MULTIFUNCTIONAL NANOMATERIALS: ROLE AND PERSPECTIVES IN COMBINATION THERAPIES AGAINST CANCER

EDITED BY: Wang Zheng, Junjie Li and Jinbing Xie
PUBLISHED IN: Frontiers in Bioengineering and Biotechnology and Frontiers in Materials

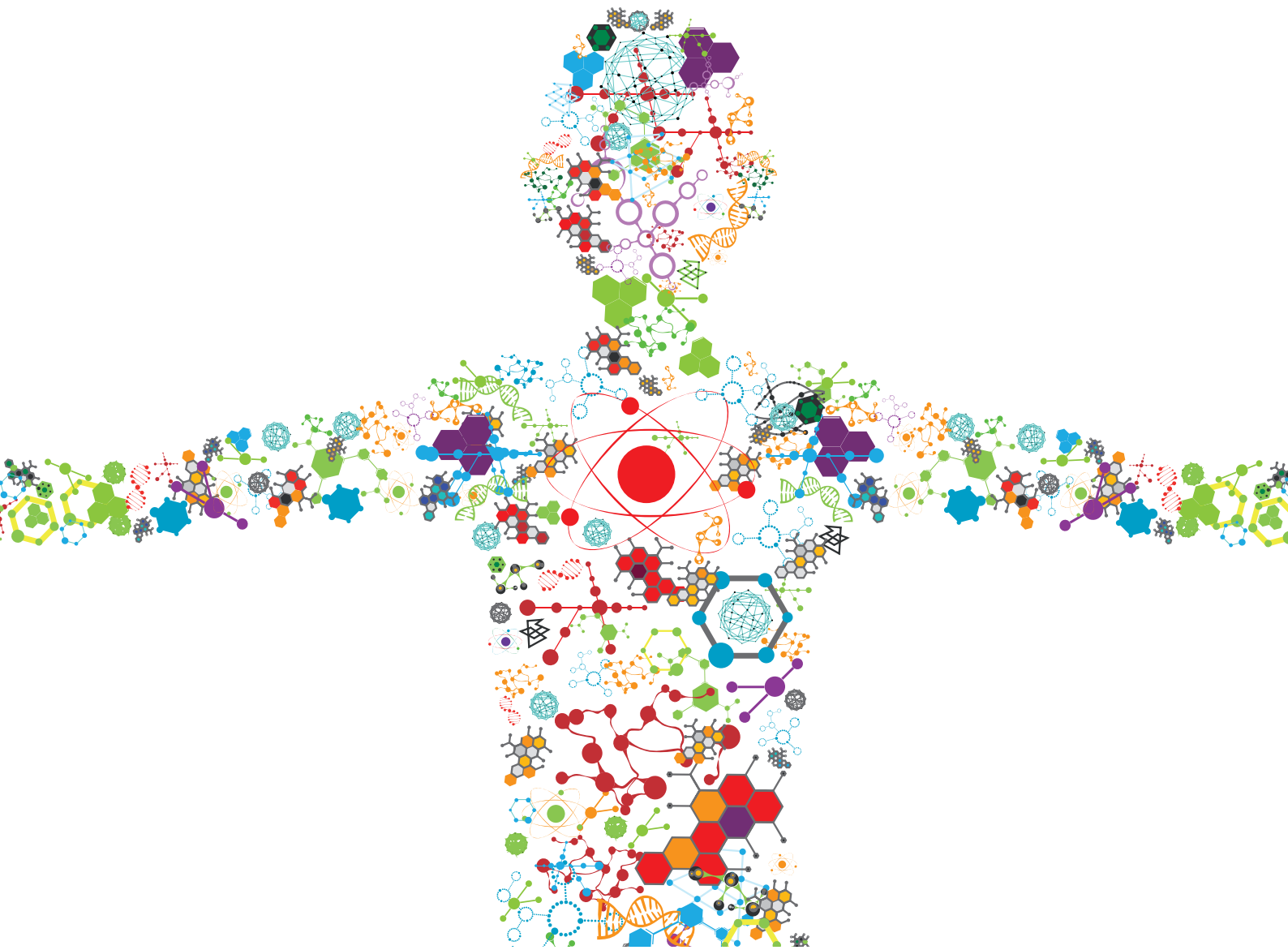

frontiers Research Topics

ISSN 1664-8714
ISBN 978-2-88976-462-4
DOI 10.3389/978-2-88976-462-4

About Frontiers

Frontiers is more than just an open-access publisher of scholarly articles: it is a pioneering approach to the world of academia, radically improving the way scholarly research is managed. The grand vision of Frontiers is a world where all people have an equal opportunity to seek, share and generate knowledge. Frontiers provides immediate and permanent online open access to all its publications, but this alone is not enough to realize our grand goals.

Frontiers Journal Series

The Frontiers Journal Series is a multi-tier and interdisciplinary set of open-access, online journals, promising a paradigm shift from the current review, selection and dissemination processes in academic publishing. All Frontiers journals are driven by researchers for researchers; therefore, they constitute a service to the scholarly community. At the same time, the Frontiers Journal Series operates on a revolutionary invention, the tiered publishing system, initially addressing specific communities of scholars, and gradually climbing up to broader public understanding, thus serving the interests of the lay society, too.

Dedication to Quality

Each Frontiers article is a landmark of the highest quality, thanks to genuinely collaborative interactions between authors and review editors, who include some of the world's best academicians. Research must be certified by peers before entering a stream of knowledge that may eventually reach the public - and shape society; therefore, Frontiers only applies the most rigorous and unbiased reviews.
Frontiers revolutionizes research publishing by freely delivering the most outstanding research, evaluated with no bias from both the academic and social point of view. By applying the most advanced information technologies, Frontiers is catapulting scholarly publishing into a new generation.

What are Frontiers Research Topics?

Frontiers Research Topics are very popular trademarks of the Frontiers Journals Series: they are collections of at least ten articles, all centered on a particular subject. With their unique mix of varied contributions from Original Research to Review Articles, Frontiers Research Topics unify the most influential researchers, the latest key findings and historical advances in a hot research area! Find out more on how to host your own Frontiers Research Topic or contribute to one as an author by contacting the Frontiers Editorial Office: frontiersin.org/about/contact

MULTIFUNCTIONAL NANOMATERIALS: ROLE AND PERSPECTIVES IN COMBINATION THERAPIES AGAINST CANCER

Topic Editors:
Wang Zheng, Suzhou Institute of Nano-tech and Nano-bionics, Chinese Academy of Sciences (CAS), China
Junjie Li, Innovation Centre of NanoMedicine (iCONM), Japan
Jinbing Xie, Southeast University, China

Citation: Zheng, W., Li, J., Xie, J., eds. (2022). Multifunctional Nanomaterials: Role and Perspectives in Combination Therapies Against Cancer.
Lausanne: Frontiers Media SA. doi: 10.3389/978-2-88976-462-4

Table of Contents

frontiers in Bioengineering and Biotechnology

REVIEW
published: 25 June 2021
doi: 10.3389/fbioe.2021.707319

Stimuli-Responsive Polymeric Nanoplatforms for Cancer Therapy

Di Chang†, Yuanyuan Ma†, Xiaoxuan Xu, Jinbing Xie and Shenghong Ju**

Jiangsu Key Laboratory of Molecular and Functional Imaging, Department of Radiology, Zhongda Hospital, Medical School of Southeast University, Nanjing, China

Polymeric nanoparticles have been widely used as carriers of drugs and bioimaging agents due to their excellent biocompatibility, biodegradability, and structural versatility. The principal application of polymeric nanoparticles in medicine is for cancer therapy, with increased tumor accumulation, precision delivery of anticancer drugs to target sites, higher solubility of pharmaceutical properties and lower systemic toxicity. Recently, the stimuli-responsive polymeric nanoplatforms attracted more and more attention because they can change their physicochemical properties responding to the stimuli conditions, such as low pH, enzyme, redox agents, hypoxia, light, temperature, magnetic field, ultrasound, and so on. Moreover, the unique properties of stimuli-responsive polymeric nanocarriers in target tissues may significantly improve the bioactivity of delivered agents for cancer treatment. This review introduces stimuli-responsive polymeric nanoparticles and their applications in tumor theranostics with the loading of chemical drugs, nucleic drugs and imaging molecules. In addition, we discuss the strategy for designing multifunctional polymeric nanocarriers and provide the perspective for the clinical applications of these stimuli-responsive polymeric nanoplatforms.

Keywords: theranostic, nanomedicine, polymeric nanoparticle, stimuli-responsive, cancer therapy

OPEN ACCESS

Edited by:
Valerio Voliani,
Italian Institute of Technology (IIT), Italy

Reviewed by:
Yonger Xue,
The Ohio State University, United States
Ling Zhi Wu,
Nanjing University of Posts and Telecommunications, China
Jing Lin,
Shenzhen University, China

****Correspondence:***
Jinbing Xie
xiejb@seu.edu.cn
Shenghong Ju
jsh0836@hotmail.com

† These authors have contributed equally to this work and share first authorship

Specialty section:
This article was submitted to Nanobiotechnology, a section of the journal Frontiers in Bioengineering and Biotechnology

Received: *09 May 2021*
Accepted: *27 May 2021*
Published: *25 June 2021*

Citation:
Chang D, Ma Y, Xu X, Xie J and Ju S (2021) Stimuli-Responsive Polymeric Nanoplatforms for Cancer Therapy. Front. Bioeng. Biotechnol. 9:707319. doi: 10.3389/fbioe.2021.707319

INTRODUCTION

Polymeric nanomaterials have gained much attention in medicine due to their unique advanced properties in cancer theranostics at the molecular level (Ren et al., 2016; Ekladious et al., 2019). Polymer molecules could be spontaneously self-assembled into nanomaterials under hydrophobic or electrostatic adsorption interactions. The polymeric nanocarriers with the loading of therapeutic drugs and imaging agents are promising to overcome the biological barriers for the theranostics of cancer (Li and Pu, 2020; Xu et al., 2021). Within these polymeric nanoplatforms, the designed smart

Abbreviations: DOX, doxorubicin; PEG, polyethylene glycol; MRI, magnetic resonance imaging; IONPs, iron oxide nanoparticles; QDs, quantum dots; AuNPs, gold nanoparticles; CT, computed tomography; CNTs, carbon nanotubes; SWCNTs, single-walled carbon nanotubes; MWCNTs, multi-walled carbon nanotubes; EPR, permeability and retention; HPMA, N-(2-Hydroxypropyl) methacrylamide; PLGA, poly (lactic co-glycolic acid); NIR, near infrared; HBPs, hyperbranched polymers; PLA, poly (lactic acid); PGA, poly glycolic acid; Gd, gadolinium; PDT, photodynamic therapy; PEI, polyethylene imine; CHT, chemotherapy; RT, radiation therapy; TME, tumor microenvironment; PEO, poly(ethylene oxide); PCL, poly(ε-caprolactone); GSH, glutathione tripeptide (γ-glutamyl-cysteinyl-glycine); ROS, reactive oxygen species; MDR, multidrug resistance; MMPs, matrix metalloproteinases; ECM, extracellular matrixes; CMD, carboxymethyl dextran; PTT, photothermal therapy; SPNpd, semiconducting polymer nanoprodrug; UCNPs, upconversion nanoparticles; QDs, quantum dots; LCST, lower critical solution temperature; UCST, upper critical solution temperature; MHT, magnetic hyperthermia; TR-cubes, thermo-responsive iron oxide nanocubes; AMF, alternating magnetic field; PLL, polymer poly-L-lysine; MPUs, multiblock polyurethanes; siRNA, small interfering RNA; NSCLC, non-small cell lung cancer.

polymeric nanocarriers responsive to the special stimuli conditions of tumor microenvironment have shown excellent effects in diagnosing and treating cancer (Montero de Espinosa et al., 2017; Wang F. et al., 2018). In particular, stimuli-responsive polymeric nanocarriers could enable the controlled release of drugs at the target sites. The distinct features of polymers to respond to the specific stimuli facilitate a high-throughput detection of molecular alterations as a result of the biological environment and allows regulation of pharmacokinetics of poorly soluble molecules, which becomes a novel trend for cancer therapy and should be engineered to realize different goals in the process of drug delivery (Li and Liu, 2014; Jiang et al., 2015). However, the multifunctional and stimuli-responsive nanocarriers also face several challenges, such as the need for better characterization, possible toxicity issues, limited absorption, and clinical transition of these nanocarrier-based delivery systems. Hence, a better understanding of the physiological environments-based stimuli of cancers and further improvement of the polymer-based nanocarrier systems are necessary for targeted therapeutic drug delivery applications. In this review, we focus on introducing stimuli-responsive polymer-based nanoplatforms and combined with imaging agents and drug/gene molecules for cancer treatment and diagnosis.

THERANOSTIC NANOMATERIALS

Overview

Theranostic nanomaterials refer to the application of nanotechnology for both diagnosis and therapy in various diseases (Jain and Stylianopoulos, 2010; Xie et al., 2010; Bobo et al., 2016). As a rapidly evolving field combining nanotechnology, biomedical and pharmaceutical sciences, the progress of multifunctional nanocarriers has shown tremendous potential for enhancing therapeutics and diagnostics, especially for cancer treatment. Several nanomaterial-based drug delivery systems have already successfully improved the therapeutic profile of conventional drugs (Caster et al., 2017). Decreased toxicity and improved therapeutic effects are obtained by utilizing nanocarriers to increase selectivity by delivering chemicals or other agents toward a specific target (**Table 1**).

Recently, the progress of stimuli-responsive nanomaterials has improved dramatically, especially in cancer treatment. The stimuli can be divided into internal and external stimuli. The internal stimuli generally include pH, redox potential, enzymes, and hypoxia (Fleige et al., 2012), while the external stimuli include light, magnetic field, ultrasound, temperature, radiation, and others (Karimi et al., 2016). The unique properties of nanomaterials enable them to respond to the stimuli, realizing different goals in diagnosing and drug delivery systems. Stimuli-responsive nanomaterials will become a new trend, and more novel nanoparticles should be engineered for treating cancers.

Theranostic Platforms

The most commonly used theranostic nanoplatforms in basic research and clinical practice are liposomes (Al-Jamal and Kostarelos, 2011; Wen et al., 2012), inorganic nanomaterials (Cabral et al., 2014; McHugh et al., 2018), and polymeric nanoparticles (Wang Z. et al., 2014; Kamaly et al., 2016), which are extensively employed theranostic nanocarriers in cancer treatment.

Liposomes (**Figure 1**) are bilayered phospholipid vesicles that can self-close to form spheres (Xing et al., 2016; Carita et al., 2018). Due to their size, biocompatibility, biodegradability, low immunogenicity and toxicity, and the encapsulating capacity for hydrophilic and hydrophobic agents, liposomes have been well applied in preclinical studies as drug and imaging agent carriers. The liposomal formulation is the first nanomedicine approved by the United States Food and Drug Administration (US FDA) for clinical application. The best application of liposomal formulation in the clinic is liposomal doxorubicin (DOX), which encapsulates DOX inside of the aqueous core and shields by polyethylene glycol (PEG) to overcome opsonization, prolong systemic drug circulation, improve therapeutic efficacy, and have been used for the treatment of Kaposi's sarcoma, ovarian cancer and multiple myeloma (Xing et al., 2016). Grange et al. evaluated the therapeutic efficiency of DOX-loaded liposomes in Kaposi's sarcoma model, and tracked the liposome tissue distribution as well as monitored drug release by *in vivo* magnetic resonance imaging (MRI) (Grange et al., 2010). Wen et al. evaluated the brain targeting theranostic liposomes loaded with quantum dots and apomorphine (Wen et al., 2012). They studied the distribution of theranostic liposomes by visualizing the fluorescence derived from quantum dots and found a significant increase in the accumulation of theranostic liposomes in the brain compared with free quantum dots.

Numerous inorganic nanomaterials have been investigated for biomedical applications because of their physical functions, such as magnetic properties of iron oxide nanoparticles, light emission of quantum dots, and optical and thermal properties of gold nanoparticles (Vigderman and Zubarev, 2013; Sharma et al., 2015; Her et al., 2017; He et al., 2021). These nanomaterials can be prepared in ultra-small sizes, susceptible to renal excretion (Prasad, 2012; Cabral et al., 2014). Currently, iron oxide nanoparticles (IONPs) (**Figure 1**) are nanocrystals made from magnetite or hematite and have been widely utilized as a T2WI contrast agent due to their T2 substantial relaxation rate effect for *in vivo* tumor MRI (Xie et al., 2010). Quantum dots (QDs) (**Figure 1**) are semiconductor nanocrystals with available diameters ranging from 2 to 10 nm. They are typically composed of Groups II-VI such as CdSe and CdTe, III–V such as InP and InAs (Prabhu and Patravale, 2012). QDs exhibit optical properties with less photobleaching, longer photoluminescence lifetime, and brighter fluorescence than other fluorophores. Gold nanoparticles (AuNPs) (**Figure 1**) are helpful for cancer diagnosis and photothermal therapy because of their optical properties (Sharma et al., 2015). They can be synthesized in different sizes and shapes such as spherical, rod-like, cage, or even irregular shapes (Vigderman and Zubarev, 2013). In addition, AuNPs can also be utilized as computed tomography (CT) contrast agents. Carbon nanotubes (CNTs) (**Figure 1**) are cylinder nanomaterials consisting of one or more graphene layers. CNTs can be single-walled (SWCNTs) with a diameter typically 0.8 to 2 nm and length ranging from less than 100 nm to several centimeters.

TABLE 1 | Representative theranostic nanomaterials utilized in drug delivery system.

Type		Size (nm)	Pros	Cons
Liposomes		80–150	♦ Biocompatibility and biodegradability ♦ Ability to deliver both the hydrophilic and hydrophobic payloads ♦ Controlled pharmacokinetics and reduced toxicity ♦ Diverse surface modification	♦ Limited loading efficiency ♦ Limited stability *in vivo* ♦ Rapid clearance from the blood
Polymers	♦ Polymer conjugate complexes ♦ Polymer nanospheres ♦ Polymer micelles ♦ Dendrimers	1–20 10–200 20–200 3–50	♦ Tunable physiochemical properties ♦ Controllable size and composition ♦ Diverse surface modification ♦ High loading efficiency and sustained release ♦ Good circulation stability	♦ Limited storage stability ♦ Potential toxicity ♦ Limited capability for hydrophilic drugs ♦ Limited chemical synthesis
Iron oxide nanoparticles		varies	♦ Clinical used MRI contrast agent ♦ Magnetic hyperthermia and PAI ♦ Easy surface modification	♦ Limited stability under aqueous conditions
Quantum dots		2–10	♦ Unique optical properties ♦ Utilization for PDT	♦ Limited biodegradability and potential toxicity
Carbon nanotubes		0.8-exceed 100 nm (diameter) less than 100 nm-several cm (length)	♦ Strong optical absorbance and utilization for PTT, PAI ♦ Unique electrical property ♦ Easy surface modification	♦ Potential toxicity ♦ Limited biodegradability
Gold nanoparticles	♦ Gold nanosphere ♦ Gold nanorod ♦ Gold nanoshell ♦ Gold nanocage	5–150 20 nm-several μm 10–400 20–200	♦ Utilization for PTT, PAI, SERS ♦ Controllable size and structure and easy surface modification ♦ Optical quenching ability	♦ Limited stability under aqueous conditions
Upconversion nanoparticles		<100	♦ Unique optical property and utilization for luminescence imaging ♦ Utilization for PDT, PTT ♦ Easy surface modification and functionalization	♦ Potential toxicity ♦ Limited biodegradability

MRI, magnetic resonance imaging; PTT, photothermal therapy; PAI, photoacoustic imaging; SERS, surface-enhanced Raman spectroscopy.

Another form of CNTs is multi-walled (MWCNTs) with a 5 to 20 nm diameter and can exceed 100 nm (De Volder et al., 2013). CNTs have thermal, mechanical and electrical properties related to their structure, stability, ease for modification and morphology (Kumar et al., 2017), thus having a potential application in Raman and photoacoustic imaging and drug delivery (Wong et al., 2013).

Polymeric nanomaterials have been widely used as carriers of drugs and bioimaging agents because of their excellent biocompatibility, biodegradability and structural versatility (Luk and Zhang, 2014; Wang Z. et al., 2014; Butowska et al., 2021). Polymers could simultaneously self-assemble into polymeric nanoparticles with encapsulating therapeutic drugs or imaging agents, thus enabling multiple functions in one nanosystem to meet the theranostic requirements. Polymeric nanomaterials such as PEG, poly(D, L-glycolic acid), and poly(D, L-lactic acid) have already been approved for clinical application (Luk and Zhang, 2014). With different nanomaterials, polymers possess different capabilities, including enhanced drug efficacy than free drugs by improved drug encapsulation and delivery, prolonged circulating half-life and triggered drug release, and so on (Wong and Choi, 2015; Luque-Michel et al., 2017). For example, by coating with PEG, they can circulate for a prolonged circulating time in the blood, avoid quick recognition and elimination by the immune system, then gradually release drugs in tumors and simultaneously facilitate tumor imaging. Polymers can still accumulate in the targeted areas of diseased tissues by either passive targeting via enhanced permeability and retention (EPR) effect or active targeting via cell surface ligands/receptors (Luk and Zhang, 2014).

Polymeric nanomaterials can also combine their unique properties with other modalities of theranostic agents, such as combined with inorganic nanomaterials to form polymer-based hybrid nanomaterials. For example, IONPs surface-modified with targeting ligands or conjugated with polymers

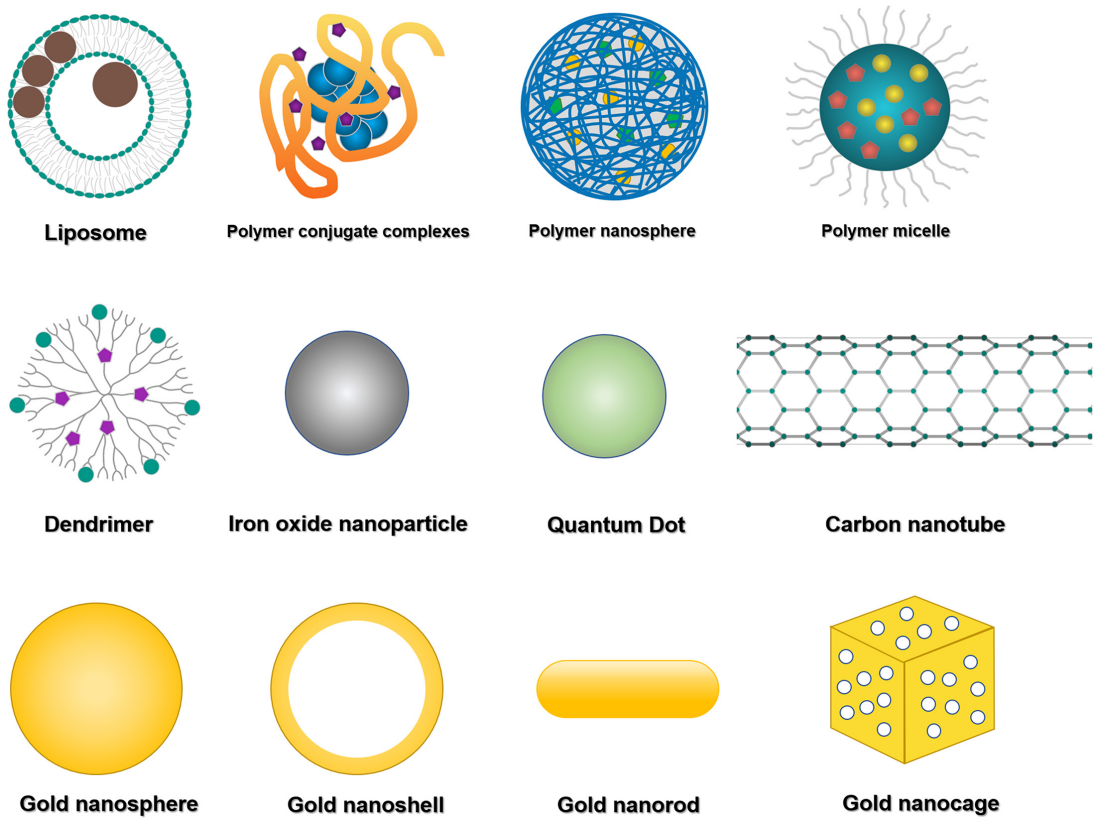

FIGURE 1 | Representative theranostic nanomaterials. The most commonly used theranostic platforms in basic research and clinical practice are liposomes, polymeric nanoparticles (mainly including polymer conjugate complexes, polymeric nanospheres, polymeric micelles, and dendritic polymers), and inorganic nanomaterials (mainly including iron oxide nanoparticles, quantum dots, carbon nanotubes, and various kinds of gold nanoparticles).

can be monitored in real-time through MRI, improving active accumulation at the lesion sites (Caldorera-Moore et al., 2011; Wang Z. et al., 2014; Sharma et al., 2017). These polymer-based nanoparticles possess a powerful theranostic vehicle in both preclinical and clinical use. So far, the distinctive properties of polymeric nanomaterials have led to their extensive research and application in cancer therapy.

More importantly, the stimuli-responsive polymeric nanoparticles attract much attention, as they can alter their physicochemical properties responding to external stimuli, such as temperature, light, enzyme, and pH changes. After stimulation, the volume, interior network permeability, or hydrophilicity-hydrophobicity of the nanoparticles are possibly changed, leading to imaging agents or drugs/genes release to generate signals for imaging or affecting cell functions. For example, pH-responsive polymeric nanoparticles could be stimulated at pH 5.7–7.0 in the solid tumor microenvironment, stable at pH 7.4 in the blood. Bae et al. synthesized pH-responsive polymeric nanoparticles using poly(L-histidine)-PEG block copolymer for cancer treatment (Prasad, 2012; Cabral et al., 2014). The hydrophobic poly histidine (PHis) was the pH-responsive moiety, which can become hydrophilic by protonation at low pH to induce drug release. These unique characteristics make polymeric nanoparticles ideal nanocarriers for tumor-targeted drug delivery.

Passive and Active Targeting of Nanomaterials

In past decades, many responsive theranostic nanomaterials have been developed to control the release and the rate of loading drugs in cancer treatment (Choi et al., 2019; Zhang et al., 2020). Theranostic nanomaterials carry therapeutic agents to the target tissues and release them to kill the diseased cells. The degree of drug delivery efficacy is highly dependent on the structures and properties of the nanomaterials. The effective localization and release rate of nanomaterials to tumor sites are mainly achieved through passive or active targeting of controlled chemicals or drugs to diseased tissues (Bertrand et al., 2014; Wang et al., 2016b,c).

Passive Targeting

Passive targeting in cancer refers to the preferential accumulation of nanoparticles to the tumor tissues. Due to the leaky tumor vasculature and impaired lymphatic drainage, and the unique microenvironment surrounding the cancer cells, theranostic nanomaterials can accumulate and be retained in tumor tissues longer than in normal tissues, which is also called EPR effect (Overchuk and Zheng, 2018; He et al., 2019; Maeda, 2021). Passive targeting is directly associated with the nanoparticles' inherent properties, including size, shape, charge, flexibility, *etc.* Nanotechnology has accelerated the

development of polymeric drugs for cancer therapy because polymeric nanomaterials can alter the physicochemical features such as size, shape and charge potential to enhance the EPR effect directly or indirectly (Maeda et al., 2009; Huang et al., 2021). The typical size of nanosystems ranges from 5 to 200 nm to avoid kidney filtration and extravasate the leaky vasculature in tumor (Dai et al., 2017). The size of nanomaterials can affect the penetration rates in solid tumors and influence the biodistribution and tumor accumulation behavior *in vivo* (Schadlich et al., 2011). In addition, the shape can also affect the properties of nanomaterials. Nanomaterials with different shape characters such as spherical, cubic, star-like have been designed in the drug delivery system, which can influence the cellular uptake and efficacy of loading drugs. The surface charge is another crucial parameter for the design and synthesis of nanomaterials. Positively charged nanomaterials show a higher affinity to cells and enhance cellular uptake due to the electrostatic interaction between negatively charged cells surface. However, positively charged nanomaterials have relatively high systemic toxicity and are more vulnerable to be cleared by the mononuclear phagocyte system, limiting their applications. In contrast, the neutral and negatively charged nanomaterials can avoid the non-specific interactions with proteins in the blood and have an extended circulation period.

Active Targeting

Active targeting is developed to enhance the accumulation of nanomaterials at the target sites in tumor tissues as a complementary strategy of passive targeting (Rosenblum et al., 2018; Ganguly et al., 2021; Wang et al., 2021). The theranostic nanomaterials modified with affinity ligands (antibodies, proteins, peptides, nucleic acids, aptamers or small molecules) could be selectively recognized by the receptors expressed on the target cells, or tissues could be delivered to the subcellular locations through an endocytosis pathway (Tanner et al., 2011; Choi et al., 2019; Mi et al., 2020). The targeting specificity and the delivering capacity are known as the two principal features in evaluating the targeting efficiency of nanomaterials (Bertrand et al., 2014). Recently, Shmidt et al. found that for nanomaterials with relatively large sizes (diameter $\geq$ 50 nm), active targeting does not significantly increase the tumor localization than non-targeted nanomaterials. However, the incorporation of targeting ligands on the surface of nanomaterials increases their cellular internalization by the target cells in the tumor, which is a prominent role of active targeting nanomaterials (Schmidt and Wittrup, 2009). Thus, active targeting has been utilized to enhance the delivery of high molecular weight molecules (macromolecules, e.g., proteins, RNA, DNA, *etc.*) to their target cells. For example, when the nanoparticles are functionalized with these targeting ligands, they can recognize the receptors on the target cells and bind via receptor-ligand interactions, whereby they are internalized through ligands-mediated endocytosis (Sahay et al., 2010). After cellular internalization, these nanoparticles trigger anticancer drugs inside the cancer cells based on biological stimuli, leading to cell death (Rosenblum et al., 2018).

POLYMERIC NANOMATERIALS

Polymeric nanoparticles are organic-based nanomaterials and have been explored widely as theranostic agents due to the plethora of benefits and significant efficacy in cancer treatment (Luk et al., 2012; Senapati et al., 2018; Zielinska et al., 2020; Mitchell et al., 2021). Various subtypes of polymeric nanomaterials have been developed to aid in drug delivery to cancerous sites, mainly including polymer conjugate complexes, polymeric micelles, polymeric nanospheres, and dendritic polymers (Luk and Zhang, 2014).

Polymer Conjugate Complexes

Conjugation of polymeric macromolecules with drugs and functional imaging agents to form polymer conjugate complexes is a new paradigm for delivering drugs and imaging agents, improving the solubility of hydrophobic molecules, prolonging their circulation time *in vivo*, and enhancing their specific accumulation in tissues (**Figure 1**). N-(2-Hydroxypropyl) methacrylamide (HPMA), poly (lactic-co-glycolic acid) (PLGA), poly (lactic acid) (PLA) and poly glycolic acid (PGA) are the commonly used polymers to synthesize nanoparticles because of their stability and biocompatibility (Prabhu and Patravale, 2012). For example, Li et al. conjugated PGA with gadolinium (Gd) and paclitaxel and imaged tumor necrosis after administration using MRI (Jackson et al., 2007); Lu et al. monitored the therapeutic efficacy of photodynamic therapy (PDT) on xenograft tumors by administration of PGA-photo-sensitizer/Gd conjugates with contrast-enhanced MRI (Vaidya et al., 2006).

Polymeric Micelles

Polymeric micelles are an essential subtype of polymeric nanoparticles, self-assembled structures with a hydrophobic core and hydrophilic exterior with an approximate size range of 20–200 nm (Zhou et al., 2018; **Figure 1**). They have been widely used in theranostic systems for cancer therapy owing to unique biocompatibility, high solubility and longer circulation time *in vivo* (when crosslinked). For instance, Wan et al. have developed a synergistic method with both photothermal therapy and chemotherapy capabilities using cyanine dye and DOX-loaded polymeric micelles in mice with lung cancer, which achieved better synergistic therapeutic efficacy compared to a single therapy (Wan et al., 2014). The micelles were triggered successfully by photo-irradiation, which caused photothermal damage to tumor cells and led to cytotoxic damage induced by DOX simultaneously. General-PM^{TM} is the best example of a clinical polymeric micellar nanoparticle for cancer therapy, which encapsulated paclitaxel in a polymeric micelle formed by monomethoxy poly(ethylene glycol)-block-poly(D, L-lactide) (Oerlemans et al., 2010; Martinelli et al., 2019). However, due to the dynamic behavior of micelles and the existence of critical micellar concentration, micelles often face challenges such as lower *in vivo* stability and poor drug loading capacity when applied in theranostic systems, which call for improved nanotechnology in optimizing the physicochemical features of micelles.

Polymeric Nanospheres

Polymeric nanospheres possess a predominantly hydrophobic feature to achieve an optimal nanosphere loading (Shim et al., 2004; Guo et al., 2015; **Figure 1**). Polymeric nanospheres could be spontaneously assembled by themselves in aqueous media with hydrophobic blocks in the core and hydrophilic blocks outside. As a result, hydrophobic drug or imaging agents could be encapsulated in the core, while hydrophilic small molecular therapeutics and macromolecules, such as proteins and nucleic acids, could be loaded corona. As different hydrophobic and hydrophilic blocks with various charges, lengths and structures, have been utilized to form polymeric nanospheres for drug and imaging agent delivery, the sizes, shapes, and stabilities of polymeric nanospheres were different. Most have relatively narrow size distributions with diameters ranging from 10 to 200 nm. Boltnarova et al. have prepared polymer nanospheres based on PLGA with low molar weight for macrophage-targeted drug delivery using both nanoprecipitation and emulsification solvent evaporation methods, which serves as a compelling, biodegradable and biocompatible drug delivery platform for macrophages (Boltnarova et al., 2021).

Dendritic Polymers

Dendritic polymers are highly branched polymers with controllable structures and many terminal functional groups (Xie et al., 2010; Rizzo et al., 2013; Ma et al., 2016; **Figure 1**). With three-dimensional architectures, various application-related properties of dendritic polymers, such as self-assembly, biodegradability, biocompatibility, and stimuli-responsiveness ability, have been adjusted and controlled through synthetic procedures. To date, progress has been made for dendritic polymers in solving fundamental and technical problems toward their theranostic applications. Ma et al. classified at least six subclasses, including dendrimers, hyperbranched polymers (HBPs), multi-arm star polymers, dendronized or dendrigraft polymers, hypergraphs or hypergrafted polymers, and dendritic-linear block polymers (Ma et al., 2016). Among them, dendrimers and hyperbranched polymers and the two major subclasses of dendritic polymers. Dendrimers are an important class of dendritic polymers known for their well-defined spherical-shaped structures, high functionality, and versatile drug delivery capabilities (Madaan et al., 2014). Dendrimers have potential abilities in entrapping and conjugating various hydrophilic/hydrophobic entities by host-guest interactions, and the high surface group functionality, tunable size and low polydispersity have made them ideal candidates for theranostic applications. For instance, Yousef et al. have successfully applied galactosamine targeted G4 polyamidoamine dendrimer to fulfill the efficient delivery of anticancer curcumin derivative for hepatocellular cellular carcinoma treatment (Yousef et al., 2018). HBP is another class of dendritic polymers with ill-defined structures and can merge multiple functionalities into a single entity (Ma et al., 2016). HBPs have unique advantages of facile one-pot fabrication (Zheng et al., 2015). Compared with other polymeric variants, the high end-group functionality and structural versatility of HBPs allow the attachment of a higher density of targeting ligands via non-covalent or covalent interactions, which can trigger stimuli-responsive drug release on the target site.

Biophysicochemical Features of Polymeric Nanomaterials

Polymeric nanomaterials can alter their physicochemical features such as size, shape and charge potential to enhance the EPR effect directly or indirectly (Maeda et al., 2009). For example, Schädlich et al. investigated the influence of size on the biodegradable polymeric nanoparticles (Schadlich et al., 2011). The nanoparticles were synthesized by polyethylene glycol-polyesters poly(lactide) block polymers (PEG-PLA) loading near-infrared (NIR)-dye which could be used to evaluate the distribution *in vivo*. Three PEG_2-PLA_{20} or PEG_2PLA_{40} (numbers in kDa) nanoparticle formulations with different and defined sizes were tested at two different xenograft tumor types, the HT29 (colorectal carcinoma) and the A2780 (ovarian carcinoma) cell lines in the research. The results showed that nanoparticles with 111 nm and 141 nm in diameter could efficiently accumulate in the tumor tissue, while the slightly larger nanoparticle whose diameter was 166 nm tended to be eliminated by the liver. Rampersaud et al. investigated the influence of shape on the drug release and anticancer efficacy of IONPs (Rampersaud et al., 2016). They used IONPs capped by dextran, a neutral and hydrophilic polymer, with a cage shape or a solid spherical shape, respectively loading riluzole, and found that the anticancer efficacy increased 3-fold in LM7 cells with the cage-shaped IONPs. The porous nature of dextran allows drugs to be released at a controlled rate, and the difference for anticancer efficacy was mainly based on the surface charge caused by different shapes of nanomaterials. The charge of riluzole-incorporated cage-shaped IONPs was more damaging than the spherical ones, leading to a longer time for riluzole to block membrane ion channels and kill more cancer cells apoptosis.

Additionally, Ramos et al. investigated the influence of cationic surface charge of the polymeric nanoparticles (Ramos et al., 2014). Polyethylene imine (PEI), a typical example of cationic polymer nanoparticles, showed increased membrane permeability with repeating units of amine groups. The positively charged nanomaterials can interact with the negatively charged gene, which could be entrapped or conjugated in the polymer nanosystem. Nevertheless, positively charged nanomaterials have some limitations, such as systemic toxicity. In contrast, neutrally and negatively charged nanomaterials have advantages in avoiding non-specific interactions and prolonging circulation time. Therefore, multiple cancer microenvironmental stimuli-responsive nanomaterials have been developed, which could alter their physicochemical features, such as reverse the surface charge and release the loading agents at the target sites to enhance drug/gene delivery (Han et al., 2012; Yuan et al., 2012; Amin et al., 2015).

STIMULI-RESPONSIVE POLYMERIC NANOPARTICLES FOR CANCER THERAPY

Cancer Therapy and Stimuli-Responsive Microenvironment

Cancer is one of the most important public health problems and the leading cause of death worldwide. Data from GLOBOCAN in the year 2020, about 19.3 million new cancer cases and 10.0 million cancer deaths lead to a considerable burden on society all over the world (Sung et al., 2021). The therapeutic methods employed globally for cancer treatment are surgery, chemotherapy (CHT), radiation therapy (RT) and immunotherapy (Luque-Michel et al., 2017). Surgery is the primary treatment modality for most solid tumors (Nguyen and Tsien, 2013). However, not all tumors can be removed via surgery due to their progression and stages, and surgical margins cannot be eradicated because of the poor differentiation from normal tissues. CHT and RT have shown their success in suppressing the proliferation and increasing the survival rate of patients, but the efficacy of CHT and RT is far from satisfactory due to the high toxicity and the damage of healthy tissues. Immunotherapy only works in a subset of cancers, and the percentage of patients who respond is low (Nguyen and Tsien, 2013; Yang, 2015). Thus, some breakthroughs should be made in the field of cancer treatment.

The tumor microenvironment (TME) is widely known as a main contributor to the development and progression of many cancers. TME in solid tumors mainly consists of immune cells, such as tumor-associated macrophages, dendritic cells, T and B lymphocytes; stromal cells such as cancer-associated fibroblasts and mesenchymal stromal cells; extracellular matrix and other secreted molecules, such as enzymes, cytokines, growth factors, *etc*. In addition, abnormal physiological environments, such as acidic extracellular pH and hypoxia, also play key roles in cancer progression, metastasis and drug resistance (Spill et al., 2016; Wang Y.A. et al., 2018; Bejarano et al., 2021; **Figure 2**). For example, the extracellular pH in tumor tissues is more acidic (5.7–6.9) than in the blood pH (7.4) at 37°C (Alfarouk et al., 2011). Compared to normal tissues, physiochemical properties in solid tumors are largely different, such as temperature is higher, oxygen partial pressure is reduced (hypoxia), and many enzymes and cytokines are overexpressed in the TME (Li et al., 2014; Chen et al., 2016; Hao et al., 2017).

Theranostic Polymeric Nanomaterials for Cancer

The field of drug delivery systems becomes popular in recent years by using synthetic polymers for drug development in cancer therapy. These polymer-based new drug entities are called "polymer therapeutics," and theranostic polymeric nanomaterials have already been utilized in numerous cancers for drug delivery (Duncan, 2003; Duncan et al., 2005; Vicent and Duncan, 2006). In general, polymer nanomedicines are designed to improve drug performance by utilizing pathophysiological characteristics of solid tumors, of which conventional low molecular weight drugs are incapable. Improved tumor-selective targeting of polymer nanomedicines and macromolecular drugs is shown due to the prolonged circulation time of these nanoparticles, leading to improved therapeutic efficacy and fewer side effects (Duncan, 2006; Greco and Vicent, 2009). Polymer-based theranostic nanomaterials can load therapeutic agents to targeted tissues or cells and regulate the release of drugs at a customized dose and time, increasing the therapeutic efficiency and reducing the side effect.

In particular, stimuli-responsive features of the polymeric nanoparticles would make an unprecedented control over the delivery and release of therapeutics at the disease site (Ke et al., 2019). Hence, developing stimuli-responsive polymeric nanoparticles that can specifically respond to TME offers promising strategies for combating cancer (Jiang et al., 2020; Qi et al., 2021). Recently, the progress of stimuli-responsive nanomaterials has improved dramatically in cancer treatment (Fleige et al., 2012; Yu J. et al., 2014; Karimi et al., 2016; Alsehli, 2020; Pham et al., 2020; Xie et al., 2020). The stimuli can be divided into internal and external stimuli. The internal stimuli generally include pH, redox potential, enzymes, hypoxia, *etc*. In contrast, the external stimuli include light, magnetic field, ultrasound, temperature, radiation, *etc*. (Karimi et al., 2016). After stimulation, the physicochemical features of the nanoparticles, such as the interior network permeability or hydrophilicity-hydrophobicity, are changed, which lead to imaging agent or drug/gene release to target sites. Thus, the following part will introduce different types of stimuli and the applications of their corresponding stimuli-responsive polymeric nanomaterials that expand the biomedical applications of theranostic nanomaterials.

Internal Stimuli

pH-Responsive Polymers

Appreciable pH variation is one of the most commonly used factors for the design of stimuli-responsive nanomaterials. Because of the abnormally fast metabolism and proliferation, a great amount of lactic acid and some end-products were produced by tumor cells, which may induce toxic effects to the adjacent tissue and an acidic pH ranging from 5.7–6.9 (Liu J. et al., 2014). Thus, many responsive polymer nanoparticles are designed to deliver drugs or genes and control release at the target sites in cancer treatment (Du et al., 2015; Kanamala et al., 2016; Li et al., 2016). For example, Chang et al. developed a polymer micelle consisting of poly[(D,L-lactide)-co-glycolide]-PEG-poly[(D,L-lactide) coglycolide] copolymer capped with N-Boc-histidine (Chang et al., 2010). Modification with N-Bochistidine enhanced the biodegradability and biocompatibility of the micelles, and DOX was loaded into micelles as an anticancer drug. Compared to pH 7.4 of normal tissues, the acidic pH microenvironment in breast cancer triggered significantly higher DOX release at pH 6.2. The pH-sensitive polymer nanoparticles released anticancer drugs with lower systemic toxicity compared with free drugs. The drugs should be released rapidly from the polymeric nanosystems under an acidic pH microenvironment in the tumor cells to

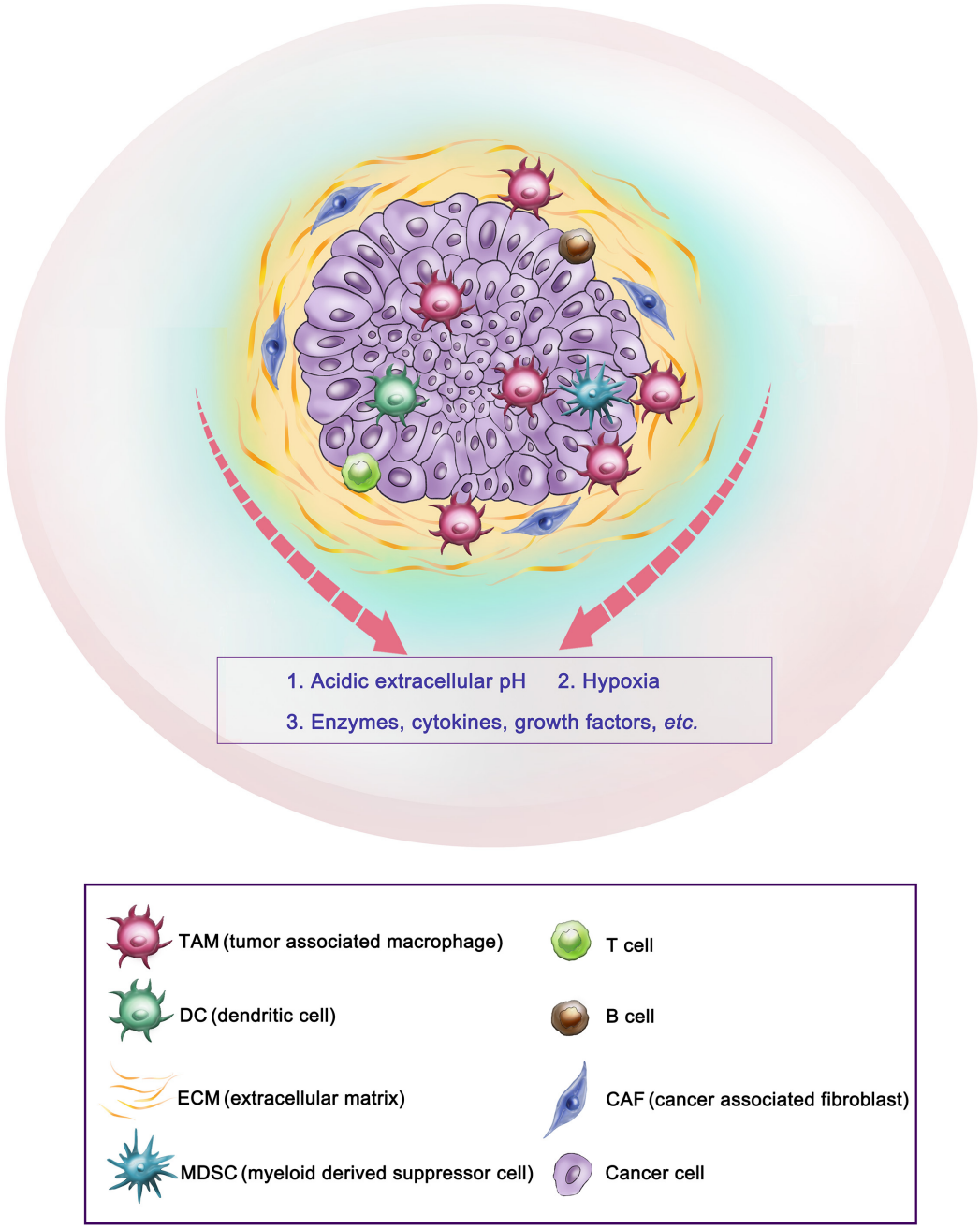

FIGURE 2 | Representative tumor microenvironment of a solid tumor. This scheme shows the representative tumor microenvironment of a solid tumor (pancreatic ductal adenocarcinoma). The tumor microenvironment in solid tumors commonly consists of tumor-associated macrophages (TAM), cancer-associated fibroblasts (CAF), extracellular matrix (ECM), *etc.*, and abnormal physiological environments such as acidic extracellular pH and hypoxia, as well as overexpressed enzymes, cytokines, *etc.*

improve the pharmacological effects of drug-loaded polymers and reduce multidrug resistance. Polymeric nanosystems that can maximize intracellular drug delivery and minimize drug release in the extracellular space are preferred. Hu et al. used PEG-cis-aconityl-chitosan-stearic acid polymeric micelles for pH-trigged DOX release, which reduced cytotoxicity due to the high internalization of the micelles into the tumor cells (Hu et al., 2012). In another study, Yu et al. designed polymeric micelles based on PbAE, altering their size and surface charge at tumor sites (Yu Y. et al., 2014). The micelles were synthesized by poly(ethylene glycol)-poly(lactide)-poly(β-amino ester) (MPEG-PLA-PAE) copolymers. In the circulation system, the micelles remained a larger size and were composed of a hydrophobic PLA/PAE core and hydrophilic PEG shell. When

the micelles were exposed to the acidic environment, the tertiary amine group in the PAE underwent protonation and switched from hydrophobic to hydrophilic, leading to a shrinking size to 20–30 nm the release of the loading drugs. This important change caused a lower diffusional hindrance in the interstitial matrix and an improved cellular uptake of the tumor tissues. Zhao et al. reported mixed micelles consisting of poly[(D, L-lactide)-co-glycolide]-PEG-folate (PLGA-PEGFOL) and poly (b-amino ester)-poly(ethylene glycol)-folate (PAE-PEG-FOL) for endosomal pH-triggered DOX release (Zhao et al., 2010). These polymer micelles also showed improved cytotoxicity, which is attributed to the specific binding of the ligands of micelles to the cell membrane, and the micelles are internalized by endocytosis. In another study, Xiong et al. reported a kind of pH-responsive polymeric micelles that could deliver siRNA and chemotherapeutic agent DOX in one system simultaneously (Xiong and Lavasanifar, 2011; **Figure 3**). A micellar system was constructed from degradable poly(ethylene oxide)-block-poly(ε-caprolactone) (PEO-b-PCL) block copolymers with functional groups on both blocks. The functional group on the PCL block was used to incorporate short polyamines for complexation with siRNA or to chemically conjugate DOX via a pH-sensitive hydrazone linkage. The DOX could be released in cancer cells via a pH-sensitive hydrazone linkage in the acid environment. With the combination of siRNA delivery, the P-glycoprotein expression could be inhibited, leading to the inhibition of P-GP-mediated DOX resistance in MDA-MB-435 tumor models. Additionally, this kind of nanocarriers could incorporate fluorescent probes in the micellar core to track the siRNA so that the theranostic goals could be achieved (Xiong and Lavasanifar, 2011). Moreover, pH alterations can modulate the imaging state of nanomaterials and trigger anticancer therapy. Ling et al. developed a new class of nanomaterials composed of self-assembled IONPs and pH-responsive ligands (Ling et al., 2014). This multifunctional system consists of a pH-sensitive polymer, which could target the cancerous tissues through surface-charge switching induced by the acidic extracellular microenvironment and extremely small IONPs that can disassemble into the cancer cells, causing a significant MR contrast effect as well as a photosensitizer with fluorescence and photodynamic therapeutic ability. Because of a lower pH in the subcellular compartments, the photosensitizers were exposed and generated the singlet oxygen to enable the photodynamic therapy to kill cancer cells selectively. These pH-responsive nanoparticles showed superior therapeutic efficacy in highly heterogeneous drug-resistant tumors (Ling et al., 2014). However, the bioavailability of these nanomaterials still requires to be improved, and the response rate to the pH stimulus must be tuned for proper applications (Liu J. et al., 2014).

Redox-Responsive Polymers

Redox potential is another property that can control the release of loading drugs in polymeric nanoparticle delivery systems (Zhang et al., 2017). Similar to the pH, a gradient of redox potential exists between healthy and cancerous tissues and intracellular and extracellular compartments, which leads to the development

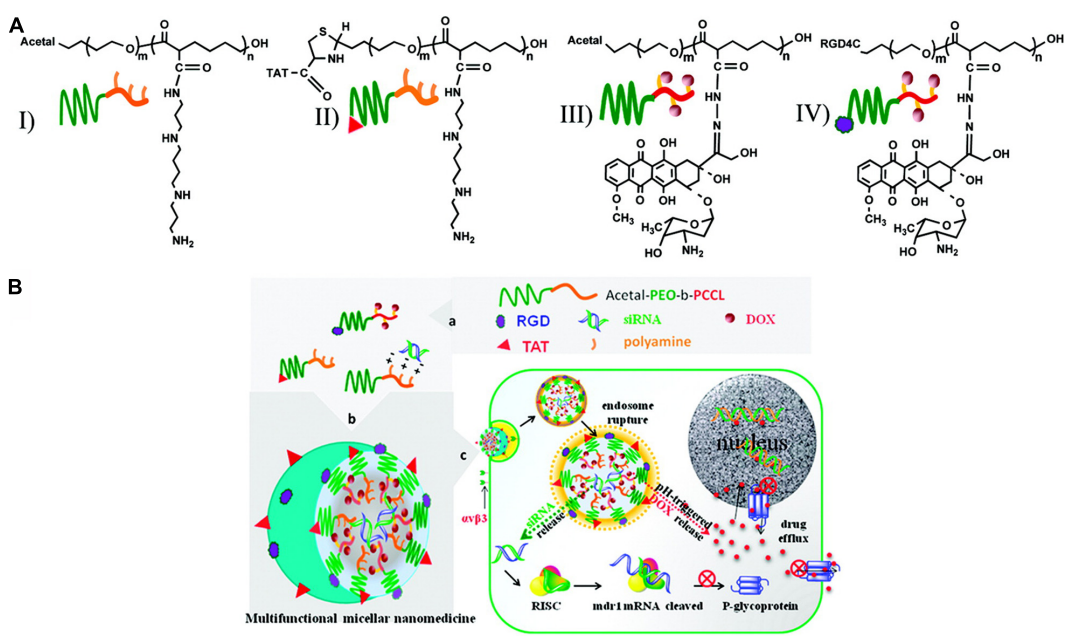

FIGURE 3 | Schematic representation of multifunctional micellar nanocarriers triggered by acidic pH. **(A)** Schematic illustration of acetal- and TAT-PEO-bP(CL-g-SP) (I and II) and acetal- and RGD4C-PEO-bP(CL-Hyd- DOX) (III and IV). **(B)** Rational design of a multifunctional micellar nanomedicine for cancer-targeted co-delivery of MDR-1 siRNA and DOX to overcome multidrug resistance. DOX release from NON-micelles triggered by acidic pH. Reprinted from Xiao-Bing Xiong and Afsaneh Lavasanifar. Traceable Multifunctional Micellar Nanocarriers for Cancer-Targeted Co-delivery of MDR-1 siRNA and Doxorubicin. ACS Nano. 2011;5(6):5202–13. With the permission of ACS publications/from reference (Xiong and Lavasanifar, 2011). MDR, multidrug resistance; PEO, poly(ethylene oxide); RGD, Arg-GLT-Asp (the integrin αvβ3-specific ligand); DOX, doxorubicin; TAT, trans-activating transcriptional activator.

of redox-responsive nanomaterials (Han et al., 2017). For example, the level of glutathione tripeptide(γ-glutamyl-cysteinyl-glycine) (GSH) in tumor tissues is at least four times higher than that in normal tissues (Karimi et al., 2016; Thambi et al., 2016). In addition, the intracellular concentration (2–10 mM) of GSH is about 100–1000 times higher than that in extracellular compartments (2–10 μM) (Han et al., 2017). Therefore, many redox-responsive nanomaterials have been developed with the ability to trigger the release of therapeutic agents. Wang et al. developed an amphiphilic polyanhydride copolymer containing disulfide bonds between the hydrophilic and hydrophobic segments (Wang J. et al., 2014). The copolymer can self-assemble into stable micelles with well-defined core-shell structure, and GSH triggered the disassembly behaviors of the micelles. These micelles showed excellent efficiency in inhibiting the growth of cancer cells in 4T1 tumor-bearing BALB/c mice due to the rapidly intracellular delivery of therapeutic agents. Quantitative analysis revealed that the redox-responsive micelles had enhanced therapeutic effects in solid tumors compared with the redox-insensitive micelles. In addition, redox-sensitive prodrug polymeric nanoparticles exhibit a unique advantage in overcoming multidrug resistance (MDR) and improving the overall therapeutic efficiency of anticancer drugs in cancer treatment. Liu et al. developed a redox-responsive DOX prodrug by conjugating DOX to DEX-PEI polymers via disulfide linkers (Liu et al., 2013). The prodrug self-assembled into polymeric micelles with an average size of 100–140 nm and exhibited a rapid drug release rate under the intracellular reduction environment (10 mM DTT). In the absence of DTT, a minimal amount of DOX was released within 48 h; however, around 50% of DOX was released within 4 h in 10 mM DTT. Additionally, the redox-responsive prodrug micelles enhanced the cellular accumulation of the DOX and achieved endosomal escape in human breast cancer multidrug-resistant cells (MCF-7/ADR) compared to free DOX. In another study, Han et al. developed self-assembled redox-responsive polymeric nanoparticles based on hyaluronic acid (HA)-polycaprolactone (PCL) block copolymer as drug carriers for cancer therapy (Han et al., 2015). The HA shell was crosslinked via a disulfide linkage. The anticancer drug DOX was efficiently encapsulated into the nanoparticles with a high drug loading rate. The DOX-loaded HA nanoparticles significantly retarded the drug release under physiological conditions (pH 7.4). The drug release rate showed a marked increase in the existence of GSH bonds in the cytoplasm. Improved antitumor efficacy was investigated using such tumor-targeted crosslinked polymeric nanoparticles than non-cross-linked nanoparticles and free chemotherapeutic drugs. In addition, Chiang et al. generated the dual redox-responsive micelles for selective cytotoxicity of cancer (Chiang et al., 2015; **Figure 4**). This kind of micelles could release the anticancer drug camptothecin in the cancer cells after the explosion of reactive oxygen species (ROS) and GSH. ROS is another essential factor in controlling the balance of redox in cancer cells, and the concentration in tumor tissues is about 100 times higher than that in normal cells because of the oncogene stimulation, mitochondrial malfunction and chronic inflammation. The ROS-responsive diethyl sulfide of the micelles could cause a swollen effect, and the GSH-responsive disulfide-containing cystamine further promoted the process of copolymer fragmentation, which led to the release of drugs in cancer cells. Redox-responsive polymeric nanoparticles can also be used for effective gene delivery. Jia et al. synthesized the chitosan oligosaccharide-based disulfide-containing polyethyleneimine derivative PEG-ss-COS-ss-PEI as a non-viral gene delivery carrier (Jia et al., 2013). The achieved PEG-ss-COS-ss-PEI copolymers could effectively condense DNA into small particles with an average diameter smaller than 120 nm. In the existence of 10 mM GSH, polyplexes of PEG-ss-COS-ss-PEI were rapidly unpacked, as revealed by a significant increase of particle sizes to over 800 nm. The PEG-ss-COS-ss-PEI copolymers had much lower cytotoxicity and displayed high transfection efficiency than the control branch, indicating that a redox-responsive copolymer composed of low molecular weight PEI, chitosan oligosaccharide and PEG via disulfide-containing linkages can be a useful gene delivery nanocarrier.

Enzymes-Responsive Polymers

Enzymes serve various functions in all biological and metabolic processes and exhibit abnormal expression levels in many disease-associated microenvironments, especially cancer (Mu et al., 2018). Compared with other stimuli, most enzymic reactions are fast and efficient, and the reaction conditions are moderate. Additionally, most enzyme-responsive nanomaterials, based on polymers, liposomes, small organic molecules, and inorganic/organic hybrid materials, can be triggered with higher specificity, and biocompatibility is beneficial for clinical translation (Mu et al., 2018). So far, several classes of enzymes such as proteases and phosphatases have been regarded as biomarkers for diagnosis and treatment, and many of them have been exploited to generate stimuli-responsive nanomaterials for diagnosis, imaging and drug delivery (He et al., 2016). Among all those enzymes, matrix metalloproteinases (MMPs) are the most well-established ones utilized as stimuli in the enzyme-responsive systems, especially cancer theranostics. MMPs are zinc-dependent endopeptidases responsible for the degradation of extracellular matrixes (ECM) proteins and the modulation of bioactive molecules on the cell surface (Khokha et al., 2013). In cancerous tissue, their expression is much higher than that in normal tissue. They could promote tumor metastases and invasion because of the ability to degrade connective tissue between cells and blood vessels lining, facilitating tumor cells to escape from their original location (Vandenbroucke and Libert, 2014). According to the expression level difference, MMPs have served as triggers, and various nanomaterials have been developed for different purposes (Ansari et al., 2014; Gallo et al., 2014; Wang H.X. et al., 2014; Callmann et al., 2015). For example, Chien et al. developed an enzyme-responsive polymer composed of a hydrophobic backbone and a hydrophilic MMP-responsive peptide (Chien et al., 2013). To date, MMP2 and MMP9 are the most widely explored enzymes for enzyme-responsive drug delivery. Zhu et al. reported a tumor-targeted micellar drug delivery platform prepared by self-assembly of the block copolymers of MMP2-sensitive PEG2000-PTX conjugate, transactivating transcriptional activator peptide-PEG1000-phosphoethanolamine (PE), and PEG1000-PE,

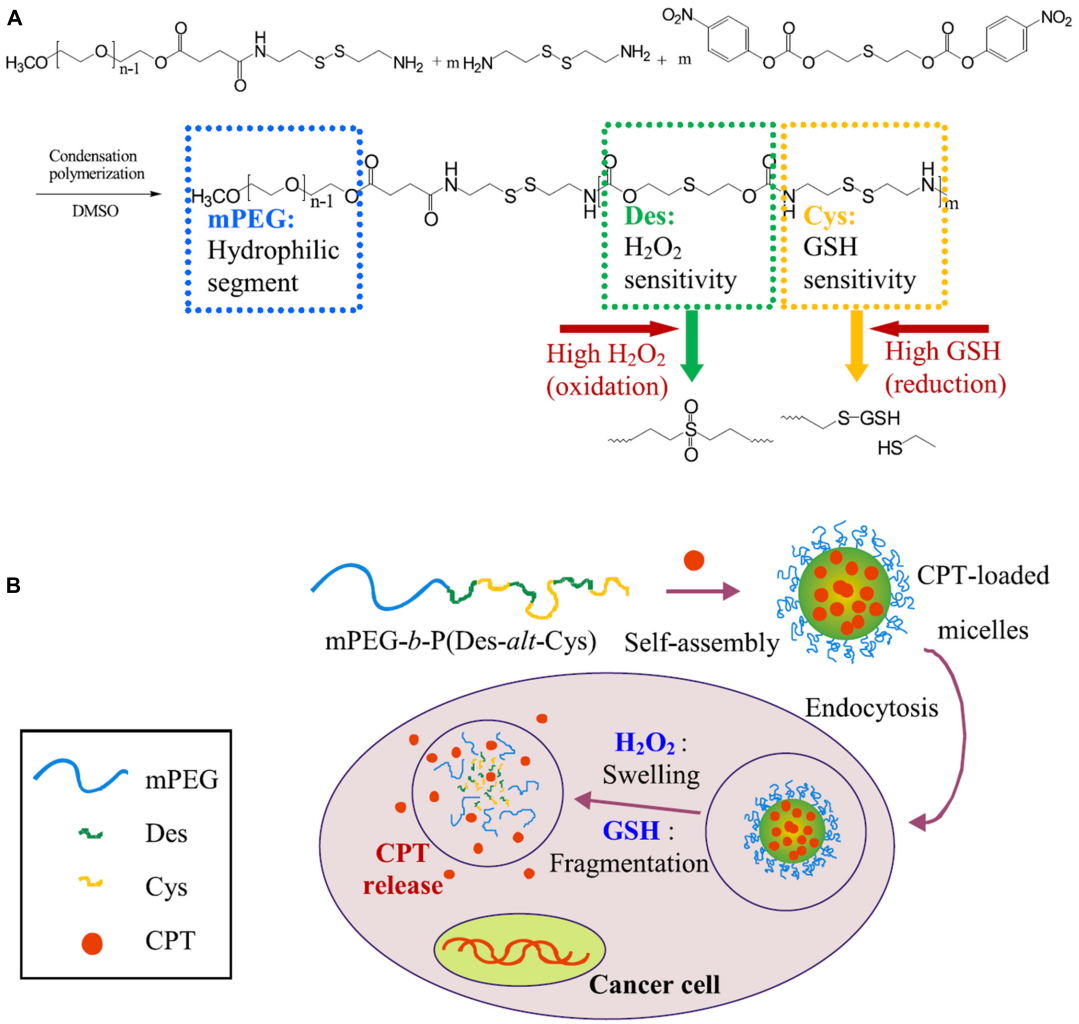

FIGURE 4 | Schematic illustration of dual redox-responsive micelles. **(A)** Chemical structure of mPEG-b-P(Des-alt-Cys) copolymer and **(B)** dual redox-responsive micelles and CPT release triggered by ROS and GSH. The dual redox-responsive micelles enter into cancer cells and exhibited high levels of ROS and GSH, then the structures of micelles are deformed, and the encapsulated CPT could be liberated from micelles, leading to selectively location-controlled drug release. Reprinted from Yi-Ting Chiang, Yu-Wei Yen, and Chun-Liang Lo. Reactive oxygen species and glutathione dual redox-responsive micelles for selective cytotoxicity of cancer. Biomaterials. 2015;61:150–61. With permission from reference (Chiang et al., 2015). PEG, poly(ethylene glycol); Des, diethyl sulfide; Cys, cystamine; CPT, camptothecin; ROS, reactive oxygen species; GSH, glutathione.

acting as MMP2-sensitive functional polymer, cell-penetrating enhancer, and nanocarrier building block, respectively (Zhu et al., 2013). Compared to non-sensitive counterparts, this MMP2 sensitivity of PEG2000-peptide-PTX micelle showed superior cell internalization, cytotoxicity, tumor targeting, and antitumor efficacy, which is promising for effective intracellular drug delivery in cancer therapy. Furthermore, Zhu et al. recently designed another MMP2-sensitive multifunctional polymeric micelle for tumor-targeting co-delivery of siRNA and hydrophobic drugs (Zhu et al., 2014). This micellar nanoplatform was constructed by an MMP2-sensitive copolymer (PEG-pp-PEI-PE) via self-assembly, which displayed exceptional stability, efficient siRNA condensation by PEI, PTX solubilization in the lipid core, and tumor targeting via both the EPR effect and MMP2 sensitivity. Several enzymes can be used as markers to monitor anticancer efficacy. Kulkarni et al. used caspases-3–cleavable sequence as an enzyme reporter element consisting of L-amino acids GKDEVDAPC-CONH2 (Kulkarni A. et al., 2016; **Figure 5**). The effector element is conjugated to the polymeric backbone via an esterase-cleavable bond, whereas the reporter element is conjugated via an amide bond with the Gly residue. In general, the reporter nanoparticles are engineered from a novel two-staged stimuli-responsive polymeric material with an optimal ratio of an enzyme-cleavable drug or immunotherapy (effector elements) and a drug function-activatable reporter element. In a drug-sensitive cell, the loading drug was released due to initiated apoptosis through the activation of the caspase-3 enzyme, which then cleaved the specific peptide, leading to a positive fluorescent signal. However, in a non-responder cell, the process of apoptosis could not be initiated, and the fluorescent

signal was silent. This distinction allowed the nanoparticles to monitor the efficacy of treatment and evaluated the tumor resistance to specific anticancer drugs (Kulkarni A. et al., 2016). Although enzyme-responsive polymeric nanomaterials have gained rapid progress and show great therapeutic and diagnostic potentials, especially for cancer at both pre- and clinical levels, challenges remain to be conquered. Different cancers and different stages make the modulation of enzymes difficult. Thus, more effective designing strategies are in need to make the polymeric nanomaterials more precise (Hu et al., 2014; Chandrawati, 2016).

Hypoxia-Responsive Polymers

Hypoxia is a specific microenvironment involved in the pathogenesis of cancer. Hypoxia-associated pathological state with insufficient oxygen plays an essential role in metastasis and chemotherapy resistance in various kinds of cancers, which provide an opportunity for cancer-specific drug delivery using reduced oxygen partial pressure as a trigger (Brown and Wilson, 2004; Rao et al., 2018). Hydrophobic nitroimidazole is a well-known hypoxia-responsive electron acceptor which can convert into hydrophilic 2-aminoimidazole under hypoxia condition, resulting in the delivery of the loaded DOX from the nanocarrier system to the microenvironment (Uthaman et al., 2018). Thambi et al. developed hypoxia-responsive polymers composed of a 2-nitroimidazole derivative and the backbone of a carboxymethyl dextran (CMD), selectively release drugs under hypoxic conditions (Thambi et al., 2014; **Figure 6**). The anticancer drug DOX was encapsulated in the polymeric nanoparticles, released at a markedly elevated rate under hypoxic conditions

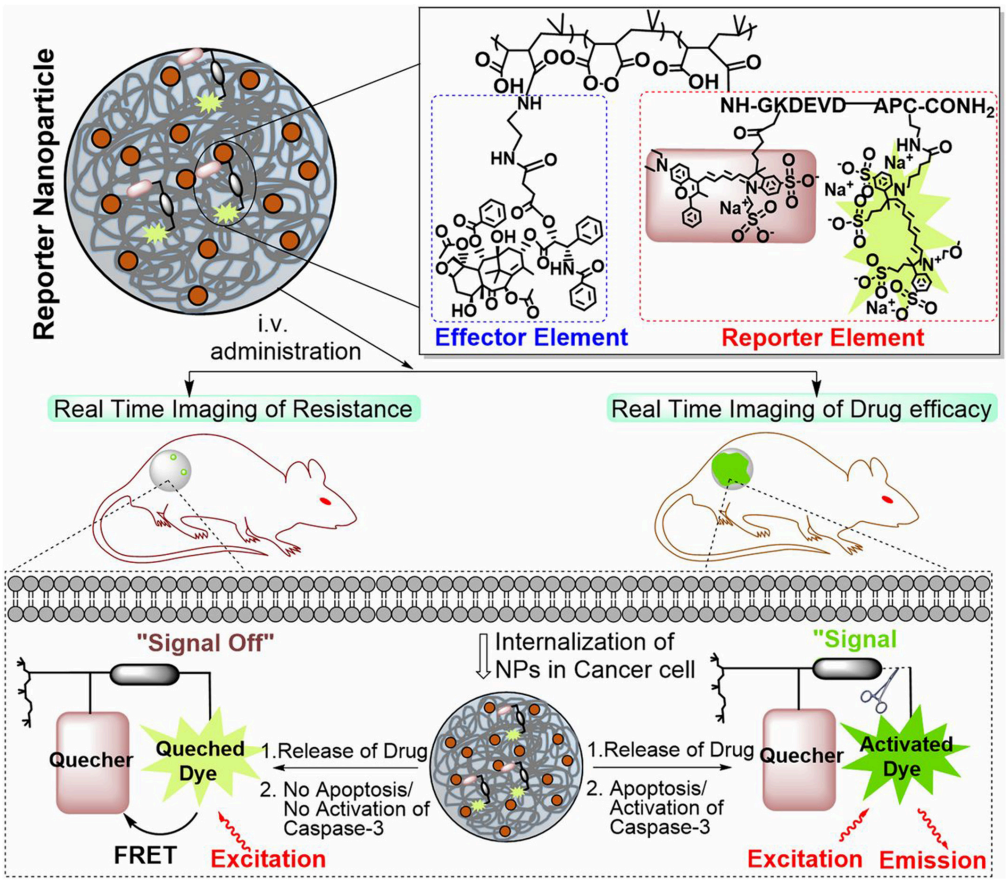

FIGURE 5 | Schematic illustration of the construct of a caspase-3 enzyme-responsive nanoparticle. The reporter nanoparticle comprises three components: a polymeric backbone, an esterase-cleavable prodrug synthesized from an anticancer drug [effector element (EE)], and an activatable reporter element (RE). At the optimal ratio of EE: RE, this stimuli-responsive polymer self-assembles into a nanoparticle. The reporter element is a caspase-3–cleavable sequence consisting of L-amino acids GKDEVDAPC-CONH2, to which we conjugated a FRET pair such that cleavage of the DEVD sequence results in removal of the quenching of the fluorescent signal. The effector element is conjugated to the polymeric backbone via an esterasecleavable bond, whereas the reporter element is conjugated via an amide bond with the Gly residue. In normal conditions, the fluorescent signal from the reporter element is in the off-state because the drug is intact inside the nanoparticle. In a drug-sensitive cell (lower right of the schematic), the released drug initiates apoptosis via the activation of the caspase-3 enzyme, which then cleaves the DEVD peptide, unquenching the fluorescent signal (on the state). However, in a non-responder cell (lower left), the failure of the released drug to induce apoptosis means the reporter element remains in the off state. Reprinted from Ashish Kulkarni, Poornima Rao, Siva Natarajan, et al. Reporter nanoparticle monitors its anticancer efficacy in real-time. Proc Natl Acad Sci U S A. 2016;113(15): E2104–13. With permission from reference (Kulkarni A. et al., 2016). FRET, Förster resonance energy transfer; DEVD, Asp-Glu-Val-Asp.

compared with normoxic conditions. In another report, He et al. designed fabrication of dual-sensitive nanoparticles with hypoxia and photo-triggered release of the drug DOX. Dual stimuli nanoparticles were developed through the self-assembly of polyethyleneimine-nitroimidazole micelles (PEI-NI), further co-assembled with Ce6-linked hyaluronic acid (HC), and nitroimidazole was incorporated in the micelles as a hypoxia-responsive electron acceptor that converted to hydrophilic 2-aminoimidazole under hypoxic conditions (He et al., 2018). The Azobenzene group is another hypoxia-sensitive moiety. Kulkarni et al. reported self-assembled polymersomes consisting of poly(lactic acid)–azobenzene–poly(ethylene glycol) and anticancer drugs gemcitabine and erlotinib (Kulkarni P. et al., 2016). This polymeric nanoparticle released the encapsulated anticancer drugs to the pancreatic cancer cells under hypoxic conditions. Biomacromolecules such as siRNA can also be delivered selectively to tumor sites by hypoxia-responsive polymeric nanoparticles. Perche et al. reported hypoxia-induced siRNA delivery using a polymer nanocarrier consisting of PEG, azobenzene, polyethyleneimine, and phospholipid (Perche et al., 2014). The siRNA polymer nanocarriers can be activated to disassemble in oxygen-deprived microenvironments by introducing an azobenzene group between PEG and PEI polymer segments. In the hypoxic environment, the azobenzene bond of the nanoparticles cleaved and deshielded the PEG coating. The responsive polymer nanoparticles with siRNA loading induced efficient gene silencing that mimic the hypoxic tumor microenvironment, representing an ideal hypoxia-responsive nanocarrier for cancer therapy. Although hypoxia-responsive nanoparticles have unique advantages in cancer therapy, it is challenging to deliver polymeric nanoparticles to hypoxic areas because they are commonly far from the vasculatures. Hence, the diffusion rate of the nanoparticles is sometimes insufficient. Thus, polymeric nanocarriers which can release hypoxia-responsive prodrugs to the hypoxic areas should be a better option due to the higher diffusion rates of small molecules.

Other Internal Stimuli

In addition to the internal stimuli mentioned above, there are still some other internal ones, such as adenosine triphosphate (ATP) (Lai et al., 2015; Saravanakumar et al., 2017). To conclude, the internal stimuli can increase the accumulation of polymer-based nanoparticles and facilitate drug delivery in targeting tissues because of the changes in pathophysiological properties.

External Stimuli

Light-Triggered Polymers

Among all external stimuli, light is the most commonly exploited one due to the ease of control and utilization (Zhang et al., 2019). The light-responsive polymeric nanomaterials have been widely applied for cancer therapy, mainly photothermal therapy (PTT) and photodynamic therapy (PDT). PTT refers to the use the light-sensitive materials that can convert the light energy to heat to increase the temperature and trigger the death of the surrounding

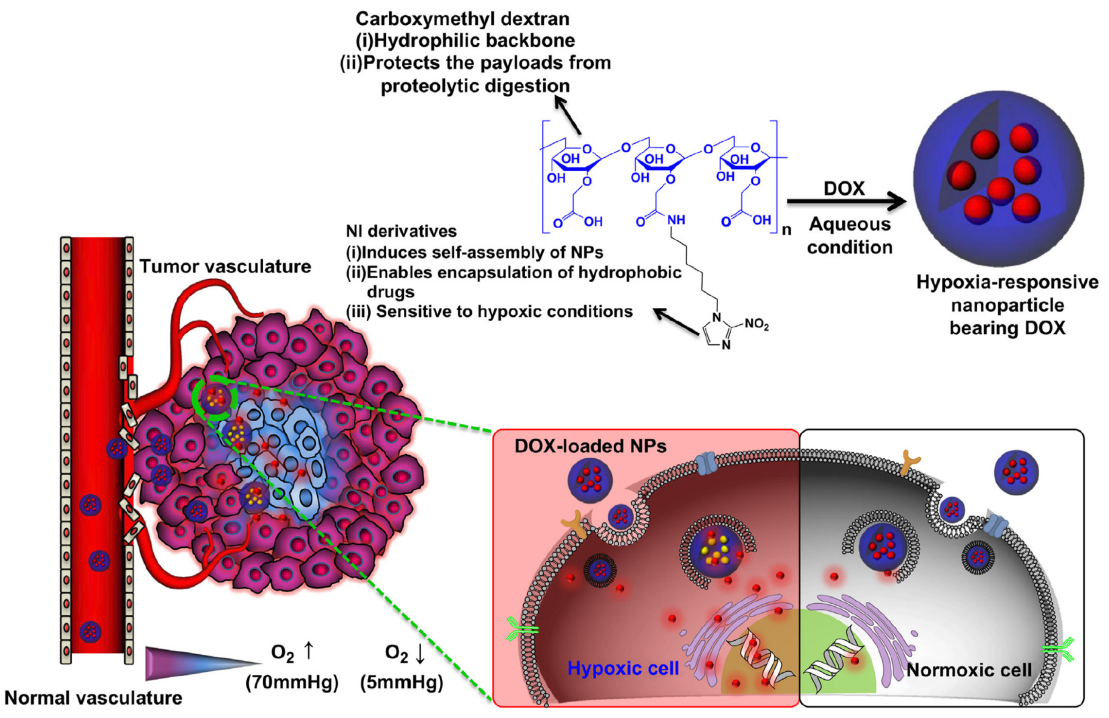

FIGURE 6 | Schematic illustration of a drug-loaded hypoxia-responsive polymer nanoparticle. The hypoxia-responsive polymers can reach the tumor site via the EPR effect, followed by intracellular drug release at hypoxic tissue. Reprinted from Thavasyappan Thambi, V.G. Deepagan, Hong Yeol Yoon, et al. Hypoxia-responsive polymeric nanoparticles for tumor-targeted drug delivery. Biomaterials. 2014;35(5):1735–43. With permission from reference (Thambi et al., 2014). NPs, nanoparticles; EPR, enhanced permeation and retention; DOX, doxorubicin.

cancer cells (Kim et al., 2016; Liu et al., 2019). Compared with other therapies, PTT allows the precise dosage of external irradiation to diminish the side-effect of the surrounding tissues. Furthermore, studies have shown that PTT is highly effective for various cancer and has multiple functions in treatment (Liu et al., 2019). PTT can combine with other therapies such as surgery (Wang S. et al., 2018), chemotherapy (Liu T. et al., 2014), radiotherapy (Yong et al., 2015), immunotherapy (Wang C. et al., 2014) to improve the overall treatment results and benefit from the outcomes or effects. So far, many nanomaterials such as semiconducting polymers have been explored for PTT, and some of them have been under clinical investigation for tumors such as head and neck cancers and primary/metastatic lung cancers (Shi et al., 2017; Liu et al., 2019). For example, Cao et al. reported a light-breakable amphiphilic block copolymer micelle with a NIR dye cypionate (Ex/Em: 780/808 nm) encapsulated into the hydrophobic core (Cao et al., 2013). A dual NIR emission induced a faster photocleavage reaction when irradiated by NIR light (765 nm), which facilitated the faster dissociation of the micelles under NIR illumination ablate the tumor tissues *in vivo* through PTT. Bagheri et al. developed an *in situ*, one-pot polymerization-induced self-assembly method to synthesize light-responsive pyrene-containing nanoparticles (Bagheri et al., 2019). Cleavage of the pyrene moieties triggered a hydrophobic-to-hydrophilic transition of the core-forming block and the dissociation of the nanoparticles, and PTT triggered the therapeutic compounds to release into the tumor. PDT is another important application for light-responsive nanomaterials and has emerged as a precise treatment modality. It utilizes the photosensitizers, which can be activated by the light of a certain wavelength, to generate cytotoxic ROS that can oxidize key cellular macromolecules and induce tumor cell ablation (Lucky et al., 2015). Nanoparticles utilized in PDT can serve as the carriers of photosensitizers or the energy transducers themselves. Polymers capable of encapsulating the photosensitizers can target the tumor sites and release the payloads to generate ROS (Synatschke et al., 2014). Similar to PTT, PDT also can combine with other therapies or improve the overall outcomes (Yu et al., 2015; Wang et al., 2016a, 2017). For example, Cui and co-workers synthesized a semiconducting polymer nanoprodrug (SPNpd) that can specifically release the chemo drugs under a photoirradiation-promoted hypoxic environment to exert synergetic PDT and chemotherapy (Cui et al., 2019; **Figure 7**). SPNpd is self-assembled from an amphiphilic polymer brush comprising a light-responsive photodynamic backbone grafted with PEG and conjugated with the chemodrug molecules via hypoxia-cleavable linkers. SPNpd (30 nm) enabled effective accumulation to the target site of breast cancer xenograft and possessed a synergistic photodynamic efficacy and chemotherapy, which acted as a promising photoirradiation-promoted and hypoxia-responsive polymeric nanoprodrug system for cancer therapy.

Light responsive polymeric nanomaterials can also be used for photo-triggered drug release when illuminated by external light. The mechanisms generally include photo-induced chemical effects, decreased hydrophobicity, and photothermal effect (Shim et al., 2017; Son et al., 2019). These strategies allow the nanomaterials to release therapeutic agents at the target sites upon the external light. For example, Cao et al. developed the biocompatible diblock copolymer micelles for controlled drug delivery. Upon the NIR irradiation, the NIR-sensitive hydrophobic core could increase the polarity and destabilize the micelles, leading to a shifted hydrophilic–hydrophobic balance which could control the release of loading drugs (Cao et al., 2016). Bagheri et al. developed a drug delivery system using NIR light and upconversion nanoparticles (UCNPs), emphasizing the use of photo-responsive compounds and polymeric materials

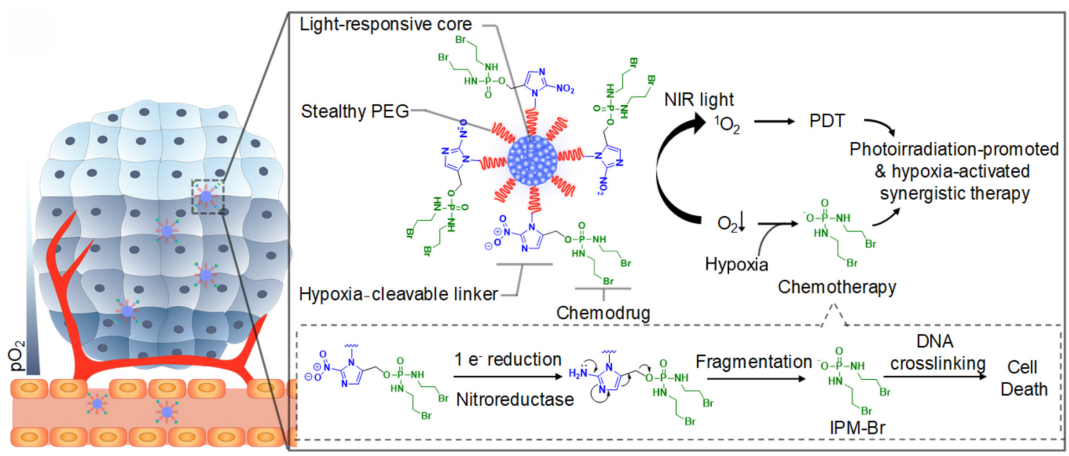

FIGURE 7 | Schematic illustration of the light-responsive SPNpd for synergistic cancer therapy. The nano-prodrug is assembled from an amphiphilic semiconducting brush polymer grafted with chemo drug side chains through a hypoxia-cleavable linker. It has three critical units: the light-responsive photodynamic SPN core, hypoxia-cleavable linker and the chemotherapeutic drug, a bromoisophosphoramide mustard intermediate (IPM-Br). Upon the photoirradiation at 808 nm, this organic photodynamic nano-prodrug (SPNpd) can specifically release the chemodrug under photoirradiation-promoted hypoxia tumor microenvironment to exert synergetic PDT and chemotherapy. Reprinted from Dong Cui, Jiaguo Huang, Xu Zhen, et al. Semiconducting Polymer Nano-prodrug for Hypoxia-activated Synergetic Photodynamic Cancer therapy. Angew Chem Int Ed Engl 2019;58(18):5920–24. With permission from reference (Cui et al., 2019). SPNpd, semiconducting polymer nanoprodrug; SPN, semiconducting polymer nanoparticle; PDT, photodynamic therapy.

conjugated onto UCNPs. This drug delivery system can be activated by low-intensity NIR illumination; thus, it is highly desirable to avoid exposing living tissues to excessive heat and reduce the *in vivo* application of this polymeric nanomaterials (Bagheri et al., 2016).

Temperature-Responsive Polymers

Temperature is another commonly utilized external stimulus to trigger the thermo-sensitive nanomaterials to release the loading agents. The temperature-responsive polymers can respond to the temperature changes and switch their structure or the aqueous solubility. Thus, the encapsulated drugs could be released at the target tissues (Karimi et al., 2016). The polymer undergoes a reversible change of phase at the specific temperature, called lower critical solution temperature (LCST) or upper critical solution temperature (UCST). The therapeutic agents can be easily encapsulated into the polymers at LCST and released at the targeting sites upon the external temperature changes (Bikram and West, 2008). Poly(N-isopropyl acrylamide) (PNIPAM) and its derivatives have been widely investigated because of the attractive LCST, which is close to the physiological temperature of the human body. The LCST of PNIPAM is around 32°C, and by coupling other materials (e.g., polymers, liposomes, proteins), the LCST could be optimized to control the drug release (Bikram and West, 2008; Karimi et al., 2016). For example, Kakwere et al. developed the nanohybrids by incorporating cubic-IONPs within a thermo-responsive polymer shell composed of PNIPAM/PEGA. The LCST of these nanohybrids was about 37°C. The phase transition may occur, leading to the release of the loading drugs upon the temperature changes (Kakwere et al., 2015). In another study, Neradovic et al. developed block copolymers of PEG as a hydrophilic block and poly(N-isopropyl acrylamide) (PNIPAAm) or poly(NIPAAm-co-N-(2-hydroxypropyl) methacrylamide-dilactate) [poly(NIPAAm-co-HPMAm-dilactate)] as the thermosensitive block that could self-assemble into nanoparticles (Neradovic et al., 2004). These copolymers formed a novel type of thermosensitive micelle, and the micelles were destabilized to release their cargo at temperatures above the LCST of 37°C with a triggered drug release profile. Qin et al. used poly(ethylene oxide)-block-poly(N-isopropyl acrylamide) (PEO-bpNIPAm) block copolymers to generate polymer micelles which became amphiphilic in water above 37°C and self-assemble into micelles encapsulating both hydrophilic and hydrophobic molecules (Qin et al., 2006). When the temperature is decreased, however, the micelles disassemble and release the molecules triggered by temperature. In addition, temperature-responsive polymeric nanoplatforms can also be used to combine externally heat-triggered treatment and localized chemotherapy under magnetic hyperthermia (MHT) conditions and may target heat more specifically and boost the drug release on demand. Mai and co-workers have engineered magnetic thermo-responsive iron oxide nanocubes (TR-cubes) to merge MH treatment with heat-mediated drug delivery (Mai et al., 2019). IONPs with a cubic shape showed remarkable heat performance under MHT conditions, and these TR-cubes can carry chemotherapeutic doxorubicin (DOX-loaded-TR-cubes) without compromising their thermo-responsiveness. A uniform and thick polymer shell on each nanocube enabled the thermo-responsive polymer nanosystem to combine MH and heat-mediated drug delivery, making the dual MH/heat-mediated chemotherapy possible. Furthermore, the temperature-responsive polymeric nanocarriers are also effective for delivery of genes. For example, Hamner et al. used a DNA-capped thermosensitive copolymer for chemotherapy drug DOX delivery (Hamner et al., 2013; **Figure 8**). They synthesized a thermoresponsive pNIPAAm-co-pAAm polymer to regulate DNA interactions in both a DNA-mediated assembly system and a DNA-encoded drug delivery system. The temperature-responsive behavior of the polymer regulated the accessibility of the sequence-specific hybridization between complementary DNA-functionalized gold nanoparticles, with a transition temperature (T_C) of 51°C. The LCST smart polymer was shown to decrease drug release kinetics and equilibrium at $T < T_C$, but increase release at $T > T_C$, thus allowing for a successful improvement of the drug delivery. In another study, Li et al. reported a rod-shaped ternary polyplex micelle via complexation between the mixed block copolymers of PEG-b-poly [PEG-b-PAsp(DET)] and poly(N-isopropylacrylamide)-b-PAsp(DET) [PNIPAM-b-PAsp(DET)] and plasmid DNA at room temperature, which exhibited unique temperature-responsive formation of a hydrophobic intermediate layer between PEG shells and plasmid DNA cores through facile temperature increase from room temperature to body temperature (∼37°C) (Li et al., 2015). This temperature-responsive micelle system possessed great potentials as efficient systemic non-viral gene delivery systems.

Magnetic Field-Responsive Polymers

The magnetic field can serve as an external stimulus for cancer therapy by controlling the drug release of the polymeric nanomaterials. Magnetic field-responsive polymers, typically incorporating the therapeutic components and magnetic nanoparticles, can produce heat in the presence of alternating magnetic fields (AMF), and MHT is an effective therapy method used for cancers (Chen et al., 2015; Zhou et al., 2018). For example, Le et al. synthesized IONPs coated with a polycationic polymer poly-L-lysine (PLL) to prevent their aggregation and enable their administration, which exhibited superior anticancer efficacy in the magnetic hyperthermia treatment of glioblastoma (Le Fevre et al., 2017). Jaidev et al. developed tumor-targeted fluorescent IONPs and gemcitabine encapsulated poly(lactide-co-glycolide) (PLGA) nanospheres conjugated with human epidermal growth factor receptor antibodies for magnetic hyperthermia of pancreatic cancer. The nanoparticles with surface modification of polymeric nanocarriers for antibody binding could enhance tumor retention through active targeting, and their multifunctional abilities significantly inhibited tumor growth *in vivo* (Jaidev et al., 2017). Compared with PTT, MHT can overcome the limitations of tissue penetration and provide an invasive method for cancer therapy. Additionally, MHT has progressed in clinical trials for different cancers, including prostate cancer, oral cancer, glioma, esophageal cancer, and so forth (Johannsen et al., 2005). Additionally,

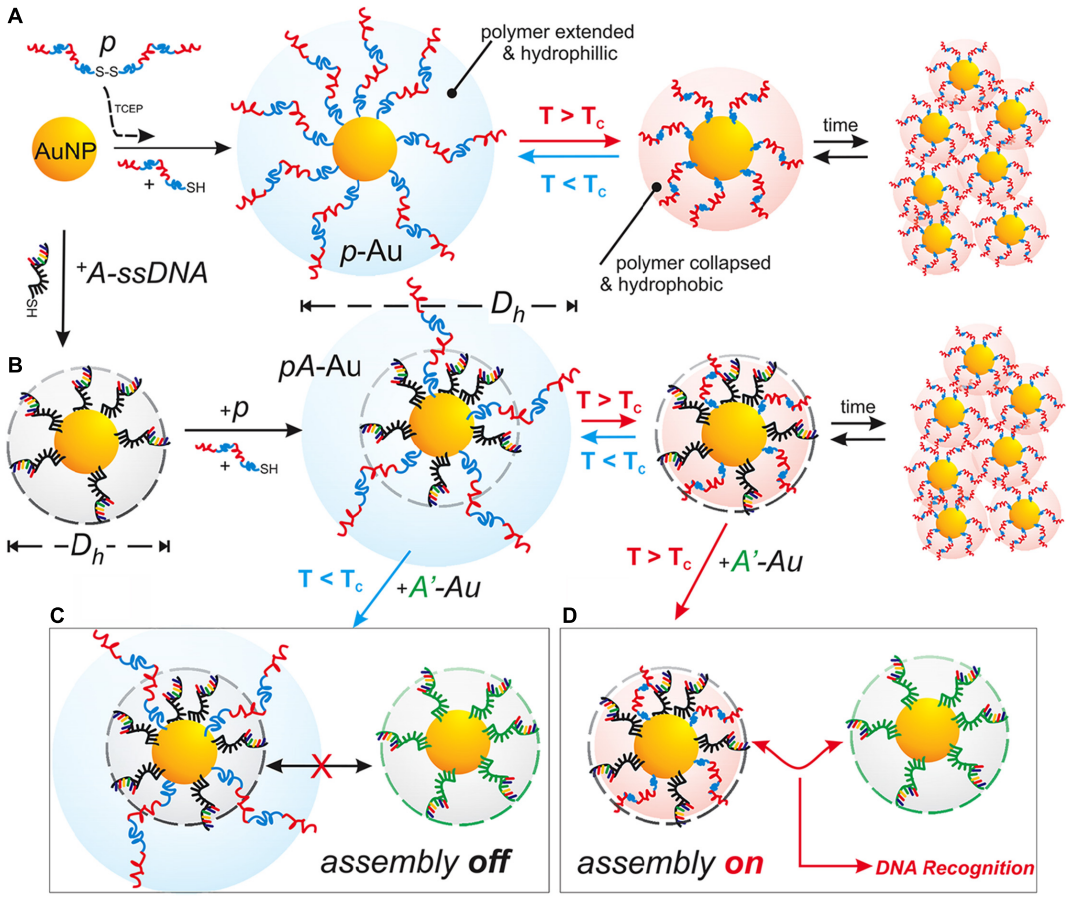

FIGURE 8 | Schematic Illustration of the temperature-responsive polymer systems. **(A)** The Au NPs were functionalized with freshly reduced pNIPAAm-*co*-pAAm copolymer (*p*), and the thermal response-based aggregation was measured. **(B)** The Au NPs were first functionalized with thiolated *A*-type ssDNA, then co-functionalized with *p*. The assembly of *Ap*-Au with complementary *A'*-Au was then blocked at $T < T_C$ **(C)**, but promoted at $T > T_C$ **(D)**. Reprinted from Hamner KL, Alexander CM, Coopersmith K, et al. Using temperature-sensitive smart polymers to regulate DNA-mediated nanoassembly and encoded nanocarrier drug release. ACS Nano. 2013;7(8):7011–20. With permission from reference (Hamner et al., 2013). Au NPs, gold nanoparticles; *Tc*, critical temperature.

magnetic-sensitive polymeric nanoparticles can control drug delivery through the heat energy produced by AMF. In a recent study, Wei et al. designed a responsive polymeric platform with a clickable and imageable nano vehicle assembled from multiblock polyurethanes (MPUs) for precise tumor diagnosis and treatment (Wei et al., 2017; **Figure 9**). The soft segments of the polymers are based on detachable PEG and degradable PCL, and the hard segments are constructed from lysine- and cystine-derivatives bearing reduction-responsive disulfide linkages and click-active alkynyl moieties, allowing for post-conjugation of targeting ligands via click chemistry. They found that the cleavage of PEG corona bearing a pH-sensitive benzoic-imine linkage could act as an on-off switch, which can activate the clicked targeting ligands under extracellular acidic microenvironment, followed by triggering the core degradation and payload release in the tumor cells. Moreover, in combination with superparamagnetic IONPs entrapped in the micellar core, the prepared micelles present excellent MRI contrast effects and T2 relaxation *in vitro* and magnetically guided MRI multimodal targeting therapeutics to tumor resulting in precise anticancer therapy and specifically enhanced MR imaging. Lee et al. developed the pluronic/polyethyleneimine shell crosslinked nanocapsules entrapping magnetite nanocrystals (PMCs) that could deliver siRNA and enhance the intracellular uptake upon exposure to a magnet (Lee et al., 2010). Although only *in vitro* experiments were conducted in this study and the effect of magnetic force for triggered release still needs additional *in vivo* tests, this study provided a novel polymer-based nanoplatform for magnetically triggered delivery of negatively charged therapeutic agents, as well as for diagnostic MRI.

Other External Stimuli

Some other external stimuli also have great promises for cancer theranostics, such as ultrasound (Paris et al., 2015; Jin et al., 2017), radiation (Fan et al., 2015; Liu et al., 2017), radiofrequency (Rejinold et al., 2015; Liu et al., 2018), and electric field (Ge et al., 2012; Kolosnjaj-Tabi et al., 2019). The corresponding polymeric nanomaterials have different properties, which can combine with the external stimuli to realize different requirements, including trigger the release of

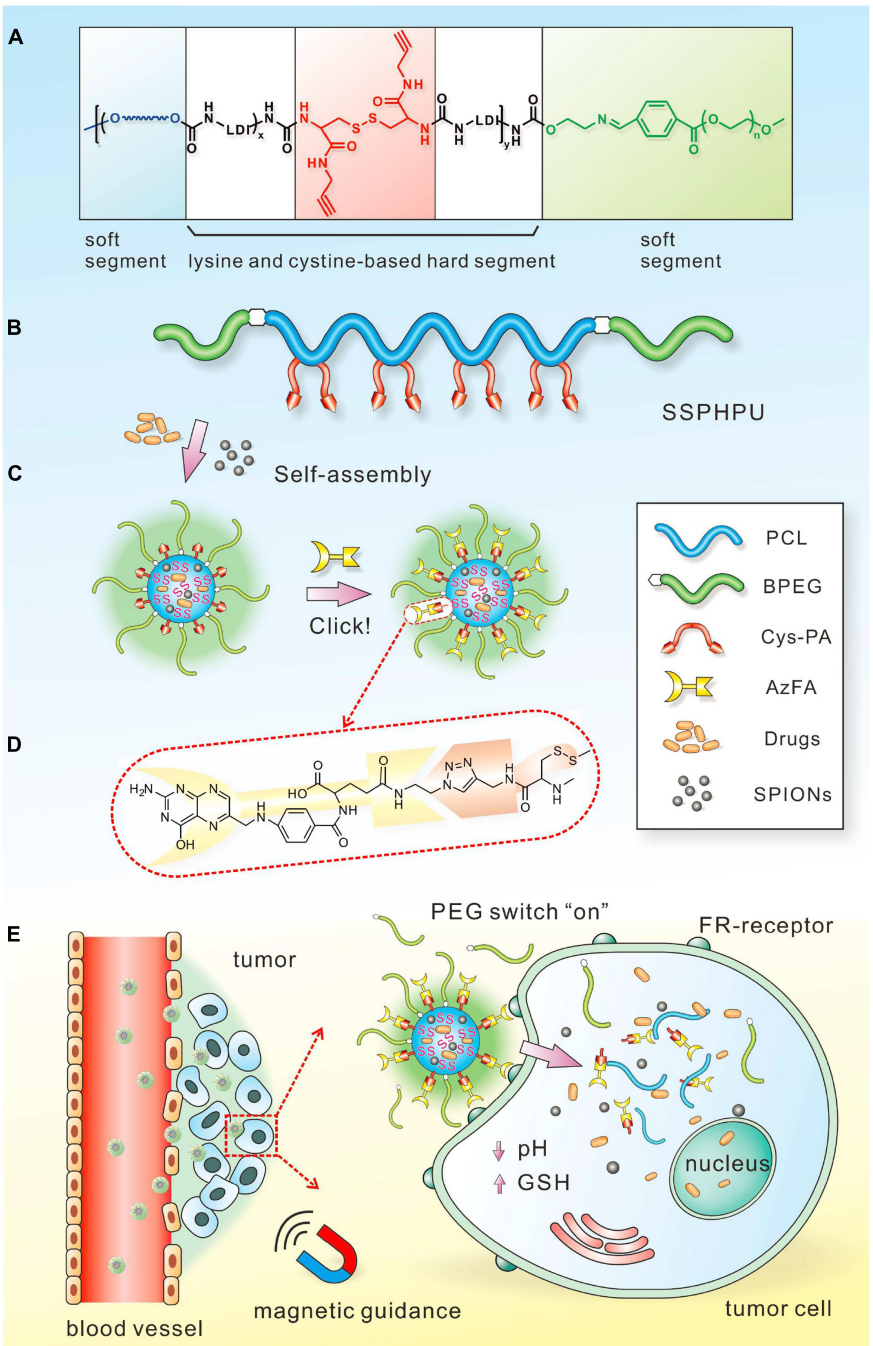

FIGURE 9 | Schematic illustration of the magnetic field-responsive polymer micelles. Schematic chemical structure **(A)** and molecular architecture **(B)** of clickable multiblock polyurethanes (MPUs). **(C)** Self-assembly of MPU micelles and post-conjugation of folic acid via click chemistry. **(D)** Schematic illustration of FA residues on the interface of polymer micelles. **(E)** Illustration of magnetic-guided and PEG-switched targeting and release properties of MPU nanocarriers. Reprinted from Jing Wei, Xiaoyu Shuai, Rui Wang, et al. Clickable and imageable multiblock polymer micelles with magnetically guided and PEG-switched targeting and release property for precise tumor theranostics. Biomaterials. 2017;145:138–53. With permission from reference (Wei et al., 2017).

loading drugs, kill the cancer cells through different mechanisms, enhance the anticancer efficacy with another treatment method, and fulfill cancer imaging/detection/diagnosis (Fleige et al., 2012; Sadhukha et al., 2013; Chen et al., 2015; Mohamed et al., 2019).

Dual/Multi-Stimuli Responsive Polymers

Every kind of stimuli-responsive polymeric nanomaterials has its limitations. For instance, the internal stimuli, such as pH, redox potential, enzymes induced by the pathophysiological property

between cancerous and normal tissues undergo dynamical changes affected by multiple factors *in vivo*. Thus, it is not easy to control these nanomaterials precisely, and the speed of response *in vivo* could limit their usage. As for the external stimuli, the key points are supposed to focus on how to increase the tissue penetration for the deep localized tumors and minimize the damage of the surrounding normal tissues with a maximized specificity and selectivity. In recent years, dual/multi-stimuli responsive polymeric nanomaterials have been generated for cancer theranostics, which can combine the advantages of each kind of materials and overcome the limitations of single-stimulus (Cheng et al., 2013; Fu et al., 2018). Dual-stimuli responsive polymeric nanoparticles have been developed that respond to a combination of two signals such as pH/redox, pH/magnetic field, pH/temperature, double pH, temperature/reduction, temperature/enzyme, temperature/magnetic field, and so on. Multi-stimuli responsive polymeric nanoparticles have been developed that respond to more signals such as temperature/pH/redox, temperature/pH/magnetic, pH/redox/magnetic, temperature/redox/guest molecules, temperature/pH/guest molecules, and so on. To date, the majority of multi-stimuli-responsive polymer nanoparticles are based on pH responsiveness due to the significant pH variations between the acidic tumor microenvironments and the normal tissues.

For example, Li et al. designed a transformable polymer nanoparticle system with pH and Light dual-stimuli (Li et al., 2017a). The pH/Light dual-stimuli polymer nanoparticles accumulated in the tumor sites based on the EPR effect, the sheddable modifications on the nanoparticles were stripped in the trigger of acidic pH. Then TAT peptides were exposed, causing improved cell association and internalization. IR-780 light irradiation promoted the DOX release loaded in the nanoparticles, leading to the death of tumor cells. Li et al. constructed a polymer nanoparticle with tumor-specific pH-responsive activation and H_2O_2 induced self-destruction based on optimized block copolymer, PEG-b-P(PBEM-co-PEM), for efficient *in vivo* antitumor application (Li et al., 2017b). The novel glucose oxidase-loaded therapeutic polymeric nanoreactors efficiently kill tumor cells and eliminate tumor via the synergistic effect. Furthermore, a block copolymer prodrug-based polymersome nanoreactor was constructed by Li and co-workers that can be specifically activated by acidic pH at the tumor site and produce H_2O_2 to further trigger the rapid release of camptothecin, which can achieve orchestrated oxidation/chemo-therapy of cancer via specific activation of increased tumor oxidative stress and higher released camptothecin drugs for cancer therapy (Li et al., 2017c). In another study, An et al. synthesized a star quaterpolymer with suitable LCST (44.7°C) and cleavable acetal and disulfide moieties assembled into the NIR light/pH/reduction-responsive nanoparticles (An et al., 2016; **Figure 10**). The multi-stimuli-responsive nanoparticles with a NIR photothermal agent and chemotherapeutic compound can exhibit smart drug release in

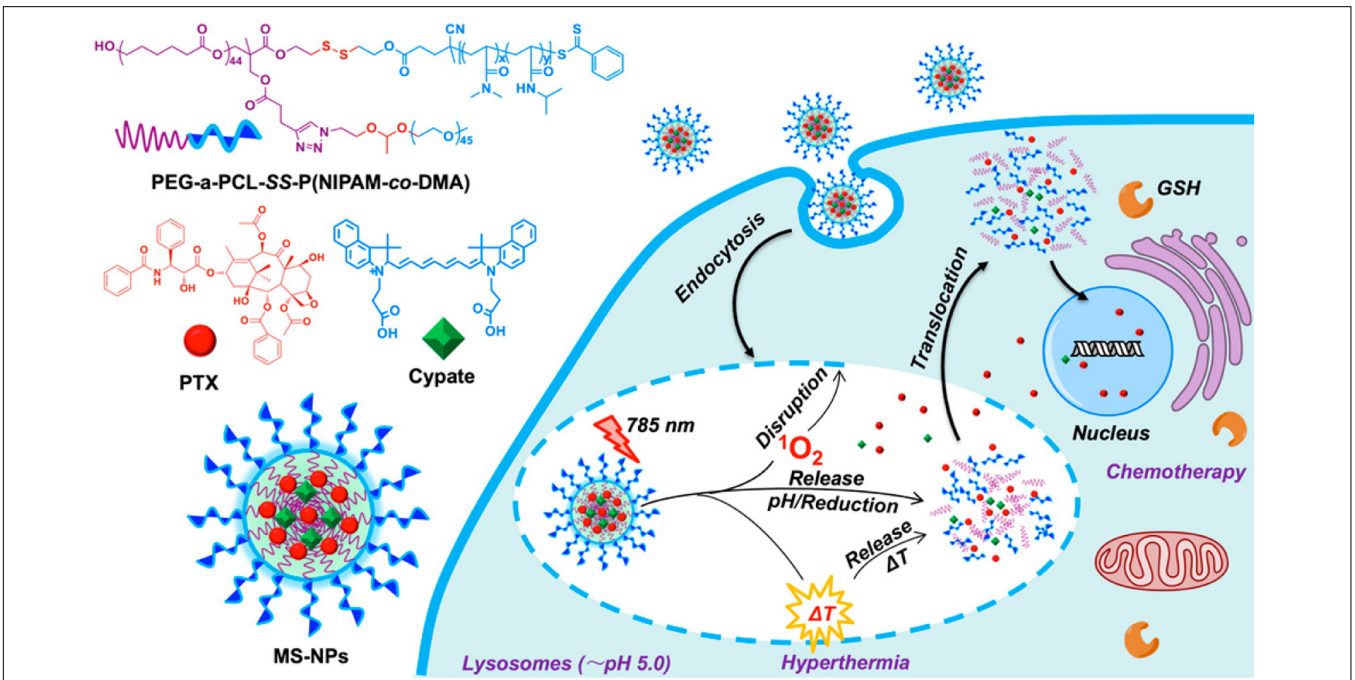

FIGURE 10 | Schematic illustration of NIR light/pH/reduction-responsive nanoparticles. The NIR Light/pH/Reduction–responsive nanoparticles consist of PEG-a-PCL-SSP(NIPAM-co-DMA) (S1) star quaterpolymer for precise cancer therapy synergistic effects. Reprinted from Xiaonan An, Aijun Zhu, Huanhuan Luo, et al. Rational Design of Multi-Stimuli-Responsive Nanoparticles Precise Cancer Therapy. ACS Nano. 2016;10(6):5947–58. With permission from reference (An et al., 2016). NIR, near-infrared; PEG, poly(ethylene glycol); PCL, poly(ε-caprolactone); NIPAM, N-isopropylacrylamide; DMA, dimethylacrylamide; GSH, cytoplasmic glutathione; MS-NPs, multi-stimuliresponsive nanoparticles.

response to intrinsic pH and reduction stimuli and can be further boosted by NIR light irradiation. The NIR light/pH/reduction-responsive nanoparticles also exhibited enhanced tumor accumulation and intracellular drug translocation in cancer cells, which synergized the photo-induced thermo-chemotherapeutic efficacy with anticancer efficiency. The dual/multi-stimuli responsive nanoparticles are highly desired for biomedical applications, especially drug delivery in cancer therapy. However, there are also several limitations, such as the low drug loading capacity, insufficient biocompatibility, *etc*. Future research should devote the effort to increase the loading efficiency and improve the biocompatibility and degradability of dual/multi stimuli-responsive polymeric nanomaterials for cancer therapy.

TABLE 2 | Clinical studies of polymeric delivery systems for cancer therapy.

Name	Polymer	Drug	Indication	Clinical status
Genexol-PM®	mPEG-PLA	Paclitaxel	♦ Recurrent breast cancer ♦ Unresectable locally advanced or metastatic pancreatic cancer ♦ Advanced Urothelial Cancer	♦ Phase IV (NCT00912639) ♦ Phase II (NCT00111904) ♦ Phase II (NCT01426126)
Docetaxel-PM	mPEG-PLA	Docetaxel	♦ Head and Neck Squamous Cell Carcinoma	Phase II (NCT02639858)
NK105	PEG-modified poly(α,β-Asp)	Paclitaxel	♦ Recurrent or metastatic breast cancer	♦ Phase III (NCT01644890)
NC-4016	mPEG-PGA	Oxaliplatin	♦ Advanced solid tumors or lymphoma	♦ Phase I (NCT01999491)
Cripecdocetaxel	Thermosensitive PEG-β-poly(N-(2-hydroxypropyl)-methacryla-mide-lactate)	Docetaxel	♦ Cancer, Solid tumors	♦ Phase I (NCT02442531)
NK012	PEG modified PGA	SN38	♦ Triple negative breast cancer ♦ Refractory solid tumors ♦ Metastatic colorectal cancer in combination with 5-fluorouracil	♦ Phase II (NCT00951054) ♦ Phase I (NCT00542958) ♦ Phase II (NCT01238939)
SPI-77	PEG	Cisplatin	♦ Ovarian tumor ♦ Osteosarcoma Metastatic	♦ Phase II (NCT00004083) Phase II (NCT00102531)
NC-6004	PEG-PGlu	Cisplatin	♦ Recurrent or Metastatic Squamous Cell Carcinoma of the Head and Neck	♦ Phase I/II (NCT03109158)
CT-2106	Poly(L-glutamic acid)	Camptothecin	♦ Ovarian Cancer ♦ Colorectal Cancer ♦ Unspecified Adult Solid Tumor	♦ Phase II(NCT00291837) ♦ Phase I/II(NCT00291785) ♦ Phase I (NCT00059917)
EZN-2208	4-arm PEG	SN38	♦ Advanced Solid Tumors, Lymphoma	♦ Phase I (NCT00520637)
NKTR-102	4-arm PEG	Irinotecan	♦ Advanced Cancer, Metastatic Solid Tumors ♦ Metastatic and recurrent NSCL	♦ Phase I (NCT01976143) ♦ Phase II (NCT01773109)
XYOTAX (CT-2103) Paclitaxel	Poly(L-glutamic acid)	Paclitaxel	♦ Glioblastoma Multiforme, Non-small Cell ♦ Lung Cancer	♦ Phase II (NCT01402063) ♦ Phase II (NCT00487669)
NK911	PEGpoly(α,β-Asp)	Doxorubicin	♦ Metastatic pancreatic cancer	♦ Phase II (Cabral et al., 2014)
SP1049C	Pluronic® P-61 and F-127 block copolymers	Doxorubicin	♦ Advanced refractory adenocarcinoma of the esophagus or GEJ	♦ Phase II (Valle et al., 2011)
NKTR-105	4-arm PEG	Docetaxel	♦ Metastatic or locally recurrent breast cancer	♦ Phase III (NCT01492101)
XMT-1001	PHF (Succinamidoester)	Camptothecin	♦ Advanced solid tumors	♦ Phase I (NCT00455052)
Doxorubicin Transdrug (Livatag)	PIHCA	Doxorubicin	♦ Advanced hepatocellular carcinoma	♦ Phase III (NCT01655693)
CRLX301	Cyclodextrin-PEG	Docetaxel	♦ Advanced solid tumors	♦ Phase I/IIa (NCT02380677)

Asp, aspartic acid; PEG, poly(ethylene glycol); GEJ, gastroesophageal junction; mPEG, methoxypoly(ethylene glycol); NCT#, ClinicalTrials.gov registry number; PGA, poly(L-glutamic acid); PLA, poly (D,L lactic acid); PHF, poly(1-hydroxyl-methylethylene hydroxyl-methyl-formal); PIHCA, poly(isohexyl cyanoacrylate).

CLINICAL STUDIES OF POLYMERIC DELIVERY SYSTEMS

Over the last two decades, polymer-based nanoplatforms have been extensively applied for various medical applications and human studies (Hua et al., 2018). Polymer-based nanoplatforms and liposomes are the most clinically available nanomaterials for human use and have been evaluated for therapeutic delivery in cancer therapy (De Jong and Borm, 2008; Majumder and Minko, 2021). Because of the unique features of polymer-containing nanodrugs in prolonging circulating half-life and improving passive tumor targeting by increasing the size of a drug, rapid progress has been made on developing polymeric nanosystems for targeted therapeutic delivery and diagnostic applications. As reported, some polymer micelles are already available for clinical use, and some polymer-drug conjugates and nanospheres are under clinical development in cancer treatment (Luque-Michel et al., 2017).

Many polymer-containing nanodrugs are being investigated in clinical trials due to the broad applicability of polymer-based nanoformulations (Ventola, 2017). For example, Opaxio (Xyotax) is a nano drug-containing polyglutamic acid-conjugated (poliglumex) paclitaxel, and early stage trials of Opaxio in patients with ovarian cancer and fallopian tube cancers showed promising clinical results (Caster et al., 2017). Furthermore, the ongoing phase III trial of Opaxio as maintenance therapy for ovarian cancer patients obtained complete responses after taxane and platinum therapy. CRLX-101, drug–conjugate formulation of camptothecin and a cyclodextrin-PEG polymer, has shown promising early therapeutic profiles in phase I/II clinical trials in patients with solid tumors such as lung cancers (SCLC and NSCLC) and gynecological malignancies (Weiss et al., 2013; Caster et al., 2017). CRLX-301(NCT02380677) is another docetaxel-conjugate polymer, which has been studied in a phase I/IIa clinical trial in the treatment of advanced solid tumors. In addition, NK012 is a polymeric formulation of SN-38 (an active metabolite of the topoisomerase inhibitor irinotecan), and two phase I trials and several phase II trials utilizing this micellar nanoformulation of SN-38 have been completed or still are ongoing in solid tumors including NSCLC (Caster et al., 2017) and triple-negative breast cancer (NCT00951054). Genexol-PM, a MPEG-block-D, L-PLA micellar formulation of paclitaxel, is being developed as alternative Cremophor-based paclitaxel. Recently, Genexol-PM is extensively investigated in phase I/II clinical trials in various countries, approved for treating metastatic breast cancer and advanced lung cancer in South Korea (Havel, 2016). Several phase II trials in solid tumors of metastatic breast cancer and NSCLC have shown a low rate of toxic reactions and a favorable rate of overall remission (Lee et al., 2008; Ahn et al., 2014). A summary of clinical studies of polymeric delivery systems for cancer therapy is presented in **Table 2** (Valle et al., 2011; Cabral and Kataoka, 2014). More clinical trials are being conducted, and novel techniques are being developed to reduce the toxicity issues and safe use of polymer-based nanomedicines in human health.

CONCLUSION AND PERSPECTIVE

In summary, this review introduces representative theranostic polymeric nanomaterials and their advantages and disadvantages in the practical use as well as their unique properties. In particular, recent advances of stimuli-responsive polymeric nanocarriers in the development of drug delivery are discussed in cancer therapy, where stimuli-responsive polymeric nanocarriers have been shown to own the possibility of controlled release of drugs/genes at the target sites by acting as an active participant rather than passive mediators. Various studies on stimuli-responsive polymers have been published, which showed that multifunctional polymeric nanosystems are promising to be effective platforms for drug/gene delivery in response to a range of internal (pH, redox potential, enzymes, hypoxia, *etc.*) and external stimuli (light, magnetic field, ultrasound, temperature, radiation, *etc.*). The internal stimuli-responsive polymeric nanosystem relies on the abnormal microenvironments in various cancers, such as acidic extracellular pH and hypoxia, for targeted drug delivery, while the external stimuli-responsive nanosystem requires prior information on the target-specific site for efficient therapy. Moreover, studies have shown that the applications of polymeric nanomaterials in various cancers have achieved positive effects in both diagnosis and treatment monitoring, including enhanced therapeutic outcomes and reduced systemic side effects compared to traditional anticancer drugs.

Despite various advantages of stimuli-responsive polymeric nanomaterials over conventional therapies, we should know that they are not perfect and many crucial issues and challenges still remain to be addressed. At first, there are a number of biological components that polymeric nanomaterials would encounter after *in vivo* administration, including biological molecules, cells, and tissues/organs. The features of polymeric nanomaterials, such as surface charge and size, will determine the subsequent biodistribution and cellular responses of polymeric nanomaterials. Secondly, it is essential to improve the stimuli sensitivity of polymeric nanomaterials in target sites because non-specific distribution of stimuli can lead to off-target effects. For example, low pH can also be found in some normal tissues, so the degree of acidic pH to which polymeric nanomaterials would respond may play an important role in determining the release amount and release rate to the target sites. Moreover, the heterogeneity of tumor types and stages greatly influence the status of internal stimuli, which should be examined extensively before the synthesis of polymeric nanomaterials. Thirdly, the current polymeric nanomaterials still have limitations for clinical or practical use due their complicated design, limited biostability *in vivo*, and potential toxicity.

We have given several examples published for the commonly used multifunctional and stimuli-responsive polymeric nanomaterials in different cancers and their roles in the process of treatment. However, polymeric nanomaterials for only imaging or only therapy are not included because of the topic request. Importantly, the future trend for polymeric nanomedicine should focus on combinational therapy, which refers to the combination of nanomedicine and gene therapy or immunotherapy for the improved efficacy of $1 + 1 > 2$. Moreover, with the aging population increasing worldwide, cancers are a severe threat to people's health. Therefore, a better understanding of the physiological microenvironments of cancers and the further development of polymeric nanocarrier-based drug systems are necessary for targeted therapeutic delivery applications. More attention should be paid to the progress of different cancers and what stimuli-responsive polymeric nanomedicine can do to globally reduce the social burden and contribute to the medical field.

AUTHOR CONTRIBUTIONS

DC and YM wrote the manuscript and developed the tables. DC and XX did the literature research. DC and JX developed or collected the figures. JX and SJ reviewed, edited, and supervised. All authors contributed to the article and approved the submitted version.

FUNDING

This work was supported by the National Natural Science Foundation of China (NSFC, Nos. 81801759, 81830053, and 81601465), Natural Science Foundation of Jiangsu Province (BK20180375), and Science Foundation for Creative Research Groups of the Ministry of Science and Technology of China (No. 6290002012).

REFERENCES

Ahn, H. K., Jung, M., Sym, S. J., Shin, D. B., Kang, S. M., Kyung, S. Y., et al. (2014). A phase II trial of Cremorphor EL-free paclitaxel (Genexol-PM) and gemcitabine in patients with advanced non-small cell lung cancer. *Cancer Chemother. Pharmacol.* 74, 277–282. doi: 10.1007/s00280-014-2498-5

Alfarouk, K. O., Muddathir, A. K., and Shayoub, M. E. (2011). Tumor acidity as evolutionary spite. *Cancers* 3, 408–414. doi: 10.3390/cancers3010408

Al-Jamal, W. T., and Kostarelos, K. (2011). Liposomes: from a clinically established drug delivery system to a nanoparticle platform for theranostic nanomedicine. *Acc. Chem. Res.* 44, 1094–1104. doi: 10.1021/ar200105p

Alsehli, M. (2020). Polymeric nanocarriers as stimuli-responsive systems for targeted tumor (cancer) therapy: recent advances in drug delivery. *Saudi Pharm. J.* 28, 255–265. doi: 10.1016/j.jsps.2020.01.004

Amin, M. L., Joo, J. Y., Yi, D. K., and An, S. S. (2015). Surface modification and local orientations of surface molecules in nanotherapeutics. *J. Control Release* 207, 131–142. doi: 10.1016/j.jconrel.2015.04.017

An, X., Zhu, A., Luo, H., Ke, H., Chen, H., and Zhao, Y. (2016). Rational design of multi-stimuli-responsive nanoparticles for precise cancer therapy. *ACS Nano* 10, 5947–5958. doi: 10.1021/acsnano.6b01296

Ansari, C., Tikhomirov, G. A., Hong, S. H., Falconer, R. A., Loadman, P. M., Gill, J. H., et al. (2014). Development of novel tumor-targeted theranostic nanoparticles activated by membrane-type matrix metalloproteinases for combined cancer magnetic resonance imaging and therapy. *Small* 10, 566–575. doi: 10.1002/smll.201301456

Bagheri, A., Arandiyan, H., Boyer, C., and Lim, M. (2016). Lanthanide-doped upconversion nanoparticles: emerging intelligent light-activated drug delivery systems. *Adv. Sci.* 3:1500437. doi: 10.1002/advs.201500437

Bagheri, A., Boyer, C., and Lim, M. (2019). Synthesis of light-responsive pyrene-based polymer nanoparticles via polymerization-induced self-assembly. *Macromol. Rapid Commun.* 40:e1800510. doi: 10.1002/marc.201800510

Bejarano, L., Jordao, M. J. C., and Joyce, J. A. (2021). Therapeutic targeting of the tumor microenvironment. *Cancer Discov.* 11, 933–959. doi: 10.1158/2159-8290.CD-20-1808

Bertrand, N., Wu, J., Xu, X., Kamaly, N., and Farokhzad, O. C. (2014). Cancer nanotechnology: the impact of passive and active targeting in the era of modern cancer biology. *Adv. Drug Deliv. Rev.* 66, 2–25. doi: 10.1016/j.addr.2013.11.009

Bikram, M., and West, J. L. (2008). Thermo-responsive systems for controlled drug delivery. *Expert Opin. Drug Deliv.* 5, 1077–1091. doi: 10.1517/17425247.5.10.1077

Bobo, D., Robinson, K. J., Islam, J., Thurecht, K. J., and Corrie, S. R. (2016). Nanoparticle-based medicines: a review of FDA-approved materials and clinical trials to date. *Pharm. Res.* 33, 2373–2387. doi: 10.1007/s11095-016-1958-5

Boltnarova, B., Kubackova, J., Skoda, J., Stefela, A., Smekalova, M., Svacinova, P., et al. (2021). PLGA based nanospheres as a potent macrophage-specific drug delivery system. *Nanomaterials* 11:749. doi: 10.3390/nano11030749

Brown, J. M., and Wilson, W. R. (2004). Exploiting tumour hypoxia in cancer treatment. *Nat. Rev. Cancer* 4, 437–447. doi: 10.1038/nrc1367

Butowska, K., Woziwodzka, A., Borowik, A., and Piosik, J. (2021). Polymeric nanocarriers: a transformation in doxorubicin therapies. *Materials* 14:2135. doi: 10.3390/ma14092135

Cabral, H., and Kataoka, K. (2014). Progress of drug-loaded polymeric micelles into clinical studies. *J. Control Release* 190, 465–476. doi: 10.1016/j.jconrel.2014.06.042

Cabral, H., Miyata, K., and Kishimura, A. (2014). Nanodevices for studying nano-pathophysiology. *Adv. Drug Deliv. Rev.* 74, 35–52. doi: 10.1016/j.addr.2014.06.003

Caldorera-Moore, M. E., Liechty, W. B., and Peppas, N. A. (2011). Responsive theranostic systems: integration of diagnostic imaging agents and responsive controlled release drug delivery carriers. *Acc. Chem. Res.* 44, 1061–1070. doi: 10.1021/ar2001777

Callmann, C. E., Barback, C. V., Thompson, M. P., Hall, D. J., Mattrey, R. F., and Gianneschi, N. C. (2015). Therapeutic enzyme-responsive nanoparticles for targeted delivery and accumulation in tumors. *Adv. Mater.* 27, 4611–4615. doi: 10.1002/adma.201501803

Cao, J., Chen, D., Huang, S., Deng, D., Tang, L., and Gu, Y. (2016). Multifunctional near-infrared light-triggered biodegradable micelles for chemo- and photothermal combination therapy. *Oncotarget* 7, 82170–82184. doi: 10.18632/oncotarget.10320

Cao, J., Huang, S., Chen, Y., Li, S., Li, X., Deng, D., et al. (2013). Near-infrared light-triggered micelles for fast controlled drug release in deep tissue. *Biomaterials* 34, 6272–6283. doi: 10.1016/j.biomaterials.2013.05.008

Carita, A. C., Eloy, J. O., Chorilli, M., Lee, R. J., and Leonardi, G. R. (2018). Recent advances and perspectives in liposomes for cutaneous drug delivery. *Curr. Med. Chem.* 25, 606–635. doi: 10.2174/0929867324666171009120154

Caster, J. M., Patel, A. N., Zhang, T., and Wang, A. (2017). Investigational nanomedicines in 2016: a review of nanotherapeutics currently undergoing clinical trials. *Wiley Interdiscip. Rev. Nanomed. Nanobiotechnol.* 9:e1416. doi: 10.1002/wnan.1416

Chandrawati, R. (2016). Enzyme-responsive polymer hydrogels for therapeutic delivery. *Exp. Biol. Med.* 241, 972–979. doi: 10.1177/1535370216647186

Chang, G., Li, C., Lu, W., and Ding, J. (2010). N-Boc-histidine-capped PLGA-PEG-PLGA as a smart polymer for drug delivery sensitive to tumor extracellular pH. *Macromol. Biosci.* 10, 1248–1256. doi: 10.1002/mabi.201000117

Chen, Q., Feng, L., Liu, J., Zhu, W., Dong, Z., Wu, Y., et al. (2016). Intelligent albumin-MnO2 nanoparticles as pH-/H2 O2 -responsive dissociable

nanocarriers to modulate tumor hypoxia for effective combination therapy. *Adv. Mater.* 28, 7129–7136. doi: 10.1002/adma.201601902

Chen, Q., Ke, H., Dai, Z., and Liu, Z. (2015). Nanoscale theranostics for physical stimulus-responsive cancer therapies. *Biomaterials* 73, 214–230. doi: 10.1016/j.biomaterials.2015.09.018

Cheng, R., Meng, F., Deng, C., Klok, H. A., and Zhong, Z. (2013). Dual and multi-stimuli responsive polymeric nanoparticles for programmed site-specific drug delivery. *Biomaterials* 34, 3647–3657. doi: 10.1016/j.biomaterials.2013.01.084

Chiang, Y. T., Yen, Y. W., and Lo, C. L. (2015). Reactive oxygen species and glutathione dual redox-responsive micelles for selective cytotoxicity of cancer. *Biomaterials* 61, 150–161. doi: 10.1016/j.biomaterials.2015.05.007

Chien, M. P., Carlini, A. S., Hu, D., Barback, C. V., Rush, A. M., Hall, D. J., et al. (2013). Enzyme-directed assembly of nanoparticles in tumors monitored by in vivo whole animal imaging and ex vivo super-resolution fluorescence imaging. *J. Am. Chem. Soc.* 135, 18710–18713. doi: 10.1021/ja408182p

Choi, K. Y., Han, H. S., Lee, E. S., Shin, J. M., Almquist, B. D., Lee, D. S., et al. (2019). Hyaluronic acid-based activatable nanomaterials for stimuli-responsive imaging and therapeutics: beyond CD44-mediated drug delivery. *Adv. Mater.* 31:e1803549. doi: 10.1002/adma.201803549

Cui, D., Huang, J., Zhen, X., Li, J., Jiang, Y., and Pu, K. (2019). A semiconducting polymer nano-prodrug for hypoxia-activated photodynamic cancer therapy. *Angew. Chem. Int. Ed. Engl.* 58, 5920–5924. doi: 10.1002/anie.201814730

Dai, Y., Xu, C., Sun, X., and Chen, X. (2017). Nanoparticle design strategies for enhanced anticancer therapy by exploiting the tumour microenvironment. *Chem. Soc. Rev.* 46, 3830–3852. doi: 10.1039/c6cs00592f

De Jong, W. H., and Borm, P. J. (2008). Drug delivery and nanoparticles:applications and hazards. *Int. J. Nanomed.* 3, 133–149. doi: 10.2147/ijn.s596

De Volder, M. F., Tawfick, S. H., Baughman, R. H., and Hart, A. J. (2013). Carbon nanotubes: present and future commercial applications. *Science* 339, 535–539. doi: 10.1126/science.1222453

Du, J., Lane, L. A., and Nie, S. (2015). Stimuli-responsive nanoparticles for targeting the tumor microenvironment. *J. Control Release* 219, 205–214. doi: 10.1016/j.jconrel.2015.08.050

Duncan, R. (2003). The dawning era of polymer therapeutics. *Nat. Rev. Drug Discov.* 2, 347–360. doi: 10.1038/nrd1088

Duncan, R. (2006). Polymer conjugates as anticancer nanomedicines. *Nat. Rev. Cancer* 6, 688–701. doi: 10.1038/nrc1958

Duncan, R., Vicent, M. J., Greco, F., and Nicholson, R. I. (2005). Polymer-drug conjugates: towards a novel approach for the treatment of endrocine-related cancer. *Endocr. Relat. Cancer* 12(Suppl. 1), S189–S199. doi: 10.1677/erc.1.01045

Ekladious, I., Colson, Y. L., and Grinstaff, M. W. (2019). Polymer-drug conjugate therapeutics: advances, insights and prospects. *Nat. Rev. Drug Discov.* 18, 273–294. doi: 10.1038/s41573-018-0005-0

Fan, W., Bu, W., Zhang, Z., Shen, B., Zhang, H., He, Q., et al. (2015). X-ray radiation-controlled no-release for on-demand depth-independent hypoxic radiosensitization. *Angew. Chem. Int. Ed. Engl.* 54, 14026–14030. doi: 10.1002/anie.201504536

Fleige, E., Quadir, M. A., and Haag, R. (2012). Stimuli-responsive polymeric nanocarriers for the controlled transport of active compounds: concepts and applications. *Adv. Drug Deliv. Rev.* 64, 866–884. doi: 10.1016/j.addr.2012.01.020

Fu, X., Hosta-Rigau, L., Chandrawati, R., and Cui, J. (2018). Multi-stimuli-responsive polymer particles, films, and hydrogels for drug delivery. *Chem* 4, 2084–2107. doi: 10.1016/j.chempr.2018.07.002

Gallo, J., Kamaly, N., Lavdas, I., Stevens, E., Nguyen, Q. D., Wylezinska-Arridge, M., et al. (2014). CXCR4-targeted and MMP-responsive iron oxide nanoparticles for enhanced magnetic resonance imaging. *Angew. Chem. Int. Ed. Engl.* 53, 9550–9554. doi: 10.1002/anie.201405442

Ganguly, S., Dewanjee, S., Sen, R., Chattopadhyay, D., Ganguly, S., Gaonkar, R., et al. (2021). Apigenin-loaded galactose tailored PLGA nanoparticles: a possible strategy for liver targeting to treat hepatocellular carcinoma. *Colloids Surf. B Biointerfaces* 204:111778. doi: 10.1016/j.colsurfb.2021.111778

Ge, J., Neofytou, E., Cahill, T. J. III, Beygui, R. E., and Zare, R. N. (2012). Drug release from electric-field-responsive nanoparticles. *ACS Nano* 6, 227–233. doi: 10.1021/nn203430m

Grange, C., Geninatti-Crich, S., Esposito, G., Alberti, D., Tei, L., Bussolati, B., et al. (2010). Combined delivery and magnetic resonance imaging of neural cell adhesion molecule-targeted doxorubicin-containing liposomes in experimentally induced Kaposi's sarcoma. *Cancer Res.* 70, 2180–2190. doi: 10.1158/0008-5472.CAN-09-2821

Greco, F., and Vicent, M. J. (2009). Combination therapy: opportunities and challenges for polymer-drug conjugates as anticancer nanomedicines. *Adv. Drug Deliv. Rev.* 61, 1203–1213. doi: 10.1016/j.addr.2009.05.006

Guo, H., Zheng, Y., Wang, B., and Li, Z. (2015). A note on an improved self-healing group key distribution scheme. *Sensors* 15, 25033–25038. doi: 10.3390/s151025033

Hamner, K. L., Alexander, C. M., Coopersmith, K., Reishofer, D., Provenza, C., and Maye, M. M. (2013). Using temperature-sensitive smart polymers to regulate DNA-mediated nanoassembly and encoded nanocarrier drug release. *ACS Nano* 7, 7011–7020. doi: 10.1021/nn402214e

Han, H. S., Thambi, T., Choi, K. Y., Son, S., Ko, H., Lee, M. C., et al. (2015). Bioreducible shell-cross-linked hyaluronic acid nanoparticles for tumor-targeted drug delivery. *Biomacromolecules* 16, 447–456. doi: 10.1021/bm5017755

Han, L., Zhang, X. Y., Wang, Y. L., Li, X., Yang, X. H., Huang, M., et al. (2017). Redox-responsive theranostic nanoplatforms based on inorganic nanomaterials. *J. Control Release* 259, 40–52. doi: 10.1016/j.jconrel.2017.03.018

Han, L., Zhao, J., Zhang, X., Cao, W., Hu, X., Zou, G., et al. (2012). Enhanced siRNA delivery and silencing gold-chitosan nanosystem with surface charge-reversal polymer assembly and good biocompatibility. *ACS Nano* 6, 7340–7351. doi: 10.1021/nn3024688

Hao, Y., Zheng, C., Wang, L., Zhang, J., Niu, X., Song, Q., et al. (2017). Tumor acidity-activatable manganese phosphate nanoplatform for amplification of photodynamic cancer therapy and magnetic resonance imaging. *Acta Biomater.* 62, 293–305. doi: 10.1016/j.actbio.2017.08.028

Havel, H. A. (2016). Where are the nanodrugs? An industry perspective on development of drug products containing nanomaterials. *AAPS J.* 18, 1351–1353. doi: 10.1208/s12248-016-9970-6

He, H., Sun, L., Ye, J., Liu, E., Chen, S., Liang, Q., et al. (2016). Enzyme-triggered, cell penetrating peptide-mediated delivery of anti-tumor agents. *J. Control Release* 240, 67–76. doi: 10.1016/j.jconrel.2015.10.040

He, H., Zhu, R., Sun, W., Cai, K., Chen, Y., and Yin, L. (2018). Selective cancer treatment via photodynamic sensitization of hypoxia-responsive drug delivery. *Nanoscale* 10, 2856–2865. doi: 10.1039/c7nr07677k

He, J., Li, C., Ding, L., Huang, Y., Yin, X., Zhang, J., et al. (2019). Tumor targeting strategies of smart fluorescent nanoparticles and their applications in cancer diagnosis and treatment. *Adv. Mater.* 31:e1902409. doi: 10.1002/adma.201902409

He, T., Jiang, C., He, J., Zhang, Y., He, G., Wu, J., et al. (2021). Manganese-dioxide-coating-instructed plasmonic modulation of gold nanorods for activatable duplex-imaging-guided NIR-II photothermal-chemodynamic therapy. *Adv. Mater.* 33:e2008540. doi: 10.1002/adma.202008540

Her, S., Jaffray, D. A., and Allen, C. (2017). Gold nanoparticles for applications in cancer radiotherapy: mechanisms and recent advancements. *Adv. Drug Deliv. Rev.* 109, 84–101. doi: 10.1016/j.addr.2015.12.012

Hu, F. Q., Zhang, Y. Y., You, J., Yuan, H., and Du, Y. Z. (2012). pH triggered doxorubicin delivery of PEGylated glycolipid conjugate micelles for tumor targeting therapy. *Mol. Pharm* 9, 2469–2478. doi: 10.1021/mp300002v

Hu, Q., Katti, P. S., and Gu, Z. (2014). Enzyme-responsive nanomaterials for controlled drug delivery. *Nanoscale* 6, 12273–12286. doi: 10.1039/c4nr04249b

Hua, S., de Matos, M. B. C., Metselaar, J. M., and Storm, G. (2018). Current trends and challenges in the clinical translation of nanoparticulate nanomedicines: pathways for translational development and commercialization. *Front. Pharmacol.* 9:790. doi: 10.3389/fphar.2018.00790

Huang, D., Sun, L., Huang, L., and Chen, Y. (2021). Nanodrug delivery systems modulate tumor vessels to increase the enhanced permeability and retention effect. *J. Pers. Med.* 11:124. doi: 10.3390/jpm11020124

Jackson, E. F., Esparza-Coss, E., Wen, X., Ng, C. S., Daniel, S. L., Price, R. E., et al. (2007). Magnetic resonance imaging of therapy-induced necrosis using gadolinium-chelated polyglutamic acids. *Int. J. Radiat. Oncol. Biol. Phys.* 68, 830–838. doi: 10.1016/j.ijrobp.2007.01.011

Jaidev, L. R., Chellappan, D. R., Bhavsar, D. V., Ranganathan, R., Sivanantham, B., Subramanian, A., et al. (2017). Multi-functional nanoparticles as theranostic agents for the treatment & imaging of pancreatic cancer. *Acta Biomater.* 49, 422–433. doi: 10.1016/j.actbio.2016.11.053

Jain, R. K., and Stylianopoulos, T. (2010). Delivering nanomedicine to solid tumors. *Nat. Rev. Clin. Oncol.* 7, 653–664. doi: 10.1038/nrclinonc.2010.139

Jia, L., Li, Z., Zhang, D., Zhang, Q., Shen, J., Guo, H., et al. (2013). Redox-responsive catiomer based on PEG-ss-chitosan oligosaccharide-ss-polyethylenimine copolymer for effective gene delivery. *Polym. Chem.* 4, 156–165. doi: 10.1039/C2PY20781H

Jiang, M., Mu, J., Jacobson, O., Wang, Z., He, L., Zhang, F., et al. (2020). Reactive oxygen species activatable heterodimeric prodrug as tumor-selective nanotheranostics. *ACS Nano* 14, 16875–16886. doi: 10.1021/acsnano.0c05722

Jiang, W., Zhou, Y., and Yan, D. (2015). Hyperbranched polymer vesicles: from self-assembly, characterization, mechanisms, and properties to applications. *Chem. Soc. Rev.* 44, 3874–3889. doi: 10.1039/c4cs00274a

Jin, Z., Wen, Y., Hu, Y., Chen, W., Zheng, X., Guo, W., et al. (2017). MRI-guided and ultrasound-triggered release of NO by advanced nanomedicine. *Nanoscale* 9, 3637–3645. doi: 10.1039/c7nr00231a

Johannsen, M., Gneveckow, U., Eckelt, L., Feussner, A., Waldofner, N., Scholz, R., et al. (2005). Clinical hyperthermia of prostate cancer using magnetic nanoparticles: presentation of a new interstitial technique. *Int. J. Hypertherm.* 21, 637–647. doi: 10.1080/02656730500158360

Kakwere, H., Leal, M. P., Materia, M. E., Curcio, A., Guardia, P., Niculaes, D., et al. (2015). Functionalization of strongly interacting magnetic nanocubes with (thermo)responsive coating and their application in hyperthermia and heat-triggered drug delivery. *ACS Appl. Mater. Interfaces* 7, 10132–10145. doi: 10.1021/am5088117

Kamaly, N., Yameen, B., Wu, J., and Farokhzad, O. C. (2016). Degradable controlled-release polymers and polymeric nanoparticles: mechanisms of controlling drug release. *Chem. Rev.* 116, 2602–2663. doi: 10.1021/acs.chemrev.5b00346

Kanamala, M., Wilson, W. R., Yang, M., Palmer, B. D., and Wu, Z. (2016). Mechanisms and biomaterials in pH-responsive tumour targeted drug delivery: a review. *Biomaterials* 85, 152–167. doi: 10.1016/j.biomaterials.2016.01.061

Karimi, M., Ghasemi, A., Sahandi Zangabad, P., Rahighi, R., Moosavi Basri, S. M., Mirshekari, H., et al. (2016). Smart micro/nanoparticles in stimulus-responsive drug/gene delivery systems. *Chem. Soc. Rev.* 45, 1457–1501. doi: 10.1039/c5cs00798d

Ke, W., Li, J., Mohammed, F., Wang, Y., Tou, K., Liu, X., et al. (2019). Therapeutic polymersome nanoreactors with tumor-specific activable cascade reactions for cooperative cancer therapy. *ACS Nano* 13, 2357–2369. doi: 10.1021/acsnano.8b09082

Khokha, R., Murthy, A., and Weiss, A. (2013). Metalloproteinases and their natural inhibitors in inflammation and immunity. *Nat. Rev. Immunol.* 13, 649–665. doi: 10.1038/nri3499

Kim, J., Kim, J., Jeong, C., and Kim, W. J. (2016). Synergistic nanomedicine by combined gene and photothermal therapy. *Adv. Drug Deliv. Rev.* 98, 99–112. doi: 10.1016/j.addr.2015.12.018

Kolosnjaj-Tabi, J., Gibot, L., Fourquaux, I., Golzio, M., and Rols, M. P. (2019). Electric field-responsive nanoparticles and electric fields: physical, chemical, biological mechanisms and therapeutic prospects. *Adv. Drug Deliv. Rev.* 138, 56–67. doi: 10.1016/j.addr.2018.10.017

Kulkarni, A., Rao, P., Natarajan, S., Goldman, A., Sabbisetti, V. S., Khater, Y., et al. (2016). Reporter nanoparticle that monitors its anticancer efficacy in real time. *Proc. Natl. Acad. Sci. U.S.A.* 113, E2104–E2113. doi: 10.1073/pnas.1603455113

Kulkarni, P., Haldar, M. K., You, S., Choi, Y., and Mallik, S. (2016). Hypoxia-responsive polymersomes for drug delivery to hypoxic pancreatic cancer cells. *Biomacromolecules* 17, 2507–2513. doi: 10.1021/acs.biomac.6b00350

Kumar, S., Rani, R., Dilbaghi, N., Tankeshwar, K., and Kim, K. H. (2017). Carbon nanotubes: a novel material for multifaceted applications in human healthcare. *Chem. Soc. Rev.* 46, 158–196. doi: 10.1039/c6cs00517a

Lai, J., Shah, B. P., Zhang, Y., Yang, L., and Lee, K. B. (2015). Real-time monitoring of ATP-responsive drug release using mesoporous-silica-coated multicolor upconversion nanoparticles. *ACS Nano* 9, 5234–5245. doi: 10.1021/acsnano.5b00641

Le Fevre, R., Durand-Dubief, M., Chebbi, I., Mandawala, C., Lagroix, F., Valet, J. P., et al. (2017). Enhanced antitumor efficacy of biocompatible magnetosomes for the magnetic hyperthermia treatment of glioblastoma. *Theranostics* 7, 4618–4631. doi: 10.7150/thno.18927

Lee, K. S., Chung, H. C., Im, S. A., Park, Y. H., Kim, C. S., Kim, S. B., et al. (2008). Multicenter phase II trial of Genexol-PM, a Cremophor-free, polymeric micelle formulation of paclitaxel, in patients with metastatic breast cancer. *Breast Cancer Res. Treat* 108, 241–250. doi: 10.1007/s10549-007-9591-y

Lee, K., Bae, K. H., Lee, Y., Lee, S. H., Ahn, C. H., and Park, T. G. (2010). Pluronic/polyethylenimine shell crosslinked nanocapsules with embedded magnetite nanocrystals for magnetically triggered delivery of siRNA. *Macromol. Biosci.* 10, 239–245. doi: 10.1002/mabi.200900291

Li, D., Ma, Y., Du, J., Tao, W., Du, X., Yang, X., et al. (2017a). Tumor acidity/NIR controlled interaction of transformable nanoparticle with biological systems for cancer therapy. *Nano Lett.* 17, 2871–2878. doi: 10.1021/acs.nanolett.6b05396

Li, J., and Pu, K. (2020). Semiconducting polymer nanomaterials as near-infrared photoactivatable protherapeutics for cancer. *Acc. Chem. Res.* 53, 752–762. doi: 10.1021/acs.accounts.9b00569

Li, J., Chen, Q., Zha, Z., Li, H., Toh, K., Dirisala, A., et al. (2015). Ternary polyplex micelles with PEG shells and intermediate barrier to complexed DNA cores for efficient systemic gene delivery. *J. Control Release* 209, 77–87. doi: 10.1016/j.jconrel.2015.04.024

Li, J., Dirisala, A., Ge, Z., Wang, Y., Yin, W., Ke, W., et al. (2017b). Therapeutic vesicular nanoreactors with tumor-specific activation and self-destruction for synergistic tumor ablation. *Angew. Chem. Int. Ed. Engl.* 56, 14025–14030. doi: 10.1002/anie.201706964

Li, J., Li, Y., Wang, Y., Ke, W., Chen, W., Wang, W., et al. (2017c). Polymer prodrug-based nanoreactors activated by tumor acidity for orchestrated oxidation/chemotherapy. *Nano Lett.* 17, 6983–6990. doi: 10.1021/acs.nanolett.7b03531

Li, J., Liu, F., Shao, Q., Min, Y., Costa, M., Yeow, E. K., et al. (2014). Enzyme-responsive cell-penetrating peptide conjugated mesoporous silica quantum dot nanocarriers for controlled release of nucleus-targeted drug molecules and real-time intracellular fluorescence imaging of tumor cells. *Adv. Healthc. Mater.* 3, 1230–1239. doi: 10.1002/adhm.201300613

Li, K., and Liu, B. (2014). Polymer-encapsulated organic nanoparticles for fluorescence and photoacoustic imaging. *Chem. Soc. Rev.* 43, 6570–6597. doi: 10.1039/c4cs00014e

Li, Y., Yang, H. Y., and Lee, D. S. (2016). Polymer-based and pH-sensitive nanobiosensors for imaging and therapy of acidic pathological areas. *Pharm. Res.* 33, 2358–2372. doi: 10.1007/s11095-016-1944-y

Ling, D., Park, W., Park, S. J., Lu, Y., Kim, K. S., Hackett, M. J., et al. (2014). Multifunctional tumor pH-sensitive self-assembled nanoparticles for bimodal imaging and treatment of resistant heterogeneous tumors. *J. Am. Chem. Soc.* 136, 5647–5655. doi: 10.1021/ja4108287

Liu, F., Lou, J., and Hristov, D. (2017). X-Ray responsive nanoparticles with triggered release of nitrite, a precursor of reactive nitrogen species, for enhanced cancer radiosensitization. *Nanoscale* 9, 14627–14634. doi: 10.1039/c7nr04684g

Liu, J. F., Neel, N., Dang, P., Lamb, M., McKenna, J., Rodgers, L., et al. (2018). Radiofrequency-triggered drug release from nanoliposomes with millimeter-scale resolution using a superimposed static gating field. *Small* 14:e1802563. doi: 10.1002/smll.201802563

Liu, J., Huang, Y., Kumar, A., Tan, A., Jin, S., Mozhi, A., et al. (2014). pH-sensitive nano-systems for drug delivery in cancer therapy. *Biotechnol. Adv.* 32, 693–710. doi: 10.1016/j.biotechadv.2013.11.009

Liu, P., Shi, B., Yue, C., Gao, G., Li, P., Yi, H., et al. (2013). Dextran-based redox-responsive doxorubicin prodrug micelles for overcoming multidrug resistance. *Polym. Chem.* 4, 5793–5799. doi: 10.1039/C3PY00830D

Liu, T., Wang, C., Gu, X., Gong, H., Cheng, L., Shi, X., et al. (2014). Drug delivery with PEGylated MoS2 nano-sheets for combined photothermal and chemotherapy of cancer. *Adv. Mater.* 26, 3433–3440. doi: 10.1002/adma.201305256

Liu, Y., Bhattarai, P., Dai, Z., and Chen, X. (2019). Photothermal therapy and photoacoustic imaging via nanotheranostics in fighting cancer. *Chem. Soc. Rev.* 48, 2053–2108. doi: 10.1039/c8cs00618k

Lucky, S. S., Soo, K. C., and Zhang, Y. (2015). Nanoparticles in photodynamic therapy. *Chem. Rev.* 115, 1990–2042. doi: 10.1021/cr5004198

Luk, B. T., and Zhang, L. (2014). Current advances in polymer-based nanotheranostics for cancer treatment and diagnosis. *ACS Appl. Mater. Interfaces* 6, 21859–21873. doi: 10.1021/am5036225

Luk, B. T., Fang, R. H., and Zhang, L. (2012). Lipid- and polymer-based nanostructures for cancer theranostics. *Theranostics* 2, 1117–1126. doi: 10.7150/thno.4381

Luque-Michel, E., Imbuluzqueta, E., Sebastian, V., and Blanco-Prieto, M. J. (2017). Clinical advances of nanocarrier-based cancer therapy and diagnostics. *Expert Opin. Drug Deliv.* 14, 75–92. doi: 10.1080/17425247.2016.1205585

Ma, Y., Mou, Q., Wang, D., Zhu, X., and Yan, D. (2016). Dendritic polymers for theranostics. *Theranostics* 6, 930–947. doi: 10.7150/thno.14855

Madaan, K., Kumar, S., Poonia, N., Lather, V., and Pandita, D. (2014). Dendrimers in drug delivery and targeting: drug-dendrimer interactions and toxicity issues. *J. Pharm. Bioallied Sci.* 6, 139–150. doi: 10.4103/0975-7406.130965

Maeda, H. (2021). The 35th anniversary of the discovery of EPR effect: a new wave of nanomedicines for tumor-targeted drug delivery-personal remarks and future prospects. *J. Pers. Med.* 11:229. doi: 10.3390/jpm11030229

Maeda, H., Bharate, G. Y., and Daruwalla, J. (2009). Polymeric drugs for efficient tumor-targeted drug delivery based on EPR-effect. *Eur. J. Pharm. Biopharm.* 71, 409–419. doi: 10.1016/j.ejpb.2008.11.010

Mai, B. T., Balakrishnan, P. B., Barthel, M. J., Piccardi, F., Niculaes, D., Marinaro, F., et al. (2019). Thermoresponsive iron oxide nanocubes for an effective clinical translation of magnetic hyperthermia and heat-mediated chemotherapy. *ACS Appl. Mater. Interfaces* 11, 5727–5739. doi: 10.1021/acsami.8b16226

Majumder, J., and Minko, T. (2021). Multifunctional and stimuli-responsive nanocarriers for targeted therapeutic delivery. *Expert Opin. Drug Deliv.* 18, 205–227. doi: 10.1080/17425247.2021.1828339

Martinelli, C., Pucci, C., and Ciofani, G. (2019). Nanostructured carriers as innovative tools for cancer diagnosis and therapy. *APL Bioeng.* 3:011502. doi: 10.1063/1.5079943

McHugh, K. J., Jing, L., Behrens, A. M., Jayawardena, S., Tang, W., Gao, M., et al. (2018). Biocompatible semiconductor quantum dots as cancer imaging agents. *Adv. Mater.* 30:e1706356. doi: 10.1002/adma.201706356

Mi, P., Cabral, H., and Kataoka, K. (2020). Ligand-installed nanocarriers toward precision therapy. *Adv. Mater.* 32:e1902604. doi: 10.1002/adma.201902604

Mitchell, M. J., Billingsley, M. M., Haley, R. M., Wechsler, M. E., Peppas, N. A., and Langer, R. (2021). Engineering precision nanoparticles for drug delivery. *Nat. Rev. Drug Discov.* 20, 101–124. doi: 10.1038/s41573-020-0090-8

Mohamed, S. M., Veeranarayanan, S., Maekawa, T., and Kumar, S. (2019). External stimulus responsive inorganic nanomaterials for cancer theranostics. *Adv. Drug Deliv. Rev.* 138, 18–40. doi: 10.1016/j.addr.2018.10.007

Montero de Espinosa, L., Meesorn, W., Moatsou, D., and Weder, C. (2017). Bioinspired polymer systems with stimuli-responsive mechanical properties. *Chem. Rev.* 117, 12851–12892. doi: 10.1021/acs.chemrev.7b00168

Mu, J., Lin, J., Huang, P., and Chen, X. (2018). Development of endogenous enzyme-responsive nanomaterials for theranostics. *Chem. Soc. Rev.* 47, 5554–5573. doi: 10.1039/c7cs00663b

Neradovic, D., Soga, O., Van Nostrum, C. F., and Hennink, W. E. (2004). The effect of the processing and formulation parameters on the size of nanoparticles based on block copolymers of poly(ethylene glycol) and poly(N-isopropylacrylamide) with and without hydrolytically sensitive groups. *Biomaterials* 25, 2409–2418. doi: 10.1016/j.biomaterials.2003.09.024

Nguyen, Q. T., and Tsien, R. Y. (2013). Fluorescence-guided surgery with live molecular navigation–a new cutting edge. *Nat. Rev. Cancer* 13, 653–662. doi: 10.1038/nrc3566

Oerlemans, C., Bult, W., Bos, M., Storm, G., Nijsen, J. F., and Hennink, W. E. (2010). Polymeric micelles in anticancer therapy: targeting, imaging and triggered release. *Pharm. Res.* 27, 2569–2589. doi: 10.1007/s11095-010-0233-4

Overchuk, M., and Zheng, G. (2018). Overcoming obstacles in the tumor microenvironment: recent advancements in nanoparticle delivery for cancer theranostics. *Biomaterials* 156, 217–237. doi: 10.1016/j.biomaterials.2017.10.024

Paris, J. L., Cabanas, M. V., Manzano, M., and Vallet-Regi, M. (2015). Polymer-grafted mesoporous silica nanoparticles as ultrasound-responsive drug carriers. *ACS Nano* 9, 11023–11033. doi: 10.1021/acsnano.5b04378

Perche, F., Biswas, S., Wang, T., Zhu, L., and Torchilin, V. P. (2014). Hypoxia-targeted siRNA delivery. *Angew. Chem. Int. Ed. Engl.* 53, 3362–3366. doi: 10.1002/anie.201308368

Pham, S. H., Choi, Y., and Choi, J. (2020). Stimuli-responsive nanomaterials for application in antitumor therapy and drug delivery. *Pharmaceutics* 12:630. doi: 10.3390/pharmaceutics12070630

Prabhu, P., and Patravale, V. (2012). The upcoming field of theranostic nanomedicine: an overview. *J. Biomed. Nanotechnol.* 8, 859–882. doi: 10.1166/jbn.2012.1459

Prasad, P. N. (2012). *Introduction to Nanomedicine and Nanobioengineering*. Hoboken, NJ: John Wiley & Sons.

Qi, C., He, J., Fu, L. H., He, T., Blum, N. T., Yao, X., et al. (2021). Tumor-specific activatable nanocarriers with gas-generation and signal amplification capabilities for tumor theranostics. *ACS Nano* 15, 1627–1639. doi: 10.1021/acsnano.0c09223

Qin, S., Geng, Y., Discher, D. E., and Yang, S. (2006). Temperature-controlled assembly and release from polymer vesicles of Poly(ethylene oxide)-block-poly(N-isopropylacrylamide). *Adv. Mater.* 18, 2905–2909. doi: 10.1002/adma.200601019

Ramos, J., Forcada, J., and Hidalgo-Alvarez, R. (2014). Cationic polymer nanoparticles and nanogels: from synthesis to biotechnological applications. *Chem. Rev.* 114, 367–428. doi: 10.1021/cr3002643

Rampersaud, S., Fang, J., Wei, Z., Fabijanic, K., Silver, S., Jaikaran, T., et al. (2016). The effect of cage shape on nanoparticle-based drug carriers: anticancer drug release and efficacy via receptor blockade using dextran-coated iron oxide nanocages. *Nano Lett.* 16, 7357–7363. doi: 10.1021/acs.nanolett.6b02577

Rao, N. V., Ko, H., Lee, J., and Park, J. H. (2018). Recent progress and advances in stimuli-responsive polymers for cancer therapy. *Front. Bioeng. Biotechnol.* 6:110. doi: 10.3389/fbioe.2018.00110

Rejinold, N. S., Jayakumar, R., and Kim, Y. C. (2015). Radio frequency responsive nano-biomaterials for cancer therapy. *J. Control Release* 204, 85–97. doi: 10.1016/j.jconrel.2015.02.036

Ren, J. M., McKenzie, T. G., Fu, Q., Wong, E. H., Xu, J., An, Z., et al. (2016). Star polymers. *Chem. Rev.* 116, 6743–6836. doi: 10.1021/acs.chemrev.6b00008

Rizzo, L. Y., Theek, B., Storm, G., Kiessling, F., and Lammers, T. (2013). Recent progress in nanomedicine: therapeutic, diagnostic and theranostic applications. *Curr. Opin. Biotechnol.* 24, 1159–1166. doi: 10.1016/j.copbio.2013.02.020

Rosenblum, D., Joshi, N., Tao, W., Karp, J. M., and Peer, D. (2018). Progress and challenges towards targeted delivery of cancer therapeutics. *Nat. Commun.* 9:1410. doi: 10.1038/s41467-018-03705-y

Sadhukha, T., Wiedmann, T. S., and Panyam, J. (2013). Inhalable magnetic nanoparticles for targeted hyperthermia in lung cancer therapy. *Biomaterials* 34, 5163–5171. doi: 10.1016/j.biomaterials.2013.03.061

Sahay, G., Alakhova, D. Y., and Kabanov, A. V. (2010). Endocytosis of nanomedicines. *J. Control Release* 145, 182–195. doi: 10.1016/j.jconrel.2010.01.036

Saravanakumar, G., Kim, J., and Kim, W. J. (2017). Reactive-oxygen-species-responsive drug delivery systems: promises and challenges. *Adv. Sci.* 4:1600124. doi: 10.1002/advs.201600124

Schadlich, A., Caysa, H., Mueller, T., Tenambergen, F., Rose, C., Gopferich, A., et al. (2011). Tumor accumulation of NIR fluorescent PEG-PLA nanoparticles: impact of particle size and human xenograft tumor model. *ACS Nano* 5, 8710–8720. doi: 10.1021/nn2026353

Schmidt, M. M., and Wittrup, K. D. (2009). A modeling analysis of the effects of molecular size and binding affinity on tumor targeting. *Mol. Cancer Ther.* 8, 2861–2871. doi: 10.1158/1535-7163.MCT-09-0195

Senapati, S., Mahanta, A. K., Kumar, S., and Maiti, P. (2018). Controlled drug delivery vehicles for cancer treatment and their performance. *Signal. Transduct. Target Ther.* 3:7. doi: 10.1038/s41392-017-0004-3

Sharma, H., Mishra, P. K., Talegaonkar, S., and Vaidya, B. (2015). Metal nanoparticles: a theranostic nanotool against cancer. *Drug Discov. Today* 20, 1143–1151. doi: 10.1016/j.drudis.2015.05.009

Sharma, R., Mody, N., Agrawal, U., and Vyas, S. P. (2017). Theranostic nanomedicine; a next generation platform for cancer diagnosis and therapy. *Mini Rev. Med. Chem.* 17, 1746–1757. doi: 10.2174/1389557516666160219122524

Shi, J., Kantoff, P. W., Wooster, R., and Farokhzad, O. C. (2017). Cancer nanomedicine: progress, challenges and opportunities. *Nat. Rev. Cancer* 17, 20–37. doi: 10.1038/nrc.2016.108

Shim, G., Ko, S., Kim, D., Le, Q. V., Park, G. T., Lee, J., et al. (2017). Light-switchable systems for remotely controlled drug delivery. *J. Control Release* 267, 67–79. doi: 10.1016/j.jconrel.2017.09.009

Shim, J., Seok Kang, H., Park, W. S., Han, S. H., Kim, J., and Chang, I. S. (2004). Transdermal delivery of mixnoxidil with block copolymer nanoparticles. *J. Control Release* 97, 477–484. doi: 10.1016/j.jconrel.2004.03.028

Son, J., Yi, G., Yoo, J., Park, C., Koo, H., and Choi, H. S. (2019). Light-responsive nanomedicine for biophotonic imaging and targeted therapy. *Adv. Drug Deliv. Rev.* 138, 133–147. doi: 10.1016/j.addr.2018.10.002

Spill, F., Reynolds, D. S., Kamm, R. D., and Zaman, M. H. (2016). Impact of the physical microenvironment on tumor progression and metastasis. *Curr. Opin. Biotechnol.* 40, 41–48. doi: 10.1016/j.copbio.2016.02.007

Sung, H., Ferlay, J., Siegel, R. L., Laversanne, M., Soerjomataram, I., Jemal, A., et al. (2021). Global cancer statistics 2020: GLOBOCAN estimates of incidence and mortality worldwide for 36 cancers in 185 countries. *CA Cancer J. Clin.* 71, 209–249. doi: 10.3322/caac.21660

Synatschke, C. V., Nomoto, T., Cabral, H., Fortsch, M., Toh, K., Matsumoto, Y., et al. (2014). Multicompartment micelles with adjustable poly(ethylene glycol) shell for efficient in vivo photodynamic therapy. *ACS Nano* 8, 1161–1172. doi: 10.1021/nn4028294

Tanner, P., Baumann, P., Enea, R., Onaca, O., Palivan, C., and Meier, W. (2011). Polymeric vesicles: from drug carriers to nanoreactors and artificial organelles. *Acc. Chem. Res.* 44, 1039–1049. doi: 10.1021/ar200036k

Thambi, T., Deepagan, V. G., Yoon, H. Y., Han, H. S., Kim, S. H., Son, S., et al. (2014). Hypoxia-responsive polymeric nanoparticles for tumor-targeted drug delivery. *Biomaterials* 35, 1735–1743. doi: 10.1016/j.biomaterials.2013.11.022

Thambi, T., Park, J. H., and Lee, D. S. (2016). Stimuli-responsive polymersomes for cancer therapy. *Biomater. Sci.* 4, 55–69. doi: 10.1039/c5bm00268k

Uthaman, S., Huh, K. M., and Park, I. K. (2018). Tumor microenvironment-responsive nanoparticles for cancer theragnostic applications. *Biomater. Res.* 22:22. doi: 10.1186/s40824-018-0132-z

Vaidya, A., Sun, Y., Ke, T., Jeong, E. K., and Lu, Z. R. (2006). Contrast enhanced MRI-guided photodynamic therapy for site-specific cancer treatment. *Magn. Reson. Med.* 56, 761–767. doi: 10.1002/mrm.21009

Valle, J. W., Armstrong, A., Newman, C., Alakhov, V., Pietrzynski, G., Brewer, J., et al. (2011). A phase 2 study of SP1049C, doxorubicin in P-glycoprotein-targeting pluronics, in patients with advanced adenocarcinoma of the esophagus and gastroesophageal junction. *Invest. New Drugs* 29, 1029–1037. doi: 10.1007/s10637-010-9399-1

Vandenbroucke, R. E., and Libert, C. (2014). Is there new hope for therapeutic matrix metalloproteinase inhibition? *Nat. Rev. Drug Discov.* 13, 904–927. doi: 10.1038/nrd4390

Ventola, C. L. (2017). Progress in nanomedicine: approved and investigational nanodrugs. *P T* 42, 742–755.

Vicent, M. J., and Duncan, R. (2006). Polymer conjugates: nanosized medicines for treating cancer. *Trends Biotechnol.* 24, 39–47. doi: 10.1016/j.tibtech.2005.11.006

Vigderman, L., and Zubarev, E. R. (2013). Therapeutic platforms based on gold nanoparticles and their covalent conjugates with drug molecules. *Adv. Drug Deliv. Rev.* 65, 663–676. doi: 10.1016/j.addr.2012.05.004

Wan, Z., Mao, H., Guo, M., Li, Y., Zhu, A., Yang, H., et al. (2014). Highly efficient hierarchical micelles integrating photothermal therapy and singlet oxygen-synergized chemotherapy for cancer eradication. *Theranostics* 4, 399–411. doi: 10.7150/thno.8171

Wang, C., Xu, L., Liang, C., Xiang, J., Peng, R., and Liu, Z. (2014). Immunological responses triggered by photothermal therapy with carbon nanotubes in combination with anti-CTLA-4 therapy to inhibit cancer metastasis. *Adv. Mater.* 26, 8154–8162. doi: 10.1002/adma.201402996

Wang, F., Xiao, J., Chen, S., Sun, H., Yang, B., Jiang, J., et al. (2018). Polymer vesicles: modular platforms for cancer theranostics. *Adv. Mater.* 30:e1705674. doi: 10.1002/adma.201705674

Wang, G. D., Nguyen, H. T., Chen, H., Cox, P. B., Wang, L., Nagata, K., et al. (2016a). X-ray induced photodynamic therapy: a combination of radiotherapy and photodynamic therapy. *Theranostics* 6, 2295–2305. doi: 10.7150/thno.16141

Wang, H. X., Yang, X. Z., Sun, C. Y., Mao, C. Q., Zhu, Y. H., and Wang, J. (2014). Matrix metalloproteinase 2-responsive micelle for siRNA delivery. *Biomaterials* 35, 7622–7634. doi: 10.1016/j.biomaterials.2014.05.050

Wang, J., Yang, G., Guo, X., Tang, Z., Zhong, Z., and Zhou, S. (2014). Redox-responsive polyanhydride micelles for cancer therapy. *Biomaterials* 35, 3080–3090. doi: 10.1016/j.biomaterials.2013.12.025

Wang, R., Yang, H., Khan, A. R., Yang, X., Xu, J., Ji, J., et al. (2021). Redox-responsive hyaluronic acid-based nanoparticles for targeted photodynamic therapy/chemotherapy against breast cancer. *J. Colloid Interface Sci.* 598, 213–228. doi: 10.1016/j.jcis.2021.04.056

Wang, S., Huang, P., and Chen, X. (2016b). Hierarchical targeting strategy for enhanced tumor tissue accumulation/retention and cellular internalization. *Adv. Mater.* 28, 7340–7364. doi: 10.1002/adma.201601498

Wang, S., Huang, P., and Chen, X. (2016c). Stimuli-responsive programmed specific targeting in nanomedicine. *ACS Nano* 10, 2991–2994. doi: 10.1021/acsnano.6b00870

Wang, S., Ma, X., Hong, X., Cheng, Y., Tian, Y., Zhao, S., et al. (2018). Adjuvant photothermal therapy inhibits local recurrences after breast-conserving surgery with little skin damage. *ACS Nano* 12, 662–670. doi: 10.1021/acsnano.7b07757

Wang, Y. A., Li, X. L., Mo, Y. Z., Fan, C. M., Tang, L., Xiong, F., et al. (2018). Effects of tumor metabolic microenvironment on regulatory T cells. *Mol. Cancer* 17:168. doi: 10.1186/s12943-018-0913-y

Wang, Y., Xie, Y., Li, J., Peng, Z. H., Sheinin, Y., Zhou, J., et al. (2017). Tumor-penetrating nanoparticles for enhanced anticancer activity of combined photodynamic and hypoxia-activated therapy. *ACS Nano* 11, 2227–2238. doi: 10.1021/acsnano.6b08731

Wang, Z., Niu, G., and Chen, X. (2014). Polymeric materials for theranostic applications. *Pharm. Res.* 31, 1358–1376. doi: 10.1007/s11095-013-1103-7

Wei, J., Shuai, X., Wang, R., He, X., Li, Y., Ding, M., et al. (2017). Clickable and imageable multiblock polymer micelles with magnetically guided and PEG-switched targeting and release property for precise tumor theranosis. *Biomaterials* 145, 138–153. doi: 10.1016/j.biomaterials.2017.08.005

Weiss, G. J., Chao, J., Neidhart, J. D., Ramanathan, R. K., Bassett, D., Neidhart, J. A., et al. (2013). First-in-human phase 1/2a trial of CRLX101, a cyclodextrin-containing polymer-camptothecin nanopharmaceutical in patients with advanced solid tumor malignancies. *Invest. New Drugs* 31, 986–1000. doi: 10.1007/s10637-012-9921-8

Wen, C. J., Zhang, L. W., Al-Suwayeh, S. A., Yen, T. C., and Fang, J. Y. (2012). Theranostic liposomes loaded with quantum dots and apomorphine for brain targeting and bioimaging. *Int. J. Nanomed.* 7, 1599–1611. doi: 10.2147/IJN.S29369

Wong, B. S., Yoong, S. L., Jagusiak, A., Panczyk, T., Ho, H. K., Ang, W. H., et al. (2013). Carbon nanotubes for delivery of small molecule drugs. *Adv. Drug Deliv. Rev.* 65, 1964–2015. doi: 10.1016/j.addr.2013.08.005

Wong, P. T., and Choi, S. K. (2015). Mechanisms of drug release in nanotherapeutic delivery systems. *Chem. Rev.* 115, 3388–3432. doi: 10.1021/cr5004634

Xie, A., Hanif, S., Ouyang, J., Tang, Z., Kong, N., Kim, N. Y., et al. (2020). Stimuli-responsive prodrug-based cancer nanomedicine. *EBioMedicine* 56:102821. doi: 10.1016/j.ebiom.2020.102821

Xie, J., Lee, S., and Chen, X. (2010). Nanoparticle-based theranostic agents. *Adv. Drug Deliv. Rev.* 62, 1064–1079. doi: 10.1016/j.addr.2010.07.009

Xing, H., Hwang, K., and Lu, Y. (2016). Recent developments of liposomes as nanocarriers for theranostic applications. *Theranostics* 6, 1336–1352. doi: 10.7150/thno.15464

Xiong, X. B., and Lavasanifar, A. (2011). Traceable multifunctional micellar nanocarriers for cancer-targeted co-delivery of MDR-1 siRNA and doxorubicin. *ACS Nano* 5, 5202–5213. doi: 10.1021/nn2013707

Xu, C., Jiang, Y., Han, Y., Pu, K., and Zhang, R. (2021). A polymer multicellular nanoengager for synergistic NIR-II photothermal immunotherapy. *Adv. Mater.* 33:e2008061. doi: 10.1002/adma.202008061

Yang, Y. (2015). Cancer immunotherapy: harnessing the immune system to battle cancer. *J. Clin. Invest.* 125, 3335–3337. doi: 10.1172/JCI83871

Yong, Y., Cheng, X., Bao, T., Zu, M., Yan, L., Yin, W., et al. (2015). Tungsten sulfide quantum dots as multifunctional nanotheranostics for in vivo dual-modal image-guided photothermal/radiotherapy synergistic therapy. *ACS Nano* 9, 12451–12463. doi: 10.1021/acsnano.5b05825

Yousef, S., Alsaab, H. O., Sau, S., and Iyer, A. K. (2018). Development of asialoglycoprotein receptor directed nanoparticles for selective delivery of curcumin derivative to hepatocellular carcinoma. *Heliyon* 4:e01071. doi: 10.1016/j.heliyon.2018.e01071

Yu, J., Chu, X., and Hou, Y. (2014). Stimuli-responsive cancer therapy based on nanoparticles. *Chem. Commun.* 50, 11614–11630. doi: 10.1039/c4cc03984j

Yu, Y., Zhang, X., and Qiu, L. (2014). The anti-tumor efficacy of curcumin when delivered by size/charge-changing multistage polymeric micelles based on amphiphilic poly(beta-amino ester) derivates. *Biomaterials* 35, 3467–3479. doi: 10.1016/j.biomaterials.2013.12.096

Yu, Z., Sun, Q., Pan, W., Li, N., and Tang, B. (2015). A near-infrared triggered nanophotosensitizer inducing domino effect on mitochondrial reactive oxygen

species burst for cancer therapy. *ACS Nano* 9, 11064–11074. doi: 10.1021/acsnano.5b04501

Yuan, Y. Y., Mao, C. Q., Du, X. J., Du, J. Z., Wang, F., and Wang, J. (2012). Surface charge switchable nanoparticles based on zwitterionic polymer for enhanced drug delivery to tumor. *Adv. Mater.* 24, 5476–5480. doi: 10.1002/adma.201202296

Zhang, P., Gao, D., An, K., Shen, Q., Wang, C., Zhang, Y., et al. (2020). A programmable polymer library that enables the construction of stimuli-responsive nanocarriers containing logic gates. *Nat. Chem.* 12, 381–390. doi: 10.1038/s41557-020-0426-3

Zhang, X., Han, L., Liu, M., Wang, K., Tao, L., Wan, Q., et al. (2017). Recent progress and advances in redox-responsive polymers as controlled delivery nanoplatforms. *Mater. Chem. Front.* 1, 807–822. doi: 10.1039/C6QM00135A

Zhang, Y., Bo, S., Feng, T., Qin, X., Wan, Y., Jiang, S., et al. (2019). A versatile theranostic nanoemulsion for architecture-dependent multimodal imaging and dually augmented photodynamic therapy. *Adv. Mater.* 31:e1806444. doi: 10.1002/adma.201806444

Zhao, H., Duong, H. H., and Yung, L. Y. (2010). Folate-conjugated polymer micelles with pH-triggered drug release properties. *Macromol. Rapid Commun.* 31, 1163–1169. doi: 10.1002/marc.200900876

Zheng, Y., Li, S., Weng, Z., and Gao, C. (2015). Hyperbranched polymers: advances from synthesis to applications. *Chem. Soc. Rev.* 44, 4091–4130. doi: 10.1039/c4cs00528g

Zhou, Q., Zhang, L., Yang, T., and Wu, H. (2018). Stimuli-responsive polymeric micelles for drug delivery and cancer therapy. *Int. J. Nanomed.* 13, 2921–2942. doi: 10.2147/IJN.S158696

Zhu, L., Perche, F., Wang, T., and Torchilin, V. P. (2014). Matrix metalloproteinase 2-sensitive multifunctional polymeric micelles for tumor-specific co-delivery of siRNA and hydrophobic drugs. *Biomaterials* 35, 4213–4222. doi: 10.1016/j.biomaterials.2014.01.060

Zhu, L., Wang, T., Perche, F., Taigind, A., and Torchilin, V. P. (2013). Enhanced anticancer activity of nanopreparation containing an MMP2-sensitive PEG-drug conjugate and cell-penetrating moiety. *Proc. Natl. Acad. Sci. U.S.A.* 110, 17047–17052. doi: 10.1073/pnas.1304987110

Zielinska, A., Carreiro, F., Oliveira, A. M., Neves, A., Pires, B., Venkatesh, D. N., et al. (2020). Polymeric nanoparticles: production, characterization, toxicology and ecotoxicology. *Molecules* 25:3731. doi: 10.3390/molecules25163731

Conflict of Interest: The authors declare that the research was conducted in the absence of any commercial or financial relationships that could be construed as a potential conflict of interest.

frontiers in Bioengineering and Biotechnology

BRIEF RESEARCH REPORT
published: 30 June 2021
doi: 10.3389/fbioe.2021.690747

Sensitive Detection of Single-Nucleotide Polymorphisms by Solid Nanopores Integrated With DNA Probed Nanoparticles

*Ling Zhi Wu[1,2], Yuan Ye[1], Zhi Xuan Wang[2], Die Ma[1], Li Li[1], Guo Hao Xi[1], Bi Qing Bao[1] and Li Xing Weng[2]**

[1] Key Laboratory for Organic Electronics and Information Displays, Jiangsu Key Laboratory for Biosensors, Institute of Advanced Materials, National Synergetic Innovation Center for Advanced Materials, Nanjing University of Posts and Telecommunications, Nanjing, China, [2] College of Geography and Biological Information, Nanjing University of Posts and Telecommunications, Nanjing, China

OPEN ACCESS

Edited by:
Junjie Li,
Innovation Center of NanoMedicine (iCONM), Japan

Reviewed by:
Yi Cao,
Nanjing University, China
Dongbao Yao,
University of Science and Technology of China, China
Cheng Zhang,
Peking University, China

***Correspondence:**
Li Xing Weng
lxweng@njupt.edu.cn

Specialty section:
This article was submitted to Nanobiotechnology, a section of the journal Frontiers in Bioengineering and Biotechnology

Received: 23 April 2021
Accepted: 21 May 2021
Published: 30 June 2021

Citation:
Wu LZ, Ye Y, Wang ZX, Ma D, Li L, Xi GH, Bao BQ and Weng LX (2021) Sensitive Detection of Single-Nucleotide Polymorphisms by Solid Nanopores Integrated With DNA Probed Nanoparticles. Front. Bioeng. Biotechnol. 9:690747. doi: 10.3389/fbioe.2021.690747

Single-nucleotide polymorphisms (SNPs) are the abundant forms of genetic variations, which are closely associated with serious genetic and inherited diseases, even cancers. Here, a novel SNP detection assay has been developed for single-nucleotide discrimination by nanopore sensing platform with DNA probed Au nanoparticles as transport carriers. The SNP of p53 gene mutation in gastric cancer has been successfully detected in the femtomolar concentration by nanopore sensing. The robust biosensing strategy offers a way for solid nanopore sensors integrated with varied nanoparticles to achieve single-nucleotide distinction with high sensitivity and spatial resolution, which promises tremendous potential applications of nanopore sensing for early diagnosis and disease prevention in the near future.

Keywords: single nucleotide polymorphism, gold nanoparticle, gastric cancer, solid nanopore, DNA probe

INTRODUCTION

Single-nucleotide polymorphisms (SNPs) primarily refer to single-nucleotide substitution that constitutes the most common genetic variation, with an average occurrence of ∼1/1,000 base pairs, which are closely associated with various cancers and tumors (Liu et al., 2017; Varona and Anderson, 2019; Megalathan et al., 2021). As an important biomarker, numerous methods have been developed for detecting SNPs. The conventional approaches are polymerase chain reaction amplification and sequencing, which are adequate to know each gene site of DNA fragment, but overqualified with being time-consuming and costly (Halperin and Stephan, 2009; Maguin and Marraffini, 2021). A variety of biosensors have been performed involving fluorescent labeling, chemiluminescence, and microassays (Liu et al., 2017; Tian et al., 2018; Zhou et al., 2020; Zhang et al., 2021). However, the photoelectric signals obtained from these methodologies have relatively low specificity and false-positive probability for single-nucleotide discrimination in pathogenic mutants. Hence, novel SNP assays with respect to simplicity, sensitivity, high throughput, and low cost are still in demand for the earlier diagnosis and clinical prognostics.

As an emerging single-molecule detection technology, nanopores are promising sensors for DNA identification, proteomic detection, determination of epigenetic changes, and biomolecular mechanism exploration with the advantages of being label-free and high-throughput

(Wang et al., 2017; Jeong et al., 2019; Spitzberg et al., 2019; Chen et al., 2021; Fragasso et al., 2021; Hu et al., 2021). The nanopore technique is inspired by the transmembrane protein channels embedded in lipid bilayers that allow ions and molecules inside and outside the living cell to exchange freely. Based on the pore materials, nanopores have been developed into two major types of biological and solid-state pores, and both take their respective advantages to achieve single-molecule identification toward clinical detection (Wang et al., 2017, 2018, 2020; Meng et al., 2019). However, the spatial and temporal resolution of individual nucleotides discriminated by nucleotide-specific current signals remains a challenge for nanopore sensing. For instance, the natural fixed pore size and instability of biological nanopores limit their sensing application. For solid nanopores with mechanical robustness and size controllability, the accuracy and the limited bandwidth of the current measurement systems are technical hurdles at single-nucleotide resolution. In this study, a novel SNP assay system has been proposed based on the nanopore readout platform integrated with DNA-probed gold nanoparticles. The functionalized Au nanoparticle is suitable for a good transport model for nanopore sensing. For instance, Au nanoparticles with a certain volume can produce distinct ionic current signatures through nanopores. Moreover, nanoparticles loaded with DNA probes facilitate molecular translocation to improve accuracy and the signal-to-noise ratio. The DNA probes wrapped on Au nanoparticles favor hybridization with SNP sequences with a high selectivity for single-nucleotide discrimination (Ang and Lanry Yung, 2012; Venta et al., 2013, 2014; Karmi et al., 2021). The perfectly matched hybridization of SNP sequences with DNA probes absorbed on Au nanoparticles will trigger the nanoparticle assembly to form dimers. The distinction of SNP mutations can be easily achieved by observing the differences of signals between the monomers and dimers of nanoparticles translocated through the hole by a nanopore platform. Thus, with high selectivity, efficiency, and simplicity, this method can be used to successfully distinguish single-nucleotide variations of DNA targets independent of the nanopore morphology.

MATERIALS AND METHODS

Materials

The chemicals used in this experiment were obtained from commercial sources: trisodium citrate dihydrate (Fisher), $HAuCl_4.3H_2O$ (Sigma), KCl (Sigma-Aldrich), concentrated sulfuric acid (Sinopharm Chemical Reagent Co., Ltd.), aquaehydrogenii dioxide (Sinopharm Chemical Reagent Co., Ltd.), and bis(p-sulfonatophenyl)phenylphosphine dihydrate dipotassium salt (BSPP) (Sigma-Aldrich, St Louis, MO, United States). All DNA oligonucleotides were synthesized by Shanghai Sangon Biotechnology Co., Ltd. (Shanghai, China). The sequences of DNA probes are PolyA-1 (60AGCGGACTCCAACACTCCGT) and PolyA-2 (60ACTGCCCATGGTGGGGGCAG), respectively. The wild target (P53WT) of the p53 gene is GAGGTTGTGAGGCGCTGCCCCCACCATG, and that of SNP targets (P53MU) is GAGGTTGTGAGGC ACTGCCCCCACCATG. Au nanoparticles were purchased from Ted Pella (Redding, CA, United States). Milli-Q super-purified water with a resistance >18 MΩ/cm was used in all the experiments.

Preparation of DNA Modified Au Nanoparticles

The Au nanoparticles were firstly protected using phosphine moiety bis(p-sulfonatophenyl) phenylphosphine to increase their stability, as previously described (Zhu et al., 2016; Chen et al., 2017). These phosphine-coated Au nanoparticles were incubated with diblock DNA with a 1:10 ratio for 16 h with gently shaking at room temperature. Then, 1 M of sodium phosphate buffer (1 M of NaCl, 100 mM of Na_2HPO_4, and NaH_2PO_4, pH 7.4) was added into the DNA/Au nanoparticle mixture for five times with a 30-min interval to reach a final concentration of 100 mM NaCl. This mixture was incubated for 24 h at room temperature. Next, the resulting mixture was centrifuged at 12,000 rpm for 20 min to remove excess DNA. The nanoparticles were resuspended in 0.1 M sodium phosphate buffer (PBS, 0.1 M of NaCl, 10 mM of Na_2HPO_4, and NaH_2PO_4, pH 7.4). The DNA-functioned Au nanoparticles were also characterized by scanning electron microscope (SEM) images from Axiostar Plus (Zeiss Axiostar Plus).

Nanopore Fabrication and Data Acquisition

The nanopores used in all our experiments were fabricated using focused-ion-beam drilling with Ga^+ ions. The resulting pores were visualized through SEM Axiostar plus (ZEISS Axiostar plus). Chips were cleaned in piranha solution (3:1 v/v H_2SO_4:H_2O_2) at 80°C for 30 min in order to remove organic contaminants and to facilitate pore wetting. The prepared nanopore chips were then sealed into polydimethylsiloxane (PDMS) microfluidic channels. The Ag/AgCl electrodes were put in each chamber to connect to a pico-Ampere current amplifier Axopatch 700B (Molecular Devices), which applied a transmembrane voltage and recorded the nanopore ion current.

RESULTS AND DISCUSSION

Design of DNA Probe Wrapped on Au Nanoparticles

The sensing principle of single-nucleotide discrimination based on the nanopore platform is illustrated in **Figure 1A**. A diblock DNA probe has been designed to perfectly match with SNP targets. The probe consists of a binding chain of polyA sequences and a capture chain of complementary sequences. The polyA block naturally adheres to the gold surface via adenine adsorption. By rational design of the polyA length, the gold nanoparticles are wrapped by DNA probes at single-molecular level, and the appended recognition blocks with an upright conformation favor DNA recognition (Qin and Lanry Yung, 2007; Yao et al., 2015; Zhu et al., 2016;

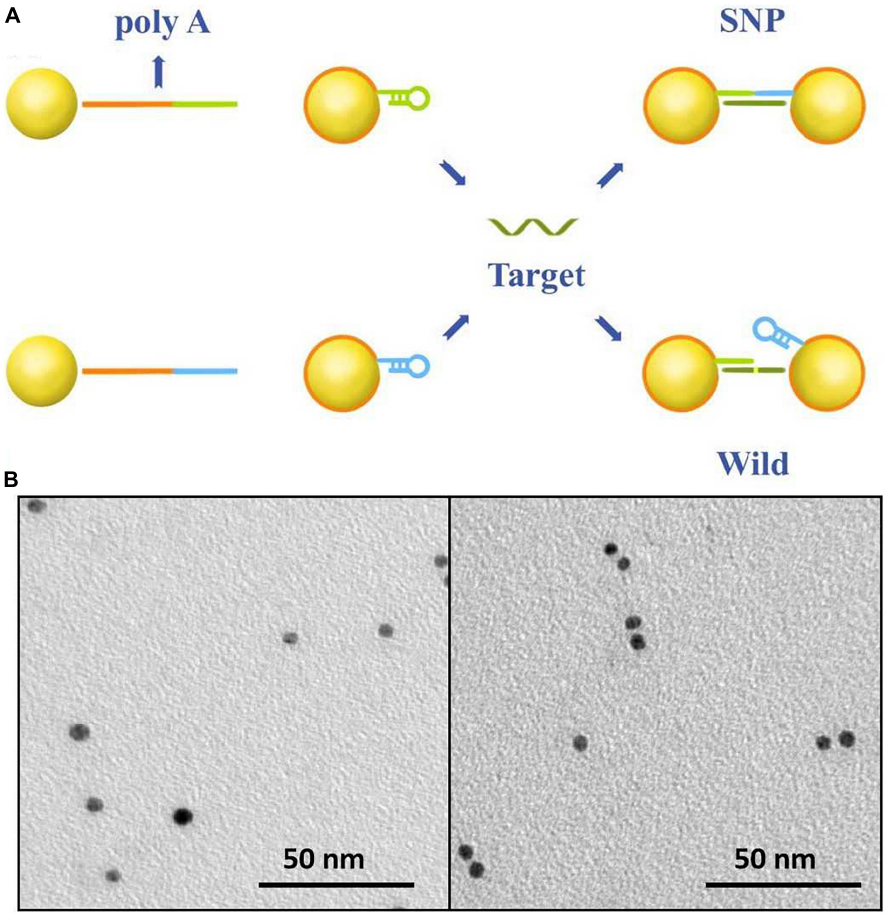

FIGURE 1 | (A) The work principle of the SNP detection system. The Au nanoparticles firstly were labeled by blocking DNA strands with the poly-adenine (polyA) block (red) and the recognition (blue and green). One block of polyA oligonucleotide could strongly absorb on the surface of gold nanoparticles; the other was designed to perfectly complementarily hybridize with SNP targets and mismatch to the wild-type targets. **(B)** SEM images of DNA-probed Au nanoparticles with wild targets in the form of monomer and SNP targets in the form of dimer.

Chen et al., 2017). The recognition strands in blue and green are perfectly complementary to SNP targets and spontaneously form hairpin structures to reduce non-specific adsorption between nucleotide sequences. After addition of SNP targets, DNA probes immobilized on the nanoparticles preferentially capture SNP targets by the perfectly matched sequence hybridization. A set of discrete Au-DNA conjugate dimers have been formed via DNA-hybridizing fragments as linkers. The wild-type target with a mismatched base is hard to open the hairpin structure and initiates self-assembly of Au nanoparticles. Thus, the Au-DNA probe has a high selectivity to discriminate the SNP and wild targets.

The recognition of the Au-DNA probes and targets is verified in **Figure 1B**. It is clear that Au nanoparticles are dispersed as monomers in the aqueous solution prior to the addition of wild-type and mutation targets. Once the SNP targets are added, DNA probes anchored on the Au particles are opened and perfectly hybridized with SNP sequences to link two Au spheres into a dimer, while the recognition of the DNA probe is hard to initiate hybridization reaction owing to sequence mismatch with wild targets. The results are further verified in light of the scattering spectra. The diameter of Au nanoparticles in mixture ranges from 5 to 10 nm after SNP targets hybridized with DNA probes. Hence, the designed DNA probes anchored on Au nanoparticles are suitable to capture SNP sequences and the discrete conjugate complex can be identified by the nanopore platform with a high selectivity for single-nucleotide discrimination.

Discrimination of Wild and Mutant Targets in Nanopore Sensing

After the hybridization of DNA probes on the nanoparticles with wild and SNP targets, the nanoparticles in the form of monomers and dimers have been transported to the nanopore platform to pick up individual distinct signals for SNP detection. In the nanopore device, the prepared nanoparticle samples have been added into reservoirs and driven through an orifice separated by a silicon nitride membrane sandwiched between two Ag/AgCl electrodes. The ionic current flowing through the nanopores is momentarily interrupted as particles pass through the pore. Thus, a set of upward pulses are observed in the current–time traces

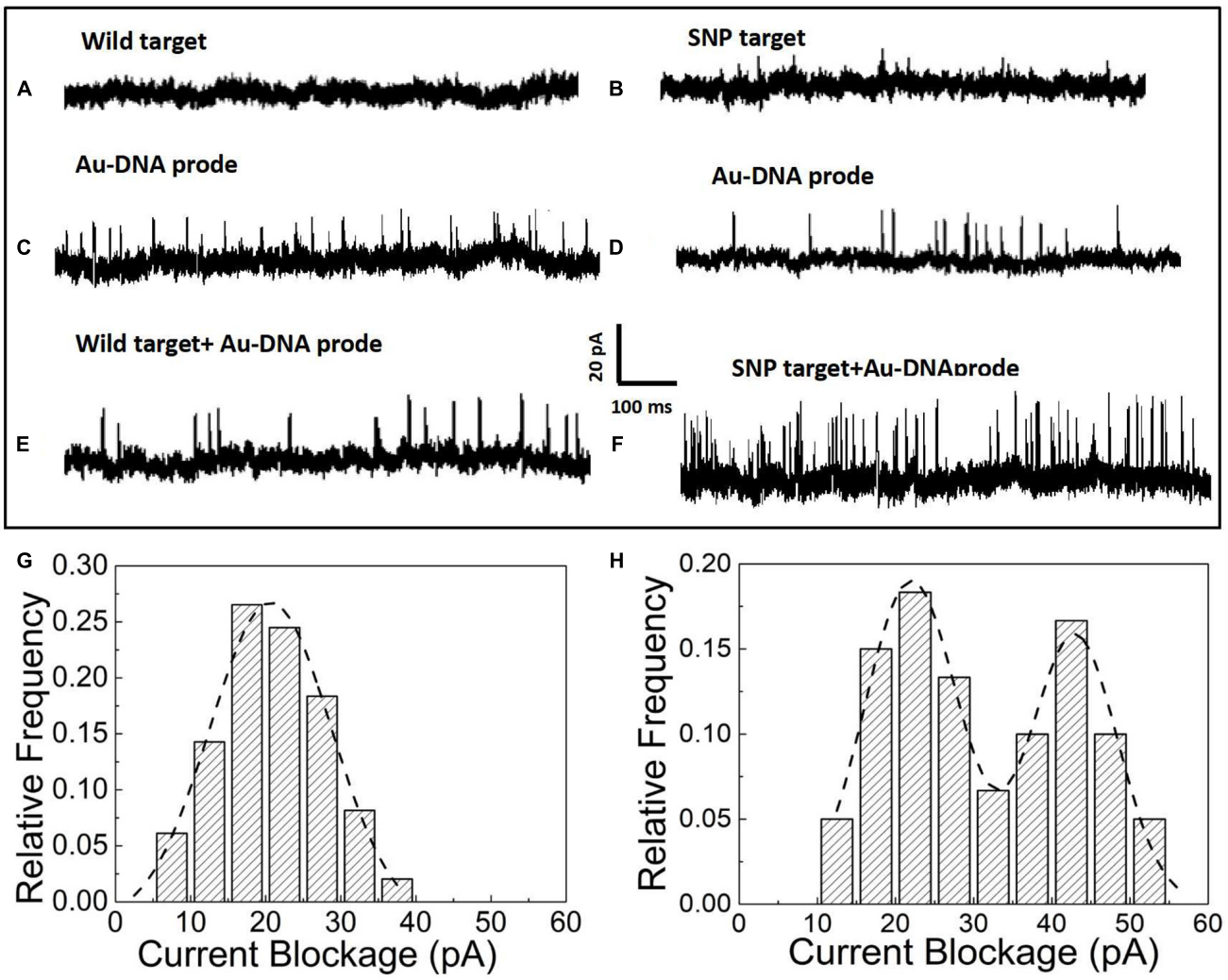

FIGURE 2 | (A) Current signal in the presence of wild targets. **(B)** Current signal in the presence of SNP targets. **(C)** Current signal in the presence of the Au-DNA probe. **(D)** Current signal in the presence of Au-DNA probes. **(E)** Current signal in the presence of wild targets with Au-DNA probes. **(F)** Current signal in the presence of SNP targets with Au-DNA probes. **(G)** Histograms of the blocked current amplitudes with wild targets. **(H)** Histograms of the blocked current amplitudes with SNP targets.

shown in **Figure 2**. The nanopore with a diameter of 35 ± 3 nm is used to capture the Au particles into the pore and acquires the optimal current pulses with a high signal-to-noise ratio. In **Figures 2A,B**, as pure wild and SNP targets are loaded into the reservoirs, no blockage signals appear in the current trace since the short DNA fragments of a dozen nucleotide bases are too small to generate discernable signals in voltage clamp mode. However, the addition of Au nanoparticles with DNA probes triggers a series of current pulse signals, shown in **Figures 2C,D**. The blockage current is induced by Au nanoparticles flowing into the pore in the form of monomers. After addition of wild and SNP targets as shown in **Figures 2E,F**, the blocked current signals have been enhanced as SNP targets are hybridized with complementary DNA probes wrapped on the Au nanoparticles, while the current pulses in the presence of wild targets are still similar to that of Au-DNA probes.

The blockage signals from individual particle translocations can be distinguished by the time duration (t_d) and the magnitude of the blockage current (I_b). The histograms of the magnitude and dwell time of the translocation events have been statistically sorted to plot the columnar statistical graphs, as shown in **Figures 2G,H**. The amplitude distribution of blockage events is fitted by Gaussian models. Based on the fitting curves, the peak values of the blocked current are maximized at 20 ± 2 pA, which corresponds to the most probable current drops induced by monomer particles through the nanopore at biased voltages. Once the SNP targets are added and react with the DNA probes, an intriguing phenomenon of double peaks appear in the current blockage statistics histograms. One of the peaks at 19 ± 3 pA is clearly similar to the most probable amplitude intensity of the blocked current events induced by monomer nanoparticles. A larger peak at the current of 41 ± 5 pA appears, which is

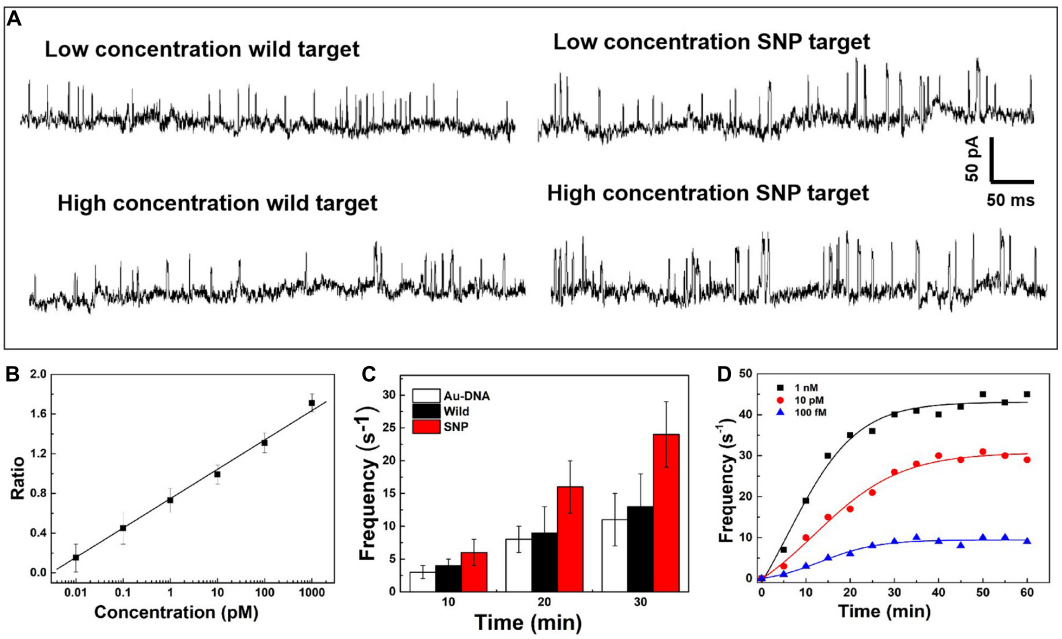

FIGURE 3 | (A) Current signals in the presence of the SNP target and wild target at low and high concentrations. **(B)** Log plot of the capture ratio of the dimer and monomer obtained from blockage current versus SNP concentrations. **(C)** Signal frequency versus experimental time. **(D)** The capture frequency of blocking events dependent on time at different concentrations.

about twice as large as the first peak. Based on the volume exclusion theory of the particles entering the pore, the blockade signals are directly proportional to the particle volume as the following formula: $\Delta I_b(t) = -\frac{\sigma\phi}{H_{eff}^2}\Lambda(t)[1 + f(\frac{d_m}{D_p}, \frac{l_m}{H_{eff}})]$, where σ is the solution conductivity, ϕ is the applied voltage between the electrodes, Λ is the excluded volume of a translocation particle inside the pore, H_{eff} is the effective length of the nanopore, d_m is the diameter, l_m is the length of a particle molecule, D_p is the nanopore diameter, and $f(d_m/D_p, l_m/H_{eff})$ is a correction factor (Talaga and Li, 2009). It is clear that Au nanoparticles are assembled into dimers by the hybridization between SNP and DNA probes. Thus, the smaller of the current peaks appears owing to monomer particle translocation, while the larger one arises from the assembled dimers passing into the pore.

Quantification of the Targets

On the nanopore readout platform, single-nucleotide discrimination between SNP and wild targets has been detected by the signal amplification of the DNA-probed nanoparticles as transport carriers through the nanopore. Considering the high-sensitivity demand in the earlier stage of cancer and tumor diagnosis, the change of the current signals has been further explored dependent on the concentration of SNP targets, as shown in **Figure 3A**. The ionic current fluctuation is observed as the DNA-probed Au nanoparticles are added into the pore, and a set of spike-like signals appears due to the volume exclusion effect of gold spheres passing through the nanopore one by one. After addition of SNP and wild targets, the recorded current trace shows an obvious change at low and high concentrations of targets. For addition of wild targets, the current trace is similar to the previous signals caused by individual Au-DNA nanoparticles. There is no visible change of the blockage current recording even though the concentration of the wild targets is increasing. The binding block of DNA probes hardly unfold the hairpin structure owing to the base-pair mismatch with wild targets. In contrast, more spike-like current signals continuously appear as increasing SNP targets. It is further verified that the designed DNA probes have high selectivity for SNP targets. From the statistical histogram of a large number of current pulse signals, the blockage current events with greater intensity and longer duration are characterized as a larger Gaussian peak position. The capture ratio of the dimer and monomer obtained from the statistical histogram of blockage current has been log-plotted as a function of SNP target concentration, as shown in **Figure 3B**. There is a linear relationship with SNP concentration increasing. At high SNP concentration, the capture frequency of dimers is greater than that of monomers, which indicates that the dimers formed by Au nanoparticle self-assembly are superior in mixed aqueous solution. The capture ratio is gradually reduced when the probability of the dimer formation is reduced with decreasing SNP concentration. By virtue of the nanopore–nanoparticle integrated approach, the SNP of the p53 gene mutation in gastric cancer is detected as low as to femtomolar under the experimental conditions. The sensitive detection limit is sufficient for the early diagnosis and treatment of cancers.

After the quantitative determination of SNP targets, experimental factors such as time and voltage have also been evaluated to optimize the detection accuracy. The reaction dynamics of the SNP assay has been checked in our experiments,

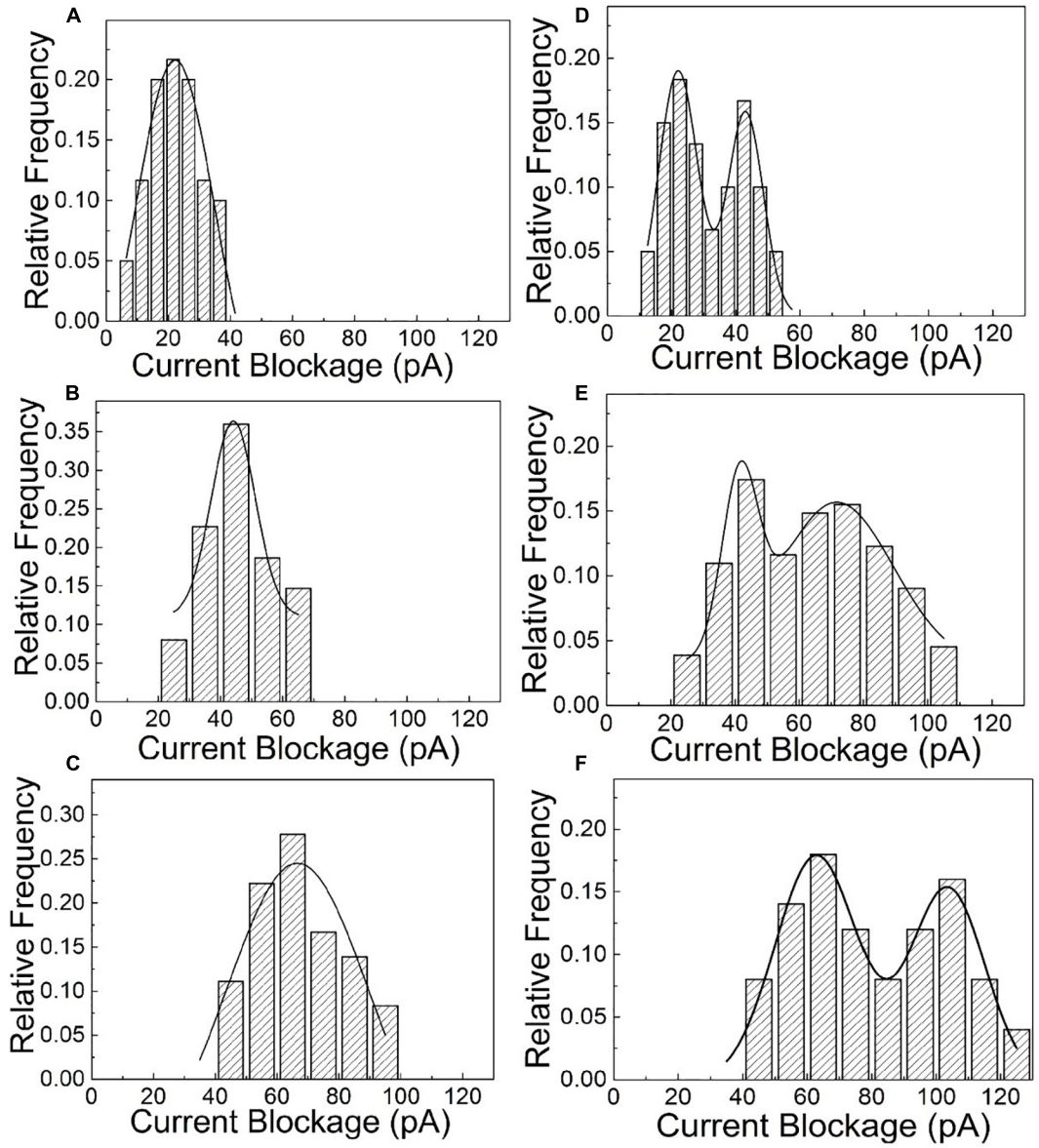

FIGURE 4 | The statistical amplitude histograms of the blocked translocation events for wild-type and mutant targets as the function of biased voltages. **(A–C)** Are statistical graphs at 250, 500, and 700 mV for wild-type targets, respectively. **(D–F)** Are statistical graphs at 250, 500, and 700 mV for SNP targets, respectively.

as shown in **Figures 3C,D**. The recognition response is rapid in the presence of SNP targets. The capture frequency is growing over time and saturated after 30 min. The capture frequency is much higher after adding SNP targets. The DNA-probed Au nanoparticles are stable in aqueous solution, and the self-assembled dimers are stabilized by the strong binding affinity of the complementary hybridization between the DNA-Au probe and SNP sequences. Likewise, the capture frequency of the SNP targets has been explored at different voltages in **Figure 4**. The results display that a single peak of the magnitude distribution for wild targets is not influenced at the varied voltages, but the peak value increases with voltage increasing, which is in line with Ohm's law of nanopore devices. For SNP targets, the double peaks of the magnitude distribution always exhibit at different biased voltages, and the capture rates of monomer and dimer particles are all enhanced at high voltages. The Au nanoparticles with appreciable size can produce distinct ionic current signatures through nanopores with a high signal-to-noise ratio.

CONCLUSION

Single-nucleotide polymorphisms are the most abundant genetic variation, which are responsible for genetic disease prevalent in a population. Therefore, the detection of the subtle single-nucleotide discrimination is important to the earlier diagnosis

and treatment of critical illness. In our work, a sensitive SNP detection system has been established by silicon nitride nanopore platform integrated with DNA-probed gold nanoparticles. The readout of single-nucleotide discrimination in nanopore sensing has been converted into the amplified signals of varied nanoparticles with comparable volume to the used nanopore. The DNA probes absorbed on nanoparticles have high selectivity and sensitivity to the SNP targets. Hence, the SNP of the p53 gene mutation in gastric cancer has been detected in the femtomolar concentration. In the same way, the robust nanopore biosensing strategy can be adapted to detect broad DNA mutations from diagnostics to targeted therapy of cancers.

DATA AVAILABILITY STATEMENT

The original contributions presented in the study are included in the article/**Supplementary Material**, further inquiries can be directed to the corresponding author.

AUTHOR CONTRIBUTIONS

YY, GX, ZW, DM, and LL did the experiments and data processing. LZW, BB, and LXW were involved in the data analysis and manuscript writing. All authors equally contributed to the manuscript and participated in the results and discussion.

FUNDING

This work was financially supported by the National Key Research and Development Program of China (2017YFA0205301 and 2017YFA0205302), the Key Research and Development Program of Jiangsu (BE2018732), the Priority Academic Program Development of Jiangsu Higher Education Institutions (PAPD, YX030003), the open research fund of Jiangsu Key Laboratory for Biosensors (51204080), the Project of Nanjing University of Posts and Telecommunications (NY220222 and 2020XZZ16), and the Open Research Fund of State Key Laboratory of Bioelectronics, Southeast University (OPSKLB202012).

SUPPLEMENTARY MATERIAL

The Supplementary Material for this article can be found online at: https://www.frontiersin.org/articles/10.3389/fbioe.2021.690747/full#supplementary-material

REFERENCES

Ang, Y. S., and Lanry Yung, L. Y. (2012). Rapid and label-free single-nucleotide discrimination via an integrative nanoparticle-nanopore approach. *ACS Nano* 6, 8815–8823. doi: 10.1021/nn302636z

Chen, K., Gularek, F., Liu, B., Weinhold, E., and Keyser, U. F. (2021). Electrical DNA sequence mapping using oligodeoxynucleotide labels and nanopores. *ACS Nano* 15, 2679–2685. doi: 10.1021/acsnano.0c07947

Chen, L., Chao, J., Qu, X., Zhang, H., Zhu, D., Su, S., et al. (2017). Probing cellular molecules with polyA-based engineered aptamer nanobeacon. *ACS Appl. Mater. Interfaces* 9, 8014–8020. doi: 10.1021/acsami.6b16764

Fragasso, A., de Vries, H. W., Andersson, J., van der Sluis, E. O., van der Giessen, E., Dahlin, A., et al. (2021). A designer FG-Nup that reconstitutes the selective transport barrier of the nuclear pore complex. *Nat. Commun.* 12:2010. doi: 10.1038/s41467-021-22293-y

Halperin, E., and Stephan, D. A. (2009). SNP imputation in association studies. *Nat. Biotechnol.* 27, 349–351. doi: 10.1038/nbt0409-349

Hu, Z. L., Huo, M. Z., Ying, Y. L., and Long, Y. T. (2021). Biological nanopore approach for single-molecule protein sequencing. *Angew. Chem.* 133. doi: 10.1002/ange.202013462

Jeong, K. B., Luo, K., Lee, H., Lim, M. C., Yu, J., Choi, S. J., et al. (2019). Alpha-hederin nanopore for single nucleotide discrimination. *ACS Nano* 13, 1719–1727. doi: 10.1021/acsnano.8b07797

Karmi, A., Dachlika, H., Sakala, G. P., Rotem, D., Reches, M., and Porath, D. (2021). Detection of Au nanoparticles using peptide-modified Si_3N_4 nanopores. *ACS Appl. Nano Mater.* 4, 1000–1008. doi: 10.1021/acsanm.0c02126

Liu, J., Lu, Y., Wang, S., Zhang, S., Zhu, X., Sheng, L., et al. (2017). Pinpoint the positions of single nucleotide polymorphisms by a nanocluster dimer. *Anal. Chem.* 89, 2622–2627. doi: 10.1021/acs.analchem.6b04981

Maguin, P., and Marraffini, L. A. (2021). From the discovery of DNA to current tools for DNA editing. *J. Exp. Med.* 218:e20201791. doi: 10.1084/jem.20201791

Megalathan, A., Wijesinghe, K. M., and Dhakal, S. (2021). Single-molecule FRET-based dynamic DNA sensor. *ACS Sens.* 6, 1367–1374. doi: 10.1021/acssensors.1c00002

Meng, F. N., Ying, Y. L., Yang, J., and Long, Y. T. (2019). A wild-type nanopore sensor for protein kinase activity. *Anal. Chem.* 91, 9910–9915. doi: 10.1021/acs.analchem.9b01570

Qin, W. J., and Lanry Yung, L. Y. (2007). Nanoparticle-based detection and quantification of DNA with single nucleotide polymorphism (SNP) discrimination selectivity. *Nucleic Acids Res.* 35:e111. doi: 10.1093/nar/gkm602

Spitzberg, J. D., Zrehen, A., van Kooten, X. F., and Meller, A. (2019). Plasmonic-nanopore biosensors for superior single-molecule detection. *Adv. Mater.* 31:e1900422. doi: 10.1002/adma.201900422

Talaga, D. S., and Li, J. (2009). Single-molecule protein unfolding in solid state nanopores. *J. Am. Chem. Soc.* 131, 9287–9297. doi: 10.1021/ja901088b

Tian, K., Chen, X., Luan, B., Singh, P., Yang, Z., Gates, K. S., et al. (2018). Single locked nucleic acid-enhanced nanopore genetic discrimination of pathogenic serotypes and cancer driver mutations. *ACS Nano* 12, 4194–4205. doi: 10.1021/acsnano.8b01198

Varona, M., and Anderson, J. L. (2019). Visual detection of single-nucleotide polymorphisms using molecular beacon loop-mediated isothermal amplification with centrifuge-free DNA extraction. *Anal. Chem.* 91, 6991–6995. doi: 10.1021/acs.analchem.9b01762

Venta, K., Wanunu, M., and Drndić, M. (2013). Electrically controlled nanoparticle synthesis inside nanopores. *Nano Lett.* 13, 423–429. doi: 10.1021/nl303576q

Venta, K. E., Zanjani, M. B., Ye, X., Danda, G., Murray, C. B., Lukes, J. R., et al. (2014). Gold nanorod translocations and charge measurement through solid-state nanopores. *Nano Lett.* 14, 5358–5364. doi: 10.1021/nl502448s

Wang, S., Wang, Y., Yan, S., Du, X., Zhang, P., Chen, H. Y., et al. (2020). Retarded translocation of nucleic acids through α-Hemolysin nanopore in the presence of a calcium flux. *ACS Appl. Mater. Interfaces* 12, 26926–26935. doi: 10.1021/acsami.0c05626

Wang, Y., Gu, L. Q., and Tian, K. (2018). The aerolysin nanopore: from peptidomic to genomic applications. *Nanoscale* 10, 13857–13866. doi: 10.1039/c8nr04255a

Wang, Y., Tian, K., Shi, R., Gu, A., Pennella, M., Alberts, L., et al. (2017). Nanolock-nanopore facilitated digital diagnostics of cancer driver mutation in tumor tissue. *ACS Sens.* 2, 975–981. doi: 10.1021/acssensors.7b00235

Yao, G., Pei, H., Li, J., Zhao, Y., Zhu, D., Zhang, Y., et al. (2015). Clicking DNA to gold nanoparticles: poly-adenine-mediated formation of monovalent

DNA-gold nanoparticle conjugates with nearly quantitative yield. *NPG Asia. Mater.* 7:e159. doi: 10.1038/am.2014.131

Zhang, W., Liu, K., Zhang, P., Cheng, W., Zhang, Y., Li, L., et al. (2021). All-in-one approaches for rapid and highly specific quantifcation of single nucleotide polymorphisms based on ligase detection reaction using molecular beacons as turn-on probes. *Talanta* 224:121717. doi: 10.1016/j.talanta.2020.121717

Zhou, Q. Y., Wang, L. J., Zhong, X. Y., Dong, J. H., Zhou, Y. L., and Zhang, X. X. (2020). Ultrasensitive multiplex detection of single nucleotide polymorphisms based on short-chain hybridization combined with online preconcentration of capillary electrophoresis. *Anal. Chem.* 92, 10620–10626. doi: 10.1021/acs.analchem.0c01675

Zhu, D., Song, P., Shen, J., Su, S., Chao, J., Aldalbahi, A., et al. (2016). PolyA-mediated DNA assembly on gold nanoparticles for thermodynamically favorable and rapid hybridization analysis. *Anal. Chem.* 88, 949–4954. doi: 10.1021/acs.analchem.6b00891

Conflict of Interest: The authors declare that the research was conducted in the absence of any commercial or financial relationships that could be construed as a potential conflict of interest.

frontiers in Bioengineering and Biotechnology

ORIGINAL RESEARCH
published: 03 August 2021
doi: 10.3389/fbioe.2021.697862

Exploring the Application of Bifunctional Metal Chelators in Treating Triple-Negative Breast Cancer

Kuo Li[1,2], *Youjiu Zhang*[2], *Xiaomei Wang*[2], *Ran Zhu*[2], *Changsheng Ma*[1]* *and Rui Hu*[3]*

[1] Department of Radiotherapy, Shandong Cancer Hospital and Institute, Shandong First Medical University and Shandong Academy of Medical Sciences, Jinan, China, [2] School of Radiation Medicine and Protection, Soochow University, Suzhou, China, [3] Department of Radiation Oncology, Suzhou Municipal Hospital, Suzhou, China

Purpose: In this study, we independently synthesised and labelled a novel bidentate bifunctional chelating agent, ^{177}Lu-3,4-HOPO-Cetuximab, that achieved tight binding between targeting and radioactivity, and evaluated its targeted killing ability of cells *in vitro* and *in vivo*.

Method: 3,4-HOPO was successfully synthesised through a series of chemical steps using malt phenol as the raw material, which was then coupled with Cetuximab labelled with ^{177}Lu. ^{177}Lu-3,4-HOPO-Cetuximab and ^{177}Lu-DOTA-Cetuximab was tested for its cell viability and cell-binding rate after different times and at different doses by CCK-8 and cell-binding experiments. ^{177}Lu-3,4-HOPO-Cetuximab (∼500 μCi) and ^{177}Lu-DOTA-Cetuximab (∼500 μCi) were injected into the tail vein of a subcutaneous metastasis mouse model of triple-negative breast cancer with a single injection, and tumour volume growth and body weight changes were regularly monitored for 20 days. The radioactivity distribution in nude mice was analysed after sacrifice, and the treated and untreated tumour tissues were analysed by HE staining.

Result: The cell viability of ^{177}Lu-3,4-HOPO-Cetuximab declined exponentially after treatment for 48 h at 50 Bq/mL to 500 kBq/mL, respectively; the cell activity was slowed down from 8 to 96 h at a dose of 500 kBq; while the binding rate of 4T1 cells in ^{177}Lu-3,4-HOPO-Cetuximab from 1 to 24 h, respectively, increased logarithmically, which was similar with ^{177}Lu-DOTA-Cetuximab. After 20 days of treatment, the body weight of nude mice with ^{177}Lu-3,4-HOPO-Cetuximab and ^{177}Lu-DOTA-Cetuximab were hardly changed, while the body weight with physiological saline decreased significantly. The tumour inhibition rate of the ^{177}Lu-3,4-HOPO-Cetuximab and ^{177}Lu-DOTA-Cetuximab were (37.03 ± 11.16)% and (38.7 ± 5.1)%; HE staining showed that tumour cells were affected by the action of ^{177}Lu causing necrosis.

Conclusion: The experiments showed that ^{177}Lu-3,4-HOPO-Cetuximab has a certain targeted therapeutic ability for triple-negative breast cancer, and it is expected to become a potential targeted nuclear medicine treatment for triple-negative breast cancer.

Keywords: triple negative breast cancer, bifunctional chelator, cetuximab, targeted internal irradiation therapy, HOPO

OPEN ACCESS

Edited by:
Wang Zheng,
Suzhou Institute of Nano-Tech and Nano-Bionics (CAS), China

Reviewed by:
Dan Shao,
South China University of Technology, China
Hang Zhou,
Harbin Medical University, China

***Correspondence:**
Changsheng Ma
machangsheng_2000@126.com
Rui Hu
huuno@sohu.com

Specialty section:
This article was submitted to Biomaterials, a section of the journal Frontiers in Bioengineering and Biotechnology

Received: *20 April 2021*
Accepted: *08 June 2021*
Published: *03 August 2021*

Citation:
Li K, Zhang Y, Wang X, Zhu R, Ma C and Hu R (2021) Exploring the Application of Bifunctional Metal Chelators in Treating Triple-Negative Breast Cancer. Front. Bioeng. Biotechnol. 9:697862. doi: 10.3389/fbioe.2021.697862

INTRODUCTION

The Transitional Breast Cancer Research Consortium (TBCRC) conducted a clinical trial (Cleere, 2010; Lisa et al., 2012; Fatima et al., 2015; Chen et al., 2017; Zimei and Zan, 2017; Pindiprolu et al., 2018) and found that although TNBC patients tolerate Cetuximab well with small adverse reactions, its efficacy is limited. This suggests that the combination of Cetuximab and EGFR inhibitor therapy is expected to be a development point for TNBC. Studies have found that EGFR ligands can drive tumour proliferation in an autocrine/paracrine manner, and Cetuximab may block ligand-receptor binding (Wang et al., 2019; Fasano et al., 2021). The studies also confirmed the ability of ^{131}I-labelled targeting molecules to target the nuclides of TNBC *via* EGFR.

Over the past few years, new ^{177}Lu-labelled radiopharmaceuticals have been researched and developed internationally. Several peptides and monoclonal antibodies (mAbs) have been conjugated to bifunctional chelators and the labelled radionuclide ^{177}Lu. Ramli et al. (2011) successfully prepared radioimmunoassays based on the anti-HER-2 monoclonal antibody compound ^{177}Lu-DOTA-trastuzumab, which showed potent anticancer effects.

With the development of nuclear medicine, the new bifunctional chelator-HOPO has been discovered by scientists and has begun to enter the field of scientific research, and some HOPO compounds have reached the experimental stage before application. Although DTPA (Stanisz and Henkelman, 2015), DOTA (Eigner et al., 2013), and NOTA (Adam et al., 2007), etc., have shown strong capabilities, research on HOPO-based chelators that link targeting molecules to lanthanide and lanthanide metal ions in nuclear medicine is gaining increasing attention (Cilibrizzi et al., 2018). Deferiprone (1,2-dimethyl-3-hydroxy-4-pyridone, DFP) has been approved in Europe as an effective iron removal agent as a bidentate 3,4-HOPO.

Previous studies in our group have proved that ^{131}I-labelled cetuximab is easy to fall off after injection in mice for a period of time. Based on the above research background, this experiment independently prepared a novel bifunctional chelating agent, 3,4-HOPO, using 3,4-HOPO as a bifunctional chelating agent for ^{177}Lu-labelled Cetuximab to investigate the effects of ^{177}Lu-3,4-HOPO-Cetuximab in the treatment of TNBC.

EXPERIMENTAL MATERIALS

Experiment Equipment

Wantong titrator (Swiss Wantong China Ltd., Switzerland); FJ-391A4 radioactivity metre (Beijing Nuclear Instrument Factory); LB 2111 Multi Crystal Gamma Counter (Berthold Technologies, Germany); KDC-20 low-speed centrifuge (Hefei Keda Innovation Co., Ltd. Zhongjia Branch).

Cell Lines and Experimental Animals

The nude mouse triple-negative breast cancer cell line 4T1 cells were provided by Soochow university laboratory. Female BALB/c nude mice were purchased from Nanjing Skrui Biotechnology Co., Ltd., aged 4–6 weeks, and were raised at the Experimental Animal Centre of Suzhou University according to SPF requirements and approved by the animal ethics committee of Soochow University.

Laboratory Supplies

3-hydroxy-2-methyl-4-pyrone (maltophenol, 99%, Jingda, Anhui Jinhe Industrial Co., Ltd.); DOTA-NHS purchased from MACROCYCLICS, Europe; Cetuximab Purchased from Shanghai Saima Biotech Co., Ltd.; $^{177}LuCl_3$ was purchased from ITG Germany.

METHODS

Synthesis of Bidentate 3,4-HOPO

The synthesis process of bidentate 3,4-HOPO is shown in **Figure 1**.

Accurately weigh 43 g of maltol (1) dissolved in 285 mL of methanol and 35 mL of 10.25 mol/L NaOH solution, add 45 mL of benzyl chloride, and reflux at 100°C for 48 h to obtain orange oily liquid benzyl maltol (2).

Take benzyl maltol (2) 73.23 g dissolved in 210 mL mixed solution of methanol and water (volume ratio 1:1), add sodium glycinate powder, reflux reaction at 100°C for 36 h, then extract with 40–100 mL dichloromethane, water phase The concentrated HCl (12 mol/L) was adjusted to a pH 2, and the precipitated yellow crystals were filtered and dried in a vacuum oven for 30 h to obtain the product Bn-3,4-HOPO (3).

After the Bn-3,4-HOPO was dissolved in methanol, a certain amount of palladium carbon (about 5% by mass of the reactant) was weighed and added slowly to the reaction solution, and hydrogen was introduced and stirred for 4 h. After completion of the reaction, the mixture was filtered to obtain palladium carbon and a product mixture; after adding DMF (N,N-dimethylformamide), the mixture was heated and stirred at 80°C until the solution became a black suspension, and the filtered filtrate was steamed to obtain rice. The white solid was dried in vacuo to give the product as 3,4-HOPO (4). The results of the nuclear magnetic resonance test were as follows: 1H NMR (400 MHz, DMSO): δ 7.53 (d, J = 7.2 Hz, 1H), 6.11 (d, J-7.2 Hz, 1H), 4.82 (s, 2H), 2.15 (s, 3H); LC-MS [M + H+] m/z: 183.87.

Preparation of 3,4-HOPO-Cetuximab and DOTA-Cetuximab (Hereinafter Referred to as 3,4-HOPO-Ab and DOTA-Ab) Solution

Take 200 μL of Ab solution from the −80°C refrigerator and thaw it in a water bath. The ratio of 3,4-HOPO:NHS = 1:1.2 in 0.25 mol/L CH_3COONH_4 solution for 5 min, add 3,4- HOPO or DOTA ratio 1.2 equivalent EDC continued to activate for 30 min; molar ratio 3,4-HOPO or DOTA: Ab = 50:1 coupling; addition of 0.25 mol/L CH_3COONH_4 solution to 0.5 mL; constant temperature mixing at room temperature for 24 h to complete coupling Union. The coupled 3,4-HOPO-Ab solution or DOTA solution was centrifuged at 4,500 rpm for 45 min at room temperature, followed by ultrafiltration at 6,000 rpm for 15 min; the conjugate was collected, 0.5 mL of 0.25 mol/L CH_3COONH_4 solution was added, and placed. Store this at 4°C.

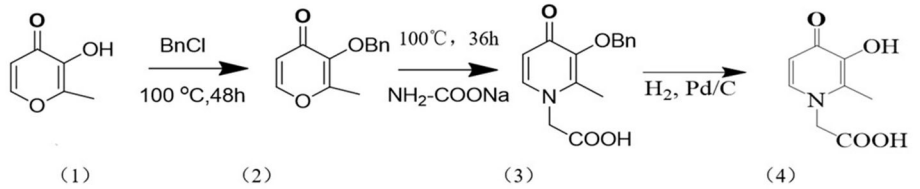

FIGURE 1 | Schematic diagram of the synthesis process of 3, 4-HOPO.

Preparation of ^{177}Lu-3,4-HOPO-Ab and ^{177}Lu-DOTA-Ab Solution

Remove 350 μL of purified 3,4-HOPO-Ab solution or ^{177}Lu-DOTA-Ab solution from a 4°C refrigerator; add 20 μL of $^{177}LuCl_3$ dilution solution to the 3,4-HOPO-Ab solution or ^{177}Lu-DOTA-Ab solution (activity is about 1 mCi); add CH_3COONH_4 buffer with pH 5. The solution was 500 μL; the mixture was shaken for 30 min at 37°C under a vortex constant temperature mixer to complete the labelling. The reaction solution after the completion of the labelling was centrifuged at 4,000 rpm for 15 min at room temperature; the buffer was discarded, the label was rinsed from the inner liner with a 0.25 mol/L CH_3COONH_4 solution, and the collected liquid was stored in an EP tube. The radiochemical purity was measured by a TLC method in a test tube in which the developing solvent was acetic acid: ammonium acetate (pH 3). The labelling rates of the ^{177}Lu-3,4-HOPO-Ab and ^{177}Lu-DOTA-Ab solutions were (89.7 ± 0.9)% and (92.6 ± 1.0)%. After purification, the radiochemical purity were both higher than 95%.

Cell-Binding Rate of ^{177}Lu-Ab and ^{177}Lu-3,4-HOPO

When the cells grow to more than 90%, the cell concentration is adjusted to about 1.0×10^5/mL, and 1 mL is added to each well in the 12-well plate and cultured overnight in the cell incubator at 37°C. When the cells adhered to the logarithmic growth phase on the second day after administration, 0.37 kBq markers were added to each hole. After 1, 2, 4, 8, and 24 h, the supernatant was added to the supernatant tube and washed twice by PBS, the cleaning fluid was also added to the supernatant tube; the cells were digested with trypsin, and the cell suspension was inhaled into the cell tube, washed with PBS for 2 times, and the radioactivity count (B) of the cell tube and the radioactivity count (F) of the supernatant tube were measured by γ counter. The cell-binding rate of the marker is B/(B+F) × 100%.

Effect of CCK-8 on the Proliferation of 4T1 Cells by ^{177}Lu

4T1 cells were uniformly inoculated into 96-well plates and the number of cells was 8,000/well. The cells were placed in a 37°C, 5% CO_2 saturated humidity incubator; the cells were fully attached for about 24 h. Six sets of parallel wells were randomly selected from each group, the medium was discarded; the medium containing $^{177}LuCl_3$, ^{177}Lu-3,4-HOPO-Ab, and ^{177}Lu-DOTA-Ab was, respectively, added to a 96-well plate by 50 Bq/mL∼ 500 kBq/mL, 100 μL per well, the medium containing 2 μg/mL of Ab was a positive control group and the blank control group was drug-free. After 4 h, replace the drug with a drug-free solution, and re-dispose it in a 37°C, 5% CO_2 saturated humidity incubator. After 48 h, discard the medium, and add 100 μL CCK-8 per well. About 0.5 h until the culture medium showed an orange colour, and the absorbance was measured by a microplate reader.

Afterwards, 100 μL of $^{177}LuCl_3$, ^{177}Lu-3,4-HOPO-Ab, and ^{177}Lu-DOTA-Ab with a radioactive dose of 500 kBq/mL were added to a 96-well plate and then placed at 37°C, 5% CO_2 saturated humidity. After the box was cultured for 4 h, the culture solution was discarded, the drug-free culture solution was replaced, and it was then discarded in the incubator for 8, 24, 48, 72, and 96 h, respectively. In total, 100 μL of medium containing 10% CCK-8 was added to each well. About 0.5 h until the culture medium showed an orange colour and was placed on a microplate reader. Cell viability (%) = [A (dosing) − A (blank)]/[A (control) − A (blank)]; A (dosing) is the absorbance of wells with cells, CCK-8 solution and drug solution; A (blank) is the absorbance of wells with medium and CCK-8 solution without cells; A (control) is the absorbance of wells with cells and CCK-8 solution without drug.

Changes in the Binding Rate of ^{177}Lu-3,4-HOPO-Ab to 4T1 Cells Over Time

After the cells were grown to more than 90% of the digested cells, the adjusted cell concentration was about 1.0×10^5 cells/mL, and 1 mL was added to each well of a 12-well plate, and cultured in a 37°C cell culture incubator overnight. When the cells were attached to the next day and were in the logarithmic growth phase, 1 mL of the culture medium containing the radioactive label was replaced (about 0.37 kBq per well), and three replicate wells were set in each group. After the markers were treated with 4T1 cells for 1, 2, 4, 8, and 24 h, the supernatant was aspirated and transferred to the supernatant EP tube. After washing twice with PBS, the washing solution was also incorporated into the supernatant EP tube. The cells were digested with a trypsin digestion solution. After the cells were completely digested, the cell suspension was inhaled into the EP tube of the cells, washed twice with PBS, and the washing solution was also added to the EP tube, and the cells were separately measured in a γ counter. The radioactivity count of the tube (B) and the radioactivity count of the supernatant tube (F). The cell-binding rate of the marker was B/(B+F) × 100%.

Tumour Growth Inhibition Experiment

In total, 30 nude mice bearing tumours with a diameter of ∼0.4–0.6 cm were randomly divided into two groups (treatment group and control group). There was no significant difference in body weight between the two groups.

In the treatment group, ^{177}Lu-3,4-HOPO-Ab was injected into the tail vein at 100 μL/mouse (∼500 μCi), and the control group was injected with an equal volume of normal saline *via* the tail vein. Treatment was administered once. After the completion of the tail vein injection, the state and activity of the nude mice were observed every day. The nude mice were weighed on day 0, day 3, day 5, day 7, day 10, and day 20 after dosing. Additionally, the long diameter and short diameter of each group of tumours were measured with a Vernier calliper, and the volume of the tumour was calculated for a total of 20 days.

The calculation method of the tumour volume was as follows:

$$V = \frac{X \times Y^2}{2},$$

where X is the long diameter and Y is the short diameter.

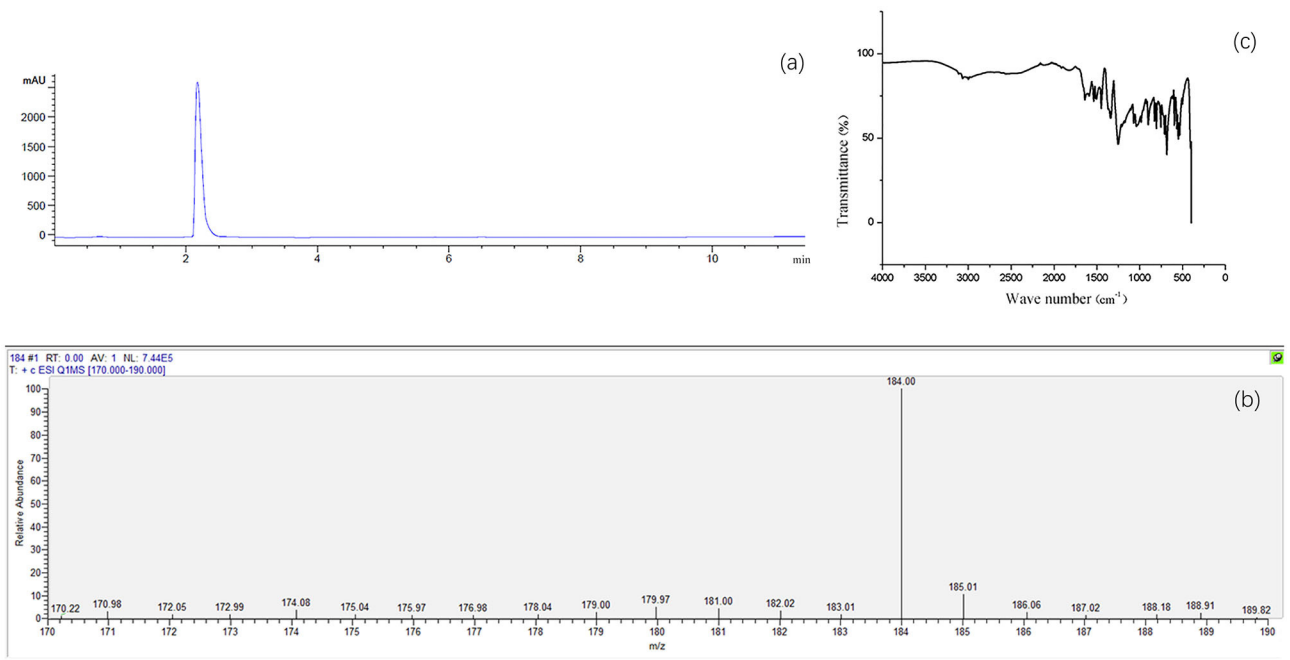

FIGURE 2 | HPLC **(a)**, mass spectrometric chromatogram **(b)** and infrared spectrum **(c)** of 3,4-HOPO.

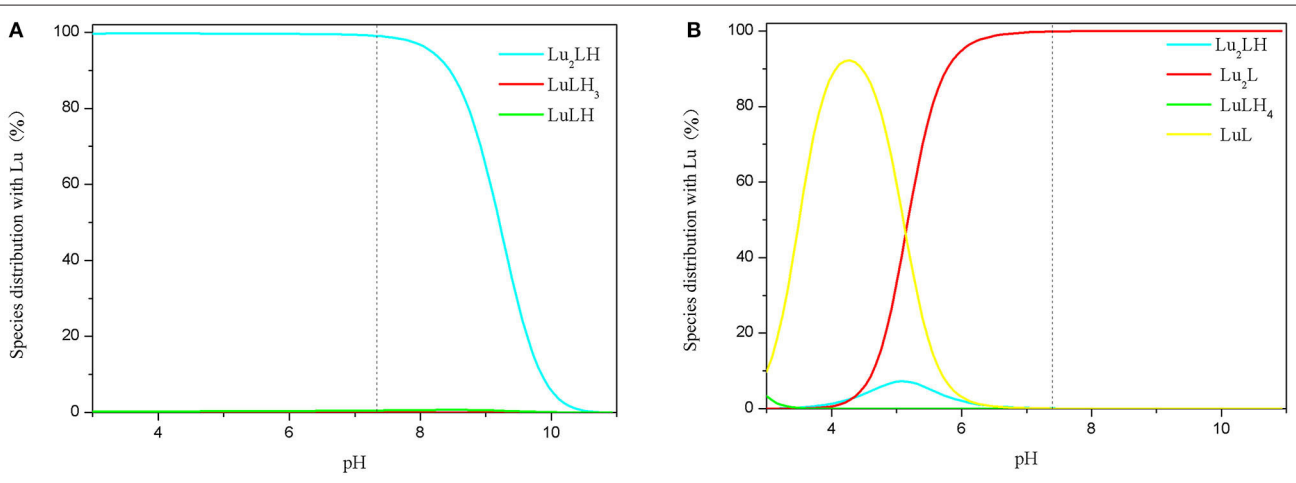

FIGURE 3 | Species distribution of 3,4-HOPO **(A)** and DOTA **(B)** with Lu^{3+} complexes (initial concentrations of Lu^{3+} ions and 3,4-HOPO were 1 × 10^{-4} M and 1 × 10^{-3} M, respectively).

The tumour growth inhibition rate (i.e., tumour inhibition rate) is the tumour inhibition rate = [(A − B)/A] × 100%, where A is the control group and B is the treatment group.

On the 20th day after administration, blood was collected from the retro-orbital sinus, and the nude mice were sacrificed. The nude mice were dissected, and organs such as the heart, liver, spleen, lung, kidneys, stomach, intestine, tumour, bone, muscle, and skin were taken, weighed, and detected by radioactive gamma count. The result was converted to %ID/g [%ID/g = radioactive count of the organ/(radioactive count rate of the injected drug × organ mass)], and the gamma counter was calibrated to be 1.2×10^6 cpm = 1 μCi.

Immunohistochemical Detection of Tumour Tissue Before and After Treatment

4T1 tumour tissues were extracted without treatment or with treatment, fixed by 4% paraformaldehyde for 24 h. HE staining and immunohistochemical analysis were entrusted to Wuhan Sevier Biotechnology Co., Ltd. The rate of EGFR positive cells is the average number of positive cells in 3 visual fields (200×) of a certain type of cells: 0–5% is grade 0, 6–25% is grade 1, 26–50% is grade 2, 51–75% is grade 3, >75% is grade 4.

Statistical Analysis

The experimental results were expressed as mean ± standard deviation ($\bar{x} \pm s$). The data were analysed by *SPSS 19.0* software. One-way analysis of variance (ANOVA) was performed in a completely randomised design. $P < 0.05$ was considered statistically significant.

RESULTS

Analysis of 3,4-HOPO

The results of UV absorption at 254 nm showed that the HPLC chromatogram of 3,4-HOPO occurred an absorption peak only at 2.2 min with no obvious impurity peaks appeared elsewhere. The purity of 3,4-HOPO is 98.6% (**Figure 2a**). Mass spectrometry (**Figure 2b**) shows the LC-MS [$M+H^+$] m/z: 184.00. Since it is the test result in H^+ mode, it is inferred that the actual molecular weight is 183.00 Infrared spectrum (**Figure 2c**) ensured that the structure of 3,4-HOPO is correct.

As shown in **Figure 3**. The dissociation constants pK_{a1} and pK_{a2} of 3,4-HOPO are 10.1 ± 0.1 and 3.7 ± 0.1, respectively. The results show that 3,4-HOPO reaches the dissociation equilibrium at pH = 10.1; the second-order dissociation constant pK_{a2} (3.7) indicates that 3,4-HOPO will be protonated at low pH and reach a deprotonation equilibrium at pH = 3.7.While the dissociation constants pKa1, pKa2, pKa3, pKa4, and pKa5 of DOTA are 2.5 ± 0.2, 2.5 ± 0.2, 4.6 ± 0.2, 8.7 ± 0.2, and 10.1 ± 0.2, respectively. The results showed that DOTA reached the first-order and second-order dissociation equilibrium at pH = 2.5, the third-order dissociation equilibrium at pH = 4.6, the fourth-order dissociation equilibrium at pH = 8.7, and the fifth-order dissociation equilibrium at pH = 10.1.

The complexation behaviours of 3,4-HOPO and Lu^{3+} ions were studied by potentiometric titration. The cumulative formation constants of $\log\beta_{0lh}$ and pM were obtained by *Hyperquad 2008* as shown in **Table 1**. The distribution of species in the range of pH 3–11 was obtained with *Hyss 2009*. The maximum enrichment zone of chelators with Lu^{3+} (enriched density above 95%) was pH < 8.2 in the form of Lu_2LH for 3,4-HOPO and pH < 6.0 in the form of Lu_2L for DOTA, respectively.

TABLE 1 | Complexation constants of 3,4-HOPO and DOTA with Lu^{3+}.

Metal ion	Coordination material					
	3,4-HOPO			DOTA		
	m l h	$\log\beta_{mlh}$	pM	m l h	$\log\beta_{mlh}$	pM
Lu^{3+}			15.3			13.6
	111	16.9 ± 0.1		114	23.6 ± 0.5	
	211	26.6 ± 0.1		110	15.3 ± 0.3	
	210	11.4 ± 0.1		211	30.1 ± 1.2	
				210	21.0 ± 0.2	

m represents coordination metal ion, l represents chelate, h represents hydrogen ion; pM = –log[m_{free}].

Effect of ^{177}Lu Labelling Material on Proliferation of 4T1 Cells

The effect of ^{177}Lu-DOTA-Ab and ^{177}Lu-3,4-HOPO-Ab on the proliferation of 4T1 cells is shown in **Figure 4A** and **Table 2**. ^{177}Lu has a certain inhibitory effect on cell proliferation. With the increase of dose (**Figure 4A** and **Table 2**), the cell activity changes from (93.85 ± 1.2)% of 50 Bq/mL to (82.2 ± 0.87)% of 500 kBq/mL for ^{177}Lu. However, the ^{177}Lu-3,4-HOPO-Ab and ^{177}Lu-DOTA-Ab have an absolute inhibitory effect on cell proliferation, the cell activity changes from (93.91 ± 1.24)% and (93.75 ± 0.64)% of 50 Bq/mL to (17.82 ± 1.03)% and (14.70 ± 0.99)% of 500 kBq/mL. Compared with ^{177}Lu, the ^{177}Lu-3,4-HOPO-Ab had a statistically significant difference in cell viability at a dose of 500 Bq/mL ($P < 0.05$), while the dose was increased to 5 kBq/mL, the difference of cell activity was statistically significant ($P < 0.05$) between ^{177}Lu and ^{177}Lu-3,4-HOPO-Ab or ^{177}Lu-DOTA-Ab.

As shown in **Figure 4B** and **Table 3**, Cetuximab promoted cell proliferation over a short period of time. With the increase of time, the cell activity decreased from (159.37 ± 2.46)% at 8 h to (104.75 ± 0.70)% at 96 h after replacement of drug-free medium. The ^{177}Lu at 500 kBq and cell culture for 8 h had a slight inhibitory effect on cell proliferation. With the increase in time, the cell activity gradually increased after the initial plateau, it was from (82.10 ± 1.75)% after 8 h of drug-free medium replacement to (90.40 ± 1.12)% at 96 h. However, ^{177}Lu-DOTA-Ab and ^{177}Lu-3,4-HOPO-Ab were cultured for 8 h had a good inhibitory effect on cell proliferation. With the increase of time, the cell activity decreased continuously (49.20 ± 1.40)% for ^{177}Lu-DOTA-Ab and (50.47 ± 1.83)% for ^{177}Lu-3,4-HOPO-Ab at 8 h after replacing the drug-free medium were changed to (7.50 ± 0.28)% and (9.24 ± 0.68)% at 96 h. And the differences at each time point were statistically significant ($P < 0.05$) compared with the cell activity at 8 h, we also found that ^{177}Lu-DOTA-Ab had a better therapeutic effect than ^{177}Lu-3,4-HOPO-Ab from 48 to 72 h, but the difference was not statistically significant ($P > 0.05$) at 96 h between ^{177}Lu-DOTA-Ab and ^{177}Lu-3,4-HOPO-Ab.

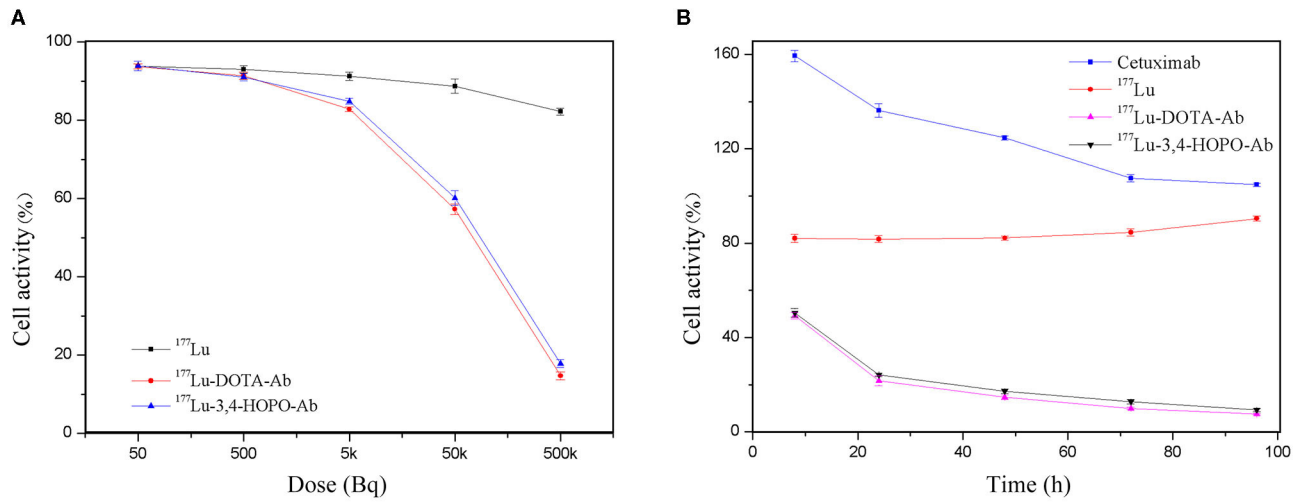

FIGURE 4 | Effect of ^{177}Lu-DOTA-Ab and ^{177}Lu-3,4-HOPO-Ab on the activity of 4T1 cells **(A)** is the effect with dose and **(B)** is the effect with time.

TABLE 2 | The effect of ^{177}Lu-DOTA-Ab and ^{177}Lu-3,4-HOPO-Ab on the activity of 4T1 cells with the dose increase.

Medicine	Dose (Bq/mL)				
	50	500	5k	50k	500k
^{177}Lu	93.85 ± 1.20	92.95 ± 0.92	91.25 ± 1.06	88.70 ± 1.84	82.20 ± 0.87
^{177}Lu-DOTA-Ab	93.75 ± 0.64	91.35 ± 0.92	82.80 ± 0.58$^{\&}$	57.25 ± 1.37$^{\&}$	14.70 ± 0.99$^{\&}$
^{177}Lu-3,4-HOPO-Ab	93.91 ± 1.24	91.01 ± 0.92$^{\&}$	84.84 ± 0.74$^{\#\&}$	60.15 ± 1.84$^{\&}$	17.82 ± 1.03$^{\#\&}$

$^{\&}$Means the difference was statistically significant ($P < 0.05$) compared with the ^{177}Lu, $^{\#}$Means ^{177}Lu-DOTA-Ab has the significant difference ($P < 0.05$) compared with the ^{177}Lu-DOTA-Ab.

TABLE 3 | The effect of ^{177}Lu-DOTA-Ab and ^{177}Lu-3,4-HOPO-Ab on the activity of 4T1 cells with the time increase.

Medicine	Time (h)				
	8	24	48	72	96
Cetuximab	159.37 ± 2.46	136.24 ± 2.83	124.63 ± 0.84	107.52 ± 1.63	104.75 ± 0.70
^{177}Lu	82.10 ± 1.75	81.70 ± 1.42	82.20 ± 0.87	84.50 ± 1.53	90.40 ± 1.12$^{\&}$
^{177}Lu-DOTA-Ab	49.20 ± 1.40$^{\%}$	21.60 ± 2.19$^{\&\%}$	14.70 ± 0.99$^{\&\%}$	9.90 ± 0.49$^{\&\%}$	7.50 ± 0.28$^{\&\%}$
^{177}Lu-3,4-HOPO-Ab	50.47 ± 1.83$^{\%}$	24.18 ± 0.74$^{\&\%}$	17.82 ± 1.03$^{\#\&\%}$	12.75 ± 0.91$^{\#\&\%}$	9.24 ± 0.68$^{\&\%}$

$^{\%}$Means ^{177}Lu-DOTA-Ab and ^{177}Lu-3,4-HOPO-Ab had significant difference ($P < 0.05$) compared with the ^{177}Lu, $^{\#}$Means ^{177}Lu-3,4-HOPO-Ab had significant difference ($P < 0.05$) compared with the ^{177}Lu-DOTA-Ab, and $^{\&}$Means the difference was statistically significant ($P < 0.05$) compared with 8 h in treatment groups.

4T1 Cell-Binding Rate of ^{177}Lu-3,4-HOPO-Ab

The results showed that 4T1 cell was no binding effect with ^{177}Lu-3,4-HOPO and ^{177}Lu in **Figure 5** and **Table 4**, while the binding rate of Cetuximab to cells increased with time. But after reaching a certain time, the growth rate decreased, and could not achieve the effect of ^{177}Lu-3,4-HOPO-Ab and ^{177}Lu-DOTA-Ab.

The change of the binding rate of ^{177}Lu-3,4-HOPO-Ab and ^{177}Lu-DOTA-Ab to 4T1 cells with time is shown in **Figure 5B**. It can be seen that the cell-binding rate is positively correlated with the time change, showing a certain targeting ability of the antibody. The binding rate of 4T1 cell with ^{177}Lu-3, 4-HOPO-Ab, and ^{177}Lu-DOTA-Ab were (1.45 ± 0.17)% and (1.67 ± 0.08)% at 1 h, increased to (10.33 ± 0.82)% and (10.17 ± 0.46)% at 24 h. There were statistically significant differences ($P < 0.05$) in the cell-binding rate between ^{177}Lu-3,4-HOPO and ^{177}Lu-3,4-HOPO-Ab as well as ^{177}Lu-DOTA-Ab all the time.

In vivo Experiment of ^{177}Lu Labelled Material on 4T1 Nude Mice

The body weight changes of the 4T1 tumour-bearing nude mice in physiological saline, ^{177}Lu-DOTA-Ab, and ^{177}Lu-3,4-HOPO-Ab over time after administration are shown in **Figure 6A** and **Table 5**. Before administration, the weight of the nude mice

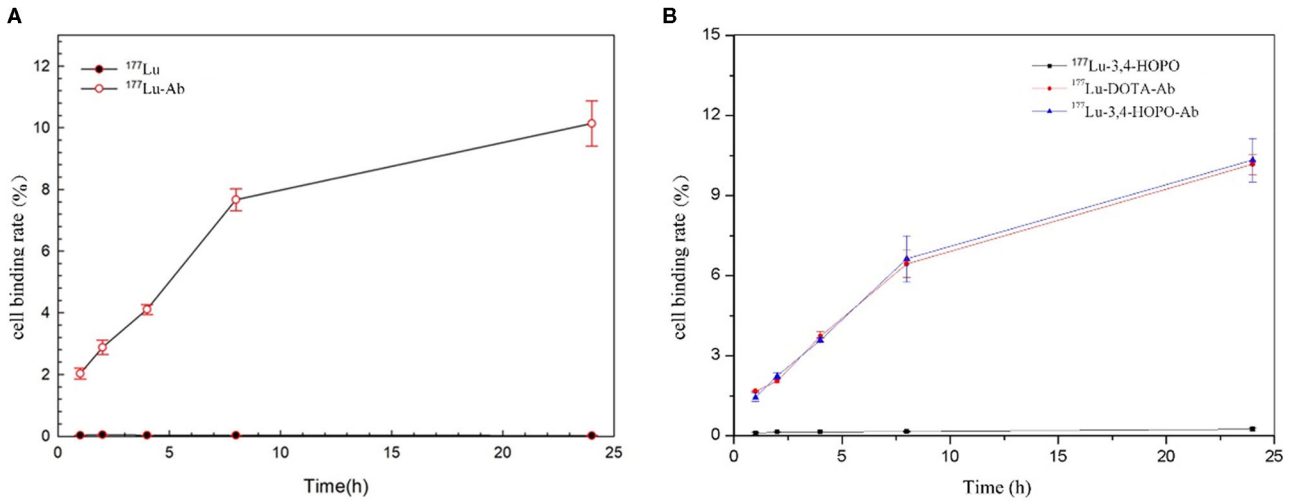

FIGURE 5 | The time-varying curve of the 4T1 cell-binding rate of ^{177}Lu and chelates. **(A)** shows the 4T1 cell-binding rate with or without Cetuximab, **(B)** shows the ^{177}Lu-DOTA-Ab, and ^{177}Lu-3,4-HOPO-Ab could have a better effect for 4T1 cell binding.

TABLE 4 | Time-varying values of 4T1 cell-binding rate of ^{177}Lu and chelates.

Medicine	Time (h)				
	1	2	4	8	24
^{177}Lu-3,4-HOPO	0.087 ± 0.040	0.142 ± 0.025	0.147 ± 0.013	0.159 ± 0.015	0.237 ± 0.042
^{177}Lu-DOTA-Ab	1.67 ± 0.02*	2.06 ± 0.08*	3.72 ± 0.19*	6.44 ± 0.51*	10.17 ± 0.37*
^{177}Lu-3,4-HOPO-Ab	1.45 ± 0.17*	2.24 ± 0.12*	3.58 ± 0.09*	6.63 ± 0.87*	10.33 ± 0.82*

** Means the difference was statistically significant ($P < 0.05$) compared with the cell-binding rate of ^{177}Lu-3,4-HOPO.*

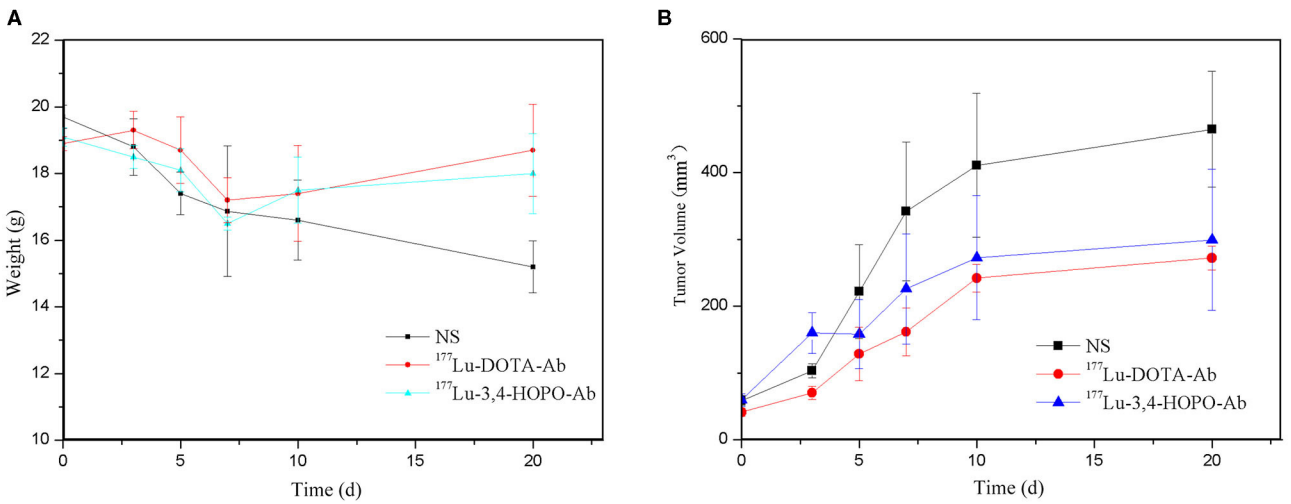

FIGURE 6 | Body weight and tumour volume changes in nude mice treated over time (NS is physiological saline). **(A)** shows the changes of body weight with time and **(B)** shows the change of tumor volume with time.

in the saline, ^{177}Lu-DOTA-Ab, and ^{177}Lu-3,4-HOPO-Ab were (19.74 ± 0.35) g, (18.9 ± 0.21) g, and (19.11 ± 0.28) g, respectively, with the difference between each group were not statistically significant ($P > 0.05$). After a period of feeding, the weight change trend of the ^{177}Lu-labelled monoclonal antibody treatment groups was increased, while it was decreased in the saline group. After 20 days, the weights of nude mice with ^{177}Lu-3,4-HOPO-Ab and ^{177}Lu-DOTA-Ab were (18.02 ± 1.20)

TABLE 5 | Weight in nude mice treated over time.

Group	Time (△)					
	0	3	5	7	10	20
NS	19.7 ± 0.4	18.8 ± 0.8	17.4 ± 0.6	16.9 ± 1.9	16.6 ± 1.2	15.2 ± 0.8
^{177}Lu-DOTA-Ab	18.9 ± 0.2	19.3 ± 0.6	18.7 ± 1.0	17.2 ± 0.7	17.4 ± 1.4*	18.7 ± 1.4*
^{177}Lu-3,4-HOPO-Ab	19.1 ± 0.3	18.5 ± 0.4	18.1 ± 0.6	16.5 ± 0.2	17.5 ± 1.0*	18.0 ± 1.2*

**Means the difference was statistically significant ($P < 0.05$) between treatment groups and NS (physiological saline) group.*

TABLE 6 | Tumour volume values in nude mice treated over time.

Group	Time (d)					
	0	3	5	7	10	20
NS	58.6 ± 7.5	103.1 ± 10.7	221.9 ± 70.2	341.8 ± 104.1	410.9 ± 107.8	465.0 ± 87.0
^{177}Lu-DOTA-Ab	51.2 ± 6.3	70.4 ± 9.8*	128.4 ± 39.9	161.3 ± 35.6*	241.9 ± 20.5*	272.2 ± 47.8*
^{177}Lu-3,4-HOPO-Ab	59.6 ± 9.6	159.7 ± 30.6#	183.6 ± 84.9#	225.8 ± 82.5*#	272.6 ± 93.2*	299.2 ± 105.7*

**Means the difference was statistically significant ($P < 0.05$) between treatment groups and NS (physiological saline) group. #Means the difference was statistically significant ($P < 0.05$) between the ^{177}Lu-3,4-HOPO-Ab group and ^{177}Lu-DOTA-Ab group.*

g and (18.7 ± 1.38) g, (15.21 ± 0.78) g in saline, and there were statistically significant differences ($P < 0.05$) between the treatment groups and the saline group from the beginning at 7th day.

As shown in **Figure 6B** and **Table 6**. Before the start of treatment, the volume of 4T1 xenografts in saline, ^{177}Lu-DOTA-Ab, and ^{177}Lu-3,4-HOPO-Ab were (58.60 ± 7.53) mm^3, (51.2 ± 6.3) mm^3, and (59.64 ± 9.60) mm^3, respectively, and there were no differences ($P > 0.05$) between each of two groups. After 20 days of treatment, the volume of tumours in ^{177}Lu-3,4-HOPO-Ab and ^{177}Lu-DOTA-Ab were (299.20 ± 105.70) mm^3 and (272.2 ± 17.8) mm^3, which in saline was (465.04 ± 87.02) mm^3. There were statistically significant differences ($P < 0.01$) in the volume of transplanted tumours within the treatment groups and the saline group from the beginning of the 7th day. The tumour inhibition rates of ^{177}Lu-3,4-HOPO-Ab and ^{177}Lu-DOTA-Ab were (37.03 ± 11.16)% and (38.7 ± 5.1)%, respectively. Tumor treatment changes in nude mice is shown in **Figure 7**.

In vivo Radioactivity Distribution in Nude Mice After 20 Days of Administration

After 20 days of injection in the tail vein, the radioactivity profile of the 4T1 tumour-bearing nude mice (**Figure 8**) showed that the radioactivity was mainly concentrated in the liver and bone, the ^{177}Lu-3,4-HOPO-Ab and ^{177}Lu-DOTA-Ab were (3.20 ± 0.30)%ID/g and (3.69 ± 0.42)%ID/g in liver and (1.83 ± 0.30)%ID/g and (2.7 ± 0.6)%ID/g in bone. However, the ^{177}Lu-3,4-HOPO-Ab group and ^{177}Lu-DOTA-Ab group had radioactivity were, respectively (1.90 ± 0.32)%ID/g and (2.2 ± 0.2)%ID/g in tumours.

HE Staining and Immunohistochemistry

HE staining of ^{177}Lu with and without treatment of 4T1 tumour, as shown in **Figure 9**. HE staining sections of the saline control group (left) showed typical mega-massive tumour cells, see multiple divisions, cell growth was strong, cells were closely arranged, and the ratio of nuclear to cytoplasm was high. Treatment group (mid and right) tumour cells showed partial necrosis and inflammation, and the cells were loosely arranged with a low nuclear-to-plasma ratio.

EGFR is mainly expressed on the cell membrane, and particles ranging from pale yellow to tan are representative of EGFR expression. For the untreated group (left), there was more EGFR expression in the tumour tissues; after treatment (mid and right), the expression of EGFR in the tumour decreased, and the proportion of positive cells was less than that in the control group.

According to the semi-quantitative scoring method, the EGFR positive rate of the untreated group was grade 10. The EGFR positive rate of the ^{177}Lu-3,4-HOPO-Ab and ^{177}Lu-3,4-HOPO-Ab groups were both grade 2.

DISCUSSION

Hydroxypyridone (HOPO) is an outstanding building block for the development of various reagents in the field of metal chelation. At present, in-depth analysis of the synthesis methods of HOPO-based ligands and many methods for achieving optimal biological activity have been reported (Ana et al., 2012).

The pH of human body fluid is close to 7.4, so we analysed the species distribution relationship and complexation constant of 3,4-HOPO interacting with different metal ions at pH 7.4. 3,4-HOPO and DOTA in Lu^{3+} system existed in the form of Lu_2LH (99.0%) and Lu_2L (99.8). In this state, the complexation constant of 3,4-HOPO is 5 orders of magnitude higher than that of DOTA.

In 1907, the French chemist G. Urbain recrystallised several times with a solution of niobium nitrate, from which a new element "Lutecium" was isolated and named "Paris" in ancient

FIGURE 7 | Tumour treatment changes in nude mice between treatment group and control group (lines 1–3 refer to the status of mice on the 0th, 7th, and 20th day after treatment, respectively. Columns 1–3 refer to the status of mice with NS, ^{177}Lu-3,4-HOPO-Ab, and ^{177}Lu-DOTA-Ab, respectively.

Latin-Lutetia named it Lutetium (Lu) (Yokel et al., 2000). Cetuximab is an FDA-approved monoclonal antibody that targets EGFR cancer cells and inhibits the growth of these cells (Listed, 2006). Cetuximab is radiolabelled with various diagnostic and therapeutic radionuclides by various bifunctional chelators and targeted in preclinical models and clinical settings (Sihver et al., 2014). Cetuximab, among the many therapeutic radionuclides, due to its excellent physical properties and its advantages in the field of tumour therapy, has been proven to be suitable for radioimmunotherapy of tumours, and its research in the field of nuclear medicine internal radiation therapy requires more attention (Kwekkeboom et al., 2003; Feng et al., 2018).

CCK-8 experiments showed that free ^{177}Lu had no killing effect for 4T1 cells, while ^{177}Lu-3,4-HOPO or ^{177}Lu-DOTA conjugated with antibody displayed little damage to cells at a low dose and cell lethality with increasing dose. It also increased exponentially because Cetuximab binds to the EGFR receptor on the surface of 4T1 cells, allowing ^{177}Lu to act on cells for a long time while free ^{177}Lu is washed after 4 h.

Due to the presence of Cetuximab, ^{177}Lu-3,4-HOPO-Cetuximab can specifically bind to EGFR-positive receptors in 4T1 cells, and the corresponding cell-binding rate increases as the duration of action increases. Since ^{177}Lu cannot penetrate the cell membrane, the β-particles emitted during cell culture damage the cells, resulting in a decrease in cell proliferation ability. However, after washing with the medium, there is almost no ^{177}Lu in the 4T1 cell culture system, and this is illustrated by the cell-binding assay. Since the cells only interacted with 500 kBq $^{177}LuCl_3$ for 4 h, the damaged cells were gradually repaired, and the cell activity gradually increased with time, reaching 90.40% at 96 h, which was significantly increased compared with 82.10% at 8 h. The cells were treated with 500 kBq ^{177}Lu-3,4-HOPO-Cetuximab for 8 h, ^{177}Lu-3,4-HOPO-Cetuximab was retained in the cells by binding of the antibody Cetuximab to the EGFR receptor positively expressed on the surface of 4T1 cells, and sustained beta-ray damage Cells, causing cell activity to decrease over time.

Intravenous injection of ^{177}Lu-3,4-HOPO-Cetuximab in the treatment of 4T1 nude mice xenografts showed that the weight of nude mice in the treatment group will decrease in a short period of time because of the strong growth of tumour cells at this stage and rapid consumption of nutrition in nude mice. Substance, after 7 days, showed the weight of nude mice in the treatment group began to rise, indicating that the tumour cell activity in nude mice decreased, and the metabolic capacity decreased. From the growth of transplanted tumour volume, the growth rate of xenografts in the treated group compared with the control group. As it slows down significantly, the growth curve slope prediction is expected to reach a negative value after a certain time, and it reaches a significant anti-tumour effect after 20 days. This series of data confirms the second part of ^{177}Lu-3,4-HOPO-Cetuximab for 4T1 The killing effect of ^{177}Lu *in vitro* and the targeting ability of Cetuximab. After 20 days of administration, the data of the radioactive distribution of the nude mice in the treatment group showed that the liver, tumour, and bone were the three organs with the highest radioactivity accumulation, and the ^{177}Lu accumulation of ^{177}Lu-3,4-HOPO-Cetuximab in the bone site was relatively low. The clinical case shows that ^{177}Lu-labelled DOTA-coupled targeting material can cause severe bone metastasis after treatment for a period of time, *in vivo* radioactivity distribution data show that the dose deposition of HOPO in the liver and bone were lower than that of DOTA, and this indicates that HOPO has a better ability to promote the

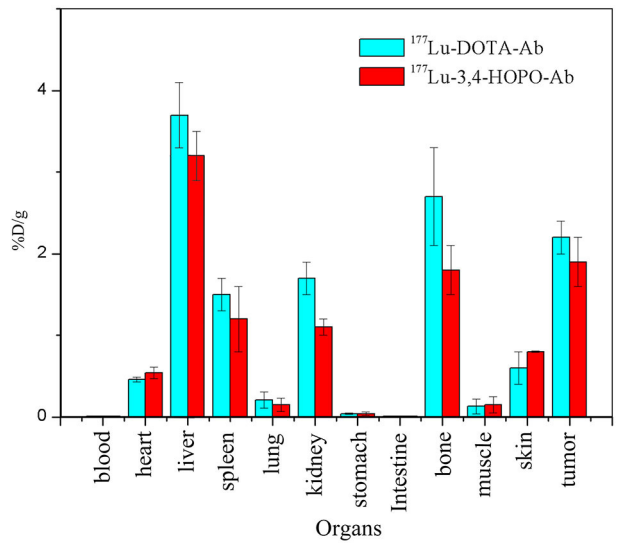

FIGURE 8 | *In vivo* distribution of nude mice after injection for 20 days.

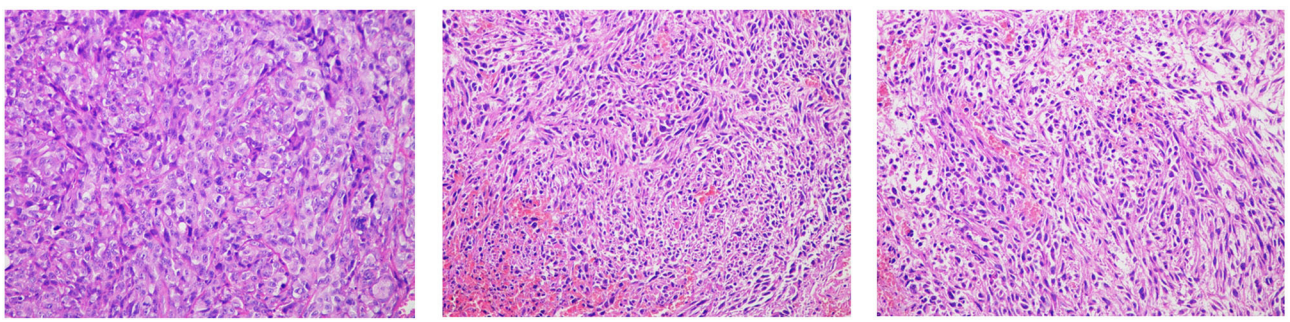

FIGURE 9 | Tumour tissue sections and EGFR immunohistochemistry (10 × 20; the left is the saline control group, middle is the ^{177}Lu-DOTA-Ab group, and right is the ^{177}Lu-3,4-HOPO-Ab group).

excretion of metal ions than DOTA. 3,4-HOPO is expected to become a new targeted therapy drug for clinical nuclear medicine to solve the problem of bone metastasis.

3,4-HOPO is a bidentate chelating agent synthesised by malt phenol as a template through a series of chemical synthesis steps. At present, the medical community has little research and application on HOPO chelate. Hagemann et al. (2017) showed that 3,2-HOPO coupled with the FGFR-2 receptor by the ^{227}Th marker was visible in the *in situ* 4T1 model of invasive nude mice. The anti-tumour activity (Tinianow et al., 2016) and another independent synthesis of octadentate 3,2-HOPO-conjugated monoclonal antibody for ^{89}Zr labelling both result in the *in vivo* stability being stronger than DTPA; in addition, there exists a report (Deri et al., 2015) on nuclear label HOPO research into the use of chelators since nuclear medicine developers have shown great potential. ^{177}Lu-3,4-HOPO-Cetuximab has obvious killing and lethal effect on 4T1 tumours.

CONCLUSIONS

We have confirmed that bidentate 3,4-HOPO has shown strong chelation application value, and it is necessary to synthesise four or more teeth 3,4-HOPO must have a more powerful clinical medicine role.

DATA AVAILABILITY STATEMENT

The raw data supporting the conclusions of this article will be made available by the authors, without undue reservation.

ETHICS STATEMENT

The animal study was reviewed and approved by Soochow University.

AUTHOR CONTRIBUTIONS

KL was responsible for collecting data for cell and animal experiments and writing article. YZ and XW were responsible for the production and purification of molecular materials. RZ was responsible for data collation. CM and RH were responsible for proposing the experimental ideas and revising the article. All authors contributed to the article and approved the submitted version.

FUNDING

This work was supported by the National Nature Science Foundation of China (81800156, 81974467), the Natural Science Foundation of Shandong Province (ZR2019MH136), the Suzhou Science and Technology Development Project (SYSD2018137), the Medical Research Program of Jiangsu Provincial Commission of Health (Z2018010), and the Gusu health personnel training project (GSWS2020063).

ACKNOWLEDGEMENTS

The authors would like to thank the editor and reviewers for their insightful suggestions, which helped improve the manuscript.

REFERENCES

Adam, F. P., Prasant, K. N., Tammy, L. R., Lixin, M., Michael, R. L., Jered, C. G., et al. (2007). [64Cu-NOTA-8-Aoc-BBN(7-14)NH_2] targeting vector for positron-emission tomography imaging of gastrin-releasing peptide receptor-expressing tissues. *Proc. Natl. Acad. Sci. U.S.A.* 104, 12462–12467. doi: 10.1073/pnas.0705347104

Ana, M. C., Parra, M., Gil, S., Gotor, R., Martínez-Mañez, R., Sancenón, F., et al. (2012). Selective detection of nerve agent simulants by using triarylmethanol-based chromogenic chemodosimeters. *Euro. J. Org. Chem.* 4937–4946. doi: 10.1002/ejoc.201200570

Chen, W., Zheng, R., Zhang, S., Zeng, H., Xia, C., Zuo, T., et al. (2017). Cancer incidence and mortality in China, 2013. *Cancer Lett.* 401, 63–71. doi: 10.1016/j.canlet.2017.04.024

Cilibrizzi, A., Abbate, V., Chen, Y.-L., Ma, Y., Zhou, T., and Robert, C. H. (2018). Hydroxypyridinone journey into metal chelation. *Chem. Rev.* 118, 7657–7701. doi: 10.1021/acs.chemrev.8b00254

Cleere, D. W. (2010). Triple-negative breast cancer: a clinical update. *Commun. Oncol.* 7, 203–211. doi: 10.1016/S1548-5315(11)70394-1

Deri, M., Ponnala, S., Kozlowski, P., Burton-Pye, B. P., Cicek, H. T., Hu, C., et al. (2015). p-SCN-BN-HOPO: a superior bifunctional chelator for 89Zr immuno-PET. *Bioconjug. Chem.* 26:2579. doi: 10.1021/acs.bioconjchem.5b00572

Eigner, S., Vera, D. B., Fellner, M., Loktionova, N., Piel, M., Lebeda, O., et al. (2013). Imaging of protein synthesis: *in vitro* and *in vivo* evaluation of 44Sc-DOTA-puromycin. *Mol. Imaging Biol.* 15, 79–86. doi: 10.1007/s11307-012-0561-3

Fasano, M., Corte, C. M. D., Viscardi, G., Di Liello, R., Paragliola, F., Sparano, S., et al. (2021). Head and neck cancer: the role of anti-EGFR agents in the era of immunotherapy. *Ther. Adv. Med. Oncol.* 13, 1–15. doi: 10.1177/1758835920949418

Fatima, Z. M., Mohammed, E. M., Meriem, S., and Mariam, A. (2015). Progress in research on triple negative breast cancer. *Asian Pacific J. Cancer Prev.* 17, 1595–1608. doi: 10.7314/APJCP.2016.17.4.1595

Feng, T., Cheng, W., Wang, B., and Fan, H. (2018). The progress in clinical research of 177Lu labeled radiopharmaceuticals. *Labeled Immunoassays Clin. Med.* 25, 180–186.

Hagemann, U. B., Sommer, A., Kristian, A., Wang, E., Larsen, A., and Wirnitzer, U. (2017). Abstract 5199: preclinical activity of the FGFR2-targeted thorium-227 conjugate in preclinical models of colorectal, gastric and triple-negative breast cancer. *Cancer Res.* 77, 5199–5199. doi: 10.1158/1538-7445.AM2017-5199

Kwekkeboom, D. J., Bakker, W. H., Kam, B. L., Teunissen, J. J. M., Kooij, P. P. M., Herder, W. W., et al. (2003). Treatment of patients with gastro-entero-pancreatic (GEP) tumours with the novel radiolabelled somatostatin analogue [177Lu-DOTA0, Tyr3] octreotate. *Euro. J. Nucl. Med. Mol. Imaging* 30, 417–422. doi: 10.1007/s00259-002-1050-8

Lisa, A. C., Hope, S. R., Marcom, P. K., Erica, L. M., Francisco, J. E., Cynthia, X. M., et al. (2012). TBCRC 001: randomized phase II study of Cetuximab in combination with carboplatin in stage IV triple-negative breast cancer. *J. Clin. Oncol.* 30, 2615–2623. doi: 10.1200/JCO.2010.34.5579

Listed, N. (2006). Cetuximab approved by FDA for treatment of head and neck squamous cell cancer. *Cancer Biol. Ther.* 5:340. doi: 10.4161/cbt.5.4.2666

Pindiprolu, S. K. S. S., Krishnamurthy, P. T., and Chintamaneni, P. K. (2018). Pharmacological targets of breast cancer stem cells: a review. *Naunyn Schmiedeberg's Arch. Pharmacol.* 391, 1–17. doi: 10.1007/s00210-018-1479-3

Ramli, M., Hidayat, B., Ardiyatno, C. N., Aguswarini, S., Rustendi, K. C. T., Subur, M., et al. (2011). "Preclinical study of 177Lu-DOTA-trastuzumab, a potential radiopharmaceutical for therapy of breast cancer positive HER-2," in *Proceedings of the 2nd International Seminar on Chemistry* (Bandung), 71–78.

Sihver, W., Pietzsch, J., Krause, M., Baumann, M., Steinbach, J., and Pietzsch, H.-J. (2014). Radiolabeled cetuximab conjugates for EGFR targeted cancer diagnostics and therapy. *Pharmaceuticals* 7, 311–338. doi: 10.3390/ph7030311

Stanisz, G. J., and Henkelman, R. M. (2015). Gd-DTPA relaxivity depends on macromolecular content. *Magnetic Resonance Med.* 44, 665–667. doi: 10.1002/1522-2594(200011)44:5<665::AID-MRM1>3.0.CO;2-M

Tinianow, J. N., Pandya, D. N., Pailloux, S. L., Ogasawara, A., Vanderbilt, A. N., Gill, H. S., et al. (2016). Evaluation of a 3-hydroxypyridin-2-one (2,3-HOPO) based macrocyclic chelator for 89Zr4+ and its use for immuno-PET imaging of HER2 positive model of ovarian carcinoma in mice. *Theranostics* 6, 511–521. doi: 10.7150/thno.14261

Wang, Z., Zhang, F., Shao, D., Chang, Z., and Dong, W. (2019). Janus nanobullets combine photodynamic therapy and magnetic hyperthermia to potentiate synergetic anti-metastatic immunotherapy. *Adv. Sci.* 6:1901690. doi: 10.1002/advs.201901690

Yokel, R. A., Fredenburg, A. M., Durbin, P. W., Jide, X.u, Mart, K. R., Kenneth, N. R., et al. (2000). The hexadentate hydroxypyridinonate TREN-(Me-3,2-HOPO) is a more orally active iron chelator than its bidentate analogue. *J. Pharm. Sci.* 89, 545–555. doi: 10.1002/(SICI)1520-6017(200004)89:4<545::AID-JPS12>3.0.CO;2-J

Zimei, L., and Zan, S. (2017). The latest developments in targeted therapy for triple-negative breast cancer. *China Oncol.* 27, 36–40. doi: 10.19401/j.cnki.1007-3639.2017.01.007

Conflict of Interest: The authors declare that the research was conducted in the absence of any commercial or financial relationships that could be construed as a potential conflict of interest.

Publisher's Note: All claims expressed in this article are solely those of the authors and do not necessarily represent those of their affiliated organizations, or those of the publisher, the editors and the reviewers. Any product that may be evaluated in this article, or claim that may be made by its manufacturer, is not guaranteed or endorsed by the publisher.

frontiers in Bioengineering and Biotechnology

ORIGINAL RESEARCH
published: 04 August 2021
doi: 10.3389/fbioe.2021.691091

Facile Assembly of Thermosensitive Liposomes for Active Targeting Imaging and Synergetic Chemo-/Magnetic Hyperthermia Therapy

*Yanli An[1], Rui Yang[2], Xihui Wang[3], Yong Han[3], Gang Jia[3], Chunmei Hu[4], Zhiyuan Zhang[5], Dongfang Liu[3] and Qiusha Tang[3]**

[1] Jiangsu Key Laboratory of Molecular and Functional Imaging, Department of Radiology, Zhongda Hospital, Medical School of Southeast University, Nanjing, China, [2] Research Institute for Reproductive Health and Genetic Diseases, The Affiliated Wuxi Maternity and Child Health Care Hospital of Nanjing Medical University, Wuxi, China, [3] School of Medicine, Southeast University, Nanjing, China, [4] Department of Tuberculosis, The Second Affiliated Hospital of Southeast University (The Second Hospital of Nanjing), Nanjing, China, [5] Department of Neurosurgery, Nanjing Jinling Hospital, School of Medicine, Nanjing University, Nanjing, China

OPEN ACCESS

Edited by:
Wang Zheng,
Suzhou Institute of Nano-Tech and Nano-Bionics (CAS), China

Reviewed by:
Min Yang,
Jiangsu Institute of Nuclear Medicine, China
Wei Wu,
Nanjing University, China
Luzhong Zhang,
Nantong University, China

***Correspondence:**
Qiusha Tang
panyixi-tqs@163.com

Specialty section:
This article was submitted to Nanobiotechnology, a section of the journal Frontiers in Bioengineering and Biotechnology

Received: *05 April 2021*
Accepted: *01 June 2021*
Published: *04 August 2021*

Citation:
An Y, Yang R, Wang X, Han Y, Jia G, Hu C, Zhang Z, Liu D and Tang Q (2021) Facile Assembly of Thermosensitive Liposomes for Active Targeting Imaging and Synergetic Chemo-/Magnetic Hyperthermia Therapy. Front. Bioeng. Biotechnol. 9:691091. doi: 10.3389/fbioe.2021.691091

Cancer stem cells (CSCs) are thought to be responsible for the recurrence of liver cancer, highlighting the urgent need for the development of effective treatment regimens. In this study, 17-allylamino-17-demethoxygeldanamycin (17-AAG) and thermosensitive magnetoliposomes (TMs) conjugated to anti-CD90 (CD90@17-AAG/TMs) were developed for temperature-responsive CD90-targeted synergetic chemo-/magnetic hyperthermia therapy and simultaneous imaging *in vivo.* The targeting ability of CD90@DiR/TMs was studied with near-infrared (NIR) resonance imaging and magnetic resonance imaging (MRI), and the antitumor effect of CD90@17-AAG/TM-mediated magnetic thermotherapy was evaluated *in vivo*. After treatment, the tumors were analyzed with Western blotting, hematoxylin and eosin staining, and immunohistochemical (IHC) staining. The relative intensity of fluorescence was approximately twofold higher in the targeted group than in the non-targeted group, while the T_2 relaxation time was significantly lower in the targeted group than in the non-targeted group. The combined treatment of chemotherapy, thermotherapy, and targeting therapy exhibited the most significant antitumor effect as compared to any of the treatments alone. The anti-CD90 monoclonal antibody (mAb)-targeted delivery system, CD90@17-AAG/TMs, exhibited powerful targeting and antitumor efficacies against $CD90^+$ liver cancer stem cells *in vivo*.

Keywords: CD90, combined therapy, imaging, LCSCs, hyperthermia therapy

INTRODUCTION

Tumorigenesis and heterogeneity, progression, and recurrence of tumors are largely caused by a small subpopulation of tumor cells with stem cell properties, known as the cancer stem cells (CSCs) (Chen et al., 2013). The conventional anticancer drugs generally affect normal cancer cells; however, recurrence is highly frequent owing to the activity of residual CSCs that are resistant to

radiotherapy and chemotherapy. Some of the resistance mechanisms involve the dormant or slow-growing phase of the cell cycle such as those that target the ATP-binding cassette (ABC) superfamily (Schätzlein, 2006; Kobayashi et al., 2014; Moitra, 2015). Thus, therapeutic strategies targeting the minor population of CSCs may be one of the most promising approaches for the treatment of resistant tumors.

In general, drugs effective against CSCs may face difficulty in entering and accumulating in the tumor where CSCs are located, resulting in inefficient therapeutic outcomes. Nanoparticles conjugated with specific CSC biomarkers have been recently successfully synthesized to selectively eliminate CSCs (Wang et al., 2013). Wang et al. (2012) showed that the delivery of suicide gene and doxorubicin through CD44-conjugated liposomal nanoparticles that specifically target $CD44^+$ tumorigenic cells of hepatocellular carcinoma (HCC) resulted in the induction of apoptosis and inhibition of tumor growth. Furthermore, Rao et al. (2015) developed a doxorubicin-encapsulated polymeric nanoparticle covered with chitosan to target and kill $CD44^+$ mammary cancer stem-like cells. This drug delivery system was found to be effective in eliminating cancer stem-like cells, decreasing the tumor volume, and exhibiting low systemic toxicity. Hence, the development of nanoparticles specifically targeted to affect CSC function and maintenance may be an attractive option to cure cancer such that these particles directly target and kill CSCs, reduce systemic toxicity, allow better tolerance to a larger drug dose and longer course, and eliminate the risk of metastasis and tumor recurrence.

At present, therapeutic strategies for CSC-targeted therapy overlap with the multidisciplinary therapies employed for the elimination of non-CSCs. These cells represent a considerable population of tumor cells and play a significant role in CSC growth regulation (Ye et al., 2014). Therefore, the eradication of differentiated cells in tumors may provide a synergetic effect for the clearance of CSCs. CD90 is an important marker for liver cancer stem cells (LCSCs), and study has shown that the expression of CD90 was related to the formation, growth, metastasis, and drug resistance of liver cancer. This makes the treatment of targeting $CD90^+$ LCSCs of important practical significance (Liu et al., 2020). It is important and of potential clinical value to find novel therapeutic approaches that specifically kill CSCs and serve as effective supplementary treatments to reduce tumor recurrence and metastasis by improving the therapeutic response. Magnetic hyperthermia is the delivery of magnetic nanoparticles into the target tissue heated to 41–46°C with an alternating current magnetic field (AMF), an adjuvant strategy in cancer treatment (Grumezescu et al., 2014). Thermotherapy has a strong anticancer activity when combined with other treatments (Paunesku et al., 2015; Wang et al., 2019). Thus, magnetic thermotherapy is a novel technique to heat the deep-seated tumors; however, its application is limited owing to its inability to target tumors (Rao et al., 2016). Thermosensitive magnetoliposomes (TMs) are promising agents in the field of targeted liposomes, as these particles render the treatment more effective and safer based on the dual effect of liposomes and magnetic thermotherapy (Wang et al., 2018). In addition, drug-loaded TMs surface modified with a targeting ligand may enhance the accumulation and release of the drug at the target site upon exposure to AMF, serving as a novel approach for targeted liposomal therapeutics (Deshpande et al., 2013).

In our previous study, we prepared anti-CD90 monoclonal antibody (mAb)-targeted TMs encapsulating heat shock protein (HSP) inhibitor, 17-allylamino-17-demethoxygeldanamycin (17-AAG) (CD90@17-AAG/TMs), to target and kill $CD90^+$ LCSCs *in vitro* (Yang et al., 2015). In combination with magnetic thermotherapy, CD90@17-AAG/TMs showed good targeting efficiency against $CD90^+$ LCSCs and effectively killed these cells *in vitro*. In addition, the upregulation of HSP90 by heat treatment caused thermoresistance *in vitro* and exerted a direct impact on the effectiveness of hyperthermia therapy. HSP inhibitor 17-AAG may reverse thermoresistance and promote apoptosis of $CD90^+$ LCSCs *in vitro* (Yang et al., 2015). We collectively studied the targeting property of CD90@17-AAG/TMs in HCC-bearing mice and explored the antitumor effect and mechanism of CD90@17-AAG/TMs against $CD90^+$ LCSCs under hyperthermic conditions *in vivo*.

MATERIALS AND METHODS

Cells and Animals

The HCC cell line Huh7 was purchased from the Institute of Biochemistry and Cell Biology (Shanghai, China). $CD90^+$ LCSCs were sorted from Huh7, as previously reported (Yang et al., 2015). BALB/c nude mice (female, average weight: 20 g, 5 weeks old) were purchased from the Comparative Medicine Centre of Yangzhou University (Yangzhou, Jiangsu, China).

Synthesis of CD90@17-AAG/TMs

We prepared 17-AAG/TMs using the rotary evaporator hydration method, as previously reported (Yang et al., 2015). 17-AAG-loaded thermosensitive liposomes (17-AAG/TSLs) comprised dipalmitoylphosphatidylcholine (DPPC), 17-AAG, cholesterol, and 1,2-distearoyl-sn-glycero-3-phosphoethanolamine-N-(methoxy[polyethylene glycol]-2000) n, (PEG2000-DSPE) (54:6:1:1 m/m). CD90@17-AAG/TMs were synthesized as described in our previous report (Deshpande et al., 2013). Anti-CD90 mAb-targeted TMs encapsulating DiR (CD90@DiR/TMs) were prepared using a similar method. The average size of the liposomes used in this study was approximately 130 nm. CD90@17-AAG/TMs were stable in phosphate-buffered saline when stored at 4°C. The phase transition temperature of CD90@17-AAG/TMs was 41.9°C. The liposomes showed good temperature-sensitive release properties at temperatures higher than the phase transition temperature. CD90@17-AAG/TMs could reach the effective thermotherapy temperature of 41°C–44°C upon exposure to AMF.

Establishment of Tumor-Bearing Mice Model With $CD90^+$ LCSCs

Tumors were developed in BALB/c nude mice with a subcutaneous injection of 1×10^5 $CD90^+$ LCSCs into the hindlimb. The experimental analysis was initiated once the

tumor volume reached 200 mm^3. Mice were housed in the Sterile Barrier System of the Medical School, Southeast University, Nanjing, China.

Targeting Ability of CD90@TMs Against CD90$^+$ LCSCs *in vivo*

Near-Infrared Imaging

Irrelevant mAb-modified DiR/TMs (IgG@DiR/TMs) were used as the control for the targeting experiment. The mice were randomly divided into three groups (five mice per group) as follows: IgG@DiR/TMs, DiR/TMs, and CD90@DiR/TMs. Mice were intravenously injected with DiR at 0.2 mg/kg. Near-infrared (NIR) images were acquired with the Maestro *in vivo* optical imaging system (excitation: 748 nm, emission: 780 nm, exposure time: 400 ms; Caliper Life Sciences, Hopkinton, MA, United States) at preinjection and at 1, 4, 6, 8, 24, 48, and 72 h post-injection and analyzed using the Maestro 2.10.0 software (Caliper Life Sciences, Hopkinton, MA, United States). The relative fluorescence intensity of the tumor was calculated as follows:

Relative fluorescence intensity = fluorescence intensity of the tumor/fluorescence intensity of the muscle.

The fluorescence intensity was measured by manually drawing a region of interest (ROI) within the tumor and muscle areas.

Magnetic Resonance Imaging

Based on the treatment, mice were divided into three groups (five mice per group) as follows: IgG@DiR/TMs, DiR/TMs, and CD90@DiR/TMs. The agents were administered through the tail vein under anesthesia (10 mg Fe/kg). The magnetic resonance imaging (MRI) of the tumor was performed at 1, 6, 8, 24, 48, and 72 h post-injection. The mapping sequence for the tumor was as follows: multi-slice multi-echo T_2-weighted imaging (MSME-T2WI): field of view (FOV) = 35 mm × 35 mm, repetition time (TR) = 3000 ms, echo time (TE) = 20 ms, slice thickness = 0.8 mm, and matrix = 256 × 256; FLASH-T2* sequence: FOV = 35 mm × 35 mm, TR = 408 ms, TE = 3.5 ms, slice thickness = 0.8 mm, and matrix = 256 × 256. The relative signal intensity of the tumor was calculated as follows:

Relative signal intensity = T_2 value of the tumor/T_2 value of the muscle

where T_2 = relaxation times measured by manually drawing an ROI within the tumor and muscle areas.

Prussian Blue Staining

After the imaging assays, mice were euthanized. Tumor tissues were excised and fixed in 10% neutral-buffered formalin. Tissues were embedded in paraffin, and 4-μm thick sections were obtained. The sections were successively stained by Prussian blue for ferric ions and nuclear fast red for the cell nucleus and examined using an optical microscopy.

In vivo Targeted Therapy of CD90@17-AAG/TMs

Once the tumor volume reached approximately 200 mm^3, CD90$^+$ LCSC-bearing mice were randomly divided into eight groups (12 mice per cohort) as shown in **Table 1**. After receiving anesthesia, mice were injected with different liposomes (10 mg Fe/kg, 40 mg 17-AAG/kg) in the caudal vein, as previously reported (Xie et al., 2014, 2016). The frequency of the injection was once a day. After 24 h, hyperthermia groups were placed on AMF (f = 200 kHz; I = 20 A) for 60 min every other day. Seven days later, half of the mice in each group were euthanized and weighed. The tumors were sectioned, followed by hematoxylin and eosin (H&E) staining. The expression levels of CD90 and HSP90 in the tumor were detected using immunohistochemical (IHC) staining. The inhibition rate (IR) of tumor volume was calculated as follows:

IR of tumor volume = (1 − volume of experimental group/volume of control groups) × 100%.

IR of the tumor mass was calculated as follows:

IR of tumor mass = (1 − weight of experimental group/weight of control groups) × 100%.

The other half of the mice were fed until their natural death, and the survival time of each mouse in eight groups was recorded and plotted as a survival curve.

TABLE 1 | Groups and treatments of targeted therapy of CD90@17-AAG/TMs.

Groups	Treatments
Control group	tumors injected with NS and unexposed to AMF
NS + AMF group	tumors injected with NS and exposed to AMF
TMs group	tumors injected with TMs and unexposed to AMF
TMs + AMF group	tumors injected with TMs and exposed to AMF
TSLs group	tumors injected with TSLs and unexposed to AMF
17-AAG/TSL group	tumors injected with 17-AAG/TSLs and unexposed to AMF
17-AAG/TMs +AMF group	tumors injected with 17-AAG/TMs and exposed to AMF
CD90@17-AAG/TMs +AMF group	tumors injected with CD90@17-AAG/TMs and exposed to AMF

Western Blotting Analysis

Tumor proteins were extracted from different groups and quantified at the end of the treatment. Protein extracts (40 μg) were separated by 12% sodium dodecyl sulfate polyacrylamide gel electrophoresis (SDS-PAGE) and transferred onto polyvinylidene fluoride membranes. Blots were blocked in 5% non-fat milk and incubated with anti-HSP90 (1:500, Zhong Shan Golden Bridge Biotechnology, Beijing, China) and β-actin (1:10,000, Sigma, St. Louis, MO, United States) antibodies at 4°C overnight. Blots were treated with a secondary antibody (1:10,000, Thermo, Waltham, MA, United States) for 1 h and visualized with SuperSignal® West Pico Chemistry Luminescent Substrate (Thermo, Waltham, MA, United States).

Statistical Analysis

Values represent the mean ± standard deviation (SD). The data were analyzed using the SPSS 16.0 software (IBM). A value of $p < 0.05$ was considered as statistically significant. All experiments were performed in triplicates.

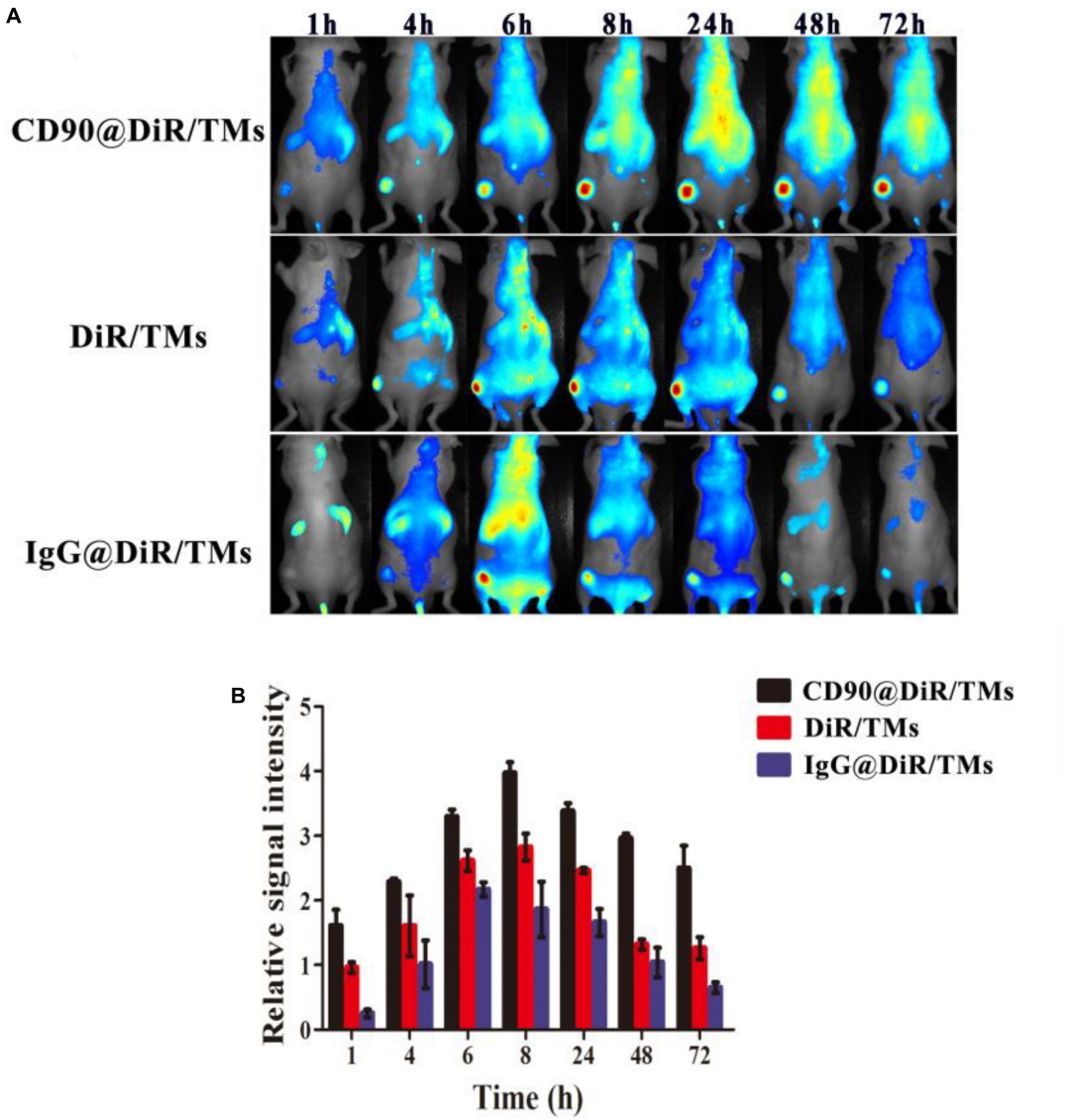

FIGURE 1 | Targeting ability of CD90@DiR/TMs in CD90$^+$ LCSC-bearing mice detected using NIR imaging. **(A)** NIR images at different time points following the injection of IgG@DiR/TMs, DiR/TMs, and CD90@DiR/TMs. **(B)** Relative fluorescence intensity of the tumor at different time points following the injection of IgG@DiR/TMs, DiR/TMs, and CD90@DiR/TMs.

RESULTS AND DISCUSSION

Near-Infrared Imaging

Liposomes, as targeted drug delivery systems, have offered a new platform for therapies against CSCs. Liposomes modified with antisurface CSC antigens may not only ameliorate the *in vivo* drug distribution but also allow specific delivery of drugs to the target cells. Hence, establishing target evaluation systems is desirable.

The *in vivo* targeting ability of CD90@17-AAG/TMs was evaluated by the encapsulation of an NIR dye DiR into the liposomes (CD90@DiR/TMs). The accumulation of CD90@DiR/TMs, IgG@DiR/TMs, and DiR/TMs in the tumor tissue was observed using NIR imaging. The highest accumulation in the tumor was detected for the two groups from 6 to 8 h after tail vein injection with the same dose of DiR, and a gradual decrease in the signal intensity was observed after 8 h (**Figure 1A**). However, the fluorescence intensity reported for the tumor injected with CD90@DiR/TMs remained high for more than 1 h after injection ($p < 0.05$; **Figure 1B**). The fluorescence intensity reported for tumors from IgG@DiR/TM and DiR/TMs group significantly decreased over time. The relative fluorescence intensity observed for the tumor from CD90@DiR/TM group was higher than that observed for the tumor from the DiR/TM group at different time points ($p < 0.05$). The relative fluorescence intensity from 8 to 72 h was 1.5 times higher in the CD90@DiR/TM group than in the DiR/TM and IgG@DiR/TM groups, indicating that anti-CD90

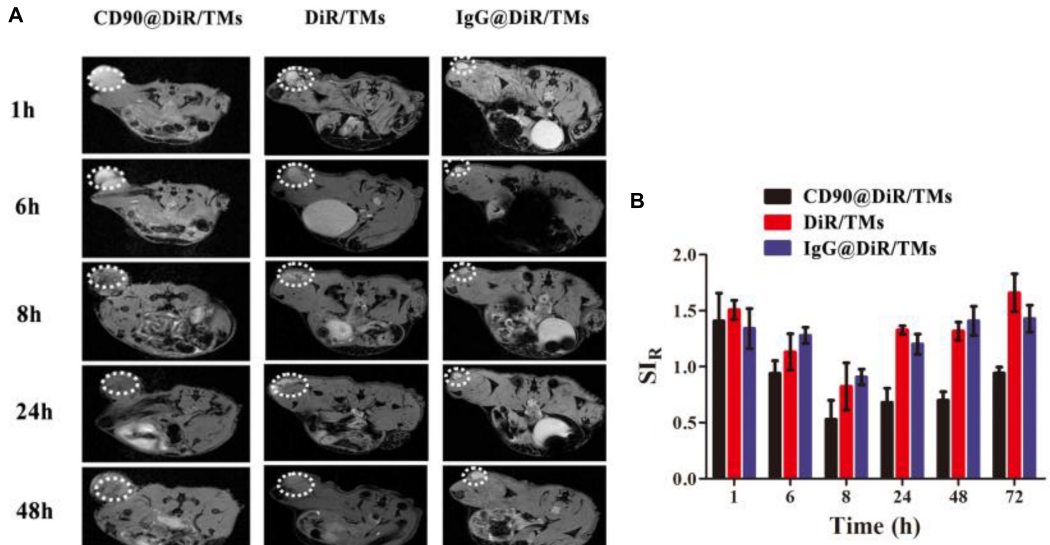

FIGURE 2 | Targeting ability of CD90@DiR/TM in CD90$^+$ LCSC-bearing mice observed using MRI. **(A)** MRI images at different time points following the injection of IgG@DiR/TMs, DiR/TMs, and CD90@DiR/TMs. **(B)** Relative signal intensities at different time points following the injection of IgG@DiR/TMs, DiR/TMs, and CD90@DiR/TMs.

mAb-modified liposomes may effectively bind to CD90$^+$ LCSCs and show improved cellular uptake.

Magnetic Resonance Imaging Analysis

Although the distribution of CD90@DiR/TMs in the tumor as well as in mice bodies can be studied using NIR fluorescent dyes, the spatial and temporal distribution may not be clearly observed. In addition, each drug has varying characteristics and specific location within cells, and NIR fluorescent dyes may be unable to simulate these features.

Drugs used as imaging tracers should be more powerful and useful for the investigation of the interaction between drug-loaded liposomes and cells. To confirm the targeting ability of CD90@DiR/TMs, the cellular uptake of IgG@DiR/TMs, DiR/TMs, and CD90@DiR/TMs was studied using MRI based on the principle that ferric oxide (Fe_3O_4) effectively decreases the T_2 relaxation time of the surrounding hydrogen proton (Hu et al., 2013). The accumulation of IgG@DiR/TMs, DiR/TMs, and CD90@DiR/TMs in the tumors increased and then gradually decreased over time, consistent with NIR imaging results (**Figure 2A**). The value of the relative signal intensity for tumors from the CD90@DiR/TM group was lower after 72 h of injection than that reported at 1 h after injection. In addition, the SI_R from 8 h was lower in the CD90@DiR/TM group than in the DiR/TMs and IgG@DiR/TMs ($p < 0.05$; **Figure 2B**). It means that the nanomaterials in the targeted group are more enriched in tumor tissues than in the non-targeted group and the irrelevant antibody group. In contrast, the relative signal intensities for tumors from the IgG@DiR/TM and DiR/TM groups showed no significant difference at the same time points ($p > 0.05$).

Prussian Blue Staining

The targeting abilities of CD90@DiR/TMs, IgG@DiR/TMs, and DiR/TMs against CD90$^+$ LCSCs in tumor tissues were further confirmed using Prussian blue staining, based on the principle that three-valent iron ions may react with potassium ferrocyanide to produce blue compounds under acidic conditions (Sluimer et al., 2015). The number of blue-stained particles in the tumor tissue from the CD90@DiR/TM group was significantly higher than that in the tumor tissue from the DiR/TM group (**Figure 3**). This result is consistent with NIR imaging and MRI results.

According to the enhanced permeability and retention (EPR) effect theory, the microvascular endothelial cells in human normal tissues are closely arranged; thus, polymeric drugs and lipid globules may not be able to penetrate through the blood vessels (Maeda et al., 2013). On the contrary, many solid tumors allow penetration of these particles as compared with normal tissues, thereby facilitating the extravasation of nanosized macromolecular anticancer drugs (particle size distribution range: 10–200 nm) owing to the abnormal vasculature in the rapidly proliferating tumors (Maeda, 2012). Polymeric drugs or lipid globules are easily intercepted due to the blockage of the lymphatic drainage. The particle size of the liposomes prepared was approximately 130 nm, which facilitated the easy accumulation of CD90@17-AAG/TMs in the tumor, attributable to the EPR effect and CD90 expression on the surface of LCSCs. Hence, Dir/TM and CD90@17-AAG/TMs were found

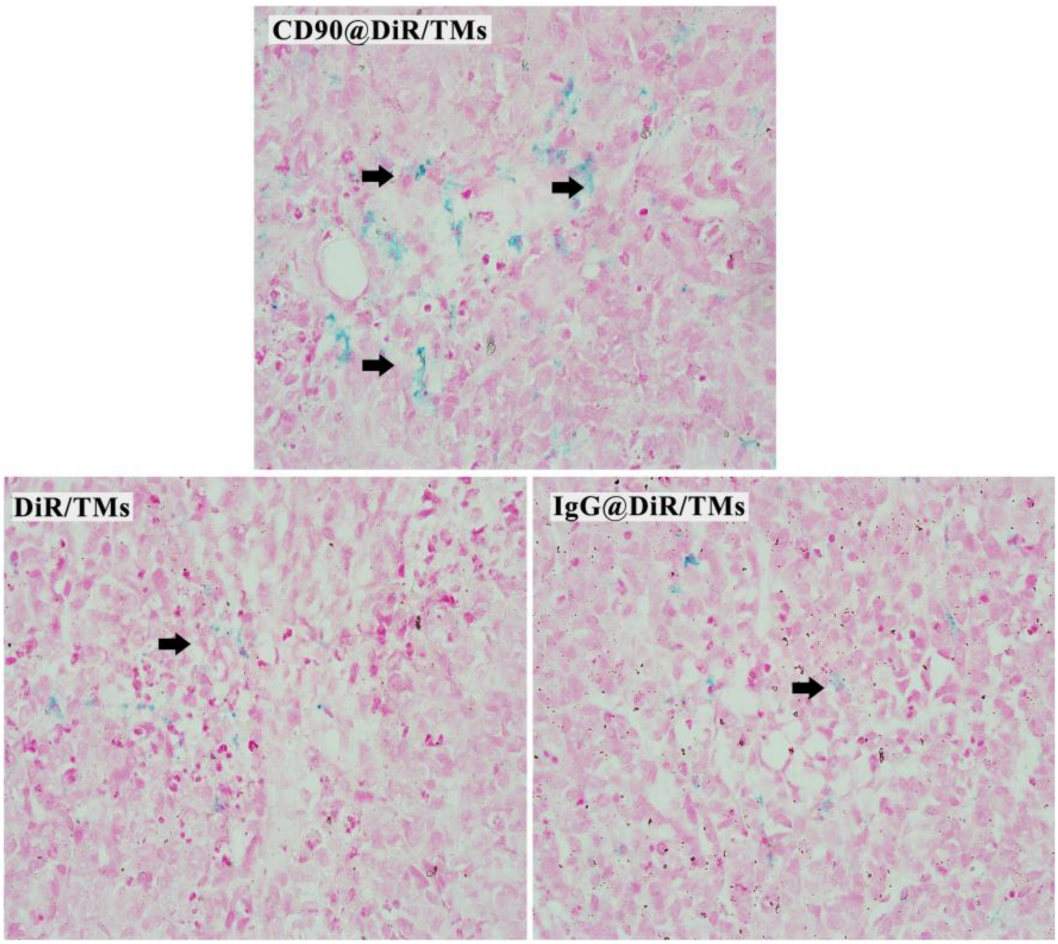

FIGURE 3 | Prussian blue staining of the tumor tissues injected with DiR/TMs and CD90@DiR/TM (×40).

to be distributed in the tumor using NIR imaging, MRI, and Prussian blue staining.

In vivo Targeted Therapy With CD90@17-AAG/TMs

To enhance the treatment effect, tumors were treated with different therapies after 24 h of injection. NIR imaging and MRI results revealed CD90@17-AAG/TM enrichment and showed its ability to induce toxicity against non-LCSCs while affecting $CD90^+$ LCSCs, owing to EPR effects and initial targeting function. The antitumor effect of CD90@17-AAG/TMs in $CD90^+$ LCSC-bearing mice was first determined by calculating the tumor volume and tumor mass IRs. **Table 2** shows that no significant differences were observed in tumor volume or tumor mass IRs among the normal saline (NS), NS + AMF, TM, and TSL groups; thus, AMF, TSLs, or TMs alone were non-toxic to tumors. The tumor volume and tumor mass IRs observed for the group treated with CD90@17-AAG/TMs in combination with hyperthermia were significantly higher than those reported for other groups ($p < 0.05$). The non-target group (17-AAG/TMs + AMF) also showed inhibition of tumor growth, possibly attributed to the enrichment of 17-AAG/TMs in the tumor tissues due to the EPR effect (**Figures 1**, **2**). The combination of 17-AAG/TMs + AMF and hyperthermia may eliminate both LCSCs and non-LCSCs. Furthermore, the injection method (injection every other day) was conducive for better enrichment. The tumor volume and tumor mass IRs in the 17-AAG/TMs + AMF group were higher than those reported for the TMs + AMF and 17-AAG/TSL groups. This observation may be associated with the reversal of thermoresistance by 17-AAG, resulting in the apoptosis of tumor cells as previously reported (Yang et al., 2015).

To further confirm the therapeutic effect of CD90@17-AAG/TMs, H&E staining of the tumors was performed. Dark brown Fe_3O_4 sediment was observed in tumors treated with different TMs (**Figure 4A**). The non-targeted groups such as TMs + AMF, 17-AAG/TSLs, and 17-AAG/TMs + AMF caused varying degrees of damages to tumors, probably attributable to the EPR effect in tumor tissues. NS, NS + AMF, TM, and TSL groups showed no effect on tumor tissues. Necrosis was predominant in the CD90@17-AAG/TMs + AMF group, indicating that CD90@17-AAG/TMs in combination with hyperthermia may kill $CD90^+$ LCSCs as well as $CD90^-$ tumor cells. Tumor cells in this group were almost completely

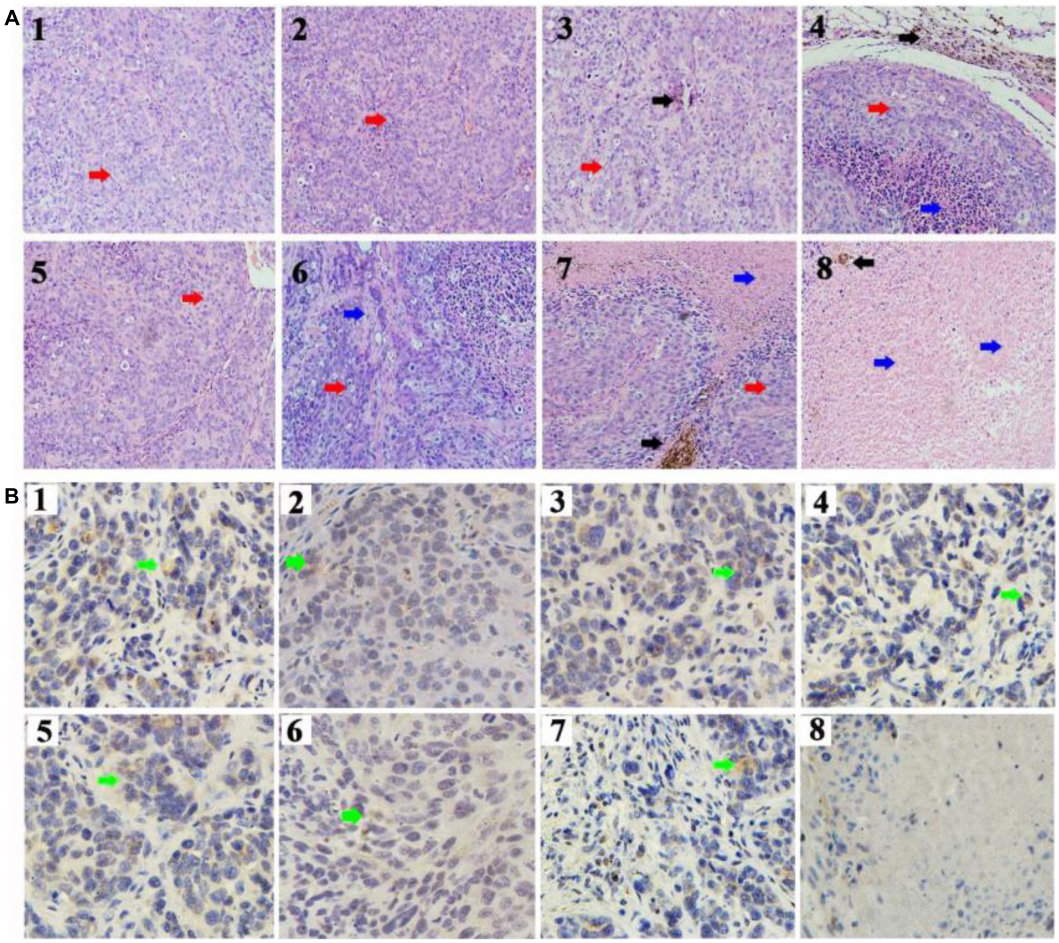

FIGURE 4 | Targeted therapy of CD90@17-AAG/TMs in different groups. **(A)** H&E staining of the tumor tissues in different groups (×20, black arrows represent Fe_3O_4 nanoparticles, red arrows represent tumor tissues, and blue arrows represent necrotic tissue). **(B)** CD90 IHC staining of the tumor tissues in different groups (×40, green arrows represent the CD90-positive cells). 1. NS, 2. NS + AMF, 3. TMs, 4. TMs + AMF, 5. TSLs, 6. 17-AAG/TSLs, 7. 17-AAG/TMs + AMF, and 8. CD90@17-AAG/TMs + AMF.

TABLE 2 | Tumor volume and tumor mass IRs in the different groups (%).

No.	Groups	IRs of tumor volume ($\bar{x} \pm s$, $n = 6$)	IRs of tumor mass ($\bar{x} \pm s$, $n = 6$)
1	NS	0	0
2	NS +AMF	0.47 ± 1.19^{ac}	0.18 ± 1.16^{ac}
3	TMs	1.08 ± 1.11^{ac}	0.53 ± 1.62^{ac}
4	TMs +AMF	24.53 ± 2.48^{bc}	18.63 ± 2.42^{bc}
5	TSLs	0.53 ± 1.12^{ac}	0.19 ± 0.96^{ac}
6	17-AAG/TSLs	21.27 ± 5.95^{bc}	21.13 ± 5.02^{bc}
7	17-AAG/TMs +AMF	64.13 ± 5.06^{c}	41.7 ± 3.47^{c}
8	CD90@17-AAG/TMs +AMF	88.0 ± 4.42^{b}	76.53 ± 5.04^{b}

[a]Comparison of experimental groups with the TMs + AMF group, $p < 0.05$; [b]comparison of experimental groups with the 17-AAG/TMs + AMF group, $p < 0.05$; [c]comparison of experimental groups with the CD90@17-AAG/TMs +AMF group, $p < 0.05$.

TABLE 3 | CD90 expression rates in tumor tissue of mice (%).

No.	Groups	Expression rates of CD90
1	NS	31.8 ± 2.7
2	NS +AMF	34.9 ± 6.2^{ac}
3	TMs	30.3 ± 3.0^{ac}
4	TMs +AMF	17.9 ± 1.4^{bc}
5	TSLs	34.2 ± 6.0^{ac}
6	17-AAG/TSLs	16.3 ± 1.1^{bc}
7	17-AAG/TMs +AMF	9.1 ± 1.2^{c}
8	CD90@17-AAG/TMs +AMF	1.9 ± 2.5

[a]Comparison of experimental groups with the NS group, $p > 0.05$; [b]comparison of experimental groups with the 17-AAG/TMs + AMF group, $p < 0.05$; [c]comparison of experimental groups with the CD90@17-AAG/TMs +AMF group, $p < 0.05$.

destroyed. CD90 expression was detected using IHC staining to confirm this hypothesis. CD90 expression in tumors treated with TMs + AMF, 17-AAG/TSLs, 17-AAG/TMs + AMF, and CD90@17-AAG/TMs decreased by varying levels (**Table 3** and **Figure 4B**). The expression rate of CD90 in CD90@17-AAG/TMs was significantly lower than that in other groups ($p < 0.05$). Taken together, the results of H&E staining and CD90 IHC staining

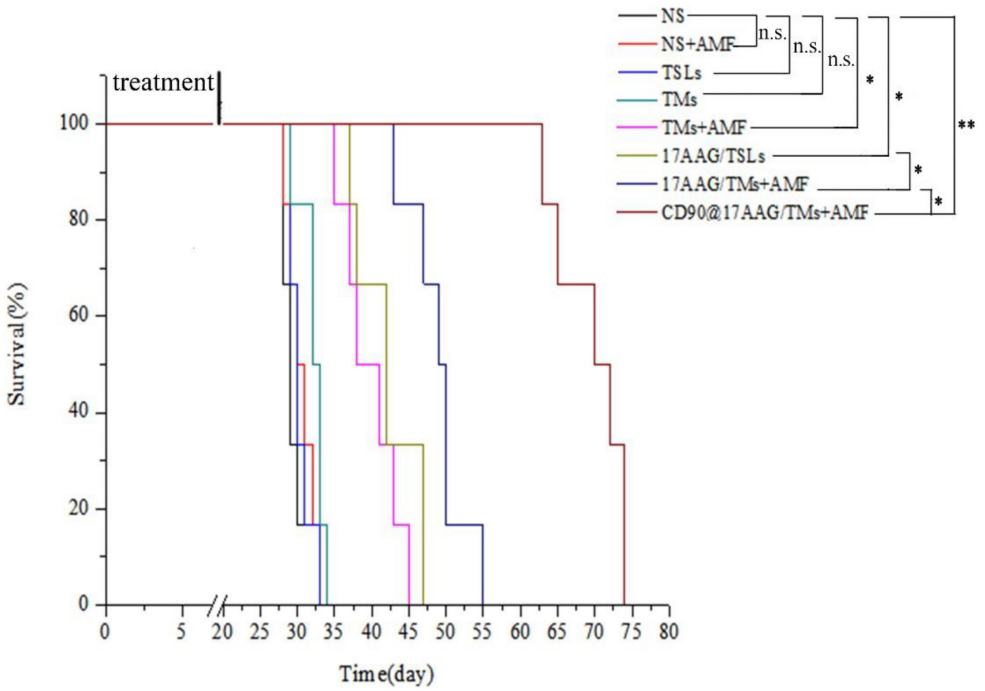

FIGURE 5 | Kaplan–Meier survival curve of CD90$^+$ LCSC-bearing mice in different groups. $n = 6$ mice per group. Data are the mean ± SD. $^*p < 0.05$, $^{**}p < 0.01$.

demonstrated the high killing ability of CD90@17-AAG/TMs against CD90$^+$ LCSCs and CD90$^-$ cells.

To evaluate the long-term effect of CD90@17-AAG/TMs + AMF therapy, overall survival of mice in each group was recorded. Kaplan–Meier survival curve was plotted according to the average survival time and SD (**Figure 5**). The results of the survival analysis were consistent with those of tumor volume IRs. No significant difference was observed between the NS, NS + AMF, TM, and TSL groups, suggestive of the absence of any effect of AMF, TSLs, or TMs on the survival time. The survival time was significantly longer for mice from the CD90@17-AAG/TM combined with hyperthermia group than those from other groups ($p < 0.01$). The non-targeted group (17-AAG/TMs + AMF) also showed prolonged survival as compared with the other four groups ($p < 0.05$) because of the inhibition ability reported due to the EPR effect. Furthermore, the survival time was longer for mice from the 17-AAG/TMs + AMF group than those from the TMs + AMF and 17-AAG/TSL groups ($p < 0.05$). All these results indicate that the tumor inhibition effect may transform into long-term survival benefit in CD90$^+$ LCSC-bearing mice.

Given their involvement in tumor formation, progression, metastasis, recurrence, and therapeutic resistance, CSCs serve as an excellent target for cancer treatment. However, the tumor microenvironment is mostly composed of non-CSCs, which play an important role in protecting and regulating the growth of CSCs (Luo et al., 2015). Therapeutic strategies that target only CSCs or non-CSCs have several limitations. Comprehensive therapeutic agents affecting both CSCs and non-CSCs hold great potential to eliminate all tumor cells and completely cure cancer. CD90@17-AAG/TMs combined with hyperthermia effectively eliminated CD90$^+$ LCSCs and CD90$^-$ cells. Hence, we hypothesized that the therapeutic effect is attributed to the following reasons: CD90@17-AAG/TMs were enriched in the stroma of tumor cells and CD90$^+$ LCSCs, owing to the EPR effect and CD90-targeting ability, which may be the most substantial reason for common elimination. The ability of tumor cells to engulf Fe_3O_4 is 4–800 times higher than that of normal cells. In addition, Fe_3O_4 endocytosed may be uniformly passed on to their progenies (Tay et al., 2018). If CD90@17-AAG/TMs were taken up by CD90$^+$ LCSCs, the Fe_3O_4 particles may be transferred to their progenies (CD90$^+$ LCSCs and CD90$^-$ cells). AMF application may now kill both CD90$^+$ LCSCs and CD90$^-$ cells. The disintegration of CD90$^+$ LCSC structure after treatment may result in the release of Fe_3O_4 particles into the surrounding environment, followed by their engulfment by other tumor cells (Jordan et al., 1999). Thus, multiple dosing and repeated treatments may potentially kill all types of tumor cells. The lysosomes from CD90$^+$ LCSCs that have endocytosed CD90@17-AAG/TMs may show sudden and substantial destruction upon exposure to AMF (Baeza et al., 2013). This would result in the release and activation of lysosomal enzymes, which would damage CD90$^+$ LCSCs and trigger injury to surrounding cells.

Mechanism Underlying Antitumor Effects of CD90@17-AAG/TM in CD90$^+$ LCSC-Bearing Mice

Magnetic thermotherapy is a novel technique to heat deep-seated tumors and effectively kill CSCs. However, the application of

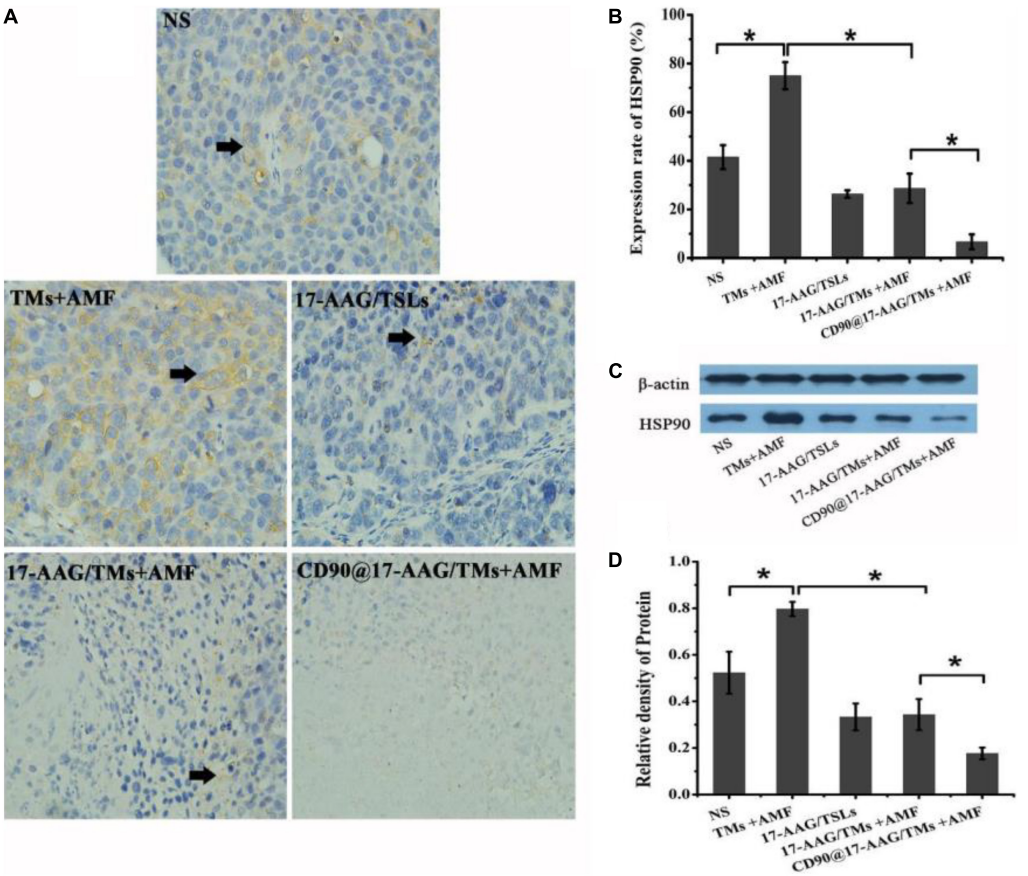

FIGURE 6 | Antitumor mechanism of CD90@17-AAG/TMs in CD90$^+$ LCSC-bearing mice. **(A)** HSP90 IHC staining of tumor tissues in different groups (×40). **(B)** Expression rate of HSP90, $^*p < 0.05$. **(C)** HSP90 expression observed using Western blot analysis. **(D)** Relative density of HSP90, $^*p < 0.05$.

hyperthermia alone has certain drawbacks, and the inclusion of heating time to enhance the effect of hyperthermia is more desirable. Thermotolerance may be developed in tumor cells undergoing multiheating treatment, resulting in reduced apoptosis and decreased cell death (Dai et al., 2013). HSPs are associated with thermoresistance and the induction of the heat shock response (Ahmed and Zaidi, 2013). The upregulation in HSP90 expression may affect the features or duration of thermotolerance (Millson and Piper, 2014). Inhibition of HSP90 may sensitize tumor cells to hyperthermia and result in increased apoptosis of tumor cells. 17-AAG is an HSP90 inhibitor derived from geldanamycin and may kill tumor cells by reversibly associating with HSP90 (Pacey et al., 2012). As a unique treatment, 17-AAG may effectively inhibit several cell signal transduction pathways involved in the maintenance of tumor cell proliferation and survival (Wang et al., 2014). To reduce the thermotolerance caused by magnetic thermotherapy, CD90@TMs encapsulating 17-AAG were prepared. The expression of HSP90 in NS, TMs + AMF, 17-AAG/TSLs, 17-AAG/TMs + AMF, and CD90@17-AAG/TMs was detected using HSP90 IHC staining and Western blot analysis. The expression rate of HSP90 was maximum in the TM + AMF group as compared to other groups ($p < 0.05$; **Figures 6A,B**), suggesting that multiheating treatment may induce thermotolerance. The encapsulation of 17-AAG in TMs resulted in a threefold decrease in the expression of HSP90 as compared to its encapsulation in TMs (28.7% ± 6.0% versus 75.0% ± 5.6%, $p < 0.05$), confirming the association between 17-AAG and HSP90$^+$ cells to overcome thermotolerance and induce cell death. The group treated with CD90@17-AAG/TMs showed minimum HSP90 expression, suggestive of the application of HSP90 to sensitize tumor cells to hyperthermia to achieve increased cell death. HSP90 protein quantitative test was performed using Western blot analysis. The trend observed in the relative expression of HSP90 coincided with the results of IHC staining. The relative intensity of HSP90 in the TM group was significantly higher than that observed in the NS and 17-AAG/TM groups ($p < 0.05$; **Figures 5C,D**), indicating that hyperthermia may upregulate the expression of HSP90 and that 17-AAG could effectively sensitize HSP90$^+$ tumor cells to magnetic hyperthermia. This observation also explains why the combination of 17-AAG/TMs and hyperthermia was more effective than the combination of TM and hyperthermia.

Hepatocellular carcinoma is one of the most common malignant tumors in the world, especially in Southeast Asia (Johnson et al., 2013). Although surgery and radiofrequency

ablation were used to treat HCC, and the common idea of these treatments is to decrease the volume of tumor tissues and the number of tumor cells in the greatest extent, recurrence is common after a certain period of time (Peng et al., 2012; Wald et al., 2013; Kwon et al., 2015). Hepatic artery embolism chemotherapy is the main treatment for advanced liver cancer and has a remission rate of only 30% (Song et al., 2015). Liu et al. (2018) synthesized the ^{131}I-labeled copper sulfide-loaded microspheres and combined embolization therapy, chemotherapy, radiotherapy, and photothermal therapy to treat hepatic tumors via hepatic artery embolization; the results showed that the embolization therapy in combination with chemotherapy, radiotherapy, and photothermal therapy could completely ablate the transplanted hepatic tumors *in situ*, while embolization combined with one or two therapy modalities slowed but did not stop tumor growth (Liu et al., 2018). In our study, the hyperthermia combined with one therapy modality can also inhibit the growth of tumor. One of the differences in our study is that the tumor model is ectopic. In future study, we will use orthotopic HCC model to verify the efficacy of CD90@17-AAG/TMs. In addition, the common occurrence of drug resistance often leads to chemotherapy failure. The first-line and second-line treatments for HCC, including sorafenib, regorafenib, and lenvatinib, can effectively treat HCC when combined with radiation therapy and chemotherapy. However, a study showed that the therapeutic effects are limited because of the high recurrence and drug resistance of LCSCs (Vu et al., 2013; Liu et al., 2020). The CSC theory explains the reason for treatment failure and demands new targets and orientation for HCC therapy. LCSCs cause tumor formation, recurrence, metastasis, and drug resistance (Chen et al., 2013). Hence, the permanent cure necessitates the complete eradication of CSCs. However, therapeutic strategies for CSCs are not different from those for non-CSCs. Non-CSCs have a protective effect on the growth of CSCs. In the present study, we enhanced the therapeutic effect against $CD90^+$ LCSCs by subjecting tumors to CD90@17-AAG/TM therapy every other day to strengthen the EPR effect and increase the endocytosis of liposomes. The treatment was continued for 7 days. CD90@17-AAG/TMs in combination with thermotherapy effectively killed $CD90^+$ LCSCs and $CD90^-$ cells *in vivo*. Although this study focused on the application of CD90@17-AAG/TMs in the treatment of HCC, other anticancer drugs could be encapsulated in these nanoparticles to eliminate CSCs and non-CSCs.

CONCLUSION

In this study, we constructed an anti-CD90 mAb-modified 17-AAG-loaded magnetic thermosensitive liposome (CD90@17-AAG/TMs) to target killing liver cancer cells. *In vivo*, it can remain in the tumor tissue through the CD90. The treatment results showed that CD90@17-AAG/TMs can effectively kill $CD90^+$ LCSCs and $CD90^-$ cells and inhibit tumor growth. In summary, CD90@17-AAG/TMs have great potential and application value in the targeted treatment of liver cancer.

DATA AVAILABILITY STATEMENT

The raw data supporting the conclusions of this article will be made available by the authors, without undue reservation.

ETHICS STATEMENT

The animal study was reviewed and approved by Institutional Animal Care and Use Committee (IACUC) of Southeast University.

AUTHOR CONTRIBUTIONS

QT was contributed to the design and conception of the subject. YA gave great support in animal imaging. XW is responsible for the implementation of the experiments, the results sorting, and manuscript writing. RY and YH gave lots of guidances on experiments details and manuscript submission. CH, ZZ, and DL was helpful in flow cytometry, animal model construction, and pictures processing. All authors contributed to the article and approved the submitted version.

FUNDING

This work was supported by the National Natural Science Foundation of China (81571789, 81271635, 81301270, and 81201131), the Natural Science Foundation of Jiangsu Province (BK2012335), the Regular University Graduate Student Scientific Research Innovation Projects of Jiangsu Province (KYCX18_0179), the Scientific Research Foundation of Graduate School of Southeast University and Southeast University Excellent Doctor Degree Thesis Training Fund (YBJJ1459), social development project of key research and development plan of Jiangsu province (grant no. BE2018606), and Six talent peaks project in Jiangsu Province (wsw-028).

REFERENCES

Ahmed, K., and Zaidi, S. F. (2013). Treating cancer with heat: hyperthermia as promising strategy to enhance apoptosis. *J. Pak. Med. Assoc.* 63, 504–508.

Baeza, A., Arcos, D., and Vallet-Regí, M. (2013). Thermoseeds for interstitial magnetic hyperthermia: from bioceramics to nanoparticles. *J. Phys. Condens. Matter.* 25:484003. doi: 10.1088/0953-8984/25/48/484003

Chen, K., Huang, Y. H., and Chen, J. L. (2013). Understanding and targeting cancer stem cells: therapeutic implications and challenges. *Acta Pharmacol. Sin.* 34, 732–740. doi: 10.1038/aps.2013.27

Dai, B., Gong, A., Jing, Z., Aldape, K. D., Kang, S. H., Sawaya, R., et al. (2013). Forkhead box M1 is regulated by heat shock factor 1 and promotes glioma cells survival under heat shock stress. *J. Biol. Chem.* 288, 1634–1642. doi: 10.1074/jbc.M112.379362

Deshpande, P. P., Biswas, S., and Torchilin, V. P. (2013). Current trends in the use of liposomes for tumor targeting. *Nanomedicine* 8, 1509–1528. doi: 10.2217/nnm.13.118

Grumezescu, A. M., Holban, A. M., Andronescu, E., Mogoşanu, G. D., Vasile, B. S., Chifiriuc, M. C., et al. (2014). Anionic polymers and 10 nm Fe_3O_4@UA wound dressings support human foetal stem cells normal development and exhibit great antimicrobial properties. *Int. J. Pharm.* 463, 146–154.

Hu, Y., Meng, L., Niu, L., and Lu, Q. (2013). Highly cross-linked and biocompatible polyphosphazene-coated superparamagnetic Fe_3O_4 nanoparticles for magnetic resonance imaging. *Langmuir* 29, 9156–9163. doi: 10.1021/la402119s

Johnson, P. J., Qin, S., Park, J. W., Poon, R. T., Raoul, J. L., Philip, P. A., et al. (2013). Brivanib versus sorafenib as first-line therapy in patients with unresectable, advanced hepatocellular carcinoma: results from the randomized phase III BRISK-FL study. *J. Clin. Oncol.* 31, 3517–3524. doi: 10.1200/JCO.2012.48.4410

Jordan, A., Scholz, R., Wust, P., Fähling, H., and Felix, R. (1999). Magnetic fluid hyperthermia (MFH): cancer treatment with magnetic fluid induced excitation of biocompatible superparamagnetic nanoparticles. *J. Magn. Magn. Mater.* 201, 413–419. doi: 10.1016/S0304-8853(99)00088-8

Kobayashi, Y., Sugiura, T., Imajyo, I., Shimoda, M., Ishii, K., Akimoto, N., et al. (2014). Knockdown of the T-box transcription factor Brachyury increases sensitivity of adenoid cystic carcinoma cells to chemotherapy and radiation in vitro: implications for a new therapeutic principle. *Int. J. Oncol.* 44, 1107–1117. doi: 10.3892/ijo.2014.2292

Kwon, S., Scovel, L., Yeh, M., Dorsey, D., Dembo, G., Krieger, E. V., et al. (2015). Surgical management of hepatocellular carcinoma after Fontan procedure. *J. Gastrointest. Oncol.* 6, E55–E60. doi: 10.3978/j.issn.2078-6891.2015.009

Liu, Q., Qian, Y., Li, P., Zhang, S., Liu, J., Sun, X., et al. (2018). 131I-labeled copper sulfide-loaded microspheres to treat hepatic tumors via hepatic artery embolization. *Theranostics* 8, 785–799. doi: 10.7150/thno.21491

Liu, Y. C., Yeh, C. T., and Lin, K. H. (2020). Cancer stem cell functions in hepatocellular carcinoma and comprehensive therapeutic strategies. *Cells* 9:1331. doi: 10.3390/cells9061331

Luo, M., Brooks, M., and Wicha, M. S. (2015). Epithelial-mesenchymal plasticity of breast cancer stem cells: implications for metastasis and therapeutic resistance. *Curr. Pharm. Des.* 21, 1301–1310. doi: 10.2174/1381612821666141211120604

Maeda, H. (2012). Macromolecular therapeutics in cancer treatment: the EPR effect and beyond. *J. Control. Release* 164, 138–144. doi: 10.1016/j.jconrel.2012.04.038

Maeda, H., Nakamura, H., and Fang, J. (2013). The EPR effect for macromolecular drug delivery to solid tumors: improvement of tumor uptake, lowering of systemic toxicity, and distinct tumor imaging in vivo. *Adv. Drug Deliv. Rev.* 65, 71–79. doi: 10.1016/j.addr.2012.10.002

Millson, S. H., and Piper, P. W. (2014). Insights from yeast into whether the inhibition of heat shock transcription factor (Hsf1) by rapamycin can prevent the Hsf1 activation that results from treatment with an Hsp90 inhibitor. *Oncotarget* 5, 5054–5064. doi: 10.18632/oncotarget.2077

Moitra, K. (2015). Overcoming multidrug resistance in cancer stem cells. *Biomed. Res. Int.* 2015:635745. doi: 10.1155/2015/635745

Pacey, S., Gore, M., Chao, D., Banerji, U., Larkin, J., Sarker, S., et al. (2012). A phase II trial of 17-allylamino, 17-demethoxygeldanamycin (17-AAG, tanespimycin) in patients with metastatic melanoma. *Invest. New Drugs* 30, 341–349. doi: 10.1007/s10637-010-9493-4

Paunesku, T., Gutiontov, S., Brown, K., and Woloschak, G. E. (2015). Radiosensitization and nanoparticles. *Cancer Treat. Res.* 166, 151–171. doi: 10.1007/978-3-319-16555-4_7

Peng, Z. W., Lin, X. J., Zhang, Y. J., Liang, H. H., Guo, R. P., Shi, M., et al. (2012). Radiofrequency ablation versus hepatic resection for the treatment of hepatocellular carcinomas 2 cm or smaller: a retrospective comparative study. *Radiology* 262, 1022–1033. doi: 10.1148/radiol.11110817

Rao, W., Wang, H., Han, J., Zhao, S., Dumbleton, J., Agarwal, P., et al. (2015). Chitosan-decorated doxorubicin-encapsulated nanoparticle targets and eliminates tumor reinitiating cancer stem-like cells. *ACS Nano* 9, 5725–5740. doi: 10.1021/nn506928p

Rao, W., Wang, H., Zhong, A., Yu, J., Lu, X., and He, X. (2016). Nanodrug-mediated thermotherapy of cancer stem-like cells. *J. Nanosci. Nanotechnol.* 16, 2134–2142. doi: 10.1166/jnn.2016.10942

Schätzlein, A. G. (2006). Delivering cancer stem cell therapies – a role for nanomedicines? *Eur. J. Cancer* 42, 1309–1315. doi: 10.1016/j.ejca

Sluimer, J. C., Gijbels, M. J., and Heeneman, S. (2015). Detection of intraplaque hemorrhage in mouse atherosclerotic lesions. *Methods Mol. Biol.* 1339, 339–348. doi: 10.1007/978-1-4939-2929-0_24

Song, D. S., Song, M. J., Bae, S. H., Chung, W. J., Jang, J. Y., Kim, Y. S., et al. (2015). A comparative study between sorafenib and hepatic arterial infusion chemotherapy for advanced hepatocellular carcinoma with portal vein tumor thrombosis. *J. Gastroenterol.* 50, 445–454. doi: 10.1007/s00535-014-0978-3

Tay, Z. W., Chandrasekharan, P., Chiu-Lam, A., Hensley, D. W., Dhavalikar, R., Zhou, X. Y., et al. (2018). Magnetic particle imaging-guided heating in vivo using gradient fields for arbitrary localization of magnetic hyperthermia therapy. *ACS Nano* 12, 3699–3713. doi: 10.1021/acsnano.8b00893

Vu, N. B., Nguyen, T. T., Tran, L. C., Do, C. D., Nguyen, B. H., Phan, N. K., et al. (2013). Doxorubicin and 5-fluorouracil resistant hepatic cancer cells demonstrate stem-like properties. *Cytotechnology* 65, 491–503. doi: 10.1007/s10616-012-9511-9

Wald, C., Russo, M. W., Heimbach, J. K., Hussain, H. K., Pomfret, E. A., and Bruix, J. (2013). New OPTN/UNOS policy for liver transplant allocation: standardization of liver imaging, diagnosis, classification, and reporting of hepatocellular carcinoma. *Radiology* 266, 376–382. doi: 10.1148/radiol.12121698

Wang, B., Chen, L., Ni, Z., Dai, X., Qin, L., Wu, Y., et al. (2014). Hsp90 inhibitor 17-AAG sensitizes Bcl-2 inhibitor (−)-gossypol by suppressing ERK-mediated protective autophagy and Mcl-1 accumulation in hepatocellular carcinoma cells. *Exp. Cell Res.* 328, 379–387. doi: 10.1016/j.yexcr.2014.08.039

Wang, K., Wu, X., Wang, J., and Huang, J. (2013). Cancer stem cell theory: therapeutic implications for nanomedicine. *Int. J. Nanomed.* 8, 899–908. doi: 10.2147/IJN.S38641

Wang, L., Su, W., Liu, Z., Zhou, M., Chen, S., Chen, Y., et al. (2012). CD44 antibody-targeted liposomal nanoparticles for molecular imaging and therapy of hepatocellular carcinoma. *Biomaterials* 33, 5107–5114.

Wang, X., Yang, R., Yuan, C., An, Y., Tang, Q., and Chen, D. (2018). Preparation of folic acid-targeted temperature-sensitive magnetoliposomes and their antitumor effects in vitro and in vivo. *Target Oncol.* 13, 481–494. doi: 10.1007/s11523-018-0577-y

Wang, Z., Zhang, F., Shao, D., Chang, Z., Wang, L., Hu, H., et al. (2019). Janus nanobullets combine photodynamic therapy and magnetic hyperthermia to potentiate synergetic anti-metastatic immunotherapy. *Adv. Sci.* 6:1901690. doi: 10.1002/advs.201901690

Xie, J., Yan, C., Yan, Y., Chen, L., Song, L., Zang, F., et al. (2016). Multi-modal Mn-Zn ferrite nanocrystals for magnetically-induced cancer targeted hyperthermia: a comparison of passive and active targeting effects. *Nanoscale* 8, 16902–16915. doi: 10.1039/c6nr03916b

Xie, J., Zhang, Y., Yan, C., Song, L., Wen, S., Zang, F., et al. (2014). High-performance PEGylated Mn-Zn ferrite nanocrystals as a passive-targeted agent for magnetically induced cancer theranostics. *Biomaterials* 35, 9126–9136.

Yang, R., Tang, Q., Miao, F., An, Y., Li, M., Han, Y., et al. (2015). Inhibition of heat-shock protein 90 sensitizes liver cancer stem-like cells to magnetic hyperthermia and enhances anti-tumor effect on hepatocellular carcinoma-burdened nude mice. *Int. J. Nanomed.* 10, 7345–7358. doi: 10.2147/IJN.S93758

Ye, J., Wu, D., Wu, P., Chen, Z., and Huang, J. (2014). The cancer stem cell niche: cross talk between cancer stem cells and their microenvironment. *Tumour Biol.* 35, 3945–3951. doi: 10.1007/s13277-013-1561-x

Conflict of Interest: The authors declare that the research was conducted in the absence of any commercial or financial relationships that could be construed as a potential conflict of interest.

The reviewer WW declared a shared affiliation, with no collaboration, with one of the author ZZ to the handling editor at the time of the review.

Publisher's Note: All claims expressed in this article are solely those of the authors and do not necessarily represent those of their affiliated organizations, or those of the publisher, the editors and the reviewers. Any product that may be evaluated in this article, or claim that may be made by its manufacturer, is not guaranteed or endorsed by the publisher.

frontiers in Bioengineering and Biotechnology

ORIGINAL RESEARCH
published: 24 August 2021
doi: 10.3389/fbioe.2021.747637

Self-Assembly Engineering Nanodrugs Composed of Paclitaxel and Curcumin for the Combined Treatment of Triple Negative Breast Cancer

Shuting Zuo[1], Zhenyu Wang[1], Xianquan An[2], Jing Wang[1], Xiao Zheng[3], Dan Shao[3] and Yan Zhang[1]**

[1]Department of Breast Surgery, The Second Hospital of Jilin University, Changchun, China, [2]Department of Anesthesiology, The Second Hospital of Jilin University, Changchun, China, [3]School of Biomedical Sciences and Engineering, South China University of Technology, Guangzhou, China

The clinical outcomes of triple-negative breast cancer (TNBC) chemotherapy are unsatisfactory. Water solubility and biosafety of chemo drugs are also major barriers for achieving satisfactory treatment effect. In this study, we have reported a combinational strategy by self-assembly engineering nanodrugs PC NDs, which were composed of paclitaxel (PTX) and curcumin (Cur), for effective and safe TNBC chemotherapy. PC NDs were prepared through reprecipitation method without using any additional carriers. The PC NDs were preferentially taken up by TNBC cells and we also observed pH-related drug release. Compared with free PTX and simple PTX/Cur mixture, PC NDs have shown higher therapeutic efficiency and better prognosis while the metastasis rate was significantly lower than that of either PTX or PTX/Cur mix group. Therefore, the self-assembly engineered PC NDs might be a promising nanodrugs for efficient and safe TNBC chemotherapy.

Keywords: triple-negative breast cancer, paclitaxel, curcumin, self-assembly, nanodrug

OPEN ACCESS

Edited by:
Jinbing Xie,
Southeast University, China

Reviewed by:
Jinfeng Liao,
Sichuan University, China
Qianyu Zhang,
Chongqing University, China

****Correspondence:***
Yan Zhang
zhangy01@jlu.edu.cn
Dan Shao
stanauagate@outlook.com

Specialty section:
This article was submitted to Nanobiotechnology, a section of the journal Frontiers in Bioengineering and Biotechnology

Received: *26 July 2021*
Accepted: *11 August 2021*
Published: *24 August 2021*

Citation:
Zuo S, Wang Z, An X, Wang J, Zheng X, Shao D and Zhang Y (2021) Self-Assembly Engineering Nanodrugs Composed of Paclitaxel and Curcumin for the Combined Treatment of Triple Negative Breast Cancer. Front. Bioeng. Biotechnol. 9:747637. doi: 10.3389/fbioe.2021.747637

INTRODUCTION

Breast cancer is the most common cancer type among women worldwide and threatens their health seriously (McDonald et al., 2016; Yeo and Guan, 2017; Fahad Ullah, 2019). Many chemotherapeutic, hormone-based, and combination drug regimens have been used to treat breast cancer, although patients with advanced aggressive disease (especially triple-negative breast cancer, TNBC) still have poor survival outcomes (Bergin and Loi, 2019). In this context, TNBC is characterized by non-expression of protein receptors, including progesterone receptor, estrogen receptor, and human epidermal growth receptor 2. Relative to other subtypes, TNBC is more aggressive, has a poorer prognosis and higher rates of visceral and central nervous system metastases, with no currently approved targeted therapies (Kumar and Aggarwal, 2016; Akram et al., 2017). Chemotherapy, including neoadjuvant chemotherapy, remains the only standard treatment option for TNBC, although patients have a poor response because of rapidly acquired drug resistance and distant metastasis, and also inevitably experience adverse effects (Lyons, 2019; Yin et al., 2020). Thus, there is a need for combination therapies that can improve the efficacy of current chemotherapeutic strategies for TNBC.

Paclitaxel (PTX) is a first-line chemotherapy drug that is used to treat TNBC by preventing microtubule depolymerization and arresting mitosis at G2/M stages of cell cycle. However, paclitaxel

has poor solubility, unavoidable toxicity, and tumors can develop resistance (Bielopolski et al., 2017; Abu Samaan et al., 2019). There is growing evidence that combining PTX with other chemotherapeutic agents (e.g., small molecule inhibitors or natural products) could enhance the anti-tumor effect (Schmid et al., 2018; Kang and Syed, 2020; Mittendorf et al., 2020). Curcumin (Cur) is a hydrophobic polyphenol derived from Curcuma longa (the spice turmeric). It exhibits anti-bacterial, anti-inflammatory, and anti-cancer properties. Furthermore, Cur has been proved to have excellent safety and widespread availability with low cost. Previous studies have indicated that Cur can downregulate the NF-kB and PI3K/Akt signaling pathways in cancer cells, which can inhibit cell growth, induce apoptosis, and increase drug sensitization (Hamzehzadeh et al., 2018; Subramaniam et al., 2018; Chen et al., 2019; Ghasemi et al., 2019; Maiti et al., 2019; Zusso et al., 2019; Borges et al., 2020; Keyvani-Ghamsari et al., 2020). In addition, the combination of PTX and Cur provided synergistic anti-cancer effects and eliminated cancer stem cells in TNBC (Baek and Cho, 2017; Calaf et al., 2018; Saghatelyan et al., 2020). However, similar to PTX, Cur has poor solubility and low bioavailability, which has limited its clinical application. Therefore, it would be useful to develop an efficient and safe system that could simultaneously deliver PTX and Cur to treat TNBC.

Significant work has been dedicated to developing drug delivery system that can concurrently deliver PTX and Cur to the tumor site, which might provide improved therapeutic activity and safety. However, most reported carriers have limited loading capacity and there are also concerns regarding their possible toxicity and biodegradation (Hiremath et al., 2019; Li et al., 2019; Zhao et al., 2019; Shao et al., 2020; Xiong et al., 2020; Hu et al., 2021; Liao et al., 2021; Zhang et al., 2021). Carrier-free drug delivery systems are recently developed alternatives that do not rely on inert carriers and thus avoid potential toxicity. Common strategies for preparing carrier-free nanodrugs include nanoprecipitation, thin-film hydration, template-assisted nanoprecipitation, supercritical fluid techniques, spray drying, and wet media milling (Zhang et al., 2018; Zheng et al., 2018; Sun et al., 2019; Zhou et al., 2019). Relative to free drugs, carrier-free nanodrugs have prolonged blood circulation times, better cellular penetration, and greater tumor accumulation (Yang et al., 2019), which has generated interest regarding their clinical applications. Therefore, we developed a carrier-free nanodrug that is composed of PTX and Cur (PC NDs) using a one-pot self-assembly nanoprecipitation method. Physicochemical, optical and drug release properties of PC NDs were characterized, and we then evaluated their effects against TNBC cells *in vitro* and *in vivo*. The results suggest that PC NDs may be a highly effective and safe option for treating TNBC.

MATERIALS AND METHODS

Chemicals and Reagents

Cur (purity: >94%) and sulforhodamine B (SRB) were obtained from Sigma-Aldrich (St. Louis, MO, United States). PTX was purchased from Solarbio Science and Technology Co., Ltd. (Beijing, China). Dulbecco's Modified Eagle Medium (DMEM), fetal bovine serum (FBS), trypsin and penicillin-streptomycin (10,000 U/ml) were obtained from GIBCO (Carlsbad, CA, United States). Matrigel was purchased from Corning Inc. (Billerica, MA, United States). Hoechst 33,258 and Lysotracker Red were purchased from Thermo Fisher Scientific (Waltham, MA, United States). Assay kits for determing alanine aminotransferase (ALT), aspartate aminotransferase (AST), alkaline phosphatase (ALP), blood urea nitrogen (BUN), and creatinine (CRE) were obtained from Nanjing Jiancheng Bioengineering Institute (Nanjing, Jiangsu, China). All reagents were directly used without any further purification.

Preparation and Characterization of PC NDs

The PC NDs were prepared using a reprecipitation method. First, Cur and PTX were dissolved in ethyl alcohol to provide solutions with concentrations of 2 mg/ml. Next, 0.4 ml of the PTX solution and 0.1 ml of the Cur solution were quickly added to 4.5 ml of deionized water, vortexed for 1 min and allowed to stand for 15 min to produce PC NDs. Finally, PC NDs were purified *via* ultrafiltration and collected *via* lyophilization, which provided a 4:1 weight ratio (PTX to Cur) after quantified by UV-vis method.

The morphology of PC NDs was inspected by a transmission electron microscope (JEOL, Ltd., Japan) and a scanning electron microscope (FESEM, S4800, Hitachi Co. Ltd., Tokyo, Japan). Fluorescence spectroscopy was performed using a Shimadzu RF-5301 PC spectrophotometer. UV–vis absorption spectra were obtained using a Shimadzu 3100 UV–vis spectrophotometer. Fourier transform infrared (FTIR) spectra were performed with a Nicolet AVATAR 360 FTIR instrument. X-ray powder diffraction (XRD) investigation was carried out on a Rigaku X-ray diffractometer using Cu Kα radiation. A Nano-ZS 90 Nanosizer (Malvern Instruments Ltd., Worcestershire, United Kingdom) was used to determine the size distribution and zeta potential of PC NDs.

Drug Release

Drug release behavior was evaluated by adding 5 mg of the PC NDs to a dialysis bag (5,000 Da), which was then placed in 50 ml of phosphate-buffered saline solution (PBS, pH: 7.4 or 5.5) on a shaking table at 37°C for 48 h. Supernatant was then collected and the amounts of PTX and Cur were analyzed *via* high-performance liquid chromatography.

Cell Culture and Uptake

A mouse breast cancer cell line (4T1), a human TNBC cell line (MDA-MB-231), and a non-neoplastic breast cell line (MCF-10A) were purchased from the American Type Culture Collection. All cells were cultured in DMEM with 10% FBS, 100 U/ml penicillin and 100 U/ml streptomycin in a humidified incubator with an atmosphere of 5% CO_2. Cellular uptake of PC NDs was evaluated after a 3-h incubation with cells, which were then washed with PBS and co-incubated with Lysotracker Red and Hoechst 33,258. Then cells were observed under an Olympus

IX71 fluorescence microscope (Olympus Corporation, Tokyo, Japan). Quantification of cellular uptake was conducted through flow cytometry (FACS, Becton Dickinson Biosciences, Franklin Lakes, United States).

Cytotoxicity

Cells were first seeded into 96-well culture plates at the density of 5,000 cells per well and then cultured overnight for fully attaching. Free Cur and PTX were dissolved deionized water at a concentration of 1 mg/ml, respectively. Next cells were treated with different final concentrations of free PTX, free Cur, PTX/Cur mixture (PTX/Cur mix) or PC NDs. After being treated for 24 or 48 h, cells were subjected to standard SRB assay and absorbance at 540 nm was analyzed using a multifunctional microplate reader. IC_{50} values were calculated by GraphPad Prism software.

In vivo Experiments

All mice were treated in compliance with the Guide for the Care and Use of Laboratory Animals, and all procedures were approved by the Animal Care and Use Committee of Jilin University (China). 50 μL of 4T1 cells (5×10^5) were mixed with 50 μL of matrigel and then orthotopically injected into the second mammary fat pad of female BALB/c mice (six to eight weeks old). Mice were randomly divided into five groups (n = 6) when tumor volume reached approximately 100 mm3, which were treated using saline, PTX (10 mg/kg, intraperitoneally), Cur (2.5 mg/kg, intraperitoneally), PTX/Cur mix (10 mg/kg of PTX and 2.5 mg/kg of Cur, intraperitoneally), or PC NDs (10 mg/kg, intravenously), respectively. All drug treatments were administered every 3 days, and measurements of tumor volume and body weight were performed at the same time. Tumor volume was calculated according to the following formula: volume = 0.5 × (longest dimension) × (shortest dimension)^2.

After 21 days of treatment, all mice were sacrificed on day 22. Tumors were measured and weighed. Main organs (liver, spleen, kidneys, hearts, and lungs) were collected, fixed and stained using hematoxylin and eosin (H and E) before being photographed. Biosafety was evaluated based on changes in body weight, pathological changes in organs mentioned above and serum biochemistry indexes including ALT, AST, ALP, BUN, and CRE.

Statistical Analysis

All experiments were performed at least three times and results were exhibited as mean ± standard deviation. Comparison between groups were calculated by Student's t-test (two groups) or Bonferroni's post hoc test (three groups or more). Data were analyzed on SPSS software. Differences were considered statistically significant when *p*-values were less than 0.05.

RESULTS AND DISCUSSION

The PC NDs were created by quickly adding ethanol solution containing PTX and Cur into excessive volume of deionized water and vortexing the mixture for 1 min (**Figure 1A** and **Supplementary Figure S1**). During the nanoprecipitation process, PTX, and Cur molecules were precipitated to form nanoparticles *via* intermolecular interactions, such as hydrogen bonding, π–π stacking and hydrophobic interactions (Li et al., 2018; Hupfer et al., 2021). The PC NDs had a spherical structure (diameter: 120–140 nm) based on characterization *via* TEM and SEM (**Figures 1B,C**). Zeta potential measurements revealed that the PC NDs had a negative surface charge (−14.6 ± 0.513 mV), which was similar to that of raw Cur (−22.2 ± 3.96 mV) and suggested that the surface of the PC NDs was mostly composed of Cur with phenolic hydroxyl groups. The ultraviolet-visible light absorption and fluorescence spectra of free PTX, free Cur, free PTX/Cur mix, and PC NDs were analyzed. The PC NDs had the same absorption peaks as free PTX and Cur, albeit with variable peak heights (**Figures 1D,E**). Furthermore, PC NDs have exhibited weaker green fluorescence than free Cur when excited with 420-nm laser, although free Cur, free PTX/Cur, and PC NDs shared the same emission peak (550 nm, **Figure 1D**). We used FTIR spectra to evaluate whether the bioactive groups of PTX and Cur were preserved in the PC NDs (**Figure 1F**), which revealed that the PC NDs exhibited N-H stretching vibration at 3,515 cm^{-1} and C=C stretching vibration of the conjugate system in Cur and PTX at 1,513 cm^{-1}, as well as disappearance of the strong O-H stretching vibration at 3,511 cm^{-1}. Based on these results, we conclude that the PC NDs contained most of the bioactive groups of PTX and Cur, with Cur potentially being "surrounded" by PTX to create the spherical structure of the PC NDs. In addition, we performed XRD measurements to determine whether the PC NDs formed drug eutectics or amorphous formations (**Figure 1G**), which revealed that the PC NDs had an XRD spectrogram that was similar to that of PTX crystal, with amorphous Cur structures. These findings suggest that the PC NDs were probably composed of crystalline formations containing PTX nanocrystals and Cur.

The release profiles of PTX and Cur from PC NDs were evaluated using a dialysis bag and PBS solution, with a pH value of 7.4 to mimic normal conditions in bodily fluids or a pH value of 5.5 to mimic the acidic tumor microenvironment, respectively. As shown in **Figure 2A**, PTX release showed a time-dependent behavior and reached approximately 33.3% over a 48-h period at a pH of 7.4. However, when the pH was 5.5, PTX release increased substantially and reached 83.2% over a 48-h period. Similar trends were observed in the acid- and time-dependent release of Cur (**Figure 2B**). Thus, the PC NDs might facilitate simultaneous and preferred release of PTX and Cur in the acidic tumor microenvironment. As shown in **Supplementary Figure S2**, PC NDs disintegrated quickly in acidic PBS, while the hydration radius has increased by about 25% during 72 h in neutral PBS. Therefore, PCNDs were used just after preparation. Fluorescence microscopy was subsequently used to evaluate cellular uptake of the two drugs. After incubation of 4T1 and MDA-MB-231 cells with PC NDs for 2 h, we labelled the nuclei with Hoechst dye (blue) and lysosomes with LysoTracker RED DND (red). Green fluorescence (Cur) was observed in the cytoplasm and lysosomes (**Figure 3B** and **Supplementary**

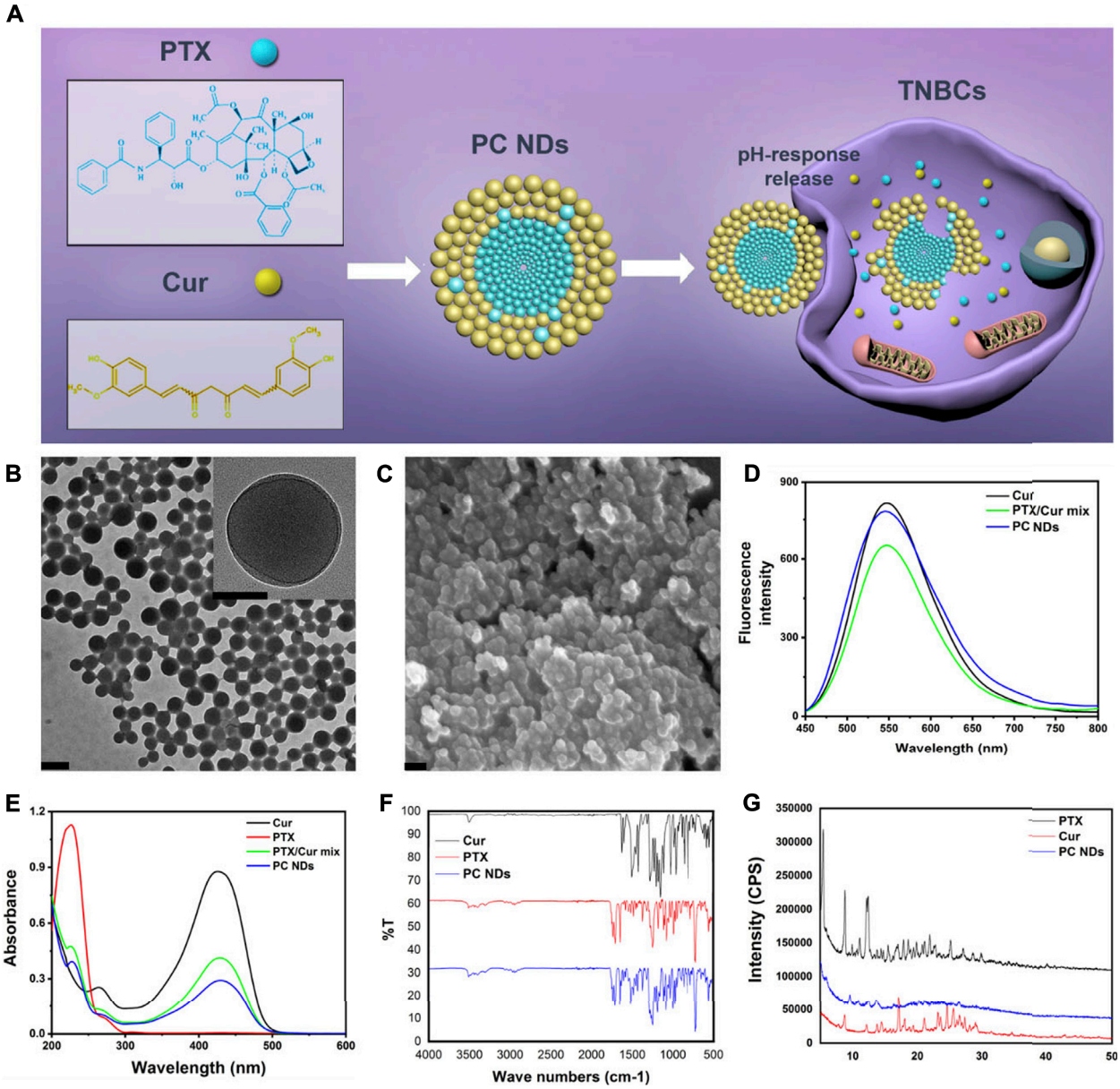

FIGURE 1 | Scheme of PC NDs preparation and its characterization. **(A)** Scheme of PC NDs preparation. PC NDs has been prepared using a reprecipitation method and shown pH-sensitive drug release behavior in tumor cells. **(B)** TEM images of PC NDs. Scale bars are 200 and 50 nm (inset), respectively. **(C)** SEM image of PC NDs. Scale bar is 200 nm. **(D)** Emission spectra of Cur, PTX/Cur mix, and PC NDs. **(E)** UV-vis absorption spectra of Cur, PTX, PTX/Cur mix, and PC NDs. **(F)** FTIR spectra of Cur, PTX, and PC NDs. **(G)** XRD spectra of Cur, PTX, and PC NDs.

Figure S3), and the overlap of the green and red fluorescence signals suggested that the PC NDs were accumulated in lysosomes. Furthermore, the intensity of the PC ND staining increased with incubation time in the TNBC cells (**Figure 3A**), which suggested a time-dependent drug release mechanism. As expected, the PC NDs had stronger fluorescence intensity (vs free Cur), which confirmed their higher rate of cellular uptake. However, relative to in the cancer cells, there was significantly less Cur uptake into normal breast cells (MCF-10A), which is likely related to the higher pH in normal cells. When considered together, these findings indicate that PC NDs can be taken up by TNBC cells and their contents released in a pH-dependent manner.

SRB assay was used to determine the viability of 4T1, MDA-MB-231, and MCF-10A cells after 24–48 h of treatment using various concentrations of free PTX, free PTX/Cur mix, and PC NDs. Relative to the control group, 4T1 cell viability of all PTX-containing groups has exhibited a dose- and time-dependent decrease manner (**Figures 4A,B**), while the addition of Cur provided even greater decreases. Similar

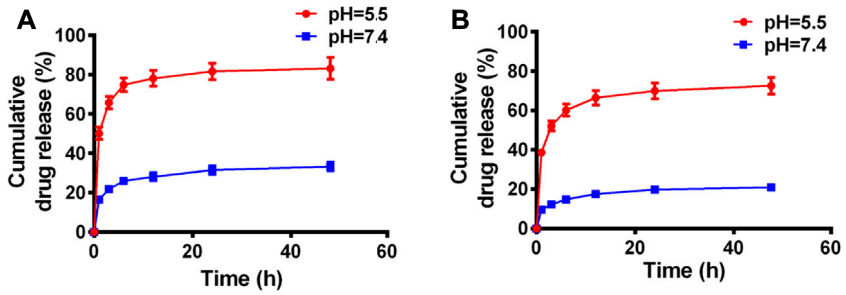

FIGURE 2 | Drug release profiles of PC NDs in PBS of different pH values during 48 h **(A)** PTX and **(B)** Cur release of PC NDs in neutral and acidic PBS.

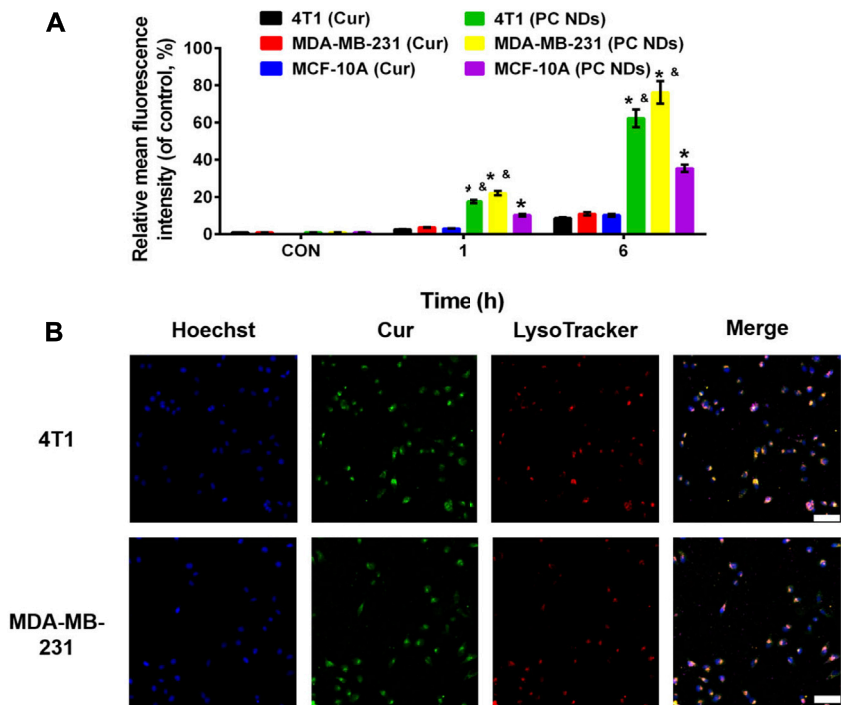

FIGURE 3 | Cellular uptake of PC NDs in 4T1, MDA-MB-231, and MCF-10A cells. **(A)** Quantitative analysis of the internalization of Cur and PC NDs in 4T1, MDA-MB-231, and MCF-10A cells through FACS. Statistical significance: *$p < 0.05$ vs control and $p < 0.05$ vs Cur.**(B)** CLSM images of 4T1 and MDA-MB-231 cells after incubation with PC NDs for 2 h. Scale bars are 200 μm.

results were also observed in MDA-MB-231 cells (**Figures 4C,D**). At 48 h, the IC_{50} values in 4T1 cells were 16.52 ± 0.16 μM for free PTX, 4.05 ± 0.13 μM for PTX/Cur mix, and 3.87 ± 0.14 μM for PC NDs. Similarly, the IC50 values in MDA-MB-231 cells at 48 h were 7.34 ± 0.19 μM for free PTX, 2.79 ± 0.10 μM for PTX/Cur mix, and 2.58 ± 0.11 μM for PC NDs. Moreover, to our expect, cells incubated with Cur have shown little to no decease on cell viability due to its low concentration (**Supplementary Figure S4**). These results suggest that combining PTX and Cur provided a significantly greater decrease in TNBC cell viability, relative to PTX alone, which might be related to Cur-induced sensitization of the TNBC cells to PTX (Saha et al., 2012; Yoshida et al., 2017). The small differences between the PTX/Cur mix and PC NDs might be the result of long treatment time, which has given enough time for cells to uptake nearby drugs. It is also worth noting that the PC NDs had less effect on MCF-10A cells than free PTX (**Figures 4E,F**), which might be related to preferred pH-related drug release in cancer cells (vs in normal cells). When considered together, these results suggest that the PC NDs provided a greater decrease in TNBC cell viability (vs PTX alone), as well as less toxicity in normal cells.

The BALB/c mice bearing 4T1 tumors were treated using saline (control group), free Cur, free PTX, free PTX/Cur mix, and PC NDs (**Figure 5A**). Relative to control group, decreased tumor growth and lower tumor weights were observed at the end of treatment using free PTX, free PTX/Cur mix, and PC NDs

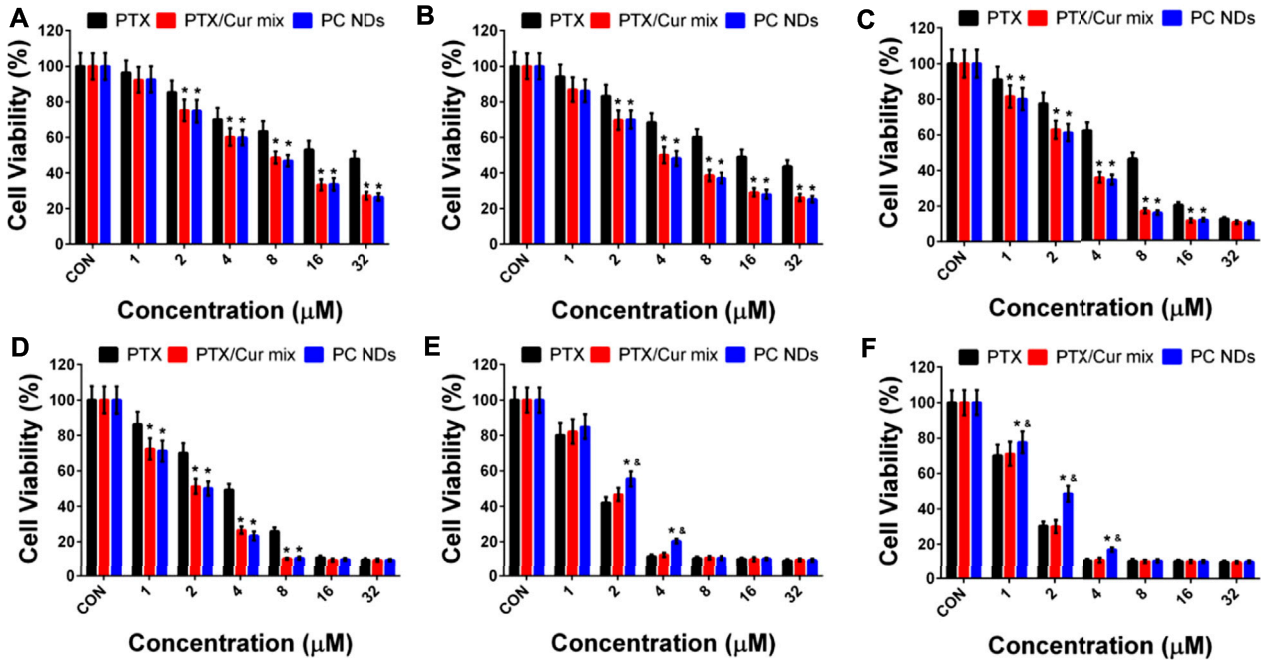

FIGURE 4 | Cytotoxicity of PTX, PTX/Cur mix, and PC NDs in 4T1, MDA-MB-231 and MCF-10A cells after 24 and 48 h incubation. Cell viability of **(A)** 4T1 cells, **(C)** MDA-MB-231 cells, and **(E)** MCD-10A cells after 24 h incubation. Cell viability of **(B)** 4T1 cells, **(D)** MDA-MB-231 cells, and **(F)** MCD-10A cells after 48 h incubation. Statistical significance: $^{*}p < 0.05$ vs control and $p < 0.05$ vs PTX.

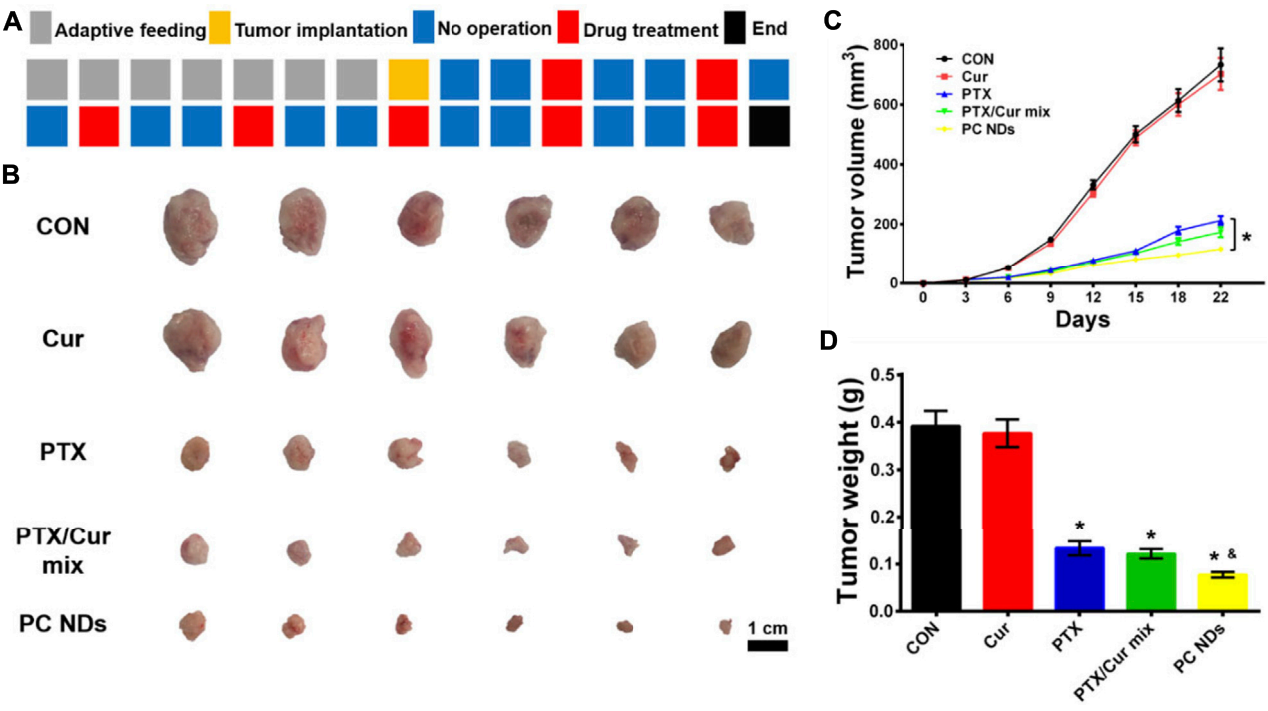

FIGURE 5 | *In vivo* anti-TNBC effect of PC NDs. **(A)** Dosage regimen of treatment for 22 days **(B)** Tumor image, **(C)** Tumor volume, and **(D)** tumor weight. Statistical significance: $^{*}p < 0.05$ vs PTX in **(C)**; $^{*}p < 0.05$ vs control and $p < 0.05$ vs PTX in **(D)**.

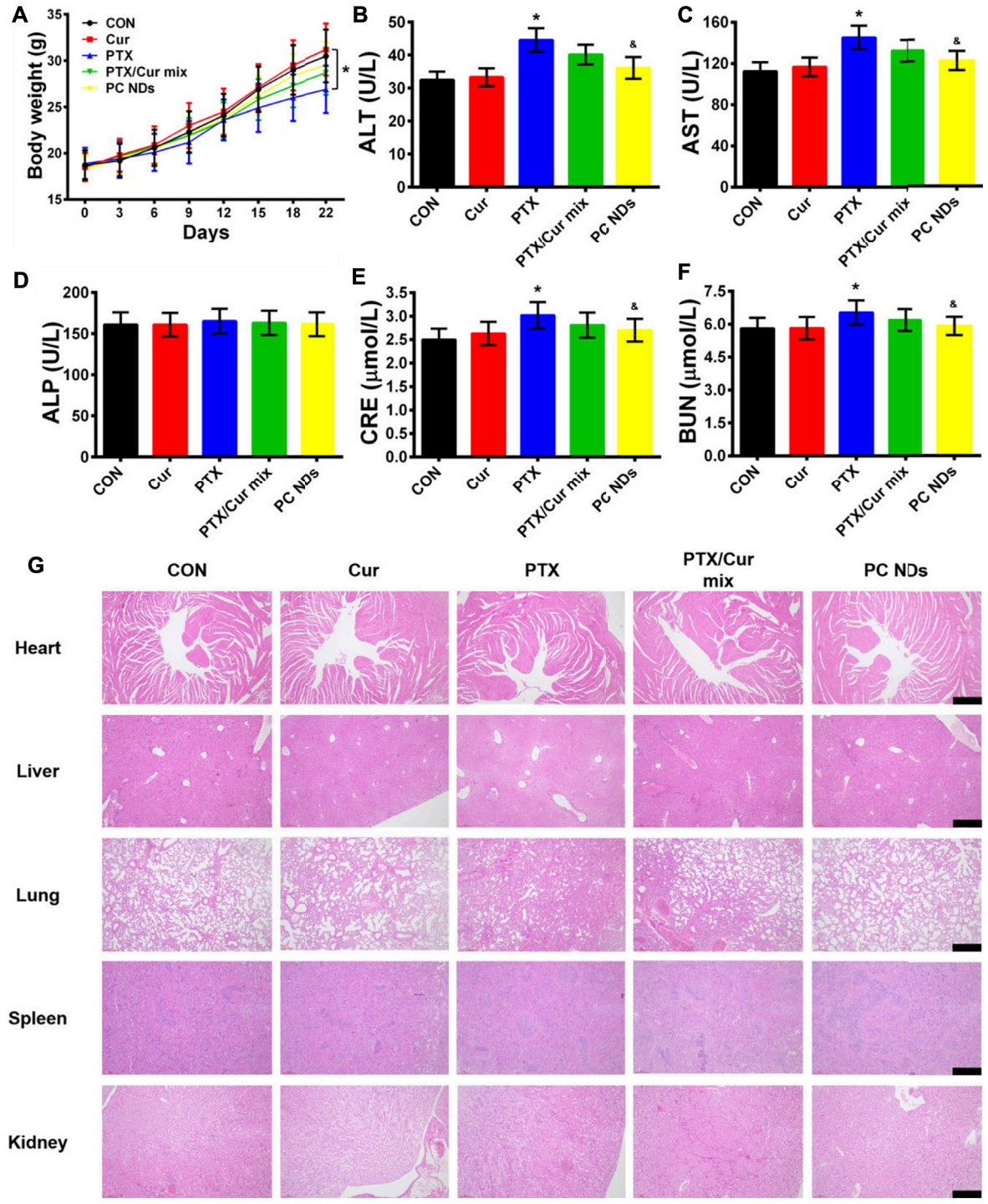

FIGURE 6 | Biosafety profile of PC NDs. **(A)** Body weight, **(B)** ALT, **(C)** AST, **(D)** ALP, **(E)** CRE, **(F)** BUN, and **(G)** H and E staining image of heart, liver, lung, spleen, and kidney from each group. Scale bars are 50 μm. Statistical significance: $^*p < 0.05$ vs control and $p < 0.05$ vs PTX.

(**Figures 5B–D**), although free Cur did not significantly influence tumor growth. Furthermore, the PC NDs appear to provide substantially more promising results (vs the other formulations), based on a tumor growth inhibition rate of 80.36%. Interestingly, free PTX provided considerable anti-tumor effects, while mice were suffered from a decrease in body weight and abnormal high levels of liver and kidney enzymes (ALT, AST, BUN, and CRE) (**Figures 6A–F**). In contrast, the PC ND group only exhibited a small decrease in body weight after 21 days of treatment and no histopathological

changes in the liver, spleen, kidneys, heart, and lungs (**Figures 6A–G**) (Edwards et al., 2017; Farhood et al., 2019). Moreover, we observed severe lung metastasis in the PTX and PTX/Cur mix groups, which was not observed in the PC ND group (**Supplementary Figure S5**) (Sesarman et al., 2018; Tan and Norhaizan, 2019). Thus, co-delivery of PTX and Cur *via* the PC NDs might improve the efficacy of treatment for TNBC (vs free PTX alone), with less systemic toxicity observed in our mouse model, although the underlying mechanisms remain unclear.

In summary, we created biocompatible and carrier-free nanodrugs composed of PTX and Cur *via* a simple nanoprecipitation method. The PC NDs were preferentially taken up by TNBC cells and we also observed pH-related drug release. The cytotoxicity assay revealed that the PC NDs had a greater effect on TNBC cells (vs free PTX), as well as less toxicity in normal cells. The *in vivo* data also clearly indicated that the PC NDs had considerably greater therapeutic efficacy than the free PTX/Cur mixture, with no signs of systemic toxicity. Therefore, the PC NDs might be a promising carrier-free strategy for safely and effectively delivering PTX and Cur to treat TNBC. Further studies are needed to determine whether this nanotherapeutic strategy holds clinical value.

DATA AVAILABILITY STATEMENT

The raw data supporting the conclusions of this article will be made available by the authors, without undue reservation, to any qualified researcher.

ETHICS STATEMENT

The animal study was reviewed and approved by Animal Care and Use Committee of Jilin University. Written informed consent was obtained from the owners for the participation of their animals in this study.

AUTHOR CONTRIBUTIONS

SZ, ZW, DS, and YZ designed the research. SZ, ZW, XA, JW, and XZ performed the research. SZ, XA, and JW analyzed the data. SZ, DS, and YZ wrote the manuscript.

FUNDING

This study was supported by Scientific Development Program of Jilin Province (20180201054YY), Finance Department Program of Jilin Province (2020SCZT028), and the Fundamental Research Funds for the Central Universities.

SUPPLEMENTARY MATERIAL

The Supplementary Material for this article can be found online at: https://www.frontiersin.org/articles/10.3389/fbioe.2021.747637/full#supplementary-material

REFERENCES

Abu Samaan, T. M., Samec, M., Liskova, A., Kubatka, P., and Büsselberg, D. (2019). Paclitaxel's Mechanistic and Clinical Effects on Breast Cancer. *Biomolecules* 9 (12), 789. doi:10.3390/biom9120789

Akram, M., Iqbal, M., Daniyal, M., and Khan, A. U. (2017). Awareness and Current Knowledge of Breast Cancer. *Biol. Res.* 50 (1), 33. doi:10.1186/s40659-017-0140-9

Baek, J.-S., and Cho, C.-W. (2017). A Multifunctional Lipid Nanoparticle for Co-delivery of Paclitaxel and Curcumin for Targeted Delivery and Enhanced Cytotoxicity in Multidrug Resistant Breast Cancer Cells. *Oncotarget* 8 (18), 30369–30382. doi:10.18632/oncotarget.16153

Bergin, A. R. T., and Loi, S. (2019). Triple-negative Breast Cancer: Recent Treatment Advances. *F1000Res* 8, 1342. doi:10.12688/f1000research.18888.1

Bielopolski, D., Evron, E., Moreh-Rahav, O., Landes, M., Stemmer, S. M., and Salamon, F. (2017). Paclitaxel-induced Pneumonitis in Patients with Breast Cancer: Case Series and Review of the Literature. *J. Chemother.* 29 (2), 113–117. doi:10.1179/1973947815y.0000000029

Borges, G. A., Elias, S. T., Amorim, B., Lima, C. L., Coletta, R. D., Castilho, R. M., et al. (2020). Curcumin Downregulates the PI3K-AKT-mTOR Pathway and Inhibits Growth and Progression in Head and Neck Cancer Cells. *Phytotherapy Res.* 34 (12), 3311–3324. doi:10.1002/ptr.6780

Calaf, G., Ponce-Cusi, R., and Carrión, F. (2018). Curcumin and Paclitaxel Induce Cell Death in Breast Cancer Cell Lines. *Oncol. Rep.* 40 (4), 2381–2388. doi:10.3892/or.2018.6603

Chen, P., Huang, H.-P., Wang, Y., Jin, J., Long, W.-G., Chen, K., et al. (2019). Curcumin Overcome Primary Gefitinib Resistance in Non-small-cell Lung Cancer Cells through Inducing Autophagy-Related Cell Death. *J. Exp. Clin. Cancer Res.* 38 (1), 254. doi:10.1186/s13046-019-1234-8

Edwards, R. L., Luis, P. B., Varuzza, P. V., Joseph, A. I., Presley, S. H., Chaturvedi, R., et al. (2017). The Anti-inflammatory Activity of Curcumin Is Mediated by its Oxidative Metabolites. *J. Biol. Chem.* 292 (52), 21243–21252. doi:10.1074/jbc.ra117.000123

Fahad Ullah, M. (2019). Breast Cancer: Current Perspectives on the Disease Status. *Adv. Exp. Med. Biol.* 1152, 51–64. doi:10.1007/978-3-030-20301-6_4

Farhood, B., Mortezaee, K., Goradel, N. H., Khanlarkhani, N., Salehi, E., Nashtaei, M. S., et al. (2019). Curcumin as an Anti-inflammatory Agent: Implications to Radiotherapy and Chemotherapy. *J. Cel. Physiol.* 234 (5), 5728–5740. doi:10.1002/jcp.27442

Ghasemi, F., Shafiee, M., Banikazemi, Z., Pourhanifeh, M. H., Khanbabaei, H., Shamshirian, A., et al. (2019). Curcumin Inhibits NF-kB and Wnt/β-Catenin Pathways in Cervical Cancer Cells. *Pathol. - Res. Pract.* 215 (10), 152556. doi:10.1016/j.prp.2019.152556

Hamzehzadeh, L., Atkin, S. L., Majeed, M., Butler, A. E., and Sahebkar, A. (2018). The Versatile Role of Curcumin in Cancer Prevention and Treatment: A Focus on PI3K/AKT Pathway. *J. Cel. Physiol.* 233 (10), 6530–6537. doi:10.1002/jcp.26620

Hiremath, C. G., Heggnnavar, G. B., Kariduraganavar, M. Y., and Hiremath, M. B. (2019). Co-delivery of Paclitaxel and Curcumin to Foliate Positive Cancer Cells Using Pluronic-Coated Iron Oxide Nanoparticles. *Prog. Biomater.* 8 (3), 155–168. doi:10.1007/s40204-019-0118-5

Hu, H., Yang, C., Zhang, F., Li, M., Tu, Z., Mu, L., et al. (2021). A Versatile and Robust Platform for the Scalable Manufacture of Biomimetic Nanovaccines. *Adv. Sci.* 8, 2002020. doi:10.1002/advs.202002020

Hupfer, M. L., Herrmann-Westendorf, F., Dietzek, B., and Presselt, M. (2021). *In Situ* Photothermal Deflection Spectroscopy Revealing Intermolecular Interactions upon Self-Assembly of Dye Monolayers. *Analyst* 146 (16), 5033–5036. doi:10.1039/d1an00582k

Kang, C., and Syed, Y. Y. (2020). Atezolizumab (In Combination with Nab-Paclitaxel): A Review in Advanced Triple-Negative Breast Cancer. *Drugs* 80 (6), 601–607. doi:10.1007/s40265-020-01295-y

Keyvani-Ghamsari, S., Khorsandi, K., and Gul, A. (2020). Curcumin Effect on Cancer Cells' Multidrug Resistance: An Update. *Phytotherapy Res.* 34 (10), 2534–2556. doi:10.1002/ptr.6703

Kumar, P., and Aggarwal, R. (2016). An Overview of Triple-Negative Breast Cancer. *Arch. Gynecol. Obstet.* 293 (2), 247–269. doi:10.1007/s00404-015-3859-y

Li, M., Sun, X., Zhang, N., Wang, W., Yang, Y., Jia, H., et al. (2018). NIR-activated Polydopamine-Coated Carrier-free "Nanobomb" for *In Situ* On-Demand Drug Release. *Adv. Sci.* 5 (7), 1800155. doi:10.1002/advs.201800155

Li, Q., Wen, J., Liu, C., Jia, Y., Wu, Y., Shan, Y., et al. (2019). Graphene-nanoparticle-based Self-Healing Hydrogel in Preventing Postoperative Recurrence of Breast Cancer. *ACS Biomater. Sci. Eng.* 5 (2), 768–779. doi:10.1021/acsbiomaterials.8b01475

Liao, J., Han, R., Wu, Y., and Qian, Z. (2021). Review of a New Bone Tumor Therapy Strategy Based on Bifunctional Biomaterials. *Bone Res.* 9 (1), 1–13. doi:10.1038/s41413-021-00139-z

Lyons, T. G. (2019). Targeted Therapies for Triple-Negative Breast Cancer. *Curr. Treat. Options. Oncol.* 20 (11), 82. doi:10.1007/s11864-019-0682-x

Maiti, P., Plemmons, A., and Dunbar, G. L. (2019). Combination Treatment of Berberine and Solid Lipid Curcumin Particles Increased Cell Death and Inhibited PI3K/Akt/mTOR Pathway of Human Cultured Glioblastoma Cells More Effectively Than Did Individual Treatments. *PloS one* 14 (12), e0225660. doi:10.1371/journal.pone.0225660

McDonald, E. S., Clark, A. S., Tchou, J., Zhang, P., and Freedman, G. M. (2016). Clinical Diagnosis and Management of Breast Cancer. *J. Nucl. Med.* 57 (Suppl. 1), 9s–16s. doi:10.2967/jnumed.115.157834

Mittendorf, E. A., Zhang, H., Barrios, C. H., Saji, S., Jung, K. H., Hegg, R., et al. (2020). Neoadjuvant Atezolizumab in Combination with Sequential Nab-Paclitaxel and Anthracycline-Based Chemotherapy versus Placebo and Chemotherapy in Patients with Early-Stage Triple-Negative Breast Cancer (IMpassion031): a Randomised, Double-Blind, Phase 3 Trial. *The Lancet* 396 (10257), 1090–1100. doi:10.1016/s0140-6736(20)31953-x

Saghatelyan, T., Tananyan, A., Janoyan, N., Tadevosyan, A., Petrosyan, H., Hovhannisyan, A., et al. (2020). Efficacy and Safety of Curcumin in Combination with Paclitaxel in Patients with Advanced, Metastatic Breast Cancer: A Comparative, Randomized, Double-Blind, Placebo-Controlled Clinical Trial. *Phytomedicine* 70, 153218. doi:10.1016/j.phymed.2020.153218

Saha, S., Adhikary, A., Bhattacharyya, P., Das, T., and Sa, G. (2012). Death by Design: where Curcumin Sensitizes Drug-Resistant Tumours. *Anticancer Res.* 32 (7), 2567–2584.

Schmid, P., Adams, S., Rugo, H. S., Schneeweiss, A., Barrios, C. H., Iwata, H., et al. (2018). Atezolizumab and Nab-Paclitaxel in Advanced Triple-Negative Breast Cancer. *N. Engl. J. Med.* 379 (22), 2108–2121. doi:10.1056/NEJMoa1809615

Sesarman, A., Tefas, L., Sylvester, B., Licarete, E., Rauca, V., Luput, L., et al. (2018). Anti-angiogenic and Anti-inflammatory Effects of Long-Circulating Liposomes Co-encapsulating Curcumin and Doxorubicin on C26 Murine colon Cancer Cells. *Pharmacol. Rep.* 70 (2), 331–339. doi:10.1016/j.pharep.2017.10.004

Shao, D., Zhang, F., Chen, F., Zheng, X., Hu, H., Yang, C., et al. (2020). Biomimetic Diselenide-Bridged Mesoporous Organosilica Nanoparticles as an X-ray-Responsive Biodegradable Carrier for Chemo-Immunotherapy. *Adv. Mater.* 32 (50), 2004385. doi:10.1002/adma.202004385

Subramaniam, D., Kaushik, G., Dandawate, P., and Anant, S. (2018). Targeting Cancer Stem Cells for Chemoprevention of Pancreatic Cancer. *Cmc* 25 (22), 2585–2594. doi:10.2174/0929867324666170127095832

Sun, M., Zhang, Y., He, Y., Xiong, M., Huang, H., Pei, S., et al. (2019). Green Synthesis of Carrier-free Curcumin Nanodrugs for Light-Activated Breast Cancer Photodynamic Therapy. *Colloids Surf. B: Biointerfaces* 180, 313–318. doi:10.1016/j.colsurfb.2019.04.061

Tan, B. L., and Norhaizan, M. E. (2019). Curcumin Combination Chemotherapy: the Implication and Efficacy in Cancer. *Molecules* 24 (14), 2527. doi:10.3390/molecules24142527

Xiong, K., Zhang, Y., Wen, Q., Luo, J., Lu, Y., Wu, Z., et al. (2020). Co-delivery of Paclitaxel and Curcumin by Biodegradable Polymeric Nanoparticles for Breast Cancer Chemotherapy. *Int. J. pharmaceutics* 589, 119875. doi:10.1016/j.ijpharm.2020.119875

Yang, M.-Y., Zhao, R.-R., Fang, Y.-F., Jiang, J.-L., Yuan, X.-T., and Shao, J.-W. (2019). Carrier-free Nanodrug: A Novel Strategy of Cancer Diagnosis and Synergistic Therapy. *Int. J. pharmaceutics* 570, 118663. doi:10.1016/j.ijpharm.2019.118663

Yeo, S. K., and Guan, J.-L. (2017). Breast Cancer: Multiple Subtypes within a Tumor? *Trends Cancer* 3 (11), 753–760. doi:10.1016/j.trecan.2017.09.001

Yin, L., Duan, J.-J., Bian, X.-W., and Yu, S.-c. (2020). Triple-negative Breast Cancer Molecular Subtyping and Treatment Progress. *Breast Cancer Res.* 22 (1), 61. doi:10.1186/s13058-020-01296-5

Yoshida, K., Toden, S., Ravindranathan, P., Han, H., and Goel, A. (2017). Curcumin Sensitizes Pancreatic Cancer Cells to Gemcitabine by Attenuating PRC2 Subunit EZH2, and the lncRNA PVT1 Expression. *Carcinogenesis* 38 (10), 1036–1046. doi:10.1093/carcin/bgx065

Zhang, F., Chen, F., Yang, C., Wang, L., Hu, H., Li, X., et al. (2021). Coordination and Redox Dual-Responsive Mesoporous Organosilica Nanoparticles Amplify Immunogenic Cell Death for Cancer Chemoimmunotherapy. *Small* 17, 2100006. doi:10.1002/smll.202100006

Zhang, F., Zhang, M., Zheng, X., Tao, S., Zhang, Z., Sun, M., et al. (2018). Berberine-based Carbon Dots for Selective and Safe Cancer Theranostics. *RSC Adv.* 8 (3), 1168–1173. doi:10.1039/c7ra12069a

Zhao, M.-D., Li, J.-Q., Chen, F.-Y., Dong, W., Wen, L.-J., Fei, W.-D., et al. (2019). Co-Delivery of Curcumin and Paclitaxel by "Core-Shell" Targeting Amphiphilic Copolymer to Reverse Resistance in the Treatment of Ovarian Cancer. *Ijn* Vol. 14, 9453–9467. doi:10.2147/ijn.s224579

Zheng, X., Zhang, F., Shao, D., Zhang, Z., Cui, L., Zhang, J., et al. (2018). Gram-scale Production of Carrier-free Fluorescent Berberine Microrods for Selective Liver Cancer Therapy. *BioFactors* 44 (5), 496–502. doi:10.1002/biof.1450

Zhou, M., Wei, W., Chen, X., Xu, X., Zhang, X., and Zhang, X. (2019). pH and Redox Dual Responsive Carrier-free Anticancer Drug Nanoparticles for Targeted Delivery and Synergistic Therapy. *Nanomedicine: Nanotechnology, Biol. Med.* 20, 102008. doi:10.1016/j.nano.2019.04.011

Zusso, M., Lunardi, V., Franceschini, D., Pagetta, A., Lo, R., Stifani, S., et al. (2019). Ciprofloxacin and Levofloxacin Attenuate Microglia Inflammatory Response via TLR4/NF-kB Pathway. *J. Neuroinflammation* 16 (1), 148. doi:10.1186/s12974-019-1538-9

Conflict of Interest: The authors declare that the research was conducted in the absence of any commercial or financial relationships that could be construed as a potential conflict of interest.

Publisher's Note: All claims expressed in this article are solely those of the authors and do not necessarily represent those of their affiliated organizations, or those of the publisher, the editors and the reviewers. Any product that may be evaluated in this article, or claim that may be made by its manufacturer, is not guaranteed or endorsed by the publisher.

frontiers in Bioengineering and Biotechnology

ORIGINAL RESEARCH
published: 11 November 2021
doi: 10.3389/fbioe.2021.783661

Multifunctional Gold Nano-Cytosensor With Quick Capture, Electrochemical Detection, and Non-Invasive Release of Circulating Tumor Cells for Early Cancer Treatment

Rui Zhang[1,2], *Qiannan You*[1,2], *Mingming Cheng*[1,2], *Mingfeng Ge*[2], *Qian Mei*[2], *Li Yang*[3,4]*, *Wen-Fei Dong*[2] *and Zhimin Chang*[2,5]*

[1]School of Biomedical Engineering (Suzhou), Division of Life Sciences and Medicine, University of Science and Technology of China, Hefei, China, [2]CAS Key Laboratory of Biomedical Diagnostics, Suzhou Institute of Biomedical Engineering and Technology, Chinese Academy of Science (CAS), Suzhou, China, [3]College of Life Science and Biotechinology, Mianyang Teachers' College, Mianyang, China, [4]Chongqing Institute of Green and Intelligent Technology, Chinese Academy of Sciences, Chongqing, China, [5]Jinan Guokeyigong Science and Technology Development Co., Ltd, Jinan, China

OPEN ACCESS

Edited by:
Jinbing Xie,
Southeast University, China

Reviewed by:
Huang Yuanyuan,
Suzhou Institute of Nano-Tech and Nano-Bionics (CAS), China
Jianati Dawulieti,
South China University of Technology, China

***Correspondence:**
Li Yang
ylyhp@126.com
Zhimin Chang
changzm@sibet.ac.cn

Specialty section:
This article was submitted to Nanobiotechnology, a section of the journal Frontiers in Bioengineering and Biotechnology

Received: 26 September 2021
Accepted: 21 October 2021
Published: 11 November 2021

Citation:
Zhang R, You Q, Cheng M, Ge M, Mei Q, Yang L, Dong W-F and Chang Z (2021) Multifunctional Gold Nano-Cytosensor With Quick Capture, Electrochemical Detection, and Non-Invasive Release of Circulating Tumor Cells for Early Cancer Treatment. Front. Bioeng. Biotechnol. 9:783661. doi: 10.3389/fbioe.2021.783661

Circulating tumor cells (CTCs) are metastatic tumor cells that shed into the blood from solid primary tumors, and their existence significantly increases the risk of metastasis and recurrence. The timely discovery and detection of CTCs are of considerable importance for the early diagnosis and treatment of metastasis. However, the low number of CTCs hinders their detection. In the present study, an ultrasensitive electrochemical cytosensor for specific capture, quantitative detection, and noninvasive release of EpCAM-positive tumor cells was developed. The biosensor was manufactured using gold nanoparticles (AuNPs) to modify the electrode. Three types of AuNPs with controllable sizes and conjugated with a targeting molecule of monoclonal anti-EpCAM antibody were used in this study. Electrochemical impedance spectroscopy (EIS) and differential pulse voltammetry (DPV) of the cytosensors were performed to evaluate the cell capture efficiency and performance. The captured 4T1 cells by the AuNPs hindered electron transport efficiency, resulting in increased EIS responses. The cell capture response recorded using EIS or DPV indicated that the optimal AuNPs size should be 17 nm. The cell capture response changed linearly with the concentration range from 8.0×10 to 1×10^7 cells/mL, and the limit of detection was 50 cells/mL. After these measurements, glycine-HCl (Gly-HCl) was used as an antibody eluent to destroy the binding between antigen and antibody to release the captured tumor cells without compromising their viability for further clinical research. This protocol realizes rapid detection of CTCs with good stability, acceptable assay precision, significant fabrication reproducibility with a relative standard deviation of 2.09%, and good recovery of cells. Our results indicate that the proposed biosensor is promising for the early monitoring of CTCs and may help customize personalized treatment options.

Keywords: CTCs, early diagnosis and treatment, electrochemical cytosensor, non-invasive release, multifunctional Au nanoparticles

INTRODUCTION

Because malignant tumor cells are derived from solid tumors and are present in peripheral blood, circulating tumor cells (CTCs) are critical to cancer metastasis (Mostert et al., 2009; Schindlbeck et al., 2009; Gradilone et al., 2011; Hristozova et al., 2011; Xie et al., 2015). The rapid and sensitive detection of CTCs in the peripheral blood is an effective and appropriate approach for the diagnosis of cancer patients (Paterlini-Brechot and Benali, 2007; Mostert et al., 2009; Mostert et al., 2012; Alix-Panabières and Pantel, 2013; Shahneh, 2013). Moreover, the isolation of CTCs from the peripheral blood has significant clinical implications because it can provide smart and personalized treatment (Hong, 2013; Souza e Silva et al., 2014; J Alvarez-Cubero et al., 2016; Miyamoto et al., 2016; Tan et al., 2017; Liu et al., 2018). Therefore, the development of a dynamic technique for the sensitive detection and noninvasive release of pathogenic cells is necessary.

Recently, the development of sensitive and quantitative detection of CTCs has attracted extensive research attention (Denis et al., 1997; Nakanishi et al., 2000; Wen et al., 2014; Shinden et al., 2015). Traditional cancer detection methods primarily include flow cytometry (Hu et al., 2010), reverse-transcriptase polymerase chain reaction (Zhao et al., 2011), and immunohistochemistry (Gogoi et al., 2016). Although the above methods performed well in terms of sensitivity and precision, they are expensive and time consuming in addition to requiring complex instruments, hampering their application in biological analysis and clinical diagnosis. Accordingly, the development of a low-cost, sensitive, and simple method for the detection and efficient release of captured CTCs is necessary and has considerable significance in the early diagnosis and monitoring of the relevant cancer processes.

Presently, academic attention has shifted toward electrochemical biosensors that utilize noninvasive and highly sensitive nanomaterials (Thévenot et al., 2001; Wang, 2005 a; b; 2006; Peng et al., 2020). For example, by combining aptamer and gold-magnetic core-shell nanoparticles, Khoshfetrat fabricated an aptamer-based electrochemical biosensor with a nitrogen-doped graphene-modified electrode. This aptasensor exhibited a linear response over a wide dynamic range of leukemia cancer cells, ranging from 10 to 1×10^6 cells/mL (Khoshfetrat and Mehrgardi, 2017). Pang synthesized a cytosensing device based on ZnO nanodisks@g-C3N4 quantum dots for the detection of CCRF-CEM cells ranging from 20 to 2×10^4 cells/mL (Pang et al., 2018). These studies demonstrate the advantages of using metal nanoparticles as a design strategy for electrochemical biosensors. Appropriate nanomaterials must be selected for the manufacture a new generation of electrochemical biosensors. Compared with other nanoparticles, gold nanoparticles (AuNPs) provide an ideal binding site for biomolecules, which is beneficial for electron transfer to the electrode. Such characteristics have been widely used to fabricate electrochemical biosensors with improved performance (Zhong et al., 2013; Gikunoo et al., 2014; Qian et al., 2019). However, few studies have investigated the effect of the size of the AuNPs on enhancing the detection performance because the size of AuNPs may affect the analysis results. Cancer cells overexpress specific proteins, which are often considered to be specific markers in CTC analytical technology for different types of cancer cells (Moskaluk et al., 2002). For example, the epithelial cell adhesion molecule (EpCAM), which is overexpressed in most epithelial tumor cells, is often identified as a specific biomarker for epithelial tumor cells (Moskaluk et al., 2002).

In the present study, cytosensors based on AuNPs of different sizes were used for the electrochemical detection of CTCs. The AuNPs attached on the surface of the glassy carbon electrode (GCE) act as a good electron conductor that facilitates electrochemical cytosensing. Subsequently, the EpCAM antibody (anti-EpCAM) was modified on the surface of AuNPs to enhance the specificity of EpCAM-positive tumor cells. The prepared anti-EpCAM/AuNPs electrode was specific for tumor cell anchoring. The adhesion of tumor cells on the surface of the electrode could alter the electron transfer resistance, thereby allowing the formation of an impedance-based cytosensor. We investigated the effect of the size of the AuNPs on the detection performance of the fabricated cytosensors. Electrochemical impedance spectroscopy (EIS) and differential pulse voltammetry (DPV) were used to assess the capability of the fabricated cytosensors with different particle sizes (17, 30, and 50 nm). For the cytosensor fabricated with 17 nm AuNPs, the widest range of 4T1 cell detection (8.0×10 to 1×10^7 cells/mL) was obtained with a lower LOD of 50 cells/mL, which was considerably lower than that of the other two fabricated cytosensors. As a control, HeLa and J774A.1 cells with low EpCAM expression were also applied under the same experimental conditions. The glycine hydrochloride (Gly-HCl) buffer introduced into the cytosensor system acted as an eluent that could break the combination within the antibody–antigen to release the trapped cells (**Scheme 1**). In this study, the developed cytosensor had high specificity for EpCAM-positive CTCs, good stability, biocompatibility, significant fabrication reproducibility, and noninvasive release. Thus, the developed cytosensor has promising application prospects in the early clinical diagnosis and treatment of cancer.

METHODS

Synthesis of AuNPs

Gold seeds were prepared using a standard method. Briefly, 1 ml of $HAuCl_4$ (25 mM) was mixed with sodium citrate (150 ml, 2.2 mM) and heated for 1 h. Then, the obtained solution was used as the seed solution. After synthesis, the solution was cooled to 90°C, $HAuCl_4$ solution (1 ml, 25 mM) was added, and the reaction was completed after 30 min. By repeating these steps, a series of AuNPs with gradually increasing particle sizes was obtained (Bastús et al., 2011). The nanoparticles were labeled as G0, G1, and G2. Finally, the AuNPs were characterized using UV-visible absorption spectrum (UV), TEM, and XPS.

Assembly Process of the Electrochemical Cytosensor

The assembly process of the AuNP-based electrochemical cytosensor is shown in **Scheme 1**. First, the GCE (3 mm) was polished with 0.05 μm alumina slurries and washed alternately with ethanol and water until a shiny mirror surface was obtained. Afterward, the mercapto functional group was modified on the electrode by cyclic voltammetry (CV). The potential range of CV detection was set from

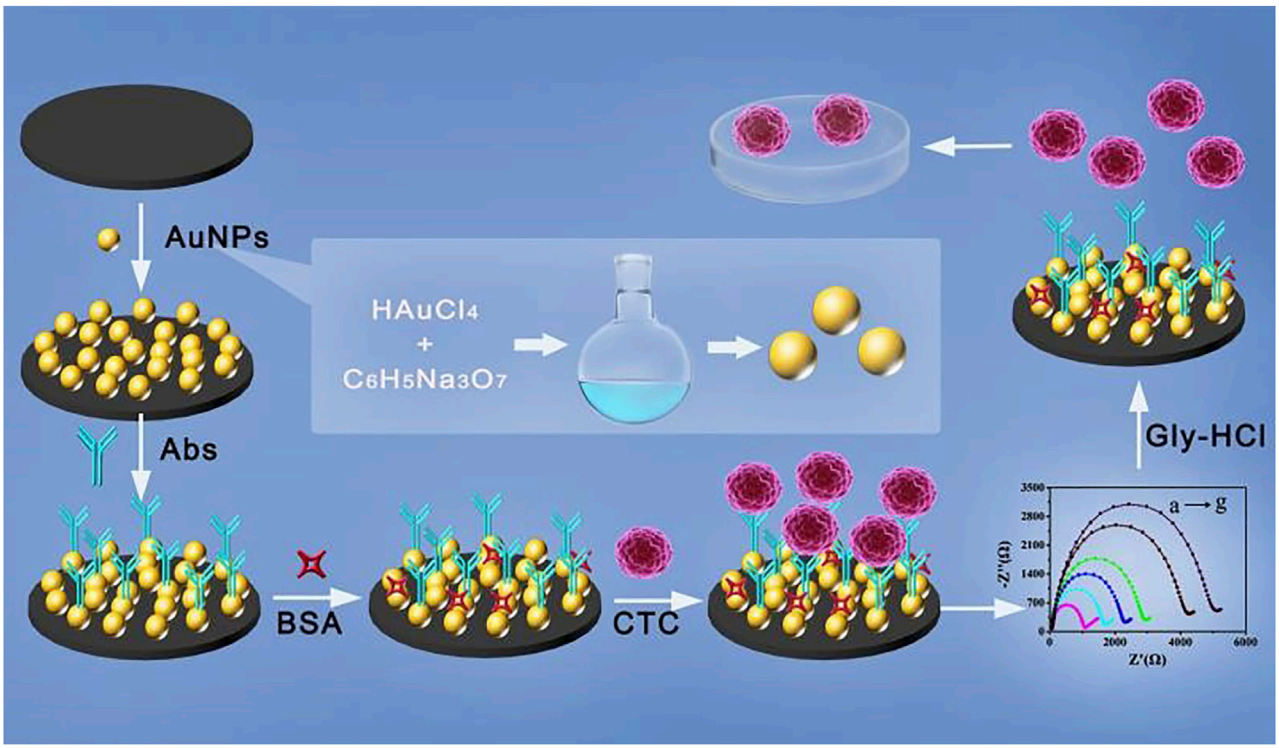

SCHEME 1 | Stepwise procedure of the electrochemical cytosensor for cell capture, detection, and release.

0.0 to 1.4 V with a scan rate of 50 mV/s, and several circles were scanned in a 1 mM aqueous solution of mercaptoethylamine until the peak current value was stable (Moskaluk et al., 2002). After the reaction, the surface-modified electrodes were washed with PBS buffer (pH 7.4). Subsequently, the electrodes were immersed in the AuNPs solution (1 ml) overnight, and the AuNPs were tightly fixed on the surface of the GCE via gold and sulfhydryl bonds. Then the electrodes were rinsed with PBS buffer (pH 7.4). Subsequently, Nafion (5 μL, 0.05% in alcohol) was dropped onto the GCE surface to prevent leakage of the AuNPs. After 2–3 washings with PBS, the AuNP/GCE electrode was fabricated. AuNPs with different particle sizes were modified on the electrode surface using the same method. For immune modification, the AuNPs/GCE electrode was immersed in anti-EpCAM solution (60 μM) and then incubated in a refrigerator at 4°C for 4 h. Then, after washing with PBS, the electrode was immersed in BSA (1%, 50 μL) for 1 h to block nonspecific binding sites. Finally, the cytosensors for immunological recognition of EpCAM-positive CTCs were obtained.

Cell Culture

4T1 cells, HeLa cells, and J774A.1 cells were cultured in a cell incubator at 37°C with 5% CO_2. 4T1 cells were cultured in RPMI-1640 medium with 10% FBS and 1% penicillin–streptomycin. After incubation, the 4T1 cells were digested with 0.25% trypsin solution. The cell sediments were redispersed in PBS (pH 7.4), and the number of cells was determined using a hemocytometer counter.

Cell Detection

For cell detection, the as prepared cytosensor was immersed into the cell suspension and incubated in a cell incubator for 2 h. After cell adsorption, the electrode was washed with PBS to remove unadsorbed cells. Finally, the prepared immunoelectrode acted as the working electrode, whereas Ag/AgCl and Pt wire electrodes were used as the reference and auxiliary electrodes, respectively. The electrode was inserted into a 0.1 M KCl, 5 mM K_4 [$Fe(CN)_6$], and 5 mM K_3 [$Fe(CN)_6$] solution. The impedance and current responses were recorded using EIS and DPV, respectively. The frequency range of the EIS detection was 0.1–10^5 Hz. The range for DPV detection was from 0 to 0.6 V, with a 50 mV pulse amplitude. The potential range of CV detections was set from −0.6 to 0.6 V with a scan rate of 50 mV/s. Meanwhile, a 10 × 10 mm indium tin oxide (ITO) substrate after mercaptosilanization pretreatment was prepared as previously described process for the modified GCE electrode and cell detection. The captured cells were analyzed by fluorescence microscopy after DAPI staining.

Cell Release

For cell release, the electrode with cell immobilization was immersed in Gly-HCl solution (0.1 M) for 30 s, and then several drops of 0.4 M NaOH solution were added to the Gly-HCl solution. The released cells were washed with PBS, centrifuged, and collected and cultured for further clinical analysis.

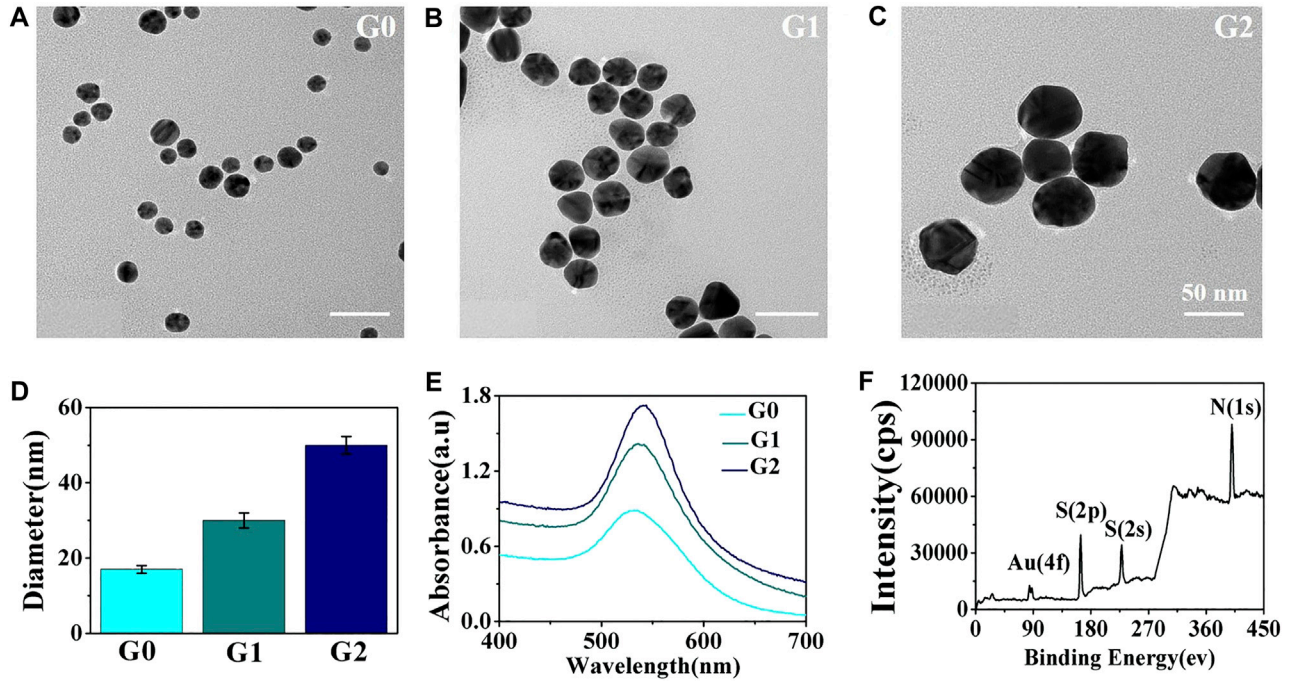

FIGURE 1 | TEM images of the prepared **(A)** G0, **(B)** G1, and **(C)** G2. **(D)** Histogram of the prepared AuNPs sizes. **(E)** UV–vis spectra of the prepared AuNPs. **(F)** XPS characterization of the AuNPs/GCE electrode.

Cell Viability Analysis

Cell viability was determined using Hoechst/PI staining assay. Briefly, Hoechst/PI solution containing 10 μg/ml Hoechst and 10 μg/ml PI in PBS was added to the cells and incubated for 5 min. The cells were washed and observed using a fluorescence microscope. The released cells were then incubated and observed under a microscope. The AuNPs were tested using a WST-1 assay to verify cytotoxicity. The working concentration of AuNPs was adjusted from 5.0 to 150.0 μM, and 4T1 cells were plated in 96-well plates and incubated for 24 h at 37°C. To evaluate cell viability, a plate reader was used to measure absorbance at 450 nm.

Blood Samples

Blood samples were obtained from the healthy mice. The animal experimental protocols were approved by the Ethics Committee for the Use of Experimental Animals of Chinese Academy of Science. To verify the performance of the cytosensors in the simulated samples with leukocyte, the healthy blood sample was centrifugated at 1,500 rpm for 5 min and the cells deposit were then resuspended in 1 ml of red blood cell lysis buffer incubated for 2 min, and the precipitate was washed with PBS and disperse with 1 ml of PBS. Subsequently, the as prepared leukocyte samples mixed with 4T1 cells at concentrations of 1×10^2, 1×10^3, 1×10^4, and 1×10^5 cells/mL to prepare the simulated samples with leukocyte.

RESULTS AND DISCUSSION

Characteristics of the AuNPs/GCE Electrode

The morphology of the AuNPs was characterized. The TEM images in **Figure 1** indicate that the synthesized AuNPs had a spherical shape with good monodispersity and uniform morphology. The average sizes of the AuNPs were 17 nm (G0), 30 nm (G1), and 50 nm (G2) (**Figure 1D**). **Figure 1E** shows the UV-visible absorption spectrum of the prepared AuNP water solution with an absorption peak at ~535 nm. As shown in **Figure 1F**, the XPS results of the AuNP/GCE electrode revealed that the AuNPs were assembled onto the GCE electrode surface with Au-S bonds to form a self-assembled AuNP/GCE electrode.

For the AuNP/GCE electrodes fabricated using AuNPs of different sizes, CV and EIS were applied to monitor the electrode fabrication steps. The CV results are shown in **Figure 2A**. There was an evident increase in the oxidation peaks of the GCE electrodes modified by the AuNPs in comparison with the unmodified GCE electrode. In addition, as the size of the AuNPs increased, the well-defined oxidation current peaks of the $[Fe(CN)_6]^{4-/3-}$ redox couple gradually decreased, indicating that the 17 nm AuNPs could provide the highest improvement in charge transfer. Therefore, 17 nm AuNPs were used under the following optimal conditions for the fabrication of the cytosensor. It is well known that the

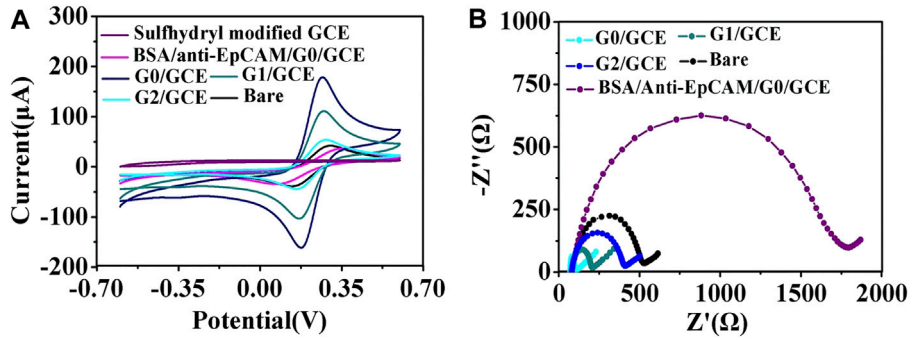

FIGURE 2 | (A) CV curves of the AuNPs/GCE fabricated using AuNPs of different sizes. **(B)** EIS of the GCE modified by AuNPs with different sizes: (G0) 17 nm, (G1) 30 nm, and (G2) 50 nm.

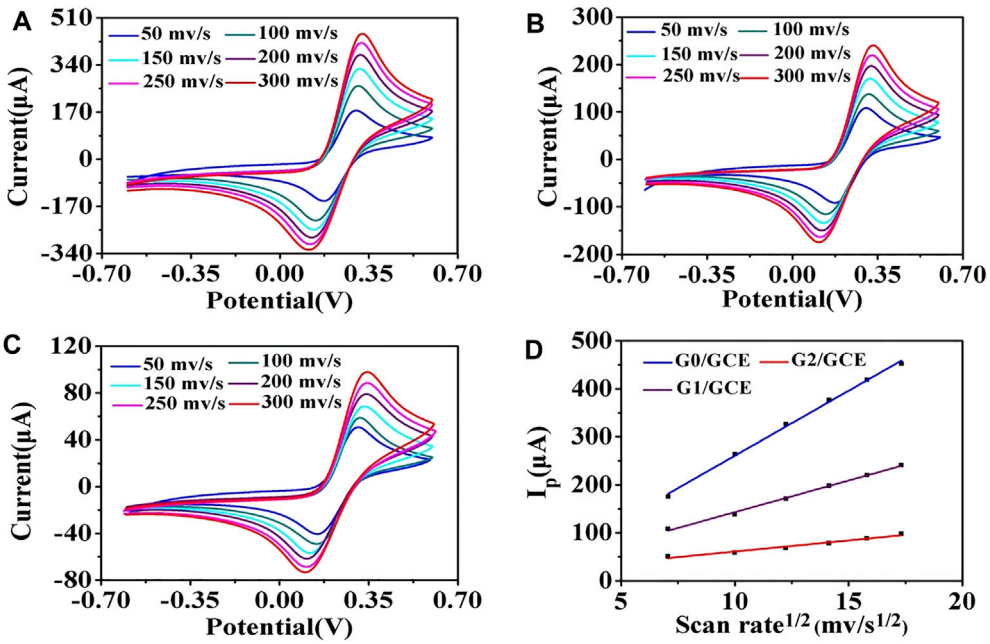

FIGURE 3 | CV of the AuNP/GCE electrodes at different scan rates: 50, 100, 150, 200, 250, and 300 mV/s. **(A)** G0/GCE, **(B)** G1/GCE, **(C)** G2/GCE, **(D)** Randles–Sevcik plots of G0/GCE, G1/GCE, and G2/GCE electrodes.

impedance spectrum consists of a semicircular portion (the high-frequency process related to electron-transfer-limited, the value recorded as R_{ct}) and a linear portion (the low-frequency process related to diffusion-limited). As demonstrated in **Figure 2B** and **Supplementary Table S1**, the R_{ct} of the AuNPs/GCE electrode was smaller than that of the GCE electrode (R_{ct} = 456.7 Ω), revealing a lower electron-transfer resistance and a faster charge exchange of $[Fe(CN)_6]^{4-/3-}$ on the AuNPs/GCE electrode in comparison to the bare GCE electrode. The R_{ct} values of the AuNPs/GCE electrodes fabricated by different AuNPs were 25.8 Ω (G0), 122.4 Ω (G1), and 319.9 Ω (G3) This shows that the impedance of the constructed electrode gradually increased as the particle size increased. After anti-EpCAM was covalently linked onto the surface of G0/GCE, the R_{ct} value and current changed significantly, which could be attributed to the weakly conductive properties of the anti-EpCAM molecule.

Additionally, the morphologies of the AuNP/GCE slides fabricated with different sizes of AuNPs were characterized using SEM. As seen in **Supplementary Figure S1**, as the size decreased, the density of particles on the surface of the GCE increased, which may result in a higher efficiency of electron transfer on the electrode surface for AuNPs with good conductivity. The AuNP/GCE electrodes were tested by CV at different scan rates. As demonstrated in **Figure 3D**, the anodic peak current value increased significantly as the AuNP size decreased, indicating that G0/GCE had the largest electron transfer efficiency on the electrode surface, which is consistent with the above conjecture.

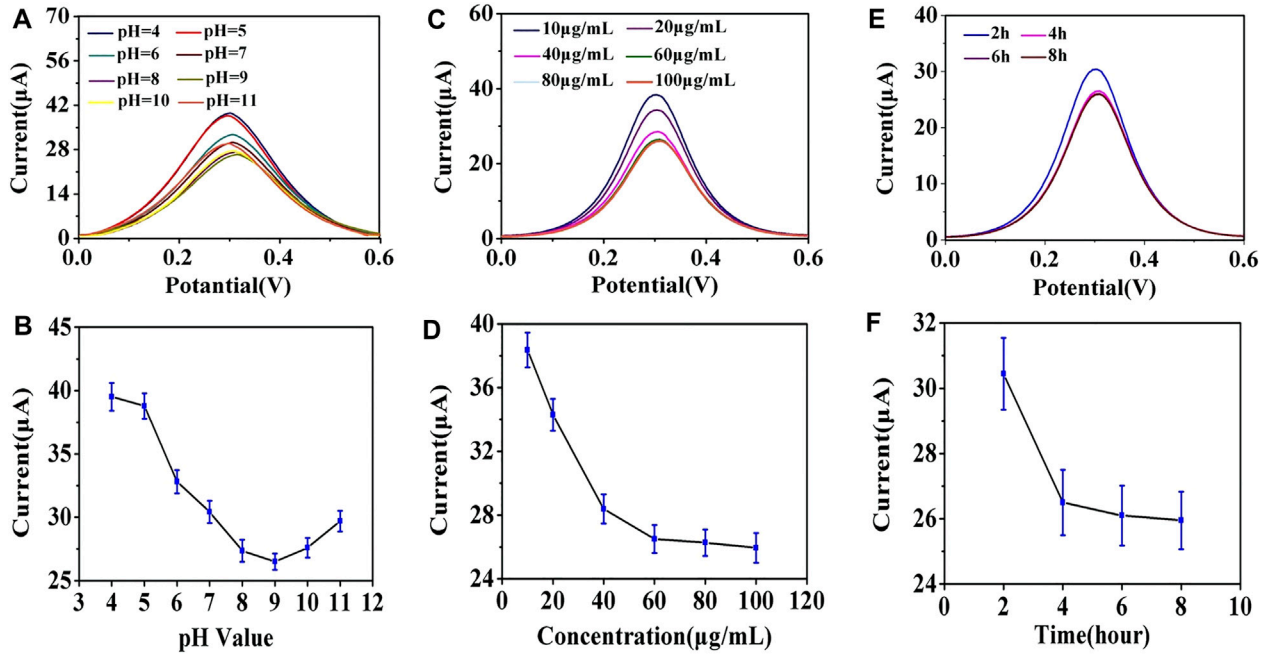

FIGURE 4 | (A) Effect of anti-EpCAM-modified pH value on DPV response. **(B)** line graph of the effect of the pH value on the peak current value of DPV. **(C)** effect of anti-EpCAM concentration on DPV response. **(D)** line graph of the effect of anti-EpCAM concentration on the peak current value of DPV. **(E)** effect of anti-EpCAM binding time on the DPV response. **(F)** line graph of the effect of anti-EpCAM binding time on the peak current value of DPV.

Fabrication of Electrochemical Cell Sensor

To achieve optimal detection performance, several parameters in the electrochemical immunoassay were explored, including the optimal pH value of antibody modification, concentrations, and incubation time of anti-EpCAM conjunction. The G0/GCE electrode was used in subsequent procedures. The pH value of the working solution has a significant influence on the binding strength between antibodies and AuNPs, and it was adjusted using K_2CO_3 or HCl in this study. As shown in **Figures 4A,B**, when the pH was adjusted from 4.0 to 9.0, the corresponding DPV signal decreased rapidly, and when the pH value exceeded 9.0, the DPV signal increased with the value. This could be attributed to the fact that the strongest covalent binding strength of the antibodies we used and AuNPs occurred in an alkaline environment (pH = 9.0) (Stonehuerner et al., 1992; Sardar et al., 2009), and the optimal pH value was determined to be 9.0.

The concentration of anti-EpCAM was a critical factor in the construction strategy because it directly affected the binding efficiency of the cells. As shown in **Figures 4C,D**, the DPV signals decreased as the anti-EpCAM concentration increased, and a minimum CV response was obtained at the concentration of 60 μg/ml, which revealed the saturation modification of anti-EpCAM. The 60 μg/ml of anti-EpCAM is recommended for further research.

Incubation times of the antibodies and AuNPs were also explored. **Figures 4E,F** illustrated the influence of the DPV signal with different incubation time. The current response saturated at 4 h, and the optimal incubation time was 4 h.

Electrochemical Characterization of Immuno-Cytosensor

Once the AuNP/GCE electrode surface antibody modification with the optimal experimental parameters was performed, the electrode was washed with PBS and blocked the nonspecific binding sites by BSA solution (1%, 50 μL) for 1 h. In the aforementioned process, the EIS method was utilized to monitor the different modification steps of the electrode for immediate and sensitive response to a change in the electrode surface (Quan et al., 2001). **Supplementary Figure S2** and **Supplementary Table S1** show the detailed changes in R_{ct} values using $[Fe(CN)_6]^{4-/3-}$ as the redox probe with anti-EpCAM and BSA modification. The results revealed that the R_{ct} value of the cell sensor was larger than that of the GCE electrode (R_{ct} = 456.7 Ω), indicating the weak conductive properties of the antibody. The cytosensors fabricated by the AuNPs with different sizes and modified by antibody were successfully assembled, and R_{ct} was 1,605.7 Ω (G0), 1,216.1 Ω (G1) and 940.4 Ω (G2).

Detection Performance of the Electrochemical Cytosensor

In the present experiment, the cytosensor was incubated with a 4T1 cells solution for 2 h at 37°C (**Supplementary Figure S3**). 4T1 cells ranging from 10 to 10^7 cells/mL were monitored for 2 h to estimate the ability of the electrochemical cytosensor. After washing three times with PBS, the EIS and DPV methods were used for the quantitative determination of tumor cells. For the EIS

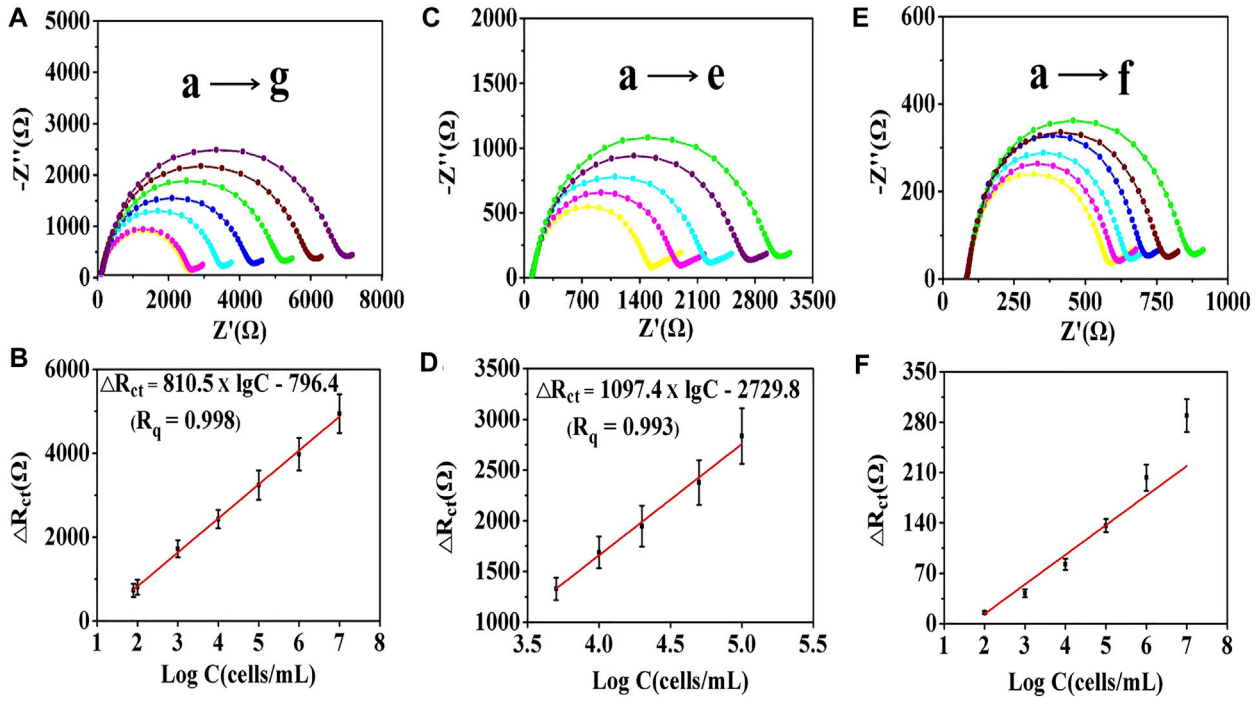

FIGURE 5 | EIS curves of the cell sensors after capturing different concentrations of 4T1 cells. **(A)** EIS curves of the G0 cytosensor. **(B)** linear relationship between the impedance value of the G0 cytosensor and the logarithm of cells concentration: (a) 8.0 × 10, (b) 1.0×10^2, (c) 1.0×10^3, (d) 1.0×10^4, (e) 1.0×10^5, (f) 1.0×10^6, and (g) 1.0×10^7 cells/mL. **(C)** EIS curves of the G0/GCE electrode. **(D)** linear relationship between the impedance value of the G0/GCE electrode and the logarithm of cells concentration: (a) 5.0×10^3, (b) 1.0×10^4, (c) 2.0×10^4, (d) 5.0×10^4, and (e) 1.0×10^5 cells/mL. **(E)** EIS curves of the GCE electrode and **(F)** linear relationship between the impedance value of the GCE electrode and the logarithm of cells concentration: (a) 1.0×10^2, (b) 1.0×10^3, (c) 1.0×10^4, (d) 1.0×10^5, (e) 1.0×10^6, and (f) 1.0×10^7 cells/mL. The error bars represent the standard deviation of three independent measurements.

method, as shown in **Figure 5** and **Supplementary Figure S4**, the R_{ct} values increased with the cell concentration owing to the trapped cells hindering the electron transfer. For the G0 AuNP cytosensor, when the cell concentration ranged from 8.0 × 10 to 10^7 cells/mL, the equation ΔR_{ct} (Ω) = 810.5 × lgC -796.4 (R^2 = 0.998) was applied to record the relationship between 4T1 cell concentration (C) and impedance change value (ΔR_{ct}). As an LOD, 55 cells/mL (S/N = 3) of 4T1 cells could be detected by EIS. The detection equations of the G1 and the G2 AuNPs cytosensors were ΔR_{ct} (Ω) = 598.1 × lgC - 754.5 (2.0×10^2–10^6 cells/mL, LOD = 112 cells/mL, R^2 = 0.997) and ΔR_{ct} (Ω) = 316.4 × lgC - 517.1 (5.0×10^2–5.0×10^5 cells/mL, LOD = 500 cells/mL, R^2 = 0.995) respectively (**Supplementary Figures S4A–D**). This revealed that the G0 AuNP cytosensor was optimal for the quantitative detection of tumor cells. For the G0 AuNP cytosensor, when the DPV method was adopted, as shown in **Supplementary Figures S4E,F**, the current response (I) decreased linearly with increasing logarithm values of the target cell concentrations within the range of 8.0 × 10 to 10^7 cells/mL. The equation was I = −2.3 × lgC +22.1 (R^2 = 0.996), and the LOD was 50 cells/mL (S/N = 3). Compared with other methods that were used for quantitative analysis of CTCs, the aforementioned assay revealed significant detection sensitivity and lower LOD (**Supplementary Table S2**) (Zhang et al., 2010; Zhu et al., 2012; Cao et al., 2017; Bolat et al., 2021).

G0/GCE and bare GCE electrodes were employed to investigate their self-sensing properties. As shown in **Figure 5C**, for the G0/GCE electrode, the Nyquist diagrams changed proportionally to the logarithm of cells concentration with the range from 5.0×10^3 to 1.0×10^5 cells/mL. The linear relationship can be depicted as ΔR_{ct} (Ω) = 1097.4 × lgC - 2729.8 (R^2 = 0.993), and the LOD was 5,000 cells/mL (**Figure 5D**). For the bare GCE electrode, there was a minor response between the ΔR_{ct} value and the logarithm of the cell concentration (**Figures 5E,F**). The obtained analytical performance of the G0/GCE sensor could give the credit to the good conductivity of the AuNPs (**Supplementary Figure S5**). After covalent coupling of the anti-EpCAM, EpCAM-positive tumor cells could be specifically captured on the surface of the electrode. Compared with the bare AuNPs/GCE cytosensor, the immunocytosensor has excellent EIS detection capability, which is largely due to the highly specific antigen–antibody immunoreaction.

To analyze the number of captured tumor cells, a 10 × 10 mm ITO substrate after mercaptosilanization pretreatment was prepared by the same procedure and then incubated with 4T1 cells (1×10^5 cells/mL) in PBS for 2 h. After the cleaning step with PBS, the captured cells were stained with DAPI for 20 min and detected using a fluorescence microscope. As shown in **Figure 6**, the number of cells captured by the constructed cytosensor decreased with the increase in the particle size of the AuNPs. This could be attributed to the fact that with the decrease in the

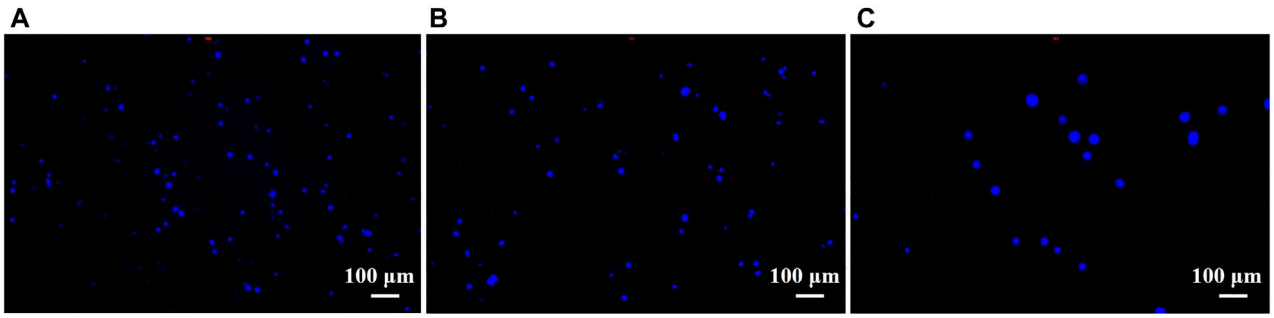

FIGURE 6 | Fluorescence images of 4T1 cells captured by cell sensors. 4T1 cells captured by **(A)** G0, **(B)** G1, and **(C)** G2 cytosensors.

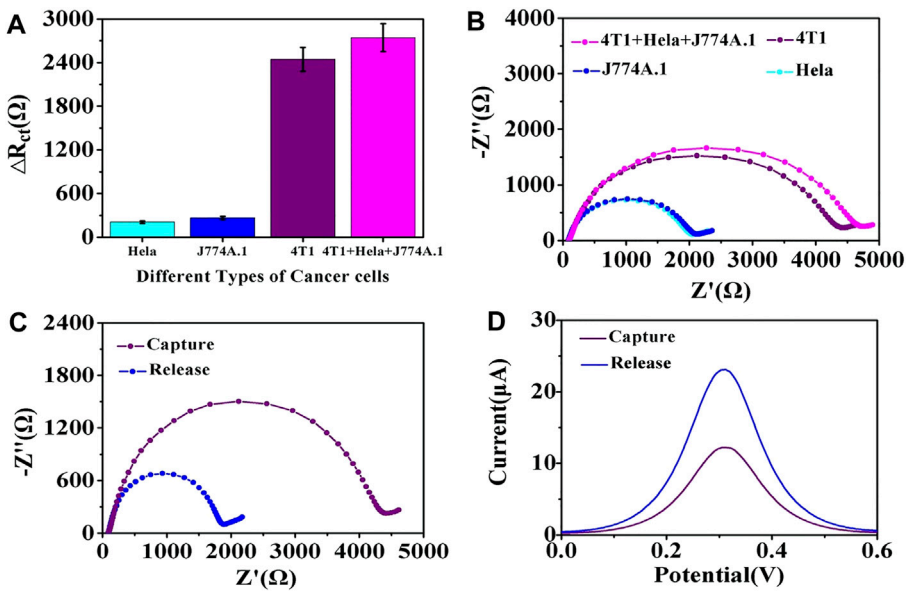

FIGURE 7 | (A) Specificity of the proposed cytosensing strategy, with the ΔR_{ct} value of the G0 cytosensor after incubation with HeLa, J774A.1, or 4T1 cells measured in a solution containing $[Fe(CN)_6]^{3-/4-}$ (5 mM, 1:1) and 0.1 M KCl. The error bars represent the standard deviation of five replicate determinations. **(B)** typical EIS responses after capturing different types of cancer cells. **(C)** comparison of the EIS results and **(D)** comparison of the DPV results of the cytosensor after the capture of cells and after the release of cells.

particle size of the AuNPs, more AuNPs with larger surface area were modified onto the surface of GCEs, resulting in better capture performance of the sensor.

Specificity and Reproducibility of the Electrochemical Cytosensor

To assess the specificity of the immunecytosensor, two EpCAM-negative cell lines, HeLa and J774A.1, were selected as controls. The cell lines (1.0×10^4 cells/mL) were co-incubated with the fabricated cytosensor for 2 h and investigated via EIS. **Figures 7A,B** show that only EpCAM-positive 4T1 cells showed a noticeable R_{ct} change, whereas the EpCAM-negative cells only showed a slight increase in the R_{ct} value. Furthermore, the R_{ct} value of the mixture sample (1.0×10^4 cells/mL of 4T1 cells, HeLa cells, and J774A.1 cells) was slightly higher than that of 4T1 cells, which could be due to the nonspecific adsorption of EpCAM-negative cells, revealing that the construction strategy results in significant selectivity for EpCAM-positive 4T1 cells.

The electrode reproducibility in the aforementioned method was determined using five freshly fabricated electrodes to detect the target cells five times at the same concentrations (10^4 and 10^5 cells/mL), with relative standard deviations of 2.09 and 3.15% (**Supplementary Table S3**), respectively. These data indicate the excellent reproducibility of this method.

Stability was also investigated as a vital property of the fabricated cytosensor. When the G0 cytosensor was stored at 4°C for 7 and 15 days, 96.5 and 92.1% of the initial current responses for 10^5 cells/mL 4T1 cells were retained, respectively. These data suggest that this method exhibited good stability.

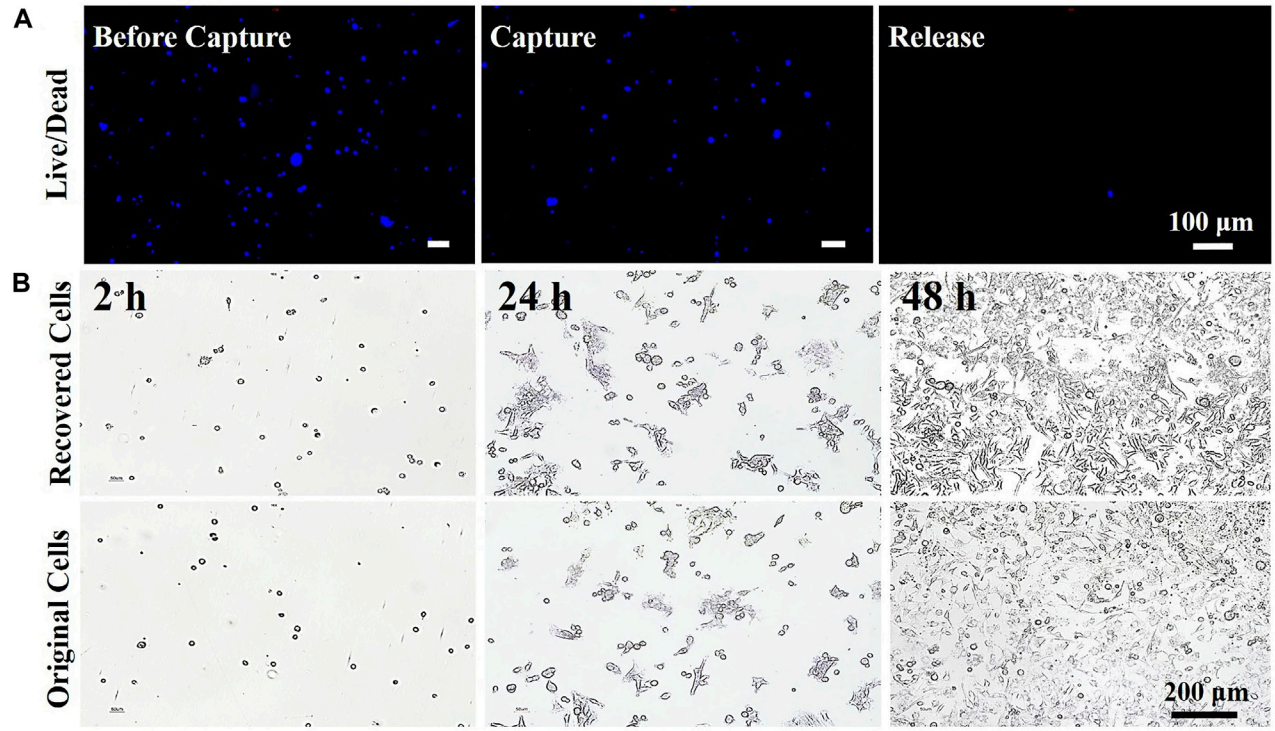

FIGURE 8 | Microscope image of 4T1 cells after three cycles of capture and release. **(A)** Live/dead cell-staining images and **(B)** cell adhesive status and proliferation profiles of the original and recovered 4T1 cells over 3 days.

Cell Release and Cell Viability Analysis

The release of captured target cells will facilitate subsequent biological analyses. After the Gly-HCl eluent destroyed the binding between the antigen and antibody, the captured 4T1 cells were released into the solution from the surface of the cytosensor. As shown in **Figure 7C**, the impedance of the electrode decreased after treatment with the Gly-HCl eluent and the release of captured cells. Similarly, the DPV results (**Figure 7D**) also reveal that the current signal of the electrode significantly increased after the release procedure. These results were due to the release of nonconductive cell entities from the electrodes and elimination of the electronic transmission screen, which led to the recovery of electrochemical signals.

The viability of 4T1 cells during the capture/release cycle was studied using Hoechst and PI staining assays. From the fluorescence microscope image in **Figure 8A**, the cell release rate was determined to be approximately 91.9%, and the captured cells were completely released. We also found that there were no significant differences in cell viability during the capture/release cycle. The long-term cell culture and proliferation ability of the recovered 4T1 cells were also studied. The proliferation test results are shown in **Figure 8B**. The 4T1 cells started to proliferate after 24 h, and there was no evident difference between cell adhesion and growth behavior. Therefore, it could be inferred that the recovery of CTCs without loss of bioactivity could be achieved using this method. The prepared biosensor is suitable for the detection of specific target cells and can release the captured cells in a nondestructive manner for further analysis.

Detection of CTCs in Simulated Samples With Leukocyte

To examine the applicability of our method in a simulated sample, leukocyte samples spiked with 4T1 cells at concentrations of 1×10^2, 1×10^3, 1×10^4, and 1×10^5 cells/mL were tested using the proposed cytosensor, and the corresponding results are shown in **Supplementary Table S3**. The recovery results were consistent with the corresponding spiked amounts of 4T1 cells. These results reveal that the fabricated biosensor could resist leukocyte interference for highly sensitive and specific CTCs detection.

CONCLUSION

In conclusion, the timely discovery and detection of CTCs is important for the early diagnosis and treatment of cancer. In the present study, the promising application prospects of AuNPs in the construction of biosensors for sensitive detection and noninvasive release of CTCs were demonstrated. To realize sensitive, specific detection of CTCs, an electrochemical cell sensor based on AuNPs was developed. The AuNPs were modified onto the surface of the electrode and then covalently bonded by anti-EpCAM for specific recognition of EpCAM-positive cells. The captured cells on the electrode influenced the hot electron transport efficiency, leading to increased R_{ct} values. The changes in R_{ct} values or current values varied with the logarithm of CTCs concentration, and a sensitive, specific electrochemical strategy for CTCs detection was then

reperted. Furthermore, the size effect of the AuNPs was studied. As the size of the AuNPs increased, the specific surface area of the cytosensors decreased, which led to fewer cells being captured by the sensors per unit area. The cell sensor constructed based on 17 nm AuNPs had a wider linear detection range from 8.0×10 to 1.0×10^7 cells/mL and a lower LOD of 50 cells/mL for the 4T1 cells. The constructed cytosensor released the captured cells in a nondestructive manner when the Gly-HCl eluent was introduced. The recovered cells could be of great significance for early screening, postoperative monitoring, and selection of personalized treatment schemes for cancer patients.

DATA AVAILABILITY STATEMENT

The original contributions presented in the study are included in the article/**Supplementary Material**, further inquiries can be directed to the corresponding authors.

ETHICS STATEMENT

The animal study was reviewed and approved by the Ethics Committee for the use of Experimental Animals of Chinese Academy of Science.

AUTHOR CONTRIBUTIONS

Conception of experiments: RZ and ZC. Laboratory experiments and analysis: RZ and QY. Writing: RZ. Review and editing: ZC. MC and MG provide purely technical help. LY and QM: visualization. W-FD: project administration and funding acquisition. All of the authors have read and agreed to the published version of the manuscript.

FUNDING

The present study was funded by the National Key R&D Program of China (No. 2020YFC2004500), the National Natural Science Foundation of China (Nos. 81771982, 91959112, 21803075 and 81902166), the Science Foundation of the Chinese Academy of Sciences (No. 2020SYHZ0041), the Instrument Developing Project of Chinese Academy of Science (No. YJKYYQ20200038), and the Science and Technology Department of Jinan City (No. 2018GXRC016).

SUPPLEMENTARY MATERIAL

The Supplementary Material for this article can be found online at: https://www.frontiersin.org/articles/10.3389/fbioe.2021.783661/full#supplementary-material

REFERENCES

Alix-Panabières, C., and Pantel, K. (2013). Circulating tumor cells: liquid biopsy of cancer. *Clin. Chem.* 59, 110–118. doi:10.1373/clinchem.2012.194258

Bastús, N. G., Comenge, J., and Puntes, V. (2011). Kinetically controlled seeded growth synthesis of citrate-stabilized gold nanoparticles of up to 200 nm: size focusing versus Ostwald ripening. *Langmuir* 27, 11098–11105. doi:10.1021/la201938u

Bolat, G., Vural, O. A., Yaman, Y. T., and Abaci, S. (2021). Polydopamine nanoparticles-assisted impedimetric sensor towards label-free lung cancer cell detection. *Mater. Sci. Eng. C* 119, 111549. doi:10.1016/j.msec.2020.111549

Cao, J., Zhao, X.-P., Younis, M. R., Li, Z.-Q., Xia, X.-H., and Wang, C. (2017). Ultrasensitive Capture, Detection, and Release of Circulating Tumor Cells Using a Nanochannel-Ion Channel Hybrid Coupled with Electrochemical Detection Technique. *Anal. Chem.* 89, 10957–10964. doi:10.1021/acs.analchem.7b02765

Denis, M. G., Lipart, C., Leborgne, J., Lehur, P.-A., Galmiche, J.-P., Denis, M., et al. (1997). Detection of disseminated tumor cells in peripheral blood of colorectal cancer patients. *Int. J. Cancer* 74, 540–544. doi:10.1002/(sici)1097-0215(19971021)74:5<540:aid-ijc11>3.0.co;2-a

Gikunoo, E., Abera, A., and Woldesenbet, E. (2014). Achieving ultra-low detection limit using nanofiber labels for rapid disease detection. *Aid* 04, 214–222. doi:10.4236/aid.2014.44030

Gogoi, P., Sepehri, S., Zhou, Y., Gorin, M. A., Paolillo, C., Capoluongo, E., et al. (2016). Development of an automated and sensitive microfluidic device for capturing and characterizing circulating tumor cells (CTCs) from clinical blood samples. *PloS one* 11, e0147400. doi:10.1371/journal.pone.0147400

Gradilone, A., Naso, G., Raimondi, C., Cortesi, E., Gandini, O., Vincenzi, B., et al. (2011). Circulating tumor cells (CTCs) in metastatic breast cancer (MBC): prognosis, drug resistance and phenotypic characterization. *Ann. Oncol.* 22, 86–92. doi:10.1093/annonc/mdq323

Hong, B. (2013). *Targeted cell separation and enumeration device and the use thereof*. United States: Google Patents.

Hristozova, T., Konschak, R., Stromberger, C., Fusi, A., Liu, Z., Weichert, W., et al. (2011). The presence of circulating tumor cells (CTCs) correlates with lymph node metastasis in nonresectable squamous cell carcinoma of the head and neck region (SCCHN). *Ann. Oncol.* 22, 1878–1885. doi:10.1093/annonc/mdr130

Hu, Y., Fan, L., Zheng, J. E., Cui, R., Liu, W., He, Y., et al. (2010). Detection of circulating tumor cells in breast cancer patients utilizing multiparameter flow cytometry and assessment of the prognosis of patients in different CTCs levels. *Cytometry A: J. Int. Soc. Adv. Cytometry* 77, 213–219. doi:10.1002/cyto.a.20838

J Alvarez-Cubero, M., Vázquez-Alonso, F., Puche-Sanz, I., Gabriel Ortega, F., Martin-Prieto, M., Garcia-Puche, L. J., et al. (2016). Dormant circulating tumor cells in prostate cancer: therapeutic, clinical and biological implications. *Curr. Drug Targets* 17, 693–701. doi:10.2174/1389450116666150309121346

Khoshfetrat, S. M., and Mehrgardi, M. A. (2017). Amplified detection of leukemia cancer cells using an aptamer-conjugated gold-coated magnetic nanoparticles on a nitrogen-doped graphene modified electrode. *Bioelectrochemistry* 114, 24–32. doi:10.1016/j.bioelechem.2016.12.001

Liu, X., Li, C., Li, J., Yu, T., Zhou, G., Cheng, J., et al. (2018). Detection of CTCs in portal vein was associated with intrahepatic metastases and prognosis in patients with advanced pancreatic cancer. *J. Cancer* 9, 2038. doi:10.7150/jca.23989

Miyamoto, D. T., Zheng, Y., Wittner, B. S., Lee, R. J., Zhu, H., Broderick, K. T., et al. (2016). *Abstract IA09: Single cell RNA-sequencing of circulating tumor cells"*. Pennsylvania: AACR.

Moskaluk, C. A., Abdrabbo, M. K., Harper, J., Yoshida, C., Riggins, G. J., Frierson, H. F., et al. (2002). Gastric cancers overexpress S100A calcium-binding proteins. *Cancer Res.* 62, 6823–6826.

Mostert, B., Kraan, J., Sieuwerts, A. M., Van Der Spoel, P., Bolt-De Vries, J., Prager-Van Der Smissen, W. J., et al. (2012). CD49f-based selection of circulating tumor cells (CTCs) improves detection across breast cancer subtypes. *Cancer Lett.* 319, 49–55. doi:10.1016/j.canlet.2011.12.031

Mostert, B., Sleijfer, S., Foekens, J. A., and Gratama, J. W. (2009). Circulating tumor cells (CTCs): detection methods and their clinical relevance in breast cancer. *Cancer Treat. Rev.* 35, 463–474. doi:10.1016/j.ctrv.2009.03.004

Nakanishi, H., Kodera, Y., Yamamura, Y., Ito, S., Kato, T., Ezaki, T., et al. (2000). Rapid quantitative detection of carcinoembryonic antigen–expressing free

tumor cells in the peritoneal cavity of gastric-cancer patients with real-time RT-PCR on the lightcycler. *Int. J. Cancer* 89, 411–417. doi:10.1002/1097-0215(20000920)89:5<411:aid-ijc3>3.0.co;2-5

Pang, X., Cui, C., Su, M., Wang, Y., Wei, Q., and Tan, W. (2018). Construction of self-powered cytosensing device based on ZnO nanodisks@ g-C3n4 quantum dots and application in the detection of CCRF-CEM cells. *Nano Energy* 46, 101–109. doi:10.1016/j.nanoen.2018.01.018

Paterlini-Brechot, P., and Benali, N. L. (2007). Circulating tumor cells (CTC) detection: clinical impact and future directions. *Cancer Lett.* 253, 180–204. doi:10.1016/j.canlet.2006.12.014

Peng, Y., Peng, Y., Tang, S., Shen, H., Sheng, S., Wang, Y., et al. (2020). PdIrBP mesoporous nanospheres combined with superconductive carbon black for the electrochemical determination and collection of circulating tumor cells. *Microchimica Acta* 187, 1–11. doi:10.1007/s00604-020-4213-z

Qian, X., Zhou, X., Ran, X., Ni, H., Li, Z., Qu, Q., et al. (2019). Facile and clean synthesis of dihydroxylatopillar [5] arene-stabilized gold nanoparticles integrated Pd/MnO2 nanocomposites for robust and ultrasensitive detection of cardiac troponin I. *Biosens. Bioelectron.* 130, 214–224. doi:10.1016/j.bios.2019.01.041

Quan, Z.-L., Wu, X.-J., Chen, S.-H., Zhao, S., and Ma, H. (2001). Self-assembled monolayers of Schiff bases on copper surfaces. *Corrosion* 57. doi:10.5006/1.3290344

Sardar, R., Funston, A. M., Mulvaney, P., and Murray, R. W. (2009). Gold nanoparticles: past, present, and future. *Langmuir* 25, 13840–13851. doi:10.1021/la9019475

Schindlbeck, C., Rack, B., Jueckstock, J., Schneeweiss, A., Thurner-Herrmanns, E., Schneider, A., et al. (2009). *Prognostic relevance of circulating tumor cells (CTCs) in peripheral blood of breast cancer patients before and after adjuvant chemotherapy–translational research program of the German SUCCESS-trial.* Pennsylvania: AACR.

Shahneh, F. Z. (2013). Sensitive antibody-based CTCs detection from peripheral blood. *Hum. antibodies* 22, 51–54. doi:10.3233/hab-130270

Shinden, Y., Ueo, H., Tobo, T., Ganachi, A., Komatsu, H., Nambara, S., et al. (2015). *The new and rapid technique of detecting breast cancer cells using new fluorescent probe 'gGlu-HMRG'and its clinical application)*. Pennsylvania: AACR.

Souza E Silva, V., Fanelli, M. F., Soares, F. A., Felismino, T. C., Eliza Cavicchioli Buim, M., Silva, V. A., et al. (2014). *Evaluation of circulating tumor cells (CTCs) as a potential biomarker in patients with colorectal cancer (CRC): A prospective analysis*. Pennsylvania: American Society of Clinical Oncology.

Stonehuerner, J., Zhao, J., O'daly, J., Crumbliss, A., and Henkens, R. (1992). Comparison of colloidal gold electrode fabrication methods: the preparation of a horseradish peroxidase enzyme electrode. *Biosens. Bioelectron.* 7, 421–428. doi:10.1016/0956-5663(92)85041-8

Tan, S. J., Yeo, T., Sukhatme, S. A., Kong, S. L., Lim, W.-T., and Lim, C. T. (2017). Personalized treatment through detection and monitoring of genetic aberrations in single circulating tumor cells. *Isolation Mol. Characterization Circulating Tumor Cell*, 255–273. doi:10.1007/978-3-319-55947-6_14

Thévenot, D. R., Toth, K., Durst, R. A., and Wilson, G. S. (2001). Electrochemical biosensors: recommended definitions and classification. *Biosens. Bioelectron.* 16, 121–131. doi:10.1016/s0956-5663(01)00115-4

Wang, J. (2005a). Carbon-nanotube based electrochemical biosensors: A review. *Electroanalysis: Int. J. Devoted Fundam. Pract. Aspects Electroanalysis* 17, 7–14. doi:10.1002/elan.200403113

Wang, J. (2006). Electrochemical biosensors: towards point-of-care cancer diagnostics. *Biosens. Bioelectron.* 21, 1887–1892. doi:10.1016/j.bios.2005.10.027

Wang, J. (2005b). Nanomaterial-based electrochemical biosensors. *Analyst* 130, 421–426. doi:10.1039/b414248a

Wen, C.-Y., Wu, L.-L., Zhang, Z.-L., Liu, Y.-L., Wei, S.-Z., Hu, J., et al. (2014). Quick-response magnetic nanospheres for rapid, efficient capture and sensitive detection of circulating tumor cells. *ACS nano* 8, 941–949. doi:10.1021/nn405744f

Xie, J., Dong, H., Chen, H., Zhao, R., Sinko, P. J., Shen, W., et al. (2015). Exploring cancer metastasis prevention strategy: interrupting adhesion of cancer cells to vascular endothelia of potential metastatic tissues by antibody-coated nanomaterial. *J. nanobiotechnology* 13, 1–13. doi:10.1186/s12951-015-0072-x

Zhang, J.-J., Cheng, F.-F., Zheng, T.-T., and Zhu, J.-J. (2010). Design and implementation of electrochemical cytosensor for evaluation of cell surface carbohydrate and glycoprotein. *Anal. Chem.* 82, 3547–3555. doi:10.1021/ac9026127

Zhao, S., Liu, Y., Zhang, Q., Li, H., Zhang, M., Ma, W., et al. (2011). The prognostic role of circulating tumor cells (CTCs) detected by RT-PCR in breast cancer: a meta-analysis of published literature. *Breast Cancer Res. Treat.* 130, 809–816. doi:10.1007/s10549-011-1379-4

Zhong, L., Gan, S., Fu, X., Li, F., Han, D., Guo, L., et al. (2013). Electrochemically controlled growth of silver nanocrystals on graphene thin film and applications for efficient nonenzymatic H2O2 biosensor. *Electrochimica Acta* 89, 222–228. doi:10.1016/j.electacta.2012.10.161

Zhu, J., Nguyen, T., Pei, R., Stojanovic, M., and Lin, Q. (2012). Specific capture and temperature-mediated release of cells in an aptamer-based microfluidic device. *Lab. Chip* 12, 3504–3513. doi:10.1039/c2lc40411g

Conflict of Interest: Author ZC was employed by Jinan Guokeyigong Science and Technology Development Co., Ltd.

The remaining authors declare that the research was conducted in the absence of any commercial or financial relationships that could be construed as a potential conflict of interest.

Publisher's Note: All claims expressed in this article are solely those of the authors and do not necessarily represent those of their affiliated organizations, or those of the publisher, the editors and the reviewers. Any product that may be evaluated in this article, or claim that may be made by its manufacturer, is not guaranteed or endorsed by the publisher.

frontiers in Bioengineering and Biotechnology

REVIEW
published: 01 December 2021
doi: 10.3389/fbioe.2021.785937

Kinetics of Nanomedicine in Tumor Spheroid as an *In Vitro* Model System for Efficient Tumor-Targeted Drug Delivery With Insights From Mathematical Models

Sayoni Maitra Roy[1†], *Vrinda Garg*[2†], *Sourav Barman*[1], *Chitrita Ghosh*[3], *Amit Ranjan Maity*[1*] *and Surya K. Ghosh*[2*]

[1]*Amity Institute of Biotechnology, Amity University, Kolkata, India,* [2]*Department of Physics, National Institute of Technology, Warangal, India,* [3]*Department of Pharmacology, Burdwan Medical College and Hospital, Burdwan, India*

OPEN ACCESS

Edited by:
Wang Zheng, Suzhou Institute of Nano-tech and Nano-bionics (CAS), China

Reviewed by:
Suresh Sarkar, University of Illinois at Urbana-Champaign, United States
Arnab Basu, Ramakrishna Mission Vivekananda Educational and Research Institute, India

***Correspondence:**
Amit Ranjan Maity
armaity@kol.amity.edu
Surya K. Ghosh
skghosh@nitw.ac.in

[†]*These authors have contributed equally to this work and share first authorship*

Specialty section:
This article was submitted to Nanobiotechnology, a section of the journal Frontiers in Bioengineering and Biotechnology

Received: *29 September 2021*
Accepted: *27 October 2021*
Published: *01 December 2021*

Citation:
Roy SM, Garg V, Barman S, Ghosh C, Maity AR and Ghosh SK (2021) Kinetics of Nanomedicine in Tumor Spheroid as an In Vitro *Model System for Efficient Tumor-Targeted Drug Delivery With Insights From Mathematical Models. Front. Bioeng. Biotechnol. 9:785937. doi: 10.3389/fbioe.2021.785937*

Numerous strategies have been developed to treat cancer conventionally. Most importantly, chemotherapy shows its huge promise as a better treatment modality over others. Nonetheless, the very complex behavior of the tumor microenvironment frequently impedes successful drug delivery to the tumor sites that further demands very urgent and effective distribution mechanisms of anticancer drugs specifically to the tumor sites. Hence, targeted drug delivery to tumor sites has become a major challenge to the scientific community for cancer therapy by assuring drug effects to selective tumor tissue and overcoming undesired toxic side effects to the normal tissues. The application of nanotechnology to the drug delivery system pays heed to the design of nanomedicine for specific cell distribution. Aiming to limit the use of traditional strategies, the adequacy of drug-loaded nanocarriers (i.e., nanomedicine) proves worthwhile. After systemic blood circulation, a typical nanomedicine follows three levels of disposition to tumor cells in order to exhibit efficient pharmacological effects induced by the drug candidates residing within it. As a result, nanomedicine propounds the assurance towards the improved bioavailability of anticancer drug candidates, increased dose responses, and enhanced targeted efficiency towards delivery and distribution of effective therapeutic concentration, limiting toxic concentration. These aspects emanate the proficiency of drug delivery mechanisms. Understanding the potential tumor targeting barriers and limiting conditions for nanomedicine extravasation, tumor penetration, and final accumulation of the anticancer drug to tumor mass, experiments with *in vivo* animal models for nanomedicine screening are a key step before it reaches clinical translation. Although the study with animals is undoubtedly valuable, it has many associated ethical issues. Moreover, individual experiments are very expensive and take a longer time to conclude. To overcome these issues, nowadays, multicellular tumor spheroids are considered a promising *in vitro* model system that proposes better replication of *in vivo* tumor properties for the future development of new therapeutics. In this review, we will discuss how tumor spheroids could be used as an *in vitro* model system to screen nanomedicine used in targeted drug delivery, aiming for better

therapeutic benefits. In addition, the recent proliferation of mathematical modeling approaches gives profound insight into the underlying physical principles and produces quantitative predictions. The hierarchical tumor structure is already well decorous to be treated mathematically. To study targeted drug delivery, mathematical modeling of tumor architecture, its growth, and the concentration gradient of oxygen are the points of prime focus. Not only are the quantitative models circumscribed to the spheroid, but also the role of modeling for the nanoparticle is equally inevitable. Abundant mathematical models have been set in motion for more elaborative and meticulous designing of nanomedicine, addressing the question regarding the objective of nanoparticle delivery to increase the concentration and the augmentative exposure of the therapeutic drug molecule to the core. Thus, to diffuse the dichotomy among the chemistry involved, biological data, and the underlying physics, the mathematical models play an indispensable role in assisting the experimentalist with further evaluation by providing the admissible quantitative approach that can be validated. This review will provide an overview of the targeted drug delivery mechanism for spheroid, using nanomedicine as an advantageous tool.

Keywords: *in vitro* cell culture, multicellular tumor spheroids, tumor microenvironment, nanomedicine, tumor-targeted drug delivery, tumor penetration and accumulation, mathematical modeling

1 INTRODUCTION

Cancer tissues are anomalous cell mass exhibiting escalated growth and unregulated cell proliferation. They divide at abnormal rates, which enable them to escape apoptosis when they ought to. For the last several decades, among various strategies (Nakamura and Harashima, 2017) used to treat intractable cancer, chemotherapy has shown its promise as a better therapeutic strategy over others. However, a complex tumor microenvironment and its hierarchical structure often impede successful drug delivery to tumor sites (Junttila and Sauvage, 2013; Frankel et al., 2017; Musetti and Huang, 2018; Wang et al., 2018; Arneth, 2019; Baghban et al., 2020). It further demands a commendable and effective delivery strategy of anticancer drug candidates, like small molecular anticancer drugs, therapeutic nucleic acid, therapeutic protein, and therapeutic peptide, specifically to the diseased site (Maity and Stepensky, 2016; Takashi et al., 2017). Furthermore, the poor water solubility of many anticancer drugs, untoward pharmacokinetics, and the related underlying risk of cytotoxic effects in normal tissue put drug candidates to use for further clinical applications (Li et al., 1986; Kusumoto et al., 1990; Onoue et al., 2014). Additionally, the limited delivery efficiency of drug candidates to selective tumor sites makes treatment efficacy remarkably poor. Hence, targeted delivery of drugs to tumor sites has become a major scientific challenge for cancer therapy by assuring drug efficacy to selectively diseased sites and overcoming undesired cytotoxic side effects to normal tissue (Iqbal et al., 2017; Srinivasarao and Low, 2017; Unsoy and Gunduz, 2018).

Toward this, nanomedicine has already proven its indispensable part in addressing these issues. An efficient nanomedicine can circulate in the blood compartment stably for a longer period of time and get partially engulfed by macrophages of the reticuloendothelial system with extravasation to the tumor site. This successful extravasation facilitates its interaction with tumor tissue for further recognition and uptake by target cells. At the same time, nanomedicine also exhibits poor extravasation at the normal tissue region and a reasonably small amount of distribution over there due to tight and continuous vasculature. After systemic circulation of nanomedicine in blood, it follows three levels of disposition to tumor cells in order to exhibit the required pharmacological effects induced by the drug candidates residing within (**Figure 1**). At the first level, nanomedicine relocates itself from blood capillaries to tumor sites, which is beneficial for treatment efficiency. Subsequently, at the tumor site, nanomedicine distributes itself to each and individual tumor cell, which is highly desirable, although multiple complex factors in the tumor microenvironment resist its entry to the tumor cell. Ultimately, individual drug candidates reach subcellular organelles to perform their actions. So, nanomedicine helps improve the bioavailability of drug candidates, increase dose responses, and enhance targeting efficiency towards delivering and distribution of effective therapeutic concentration and by limiting toxic concentration. This characteristic of nanomedicine shows its promise towards improved therapeutic efficacy of anticancer drugs (Martin et al., 2017; John et al., 2020; Ferreira et al., 2021). In the preclinical study, the distribution of nanomedicine in tumor cells following its disposition in tumor tissue is the key investigation to determine the efficiency of drug treatment and subsequent disease management strategy.

Before reaching clinical translation, understanding the pharmacokinetics of the anticancer drug at different levels of drug disposition in *in vivo* animal modeling is a very important step. Hence, screening nanomedicine in animal models is essential. Although performing experiments with animal

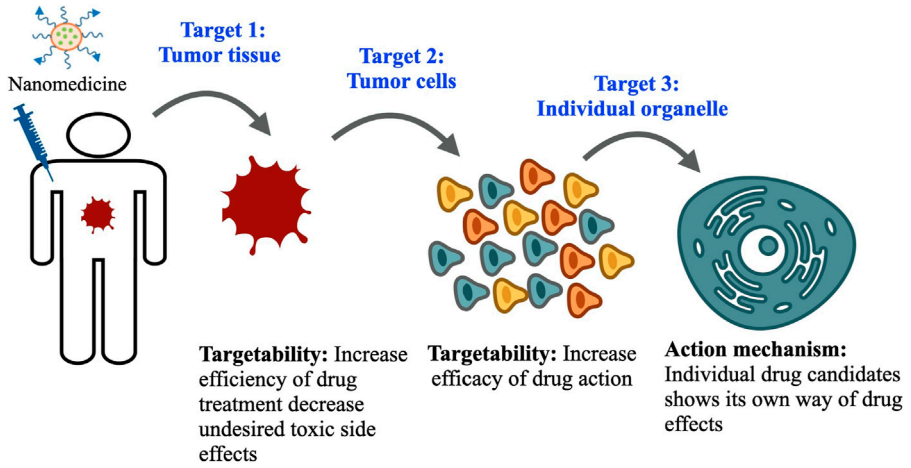

FIGURE 1 | Three levels of drug disposition: The nanomedicine faces three levels of dispositions before reaching its final target. First, they enter the tumor tissue, where multiple complex factors in the tumor microenvironment limit their delivery; second, they follow cellular endocytosis mechanisms and enter inside the tumor cell and exert desired therapeutic effects. Finally, the drug candidate inside nanomedicine reaches individual organelles to exhibit its action mechanism.

models is undoubtedly valuable, many ethical protocols should be followed to conduct an experiment with animals (Patel et al., 2015). Moreover, animal experiments are very expensive, take a longer time to finish, and require repeated experimentation on individual groups to reach the final conclusion. Cancer cells are now being grown in a controlled environment in the laboratory to reproduce the characteristics of *in vivo* solid tumors. Creating the same environment artificially as the real tumor is subject to a lot of constraints in terms of progressive cell accumulation, properties that help cancer cells persist within the tissue leading to a tumor, and physicochemical traits that result in their invasiveness and drug resistance. To overcome these issues, multicellular tumor spheroids are considered promising *in vitro* three-dimensional (3D culture) models, which are intermediate between *in vitro* cellular monolayer and *in vivo* animal models in terms of complexity, cell-cell communication, and gradients of nutrients and oxygen (Kostarelos et al., 2004; Mehta et al., 2012; Solomon et al., 2016). Thus, these *in vitro* tumor models overcome the ethical issues concerned with animal models as well. Tumor spheroids are formed artificially and very easily under laboratory conditions by aggregation and inducing self-assembly of tumor cells, representing a three-dimensional architecture, and can closely mimic drug penetration, distribution, and final accumulation in cancer cells as that of the solid tumor in the body (Sant and Johnston, 2017b; Gianpiero et al., 2017). Moreover, they can assess the efficacy of anticancer drugs as they can serve as a close representative of tumor tissue and cellular microenvironment in terms of cell proliferation, heterogeneity, and drug resistance. Tumor spheroid can replicate the tumor microenvironment where *in vivo* parameters like gradients of soluble cell culture components (e.g., oxygen, nutrients, and growth factor) and cellular waste are generated after metabolic activities (paracrine factors, different metabolites, etc.). These gradients impose a barrier for the diffusion of nanomedicine in the spheroid architecture. Moreover, spheroids build a complex cell-cell network and cell-extracellular matrix adhesions. Thus, 3D tumor spheroid models possess several characteristics like solid tumors such as cell-cell interactions, cellular microenvironments (e.g., hypoxia), drug penetration, reaction, resistance, and extracellular matrix (ECM) production and deposition. Cellular organization within the tumor spheroid is the key aspect governing impaired therapeutic efficacy of anticancer drugs. The proliferating external cell layer of the spheroid causes higher consumption of oxygen and the concentrations of oxygen and nutrients are reduced dramatically towards the center of the spheroid. This hypoxic environment at the center displays an unregulated expression of the hypoxia-inducible factor (HIF), which contributes to establishing therapeutic resistance mechanisms. Both hypoxia and necrosis play crucial roles in anticancer drug resistance mechanisms (Karsch-Bluman et al., 2019; Sharma et al., 2019; Karsch Bluman and Benny, 2020).

For several decades, traditional two-dimensional *in vitro* monolayer cell cultures (2D culture) have been used to screen therapeutics for different intractable diseases, including cancer. Matching between the intrinsic microenvironment and heterogeneity as a real solid tumor is lacking in these cell cultures. Additionally, despite their relative ease of handling, reproducibility, and affordable establishment cost, 2D monolayer cell cultures lag in cell-cell signaling, penetration profile of drugs, and their accumulation as solid tumors (Kapałczyńska et al., 2018). Thus, the therapeutic strategies and *in vitro* methodologies can be indeed improved by considering that the three-dimensional cell cultures maintain the similar complex physiology and microenvironment as a real solid tumor. The tumor spheroid bridges the gap between the 2D cultures and animal models. This model allows replicating the architecture of solid tumors and better investigates the pathobiology of human cancer (**Figure 2**). The potential of the tumor spheroid model is reported to be particularly needful for the development of new anticancer strategies and better measures for cancer treatment and is well acclimated for high-throughput drug screening. Currently, chemotherapy is considered one of the most

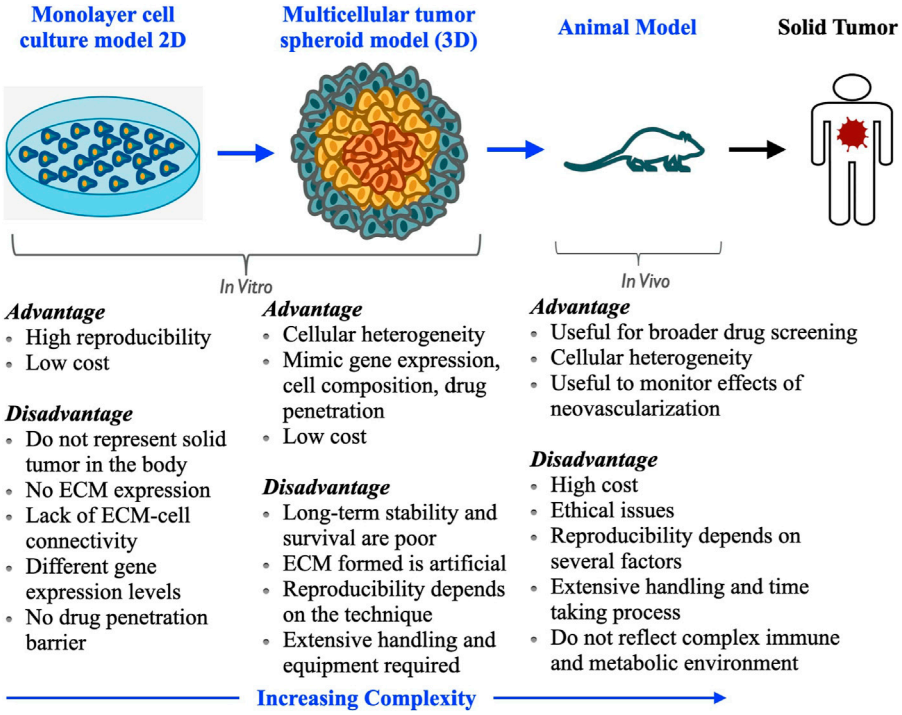

FIGURE 2 | Comparison of various tumor models used for drug screening: importance of multicellular tumor spheroid as an *in vitro* model in preclinical level for screening of new anticancer drugs and development of treatment.

promising and first-line treatment methods among different anticancer therapies; thereby, before reaching any conclusion about performing animal experiments to translate nanomedicine formulations from bench to bedside, initial screening of the tumor spheroid model is highly needed. For a more elaborative view and a thorough understanding of the mechanism, mathematical modeling can be used. It can give a direction to the new approaches for treating the system quantitatively (Goodman et al., 2008; Altrock et al., 2015). The essence of numerical modeling lies in developing the mathematical formulations representing the underlying physical mechanisms of the 3D tumor spheroid growth rate and kinetics of nanoparticles through its cellular organization (Chou et al., 2013). The quantitative approach at distinct cellular scales of tumor spheroid architecture and diffusion of drug molecules or nanodrug formulations (i.e., nanomedicine) inside a tumor and its crowded environment (Ghosh et al., 2012; Ghosh et al., 2015; Ghosh et al., 2016) provides the momentum for the optimized study of these mechanisms. These models can be validated by experimental data bringing forth the unknown parameters that can assist the qualitative approach more precisely (Hori et al., 2021).

In this article, we will discuss how tumor spheroids could be used as an *in vitro* model system to screen nanomedicine used in tumor-targeted drug delivery aiming to better therapeutic benefits of anticancer drugs for future development of new therapeutics and treatment strategies at the preclinical stage (Mu et al., 2018; Raza et al., 2018; Baker et al., 2020). Here, we will also provide an overview of qualitative description, including the strategies to approach the system quantitatively at distinct scales and coordinates integrating both solid tumor and nanomedicine as one system for tumor-targeted drug delivery (Altrock et al., 2015) Beginning with the hierarchical architecture of the tumor spheroid and then its microenvironment (Laird, 1964), we will discuss the mathematical modeling at the cellular, subcellular, and extracellular scale using molecular dynamics, reaction-diffusion mechanism, and hybrid models (Kim and Stolarska, 2007). The latter section will elucidate the physicochemical properties of nanomedicines with a quantitative description of the concentration of drug molecules, and binding sites on cell surface, along with models for adsorption, internalization (Wilhelm et al., 2002; Gao et al., 2013), and diffusion of nanomedicine through the spheroid taking intricate cell-cell interaction, cell-ECM adhesions, and porous gel matrix into consideration for the evaluation of nanomedicine penetration (Ghosh et al., 2015; Ghosh et al., 2016), featuring their adequacy as an insightful tool (Goodman et al., 2008; Ghosh et al., 2012). We conclude with an outlook of the future perspective of the dynamics of shape change of nanomedicine as a modified and efficient drug delivery system (Li et al., 2017b).

2 SOLID TUMOR

A tumor is an abnormal lump of cells showing dysregulated proliferation. Tumors can be largely divided into two categories: non-solid tumors and solid tumors. Non-solid tumors are generally referred to as those having a hematological origin.

Examples include lymphoma and leukemia. On the other hand, solid tumors are structures made up of an abnormal mass of tissues, which do not contain cysts or liquid areas. They may be benign or malignant (Gavhane et al., 2011). Benign tumors are generally slow-growing, resemble normal cells, and remain localized. In contrast, malignant tumors are cancerous bearing characteristics like anaplasia, invasiveness, and metastasis. The nomenclature of solid tumors is based on the type of cells that form them. For example, osteosarcoma and neurofibrosarcoma are comprised of bone cells and nerve sheath cells, respectively (Gavhane et al., 2011). Solid tumors are heterogeneous entities in which the progression is governed by crosstalk between the epithelial parenchyma of carcinomas and the supportive framework of a tumor tissue known as tumor stroma. The basic constitution of the tumor stroma includes the nonmalignant cells known as the stromal cells. Compared to nonsolid tumors, solid tumors pose distinct challenges to chemotherapy owing to the physical and biochemical complexity of their local environment, commonly referred to as the tumor microenvironment. Compared to normal tissue, tumor tissue has distinct structural properties that often hinder the delivery and distribution of anticancer drugs throughout the tumor mass and limit the efficiency and efficacy of drug treatment. Thus, understanding the detailed structural characteristics of a solid tumor with its microenvironment is indispensable for developing new treatment strategies.

2.1 Tumor Stroma

The tumor stroma is the abetting structure of tumor tissue. It is composed of non-malignant cells of tumor-like cancer-associated fibroblasts (CAFs) (Raghu et al., 2016; Tang et al., 2016; Lee et al., 2018; Liu et al., 2019; Monteran and Erez, 2019; Wang et al., 2019; Yavuz et al., 2019), tumor-associated macrophages (TAMs) (Qian et al., 2009; Noy and Pollard, 2014; Larionova et al., 2019; Lin et al., 2019), tumor-associated neutrophils (TANs), mesenchymal stem cells and extracellular matrix (ECM) with fibrous structural proteins (e.g., collagen and elastin), fibrous adhesive proteins (e.g., laminin and fibronectin), and proteoglycans. Nests of malignant tumor cells are linked through junctional proteins (e.g., claudins, desmoglein-2, and E-cadherin) in most solid tumors derived from epithelial tissues. These nests are surrounded by tumor stroma which plays a key role in regulating the behavior of cells found in the local milieu. Tumor stroma creates a niche that aids in seeding metastatic cells and intervenes in drug delivery to tumors. It generates a physical obstacle of stroma proteins that restrict drug penetration and connection between drug candidates, tumor-infiltrating immune cells, and target receptors present in the tumor cell surface. Tumor stroma generates cytokines and chemokines, which prompt synthesis of stroma proteins, prevent activation of immune cells, and activate immuno-suppressive cells such as regulatory T cells. Stroma is associated with characteristic tissue development and homeostasis in the tumor microenvironment, distinct from those associated with normal tissue (Kim et al., 2013; Nunes et al., 2019). Moreover, ECMs produced in most tumors make them more rigid and different types of collagen molecules are also accumulated, forming a thick network inside tumor tissue, resulting in a decrease in pores of tumor matrix, which restrict tumor penetration of nanomedicine useful for therapy. Amplified rigidity increases interstitial fluid pressure, which further restricts the distribution of nanomedicine throughout tumor mass. Therefore, targeting genetically stable stromal cells provides an additional benefit.

2.2 Tumor Stromal Cells

Stromal cells exhibit constant synthesis and release of growth factors, connective tissue components, and cytokines, cooperate with malignant cells to proliferate, invade, and metastasize, which seek major attention in tumor-targeted drug delivery using nanomedicine (Choi et al., 2013; Raghu et al., 2016; Tang et al., 2016; Lee et al., 2018; Liu et al., 2019; Monteran and Erez, 2019; Wang et al., 2019; Yavuz et al., 2019). Cancer-associated fibroblasts (CAF) are major cells found in tumor-associated stroma compared to stroma cells in healthy tissue (Kalluri, 2016). CAF are spindle-shaped mesenchymal cells characterized by constant activation, faster proliferation, and accumulation of large amounts of ECM compared to fibroblast in normal tissue (Kim and Bae, 2016). Tumor cells and stromal cells upregulate different types of profibrotic growth factors in the tumor microenvironment to transdifferentiate stromal fibroblast in CAF. They release various growth factors, for instance, epidermal growth factor (EGF), hepatocyte growth factor (HGF), and insulin-like growth factor-1 (IGF-1) and affect cell proliferation, invasion, and metastasis. They are involved in angiogenesis along with inflammatory cell recruitment. CAF are also engaged in the arousal of angiogenic processes and engages more inflammatory cells. Another very important cell type present in tumor stroma is tumor-associated macrophages (TAMs), which are immune cells of the tumor microenvironment. TAMs suppress antitumor immune responses, generate an immune suppressive microenvironment, and control tumor-associated changes in ECM by secretion of profibrotic growth factors. They produce cytokines (IL-I and IL-8), tumor necrosis factor-α (TNF-α), growth factors (EGF, HGF, bFGF, and VEGF), and various enzymes (Li et al., 2017a). TAMs regulate cancer stem cell activities in solid tumors. Tumor-associated neutrophils (TANs) are also a dominant form of immune cell infiltrates, found in various types of cancer (Masucci et al., 2019; Wu et al., 2019). They generate neutrophils, reactive oxygen species, cytokines, growth factors, and proteinases and play key roles in controlling tumor cell proliferation, metastasis, angiogenesis, and antitumor immune suppression (Masucci et al., 2019; Wu et al., 2019).

2.3 Characteristics of Solid Tumor that Influence Nanomedicine Penetration

Nanomedicine facilitates the transport of drug candidates from tumor surface to center. The penetration across tumor mass gets occasionally influenced by the specific properties of tumor architecture (**Figure 3**).

2.3.1 Abnormal Vasculature

The vasculature in solid tumors are heterogeneous, which leads to perfused areas, and results in abnormal blood flow in the tumor (Tong et al., 2004; Danquah et al., 2011; Mizukami et al., 2012).

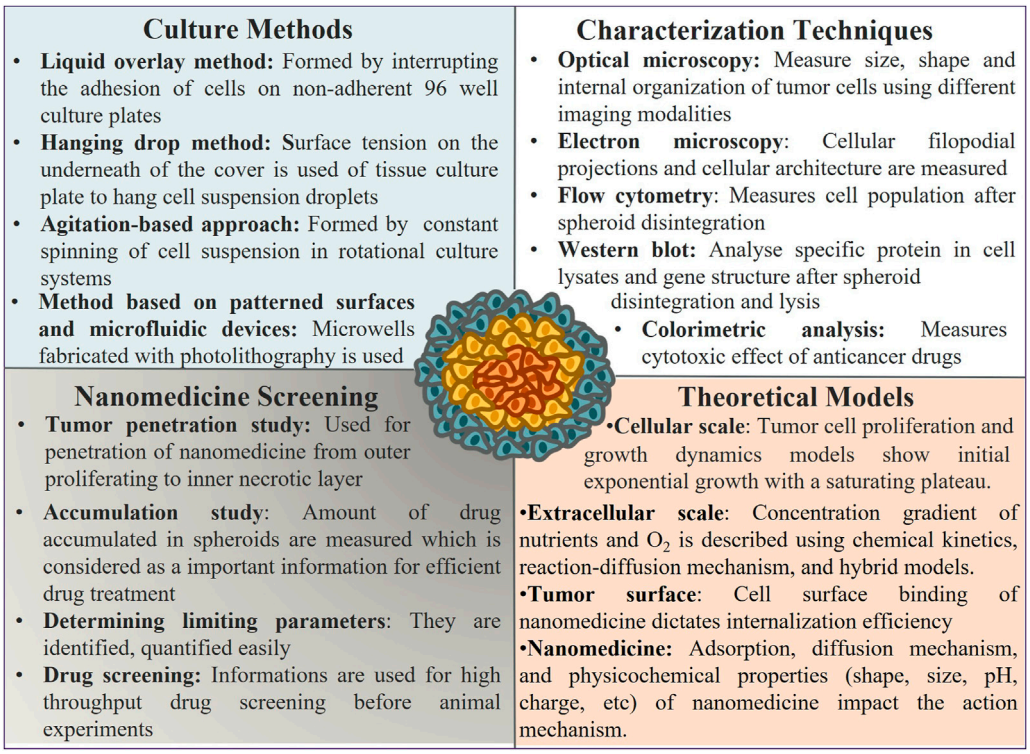

FIGURE 3 | Tumor spheroid culture, characterization, use, and parameters that affect its activity as a model system: tumor spheroids are prepared using different experimental methods, and various techniques are used to characterize their architecture, properties, and application for nanomedicine screening. Several parameters affect the structure, growth, and efficiency of nanomedicine screening, as revealed from the theoretical study.

Tumors can be sustained via the angiogenesis process to generate new blood capillaries and permit oxygen and nutrient transport by diffusion (Mark et al., 2013; Li et al., 2018; Lugano et al., 2020). Healthy tissue forms new blood capillaries and regulates a sufficient amount of blood supply for cells, whereas the new blood capillaries in tumor tissue are poorly organized and heterogeneous in nature. Due to this abnormal vasculature, some parts of tumors are not easily accessible to demonstrate the therapeutic outcomes (Tong et al., 2004; Danquah et al., 2011; Mizukami et al., 2012). Normalization of tumor vasculature is one of the theories behind using anti-angiogenic drugs, which makes it more accessible for chemotherapy (Goel et al., 2011). However, in general, this abnormal and leaky tumor vasculature with respect to healthy tissue vasculature allows nanomedicine to be distributed in the tumor region and the delivery of drug candidates by the well-known enhanced permeability and retention effect (EPR effect) (Greish, 2007; Fang et al., 2011; Maeda, 2012; Maeda et al., 2013; Prabhakar et al., 2013; Maeda et al., 2016). Moreover, the impaired lymphatic drainage of tumors allows nanomedicine to be retained over there for a long time, again fostering the sustained release of drugs. EPR effect allows nanomedicines to not touch healthy tissue and thus exhibit low therapy-related undesired toxic side effects (Greish, 2007; Fang et al., 2011; Maeda, 2012; Maeda et al., 2013; Prabhakar et al., 2013; Maeda et al., 2016).

2.3.2 Elevated Interstitial Fluid Pressure

Healthy tissue regulates interstitial fluid pressure in a way where the total pressure gradient between the tissues and the blood vessels enhances fluid flow and nutrient transport out of blood capillaries and into the cells. However, in tumor mass, there is abnormal vasculature with an increased interstitial fluid pressure along with high cell density and impaired lymphatic drainage (Heldin et al., 2004). This increased interstitial fluid pressure within the tumor causes inefficient uptake of nanomedicine. Various antagonists of vascular endothelial growth factor, antifibrotic agents, and transforming growth factor-beta are commonly used to decrease the interstitial fluid pressure to improve the transport and penetration of nanomedicine within the tumor mass.

2.3.3 Dense Extracellular Matrix

The dense extracellular matrix is a significant barrier to the nanomedicine transport to reach tumor cells (Netti et al., 2000). Low blood supply is the consequence of abnormal vasculature within tumors. Drugs are transported by diffusion due to the insufficient convective transport within tumors. Fibrous macromolecules (collagen and glycosaminoglycans) fill in the extracellular spaces in solid tumors, resulting in a relatively dense extracellular space in solid tumors compared to the healthy tissues as the collagen content is significantly higher in solids

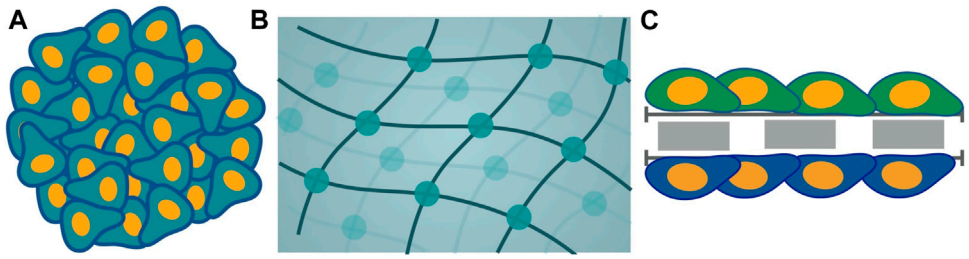

FIGURE 4 | Schematic representation of different models of cell culture is categorized into two classes: non-scaffold-based and scaffold-based. Non-scaffold-based culture is multicellular tumor spheroid **(A)** and scaffold-based cultures are hydrogel **(B)** and inserts **(C)**.

tumors than in the normal tissues (Lu and Weaver 2012; Hynes, 2009; Frantz et al., 2010; Kim et al., 2011; Lu and Weaver_2012; Eble and Niland, 2019). There is no hindrance in the diffusion of small drug molecules through this protein matrix, but impaired mobility is observed in the case of large size of nanomedicine, resulting in them being confined in the areas surrounding the blood vessels (Greish, 2007; Fang et al., 2011; Lu et al., 2012; Eble and Niland, 2019). The impaired transport of nanomedicine through the dense extracellular matrix could be overcome by the degradation of extracellular matrix proteins.

2.4 Solid Tumor Models

Among the plethora of models for tumor cell culture consisting of the monolayer, 2D, and 3D culture, there is a foremost requirement of models congruent with intended efficient pathways of drug delivery (Waite and Roth, 2012). Different tumor cells are cultured as *in vitro* models to understand the underlying physical mechanism and chemical basis for the biological phenomena exhibited during tumor growth. The 3D tumor spheroids models with complex physiology and the microenvironment as a real solid tumor are highly persuasive. Various criteria take heed for the appropriate 3D cell culture model for targeted drug delivery with impaired efficacy. The 3D cell cultures are obtained mainly in two categories: non-scaffold-based cell cultures and scaffold-based cell cultures (**Figure 4**). For both non-scaffold and scaffold-based cell cultures, ECM and drug resistance are the two most primitive properties essential to be incorporated into an *in vitro* model of tumors. ECM is the non-cellular component of tissues, which acts as the link that establishes cell-cell communication for interaction among themselves and induces growth as a unit for spheroid culture. ECM components for scaffold-based cell cultures are natural like collagen, semi-synthetic like chitosan, or synthetic biomaterial like polycaprolactone (Costa et al., 2016). The obstruction to continuous flow and transport of drug molecules across the ECM, caused by the rise in interstitial fluid pressure, is known as drug resistance. Thus, this network plays an indispensable role in the proper channelizing of drug molecules to the core of a tumor with minimum resistance. Considering the impact of ECM, various kinds of scaffold and non-scaffold-based cell culture models have been developed. Scaffold-based 3D cell culture models are hydrogels and inserts, in which cells are grown embedded into platforms that mimic the ECM architecture. Hydrogel is a crosslinked polymer network (Ghosh et al., 2014; Ghosh et al., 2016). It is a colloidal gel with water as a dispersive medium. Hydrogel is cells seeded in gel-based 3D structures. For hydrogel to be used as an *in vitro* cell culture model, it should reflect a higher rate of reproducibility, which involves constructing the same results agreeing with the original study with the higher precision when produced again. In the field of biomedical research, where applications of *in vitro* cell cultures are widely increasing, reproducibility becomes one of the key components for establishing consistent results similar to *in vivo* models. Hydrogels lack reproducibility and ECM components impart resistance to drug penetration by diffusion (Achilli et al., 2012; Costa et al., 2016). Materials, such as collagen, that are used to mimic the ECM components are expensive. Hydrogel restricts the penetration of compounds leading to cell isolation for analysis, thereby losing its ability to capture spatial information (Sant and Johnston, 2017b). Thus, this restricts its use for a more useful cell culture model. On the other hand, inserts are another 3D cell culture scaffold-based model. This cell culture system consists of two parts: a plate as a scaffold with wells and insert. Inserts are like porous membranes anchored to the platform such that they will allow the nutrient media transport to them by attaching their surface to the cells regulating their growth and exchange through membranes for the transport study. More precisely, they are like cells seeded in structures constituted by different biomaterials like polycarbonate. These biomaterials may have similar properties as those of ECM. However, ECM components create the barrier that brings forth the resistance to drug flow, providing hindrances to the drug penetration. They have deficits in reproducibility, majorly dependent on the methods used for the scaffold fabrication. Thus, using these two models, hydrogel and inserts are useful but at the cost of extracellular matrix and drug resistance, which are the foremost priorities for the most efficient targeted drug delivery.

Cell culture models that are non-scaffold-based are the self-assembled aggregates of cells, such as multicellular tumor spheroid. ECM in these cell cultures is composed of protein produced by cells during the formation of cell culture (Costa et al., 2016; Han et al., 2021). Highly dense ECM components are the driving force for impaired drug penetration without any resistance. Both of the fundamental requirements are accompanied. Thus, the facets that play a pivotal role are extracellular matrix and drug resistance leading to one of the

TABLE 1 | Comparison of different 3D culture cellular models.

Model	ECM	Drug penetration	Cellular heterogeneity	Cellular organization	Gene expression
Spheroids	The deposition of this connective network is similar to the *in vivo* tumor	A highly dense connective network is responsible for impaired drug penetration	Cancer cells cultured with fibroblast, immune cells, and endothelial cells lead to heterogeneity	Spheroid of three zones: proliferating, quiescent, and necrotic varying in proliferating rate and gradient of oxygen, nutrients, waste accumulation, and CO_2	Showing similarity as the *in vivo* tumor
Hydrogel	Artificial and may have some components which are present in the native matrix	Barriers created by the connective network may be responsible for resistance to drug penetration by diffusion	Varying cell types can be grown on the scaffold	It is spontaneous and consists of heterogeneous cells. The necrotic layer may be formed	Resembles with *in vivo* tumor
Inserts	Consists of biomaterials having similar properties as ECM	Barriers established by ECM may lead to some resistance to drug penetration	Heterogeneous cells can be grown on the platform	The organization of cells is spontaneous and embedded with cellular heterogeneity. The innermost core consisting of necrotic cells may be formed	Resembles with *in vivo* tumor

appropriate platforms for non-scaffold-based multicellular spheroid as cell culture model (Costa et al., 2016). The 3D spheroid models took precedence over all other existing models, including dimensionality of 2D and 3D models (**Table 1**).

The foremost properties of the cell culture models have been discussed, paving the path for the understanding of factors on which the drug delivery mechanism of spheroid depends. The delivery competence of therapeutic drug molecules is highly dependent on the tumor architecture. Modeling the internal structure of a tumor is a matter of greater importance for the impaired efficacy of drug delivery. Spatiotemporal study of the growth of tumors is the point of prime focus primarily influenced by the complex compartmentalized tumor architecture. Consequently, for the transport and penetration of the drug molecules to the core, an insight into the modeling mechanism can state the benefit of tailoring and governing treatments. Thus, to understand the fundamental mechanism for the detailed study of critical factors admissible for targeted drug delivery, mathematical modeling of a tumor is required.

The following study will comprise a broad view of both key components, tumor and nanomedicine. The former discusses the target itself, multicellular tumor spheroid as a tumor *in vitro* model, its architecture, factors assisting cell-cell interaction, its culture methods, the characterization of tumor spheroid, and the mathematical models supporting its growth at various cellular scales. Moreover, the latter discusses the drug molecules to be treated on the target, consisting of the study of key attributes of nanoparticles affecting their efficient delivery to target and the mathematical models supporting their adsorption, internalization, and diffusion at distinct scales.

3 TUMOR SPHEROIDS

Multicellular tumor spheroids are the 3D architecture of cancer cells that potentially reflect the *in vivo* conditions of tumors in the body. They can be cultured with only cancer cells or co-cultured with cancer cells and other cell types under various conditions (Nunes et al., 2019). Just as in naturally occurring tumors, these tumor spheroids also develop similar properties, which provide insightful details to study them an important model in cancer research, bridging the gap between *in vitro* cancer cell line cultures and *in vivo* tumors. The 3D architecture of miniature cellular aggregates modeled in a tumor spheroid is widely used for studying different types of cancers *in vitro*.

3.1 Structure of Tumor Spheroids

Multicellular tumor spheroids are spherical *in vitro* self-assembly of cellular aggregation representing the characteristics of *in vivo* solid tumors. In this self-assembled organization, cells aggregate, sort, and compartmentalize to separate different regions of the spheroid (Nath and Devi 2016). To impersonate the shear properties of the *in vivo* model of solid tumors, the study of the internal structure of the *in vitro* model of a spheroid is essential. The internal structure is incorporated with different cell layers based on the concentration gradient of nutrients, oxygen to regulate cell function, differential zones of proliferation and growth factors, pH, and cellular density. All these factors of the cellular organization play an indispensable role in studying the diffusion and penetration for impaired nanomedicine delivery (Lazzari et al., 2017; Sant and Johnston, 2017b; Costa et al., 2016). In accordance with differential proliferation rate, the structure can be broadly categorized in three different zones: proliferation, senescent, and necrotic zones; see **Figure 5** (Mehta et al., 2012; Lazzari et al., 2017; Sant and Johnston, 2017). Modeling of spheroid growth can be done by taking into account the following spheroid cellular organization. These layers are characterized by the decreasing gradient of nutrients, oxygen, and pH, from the exterior to the center of the spheroid and by the increasing gradient of CO_2, lactate, and waste from the exterior to the center of the spheroid. The outer layer where cells resurge and escalate rapidly in number is called the proliferation zone. It exhibits high proliferation rates in the spheroid periphery. The proliferation is stimulated by the constant exposure of the cells to oxygen and nutrients. When the oxygen diffusion and nutrient availability become a limiting factor, the cell's proliferation rate

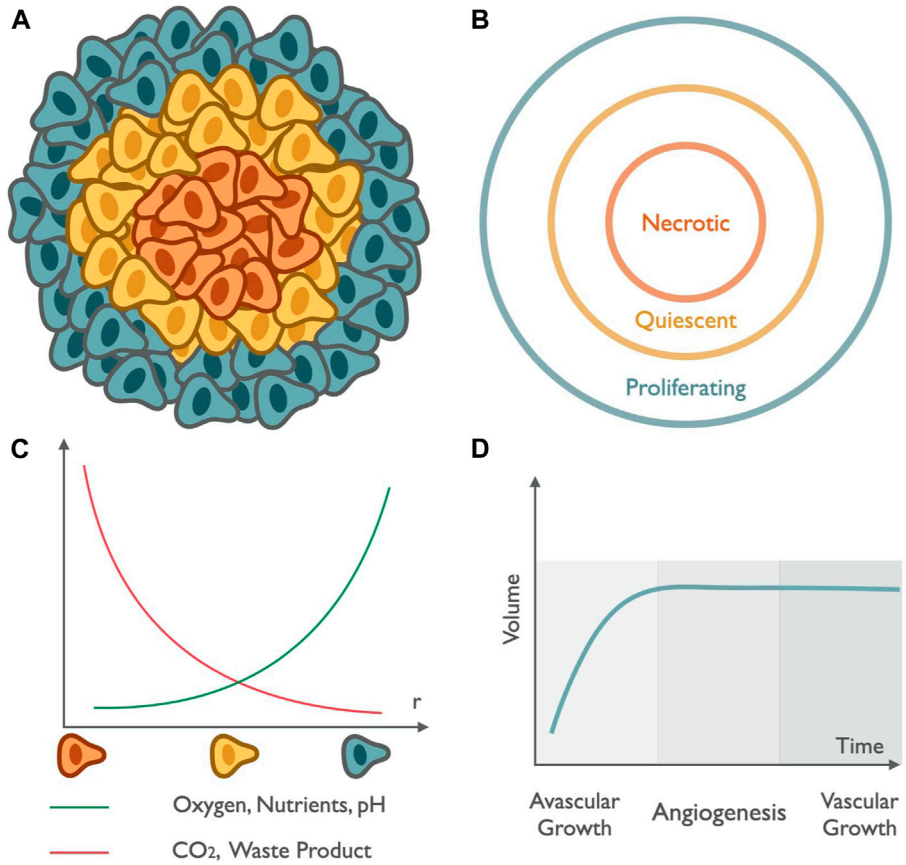

FIGURE 5 | Tumor spheroid structure and growth: Schematic **(A,B)** represents the compartmentalized structure of tumor spheroids. The peripheral region in green represents the outermost zone, rich in oxygen content, and responsible for the rapid multiplication of cell numbers known as the proliferating zone. The annular region in yellow depicts the region with depletion in nutrients and oxygen known as the quiescent region. The innermost part in orange highlights the zone with the lowest pH and also deficits in oxygen, leading to the death of healthy cells known as the necrotic zone. **(C)** The graph in green represents the increase in the availability of oxygen, nutrients, and pH and the curve in red represents the variation of CO_2 content and waste accumulation as we move radially outward from the center. **(D)** Growth curve: spheroid growth can be described in two different stages, initial avascular growth, where the volume of the tumor increases exponentially, followed by a dormant phase of saturation till the growth of spheroid reaches a plateau, and the transition from avascular growth to vascular growth occurs via angiogenesis, which represents the initiation of formation of new blood vessels led by a vascular growth dominated by the process of growth of cells rich in blood vessels that provide them with a gateway through which they enter metastasis to distant sites.

decreases, giving rise to the middle layer made up of senescent cells. In the middle zone, cells can no longer divide due to the depletion of nutrients; nevertheless, they are active and alive, which is identified as the senescent zone. The middle region is followed by a decrease in cell metabolism as the distance from the outer region increases. The supply of nutrition is also depleted as we move from the periphery to inner zones. Finally, the core region, characterized by depletion in oxygen concentration, results in hypoxia, nutrient supply, and waste accumulation leading to a critical situation of cell necrosis (**Figure 5**). It is identified as the region where cells are noxious and lead to death, known as the necrotic zone. This core is the zone of the lowest pH (6.6–7.2) within the tumor spheroid. In this hypoxic environment, the pyruvate is converted into lactate by the cancer cells to obtain energy, known as the Warburg effect. The accumulation of lactate results in an acidified core of the spheroid and makes it favorable for drug release from nanomedicine.

The annular organization of subsequent cell layers within the spheroid is reported to be the key factor behind the inadequate therapeutic efficacy of anticancer drugs, as the presence of cells in the successive region from the outer zone, that is, the quiescent and necrotic region, reduces the potency to penetrate nanomedicine. In the hypoxic region of the spheroid, different drugs that cause cell death via the formation of reactive oxygen species (ROS) have a very low therapeutic efficacy (Liang and Liu, 2016; Al-Akra et al., 2019). Moreover, many drugs (e.g., paclitaxel) that promote cytotoxicity to the cells and proliferation have a poor impact in this innermost zone and that is why even the drugs which are highly effective in rapidly multiplying cells have a poor therapeutic benefit in the interior layers of the spheroid for the same reason. Moreover, low environmental pH catalyzes the change of net charge of drug molecules (e.g., melphalan, methotrexate, and mitoxantrone), tumor penetration, and intracellular uptake. The typical low pH condition at the interior zone induces the cancer cells to

start expressing different kinds of hypoxia-inducible factor (HIF) family, which promotes the proliferation and consequent survival rate of the cancer cells (Masoud and Li, 2015; Albadari et al., 2019; Hompland et al., 2021).

3.2 Characteristics of Tumor Spheroids

The application of multicellular tumor spheroid in tumor-drug delivery is increasing rapidly. The key characteristics of a promising *in vitro* spheroid model are to accurately mimic the *in vivo* solid tumor, incorporating the real biological characteristics such as heterogeneity, microenvironment, and cellular arrangements. Spheroid is a well felicitous *in vitro* model for the aimed conveyance of nanomedicine due to its ability to transcribe the intrinsic characteristics found in solid tumors. We will elucidate the following characteristics of the spheroid in detail such as cellular heterogeneity, cell-cell signaling, internal structure, ECM deposition, gene expression, and how the external modification to spheroid could lead to efficient drug delivery, and how mathematical modeling approaches could give us the tools to decipher the underlying mechanisms (Albrecht et al., 2006; Ekert et al., 2014; Popilski and Stepensky, 2015; Shamsi et al., 2019).

Three-dimensional multicellular tumor spheroid is widely used as a model system for studying different types of cancers and screening of nanomedicine efficacy. Cellular heterogeneity is one of the critical aspects that is needed for this study and represents the diverse nature of cell types showing distinct morphological and phenotypic profiles. Cellular heterogeneity is embodied with the multiple cells that vary in their protein and gene expression. Spheroid is embraced with different heterogeneous tumor and stromal cells with varying ratios that lead to its cellular heterogeneity. The *in vitro* model can be established with homotypic cancer cells only or heterotypic cancer cells cultured with fibroblast, immune cells, or endothelial cells (Costa et al., 2016; Lazzari et al., 2017; Millard et al., 2017). In heterotypic tumor spheroids, the number of cells could be varied to closely mimic heterogeneity in solid tumors. Moreover, interacting networks among cells having this heterogeneity are demanded. Signaling established between the cells which are in close proximity helps in reproducing the spheroid's key aspects and its microenvironment. All the cells growing in close proximity provide a route to a highly interactive microenvironment for physical communication and signaling pathways of cells to drugs. This heterogeneity and signaling can help decipher how multiple cell types might impact drug delivery to the site.

Solid tumors exhibit complex cellular microenvironment and architecture, where extracellular matrix (ECM) plays a crucial role (Lu et al., 2012; Pickup et al., 2014; Bussard et al., 2016; Lazzari et al., 2017). ECM is an essential component for binding the cells together via proteoglycans and fibrous proteins. The extracellular matrix (ECM) compositions, e.g., fibronectin, laminin, proteoglycans, collagen, and tenascin, are deposited by cells within 3D spheroids like solid tumors (Frantz et al., 2010; Kim et al., 2011; Lu et al., 2012; Hynes, 2013). The ECM (α5- and β1-integrin) in the tumor spheroid form a barrier known as limited mass transport, further limiting the insertion and uniform distribution of nanomedicine in the solid tumor mass. Extracellular matrix components in a highly interactive 3D microenvironment of spheroids make the structure more compact by depositing the protein, leading to an increase in the interstitial fluid pressure and further limiting impaired therapeutic efficacy of nanomedicine. It helps tumor cells in regulating different cell functions and maintaining the complex cell network. ECM-related signaling pathways play a crucial role in tumor progression, cancer cell migration, and penetration (Frantz et al., 2010; Kim et al., 2011; Lu et al., 2012; Hynes, 2013). Tumor cells within solid tumors grow in two stages. Initially, the tumor grows very rapidly, termed the avascular growth phase. Then, cells continue to stay in a dormant phase followed by vascular growth with the generation of new blood capillaries (angiogenesis) promoted by pro-angiogenic factors (e.g., angiogenin) and ECM rebuilding mediated by proteases (e.g., MMP-2 and MMP-9). Similarly, the progress of a tumor in an *in vitro* model is the collective dynamics of interaction between tumor cells and their microenvironment. The initial volume growth increases exponentially with time until it reaches a certain value (~400 μm in diameter), but later the growth of volume decreases with time and becomes constant, referred to as the spheroid growth plateau (**Figure 5**). This avascular tumor expansion, growth plateau, and vascular expansion as spheroid growth varying with both temporal and spatial dimensions can be modeled mathematically.

Growth factors and the cellular ECM protein can be encoded with the learning of genes. Gene expression is a closely constrained process regulating the response of a cell to its changing environment. The study of gene expression is vital as it involves the conversion of DNA's instruction into functional products like protein (Costa et al., 2016). Gene expression profile is firmly affected by the cellular organization of the spheroid. The abundant target protein expression, also known as overexpressed gene, plays an essential role in studying cancer progression, invasion, and metastasis. There are various factors that influence the morphology of tumor spheroids, such as cell type, cell density, culture media, method of culture, and mechanical stress. Based on their compactness, spheroids could be compact spheroid, tight aggregates, and loose aggregates of cells. In a compact spheroid, cells are tightly bound to each other. In tight or loose aggregation, cells do not form a complete sphere and can be easily disintegrated. Aggregation of cells initially occurs by loose bonds between integrin and ECM, then forming close contact through N-cadherin to E-cadherin interactions. As the cell communication pathways, morphology, and polarity of the cells in solid tumors closely resemble the structure of multicellular tumor spheroids in many ways, the study of using tumor spheroids is a very important *in vitro* model in recent times for studying the penetration profile of nanomedicine and calculation of accumulation of anticancer drugs (England et al., 2013). Thus, cellular arrangements and internal structure in tumor spheroid closely resemble solid tumors, making it an appropriate model for the study of tumor growth and invasion as metastasis with the effect of drug candidates for screening of different nanomedicine formulations towards its efficacy and efficiency of disease management.

TABLE 2 | Tumor spheroid used as *in vitro* model for nanomedicine penetration study.

Sl no	Nanomedicine	Spheroid properties	Penetration details	Techniques	Comments	References
1	Doxorubicin-loaded NM coated with CD47 peptides (DOX/sNDF-CD47) of sub-150 nm size	Coculture of tumor-associated fibroblast MRC-5 cells with MCF-7 cells	sNDF-CD47 penetrate deeper into TS compared to control NM	CLSM	CD47 peptide assist penetration	Mo et al. (2019)
2	PG-co-PCL dendritic NM loaded with gemcitabine of 166 nm size	TS of MIA PaCa-2 pancreatic cancer cells. 150,000 cells per TS were used	NP carried gemcitabine 40 μm deeper into TS	CLSM	No ligand has been used for spheroid penetration	Ray et al. (2019)
3	pH-responsive crosslinked nanogels of 200 nm size loaded with cisplatin	TS of A549 cells with 200–300 μm size having 5 × 10^5 cells	Nanogel located at 50 μm depth	CLSM	No ligand has been used for spheroid penetration	Cheng et al. (2019)
4	PLGA NP encapsulated with tetrandrine and a magnetic material (Fe_3O_4) with a size of 199 nm and a negative surface charge	TS with A549 cancer cell prepared by liquid overlay method with 250 μm size	NP penetrate to 160 μm depth	CLSM	PLGA NP deeply penetrates A549 TS, exerts an antiproliferation effect, and induces apoptosis	Wang et al. (2019)
5	Transferrin targeted core-shell NM encapsulating sorafenib and doxorubicin, size of 110 nm	3D HCC spheroid with a size of ~200 μm	Penetration of targeted core-shell NP throughout the tissue causing uniform cell killing	CLSM	Transferrin assists in spheroid penetration	Malarvizhi et al., 2014
6	HPMA copolymer-based NM carrying pirarubicin of size 25 nm	Colon carcinoma C26 tumor cells (250–300 μm) and glioblastoma U87-MG cells (450–550 μm) were employed	C26 and U87-MG spheroids were observed with 120 and 80 μm penetration, respectively	CLSM	HPMA NM assists penetration of THP	Kudláčová et al. (2020)
7	Paclitaxel-loaded polymeric micelles with size 90 nm	The NCI/ADR-RES multicellular spheroids with 400–600 μm size were established by the liquid overlay method	The penetration capability of micelles was greater than control groups	CLSM	MMP2-sensitive peptide linker assists in tumor penetration	Yao et al. (2017a)
8	Pluronic NP and PEO-PPO-PEO triblock copolymers micelle	HeLa and U87 cells were to prepare TS of 500–600 μm size	Penetration NP observed at 80–100 μm depth	CLSM	Penetration depends on the transcellular transport of the carriers	Arranja et al. (2016)
9	Doxorubicin immobilized AuNC-cRGD-Apt NP	U87MG cells were used by a liquid overlay method of the diameter of 500–600 μm	NP located at 80 μm inside TS	CLSM	Targeting ligand cRGD assists penetration	Chen et al. (2016)
10	Theranostics thermosensitive micelle CuS functionalized by (PAAmAN–PEG) with size 8.9 nm	MDA-MB-468 cells with the size of 500 μm were formed using the hanging drop method.	NM shows a higher and homogeneous distribution in the central area of the tumor spheroids	CLSM	Targeting ligand facilitates the penetration of NP into tumor spheroids	Chen et al. (2017)
11	Gold NP coated with tiopronin with a size of 2–15 nm	MCF-7 cells were used in the liquid overlay method with 600 cells per well	NP penetration occurred in a size-dependent manner, with 2 and 6 nm AuNPs able to penetrate deeply into tumor spheroid	Bright-field and dark-field microscopy	Colloidal gold NP shows great potential to overcome delivery limitations	Huang et al. (2012)
12	Paclitaxel-loaded Ft-NP with a size of 150 nm and delivered via neuropilin-1- and tenascin C-mediated specific penetration	U87 glioma TS having 5 × 10^5 cells were used by liquid overlay technique	Ft-NP-PTX penetrated deeper into TS compared to control NM	CLSM	Ft peptide- (fused FHK and tLyp-1 peptide together via cysteine linkage) functionalization facilitated its deep penetration	Kang et al. (2016)
13	Micelle with paclitaxel and 40 nm size	4T1 cells were used in TS with 100 μm size	Deeper penetration and improved cellular internalization of NP was observed in tumor tissues at pH 6.8	CLSM	No ligand has been used for spheroid penetration	Ke et al. (2018)
14	Ce6 conjugated mPEG-PLA NP	Avascular A549 spheroid model of 400–500 μm size was prepared by liquid overlay method	NP located at 70 μm depth	CLSM	The small size and the negative surface of NP help in easy penetration into the spheroids	Kumari et al. (2020)
15	Hyaluronic acid grafted micelles encapsulating optimal molar ratio (1:1) of Gem-C12 and HNK, with 53 nm size	TS of U87MG cells with 200 μm size	NP located to a depth of 50 μm	CLSM	The enhanced penetration results from active endocytosis by CD44 on the U87 cell surface	Liu et al. (2018)

(Continued on following page)

TABLE 2 | (*Continued*) Tumor spheroid used as *in vitro* model for nanomedicine penetration study.

Sl no	Nanomedicine	Spheroid properties	Penetration details	Techniques	Comments	References
16	NP with a mesoporous silica nanoparticle (MSN)-supported PEGylated liposome yolk and CCM coating, with 180 nm size	MCF-7 MCSs were cultured and prepared using a lipid overlay system with 10^4 MCF-7 cells	Penetration throughout TS up to a 23.3-fold increase compared to the penetration of membrane vesicles	CLSM	NP exhibited moderate rigidity, which was attributed to its yolk-shell structure, leading to an improved tumor penetration	Nie et al. (2020)
17	Lipid-core micelles and liposomes as nanocarriers for encapsulation and delivery of NCL-240, with 200 nm size	NCI/ADR-RES spheroids with a diameter of ~550 μm	Micelles located up to a depth of 100 μm	CLSM	Transferrin targeting enhanced penetration	Pattni et al. (2016)
18	Nanoformulations of CUR and DOX with scFv-targeted micelles	Multicellular 3D cancer cell spheroids of U87MG were prepared by the liquid overlay method with 10^4 cells	Penetration observed up to a depth of 70 μm	CLSM	Using GLUT-1 scFv as the targeting ligand resulted in higher cellular internalization and better penetration	Sarisozen et al. (2016)
19	Targeted Mesoporous iron oxide nanoparticles, encapsulated perfluorohexane, and paclitaxel, with a diameter of 160 nm	Three-dimensional TS models with 200 μm in diameter prepared by using a liquid overlay method	Drug concentration was observed in the deep regions of tumor cells	CLSM	MF-induced PFH gasification increased the NP penetration and accumulation in the TS	Su et al. (2015)
20	Raloxifene encapsulated with styrene co-maleic acid (SMA) micelle, with a diameter of 65.34 ± 30.89 nm	PC3 cells TS with 8,000 cells and of 400 μm in diameter	Micelle effectively inhibits cell cycle progression, increases apoptosis, and alters the integrity of TS models	CLSM	No ligand has been used for spheroid penetration	Taurin et al. (2014)
21	Paclitaxel loaded to MHI-HGC nano-micelle forming MHI-HGC-PTX with 230 nm size	4T1-3D spheroid of 200–300 μm in radius	MHI-148 Cyanine Dye Conjugated Nanomicelle showed high penetration ability in the tumor spheroid	CLSM	Heptamethine dye as a targeting ligand, optical imaging agent, and NIR photothermal stimuli assists on-demand drug release	Thomas et al. (2018)
22	Docetaxel-loaded hybrid micelles with DSPE-PEG and TPGS (TPGS/DTX-M), with a diameter of 17–24 nm	Tumor spheroids were formed with KBv cells using the hanging drop method, size of 400 μm	TPGS has served as a permeation enhancer and assisted in drug penetration in TS	CLSM	Folate-modified TPGS hybrid micelles promote effective delivery of DTX	Wang et al. (2015)
23	iRGD-modified nanoparticles loaded with ICG and TPZ, with a diameter of 112 nm	4T1 cells- multicellular TS with 400 μm diameter	Nanoparticles located at a depth of 89 μm	CLSM	Conjugated iRGD onto the surface of the nanoparticles improves their penetration in TS	Wang et al. (2018)
24	curcumin-loaded VES-g-PLL micelles, exhibiting an ultra-small particle size of ca. 30 nm and positive Zeta potential of 19.6 mV	C6 spheroids, with a volume of 250 mm^3, were developed using the liquid overlay method	Curcumin-loaded micelles located in deeper regions of TS	CLSM	Ultra-small size and positively charged surface, Cur-Micelles promoted deeper penetration. No ligand was used	Xu et al. (2017)
25	DOX-loaded CQDs-TPGS-TPP nano micelles, size <160 nm	MCF-7/ADR-derived spheroids with a diameter of 300–400 μm	NP penetrated to a depth of 120 μm	CLSM	DOX penetration efficiency improved via CQDs-TPGS-TPP/DOX nanomicelles	Zhang et al. (2017)
26	Silver NPs functionalized with polyethylene glycol and aptamer As1411, with a diameter of 18 nm	C6 glioma spheroid model	The penetration ability of the AgNPs functionalized with PEG and As1411 was superior to that of the AgNPs modified only with PEG	CLSM	As1411 effectively increased the tumor penetration of the NPs	Zhao et al. (2019)
27	Transferrin modified (PEG-PE)-based polymeric micelles containing paclitaxel and tariquidar, with hydrodynamic diameter ca. 16 nm	3D spheroids of SKOV-3TR cells, with a diameter larger than 600μm, hypoxic micro-regions, and a necrotic spheroid core	Tf-targeted micelles penetrated deeper layers of the spheroid	CLSM	The small size of the micelles and Tf-targeting improved TS penetration	Zou et al. (2017)
28	GANT61 and curcumin-loaded PLGA nanoparticles, with a size of 347.4 nm	MCF-7 3D spheroid with 3 $\times 10^4$ cells	NP are observed in the deep regions of TS and kills all the bulk tumor cells and CSCs together by targeting EGFR and Hh pathway	CLSM	No ligand has been used for spheroid penetration	Borah et al. (2020)
29	Hyaluronic acid-coated single-walled carbon nanotubes loaded with doxorubicin	MDA-MB-231 cell spheroids	NP penetrates deep to the center of TS and induces cell apoptosis	CLSM	HA can specifically recognize CD44 acts as a targeting ligand in nanoparticles and assists tumor penetration	Liu et al. (2019)

(Continued on following page)

TABLE 2 | (*Continued*) Tumor spheroid used as *in vitro* model for nanomedicine penetration study.

Sl no	Nanomedicine	Spheroid properties	Penetration details	Techniques	Comments	References
30	siBcl-2/Dox-TPGS-LPs, size of 210 nm	3D H22 tumor spheroids with 4×10^5 cells	siBcl-2/Dox-TPGS-LPs exhibited better penetration compared to the control NM	CLSM	TPGS-modified cationic LPs assists in the penetration	Tan et al. (2019)
31	ND-PG-RGD composite loaded with doxorubicin to give the final product Nano-DOX, with a hydrodynamic diameter of 83.9 ± 32.3 nm	3D GC spheroids	Nano-DOX penetrated deeper layers of the spheroid	CLSM	TAM serves as a carrier and reservoir to release drugs to the TS	Li et al. (2017)
32	Polymeric hybrid nano micelles to co-deliver the Dox and microRNA-34a (miR-34a)	MDA-MB-231 3D multicellular spheroids (approximately 600–800 μm)	Suitable micelle size caused deeper penetration of Dox into the TS, generating efficient cell killing	CLSM	No ligand has been used for spheroid penetration	Xie et al. (2019)
33	MMP2-sensitive FR-targeted, DSB loaded polymeric nanoparticulate micelle with a size of 100–200 nm	NCI/ADR-RES multicellular spheroids a diameter of 400–600 μm	The polymeric micelle showed deeper penetration than the control NP	CLSM	Multifunctional micellar nanoparticles combined (MMP2)-sensitive tumor (site) targeting with folate receptor-mediated tumor (cell) targeting	Yao et al. (2017b)
34	Glycogen NPs for the therapeutic delivery of nucleic acids with a diameter of 20–150 nm	293T-Luc cells and PC3 cells were used for TS preparation	Glycogen constructs penetrate the spheroid ECM and are effectively internalized into the tumor cells	CLSM	The controlled size and surface charge density of glycogen-siRNA constructs minimized the interactions with serum proteins and allowed significant penetration	Wojnilowicz et al. (2018)
35	Nano-doxorubicin-loaded monocytes	U87 cell spheroids	Drug release from nano-DOX-MC was observed at deeper layers of the TS	CLSM	Nano-DOX can be effectively delivered by MC	Wang et al. (2018)
36	Small unilamellar vesicles (SUVs) probed with different lipid compositions, with a hydrodynamic diameter of approximately 85 nm	BxPC-3 and HPSC multicellular spheroids were prepared by lipid overlay method with 5,000 BxPC-3 and 5000 HPSC cells	Lip3 displayed the best penetration compared to the rest of the liposomes diffused into the MCSs	CLSM	Liposome mechanics is a design parameter for enhancing drug delivery in TS	Dai et al. (2019)

3.3 Culture Methods of Tumor Spheroids

A plethora of techniques to culture *in vitro* models are available, incorporating the use of cell attachment resistant surface forces to induce cell-cell interactions and ultimately support the formation of multicellular tumor spheroid (**Figure 3** and **Table 2**). These techniques will be discussed in the subsequent part (Ishiguro et al., 2017; Lazzari et al., 2017).

3.3.1 Liquid Overlay Method

Spheroids are formed by interrupting the adhesion of cells on non-adherent 96-well culture plates, coated with poly-2-hydroxyethyl methacrylate or agarose, which prevents attachment (Costa et al., 2014). This method allows the culture of both homotypic and heterotypic spheroids where size and morphology could be changed easily by changing the number of cells used for seeding in individual wells. Additionally, ease of handling and production of a large number of spheroids makes this approach very useful for different types of high-throughput assessments. The method demands a lower volume of culture media and testing materials. However, plate to coat with poly-2-hydroxyethyl methacrylate or agarose takes a longer time. Commercially available pre-coated low adhesion plates increase the overall cost of the experiment.

3.3.2 Hanging Drop Method

This method utilizes surface tension on the underneath of the cover of the tissue culture plate to hang cell suspension droplets (~20–50 μL). Further gravity helps cell accumulation at the liquid-air interface (cover of drop), resulting in aggregation into a single spheroid. Both homotypic and heterotypic spheroid size could be controlled by changing cell density. This method is highly reproducible. However, the limited volume of seeding suspension does not supply enough nutrients for long-term culture. It required transferring to another culture plate for experiments, which affects the integrity of cells in the spheroids. It is an extremely time-consuming and labor-intensive process, which is not suitable for large-scale applications. Some commercially available plates are to be used for better outcomes (Lin and Chang, 2008; Benien et al., 2014).

3.3.3 Agitation-Based Approach

In this technique, spheroid formation is done by a constant spinning of cell suspension in rotational culture systems that restore motion and support cell-to-cell interactions and avoid their attachment to the wall of the culture plate. The method provides control over the condition for large-scale production and long-term culture of tumor spheroids. However, controlling the number of cells per spheroid and their size

is very difficult. Moreover, manual selection and transfer into different plates are necessary before further assay. Hence, it is labor-intensive and involves requiring a large amount of culture media, which limits their wide-scale application (Gianpiero et al., 2017).

3.3.4 Patterned Surfaces and Microfluidic Devices

This technique utilizes arrays of microwells fabricated with photolithography. Low attachment surfaces are achieved by a coating of agarose or the use of non-adherent materials like polydimethylsiloxane. This method requires a limited number of cells, media, and reagents, making it suitable for high-throughput drug screening. Complexity is achieved with microfluidic devices displaying heterogeneous cell types. Various shaped channels ensure cell signaling and initiate the *in vivo*-like organization. The equipment required for this technique is expensive, hindering the wide application in the preclinical assessments of nanomedicines (Gianpiero et al., 2017).

3.4 Characterization of Tumor Spheroids

Advanced characterization techniques are utilized to characterize tumor spheroids based on, e.g., size, shape, cellular arrangements, protein and gene expression, cell cycle patterns, invasive nature, and metastatic potential of cancer cells to assess the nanomedicine (**Figure 3** and **Table 2**). Various types of techniques are described as follows (Elizabete et al., 2016).

3.4.1 Optical Microscopy

Bright field, dark field, differential interference contrast (DIC), phase contrast, and fluorescence microscope-based different imaging modalities are very important techniques for characterizing the size, shape, and internal organization of tumor cells in the spheroids (**Table 2**). An optical microscope is a more routine tool used to study the growth evolution and internal arrangements in each layer of tumor spheroids. Fluorescent microscopic techniques are commonly used to understand the amount of live and dead cells within spheroids, where calcein-AM and propidium iodide are routine stains used for the purpose. For histological analysis, hematoxylin and eosin assay, toluidine blue, and Masson's trichrome are used. Fluorescence microscopy is a very important tool to check the therapeutic efficacy of nanomedicine equipped with various anticancer drugs with fluorescence properties (e.g., doxorubicin, epirubicin, and curcumin). This technique allows determining the drug penetration and distribution profile and calculating the amount of drug accumulated in the spheroids (Mikhail et al., 2014). Currently, more advanced techniques of confocal laser scanning microscopy (CLSM) are used to measure each layer's penetration information (Zinchuk and Zinchuk, 2011; Rane and Armani, 2016). However, thick specimens are difficult to measure by CLSM where penetration of light is limited with water immersion objectives. Tumor spheroids are sliced into 5–10 μm thickness and used for measurements. To prevent distortion of tumor spheroid during sectioning, cryosectioning is commonly used with cryoprotecting agents. Penetration of the staining agent is not significantly hindered in sectioned slices but also in intact spheroids. Different fluorescence-based techniques such as light-sheet-based fluorescence microscopy (LSFM), two-photon microscopy, and multiphoton microscopy have been developed for imaging cell layers present in the interior of spheroids to avoid sectioning.

3.4.2 Electron Microscopy

Electron microscopy-based technique is used to acquire images of spheroids with high magnification and resolution with cellular filopodial projections and cellular architecture involved in cell-cell physical interaction. Cell death after nanomedicine treatment is also studied using this technique. Scanning electron microscopy (SEM) with a high vacuum technique is most commonly used to prepare a sample following four stages of fixation. The initial spheroid is preserved and stabilized in order to allow its manipulation and imaging. In the next stage (dehydration), water in the sample is replaced with acetone or alcohol and processed for critical point drying where the sample is completely dried if any ethanol or acetone present in the sample is replaced by CO_2, evaporated from the sample, and coated with sputter sample coating with gold for imaging. However, in the last two stages, disruption of the spheroid structure sometimes happens. To overcome these limitations, other advanced SEM techniques, such as low vacuum SEM and cryogenic SEM, are used as a substitution. Transmission electron microscopy (TEM) is another widely applied technique to evaluate nanomedicine penetration and accumulation in tumor spheroid. In this method, the spheroid is fixed chemically, dehydrated, and sectioned into thin slices, and before measurement, sections are stained with 2% uranyl acetate to generate more contrast.

3.4.3 Flow Cytometry

Flow cytometry is used to determine the cell population in tumor spheroids, where individual cell analysis in suspension is performed after spheroid disintegration. Flow cytometry has widely been used to quantify the cellular uptake of nanomedicine and to evaluate their toxicity; but, however, it is a less efficient technique to understand nanomedicine penetration at different layers of spheroids as this technique requires the disaggregation of spheroids (Sasaki et al., 2020; Mo et al., 2013). However, flow cytometry is used for cell cycle pattern analysis in tumor spheroid where fluorescent dyes intercalate with DNA during the different stages of the cell cycle (especially for the proliferative and senescent zone) (Tindall and Please, 2007). Specifically, fluorescent dye interacts with DNA during S-phase that distinguishes senescent from proliferating cells. This type of fluorescent dye is used to identify cells in different phases of the cell cycle, like the S-phase and S-M phases. Fluorescent probes that target cellular components or proteins of interest also could be used for flow cytometry-based analysis of cell death and gene expression.

3.4.4 Western Blot

Western blot is a very important technique that is widely used to analyze specific proteins in cell lysates and gene structure in

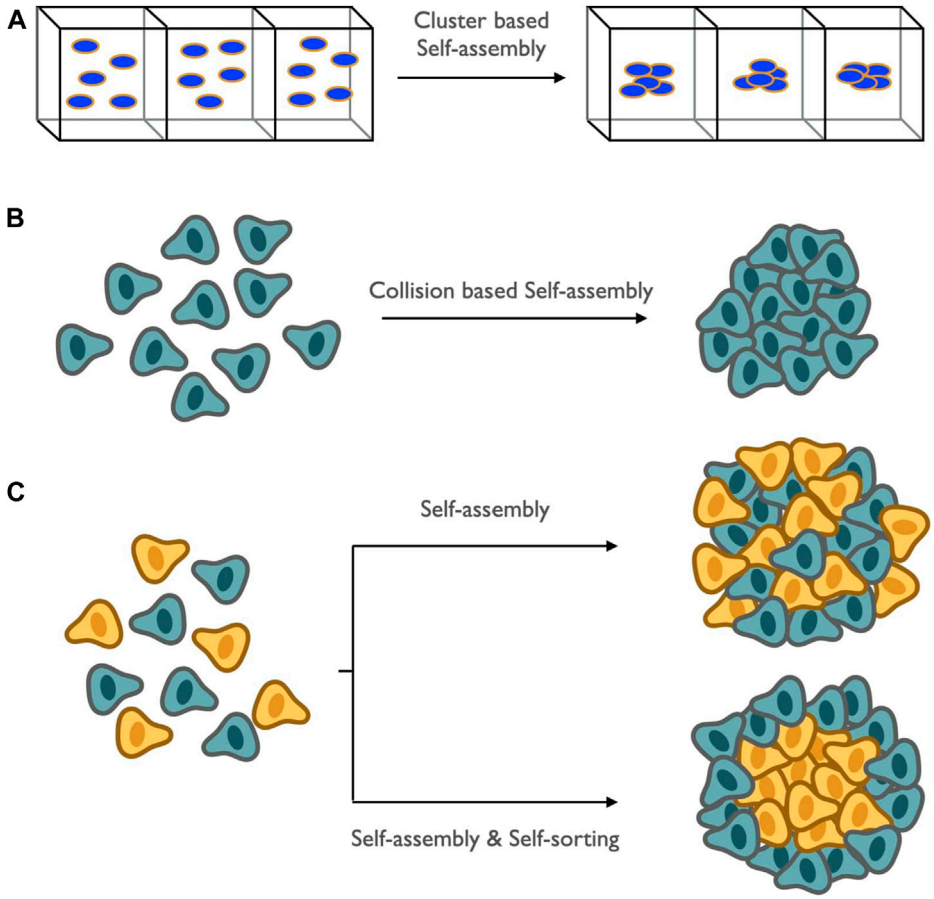

FIGURE 6 | Schematic representation of spatial arrangement and assembly of proliferating and necrotic cells: it is mediated by the soluble products among themselves and regulated by convection and diffusion and is termed as self-assembly. Two broad categories of self-assembly: **(A)** cluster-based self-assembly, which involves the formation of small compartments of mono-dispersed cells; **(B)** collision-based self-assembly, which involves the arrangements or grouping which occurs when suspended cells collide among themselves. Self-assembly is always followed by sorting of mixed cell populations leading to a particular pattern of the cellular combination known as self-sorting.

tumor spheroids. Cellular homogenates are prepared from cultured spheroids after cell lysis in the presence of detergent. Particularly, the cell lysis process damage the cell structure and releases intracellular proteins from different subcellular compartments. Western blot allows detecting a low concentration of protein. However, the western blot is a semiquantitative method and that is why RTPCR is sometimes complemented with it. In this technique, gene expression is quantified through the synthesis of complementary DNA transcripts from RNA. This technique is used to identify different essential proteins in tumor progression and analyze therapeutic efficacy by assessing the expression of pro-apoptotic markers. This technique is used widely to check the efficacy of gene therapy in tumor spheroids.

3.4.5 Colorimetric Analysis

The colorimetric analysis is based on the chemical assays used to measure cytotoxic effects of anticancer drugs. The colorimetric method is applied for assays like Alamar Blue acid phosphate, lactate dehydrogenase, MTS, MTT, and WST-8. These assays are based on the conversion of enzymes present in the subcellular compartment of live cells. Then, the formed product is determined by measuring the absorbance or fluorescence at specific wavelengths. Although colorimetric analysis is more applicable to monolayer culture, the spheroid system could be used after modification of experimental techniques. As a substitute for colorimetric assay, different spectroscopic techniques like tissue dynamic spectroscopy, Fourier transformed infrared imaging, and photon-induced X-ray emission (PIXE) are used less commonly to determine the toxic effect of drugs in tumor spheroids.

The next part of this review will address an overview of different types of mathematical models that have been developed to represent spheroid structure and how the insight drawn from these models helps in making an efficient drug delivery mechanism.

3.5 Mathematical Modeling of Spheroid Growth

The study of spheroid growth using mathematical modeling is more than half a century old (Laird, 1964). These quantitative approaches are invaluable tools for comprehending the cellular and transport phenomenon within spheroids and foreseeing the physiological acknowledgment to drug delivery. They can provide the pertinent perspective for drug delivery mechanisms and effectiveness in spheroid. Mathematical modeling of spheroid can be outlined into two distinct scales. First, the cellular scale describes cellular dynamics that lead to the model of tumor cell proliferation. The exact quantitative expression for this model is given by the Gompertz equation (Laird, 1964). It was commonly believed that tumors grow exponentially and stop until the host nutrition supply is exhausted. However, it has been observed that exponential growth is only dominant for a brief period of time and reaches a growth plateau as the tumor grows larger in size (Laird, 1964; Ward and King, 1999; Mehta et al., 2012; Costa et al., 2016). Secondly, on the other hand, the subcellular and extracellular scales describe the chemical dynamics with the help of the reaction-diffusion mechanism and hybrid models. Modeling tumor morphology starting from individual cells is usually divided into two categories incorporating both continuum and the cell-level description. Hybrid models deal with a combination of these two different descriptions. One is related to the periphery of the tumor, embraced with a cell-level description where it is advantageous to do so, and the other covers the two inner zones of tumor and the extracellular matrix pertaining to continuum description, i.e., cell population-based continuum models and individual cell-based discrete models. During the development of these models, the primary focus was on incorporating the different characteristics of spheroid growth, such as initial exponential growth and the concentration gradient of nutrients, oxygen, which are vitally important for the layered organization of spheroid and targeted nanomedicine delivery.

First, cellular dynamics can be studied mathematically by one of the pioneering models for tumor growth developed by Laird in 1964 (Laird, 1964). The growth kinetics of solid tumors is akin to spheroid, which can be classified into two levels. During the initial phase, the exponential growth of the tumor volume is observed. It is followed by a dormant phase of minimized metabolic activities until the spheroid growth plateau, where the spheroid's volume attains a constant value (**Figure 5**). In improving the exponential model, the cell population growth curve with a time-dependent growth rate is considered. Let the size of the population at time t be $W(t)$ and the growth rate decay exponentially be $a(t) = \alpha e^{-bt}$. Here, the independent variable is time t, and the dependent variable is the tumor volume or population size $W(t)$. The corresponding ordinary differential equation for $W(t)$can be written as follows:

$$\frac{dW(t)}{dt} = \alpha e^{-bt} W(t). \tag{1}$$

The solution to this model shows tumor cell proliferation that can be expressed by a modified exponential process, commonly known as the Gompertz equation for sigmoidal growth, of the following form:

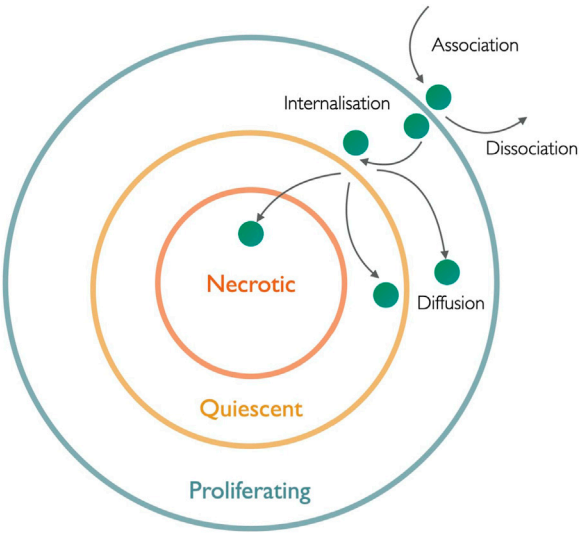

FIGURE 7 | Schematic illustration of nanomedicine penetration into the hierarchical layers of the spheroid: the whole nanomedicine internalization and diffusion process depends on different rate coefficients of association, dissociation, and internalization and is depicted by arrows.

$$\frac{W(t)}{W_0} = e^{\frac{a}{b}(1-e^{-bt})}, \tag{2}$$

where $W(t)$ is the tumor size at any time t, $W_0$is the initial tumor size, and b is constant. Now, e^{-bt} can be expressed in power series as $e^{-bt} = \sum_{n=0}^{\infty} \frac{(bt)^n}{n!}$. During the initial growth, i.e., at small t, e^{-bt}can be approximated as $e^{-bt} \approx 1 - bt$, and the growth equation takes the simple exponential form $\frac{W(t)}{W_0} = e^{at}$, which is consistent with the observation of initial tumor growth. At later times, the growth deviates from the pure exponential dependency and takes the Gompertz form. From the Gompertzian analysis, the theoretical upper limit of tumor growth for mice is typically $\approx 10^9$cells, which is also consistent with the approximate size at death (Laird, 1964; Norris et al., 2006; Altrock et al., 2015; Costa et al., 2016).

In the above formalism of growth dynamics, there is only one independent variable time t, and the dependent variable is the volume of the tumor. Nevertheless, mathematical models have been developed using partial differential equations to study the spheroid growth and architecture at higher dimensions. For instance, a model has been developed to study quantities such as oxygen distribution which has more than one dependence, one is spatial and the other is temporal. One valuable characteristic of a spheroid is their limit of diffusion of about 150–200 μm for many molecules, specifically oxygen (Mehta et al., 2012). This diffusion limit gives rise to limited mass transport, as a result of which spheroid displays the gradient of oxygen, distribution of nutrients, metabolic waste accumulation, and proliferation profile inside them. Hence, a diffusion model for the oxygen concentration is requisite. The oxygen concentration in a tissue can be represented by $\rho(r,t)$, where the position r, in general, measures from the center of the spheroid at a time t. The reaction-diffusion equation for oxygen concentration inside a

spheroid in the form of a partial differential equation can be written as follows:

$$\frac{\partial \rho(r,\,t)}{\partial t} = D\frac{\partial^2 \rho(r,\,t)}{\partial r^2} - a\rho(r,t) - bN(r,t)\rho(r,t) + c\rho(r,t)\,, \tag{3}$$

where oxygen diffuses inside the spheroid with a diffusion constant D, decays with the rate constant a, and is produced with a rate constant c. The consumption of oxygen is proportional to the group size of the tumor cells $N(r,t)$ and available oxygen concentration $\rho(r,t)$ itself with a rate constant b.

A mathematical model is required to weave the insights gained from the discrete cellular dynamics into a coherent description of the reaction-diffusion mechanism. Combining the continuum model of growth-consumption as a reaction-diffusion model along with discrete cellular dynamics of cell growth and motility, a hybrid model has been developed. The model retains the cellular description in the rapid proliferation region on the periphery of the tumor and for the dynamics of tumor cell density, extracellular matrix (ECM) cells, matrix-degrading enzymes (MDE), and oxygen concentration as continua. The corresponding coupled dynamic equations of these individual quantities can be written as partial differential equations. For instance, a partial differential equation for the dynamics of tumor cell number $N_T$is given by

$$\frac{\partial N_T}{\partial t} = D_T\frac{\partial^2 N_T}{\partial r^2} - \frac{\partial}{\partial r}\left(N_T\frac{\partial N_E}{\partial r}\right), \tag{4}$$

where the diffusion constant of tumor cells is denoted by D_T and extracellular matrix is represented by N_E. The dynamics of ECM (N_E), MDE (N_M), and oxygen concentration (ρ) are represented by

$$\begin{aligned}\frac{\partial N_E}{\partial t} &= -\phi\, N_M N_E,\\ \frac{\partial N_M}{\partial t} &= D_M\frac{\partial^2 N_M}{\partial r^2} + \lambda\, N_T - \mu\, N_M,\\ \frac{\partial \rho}{\partial t} &= D_\rho\frac{\partial^2 \rho}{\partial r^2} + f\, N_E - n\, N_T - c\rho\,.\end{aligned} \tag{5}$$

The diffusion constant associated with ECM and MDE is, respectively, represented by $D_E$and D_M. The degradation of the extracellular matrix is directly proportional to the density of matrix-degrading enzymes and extracellular matrix with a proportionality constant ϕ. Matrix-degrading enzymes are produced by the tumor cells themselves with a rate constant λ and natural decay with a rate constant μ. On the other hand, the oxygen concentration is directly proportional to the ECM density with a rate constant f. It is consumed by the tumor cell at a rate n and decays at a rate c.

The hybrid model bridges two different types of models distinguishing between individual cell and cell population-based models. This model complements a fully continuous and complex description of tumor dynamics. The discrete cell interaction can be explained by a stochastic model, which is an off-lattice model. On a 2D lattice, probabilistic rules are applied to each cell pertaining to discreteness by defining stochastic reaction rates of respective events and may depend on the microenvironment (Kim and Stolarska, 2007; Altrock et al., 2015). In a hybrid model, these stochastic rates depend on the concentration of continuous variables ρ, N_M, N_E, and N_T . Besides this, the hybrid model also specifies the guidance for processes like proliferation, which are dependent on the environment and are specific to cells. Recent research has been done considering 3D cell culture leading to new methods for drug transport. In the future, mathematical models will continue to help as a guiding path for understanding the tumor architecture and its growth and studying the transport of oxygen and nutrients among different zones within the spheroid via cellular and chemical dynamics.

3.6 Self-Assembly and Self-Sorting

The organization of interior layered composition of MCTS can be determined by the spatial arrangements, interaction, and grouping of cells combined into developmental and functional patterns. The fabrication of these similar or different cellular patterns allows them to form self-organized individual compartments assembled together, resulting in a highly stratified structure is known as self-assembly. This bio-fabricated spheroid assembly is mediated by the molecular gradients of soluble factors which are capable of binding to cellular receptors causing the signals to initiate proliferation. These soluble factors within the spheroid microenvironments are established by the process of convection and diffusion. This arrangement across the multiple length scales can be assembled in two different ways: cluster-based self-assembly and collision-based self-assembly. Cluster-based self-assembly consists of the partitioning of mono-dispersed cells into sectors followed by their settlement and aggregation, maintaining their cellular integrity as clusters and resulting in spheroid. In contrast, when the suspended cells strike into each other, leading to the formation of a spheroid is termed collision-based arrangement. Self-assembly is often followed by self-sorting. When varying cell types are organized among themselves, leading to a particular pattern of segregation, this can be stated as self-sorting (**Figure 6**). Based on this, a theoretical model has been developed for the study of spheroid formation that occurs when two cell types are differently segregated. Modeling of a spheroid based on self-assembly and sorting is affiliated with cell-to-cell adhesion and surface tension. This necessitates the sorting of cells of the highest cohesion to the interior of the spheroid and those with lower cohesion to the outer. This hypothesis is known as Differential Adhesion. From the recent study (Achilli et al., 2012), it has been shown that modeling of self-sorting processes can be done using an order parameter to describe the relationship between heterotypic interface length and size of the system, taking the geometrically driven argument as its base.

The subsequent part of the study will elucidate another key component of the targeted drug delivery mechanism, that is, the study of drug molecules and how they can be modeled mathematically and the key attributes related to their physical properties and chemical composition.

4 KINETICS OF NANOMEDICINE IN TUMOR SPHEROIDS

Anticancer drugs used for chemotherapeutic purposes to treat intractable cancers have undesired cytotoxic side effects for normal tissues due to lack of selectivity to the target diseased tissue and broad biodistribution once administered into the systemic circulation. Additionally, free drug candidates are characterized by insufficient pharmacokinetics and early degradation in the physiological environment (Duncan and Gaspar, 2011; Curtis et al., 2016; Cabral et al., 2018; Tchoryk et al., 2019). Usage of drug formulations for treating cancer having sizes greater than preferred nanometers has adverse effects such as *in vivo* instability, poor bioavailability, issues with target-specific delivery, and toxic effects. To overcome these critical medical challenges, some potential and advanced technology is needed. Nanotechnology can be used as a gateway to bridge the gap between biological phenomena and physical mechanisms. It entails the use of nanoscale materials having sizes 10–100 nm with the concept of aiming peculiar drugs to the desired cells, tissues, and body parts. To this end, drug delivery in a targeted fashion to the diseased sites is a smart strategy to combat enhanced therapeutic benefits and limit these cytotoxic side effects of drugs to normal tissue. Desired drug individuals are specially designed as nanomedicine (i.e., nano-drug formulations) so that effective therapeutic concentration of active drug molecules reaches its site of action to exhibit required pharmacological activities (Cai et al., 2019). Nanomedicine-based approaches could be used as a translational technology where drugs interact particularly with target-specific diseased tissue and individual cells with normal sites that remain thoroughly unaffected and thus ensure to mitigate undesired toxic side effects. It exerts remedial agents at the nanoscale with size ranges between 10 and 100 nm leading to the frontiers of nanomedicine drug delivery, more precisely with a controlled release (Prokop and Davidson, 2008; Jain and Stylianopoulos, 2010; Bae and Park, 2011; Carolyn and Charles, 2012; Babu et al., 2014; Marchal et al., 2015; Li et al., 2017). These remedial agents have to follow certain fundamental objectives for effective delivery mechanisms. The foremost objective of nanomedicine is to increase the concentration and the augmentative exposure of the therapeutic drug candidates to the core. Therefore, target-specific drug delivery is a very promising strategy for therapy against intractable cancer. Thus, nanomedicine ensures enhanced therapeutic efficacy and simultaneously reduces the event of systemic toxicity of anticancer drugs. But, the efficacy of nanomedicine depends on the spatiotemporal concentration distribution of the therapeutic drug candidates in the entire tumor, from the proliferation zone up to the core, which is associated with the tumor microenvironment and physicochemical properties of nanomedicine (Shyh Dar and Leaf, 2008; Markman et al., 2013; Wicki et al., 2015; Maity and Stepensky, 2016). The shape, size, charge, initial molar concentration, pH, chemical composition, the effect of targeting ligand, and cross-linking of the nanomedicines have a profound impact on its ability to diffuse, penetrate and accumulate into the solid tumor as well as tumor spheroids.

Nanomedicines are characterized by a stable circulation in the bloodstream, escape from unnecessary unspecific interactions with various blood components, successfully extravasate from blood vessel to diseased site and increase the ability of interactions and recognitions by target-tumor tissue and deliver drugs into the intracellular system. Thus, nanomedicine formulations avoid leakage and degradation of drugs in the blood compartment. A very stable blood circulation of nanomedicine is recognized by solid tumors for developing tumor-targeted drug therapy strategies. Furthermore, the tumor vasculature is leaky and non-restrictive, which offers nanomedicines an enhanced permeability to the tumor site. Once nanomedicine enters, it remains there for a long time due to impaired lymphatic drainage system (Shyh Dar and Leaf, 2008; Markman et al., 2013; Wicki et al., 2015; Maity and Stepensky, 2016b). This is enhanced permeability and retention effect (EPR), which is an outstanding mechanism for drug accumulation into tumor sites. Nanomedicine is transported through the tumor blood vessel, which is found across interendothelial gaps and follows transendothelial pathways. In addition, they have fenestration and vesicular vacuolar organelles with 50–100 nm size, which is simplified to the transport of a tiny shape nanomedicine into a tumor. Nanomedicine with 100 nm size extravasate by vascular bursts in the tumor. This process is done by intratumoral and vascular pressure gradients. It helps to ingest the nanomedicine into the tumor interstate.

Nanomedicines are internalized to target cells via the endocytosis mechanism and pass through endosomal-lysosomal vesicles. The acidic pH of the endo-lysosomal compartment acts as a trigger for some nanomedicine to release cargo drugs inside target cells and is suitable for its action. For this purpose, nanomedicine is prepared with biocompatible polymers such as PEG (polyethylene glycol), which shields the outer surface, avert elimination by RES from the bloodstream, and also extend the lifetime of nanomedicine in the bloodstream and foster further extravasation and tumor recognition processes (Li and Huang, 2009; Nie, 2010). The size and charge of nanomedicine affect the whole process. Nanomedicine size less than 150 nm accumulates in the liver and larger than 150 nm stay in the spleen. Nanomedicine with a positive charge is mostly found in the liver, spleen, and lungs, whereas neutral or negative charge nanomedicine tends to stay in the bloodstream for a longer time. A ligand-installed on the nanomedicine periphery establishes a recognition towards vascular receptors, promoting the extravasation of nanomedicines from the bloodstream into tumors (Li and Huang, 2009; Nie, 2010). Numerous nanomedicine formulations like dendrimer, liposome, drug-polymer conjugates, nanoparticles, and polymeric micelles act as tumor-targeted drug delivery vehicles (Yang et al., 2015). The design of biocompatible polymers abides by the guidelines of the FDA for biomedical applications of the polymeric micelle,

where a minimum amount of polymer is administered to avoid unwanted toxicity in the body and activation of immune responses (Ahmad et al., 2010; Sun et al., 2017; Mullis et al., 2019; Tan et al., 2020). Thus, a risk-free biodegradable polymer is designed and frequently used, which disintegrates into monomer once contributing its part, excreted from the body without accumulation and toxicity. As a result, these properties can provide an insight into the fundamental mechanisms of the underlying kinetics of drug delivery and help in building up the potency of nanomedicine delivery in a targeted way (Lane et al., 2015; Donahue et al., 2019).

The entire pathways taken by nanomedicines to reach the core of spheroids can be treated mathematically. Mathematical modeling can be perceived as an essential tool for quantitative analysis of impaired drug delivery. As a result, several mathematical models have been developed to study the penetration, kinetics, and biochemical effects of therapeutics. The succeeding section will bring forth the broad vision on the optimal delivery of nanomedicine to the core of the spheroid and facilitate their tailoring. Moreover, it will address how various mathematical models are capable of forecasting the effect of different physical parameters on the spatiotemporal dynamics and penetration of nanomedicines. Profuse mathematical models have been set in motion for more elaborative and meticulous designing of nanomedicine, which will be discussed below as:

4.1 Mathematical Modeling of Nanomedicine

The rapidly growing nanotechnology evokes the need for understanding how nanomedicine's characteristics influence the transport processes. Mathematical modeling has the potential to point to the comprehensive view of nanomedicine designing and characterize the important features prerequisite for drug delivery. In this section, we will discuss the quantitative insights for the elucidation of nanoparticle (i.e., nanomedicine) diffusion mechanisms in the bulk, penetration into the multicellular spheroid, and then the calculation of binding site availability on the spheroid surface (**Figure 7**). The viability of requisite mathematical models for the treatment of spheroids with nanomedicine will be of primary focus.

The binding of a drug molecule is essential when it comes to an unhindered drug delivery mechanism, which is proportional to the optimized value of successful binding. Molar concentration plays a major role while addressing the optimized binding and penetration of nanoparticles to and through the spheroid. Binding can be maximized in two different ways: first, it is related to the molar concentration of nanoparticles, while the other is related to the molar concentration of the cell surface binding sites in the spheroid. To study the penetration of nanomedicine to the spheroid, using stock's solution (Gao et al., 2013), the molar concentration of nanoparticle (ρ^M) in Mol/L can be calculated as follows:

$$\rho^M\ (Mol/L) = \frac{NP\ conc.\ (number/L)}{6 \times 10^{23}\ particles/mole} = \frac{6C_{stock} \times 10^{12}}{N_A\ \pi \rho d^3}, \quad (6)$$

where C_{stock} is the nanoparticle concentration in manufacturer stock solution, $N_A$is Avogadro's number, ρ is the density of nanoparticle, and d is the nanoparticle diameter in meters. The stock's solution is being prepared for the transport study of the molar concentration and aggregation of nanoparticles. Moreover, the molar concentration of cell surface binding sites in a spheroid can be defined as follows:

$$B_{max,\ spheroid} = \frac{\phi \times 10^{15}}{6 \times 10^{23} \times \frac{4}{3}\pi r_{cell}^3} B_{max,\ single\ cell.}, \quad (7)$$

where ϕ is the cell density calculated by taking the volume of total cells in spheroid divided by the total spheroid volume (with the assumption of the spherical shape of spheroid), r_{cell} is the radius of the tumor cell in the suspension of stock's solution, $B_{max,\ single\ cell}$ is the molar concentration of single-cell binding, and $B_{max,\ spheroid}$ is the molar concentration of cell surface binding site in spheroid (Gao et al., 2013).

Mathematical modeling is instrumental in aiding our understanding of the internalization of nanomedicine through the stratified structure of tumor spheroid and then followed by its diffusion inside the spheroid. The diffusion of nanomedicine at the cellular and extracellular levels is stipulated by its calculation in the interstitium and interstitial sites and taking the porosity of the spheroid into account, addressed using mathematical tools. Nanoparticle penetration to the cells can be designated as a two-step process. First, the adsorption of nanoparticles is then followed by their internalization. Fundamentally, association or this binding kinetics of negatively charged nanoparticles to cell surface termed Langmuir adsorption with the assumption that a particular cell line has a fixed capacity for particle binding through electrostatic interactions (Wilhelm et al., 2002). This process incorporates the rate of change of mass of nanoparticles bound to the cell surface, established by considering the molar concentration in the extracellular medium (M), the mass of adsorbing and desorbing nanoparticles. Langmuir adsorption can be modeled using a differential equation representing the variation of m(t) with time consisting of k_{ass}, k_{diss} as the association and dissociation rate constants:

$$\frac{dm}{dt} = k_{ass} M\,(m_0 - m) - k_{diss} m, \quad (8)$$

where m_0 and $m(t)$ are the maximum mass that can be bound to the cell surface initially and at a later time t, respectively. The above differential equation represents that the mass of absorbed nanoparticles per unit time is proportional to the molar concentration of nanoparticles, to the mass that is present on the cell surface that still can be adsorbed $(m_0 - m)$, and to the mass of desorbing nanoparticles. Initially, at t = 0, m(t) = 0, the analytical description of mass of the adsorbed particles unifying both temporal dependencies and the concentration of binding nanoparticles on the cell surface can be given by

TABLE 3 | Attributes for nanomedicine modeling considering two important objectives, extent of penetration to the core, and expense of release of drug to the core.

Modeling parameter	Range	Limitations	Remarks
Size	The domain of 20–70 nm preferred	The larger size can be used with growth inhibitors	The smaller the size, the better the penetration
Charge	Cation and anion, due to interaction with cells, both resist the penetration up to some range, whereas neutral nanoparticles show higher penetration	Charges will affect the size of nanomedicine by forming aggregates	Owning charge leads to accumulation in the outer region and retard the diffusion
Shape	Nanocylinders and nanorods with a large aspect ratio of height/diameter of their respective sizes are preferred	Variation of shape change with other parameters like size and length is needed to be further explored	Preferential penetration depends on the surface area in contact and hence the shape
pH	Once internalized, pH-sensitive nanomedicine leads to remarkable penetration up to the core	pH-insensitive nanomedicine lowers the penetration	More pH sensitivity leads to better penetration up to the core
Chemical Composition	Biodegradable nanomedicine is preferred	Degradability	Non-biodegradable with higher concentrations will induce growth inhibition comparable to biodegradable
Cross-Linking	Crosslinked nanomedicine over uncrosslinked leads to better penetration and lower cytotoxicity	Disassembly	Cross-linking is preferred due to compact structure though sometimes disassembly leads to a better release of drugs
Ligand	Expressing nanomedicine with the ligand is helpful in selective cell targeting	Limits the diffusion sometimes due to the size difference of pores in the tumor	Endowing nanomedicine with ligands leads to deeper penetration, higher inhibition of growth but sometimes limits the transport

$$m(t, M) = \frac{k_{ass} M}{k_{ass}\, M + \, k_{diss}} m_0 \left(1 - e^{-(k_{ass} M + k_{diss})t}\right). \quad (9)$$

The above expression can be modified to get maximum adsorbed mass with characteristic time $T = \frac{1}{(k_{ass} M + \, k_{diss})}$, which approximately gives. $m_{max} = \frac{k_{ass} M}{k_{ass} M + k_{diss}} m_0$.

After adsorption has occurred, the internalization of nanoparticles can be quantitatively approached in two ways. First, by considering the mass of the nanoparticle bound to the cell surface and another by taking the structural uniformity of the target, i.e., tumor spheroid, into account. Starting with the first approach, the global process of nanoparticle penetration into the tumor involves their binding mass to the cell surface represented at any time t by $m_{bind}(t)$ and their internalized mass within the cell via endocytosis represented by $m_{int}(t)$. Differential equation regulating all these phenomena can be stated as follows:

$$\frac{dm_{bind}(t,\, M)}{dt} = k_{ass} M (m_0 - m_{bind}) - k_{diss} m_{bind} - \frac{dm_{int}}{dt}. \quad (10)$$

It has been previously assumed that the fraction of cell surface absorbs the nanoparticle, termed reactive surfaces (RS) which are regenerative and remain constant. Let $f_{int}(t)$, f_0 be defined as the fraction of RS being internalized over the total available reactive surface at any time t and the maximum fraction of RS internalized by the cell, respectively. Thus, this can be represented by the differential equation with internalization rate constant (k_{int}), $\frac{df_{int}(t)}{dt} = k_{int}(f_0 - f_{int})$. This equation can be used to calculate the rate of change of internalized mass as $\frac{dm_{int}}{dt} = \frac{df_{int}}{dt} m_{bind}$. Using this equation, we can also calculate the total uptake of the mass of the nanoparticle $m(t) = m_{bind} + m_{int}$.

4.2 Influence of Spheroid Architecture on Nanomedicine Penetration and Diffusion.

Now, considering the structural uniformity, the penetration of nanomedicine into the spheroid is addressed quantitatively. Mathematical models have been developed using the nanoparticle-cell bio interface data to predict the penetration of nanomedicine into the spheroid that accounts for radial dependent changes of its internal structure. The diffusive transport and the spatial distribution of nanoparticles can be represented using nanoparticle-cell interaction parameters: association, dissociation, and internalization rate constants. The mathematical expression for the nanoparticle motion into the spheroid relationship is given by Goodman et al. (Goodman et al., 2008). The kinetics of nanoparticle internalization in 3D multicellular spheroid depends on the molar concentration of free nanoparticles available in the spheroid, bound nanoparticles, nanoparticles undergoing internalization, and concentration of available binding sites on the cell surface: M, M_b, M_{int}, and M_{bs}, respectively. The entire ensemble of defining free, bound, and unbound nanoparticles is dependent on the force, which in turn is potentially mediated by cell-cell interaction and cell-ECM interaction. A set of partial differential equations representing the rate of change of respective concentration with time taking the structural changes of the spheroid in the radial direction and nanoparticles internalization using concentration into account is given (Graff and Wittrup, 2003; Ward and King, 2003; Hori et al., 2021; Gao et al. 2013). The molar concentration of free particles per unit time in spheroid volume is proportional to the molar concentration of unbound particles present in the accessible volume intracellularly, which are varying with radial

coordinates, dissociated bound particles, and associated binding sites as well as unbound particles concentration can be written as follows:

$$\frac{\partial M}{\partial t} = \frac{D}{r^2}\frac{\partial}{\partial r}\left[\epsilon r^2 \frac{\partial}{\partial r}\left(\frac{M}{\epsilon}\right)\right] + k_{diss}M_b - k_{ass}M_{bs}\frac{M}{\epsilon}, \quad (11)$$

where k_{ass}, k_{diss}, and k_{int} are the kinetic reaction rates for nanoparticle-cell interaction corresponding to the association, dissociation, and internalization of nanoparticles in a spheroid, respectively. D is the effective diffusion coefficient, r is the radial coordinate representing nanoparticle diffusion measured from the center of the spheroid, R is the spheroid radius, and $\epsilon$is the volumetric porosity of the spheroid, which is the ratio of the spheroid volume accessible to the particles to the total available volume. The partial differential equation elucidating the change of molar concentration of bound nanoparticles with time embedded proportionality with association rate of binding sites, dissociation, and internalization rates of bound particles can be presented as follows:

$$\frac{\partial M_b}{\partial t} = k_{ass}M_{bs}\frac{M}{\epsilon} - (k_{diss} + k_{int})M_b\,. \quad (12)$$

The following differential equation represents the temporal variation of the molar concentration of remaining binding sites on the cell surface on which particles can still attach. It is proportional to dissociation and the internalization of bound particles and association rate of binding sites and unbound particles and also the rate of change of internalized particle related to internalization constant, respectively, as follows:

$$\frac{\partial M_{bs}}{\partial t} = (k_{diss} + k_{int})M_b - k_{ass}M_{bs}\frac{M}{\epsilon},\ and\ \frac{\partial M_i}{\partial t} = k_{int}M_b. \quad (13)$$

The boundary conditions for the initial and at a later time t are as follows: initially, when all particles are present on the surface of the cell, the molar concentration of free, bound, and internalized particle bears no value, i.e., at t = 0, M (0,r) = M_b (0,r) = M_{int} (0,r) = 0 for $0 \le r < R$; and at a later time t, the molar concentration of particles free in spheroid volume holds the same value as the molar concentration of nanoparticles outside the spheroid (M_0)multiplied with porosity of spheroid, i.e., t = t, r = R, we have M(t, R) = $M_0\epsilon$(R), with no radial variation of unbound particle intracellularly $\frac{\partial}{\partial r}\left(\frac{M}{\epsilon}\right)(t,0) = 0$. Here, M_0 is considered to be uniform and equal to the averaged concentration of particles due to mixing in stirred vessels under the experimental conditions. Solving the above set of partial differential equations, we get the total number of particles that are retained in spheroid at time t as $M_t(t,r) = p(r)[M(t,r) + M_b(t,r) + M_{int}(t,r)]$, where p(r) is the piecewise linear window function. $p(r)$ is used to consider the particles near the spheroid's outer rim that need to be removed with the value of r_1 approximated to $0.95R$. It acquires unity when all the particles are internalized and less than unity as per the variation of their radial position from the spheroid surface and center, i.e., $p(r) = 1$ for $r < r_1$; $p(r) = 1 - \frac{r-r_1}{R-r_1}$ for $r_1 < r \le R$.

Once the nanoparticles are internalized, diffusion sets are limited to the targeted delivery. Diffusion plays an indispensable role in how the nanomedicine gets transported to multilayers from cellular scale to extracellular scale. Diffusion is driven by gradients in concentration. It involves the penetration of nanomedicine to multilayers of cells prior to making it to the center. Out-turns of diffusion barriers in multilayer tissues such as cellular compaction, efflux system, and gap junctions have been solved via various models (Costa et al., 2016). The model by Gao et al. (Gao et al., 2013), for the diffusion coefficient of intercellular, porous spaces into the spheroid is represented in three steps. Initially, free diffusion D_0 nanoparticles in water at 37 °C are calculated using the Stokes–Einstein equation. This coefficient at a specified temperature is given by $D_0 = \frac{k_B T}{6\pi\eta a}$, where k_B is the Boltzmann constant, T is the temperature in kelvin, η is the viscosity of water, and a is the radius of the particle. Now, this is followed by diffusion in the interstitium (D_{int}). It represents the diffusion in a porous gel matrix, which acts as an extensive connective network for cell-cell interactions and is responsible for the formation of an extracellular matrix via matrix protein. It depends on the ratio of particle radius $(a)$to pore radius (a_f) and the square root of volume fraction of tumor interstitium matrix (ϕ_{int}). The corresponding relation can be expressed as $D_{int} = D_0 e^{\left(-\frac{a}{a_f}\sqrt{\phi_{int}}\right)}$, where the volume fraction of tumor interstitium matrix $(\phi_{int})$is defined as the ratio of the volume occupied by the particle diffused in the ECM to the total volume of all particles present before diffusion and $\phi_{int} > 0$ always. This ratio is always less than equal to unity depending on the volume of particles that are diffused. For the calculation of ϕ_{int}, the value of collagen is used, which can be obtained by the multiplication of interstitial collagen concentration and its effective cell volume. For movements of nanoparticles to occur through the ECM, the typical mesh size of the tumor matrix should be comparable or larger than the size of the nanoparticles. Hence, the ratio $\frac{a}{a_f}$ is usually less than unity. Collectively, this will lead to the overall value of $\left(\frac{a}{a_f}\sqrt{\phi_{int}}\right)$ less than unity. Now, incorporating diffusion at interstitial cellular scale, which mainly depends on the cellular density ϕ and porous spaces inbetween the cell $(1-\phi)$ can be represented as $D_i = D_{int}(1-\phi)^2$; i.e., $D_i = D_{int}\,\epsilon^2$, where D_i is the interstitial diffusivity constant for diffusion in a porous gel matrix with immobilized cells and ϵ is the porosity in spheroids and defined as the ratio of the volume of immobilized cells to the total volume of cells in the tumor matrix and lies in the range of $0 < \epsilon < 1$. The interstitial diffusivity (D_i) depends directly on the porosity factor, which acquires values less than unity, resulting in slightly lesser diffusion at the cellular scale. Thus, this entire process of diffusion can be summarized with an inequality relation: $D_0 > D_{int} > D_i$, evidently confirming the idea of the uneven rate of particle diffusion till they reach the spheroid's core.

Taking the shape factor of spheroid into account consisting hindrances in its pores, steric hindrances due to the presence of ligand, and the tortuosity due to structural non-uniformity, the mathematical model for the nanomedicine diffusion has been given by Goodman et al. (Goodman et al., 2008). Similar to the model by Gao et al., initially, this model also takes free diffusion in

the unbound medium that is not mediated by any force and potential due to cell-cell and cell-ECM interaction into consideration. The free diffusion given by the Stokes–Einstein relation can be written as $D_0 = \frac{k_B T}{6\pi\eta a}$, where D_0 is the diffusion coefficient in the unbounded medium, k_B is the Boltzmann constant, $\eta$is the viscosity of the liquid, and T is the absolute temperature. Now, depending on tortuosity $\tau(\epsilon)$, shape factor F, hindrances due to hydrodynamics, and the steric effects of the diffusion coefficient in the porous media $L(\lambda)$, the corresponding relation for effective diffusion constant can be presented as $D = D_0 \frac{L(\lambda)}{F\tau(\epsilon)}$. Here, $\tau(\epsilon)$ is related to the curvature consisting of structural aspects of the spheroid and has a profound impact on the diffusion and hydrodynamics in porous media. It is responsible for the increase in diffusion path length in the spheroid and related to the volumetric porosity(ϵ)as $\frac{1}{\tau(\epsilon)} = 1 - \frac{2}{3}(1+\epsilon)(1-\epsilon)^{\frac{2}{3}}$, where ϵ is the ratio of the volume of immobilized cells to the total volume of cells in a tumor and bears a value in the range $0 < \epsilon < 1$. As defined, the inverse proportionality between them leads to $\tau(\epsilon)$>1. Mobility of particles in spheroid $\lambda$is defined as the ratio of particle's radius a to the pore radiusr_p; that is, $\lambda = \frac{a}{r_p}$. The typical size of pore radius is comparable or greater than the particle size as $a < r_p$; therefore, $\lambda < 1$. The ideal situation of free diffusion is often affected by hindrances in the intercellular medium and tumor spheroid structure. Steric hindrances are defined as the obstructions in the path of a particle due to the presence of surrounding particles and ligands, often slowing down its motion and may stagnate the diffusion in the pore. This steric reduction along with the effects of hydrodynamic forces can be expressed as $L(\lambda) = (1-\lambda)^2(1 - 2.1004\lambda + 2.089\lambda^3 - 0.948\lambda^5)$. The structure factor (F) incorporates the obstructions in the spheroid pore and holds a value F > 1. Thus, the combined effect of all these defines the demeanor of diffusion in spheroid, stating an overall lesser value of D than D_0 upholding the real phenomenon.

Binding sites are the receptors on the surface of cells that help the drug molecules and ligands to bind with them for better signal transduction pathways. One of the most crucial parts of targeted drug delivery is the appropriate availability of these binding sites on the surface of cells with which drug molecules can attach and eventually internalize. For impaired efficacy of drug delivery to the target, calculation of the concentration of available binding sites on the cell surface is a requisite. For the porous media, a parallel pore model was developed, which established a relationship among the molar concentrations of the available binding sites on the cell surface (M_{bs})taken initially at t = 0 with the spheroid structure, porosity, structural dimension of a particle, and pore radius as (Goodman et al., 2008) $M_{bs}(0,r) = \frac{2}{\pi}\frac{k_\beta \beta \epsilon}{a^2 r_p N_A}$, where a is the radius of the particle, r_p is the pore radius, N_A is the Avogadro's number, and the density of remaining binding sites present on the cell surface is represented by β, whereas $k_\square$ is related to the variation in binding cell density on the monolayer cell culture surface to the cells in spheroid.

The surface of the tumor is well decorated with binding sites as receptors for the targeting ligand. Once the drug molecules bind to its surface, the next concern is about the calculation of the total number of cohesive particles that are bound and internalized. A model with several assumptions for a single cell considering bound and internalized particles to determine the number of cohesive particles, rate constants, and the number of binding sites is used. The concentration of particles surrounding the cell and the mean concentration of particles in the vessel are equal. A cell's surface area is not inhibited by any other cells. Due to the continuous turnover of the cell membrane, the cell regenerates potential binding sites as the particle internalizes, as a result of which binding sites are taken to be constant, and any exocytosis will end up in the reduced value of k_{int} (Goodman et al., 2008). The model provides the relations representing the variation of number of bound particles with time proportional to the decreasing rate of dissociation and internalized particle and the positive influence of associated binding site on the cell surface along with total particle outside the spheroid as follows:

$$\frac{dN_b}{dt} = -(k_{diss} + k_{int})N_b + k_{ass}M_0 N_{bs}. \tag{14}$$

The remaining number binding site N_{bs} on the cell surface is the difference between the number of available binding sites S, which were present initially, and the number of bound particles on the cell surface N_b:

$$N_{bs} = S - N_b \text{ , } and \text{ } \frac{dN_{int}}{dt} = k_{int}N_b \text{ ,} \tag{15}$$

where N_{int} is the number of particles that are internalized and proportional to the internalization rate constant of bound particles. The initial number of binding sites (S) can be related to the effective segment of cell surface area that is available for binding(β)as $\beta = \frac{Sa^2}{4R_c^2}$, where R_c is the individual cell's radius, and a is the particle radius. On the other hand, the growth of the number of bound particles and the total number of adhered particles can be given by solving **Eq. 15**. Thus, we get the number of bound particles (N_b) and the total number of adhered particles (N_t):

$$N_b = \alpha\left(1 - e^{-\gamma t}\right),$$
$$N_t(t) = N_b(t) + N_{int}(t) = \alpha\left[k_{int}t + \frac{\gamma - k_{int}}{\gamma}\left(1 - e^{-\gamma t}\right)\right], \tag{16}$$

where α and $\gamma$are defined as follows:

$$\alpha = \frac{k_{ass}M_0 S}{\gamma}, \text{ } and \text{ } \gamma = k_{ass}M_0 + k_{diss} + k_{int} \text{ .} \tag{17}$$

Here, as $\gamma$is the sum of all the rate constants, $\gamma > k_{ass}$ and $\gamma > k_{int}$ individually. Also, S and M_0 are definite quantities and greater than unity. Hence, $\alpha < 1$, which leads to the fact that N_b *and* N_t are less than unity and therefore sustaining our aim of greater internalization of particles into the spheroid. Solving **Eq. 16** and using experimental data, the value of particle binding to the cell, rate constants, and the number of binding sites can be calculated. Thus, the mathematical models provide us the tool and allow us to calculate all the parameters such as concentration of nanoparticles, binding sites, diffusion coefficient at distinct scales, number of adhered particles, rate coefficients, and number

of binding sites which are needed for successful targeted drug delivery. This quantitative approach to the problem makes us well equipped to deal with the system qualitatively as well by studying the physicochemical properties of drug carriers.

4.3 Role of Physiochemical Properties of Nanoparticles.

Quantitative analysis of nanomedicine in all the physical and mathematical regimes leads the way for the study of physicochemical features of the drug. The study of these properties of nanomedicine can help in establishing a suitable platform for target-oriented delivery of drugs with more adaptability (Liu et al., 2012). The following section will illustrate the key features of nanomedicines aiming at providing efficient drug delivery mechanisms, attaining the objectives, and enhancing bioactivity (**Table 3**).

4.3.1 Role of Size

The efficacy of nanomedicine largely depends on the distribution of the therapeutic concentration throughout the entire tumor, from the surface to center (i.e., proliferation zone to the necrotic core), so for the study of penetration profile of nanomedicine to the necrotic region, a key attribute that should be taken into account is the size of nanomedicine. In an ideal situation, the size of nanomedicine varies inversely with a diffusive capacity (Lazzari et al., 2017). Thus, smaller nanomedicines show better penetration in the spheroid. Treating nanomedicine with collagenase has a crucial impact on its penetration. Goodman et al., 2008 (Goodman et al., 2008; Cabral et al., 2011) have shown the effect of collagenase treatment on the penetration of particles. Nanomedicines lying in the diameter range of 20–40 nm accumulated to the interior of the spheroid show a dramatic increase in penetration upon treatment with collagenase, while those having a diameter of 100 nm experience restricted penetration after collagenase treatment. Moving further to the range of 200 nm, there is no penetration at all into the spheroid interior, even with collagenase treatment. Now, taking the accumulation into consideration and how the size of nanomedicine gets affected by it, it has been reported by Horacio et al. that with the size ranging from 30 to 100 nm, the accumulation of 30 nm nanoparticles was two times higher than that of 50 nm and four times more than that of 70 and 100 nm (Horacio et al., 2011). Moreover, 100 nm nanomedicine shows higher accumulation in the liver than any other organ, highlighting the significance of nanomedicine distribution to specific organs.

4.3.2 Role of Charge

The surface charge on nanomedicines also affects the efficiency of the drug delivery system and their penetration. The nature of the charge not only leads to the accumulation of nanomedicines in the spheroid but also affects the rate of penetration. The neutral charge exhibits the most rapid penetration rate in contrast with the positive and negative charges. Having any kind of charge, whether cationic and anionic, manifests slower penetration due to interaction between the charged particle with the cell surface of the spheroid, resulting in deceleration of their diffusion (Gao et al., 2013; Wu et al., 2020). The interaction of nanomedicines with the cell component expelled in the extracellular medium, which is already negatively charged, leads to the change in the size of charged nanomedicines remarkably as compared to the neutral drug molecules. In support of this, a confocal microscopy-based study showed that the charged particles formed aggregates over time (Gao et al., 2013; Lazzari et al., 2017). Hence, the cationic nanomedicines lead to a high accumulation in the outer layer of the spheroid and simple surface adsorption. On the other hand, the cationic drug molecules allow a more uniform distribution in the spheroid, resulting in loss of ability to work efficiently and destruction of the inner compact spheroid structure.

4.3.3 Role of Shape

The shape acts as a key component that influences the rate of tumor accumulation and therapeutic efficacy. The influence of shape on the penetration of nanomedicine is still under study. Shape affects the nanoparticle's affinity to bind with the target. Nanoparticle's aspect ratio, which is defined by the height vs. diameter ratio, may establish varying rates and patterns of extravasation for different tumors. The underlying role of shape on the penetration and size of nanoparticles go hand in hand. Studies by Stenzel et al. showed that the capacity of penetration is correlated to size. Thus, the shortest one displayed the highest capacity of penetration for MCF-7 cells. Numerous shapes of nanomedicine with varying sizes can be discerned. Disc-shaped nano cylinders and cuboidal nanorods of two different sizes interpreted in terms of low and high aspect ratios showed different penetration. It has been observed that nanocylinders and nano-cuboids of a higher aspect ratio represent more nanoparticle penetration inside the spheroid when plotting the normalized intensity against their normalized distance from the center is done. This comparison can be drawn more clearly by the two-photon microscopy highlighting the more accumulation of nanoparticles inside the spheroid for the higher aspect ratios of the nanocylinders and nano-cuboids sized drug molecules (Horacio et al., 2011; Lazzari et al., 2017; Costa et al., 2021). The higher aspect ratio, hence the larger surface area in contact, can be stated as one of the reasons for this favored penetration, which promotes a higher avidity between the cells and diffusion across spheroids.

4.3.4 Role of pH

The pH plays a very crucial role in the modeling of nanomedicine. While anticipating the tendency of penetration of nanoparticles, pH-sensitive nanoparticles take the lead over the rest. Targeting the tumor with nanomedicine involves the diffusion of nanoparticles and their controlled release up to the core. Thus, once internalization is done, the disassembly of nanomedicine to release the drug is the point of prime focus. As we move from the proliferation zone to the necrotic zone, the region becomes more acidic due to a drop in pH in the tumor extracellular space. Immediately after internalization, this redox and acidic environment proved beneficial for the sustained release of drugs that are pH-sensitive and can penetrate deeply and

more uniformly into the spheroid mass (Lazzari et al., 2017). Nonetheless, the pH-insensitive nanoparticles manifest the reduced penetration yielding to inefficient drug delivery.

4.3.5 Role of Chemical Composition

Followed by pH, another pivotal aspect in the direction of better penetration is how nanomedicine is designed chemically. Lower concentration, minimum cytotoxicity, and biodegradability are the main criteria for nanomedicine and its efficient use as a drug delivery system. Additionally, the degradability of a polymer used for nanomedicine formulation has a profound impact on the cytotoxicity and growth inhibition of cells. Biodegradable and non-biodegradable polymers prepared by self-assembly behave differently for nanomedicine-mediated targeted drug delivery (Lazzari et al., 2017). Non-biodegradable nanoparticles, such as bovine serum albumin conjugated with polymethyl methacrylate, show higher penetration and deeper accumulation in the tumor via repeated mediated endocytosis and exocytosis processes, but this higher rate of penetration will provide resistance to the sufficient intercellular release of drugs leading to comparatively lower cytotoxicity, as comparable to biodegradable nanoparticles such as bovine serum albumin conjugated with polycaprolactone. When nanoparticles are conjugated chemically with these biodegradable agents, their degradability is assured, in contrast to their higher intracellular drug concentration (Lazzari et al., 2017). These non-biodegradable nanoparticles, when taken with five times higher concentration, will induce growth inhibition comparable to bio-degradable.

4.3.6 Role of Cross-Linking

While considering the optimal attributes of nanomedicine, directing its penetration to the core, the idea of cross-linking emerges as a prominent one. Nanomedicine penetration, drug release, and cytotoxicity can be affected by cross-linking of the drug-loaded micelle (Lazzari et al., 2017). A crosslinked micelle is capable of moving via a transcellular pathway leading to greater cytotoxicity than the non-crosslinked or free counterpart, which got disassembled after penetration through the outer layer. Inefficacy of free drugs can be followed by their limited diffusion. In contrast, later on, it was observed by Lu et al. (Lu et al., 2014) that the compact structure of crosslinked micelle leads to the deepest penetration, but it displays the lowest cytotoxicity by creating hindrances for its diffusion to the core, thus slowing down disassembly and release of loaded drugs. A non-crosslinked micelle can degrade on the way to penetrate at the core of tumor spheroids, and as a consequence, the loaded anticancer drugs could be released somewhere, which may lead to a complex situation of penetration of free drug vs. integrated micelle.

4.3.7 Role of Targeting Ligand

Surface decoration of nanoparticles with specific targeting ligands is beneficial for selectively targeting the tumor site via receptor-ligand, transporter-ligand interaction. Nanoparticles modified with various targeting ligands are used as a plan of action for selective cancer cell targeting (Lazzari et al., 2017; Nagesetti et al., 2021). The ligand-mediated delivery of nanoparticles promoted by selective cell targeting and at the same time paved the way for limited accumulation in the surrounding normal tissue leading to maximizing the efficiency of drug effects to diseased sites and minimizing the toxic side effects related to anticancer drugs. Selective tumor cell targeting with ligands decorated on nanomedicine surface, some of them can be outlined here. Nanoparticles decorated with transferrin piloted the inhibition of cell proliferation, drug penetration, and resulting regression of spheroid volume but limited the drug penetration to a certain depth only, not to the core (Lazzari et al., 2017). Nanoparticles expressed with the folic acid ligand resulted in the highest inhibition of tumor growth when analyzed in the tumor spheroid model (Lazzari et al., 2017). Different carbohydrate decorated nanomedicines resulted in the efficient delivery of the drug and noteworthy regression of tumor growth. Moreover, an aptamer-modified nanomedicine leads to a reduction in spheroid volume up to five times more comparable with non-functionalized nanomedicine by higher penetration to the core. Hence, ligand-decorated nanomedicine showed intense signaling from the periphery towards the center of the spheroid, validating the better penetration ability to the core, higher capacity of inhibition of spheroid volume growth, and significant tumor regression. However, the binding of ligands strongly to cell surface receptors and transporter sometimes limits the nanomedicine transport. The larger nanoparticles with a size range of <10 nm and 100–200 nm, i.e., between capillary pore size in normal tissue and the pore size in the tumor vasculature, respectively, provide the passive tumor targeting but also retard the transport (Gao et al., 2013). Specific ligands are decorated to nanomedicine surfaces using different chemical approaches, e.g., click chemistry, maleimide-thiol coupling, and carbodiimide coupling (Maity and Stepensky, 2016; Maity and Stepensky, 2016).

5 CONCLUSION

In order to elicit a given curative response for different intractable cancers, the effective therapeutic concentration of anticancer drug candidates should reach the site of action to conjure therapeutic benefits. However, several inexorable barriers, including untoward pharmacokinetics, lack of selectivity, degradation of drugs in harsh *in vivo* environments, and drug leaching and widespread biodistribution, act as key factors that limit inadequate drug effects to diseased sites and cause toxicity to normal tissues. However, the use of nanomedicines for tumor-targeted drug delivery overcomes the spatiotemporal distribution of drugs and avoids the side effects. Desired drug individuals are specially designed into nanomedicine to exhibit the required pharmacological activities. Nanomedicine-based approaches could be used as a translational technology where drugs interact particularly with target-specific diseased tissue and individual cells with normal sites remain thoroughly unaffected. The preclinical evaluation of the therapeutic

potential of nanomedicines demands relevant models which could exactly mimic the solid tumors in the body. However, very recently, the physiological relevance and advantages of 3D tumor spheroid models and drug screening have been widely acknowledged. The conventional 2D cultures are incapable of imitating the heterogeneity and complexity of solid tumors as *in vivo* tumors grow in 3D confirmation with a specific architecture that cannot be reproduced by a 2D monolayer cellular model system. 3D tumor spheroid models possess several characteristics of real tumors, such as cell-cell interactions, cellular microenvironments (e.g., hypoxia), drug penetration, reaction and resistance, and ECM production/deposition. The tumor spheroid model bridges the gap between the 2D monolayer cultures and *in vivo* tumor tissue models. The model allows replicating the architecture of solid tumors and better investigates the pathobiology of human cancer. The potential of the spheroids model is reported to be crucial for the development of new anticancer strategies or better measures of cancer treatment. The cellular organization within the tumor spheroids is the key aspect governing the therapeutic efficacy of anticancer drugs**.** The proliferation of cells in the external layer of the spheroid causes higher consumption of oxygen. Moreover, the oxygen and nutrient gradients are reduced towards the center of the spheroid. The cell signaling pathway and the physiological communications established between cells in close contact within the spheroids makes it possible to replicate the fundamental aspects of real tumor and its microenvironments, including the proliferative rates of different cells, specific gene expressions, ECM deposition, ECM-cell, and cell-cell physical interactions, and drug resistance. Analogous to the solid tumors, the tumor spheroids display an internal layered cellular distribution, which is a result of mass transport limitations. It impedes the diffusion of nutrients, oxygen, and metabolic wastes through the tumor spheroids and creates distinct gradients. Due to the constant availability of oxygen and nutrients, highly proliferating cells form the external layers of the tumor spheroid, which is similar to solid tumors *in vivo*. Due to depletion in oxygen and nutrients, the proliferation rate decreases, and the cell metabolism decreases progressively, giving rise to the quiescent viable zone. Further decrease in oxygen, nutrient shortage, and accumulation of metabolic wastes results in cell necrosis and forms the core of tumor spheroids. The cellular organization and presence of gradients help the internal cells to exhibit specific metabolic adaptations responsible for the impaired therapeutic efficacy of anti-cancer drugs. The microenvironments act as regulating factors that govern the rate of proliferation, differentiation, and tumor progression. It imitates the physical barriers found in solid tumors, which impedes the free penetration of drug-loaded nanocarriers. The physiology and polarity of the cell signaling pathways and their gene expressions closely resemble the real tumors. These characteristics make the tumor spheroids suitable for tumor models and can be used for evaluation of drugs in the field of oncology and are well acclimated for high-throughput drug screening. Mathematical modeling of drug delivery systems is a prerequisite for effective troubleshooting during production and efficient improvement of the safety of the pharmacological treatment procedures. It provides a quantitative understanding of the underlying physical principles and profound insight into the biochemical phenomena in the drug delivery procedure. A quantitative approach to the system helps in consolidating the entire phenomenon of drug delivery as an efficient model by comprehensively characterizing the tumor growth, features assimilating the concentration gradients of various factors, tailoring nanomedicine, and the pathway taken by drug molecules. These approaches serve as invaluable tools for designing not only the tumor architecture but also the optimization of the process of diffusion through its different layers. These approaches have a contributory impact on the mathematical understanding of the wide spectrum of drug molecules administration routes starting from their adsorption on the surface till their internalization to the core. Mathematical modeling addresses the elementary components requisite for nanomedicine delivery, starting from the description of binding sites on the tumor spheroid surface to the calculation of a number of internalized particles that are sufficiently complex enough to describe the phenomenon of interest. These models describe the essential aspects of targeted drug delivery with more precision and support the experimental data and qualitative study. This mathematical vision of the problem proved significant in our better understanding of cancer biology and its treatment. It broadens the horizon of the study of nanomedicine by addressing the shortcomings of the present empirical models.

Tumor microenvironment vs. nanomedicine efficacy: despite path-breaking advancements in the modalities of cancer treatment, the mortality associated with solid tumors has not changed much in the last decade owing to the fact that various physical barriers in the tumor microenvironment limit the treatment efficacy of cancer therapeutics. Major advancements in the field of nanobiotechnology have enabled researchers to design different nanomedicines and modify their physical and chemical characteristics according to the specific tumor microenvironment. Interaction between nanomedicine and biological system at different stages of targeting to extract important factors intrinsic to the biological system, which influences the therapeutic efficacy of the targeted nanomedicine by different mechanisms including premature clearance, phagocytic engulfment by the RES system, immunological elimination, and inhibition of tumor penetration by solid tumor microenvironment complexity. However, a more clinical relevance requires a special emphasis on the analysis of structural complexity of the tumor microenvironment, which poses mechanical, chemical, biological, and hydrodynamic barriers to nanomedicine efficacy since these factors are prime for development, delivery, and screening for better therapeutic benefits.

In the pursuit of the most effective penetration, a universal shape of nanoparticles is the need of the hour. Keeping the spheroid architecture and surface properties in mind, specific shapes of nanoparticles are designed for particular spheroid model systems. However, obtaining the optimized universal shape of nanoparticles, for an effective targeted

drug delivery system generically, is yet to be achieved. The different shapes of the nanomedicines, along with their size, surface properties, and parameters, should be further explored. In this regard, we need to design nanoparticles whose shape can change dynamically depending on the tumor surface, microenvironment, and internal porosity. These shape-switchable nanoparticles allow the controllable variation in their shape as per the geometrical constraints of the tumor and are able to shrink and adjust their size according to the encountered environment. This stimuli-responsive nanomedicine is promising in designing a universal nanomedicine carrier for the application in drug delivery.

AUTHOR CONTRIBUTIONS

SR, VG, and SB contributed to the literature review and wrote, reviewed, and edited the original draft. CG contributed to the conceptualization, literature review, gave clinical aspects, and reviewed and edited the manuscript. AM and SG were responsible for the conceptualization, project administration, and literature review, wrote the original draft, reviewed and edited the manuscript, and acquired funding and resources.

FUNDING

The project is financially supported by Ramalingaswami Re-entry Fellowship, reference no. BT/RLF/Re-entry/53/2019, sponsored by the Department of Biotechnology (DBT), Government of India, and Startup Research Grant (SRG), SRG/2020/001606, sponsored by the Science and Engineering Research Board (SERB), Department of Science and Technology (DST), Government of India.

ACKNOWLEDGMENTS

AM and SB would like to acknowledge the Department of Biotechnology (DBT) for providing funding and fellowship to AM and SB. SG and VG would like to acknowledge the Science and Engineering Research Board (SERB), Department of Science and Technology (DST), for providing funding and fellowship to VG.

REFERENCES

Achilli, T.-M., Meyer, J., and Morgan, J. R. (2012). Advances in the Formation, Use and Understanding of Multi-Cellular Spheroids. *Expert Opin. Biol. Ther.* 12 (10), 1347–1360. doi:10.1517/14712598.2012.707181

Ahmad, J., Ahmad, M. Z., and Akhter, H. (2020). Surface-Engineered Cancer Nanomedicine: Rational Design and Recent Progress. *Cpd* 26 (11), 1181–1190. doi:10.2174/1381612826666200214110645

Al-Akra, L., Bae, D.-H., Leck, L. Y. W., Richardson, D. R., and Jansson, P. J. (2019). The Biochemical and Molecular Mechanisms Involved in the Role of Tumor Micro-environment Stress in Development of Drug Resistance. *Biochim. Biophys. Acta (Bba) - Gen. Subjects* 1863, 1390–1397. doi:10.1016/j.bbagen.2019.06.007

Albadari, N., Deng, S., and Li, W. (2019). The Transcriptional Factors HIF-1 and HIF-2 and Their Novel Inhibitors in Cancer Therapy. *Expert Opin. Drug Discov.* 14 (7), 667–682. doi:10.1080/17460441.2019.1613370

Albrecht, D. R., Underhill, G. H., Wassermann, T. B., Sah, R. L., and Bhatia, S. N. (2006). Probing the Role of Multicellular Organization in Three-Dimensional Microenvironments. *Nat. Methods* 3 (5), 369–375. doi:10.1038/nmeth873

Altrock, P. M., Liu, L. L., and Michor, F. (2015). The Mathematics of Cancer: Integrating Quantitative Models. *Nat. Rev. Cancer* 15, 730–745. doi:10.1038/nrc4029

Arneth, B. (2019). Tumor Microenvironment. *Medicina* 56, 15. doi:10.3390/medicina56010015

Arranja, A., Denkova, A. G., Morawska, K., Waton, G., Van Vlierberghe, S., Dubruel, P., et al. (2016). Interactions of Pluronic Nanocarriers with 2D and 3D Cell Cultures: Effects of PEO Block Length and Aggregation State. *J. Controlled Release* 224, 126–135. doi:10.1016/j.jconrel.2016.01.014

Babu, A., Templeton, A. K., Munshi, A., and Ramesh, R. (2014). Nanodrug Delivery Systems: a Promising Technology for Detection, Diagnosis, and Treatment of Cancer. *AAPS PharmSciTech* 15 (3), 709–721. doi:10.1208/s12249-014-0089-8

Bae, Y. H., and Park, K. (2011). Targeted Drug Delivery to Tumors: Myths, Reality and Possibility. *J. Controlled Release* 153 (3), 198–205. doi:10.1016/j.jconrel.2011.06.001

Baghban, R., Roshangar, L., Jahanban-Esfahlan, R., Seidi, K., Ebrahimi-Kalan, A., Jaymand, M., et al. (2020). Tumor Microenvironment Complexity and Therapeutic Implications at a Glance. *Cell commun signal* 18 (59), 1–19. doi:10.1186/s12964-020-0530-4

Baker, A., Khan, M. S., Iqbal, M. Z., and Khan, M. S. (2020). Tumor-targeted Drug Delivery by Nanocomposites. *Cdm* 21 (8), 599–613. doi:10.2174/1389200221666200520092333

Borah, A., Pillai, S. C., Rochani, A. K., Palaninathan, V., Nakajima, Y., Maekawa, T., et al. (2020). GANT61 and Curcumin-Loaded PLGA Nanoparticles for GLI1 and PI3K/Akt-Mediated Inhibition in Breast Adenocarcinoma. *Nanotechnology* 31 (18), 185102. doi:10.1088/1361-6528/ab6d20

Bussard, K. M., Mutkus, L., Stumpf, K., Gomez-Manzano, C., and Marini, F. C. (20162016). Tumor-associated Stromal Cells as Key Contributors to the Tumor Microenvironment. *Breast Cancer Res.* 18, 84. doi:10.1186/s13058-016-0740-2

Cabral, H., Matsumoto, Y., Mizuno, K., Chen, Q., Murakami, M., Kimura, M., et al. (2011). Accumulation of Sub-100 Nm Polymeric Micelles in Poorly Permeable Tumours Depends on Size. *Nat. Nanotech* 6, 815–823. doi:10.1038/NNANO.2011.166

Cabral, H., Miyata, K., Osada, K., and Kataoka, K. (2018). Block Copolymer Micelles in Nanomedicine Applications. *Chem. Rev.* 118 (14), 6844–6892. doi:10.1021/acs.chemrev.8b00199

Cai, L., Qin, X., Xu, Z., Song, Y., Jiang, H., Wu, Y., et al. (2019). Comparison of Cytotoxicity Evaluation of Anticancer Drugs between Real-Time Cell Analysis and CCK-8 Method. *ACS Omega* 4 (7), 12036–12042. doi:10.1021/acsomega.9b01142

Waite, C. L., and Roth, C. M. (2012). Nanoscale Drug Delivery Systems for Enhanced Drug Penetration into Solid Tumors: Current Progress and Opportunities. *Crit. Rev. Biomed. Eng.* 40, 21–41. doi:10.1615/CritRevBiomedEng.v40.i1.20

Chen, D., Li, B., Cai, S., Wang, P., Peng, S., Sheng, Y., et al. (2016). Dual Targeting Luminescent Gold Nanoclusters for Tumor Imaging and Deep Tissue Therapy. *Biomaterials* 100, 1–16. doi:10.1016/j.biomaterials.2016.05.017

Chen, G., Ma, B., Wang, Y., Xie, R., Li, C., Dou, K., et al. (2017). CuS-Based Theranostic Micelles for NIR-Controlled Combination Chemotherapy and Photothermal Therapy and Photoacoustic Imaging. *ACS Appl. Mater. Inter.* 9 (48), 41700–41711. doi:10.1021/acsami.7b14083

Cheng, X., Zeng, X., Li, D., Wang, X., Sun, M., He, L., et al. (2019). TPGS-grafted and Acid-Responsive Soy Protein Nanogels for Efficient Intracellular Drug Release, Accumulation, Penetration in 3D Tumor Spheroids of Drug-Resistant

Cancer Cells. *Mater. Sci. Eng. C Mater. Biol. Appl.* 102, 863–875. doi:10.1016/j.msec.2019.05.017:

Choi, I. K., Strauss, R., Richter, M., Yun, C. O., and Lieber, A. (2013). Strategies to Increase Drug Penetration in Solid Tumors. *Front. Oncol.* doi:10.3389/fonc.2013.00193

Chou, C.-Y., Huang, C.-K., Lu, K.-W., Horng, T.-L., and Lin, W.-L. (2013). Investigation of the Spatiotemporal Responses of Nanoparticles in Tumor Tissues with a Small-Scale Mathematical Model. *PLoS ONE* 8 (4), e59135. doi:10.1371/journal.pone.0059135

Costa, E. C., Gaspar, V. M., Coutinho, P., and Correia, I. J. (2014). Optimization of Liquid Overlay Technique to Formulate Heterogenic 3D Co-cultures Models. *Biotechnol. Bioeng.* 111 (8), 1672–1685. doi:10.1002/bit.25210

Costa, E. C., Moreira, A. F., de Melo-Diogo, D., Gaspar, V. M., Carvalho, M. P., and Correia, I. J. (2016). 3D Tumor Spheroids: an Overview on the Tools and Techniques Used for Their Analysis. *Biotechnol. Adv.* 34, 1427–1441. doi:10.1016/j.biotechadv.2016.11.002

Costa, M. C. F., Marangoni, V. S., Trushin, M., Carvalho, A., Lim, S. X., Nguyen, H. T. L., et al. (2021). 2D Electrolytes: Theory, Modeling, Synthesis, and Characterization. *Adv. Mater.* 33 (25), 2100442. doi:10.1002/adma.202100442

Curtis, L. T., England, C. G., Wu, M., Lowengrub, J., and Frieboes, H. B. (2016). An Interdisciplinary Computational/experimental Approach to Evaluate Drug-Loaded Gold Nanoparticle Tumor Cytotoxicity. *Nanomedicine* 11 (3), 197–216. doi:10.2217/nnm.15.195

Dai, Z., Yu, M., Yi, X., Wu, Z., Tian, F., Miao, Y., et al. (2019). Chain-Length- and Saturation-Tuned Mechanics of Fluid Nanovesicles Direct Tumor Delivery. *ACS Nano* 13 (7), 7676–7689. doi:10.1021/acsnano.9b01181

Danquah, M. K., Zhang, X. A., and Mahato, R. I. (2011). Extravasation of Polymeric Nanomedicines across Tumor Vasculature. *Adv. Drug Deliv. Rev.* 63 (8), 623–639. doi:10.1016/j.addr.2010.11.005

Donahue, N. D., Acar, H., and Wilhelm, S. (2019). Concepts of Nanoparticle Cellular Uptake, Intracellular Trafficking, and Kinetics in Nanomedicine. *Adv. Drug Deliv. Rev.* 143, 68–96. doi:10.1016/j.addr.2019.04.008

Duncan, R., and Gaspar, R. (2011). Nanomedicine(s) under the Microscope. *Mol. Pharmaceutics* 8 (6), 2101–2141. doi:10.1021/mp200394t

Eble, J. A., and Niland, S. (2019). The Extracellular Matrix in Tumor Progression and Metastasis. *Clin. Exp. Metastasis* 36 (3), 171–198. doi:10.1007/s10585-019-09966-1

Ekert, J. E., Johnson, K., Strake, B., Pardinas, J., Jarantow, S., Perkinson, R., et al. (2014). Three-Dimensional Lung Tumor Microenvironment Modulates Therapeutic Compound Responsiveness *In Vitro* - Implication for Drug Development. *PLoS One* 9 (3), e92248. doi:10.1371/journal.pone.0092248

England, C. G., Priest, T., Zhang, G., Sun, X., Patel, D. N., McNally, L. R., et al. (2013). Enhanced Penetration into 3D Cell Culture Using Two and Three Layered Gold Nanoparticles. *Int. J. Nanomedicine.* 8, 3603–3617. doi:10.2147/IJN.S51668

Fang, J., Nakamura, H., and Maeda, H. (2011). The EPR Effect: Unique Features of Tumor Blood Vessels for Drug Delivery, Factors Involved, and Limitations and Augmentation of the Effect. *Adv. Drug Deliv. Rev.* 63 (3), 136–151. doi:10.1016/j.addr.2010.04.009

Ferreira, P. L., Gaspar, M. Vitor., and Monteiro, V. M. (2021). Screening of Dual Chemo-Photothermal Cellular Nanotherapies in Organotypic Breast Cancer 3D Spheroids. *J. Control. Release* 10331, 85–102. doi:10.1016/j.jconrel.2020.12.054

Frankel, T., Lanfranca, M. P., and Zou, W. (2017). The Role of Tumor Microenvironment in Cancer Immunotherapy. *Adv. Exp. Med. Biol.* 1036, 51–64. doi:10.1007/978-3-319-67577-0_4

Frantz, C., Stewart, K. M., and Weaver, V. M. (2010). The Extracellular Matrix at a Glance. *J. Cel Sci* 123 (Pt 24), 4195–4200. doi:10.1242/jcs.023820

Gao, Y., Li, M., Chen, B., Shen, Z., Guo, P., Wientjes, M. G., et al. (2013). Predictive Models of Diffusive Nanoparticle Transport in 3-Dimensional Tumor Cell Spheroids. *AAPS J.* 15. doi:10.1208/s12248-013-9478-2

Gavhane, Y. N., Shete, A. S., Bhagat, A. K., Shinde, V. R., Bhong, K. K., Khairnar, G. A., et al. (2011). Solid Tumors: Facts, Challenges and Solutions. *Int. J. Pharma Sci. Res. (Ijpsr)* 2 (1), 1–12.

Ghosh, S. K., Kundu, T., and Sain, A. (2012). From Chemosensing in Microorganisms to Practical Biosensors. *Phys. Rev. E.* 86, 51910–51915. doi:10.1103/PhysRevE.86.051910

Ghosh, S. K., Grebenkov, D., Cherstvy, A., and Metzler, R. (2014). Deformation Propagation in Responsive Polymer Network Films. *J. Chem. Phys.* 141, 74903–74911. doi:10.1063/1.4893056

Ghosh, S. K., Cherstvy, A., and Metzler, R. (2015). Non-universal Tracer Diffusion in Crowded media of Non-inert Obstacles. *Phys. Chem. Chem. Phys.* 17, 1847–1858. doi:10.1039/c4cp03599b

Ghosh, S. K., Grebenkov, D., Cherstvy, A., and Metzler, R. (2016). Anomalous, Non-gaussian Tracer Diffusion in Crowded Two-Dimensional Environments. *New J. Phys.* 18, 013027–013042. doi:10.1088/1367-2630/18/1/013027

Ghosh, S. K., Petrov, E. P., Cherstvy, A., and Metzler, R. (2016). Interactions of Rod-like Particles on Responsive Elastic Sheets. *Soft Matter* 12 (38), 7908–7919. doi:10.1039/c6sm01522k

Gianpiero, L., Patrick, C., and Simona, M. (2017). Multicellular Tumor Spheroids: a Relevant 3D Model for the *In Vitro* Preclinical Investigation of Polymer Nanomedicines. *Polym. Chem.* 8, 4947–4969. doi:10.1039/c7py00559h

Goel, S., Duda, D. G., Xu, L., Munn, L. L., Boucher, Y., Fukumura, D., et al. (2011). Normalization Of The Vasculature For Treatment Of Cancer And Other Diseases. *Physiol. Rev.* 91 (3), 1071–1121. doi:10.1152/physrev.00038.2010

Goodman, T. T., Chen, J., Matveev, K., and Pun, S. H. (2008). Satio-Temporal Modeling of Nanoparticle Delivery to Multicellular Tumor Spheroids. *Biotechnol. Bioeng.* 101. doi:10.1002/bit.21910

Graff, C. P., and Wittrup, K. D. (2003). Theoretical Analysis of Antibody Targeting of Tumor Spheroids: Importance of Dosage for Penetration, and Affinity for Retention. *Cancer Res.* 63, 1288–1296.

Greish, K. (2007). Enhanced Permeability and Retention of Macromolecular Drugs in Solid Tumors: a Royal Gate for Targeted Anticancer Nanomedicines. *J. Drug Target.* 15 (7-8), 457–464. doi:10.1080/10611860701539584

Han, S. J., Kwon, S., and Kim, K. S. (2021). Challenges of Applying Multicellular Tumor Spheroids in Preclinical Phase. *Cancer Cel Int* 21 (1), 152. doi:10.1186/s12935-021-01853-8

Heldin, C. H., Rubin, K., Pietras, K., and Östman, A. (2004). High Interstitial Fluid Pressure - an Obstacle in Cancer Therapy. *Nat. Rev. Cancer* 4 (10), 806–813. doi:10.1038/nrc1456

Hompland, T., Fjeldbo, C. S., and Lyng, H. (2021). Tumor Hypoxia as a Barrier in Cancer Therapy: Why Levels Matter. *Cancers (Basel)* 13 (3), 499. doi:10.3390/cancers13030499

Hori, S. S., Tong, L., Swaminathan, S., Liebersbach, M., Wang, J., Gambhir, S. S., et al. (2021). A Mathematical Model of Tumor Regression and Recurrence after Therapeutic Oncogene Inactivation. *Sci. Rep.* 11, 1341. doi:10.1038/s41598-020-78947-2

Huang, K., Ma, H., Liu, J., Huo, S., Kumar, A., Wei, T., et al. (2012). Size-dependent Localization and Penetration of Ultrasmall Gold Nanoparticles in Cancer Cells, Multicellular Spheroids, and Tumors *In Vivo*. *ACS Nano* 6 (5), 4483–4493. doi:10.1021/nn301282m

Hynes, R. O. (2009). Extracellular Matrix: Not Just Pretty Fibrils. *Science* 326, 1216–1219. doi:10.1126/science.1176009

Hynes, R. O. (2013). Extracellular Matrix: Not Just Pretty Fibrils. *Science* 326, 1216–1219. doi:10.1126/science.1176009

Iqbal, J., Anwar, F., and Afridi, S. (2017). Targeted Drug Delivery Systems and Their Therapeutic Applications in Cancer and Immune Pathological Conditions. *Infect. Disord. Drug Targets* 17 (3), 149–159. doi:10.2174/1871526517666170606102623

Ishiguro, T., Ohata, H ., Sato, A ., Yamawaki, k., Enomoto, T., and Okamoto, K. (2017). Tumor-derived Spheroids: Relevance to Cancer Stem Cells and Clinical Applications. *Cancer Sci.* 108 (3), 283–289. doi:10.1111/cas.13155

Jain, R. K., and Stylianopoulos, T. (2010). Delivering Nanomedicine to Solid Tumors. *Nat. Rev. Clin. Oncol.* 7 (11), 653–664. doi:10.1038/nrclinonc.2010.139

John, D. M., Horacio, C., Triantafyllos, S., and RakeshJain, K. (2020). Improving Cancer Immunotherapy Using Nanomedicines: Progress, Opportunities and Challenges. *Nat. Rev. Clin. Oncol.* 17 (4), 251–266. doi:10.1038/s41571-019-0308-z

Junttila, M. R., and Sauvage, F. J. de. (2013). Influence of Tumour Micro-environment Heterogeneity on Therapeutic Response. *Nature* 501, 346–354. doi:10.1038/nature12626

Kalluri, R. (2016). The Biology and Function of Fibroblasts in Cancer. *Nat. Rev. Cancer* 16 (9), 582–598. doi:10.1038/nrc.2016.73

Kang, T., Zhu, Q., Jiang, D., Feng, X., Feng, J., Jiang, T., et al. (2016). Synergistic Targeting Tenascin C and Neuropilin-1 for Specific Penetration of Nanoparticles for Anti-glioblastoma Treatment. *Biomaterials* 101, 60–75. doi:10.1016/j.biomaterials.2016.05.037

Kapałczyńska, M., Kolenda, T., Przybyła, W., Zajączkowska, M., Teresiak, A., Filas, V., et al. (2018). 2D and 3D Cell Cultures - a Comparison of Different Types of Cancer Cell Cultures. *Arch. Med. Sci.* 14 (4), 910–919. doi:10.5114/aoms.2016.63743

Karsch-Bluman, A., and Benny, O. (2020). Necrosis in the Tumor Microenvironment and its Role in Cancer Recurrence. *Adv. Exp. Med. Biol.* 1225, 89–98. doi:10.1007/978-3-030-35727-6_6

Karsch-Bluman, A., Feiglin, A., Arbib, E., Stern, T., Shoval, H., Schwob, O., et al. (2019). Tissue Necrosis and its Role in Cancer Progression. *Oncogen* 38 (11), 1920–1935. doi:10.1038/s41388-018-0555-y

Ke, W., Yin, W., Zha, Z., Mukerabigwi, J. F., Chen, W., Wang, Y., et al. (2018). A Robust Strategy for Preparation of Sequential Stimuli-Responsive Block Copolymer Prodrugs via Thiolactone Chemistry to Overcome Multiple Anticancer Drug Delivery Barriers. *Biomaterials* 154, 261–274. doi:10.1016/j.biomaterials.2017.11.006

Kim, J., and Bae, J. S. (2016). Tumor-Associated Macrophages and Neutrophils in Tumor Microenvironment. *Mediators Inflamm.* 2016, 6058147. doi:10.1155/2016/6058147.3

Kim, Y., and Stolarska, M. A. (2007). A Hybrid Model for Tumor Spheroid Growth *In Vitro* I: Theoretical Development and Early Results. *Math. Models Methods Appl. Sci.* 17, 1773–1798. doi:10.1142/S0218202507002479

Kim, S. H., Turnbull, J., and Guimond, S. (2011). Extracellular Matrix and Cell Signalling: the Dynamic Cooperation of Integrin, Proteoglycan and Growth Factor Receptor. *J. Endocrinol.* 209 (2), 139–151. doi:10.1530/JOE-10-0377

Kim, S. W., Park, K. C., Jeon, S. M., Ohn, T. B., Kim, T. I., Kim, W. H., et al. (2013). Tumour-microenvironment Interactions: Role of Tumour Stroma and Proteins Produced by Cancer-Associated Fibroblasts in Chemotherapy Response. *Cel Oncol (Dordr)* 36 (2), 95–112. doi:10.1007/s13402-013-0127-7

Kostarelos, K., Emfietzoglou, D., Papakostas, A., Yang, W-H., Ballangrud, A., and Sgouros, G. (2004). Binding and Interstitial Penetration of Liposomes within Avascular Tumor Spheroids. *Int. J. Cancer* 112, 4, 713–721. doi:10.1002/ijc.20457

Kudláčová, J., Kotrchová, L., Kostka, L., Randárová, E., Filipová, M., Janoušková, O., et al. (2020). Structure-to-Efficacy Relationship of HPMA-Based Nanomedicines: The Tumor Spheroid Penetration Study. *Pharmaceutics* 12 (12), 1242. doi:10.3390/pharmaceutics12121242

Kumari, P., Paul, M., Bhatt, H., Rompicherla, S. V. K., Sarkar, D., Ghosh, B., et al. (2020). Chlorin e6 Conjugated Methoxy-Poly(Ethylene Glycol)-Poly(D,L-Lactide) Glutathione Sensitive Micelles for Photodynamic Therapy. *Pharm. Res.* 37 (2), 18. doi:10.1007/s11095-019-2750-0

Kusumoto, H., Maehara, Y., Sakaguchi, Y., Kohnoe, S ., Kumashiro, R., and Sugimach, k. (1990). Modulation of Cytotoxic Effect of Anticancer Drugs by Dipyridamole in HeLa Cells *In Vitro*. *Anticancer Res.* 10 (6), 1643–1645.

Laird, A. (1964). Dynamics of Tumor Growth. *Br. J. Cancer* 18, 490–502. doi:10.1038/bjc.1964.55

Lane, L. A., Qian, Ximei., Smith, A. M., and Nie, S. (2015). Physical Chemistry of Nanomedicine: Understanding the Complex Behaviors of Nanoparticles *In Vivo*. *Annu. Rev. Phys. Chem.* 66, 521–547. doi:10.1146/annurev-physchem-040513-103718

Larionova, I., Cherdyntseva, N., Liu, T., Patysheva, M., Rakina, M., and Kzhyshkowska, J. (2019). Interaction of Tumor-Associated Macrophages and Cancer Chemotherapy. *Oncoimmunology* 8 (7). doi:10.1080/2162402X.2019.1596004

Lazzari, G., Couvreura, P., and Mura, S. (2017). Multicellular Tumor Spheroids: a Relevant 3D Model for the *In Vitro* Preclinical Investigation of Polymer Nanomedicines. *Polym. Chem.* 8, 4947. doi:10.1039/c7py00559h

Lee, S. W., Kwak, H. S., Kang, M. H., Park, Y. Y., and Jeong, G. S. (2018). Fibroblast-associated Tumour Microenvironment Induces Vascular Structure-Networked Tumouroid. *Sci. Rep.* 8 (1), 2365. doi:10.1038/s41598-018-20886-0

Li, S-D., and Huang, L, (2009). Nanoparticles Evading the Reticuloendothelial System: Role of the Supported Bilayer. *Biochim. Biophys. Acta* 1788 (10), 2259–2266. doi:10.1016/j.bbamem.2009.06.022

Li, X. T., Lin, C., and Li, P. Y. (1986). Comparison of *In Vitro* Assays for the Cytotoxic Effect of Anticancer Drugs. *Zhonghua Zhong Liu Za Zhi* 8 (3), 184–186.

Li, T. F., Li, K., Wang, C., Liu, X., Wen, Y., Xu, Y. H., et al. (2017a). Harnessing the Cross-Talk between Tumor Cells and Tumor-Associated Macrophages with a Nano-Drug for Modulation of Glioblastoma Immune Microenvironment. *J. controlled release* 268:128–146. doi:10.1016/j.jconrel.2017.10.024

Li, Z., Tan, S., Li, S., Shen, Q., and Wang, K. (2017b). Cancer Drug Delivery in the Nano Era: An Overview and Perspectives. *Oncol. Rep.* 611–624. doi:10.3892/or.2017.5718

Li, T., Kang, G., Wang, T., and Huang, H. E. (2018). Tumor Angiogenesis and Anti-angiogenic Gene Therapy for Cancer. *Oncol. Lett.* 16 (1), 687–702. doi:10.3892/ol.2018.8733

Liang, J., and Liu, B. (2016). ROS-responsive Drug Delivery Systems. *Bioeng. Transl Med.* 1 (3), 239–251. doi:10.1002/btm2.10014

Lin, R-Z., and Chang, H-Y. (2008). Recent Advances in Three-Dimensional Multicellular Spheroid Culture for Biomedical Research. *Biotechnol. J.* 3, 1172. doi:10.1002/biot.200700228

Lin, Y., Xu, J., and Lan, H. (2019). Tumor-associated Macrophages in Tumor Metastasis: Biological Roles and Clinical Therapeutic Applications. *J. Hematol. Oncol.* 12 (176), 1–16. doi:10.1186/s13045-019-0760-3

Liu, Y., Tan, J., Thomas, A., Ou-Yang, D., and Muzykantov, V. R. (2012). The Shape of Things to Come: Importance of Design in Nanotechnology for Drug Delivery. *Ther. Deliv.* (2), 181–194. doi:10.4155/tde.11.156

Liu, X., Li, W., Chen, T., Yang, Q., Huang, T., Fu, Y., et al. (2018). Hyaluronic Acid-Modified Micelles Encapsulating Gem-C 12 and HNK for Glioblastoma Multiforme Chemotherapy. *Mol. Pharmaceutics* 15 (3), 1203–1214. doi:10.1021/acs.molpharmaceut.7b01035

Liu, D., Zhang, Q., Wang, J., Fan, L., Zhu, W., and Cai, D. (2019). Hyaluronic Acid-Coated Single-Walled Carbon Nanotubes Loaded with Doxorubicin for the Treatment of Breast Cancer. *Die Pharmazie* 74 (2), 83–90. doi:10.1691/ph.2019.8152

Liu, T., Han, C., Wang, S., Fang, P., Ma, Z., Xu, L., et al. (2019). Cancer-associated Fibroblasts: an Emerging Target of Anti-cancer Immunotherapy. *J. Hematol. Oncol.* 12 (86), 1–15. doi:10.1186/s13045-019-0770-1

Lu, P., and Weaver, V. M. (2012). The Extracellular Matrix: a Dynamic Niche in Cancer Progression. *J. Cel Biol* 196 (4), 395–406. doi:10.1083/jcb.201102147

Lu, P., Weaver, P. M., and Crossmark, Z. W. (2012). The Extracellular Matrix: A Dynamic Niche in Cancer Progression. *J. Cel Biol* 196 (4), 395–406. doi:10.1083/jcb.201102147

Lu, H., Utama, R. H., Kitiyotsawat, U., Babiuch, K., Jiang, Y., and Stenzel, M. H. (2014). Enhanced Transcellular Penetration and Drug Delivery by Crosslinked Polymeric Micelles into Pancreatic Multicellular Tumor Spheroids. *Biomater. Sci.* 3, 1085. doi:10.1039/c4bm00323c

Lugano, R., Ramachandran, M., and Dimberg, A. (2020). Tumor Angiogenesis: Causes, Consequences, Challenges and Opportunities. *Cell Mol Life Sci* 77 (9), 1745–1770. doi:10.1007/s00018-019-03351-7

Maeda, H., Nakamura, H., and Fang, J. (2013). The EPR Effect for Macromolecular Drug Delivery to Solid Tumors: Improvement of Tumor Uptake, Lowering of Systemic Toxicity, and Distinct Tumor Imaging *In Vivo*. *Adv. Drug Deliv. Rev.* 65 (1), 71–79. doi:10.1016/j.addr.2012.10.002

Maeda, H., Tsukigawa, K., and Fang, J. (2016). A Retrospective 30 Years after Discovery of the Enhanced Permeability and Retention Effect of Solid Tumors: Next-Generation Chemotherapeutics and Photodynamic Therapy--Problems, Solutions, and Prospects. *Microcirculation* 23 (3), 173–182. doi:10.1111/micc.12228

Maeda, H. (2012). Vascular Permeability in Cancer and Infection as Related to Macromolecular Drug Delivery, with Emphasis on the EPR Effect for Tumor-Selective Drug Targeting. *Proc. Jpn. Acad. Ser. B Phys. Biol. Sci.* 88 (3), 53–71. doi:10.2183/pjab.88.53

Maity, A. R., and Stepensky, D. (2016). Limited Efficiency of Drug Delivery to Specific Intracellular Organelles Using Subcellularly "Targeted" Drug Delivery Systems. *Mol. Pharm.* 13 (1), 1–7. doi:10.1021/acs.molpharmaceut.5b00697

Maity, A. R., and Stepensky, D. (2016). Delivery of Drugs to Intracellular Organelles Using Drug Delivery Systems: Analysis of Research Trends and

Targeting Efficiencies. *Int. J. Pharm.* 496, 268–274. doi:10.1016/j.ijpharm.2015.10.053

Marchal, S., Hor, A. E., Millard, M., Gillon, V., and Lina, B. (2015). Anticancer Drug Delivery: an Update on Clinically Applied Nanotherapeutics. *Drugs* 75 (14), 1601–1611. doi:10.1007/s40265-015-0453-3

Mark, E., Mami, M., Aniruddha, R., and Shyh-Dar, L. (2013). Factors Controlling the Pharmacokinetics, Biodistribution and Intratumoral Penetration of Nanoparticles. *J. Control. Release* 172 (3), 782–794. doi:10.1016/j.jconrel.2013.09.013

Markman, J. L., Rekechenetskiy, A., Holler, E., and Ljubimova, J. Y. (2013). Nanomedicine Therapeutic Approaches to Overcome Cancer Drug Resistance. *Adv. Drug Deliv. Rev.* 65 (13-14), 1866–1879. doi:10.1016/j.addr.2013.09.019

Martin, J. D., Cabral, H., Stylianopoulos, T., and Jain, R. K. (2017). Tumor-targeted Nanomedicines for Cancer Theranostics. *Pharmacol. Res.* 115, 87–95. doi:10.1016/j.phrs.2016.11.014

Masoud, G. N., and Li, W. (2015). HIF-1α Pathway: Role, Regulation and Intervention for Cancer Therapy. *Acta Pharm. Sin B* 5 (5), 378–389. doi:10.1016/j.apsb.2015.05.007

Masucci, M. T., Minopoli, M., and Carriero, M. V. (2019). Tumor Associated Neutrophils. Their Role in Tumorigenesis, Metastasis, Prognosis and Therapy. *Front. Oncol.* 9, 1146. doi:10.3389/fonc.2019.01146

Mehta, G., Hsiao, A. Y., Ingram, M., Luker, G. D., and Takayama, S. (2012). Opportunities and Challenges for Use of Tumor Spheroids as Models to Test Drug Delivery and Efficacy. *J. Control. Release* 164 (2), 192–204. doi:10.1016/j.jconrel.2012.04.045

Mikhail, A. S., Eetezadi, S., Ekdawi, S. N., Stewart, J., and Allen, C. (2014). Image-based Analysis of the Size- and Time-dependent Penetration of Polymeric Micelles in Multicellular Tumor Spheroids and Tumor Xenografts. *Int. J. Pharm.* 464 (1-2), 168–177. doi:10.1016/j.ijpharm.2014.01.010

Millard, M., Yakavets, I., Zorin, V., Kulmukhamedova, A., Marchal, S., and Bezdetnaya, L. (2017). Drug Delivery to Solid Tumors: the Predictive Value of the Multicellular Tumor Spheroid Model for Nanomedicine Screening. *Int. J. Nanomedicine* 12, 7993. doi:10.2147/IJN.S146927

Mizukami, Y., Sasajima, J., Ashida, T., and Kohgo, Y. (2012). Normal Tumor Vasculatures and Bone Marrow-Derived Pro-angiogenic Cells in Cancer. *Int. J. Hematol.* 95 (2), 125–130. doi:10.1007/s12185-012-1017-x

Mo, J., Sun, B., Zhao, X., Gu, Q., Dong, X., Liu, Z., et al. (2013). The *In-Vitro* Spheroid Culture Induces a More Highly Differentiated but Tumorigenic Population from Melanoma Cell Lines. *Melanoma Res.* 23 (4), 254–263. doi:10.1097/CMR.0b013e32836314e3

Mo, L., Zhao, Z., Hu, X., Yu, X., Peng, Y., Liu, H., et al. (2019). Smart Nanodrug with Nuclear Localization Sequences in the Presence of MMP-2 to Overcome Biobarriers and Drug Resistance. *Chemistry* 25 (8), 1895–1900. doi:10.1002/chem.201805107

Monteran, L., and Erez, N. (2019). The Dark Side of Fibroblasts: Cancer-Associated Fibroblasts as Mediators of Immunosuppression in the Tumor Microenvironment. *Front. Immunol.* 10, 1835. doi:10.3389/fimmu.2019.01835

Mu, C. F., Shen, J., Liang, J., Zheng, H. S., Xiong, Y., Wei, Y. H., et al. (2018). Targeted Drug Delivery for Tumor Therapy inside the Bone Marrow. *Biomaterials* 155, 191–202. doi:10.1016/j.biomaterials.2017.11.029

Mullis, A. S., Broderick, S. R ., Binnebose, A. M., Peroutka-Bigus, N., Bellaire, B. H., Ranjan, K., et al. (2019). Data Analytics Approach for Rational Design of Nanomedicines with Programmable Drug Release. *Mol. Pharm.* 16 (5), 1917–1928. doi:10.1021/acs.molpharmaceut.8b01272

Musetti, S., and Huang, L. (2018). Nanoparticle-Mediated Remodeling of the Tumor Microenvironment to Enhance Immunotherapy. *ACS Nano* 12 (12), 11740–11755. doi:10.1021/acsnano.8b05893

Nagesetti, A., Dulikravich, S. G., and Orlande, B. R. H. (2021). Computational Model of Silica Nanoparticle Penetration into Tumor Spheroids: Effects of Methoxy and Carboxy PEG Surface Functionalization and Hyperthermia. *Int. Numer. Methods Biomed. Eng.* 37 (8), e3504. doi:10.1002/cnm.3504

Nakamura, T., and Harashima, H. (2017). Integration of Nano Drug-Delivery System with Cancer Immunotherapy. *Ther. Deliv.* 8 (11), 987–1000. doi:10.4155/tde-2017-0071

Nath, S., and Devi, G. R. (2016). Three-dimensional Culture Systems in Cancer Research: Focus on Tumor Spheroid Model. *Pharmacol. Ther.* 163, 94–108. doi:10.1016/j.pharmthera.2016.03.013

Netti, P. A., Berk, D. A., Swartz, M. A., Grodzinsky, A. J., and Jain, R. K. (2000). Role of Extracellular Matrix Assembly in Interstitial Transport in Solid Tumors. *Cancer Res.* 60 (9), 2497–2503.

Nie, D., Dai, Z., Li, J., Yang, Y., Xi, Z., Wang, J., et al. (2020). Cancer-Cell-Membrane-Coated Nanoparticles with a Yolk-Shell Structure Augment Cancer Chemotherapy. *Nano Lett.* 20 (2), 936–946. doi:10.1021/acs.nanolett.9b03817

Nie, S. (2010). Understanding and Overcoming Major Barriers in Cancer Nanomedicine. *Nanomedicine (Lond).* 5 (4), 523–528. doi:10.2217/nnm.10.23

Norris, E. S., King, J. R., and Byrne, H. M. (2006). Mathematical and Computer Modelling Modelling the Response of Spatially Structured Tumors to Chemotherapy: Drug Kinetics. *Math. Comput. Model.* 43 (7–8), 820–837. doi:10.1016/j.mcm.2005.09.026

Noy, R., and Pollard, J. W. (2014). Tumor-associated Macrophages: from Mechanisms to Therapy. *Immunity* 41 (1), 49–61. doi:10.1016/j.immuni.2014.06.010

Nunes, A. S., Barros, A. S., Costa, E. C., Moreira, A. F., and Correia, I. J. (2019). 3D Tumor Spheroids as *In Vitro* Models to Mimic *In Vivo* Human Solid Tumors Resistance to Therapeutic Drugs. *Biotechnol. Bioeng.* 116 (1), 206–226. doi:10.1002/bit.26845

Onoue, S., Yamada, S., and Chan, H-k. (2014). Nanodrugs: Pharmacokinetics and Safety. *Int. J. Nanomedicine* 20 (9), 1025–1037. doi:10.2147/IJN.S38378

Patel, N. R., Aryasomayajula, B., Abouzeid, A. H., and Torchilin, V. P . (2015). Cancer Cell Spheroids for Screening of Chemotherapeutics and Drug-Delivery Systems. *Ther. Deliv.* 6 (4), 509–520. doi:10.4155/tde.15.1

Pattni, B. S., Nagelli, S. G., Aryasomayajula, B., Deshpande, P. P., Kulkarni, A., Hartner, W. C., et al. (2016). Targeting of Micelles and Liposomes Loaded with the Pro-apoptotic Drug, NCL-240, into NCI/ADR-RES Cells in a 3D Spheroid Model. *Pharm. Res.* 33 (10), 2540–2551. doi:10.1007/s11095-016-1978-1

Pickup, M. W., Mouw, J. K., and Weaver, V. M. (2014). The Extracellular Matrix Modulates the Hallmarks of Cancer. *EMBO Rep.*(12), 1243–1253. doi:10.15252/embr.201439246

Popilski, H., and Stepensky, D. (2015). Mathematical Modeling Analysis of Intratumoral Disposition of Anticancer Agents and Drug Delivery Systems. *Expert Opin. Drug Metab. Toxicol.* 11 (5), 767–784. doi:10.1517/17425255.2015.1030391

Prabhakar, U., Maeda, H., Jain, R. K., Sevick-Muraca, E. M., Zamboni, W., Farokhzad, O. C., . . ., and Blakey, D. C. (2013). Challenges and Key Considerations of the Enhanced Permeability and Retention Effect for Nanomedicine Drug Delivery in Oncology. *Cancer Res.* 73 (8), 2412–2417. doi:10.1158/0008-5472.CAN-12-4561

Prokop, A., and Davidson, J. M. (2008). Nanovehicular Intracellular Delivery Systems. *J. Pharm. Sci.* 97 (9), 3518–3590. doi:10.1002/jps.21270

Qian, B., Deng, Y., Im, J. H., Muschel, R. J., Zou, Y., Li, J., et al. (2009). A Distinct Macrophage Population Mediates Metastatic Breast Cancer Cell Extravasation, Establishment and Growth. *PLoS ONE* 4 (8), 1–16. doi:10.1371/journal.pone.0006562

Rane, D. T., and Armani, M. A. (2016). Two-Photon Microscopy Analysis of Gold Nanoparticle Uptake in 3D Cell Spheroids. *Plos one*, 1–13. doi:10.1371/journal.pone.0167548

Ray, P., Ferraro, M., Haag, R., and Quadir (2019). Dendritic Polyglycerol-Derived Nano-Architectures as Delivery Platforms of Gemcitabine for Pancreatic Cancer. *Macromolecular Biosci.* 19 (7), e1900073. doi:10.1002/mabi.201900073

Raza, A., Hayat, U., Rasheed, T., Bilal, M., and Iqbal, H. M. (2018). Redox-responsive Nano-Carriers as Tumor-Targeted Drug Delivery Systems. *Eur. J. Med. Chem.* 157, 705–715. doi:10.1016/j.ejmech.2018.08.034

Sant, S., and Johnston, P. A. (2017). The Production of 3D Tumor Spheroids for Cancer Drug Discovery. *Drug Discov. Today Technol.* 23, 27–36. doi:10.1016/j.ddtec.2017.03.002

Sarisozen, C., Dhokai, S., Tsikudo, E. G., Luther, E., Rachman, I. M., and Torchilin, V. P. (2016). Nanomedicine Based Curcumin and Doxorubicin Combination Treatment of Glioblastoma with scFv-Targeted Micelles: *In Vitro* Evaluation on 2D and 3D Tumor Models. *Eur. J. pharmaceutics biopharmaceutics* 108, 54–67. doi:10.1016/j.ejpb.2016.08.013

Sasaki, N., Gomi, F., Hasegawa, F., Hirano, K., Fujiwara, M., Toyoda, M., et al. (2020). Characterization of the Metastatic Potential of the Floating Cell Component of MIA PaCa-2, a Human Pancreatic Cancer Cell Line.

Biochem. Biophys. Res. Commun. 522 (4), 881–888. doi:10.1016/j.bbrc.2019.11.120

Shamsi, M., Mohammadi, A., Manshadi, M. K. D., and Sanati-Nezhad, A. (2019). Mathematical and Computational Modeling of Nano-Engineered Drug Delivery Systems. *J. Control. Release* 307, 150–165. doi:10.1016/j.jconrel.2019.06.014

Sharma, A., Arambula, J. F., Koo, S., Kumar, R., Singh, H., Sessler, J. L., et al. (2019). Hypoxia-targeted Drug Delivery. *Chem. Soc. Rev.* 48 (3), 771–813. doi:10.1039/c8cs00304a

Shyh-Dar, Li., and Leaf, H. (2008). Pharmacokinetics and Biodistribution of Nanoparticles. *Mol. Pharm.* 5 (4), 496–504. doi:10.1021/mp800049w

Solomon, M. A., Lemera, J., and D'Souza, G. G. (2016). Development of an *In Vitro* Tumor Spheroid Culture Model Amenable to High-Throughput Testing of Potential Anticancer Nanotherapeutics. *J. Liposome Res.* 26 (3), 246–260. doi:10.3109/08982104.2015.1105820

Srinivasarao, M., and Low, P. S. (2017). Ligand-Targeted Drug Delivery. *Chem. Rev.* 19, 12133–12164. doi:10.1021/acs.chemrev.7b00013

Su, Y. L., Fang, J. H., Liao, C. Y., Lin, C. T., Li, Y. T., and Hu, S. H. (2015). Targeted Mesoporous Iron Oxide Nanoparticles-Encapsulated Perfluorohexane and a Hydrophobic Drug for Deep Tumor Penetration and Therapy. *Theranostics* 5 (11), 1233–1248. doi:10.7150/thno.12843

Sun, Q., Zhou, Z., Qiu, N., and Shen, Y. (2017). Rational Design of Cancer Nanomedicine: Nanoproperty Integration and Synchronization. *Adv. Mater.* 29 (14), 628. doi:10.1002/adma.201606628

Tan, X., Fang, Y., Ren, Y., Li, Y., Wu, P., Yang, X., et al. (2019). D-α-tocopherol Polyethylene Glycol 1000 Succinate-Modified Liposomes with an siRNA corona Confer Enhanced Cellular Uptake and Targeted Delivery of Doxorubicin via Tumor Priming. *Int. J. Nanomedicine* 14, 1255–1268. doi:10.2147/IJN.S191858

Tan, Y. Y., Yap, P. K., Lim, G. L, X., Mehta, M., Chan, Y., and Ng, S. W. (2020). Perspectives and Advancements in the Design of Nanomaterials for Targeted Cancer Theranostics. *Chem. Biol. Interact* 329, 109221. doi:10.1016/j.cbi.2020.109221

Tang, D., Gao, J., Wang, S., Ye, N., Chong, Y., Huang, Y., et al. (2016). Cancer-associated Fibroblasts Promote Angiogenesis in Gastric Cancer through Galectin-1 Expression. *Tumour Biol.* 37 (2), 1889–1899. doi:10.1007/s13277-015-3942-9

Taurin, S., Nehoff, H., Van Aswegen, T., Rosengren, R. J., and Greish, K. (2014). A Novel Role for Raloxifene Nanomicelles in Management of Castrate Resistant Prostate Cancer. *Biomed. Research International*, 323594. doi:10.1155/2014/323594

Tchoryk, A., Taresco, V., Argent, H. R., Ashford, M., Gellert, R. P., et al. (2019). Penetration and Uptake of Nanoparticles in 3D Tumor Spheroids. *Bioconjug. Chem* 30 (5), 1371–1384. https://doi.org/10.1021/acs.bioconjchem.9b00136

Thomas, R. G., Moon, M. J., Surendran, S. P., Park, H. J., Park, I. K., Lee, B. I., et al. (2018). MHI-148 Cyanine Dye Conjugated Chitosan Nanomicelle with NIR Light-Trigger Release Property as Cancer Targeting Theranostic Agent. *Mol. Imaging Biol.* 20 (4), 533–543. doi:10.1007/s11307-018-1169-z

Tindall, M. J., and Please, C. P. (2007). Modelling the Cell Cycle and Cell Movement in Multicellular Tumour Spheroids. *Bull. Math. Biol.* 69 (4), 1147–1165. doi:10.1007/s11538-006-9110-z

Tong, R. T., Boucher, Y., Kozin, S. V., Winkler, F., Hicklin, D. J., and Jain, R. K. (2004). Vascular Normalization by Vascular Endothelial Growth Factor Receptor 2 Blockade Induces a Pressure Gradient across the Vasculature and Improves Drug Penetration in Tumors. *Cancer Res.* 64 (11), 3731–3736. doi:10.1158/0008-5472.CAN-04-0074

Unsoy, G., and Gunduz, U. (2018). Smart Drug Delivery Systems in Cancer Therapy. *Curr. Drug Targets* 19 (3), 202–212. doi:10.2174/1389450117666160401124624

Waite, C. L., and Roth, C. M. (2012). Nanoscale Drug Delivery Systems for Enhanced Drug Penetration into Solid Tumors: Current Progress and Opportunities. *Crit. Rev. Biomed. Eng.* 40 (1), 21–41. doi:10.1615/critrevbiomedeng.v40.i1.20

Wang, A. T., Liang, D. S., Liu, Y. J., and Qi, X. R. (2015). Roles of Ligand and TPGS of Micelles in Regulating Internalization, Penetration and Accumulation against Sensitive or Resistant Tumor and Therapy for Multidrug Resistant Tumors. *Biomaterials* 53, 160–172. doi:10.1016/j.biomaterials.2015.02.077

Wang, C., Li, K., Li, T., Chen, Z., Wen, Y., Liu, X., et al. (2018). Monocyte-mediated Chemotherapy Drug Delivery in Glioblastoma. *Nanomedicine (Lond).* 13 (2), 157–178. doi:10.2217/nnm-2017-0266

Wang, J-J., Lei, K-F., and Han, F. (2018). Tumor Microenvironment: Recent Advances in Various Cancer Treatments. *Eur. Rev. Med. Pharmacol. Sci.* 22 (12), 3855–3864. doi:10.26355/eurrev_201806_15270

Wang, F. T., Sun, W., Zhang, J. T., and Fan, Y. Z. (2019). Cancer-associated Fibroblast Regulation of Tumor Neo-Angiogenesis as a Therapeutic Target in Cancer. *Oncol. Lett.* 17 (3), 3055–3065. doi:10.3892/ol.2019.9973

Wang, K., Hu, H., Zhang, Q., Zhang, Y., and Shi, C. (2019).Synthesis, Purification, and Anticancer Effect of Magnetic Fe 3 O 4-loaded Poly (Lactic-co-glycolic) Nanoparticles of the Natural Drug Tetrandrine. *J. Microencapsulation*. 36(4): 356–370. doi:10.1080/02652048.2019.1631403

Ward, J. P., and King, J. R. (1999). Mathematical Modelling of Avascular-Tumour Growth. II: Modelling Growth Saturation. *Math. Med. Biol. A J. IMA* 16 (2), 171–211. doi:10.1093/imammb/16.2.171

Ward, J. P., and King, J. R. (2003). Mathematical Modelling of Drug Transport in Tumour Multicell Spheroids and Monolayer Cultures. *Math. Biosci.* 181 (2), 177–207. doi:10.1016/s0025-5564(02)00148-7

Wicki, A., Witzigmann, D., Balasubramanian, V., and Huwyler, J. (2015). Nanomedicine in Cancer Therapy: Challenges, Opportunities, and Clinical Applications. *J. Control. Release* 200, 138–157. doi:10.1016/j.jconrel.2014.12.030

Wilhelm, C., Gazeau, F., Roger, J., Pons, J. N., and Bacri, J. C. (2002). Interaction of Anionic Superparamagnetic Nanoparticles with Cells: Kinetic Analyses of Membrane Adsorption and Subsequent Internalization. *Langmuir* 18 (21), 8148–8155. doi:10.1021/la0257337

Wojnilowicz, M., Besford, Q. A., Wu, Y. L., Loh, X. J., Braunger, J. A., Glab, A., et al. (2018). Glycogen-nucleic Acid Constructs for Gene Silencing in Multicellular Tumor Spheroids. *Biomaterials* 176, 34–49. doi:10.1016/j.biomaterials.2018.05.024

Wu, L., Saxena, S., Awaji, M., and Singh, R. K. (2019). Tumor-Associated Neutrophils in Cancer: Going Pro. *Cancers (Basel)* 11 (4), 564. doi:10.3390/cancers11040564

Wu, H., Sarfati, R., Wang, D., and Schwartz, D. K. (2020). Electrostatic Barriers to Nanoparticle Accessibility of a Porous Matrix. *J. Am. Chem. Soc.* 142, 4696–4704. doi:10.1021/jacs.9b12096

Xie, X., Chen, Y., Chen, Z., Feng, Y., Wang, J., Li, T., et al. (2019). Polymeric Hybrid Nanomicelles for Cancer Theranostics: An Efficient and Precise Anticancer Strategy for the Codelivery of Doxorubicin/miR-34a and Magnetic Resonance Imaging. *ACS Appl. Mater. Inter.* 11 (47), 43865–43878. doi:10.1021/acsami.9b14908

Xu, H. L., Fan, Z. L., ZhuGe, D. L., Shen, B. X., Jin, B. H., and Xiao, J. (2017). Therapeutic Supermolecular Micelles of Vitamin E Succinate-Grafted ε-polylysine as Potential Carriers for Curcumin: Enhancing Tumour Penetration and Improving Therapeutic Effect on Glioma. *Colloids Surfaces. B, Biointerfaces.* 158, 295–307. doi:10.1016/j.colsurfb.2017.07.019

Yang, Q., Yang, Y., Li, L., Sun, W., Zhu, X., and Huang, Y . (2015). Polymeric Nanomedicine for Tumor-Targeted Combination Therapy to Elicit Synergistic Genotoxicity against Prostate Cancer. *ACS Appl. Mater. Inter.* 7 (12), 6661–6673. doi:10.1021/am509204u

Yao, Q., Choi, J. H., Dai, Z., Wang, J., Kim, D., Tang, X., et al. (2017a). Improving Tumor Specificity and Anticancer Activity of Dasatinib by Dual-Targeted Polymeric Micelles. *ACS Appl. Mater. andInterfaces* 9 (42), 36642–36654. doi:10.1021/acsami.7b12233

Yao, Q., Dai, Z., Hoon Choi, J., Kim, D., and Zhu, L. (2017b). Building Stable MMP2-Responsive Multifunctional Polymeric Micelles by an All-In-One Polymer-Lipid Conjugate for Tumor-Targeted Intracellular Drug Delivery. *ACS Appl. Mater. Inter.* 9 (38), 32520–32533. doi:10.1021/acsami.7b09511

Yavuz, B. G., Gunaydin, G., Gedik, M. E., Kosemehmetoglu, K., Karakoc, D., Ozgur, F., et al. (2019). Cancer Associated Fibroblasts Sculpt Tumour Microenvironment by Recruiting Monocytes and Inducing Immunosuppressive PD-1+ TAMs. *Nature* 9, 1–15. doi:10.1038/s41598-019-39553-z

Zhang, Y., Zhang, C., Chen, J., Liu, L., Hu, M., Li, J., et al. (2017). Trackable Mitochondria-Targeting Nanomicellar Loaded with Doxorubicin for Overcoming Drug Resistance. *ACS Appl. Mater. Inter.* 9 (30), 25152–25163. doi:10.1021/acsami.7b07219

Zhao, J., Liu, P., Ma, J., Li, D., Yang, H., Chen, W., et al. (2019). Enhancement of Radiosensitization by Silver Nanoparticles Functionalized with Polyethylene

Glycol and Aptamer As1411 for Glioma Irradiation Therapy. *Int. J. Nanomedicine* 14, 9483–9496. doi:10.2147/IJN.S224160

Zinchuk, V., and Zinchuk, O, (2011). Quantitative Colocalization Analysis of Confocal Fluorescence Microscopy Images. *Curr. Protoc. Cel Biol* 39, 4.19.1–4.19.16. doi:10.1002/0471143030.cb0419s52

Zou, W., Sarisozen, C., and Torchilin, V. P. (2017). The Reversal of Multidrug Resistance in Ovarian Carcinoma Cells by Co-application of Tariquidar and Paclitaxel in Transferrin-Targeted Polymeric Micelles. *J. Drug Target.* 25 (3), 225–234. doi:10.1080/1061186X.2016.1236113

Conflict of Interest: The authors declare that the research was conducted in the absence of any commercial or financial relationships that could be construed as a potential conflict of interest.

Publisher's Note: All claims expressed in this article are solely those of the authors and do not necessarily represent those of their affiliated organizations, or those of the publisher, the editors and the reviewers. Any product that may be evaluated in this article, or claim that may be made by its manufacturer, is not guaranteed or endorsed by the publisher.

frontiers in Bioengineering and Biotechnology

REVIEW
published: 07 December 2021
doi: 10.3389/fbioe.2021.798882

Emerging Nano-Based Strategies Against Drug Resistance in Tumor Chemotherapy

Lei Cao[1†], Yuqin Zhu[1†], Weiju Wang[2], Gaoxiong Wang[1], Shuaishuai Zhang[3]* and Hongwei Cheng[4]**

[1]Department of Pathology, Quanzhou Women's and Children's Hospital, Quanzhou, China, [2]Department of Pathology, Qingyuan Maternal and Child Health Hospital, Qingyuan, China, [3]School of Pharmaceutical Sciences, Southern Medical University, Guangzhou, China, [4]State Key Laboratory of Molecular Vaccinology and Molecular Diagnostics and Center for Molecular Imaging and Translational Medicine, School of Public Health, Xiamen University, Xiamen, China*

OPEN ACCESS

Edited by:
Junjie Li,
Innovation Centre of NanoMedicine (iCONM), Japan

Reviewed by:
Panyue Wen,
University of Science and Technology of China, China
Amit Ranjan Maity,
Amity University Kolkata, India
Yu Han,
Hefei Normal University, China

***Correspondence:**
Gaoxiong Wang
wanggaoxiong2013@163.com
Shuaishuai Zhang
zhangshuai2@smu.edu
Hongwei Cheng
hongwei1026@hotmail.com

[†]These authors have contributed equally to this work and share first authorship

Specialty section:
This article was submitted to Nanobiotechnology, a section of the journal Frontiers in Bioengineering and Biotechnology

Received: *20 October 2021*
Accepted: *19 November 2021*
Published: *07 December 2021*

Citation:
Cao L, Zhu Y, Wang W, Wang G, Zhang S and Cheng H (2021) Emerging Nano-Based Strategies Against Drug Resistance in Tumor Chemotherapy. Front. Bioeng. Biotechnol. 9:798882. doi: 10.3389/fbioe.2021.798882

Drug resistance is the most significant causes of cancer chemotherapy failure. Various mechanisms of drug resistance include tumor heterogeneity, tumor microenvironment, changes at cellular levels, genetic factors, and other mechanisms. In recent years, more attention has been paid to tumor resistance mechanisms and countermeasures. Nanomedicine is an emerging treatment platform, focusing on alternative drug delivery and improved therapeutic effectiveness while reducing side effects on normal tissues. Here, we reviewed the principal forms of drug resistance and the new possibilities that nanomaterials offer for overcoming these therapeutic barriers. Novel nanomaterials based on tumor types are an excellent modality to equalize drug resistance that enables gain more rational and flexible drug selectivity for individual patient treatment. With the emergence of advanced designs and alternative drug delivery strategies with different nanomaterials, overcome of multidrug resistance shows promising and opens new horizons for cancer therapy. This review discussed different mechanisms of drug resistance and recent advances in nanotechnology-based therapeutic strategies to improve the sensitivity and effectiveness of chemotherapeutic drugs, aiming to show the advantages of nanomaterials in overcoming of drug resistance for tumor chemotherapy, which could accelerate the development of personalized medicine.

Keywords: tumor chemotherapy, drug resistance, tumor microenvironment, nanomedical strategy, combination therapy

INTRODUCTION

The biggest barrier to cancer therapy is the inevitable emergence of drug resistance. Drug resistance can be divided into two categories according to the behind factors: primary and secondary (Longley and Johnston, 2005). Primary resistance indicates those factors present in the cancer cell or tissue itself before chemotherapy and reduces the efficacy of chemotherapy. However, because of various adaptive responses, such as increased expression of therapeutic targets and activation of alternative signaling pathways, secondary or acquired resistance can develop during therapeutic periods that are initially sensitive to cytotoxic agents (Lackner et al., 2012). Continuously activated proliferative signaling, inactivated growth suppressors, and activated metastasis factors are classical hallmarks of some tumors, which lead to drug resistance to chemotherapy. With the deepening of mechanism research, tumor heterogeneity, tumor microenvironment, and cancer stem cells (CSCs) were closely associated with

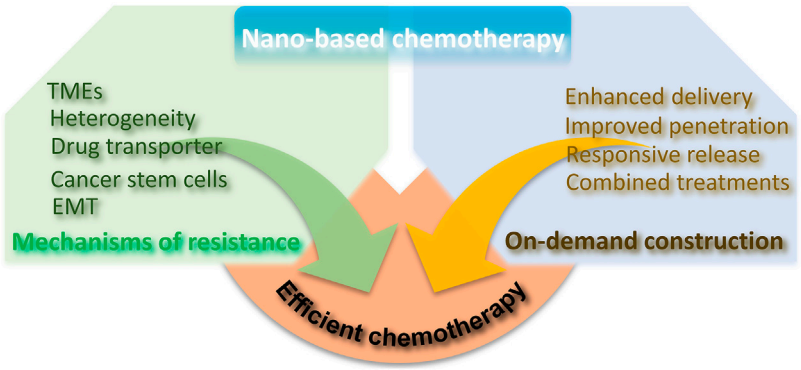

SCHEME 1 | Illustration of chemotherapy resistance mechanism and the advantages of nano-based chemotherapy to achieve efficient chemotherapy.

the occurrence and development of drug resistance in chemotherapy. Besides, the characteristic of cell motility acquired from epithelial-mesenchymal transition (EMT), genetic factors of drug transport, especially the multiple drug resistance (MDR) is also considered to be vital factors for resistance development.

Considering the drug resistance is a complex mechanism, many dexterous solutions appeared in anticancer therapies to overcome drug resistance and increase the efficacy of treatment. Among these, nanomaterials as a promising drug delivery are being investigated for solving several forms of drug resistance (Markman et al., 2013; Da Silva et al., 2017). Compared with "free" drugs, nanomaterials have remarkable advantages containing higher bioavailability, slower drug release, lower drug usage, and better treatment outcomes. Statistically, there are more than 40 therapeutic nanomaterials approved for clinical use worldwide and at least 200 nanoparticles undergoing clinical trials (Schütz et al., 2013; van Der Meel et al., 2013; Bobo et al., 2016). The classical enhanced permeability and retention (EPR) effect in solid tumors promote the selective distribution of nanomaterials, further increase pharmacodynamics and reduce systemic side effects (Fang et al., 2011; Kobayashi et al., 2013). A possible concern is that the nanomaterials may be inclined to accumulate in drug disposal organs such as the liver and kidney, leading to severe organ toxicity. To avoid the side effects introduced by nanomaterials, researchers have developed lots of methods including changing the physicochemical properties of nanomaterial, PEG polymer chains modifications, and so on (Milla et al., 2012; Zhu et al., 2013). At present, more and more novel nanomaterial-based formulations are emerging in-clinic research, many of them win success especially in solving the therapeutic impediments in cancer treatment.

Here, in this review, we mainly described the mechanisms of drug resistance and focused on recent innovation of dexterous and sophisticated nano-strategies in overcoming drug resistance, providing ideas for tumor chemotherapy and related combination therapies (**Scheme 1**).

MECHANISM OF DRUG RESISTANCE

The mechanism of drug resistance at tumor tissue level is extremely complicated. Commonly, tumor heterogeneity, tumor microenvironment (TME), drug transporter and multidrug resistance, cancer stem cells (CSCs), epithelial-mesenchymal transition (EMT) and tumor metastasis are known as the major drug resistance factors (**Figure 1**), which contribute to the off-target effect in the practice of chemotherapy. And drug transporters-mediated drug efflux impairs the cellular chemotherapeutics delivery, leading to the low therapeutic dose (Cheng et al., 2018a; Fan et al., 2018; Ke et al., 2021). Besides, low pH, hypoxic tumor microenvironment, and other anti-apoptotic molecules could enhance the survival compensation effect (Li and Kataoka, 2021). Except for the five drug resistance reasons we mentioned, other resistant reasons containing gene mutations and genomic instability, epigenetic changes such as DNA methylation and protein acetylation, inhibition of apoptotic signaling and overexpression of anti-apoptotic molecules (Min et al., 2017; Vasan et al., 2019). To comprehensively explain the innovative design and prospects of nanomedicine in overcoming of tumor resistance, this review mainly focuses on several classic resistance mechanisms. Clinical practice shows serious resistance against chemotherapeutic drugs significantly impairs the therapeutical effect and contributes to poor prognosis for cancer patients. Therefore, full understanding the mechanism of drug resistance at the molecular level might bring novel treatment strategies, which in turn will lead to deeper and longer-lasting cancer treatments.

Tumor Heterogeneity

Heterogeneity is a distinct characteristic of tumor tissues from normal tissues and is represented by different morphological profiles. The heterogeneity may cause discrepant distribution of tumor cell subpopulations across different regions of the primary tumor (spatial heterogeneity) or variations in the molecular makeup of a single lesion over time (temporal heterogeneity). Cancer cells have the powerful capacity of self-renewal and differentiation, which give rise to abundant tumor types causing heterogeneity of the tumors (Marusyk and Polyak, 2010; Dagogo-Jack and Shaw, 2018). The driving forces behind tumor heterogeneity contain heritable and non-heritable mechanisms, either as a result of a natural progression of tumor or exposure to pressures created by

clinical interventions. A substantial fraction of heterogeneity commonly results from environmental factors during tumor development and is therefore non-heritable. Tumor heterogeneity can be regarded as a process of Darwinian evolution theory (Polyak, 2014; Zellmer and Zhang, 2014). Tumor heterogeneity affects drug sensitivity and provides fuel for drug resistance in cancer therapy. The example of drug response influenced by temporal heterogeneity comes from a cellular barcoding experiment results that resistant clones often arise from the selective expansion of pre-existing populations during drug treatment (Bhang et al., 2015). Spatial heterogeneity has a greater impact on initial drug treatment response. However, analyses involving single-site biopsy sampling might result in underestimation of the degree of spatial heterogeneity. Instead, noninvasive "liquid biopsies" extracted from patient blood are a promising strategy for addressing the shortcomings of tissue sampling (Nagrath et al., 2007; Chabon et al., 2016). Recently, single-cell sequencing technology is revolutionizing biomedical research. Using single-cell genomics enables to characterize tumor heterogeneity by quantifying the gene expression of thousands of individual cells (Villani et al., 2017).

Tumor Microenvironment

The reprogramming of cellular metabolism is a common feature of cancer cells, one of which is known as the Warburg effect (Vaupel et al., 2019). Cancer cells would prefer to adopt aerobic glycolysis for growth rather than oxidative phosphorylation (OXPHOS), which strongly upregulate glucose uptake and aerobic glycolysis to increase intermediate glycolytic metabolites and the production of lactic acid (Lu et al., 2015). On the one hand, the glycolytic intermediates provide essential anabolic energy for cell proliferation and tumor growth. On the other hand, the increased by-product of lactic acid results in the accumulation of intracellular protons. The accumulation of protons in the intracellular environment activates the proton excludes (Na+/H+ exchanger, and carbonic anhydrase) and consequently changes the pH gradient in the tumor microenvironment (Izumi et al., 2003). This new biophysical setting profoundly influences the capability of drug uptake and pharmacological process in cancer cells. The lower pH value in tumor tissues gives rise to the protonation and neutralization of various chemotherapeutic drugs such as doxorubicin by preventing them from entering the targeted locus (Miraglia et al., 2005; Spugnini et al., 2015). Moreover, alteration of pH gradient easily promotes the formation of cytoplasmic acidic vesicles in tumor cells, which sequestrates chemical molecules in cell organelles eventually leading to the elimination of the drug through vesicle degranulation (Taylor et al., 2015).

Hypoxia is another common microenvironment feature in nearly all solid tumors. The uncontrolled proliferation of tumors limits the availability of oxygen supplied from the tumor vascular system, thus exposing them to low oxygen environments. On average, the oxygen level in tumor tissues is around 1–2% or below (McKeown, 2014). Hypoxia is also a key factor in cancer therapy resistance by regulating the tumor microenvironment (Rohwer and Cramer, 2011; Jing et al., 2019). The transcription

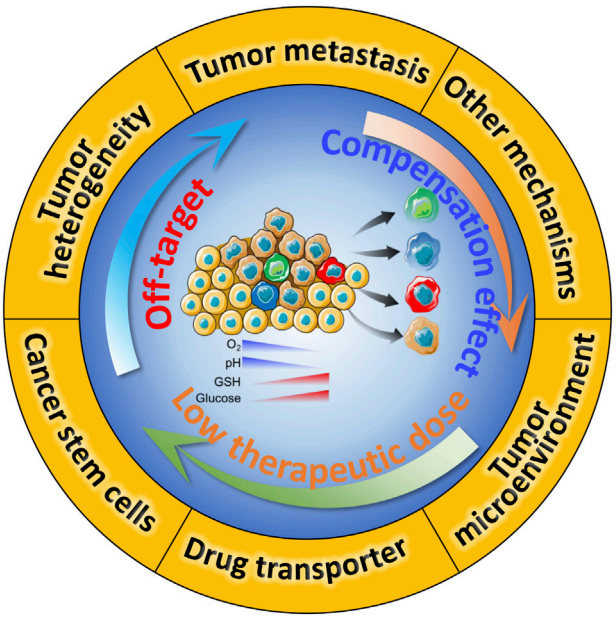

FIGURE 1 | Schematic illustration of drug resistance in chemotherapy, and the underlying crosstalk between these mechanisms.

factor hypoxia-inducible factor (HIF) usually serves as the major mediator of hypoxia response and is highly expressed in many cancers. Numerous evidence has shown that the inhibition of HIF-1α in cancer cells significantly enhanced sensitivity towards chemotherapeutic drugs (Brown et al., 2006; Liu et al., 2008). However, the underlying molecular mechanism of HIF-1α's contributions to drug resistance is complicated, multiple, and specific in some tumor types. Some studies found that HIF-1 can induce the expression of the multidrug resistance 1 (MDR1) gene in a hypoxic tumor environment (Comerford et al., 2002). The membrane-located P-glycoprotein (P-gp) is the translation product of the MDR1 gene, which belongs to the family of ATP-binding cassette (ABC) transporters. Acting as a drug efflux pump, P-gp could decrease the intracellular concentration of chemotherapy agents such as paclitaxel, vinca alkaloids (Gottesman et al., 2002). Many chemotherapeutic agents such as 5-fluorouracil (5-FU), cisplatin, and DNA damage inducer triggering cell apoptosis largely depend on p53 pathway activation. Other important findings are that HIF-1 may function as an antagonist of p53-mediated cell death upon treatment with the chemotherapeutic agent (Hao et al., 2008; Rohwer et al., 2010). Besides, other reasons of HIF-1 contribute to chemotherapeutic drug resistance involving DNA damage repair, metabolic reprogramming, and immune microenvironment (Wirthner et al., 2008; Semenza, 2010; Vaupel and Multhoff, 2018).

Drug Transporter and Multidrug Resistance

Drug transporters are integral membrane proteins that are involved in drug disposition by affecting absorption, distribution, metabolism, and excretion (ADME). Clinical pharmacokinetic drug-drug interactions (DDIs) studies have shown that transporters mainly

participate in the drug ADME process together with metabolic enzymes (Zhang et al., 2008). Based on their structure and mechanism, membrane transporters can be divided into two major superfamilies: the ATP-binding cassette (ABC) and solute-linked carrier (SLC) superfamily (Giacomini et al., 2010; Nigam, 2015). One of the drug transporter so far received the greatest attention is ABC family transporters namely ABCB1, also known as P-glycoprotein or MDR1. Tumor cells can achieve resistance to a broad range of anti-cancer drugs via activating drug efflux pumps of membrane-resident P-glycoprotein (P-gp). These hydrophobic drug substrates such as anthracyclines, vinca alkaloids, taxane, epipodophyllotoxins, topotecan, as well as several pharmaceuticals agents are presented to the transporter directly from the lipid bilayer. Such self-defense effect can occur in ATP-dependent or ATP-independent manners regardless of the concentration gradients of drugs (Pérez-Tomás, 2006; Robey et al., 2018). Research has suggested that the expression of P-gp is usually upregulated in a variety of tumors including the colon, kidney, liver, and pancreas. When exposed to chemotherapy drugs, the mRNA levels of MDR1 can be rapidly induced in tumor cells (Abolhoda et al., 1999). A more important discovery is that transporter protects against cell death not only by forcing out drugs but also via direct interference with the caspase-dependent pathway, which is called as efflux pump-independent MDR effect (Pallis et al., 2002). For the above reasons, it seems that P-gp inhibition is a clever therapeutic way to reverse the MDR phenotype. However, many of the P-gp modulators were substrates for other transporters or metabolic enzymes resulting in unpredictable pharmacokinetic interactions. For this reason, considerable efforts should be made to develop agents specifically inhibiting P-gp function in MDR-mediated drug resistance research.

Existence of Cancer Stem Cells

It is widely accepted that cancers develop from a small subset of stem cells with exclusive ability to self-renew and differentiate into the heterogeneous cancer cell types (Clarke et al., 2006; Beck and Blanpain, 2013). These intrinsic cancer stem cells or tumor-initiating cells constitute a population that is mainly responsible for cancer aggressiveness, drug resistance, and tumor relapse. There is no universal molecular feature of CSCs, although some cell-surface markers such as CD133, CD44 were associated with CSC phenotype in different types of tumors (Grosse-Gehling et al., 2013; Yan et al., 2015). Sometimes, it is assumed that the expression of these surface markers may reflect the CSC frequency rather than exact content in certain tumors. CSCs are rarely ranging from 1 per 1,000 to 1 per 100,000 in human tumors (Ishizawa et al., 2010). Nevertheless, when transplanted into the immunodeficient mice, these CSCs quickly enable the formation of secondary tumors. Chemotherapeutic drugs typically affect dividing cells, while CSCs are primarily quiescent cells with enhanced DNA repair mechanisms, always not influenced (Vitale et al., 2017). Besides, CSCs also express high levels of specific ABC drug transporters containing ABCB1, ABCG2, and ABCC1, which are known MDR genes in tumor cells, allowing for increased survival (Moitra, 2015). Although chemotherapy kills the majority of tumor cells, the resistant CSCs may still survive and expand the tumor again with self-renewing cells and differentiated offspring (Dean et al., 2005).

EMT and Tumor Metastasis

Epithelial-mesenchymal transition (EMT) is a process that epithelial cells lose their apical-basal polarity and cell-cell adhesive properties, acquire migratory and invasive properties of mesenchymal cells. These undergoing EMT cells exhibit decreased expression levels of epithelial markers (E-cadherin) and increased expression levels of mesenchymal genes (N-cadherin and vimentin) (Lamouille et al., 2014). In most cases, EMT leads to cell morphological changes and the gain of stem cell-like features. EMT is extensively involved in multiple biological pathological processes, especially in many aspects of cancer progression, including tumor metastasis and drug resistance (Du and Shim, 2016; Du et al., 2017). In diverse types of cancers, these undergoing EMT cells frequently overexpressed ABC family transporters and showed drug resistance phenotype similar to CSCs (Mani et al., 2008; Jiang et al., 2017). Studies have demonstrated that the promoters of ABC transporters contain several binding sites for EMT-related transcription factors. Overexpression of transcription factors such as Twist and Snail could increase the promoter activity and expression of ABC transporters in cancer cells, causing drug resistance in cancer treatment (Saxena et al., 2011). Besides, matrix metalloproteinases (MMPs) are involved in the regulation of EMT and other metastasis-related molecules, the combination of specific inhibitors against MMPs is an effective strategy to prevent tumor metastasis and improve tumor chemotherapy (Chen X. et al., 2021).

NANOMATERIAL THERAPEUTICS OVERCOME DRUG RESISTANCE

Nanotechnology is initially defined as the "intentional design, characterization, production, and applications of materials, structures, devices, and systems by controlling their size and shape in the nanoscale from 1 to 100 nm range." (N Engl J Med. 2010 Dec 16; 363 (25):2434–43) Nanotechnology has potential applications in medical applications because nanomaterials are similar in scale to biomolecules and systems, and can be designed to perform different functions. In cancer treatment, nanomaterials are mainly designed to aid in the transport of anticancer drugs through biological barriers. The aims of cancer nanomedicine are to use the properties and physical characteristics of nanomaterials for achieving more effective and safer cancer treatment (Nat Rev Cancer. 2017 Jan; 17 (1):20–37). In recent years, emerging evidence demonstrated that some nanomaterials have distinct advantages in reducing side effects and overcoming drug resistance. The following will focus on recent advancements in nanotherapeutic approaches to tackle drug resistance.

Precise Individualized Strategies for Overcoming Tumor Heterogeneity

Tumor heterogeneity is an important hallmark for some cancers, which contribute to the unsatisfactory treatment outcome (Liu et al., 2019). Traditional tumor treatments are mostly based on ultrasound (US), magnetic resonance imaging (MRI), computed tomography

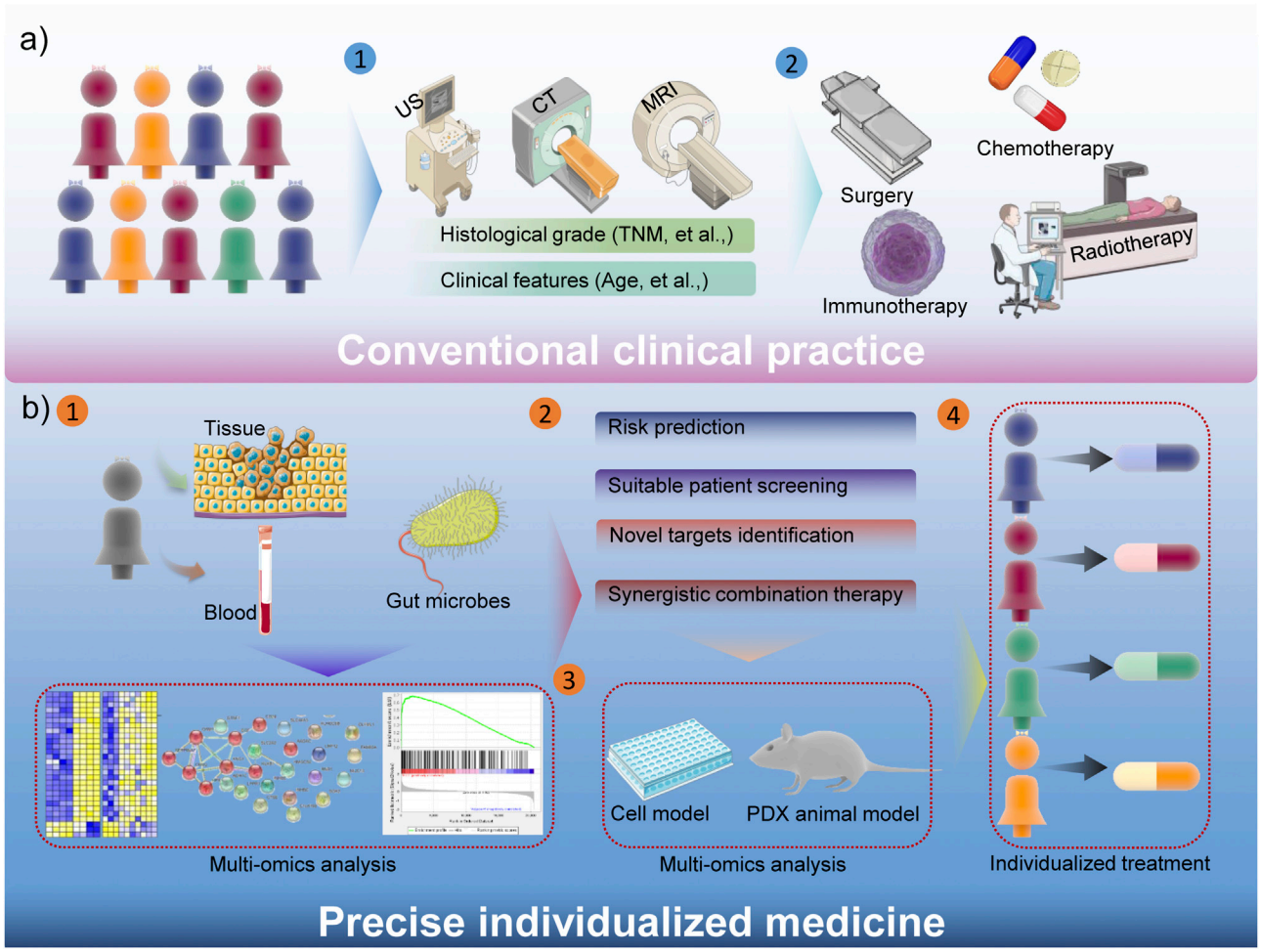

FIGURE 2 | Schematic illustration of the advantages about precise individualized medicine.

(CT) and other examinations to stage cancer patients, and then formulate treatment strategies based on histological grade (such as TNM staging, cancer thrombus formation, et al.) and some clinical characteristics of the disease, etc. (Lord et al., 2021). And then surgery, chemotherapy, radiotherapy, immunotherapy and other treatments could be chosen by median's experience. Obviously, the consistency of conventional tumor treatments is poor, and this general treatments have a certain therapeutic effect on some patients, but due to the characteristics of tumor heterogeneity and other reasons, many patients have not benefited. The inhibitor against kirsten rat sarcoma virus (KRAS) oncogene is a good example. Due to the gene mutation of KRAS in many cancer patients, the clinical performance is not satisfactory (Kim et al., 2020). Another specific example is that sex also plays a critical role in the drug response, toxicity and other aspects (Hajipour et al., 2021). Therefore, precision medicine has received more and more attention in recent years, which could significantly compensate for the shortcomings of conventional strategies (**Figure 2**). Simply, patient's sample-based multi-omics analysis could comprehensively demonstrate the underlying risk, suitable patients, novel drug targets, and promising combination therapies (Zhang and Yu, 2020). Not only that, precision medicine will also accelerate the process of clinical transformation, the cells and patient-derived xenograft (PDX)-based drug screening could enhance the efficacy of clinical trials (Wang et al., 2018a). Therefore, the precision medicine could guide the choice of clinical medication and treatment options, and more evidence also confirms that it is beneficial to improve the prognosis of cancer patients. Considering the better performance of nanomedicine in cancer therapy, the diverse functionality of nanomedicine remarkably facilitates precision nanomedicine, bringing revolutionary progress to tumor treatment.

Exploiting Novel pH-Responsive Nanoparticles Based on Tumor Acidity

Recognizing that tumors tend to be acidic environments, a class of pH-responsive nano-structures is developed and such systems could enhance uptake by tumor cells through acidic microenvironment-triggered drug release. These nanoparticles were reported as following. Self-assembled PEG-detachable polymeric micelles DOX-PMs (Xu et al., 2019), zwitterionic charge-switchable polymers S-NP/DOX (Yuan et al., 2012), pH and redox dual

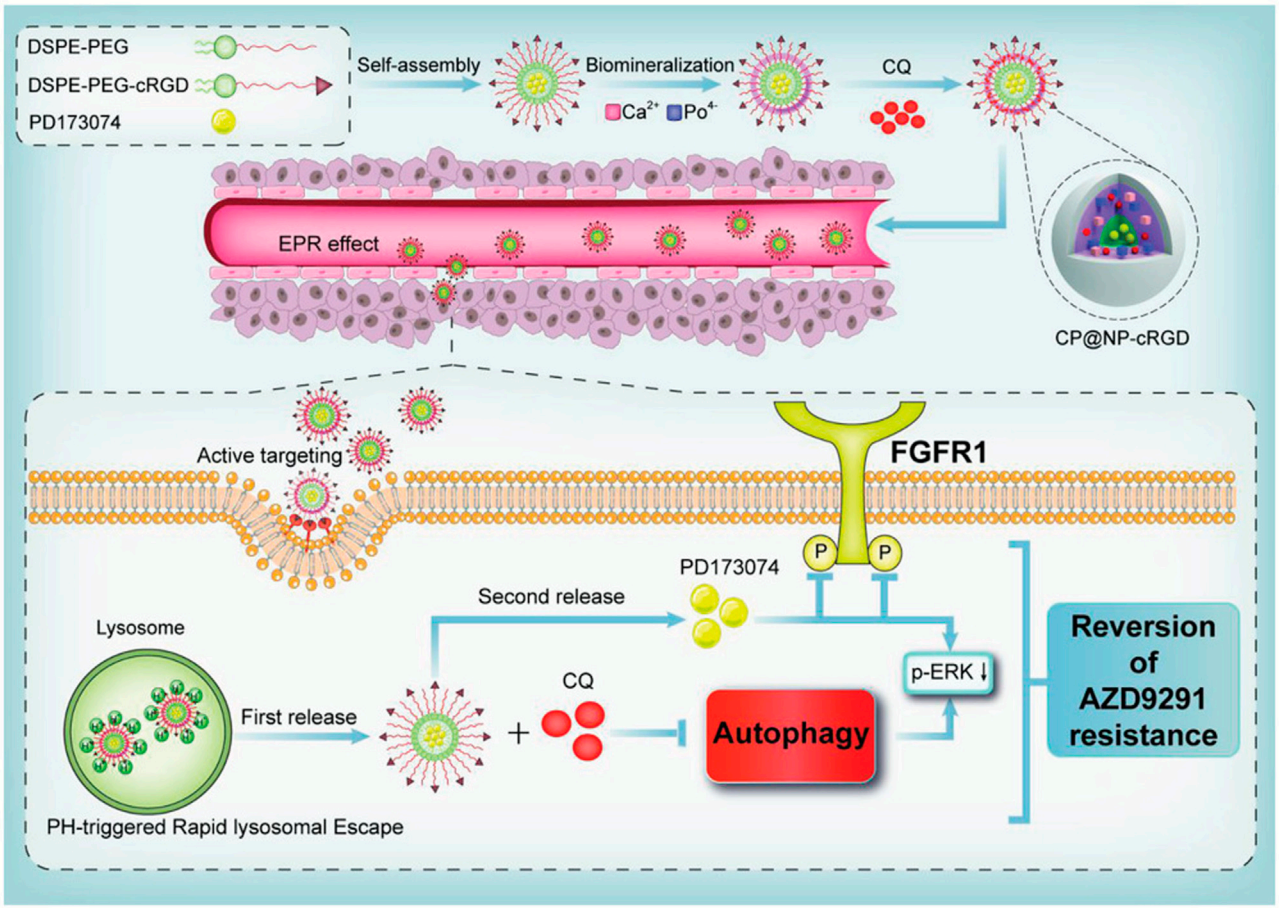

FIGURE 3 | Schematic model of a pH-responsive shell-core nanoparticles to overcome AZD9291 drug resistance. Reproduced with permission (Gu et al., 2021). Copyright 2021, Wiley.

responsive nanoparticle RPDSG/DOX (Kc et al., 2012), pH-sensitive DSF/PTX co-loaded micelles (Huo et al., 2017), dual-pH responsive BCP-DOX micelles (Mao et al., 2016), which were designed to combat chemotherapy resistance based on the low pH tumor microenvironment, and the results have implied that these pH-responsive micelles have significant potential for efficiently combating chemotherapeutic agents (DOX and PTX) resistance in cancer treatment especially in co-delivery applications (Yu et al., 2015; Wang et al., 2017). Liu et al. reported a pH-sensitive DSF/PTX co-delivery systems work in drug-resistant tumor cells model. Briefly, the micelles were composed of succinic anhydride-modified PTX (SA-PTX) and disulfiram (DSF), a P-glycoprotein (P-gp) inhibitor, was simultaneously encapsulated into the hydrophobic core of poly (ethylene glycol)-block-poly (l-lysine) (PEG-b-PLL). Such a drug carrier was characterized as follows: 1) the micelles remain negative surface charge under blood circulation, while quickly changes to positive under acidic tumor tissues owing to the hydrolysis of anhydride group. 2) the endocytosis effect increases the uptake of micelles. 3) the internalized carriers could quickly release DSF accompanied by deformation of micelles, and then PTX drugs are released in acidic organelles in a pH-dependent sustained manner. 4) Because P-gp was inhibited by DSF, the PTX could accumulate at a higher concentration and effectively kill resistant tumor cells (Huo et al., 2017). Another good example is the combined PD173074 chemotherapeutics and chloroquine (CQ) to block the autophagy and fibroblast growth factor receptor 1 (FGFR1) mediated AZD9291-resistance (**Figure 3**). In details, a pH-sensitive nanoparticle system with shell-core structure was designed to encapsulate FGFR1 inhibitor PD173074 and autophagy inhibitor CQ to overcome the resistance of tyrosine kinase inhibitors (TKIs) AZD9291 in non-small cell lung cancer (NSCLC). FGFR1 signaling was described to contribute to EMT-associated acquired resistance of EGFR-TKI in NSCLC treatment. Therefore, NSCLC cells with EGFR-TKI resistance is sensitive to FGFR1 inhibitors (Wang et al., 2016). Further, the FGFR1 signaling could regulate cell autophagy, and autophagy inhibition is beneficial to enhance the anticancer effects of FGFR1 inhibitor (Lee et al., 2016). The novelty of this study is the application of pharmacological effects for innovative nanotheranostic. Furthermore, the biomineralization with CaP favour the nanoparticles with pH-sensitive to achieve the lysosome escape and realize the pH-responsive drug release, which could be applied by the low pH tumor microenvironment. The specific pH-activation drug release is fully studied, and many combined strategies were also developed based on other tumor

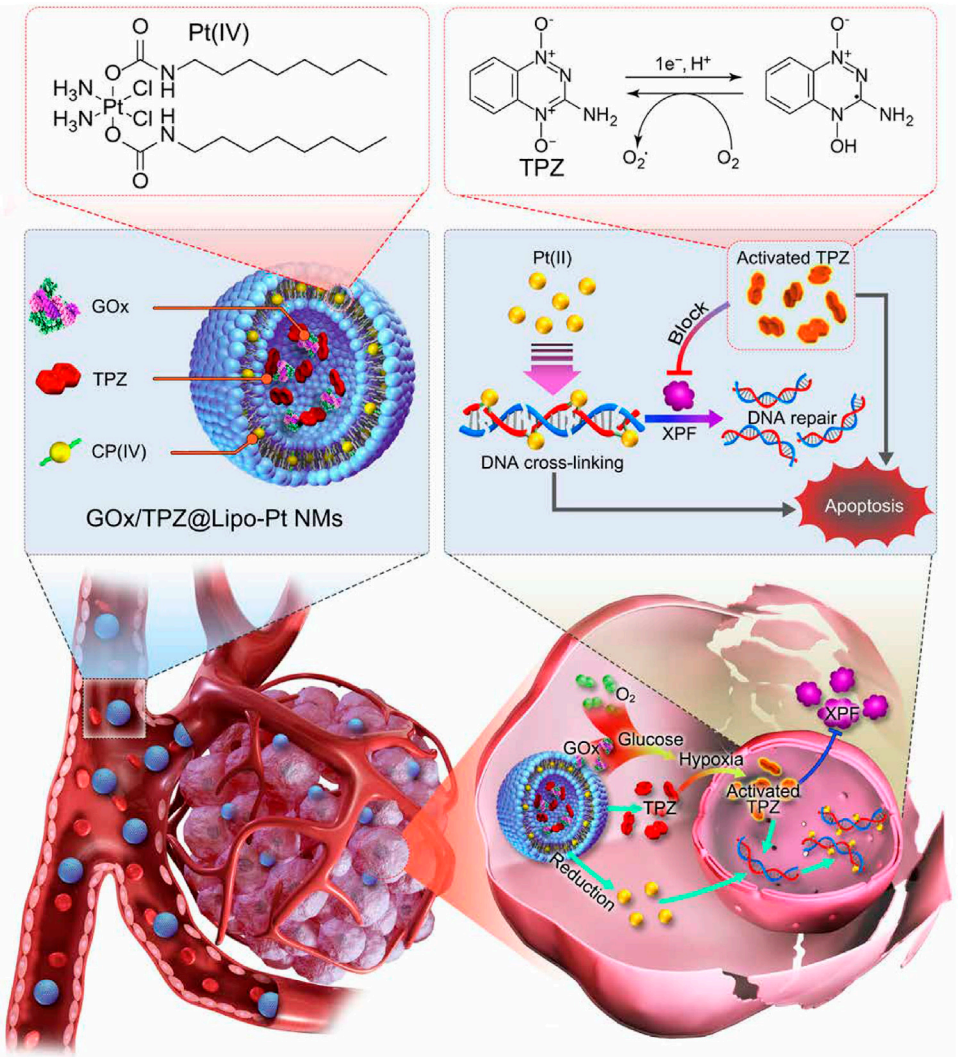

FIGURE 4 | Schematic illustration of the GOx/TPZ@Lipo-Pt nanomaterial and hypoxia-induced reversal of cisplatin resistance. Reproduced with permission (Chen J. et al., 2021). Copyright 2021, American Chemical Society.

microenvironments, such as higher glucose, low oxygen and higher Glutathione (GSH) concentration (Li et al., 2013; Li et al., 2017; Cheng et al., 2021). These pH-responsive nanoparticles not only can realize the escape of lysosome and enhance the pharmacological concentration, also achieve the responsive drug release to decrease the toxic side effects.

Nanoparticles Targeting the Hypoxic Tumor Microenvironment

Evidence has revealed that hypoxia in the tumor microenvironment has a crucial role in the clinical resistance of chemotherapy through a variety of signal transduction pathways and molecular changes (Pastorek and Pastorekova, 2015; Wang D. et al., 2021; Xu et al., 2021). The development of advanced nanomaterial delivery methods for reversing the resistance of hypoxic tumors is therefore of great interest but remains a considerable challenge. In general, strategies modulating hypoxia via nanomaterials that have been investigated can be divided into three categories including countering hypoxia, disregarding hypoxia, and exploiting hypoxia. The countering hypoxia strategy is a traditional targeting method. For example, the recent study designed a versatile tumor hypoxia-directed nanoparticle loaded with Acetazolamide (ATZ) specifically targeting the marker of tumor hypoxia marker carbonic anhydrase IX (CA IX) for reversing Sorafenib resistance in RCC treatment (Alsaab et al., 2018). Based on the biocompatibility and oxygen dissolving ability of perfluorocarbon (PFC), others developed an innovative nano-PFC as an oxygen shuttle for ultrasound-triggered tumor-specific delivery of oxygen (Song et al., 2016). This kind of efficient oxygen-enhanced nanomaterial may also provide a promising strategy to overcome the hypoxia-associated resistance in cancer treatment (Tian et al., 2017). Interestingly, some material scientists tend to

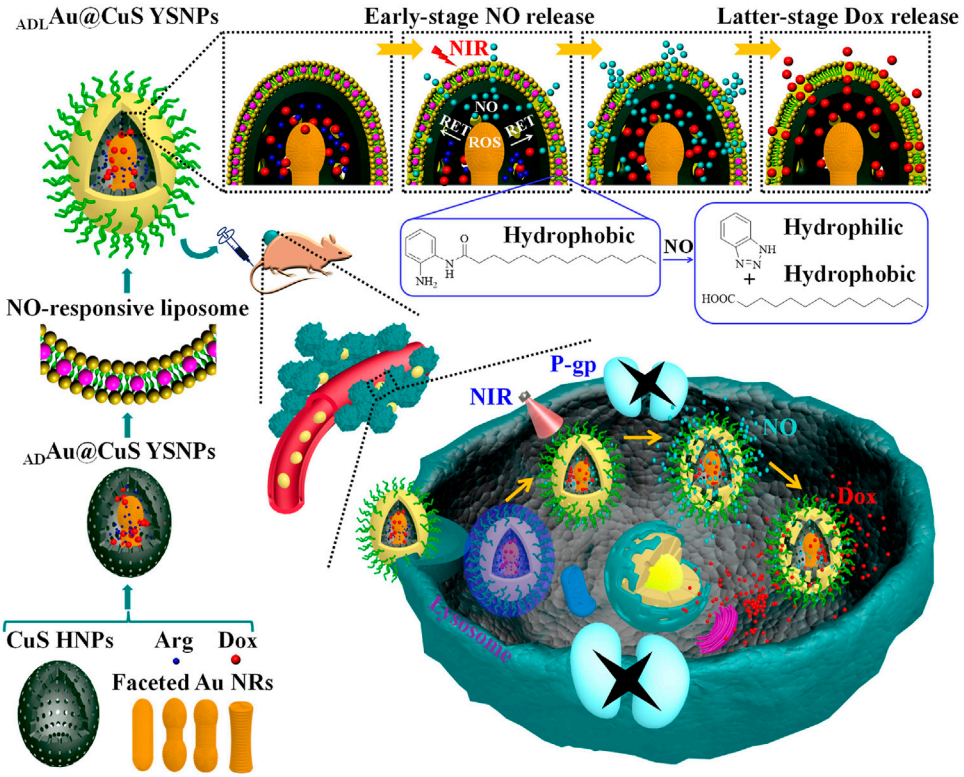

FIGURE 5 | Illustration of the NO and Dox programmable released ADLAu@CuS YSNPs in MDR cancer therapy. Reproduced with permission (Wang L. et al., 2019). Copyright 2019, American Chemical Society.

explore and make use of the hypoxic feature in drug-resistant tumor cells that is called as exploiting hypoxia strategy. Numerous studies have indicated that hypoxia-triggered DNA damage, mitochondrial activity, autophagy, and drug efflux are treatment obstacles in platinum-based clinical chemotherapy. For example, the xeroderma pigmentosum group F (XPF), an DNA self-repairing protein could be regulated by hypoxia, which causes the acquired resistance of cancer cells to cisplatin (Angew Chem Int Ed Engl. 2016 Dec 12; 55 (50):15564–15568). Recently, researchers proposed a novel nano-chemotherapy strategy that is to build a liposome nanodrug containing glucose oxidase (GOx), tirapazamine (TPZ), and platinum (IV) prodrug (Chen J. et al., 2021). The nanodrug can not only be fully utilized but also further aggravate intracellular hypoxia of cisplatin-resistant tumor cells, thus fully activating TPZ drug activity. Activated TPZ effectively inhibited the expression level of XPF protein promoting DNA repair in tumor cells, thus achieving synergistically enhanced anti-tumor therapy with platinum drug (**Figure 4**).

Typical Nanocarriers for Overcome of Drug Pump Efflux

With the development of nanotechnology, more and more new-style nanostructures were discovered. Among these, gold nanoparticles (AuNPs) are being widely used to deliver small molecules due to their unique optical properties and surface plasmon resonance effect. And PEG can be attached to the surface of gold nanoparticles to increase the stability and circulation time of chemotherapy drugs. Moreover, the surface plasmon band (SPR) of the nanoparticle will be modified by changing the shape of AuNPs from spheres to rods. One of the advantages of gold nanorods is the shift of the SPR allows for near-infrared (NIR) absorption at the cross-sections permitting a deeper penetration into living tissues (Arvizo et al., 2010). Many results have demonstrated these AuNPs or gold nanorods could be used for the circumvention of drug resistance (Song et al., 2017; Wang et al., 2018b). One notable work is the study that Vishwakarma SK et al. developed a stable colloidal suspension of sorafenib-gold nanoconjugate (SF-GNP) in an aqueous medium for reverting the drug resistance in HCC cells in a 3D model system. Owing to the potential of highly biocompatible, SF-GNP nanoconjugates significantly reduced the growth and proliferation of SF resistant tumor cells with very least or no side effect after intra-peritoneal administration of SF-GNP nanoconjugates in animals (Vishwakarma et al., 2017).

Except for gold nanoparticles, another representative nanomaterial is the nitric oxide (NO)-stimulated nanosystem for multidrug resistance cancer therapy. This system reversing the MDR effect attribute to the principle that gaseous signaling molecules nitric oxide (NO) can be used as ABC transporter inhibitors to downregulate the expression level of P-gp, thus creating a favorable microenvironment for the treatment of drug-resistant

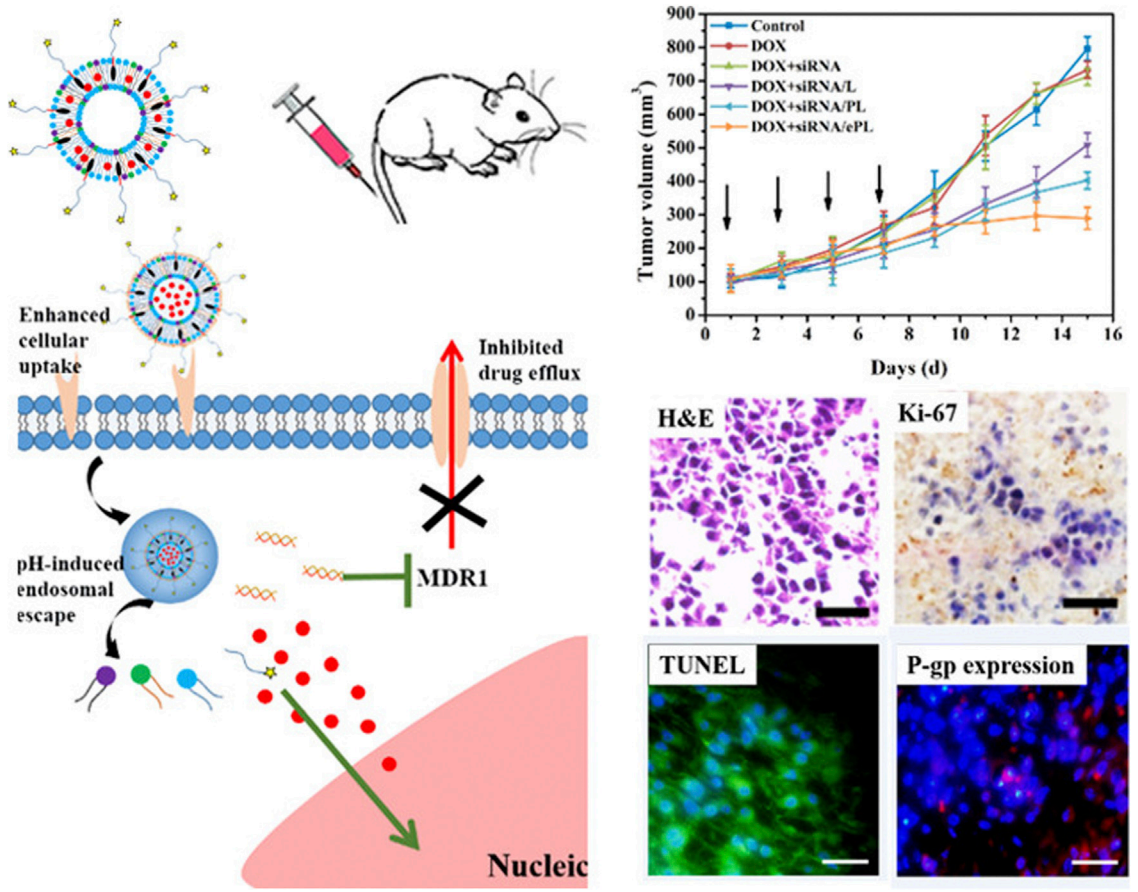

FIGURE 6 | Schematic illustration of multifunctional DOX + siRNA/ePL lipoplexes to overcome MDR effect. Reproduced with permission (Zhang et al., 2018). Copyright 2018, American Chemical Society.

cancer cells (Pieretti et al., 2020). Interestingly, Wang et al. designed a sophisticated nanosystem containing NO-responsive liposome, encapsulate L-arginine (l-Arg)/Dox-loaded gold@copper sulfide yolk-shell nanoparticles (ADAu@CuS YSNPs) to programmable release Dox in Dox-resistant cancer. Various faceted Au NRs were embedded in CuS HNPs to optimize Au@CuS YSNPs. The finally formed ADLAu@CuS YSNPs can convert L-Arg into NO upon NIR laser irradiation, leading to hydrolysis of o-phenylenediamine-containing lipid and programmable release of NO and Dox. Once internalized into MCF-7/ADR cells, the early stage NO release of ADLAu@CuS YSNPs can inhibit P-gp expression and create a favorable microenvironment for the latter stage Dox accumulation, beneficial for MDR cancer therapy (Wang L. et al., 2019). This NO and Dox sequential release of ADLAu@CuS YSNPs presenting a potential direction for drug-resistant cancer therapy (**Figure 5**).

The combination of chemotherapy and photothermal therapy is a promising strategy for cancer treatment. Despite the advantages in overcoming drug resistance, more studies have demonstrated the promising applications of these gold nanoparticles or NO-releasing nanomaterials in combined chemo-photothermal therapy (Zhang et al., 2016; Wei G. et al., 2019; Wang J. et al., 2021).

Co-Delivery Nano-Formulations for Reversal of Resistance Mechanism

The co-delivery system of chemo-pharmaceutical agents and siRNA is an excellent nano-therapeutic strategy for the effective killing of tumor cells (Xiao et al., 2017; Li et al., 2019). Since the major mechanisms of drug resistance are the overexpression of drug-resistant associated genes such as drug transporters, one approach for overcoming drug resistance is to use the co-delivery strategy that utilizes small interfering RNA (siRNA) to silence the expression of drug-resistant associated genes together with chemotherapeutic drugs. Reports have demonstrated that these co-delivery nanocarrier systems still potently reverses the multi-drug resistance effect in tumor tissues even under hypoxic and acidic conditions (Butt et al., 2016; Zeng et al., 2017; Marson et al., 2019; Joshi et al., 2020). The expression of the multidrug resistance 1 (MDR1) gene is a major obstacle that hinders the treatment of numerous cancer. Notably, the targeted resistant genes loaded in nanoparticles not only contain the MDR1 (P-gp) gene but also other genes including the

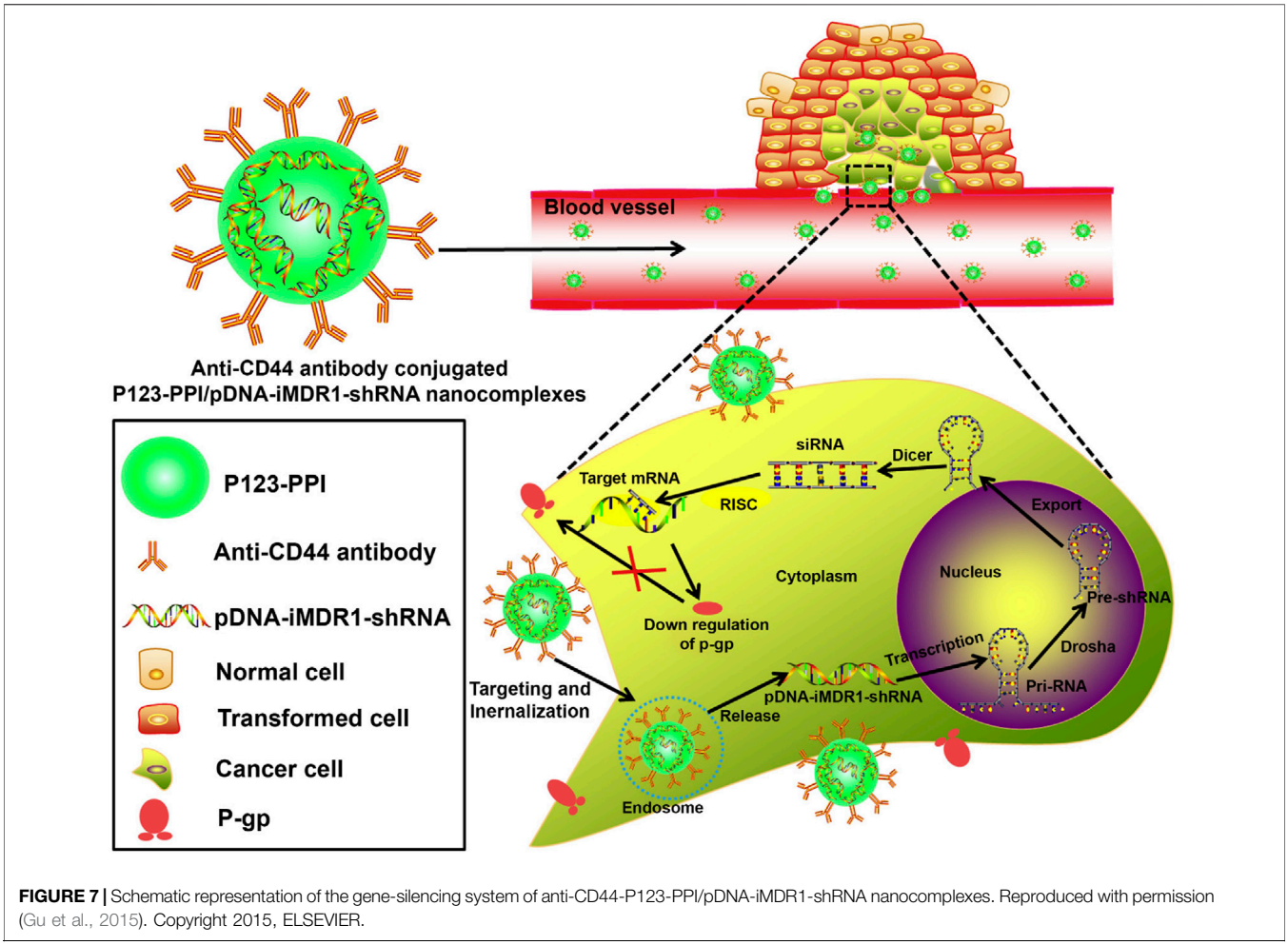

FIGURE 7 | Schematic representation of the gene-silencing system of anti-CD44-P123-PPI/pDNA-iMDR1-shRNA nanocomplexes. Reproduced with permission (Gu et al., 2015). Copyright 2015, ELSEVIER.

STC2 gene in liver cancer, K-Ras gene in lung cancer, and Bcl2 gene in breast cancer (Jeong et al., 2017; Wen et al., 2017; Cheng et al., 2018b). Recently, Zhang et al. designed a multifunctional pH-sensitive drug delivery system loaded with siRNA and DOX for drug-resistant breast cancer treatment. The nanocarrier is comprised of EphA10 antibody-conjugated pH-sensitive doxorubicin (DOX), co-loaded with MDR1-siRNA liposome (shortened as DOX + siRNA/ePL). Results from the intracellular study indicated that DOX + siRNA/ePL possessed the ability for incremental cellular uptake and rapid endosomal escape in a time-dependent manner. Meanwhile, the animal experiments suggested that DOX + siRNA/ePL could inhibit the proliferation, induce apoptosis, and downregulate the P-gp expression *in vivo* (Zhang et al., 2018). Altogether, DOX + siRNA/ePL was expected to be a suitable co-delivery system for overcoming drug-resistant effects in breast cancer treatment (**Figure 6**).

Enhanced Drug Delivery by Antibody-Modified Active Targeting

The low drug therapeutic dose is an important factor of acquired resistance in cancer treatment, efficient drug delivery could improve

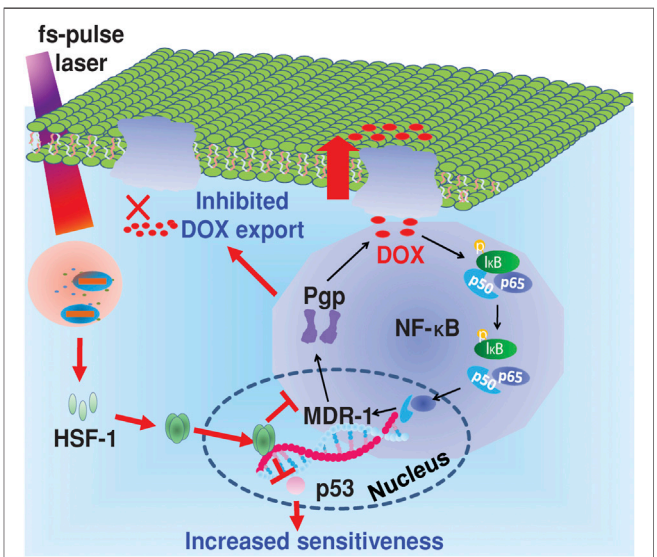

FIGURE 8 | Mechanism of the reversal of drug resistance in cancer cells under fs-pulse laser irradiation. Reproduced with permission (Wang et al., 2014). Copyright 2014, Wiley.

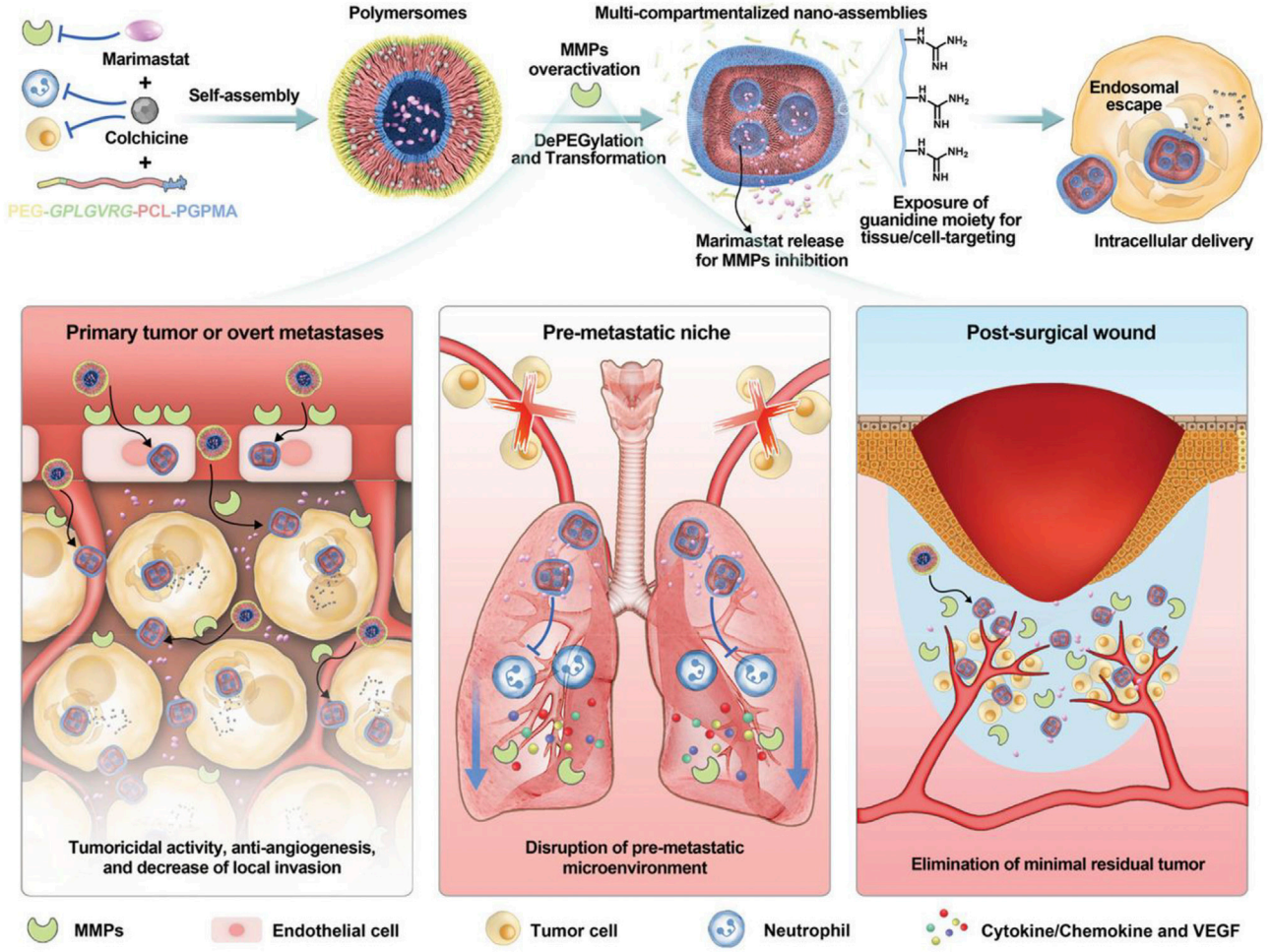

FIGURE 9 | Schematic illustration of MMPs inhibition to eliminate tumor metastasis. Reproduced with permission (Li et al., 2021). Copyright 2021, Wiley.

the pharmaceutic effect and prevent the occurrence of drug resistance. Sorafenib (SFB) is a common chemotherapeutical drug targeting vascular endothelial growth factor receptor (VEGFR), which is universally overexpressed in many tumors (Gounder et al., 2018). The therapeutic efficacy of sorafenib (SFB) in the clinic was greatly limited due to its short half-life as well as drug resistance (Wu et al., 2019). To solve these problems, Gan et al. developed a novel SFB-loaded polymeric nanoparticle for targeted therapy of liver cancer. This nanoparticle was fabricated from self-assembly of biodegradable block copolymers and drug SFB, followed by conjugating the anti-GPC3 antibody, referred to NP-SFB-Ab (Gan et al., 2018). Results have shown that NP-SFB-Ab greatly inhibits the tumor growth of xenograft tumors without obvious side effects. Other antibody-conjugated nanoparticles include HER2-antibody conjugated nanocarrier for multi-drug-resistant breast cancer therapy, ICAM-1 as well as Trop2 antibody-mediated nanoparticles for triple-negative breast cancer (TNBC) treatment (Vivek et al., 2014; Son et al., 2018; Wang M. et al., 2019). Gu et al. explored Pluronic P123-conjugated polypropylenimine (PPI) dendrimer (named as P123-PPI) to deliver shRNA against MDR1 in breast cancer cells (Gu et al., 2015). In detailed, anti-CD44 monoclonal antibody was also included to form nanocomplex, achieving the efficient gene delivery, enhanced tumor targeting and longer blood circulation. Based on the above design, the nanocomplexes significantly inhibited the P-gp expression, simultaneously drug resistant cells showed the increased cellular adriamycin (ADR) accumulation (**Figure 7**).

Combined Strategies in Reversal of Drug Resistance

The combinatorial strategy of chemo-chemo, chemo-immune, and chemo-photothermal treatments, usually called “cocktail therapy”, have been reported to be effective solutions to overcome drug resistance. For example, Zhang et al. developed an iRGD peptide-modified lipid-polymer hybrid nanosystem (LPN), co-loaded with paclitaxel (PTX) and tetrandrine (TET). As expected, the PTX + TET/iRGD LPNs significantly suppressed P-gp expression, promoted ROS production and apoptosis in PTX-resistant tumors (Zhang et al., 2017). Like “Domino-effect”, the chemotherapy combined with immunotherapy could amplify the efficacy of anti-tumor treatment. Studies have demonstrated

that many advanced nanoparticles are competent to break through barriers in combinatorial chemo-immune treatment (Wei X. et al., 2019; He et al., 2021; Yan et al., 2021). Notably, the latest study reveals the phenomenon that some nanomaterials possess the inherent biological effect on immunotherapy. These nonfunctional nanomaterials can overcome tumor resistance to PD-1 antibody and sensitize the therapeutic effect of PD-1 antibody, thus presenting a promising prospect in chemo-immune therapy (Sun et al., 2021).

Herein, the following picture simply illustrated a case that chemo-photothermal treatment applied in overcoming drug resistance (**Figure 8**). Wang et al. found that irradiation of Au@SiO2 resistant cells with femtosecond pulses at a lower intensity than photothermal therapy produced a unique photothermal effect, which induced intracellular heat shock factor (HSF-1) expression, inhibited the expression of p-glycoprotein (P-gp) on the cell membrane, and the NF-κB pathway. In addition, it can successfully induce the degradation of p53 protein mutated in drug-resistant cells, sensitize to chemotherapy drugs, and finally effectively overcome tumor drug resistance. Therefore, fs-pulsed laser irradiation provided a novel and promising strategy to combat drug resistance with the aid of a multifunctional nanocarrier (Au@SiO2) and triggered photothermal effects (Wang et al., 2014).

Interaction of Chemotherapeutics and Metastasis-Related Inhibitors

Tumor metastasis is a major risk factor for poor prognosis of cancer patients, which is the most concerned issue in surgical treatment. Moreover, chemotherapy has little benefit in the treatment of multiple metastasis (He and Shi, 2014). Herein, the efficient inhibition of tumor metastasis is an urgent work to enhance the pharmaceutical effect of chemotherapeutics. Li et al. reported an enzymatically polymer to simultaneously deliver colchicine chemotherapeutics and marimastat, which is a potent MMPs inhibitor (**Figure 9**). Based on the efficient drug delivery, this nanosystem could disrupt the microtubules of tumor cells by colchicine, and simultaneously prevent tumor metastasis microenvironment, which could reduce the primary post-surgical recurrence and distant metastasis significantly (Li et al., 2021). To be noted that, MMPs are commonly activated in some tumor tissues, some nanosystem were developed to release chemotherapeutics in MMP-responsive manner (Yao et al., 2018; Vaghasiya et al., 2020), displaying an enhanced chemotherapeutical response.

CONCLUSION AND PERSPECTIVES

Tumors are composed of mutually interacting tumor cells and tumor microenvironment. Consequently, internal cancer cells along with external environmental factors, extracellular matrix (ECM), and immune cells eventually determine the tumor fate. Tumor heterogeneity, the existence of CSCs, and the occurrence of EMT process in tumor cells are the inner driving force in chemotherapy resistance. However, alterative external pressure including hypoxia, acidic environment, and tumor-associated macrophage (TAM) directly affect drug kinetics and favor the selection of more malignant, therapy-resistant tumor cell subpopulations. Since the complexity of tumor heterogeneity and microenvironment, the causes of drug resistance may differ from individual patients and within a single tumor. Thus, the therapeutic strategies based on a single and fixed chemotherapy drug are inevitably suboptimal. In contrast, flexible and diverse drug delivery materials provided a window into the availability of better treatment. What's more, multiple nanoparticles applied in chemotherapy regimens could be effectively combined with photothermal therapy, immunotherapy, and CRISPR-mediated gene edit, thus synergistically acquiring better therapeutic efficacy in cancer treatment (Cheng et al., 2020). Considering the complexity and the heterogeneity of tumors, it is necessary to distinguish which nanotechnology strategy is most likely effective from a given context. This is just like the targeted therapy in individual patients or as we usually called precision medicine (Mitchell et al., 2021). Of course, one of approaches is to replace the traditional small molecule drugs with more smart drugs such as anti-cancer peptides (ACPs). Compared with chemical drugs, peptide-based drug delivery strategy has obvious advantages in cancer treatment, especially in overcoming drug resistance. In addition, the conjugation of peptides to nanoparticles results in advanced materials for treatment of cancer, whose properties can be adjusted to maximal efficacy for a given application (Scarberry et al., 2008; Olson et al., 2010).

In recent years, immunotherapy-combined nanoformulations have been developed based on studies of tumor escape mechanism, transforms immunosuppressive tumors into immunostimulatory phenotypes and overcomes the pathways leading to tumor escape. The therapeutic strategy has the potential to induce durable antitumor immune responses in hematologic and solid malignancies and thus has become treatment algorithms for multiple tumor types (Bhatia and Kumar, 2014). Cancer immunotherapy expands potential targets from tumors to the entire immune system, which is an area worthy of further exploration. Therapeutic approaches to manipulate various aspects of the immune system have been widely investigated including immune checkpoint inhibitors, CAR T cell adoptive immunotherapy, oncolytic viruses and vaccines (Yang, 2015). Also, increasing efforts are attempting to employ combination therapy to engage different parts of the immune system, implying the importance of this holistic approach. Through integrating with immunotherapy, nanomedicine improves the delivery of immune stimulators to create a close dialogue between tumors and immune system, which provides unique opportunities to complement each other. In turn, immunotherapy may weaken the effect of biological barriers for nanomedicine, and sometimes may not require large-scale targeted tumor killing activity because activating a small number of immune cells in the tumor or surrounding tissue can spread an immune response (Li and Kataoka, 2021). Compared with solely chemotherapeutic method, immuno-oncological or immuno-chemical nanomedicine strategies have the great potential to improve the efficiency toward tumor therapy. In

our personal view, tumor immunotherapy can be an excellent way to overcome chemotherapeutic drug resistance because this strategy directly targets the tumor microenvironment rather than the heterogeneous tumor cells to achieve efficacy. Furthermore, nano-immunotherapy strategy could also prevent the function of cancer stem cells (CSCs), which could significantly enhance the sensitivity of chemotherapy and tumor recurrence (Lang et al., 2019). All of these evidence shows the promising outcome of nanotherapeutics with combination of immunotherapy and chemotherapy.

It is challenging to design nanomaterials to share all desirable characteristics for overcoming all barriers. A concrete design should mainly depend on the specific drug cargo and tumor target. An ideal drug delivery system should adequately protect drug cargo, minimize nonspecific interactions with biological species, and allow efficient aggregation to target sites. In addition, the drug delivery system, once accumulated in tumor tissue, should provide sufficient penetration to deliver the drug throughout the tumor tissue, resulting in mass apoptosis of tumor cells (Li et al., 2014; Li et al., 2015; Li et al., 2021). For a long time, we have been tried to design more complex nanomaterials in many circumstances. However, the design itself is flawed to some extent. Besides, exploring the function of nanomaterial itself *in vivo* and its interaction with biological system at the tissue, cellular, and molecular levels are always ignored. We strongly suggest that researchers should pay more attention on the material itself biological functions and its pharmacokinetics *in vivo*. What's more, many efforts should be made to provide definitive evidence for its functional mechanism instead of creating many new complicated nanoparticle systems for similar concept.

At present, nanoparticles are trying to open a new era for tumor treatment. Though nanomedicine is still at an early stage, the reported results in cancer treatment especially in reversing drug resistance are surprising, and importantly, these advanced antitumor concepts are of great references for chemists, materials scientists, biologists, and may provide new insights into cancer and even a breakthrough in other fields.

AUTHOR CONTRIBUTIONS

LC and YZ contributed equally to this review. SZ, LC, and HC wrote the article. SZ and YZ conducted the literature analysis. WW, GW, SZ, and HC revised the article. All authors have read and agreed to the published version of the article.

FUNDING

This work was funded by Science and Technology Project of Quanzhou (2018Z155 and 2021N092S). The article processing charge was supported by Quanzhou Women's and Children's Hospital.

REFERENCES

Abolhoda, A., Wilson, A. E., Ross, H., Danenberg, P. V., Burt, M., and Scotto, K. W. (1999). Rapid Activation of MDR1 Gene Expression in Human Metastatic Sarcoma after *In Vivo* Exposure to Doxorubicin. *Clin. Cancer Res.* 5, 3352–3356.

Alsaab, H. O., Sau, S., Alzhrani, R. M., Cheriyan, V. T., Polin, L. A., Vaishampayan, U., et al. (2018). Tumor Hypoxia Directed Multimodal Nanotherapy for Overcoming Drug Resistance in Renal Cell Carcinoma and Reprogramming Macrophages. *Biomaterials* 183, 280–294. doi:10.1016/j.biomaterials.2018.08.053

Arvizo, R., Bhattacharya, R., and Mukherjee, P. (2010). Gold Nanoparticles: Opportunities and Challenges in Nanomedicine. *Expert Opin. Drug Deliv.* 7, 753–763. doi:10.1517/17425241003777010

Beck, B., and Blanpain, C. (2013). Unravelling Cancer Stem Cell Potential. *Nat. Rev. Cancer* 13, 727–738. doi:10.1038/nrc3597

Bhang, H.-e. C., Ruddy, D. A., Krishnamurthy Radhakrishna, V., Caushi, J. X., Zhao, R., Hims, M. M., et al. (2015). Studying Clonal Dynamics in Response to Cancer Therapy Using High-Complexity Barcoding. *Nat. Med.* 21, 440–448. doi:10.1038/nm.3841

Bhatia, A., and Kumar, Y. (2014). Cellular and Molecular Mechanisms in Cancer Immune Escape: a Comprehensive Review. *Expert Rev. Clin. Immunol.* 10, 41–62. doi:10.1586/1744666x.2014.865519

Bobo, D., Robinson, K. J., Islam, J., Thurecht, K. J., and Corrie, S. R. (2016). Nanoparticle-Based Medicines: A Review of FDA-Approved Materials and Clinical Trials to Date. *Pharm. Res.* 33, 2373–2387. doi:10.1007/s11095-016-1958-5

Brown, L. M., Cowen, R. L., Debray, C., Eustace, A., Erler, J. T., Sheppard, F. C. D., et al. (2006). Reversing Hypoxic Cell Chemoresistance *In Vitro* Using Genetic and Small Molecule Approaches Targeting Hypoxia Inducible Factor-1. *Mol. Pharmacol.* 69, 411–418. doi:10.1124/mol.105.015743

Butt, A. M., Amin, M. C. I. M., Katas, H., Abdul Murad, N. A., Jamal, R., and Kesharwani, P. (2016). Doxorubicin and siRNA Codelivery via Chitosan-Coated pH-Responsive Mixed Micellar Polyplexes for Enhanced Cancer Therapy in Multidrug-Resistant Tumors. *Mol. Pharmaceutics* 13, 4179–4190. doi:10.1021/acs.molpharmaceut.6b00776

Chabon, J. J., Simmons, A. D., Lovejoy, A. F., Esfahani, M. S., Newman, A. M., Haringsma, H. J., et al. (2016). Circulating Tumour DNA Profiling Reveals Heterogeneity of EGFR Inhibitor Resistance Mechanisms in Lung Cancer Patients. *Nat. Commun.* 7, 11815. doi:10.1038/ncomms11815

Chen, J., Wang, X., Yuan, Y., Chen, H., Zhang, L., Xiao, H., et al. (2021a). Exploiting the Acquired Vulnerability of Cisplatin-Resistant Tumors with a Hypoxia-Amplifying DNA Repair-Inhibiting (HYDRI) Nanomedicine. *Sci. Adv.* 7, eabc5267. doi:10.1126/sciadv.abc5267

Chen, X., Zou, J., Zhang, K., Zhu, J., Zhang, Y., Zhu, Z., et al. (2021b). Photothermal/matrix Metalloproteinase-2 Dual-Responsive Gelatin Nanoparticles for Breast Cancer Treatment. *Acta Pharmaceutica Sinica B* 11, 271–282. doi:10.1016/j.apsb.2020.08.009

Cheng, H., Fan, X., Wang, X., Ye, E., Loh, X. J., Li, Z., et al. (2018a). Hierarchically Self-Assembled Supramolecular Host-Guest Delivery System for Drug Resistant Cancer Therapy. *Biomacromolecules* 19, 1926–1938. doi:10.1021/acs.biomac.7b01693

Cheng, H., Fan, X., Ye, E., Chen, H., Yang, J., Ke, L., et al. (2021). Dual Tumor Microenvironment Remodeling by Glucose-Contained Radical Copolymer for MRI Guided Photo-Immunotherapy. *Adv. Mater.* Online ahead of print, e2107674. doi:10.1002/adma.202107674

Cheng, H., Wu, Z., Wu, C., Wang, X., Liow, S. S., Li, Z., et al. (2018b). Overcoming STC2 Mediated Drug Resistance through Drug and Gene Co -delivery by PHB-PDMAEMA Cationic Polyester in Liver Cancer Cells. *Mater. Sci. Eng. C.* 83, 210–217. doi:10.1016/j.msec.2017.08.075

Cheng, Q., Wei, T., Farbiak, L., Johnson, L. T., Dilliard, S. A., and Siegwart, D. J. (2020). Selective Organ Targeting (SORT) Nanoparticles for Tissue-specific mRNA Delivery and CRISPR-Cas Gene Editing. *Nat. Nanotechnol.* 15, 313–320. doi:10.1038/s41565-020-0669-6

Clarke, M. F., Dick, J. E., Dirks, P. B., Eaves, C. J., Jamieson, C. H. M., Jones, D. L., et al. (2006). Cancer Stem Cells-Perspectives on Current Status and Future Directions: AACR Workshop on Cancer Stem Cells. *Cancer Res.* 66, 9339–9344. doi:10.1158/0008-5472.can-06-3126

Comerford, K. M., Wallace, T. J., Karhausen, J., Louis, N. A., Montalto, M. C., and Colgan, S. P. (2002). Hypoxia-inducible Factor-1-dependent Regulation of the Multidrug Resistance (MDR1) Gene. *Cancer Res.* 62, 3387–3394.

Da Silva, C. G., Peters, G. J., Ossendorp, F., and Cruz, L. J. (2017). The Potential of Multi-Compound Nanoparticles to Bypass Drug Resistance in Cancer. *Cancer Chemother. Pharmacol.* 80, 881–894. doi:10.1007/s00280-017-3427-1

Dagogo-Jack, I., and Shaw, A. T. (2018). Tumour Heterogeneity and Resistance to Cancer Therapies. *Nat. Rev. Clin. Oncol.* 15, 81–94. doi:10.1038/nrclinonc.2017.166

Dean, M., Fojo, T., and Bates, S. (2005). Tumour Stem Cells and Drug Resistance. *Nat. Rev. Cancer* 5, 275–284. doi:10.1038/nrc1590

Du, B., and Shim, J. S. (2016). Targeting Epithelial-Mesenchymal Transition (EMT) to Overcome Drug Resistance in Cancer. *Molecules* 21, 965. doi:10.3390/molecules21070965

Du, F., Liu, H., Lu, Y., Zhao, X., and Fan, D. (2017). Epithelial-to-Mesenchymal Transition: Liaison between Cancer Metastasis and Drug Resistance. *Crit. Rev. Oncog.* 22, 275–282. doi:10.1615/critrevoncog.2018024855

Fan, X., Cheng, H., Wang, X., Ye, E., Loh, X. J., Wu, Y.-L., et al. (2018). Thermoresponsive Supramolecular Chemotherapy by "V"-Shaped Armed β-Cyclodextrin Star Polymer to Overcome Drug Resistance. *Adv. Healthc. Mater.* 7, 1701143. doi:10.1002/adhm.201701143

Fang, J., Nakamura, H., and Maeda, H. (2011). The EPR Effect: Unique Features of Tumor Blood Vessels for Drug Delivery, Factors Involved, and Limitations and Augmentation of the Effect. *Adv. Drug Deliv. Rev.* 63, 136–151. doi:10.1016/j.addr.2010.04.009

Gan, H., Chen, L., Sui, X., Wu, B., Zou, S., Li, A., et al. (2018). Enhanced Delivery of Sorafenib with Anti-GPC3 Antibody-Conjugated TPGS-B-PCL/Pluronic P123 Polymeric Nanoparticles for Targeted Therapy of Hepatocellular Carcinoma. *Mater. Sci. Eng. C.* 91, 395–403. doi:10.1016/j.msec.2018.05.011

Giacomini, K. M., Giacomini, K. M., Huang, S. M., Tweedie, D. J., Benet, L. Z., Brouwer, K. L., et al. (2010). Membrane Transporters in Drug Development. *Nat. Rev. Drug Discov.* 9, 215–236. doi:10.1038/nrd3028

Gottesman, M. M., Fojo, T., and Bates, S. E. (2002). Multidrug Resistance in Cancer: Role of ATP-dependent Transporters. *Nat. Rev. Cancer* 2, 48–58. doi:10.1038/nrc706

Gounder, M. M., Mahoney, M. R., Van Tine, B. A., Ravi, V., Attia, S., Deshpande, H. A., et al. (2018). Sorafenib for Advanced and Refractory Desmoid Tumors. *N. Engl. J. Med.* 379, 2417–2428. doi:10.1056/nejmoa1805052

Grosse-Gehling, P., Fargeas, C. A., Dittfeld, C., Garbe, Y., Alison, M. R., Corbeil, D., et al. (2013). CD133 as a Biomarker for Putative Cancer Stem Cells in Solid Tumours: Limitations, Problems and Challenges. *J. Pathol.* 229, 355–378. doi:10.1002/path.4086

Gu, J., Fang, X., Hao, J., and Sha, X. (2015). Reversal of P-Glycoprotein-Mediated Multidrug Resistance by CD44 Antibody-Targeted Nanocomplexes for Short Hairpin RNA-Encoding Plasmid DNA Delivery. *Biomaterials* 45, 99–114. doi:10.1016/j.biomaterials.2014.12.030

Gu, Y., Lai, S., Dong, Y., Fu, H., Song, L., Chen, T., et al. (2021). AZD9291 Resistance Reversal Activity of a pH-Sensitive Nanocarrier Dual-Loaded with Chloroquine and FGFR1 Inhibitor in NSCLC. *Adv. Sci.* 8, 2002922. doi:10.1002/advs.202002922

Hajipour, M. J., Aghaverdi, H., Serpooshan, V., Vali, H., Sheibani, S., and Mahmoudi, M. (2021). Sex as an Important Factor in Nanomedicine. *Nat. Commun.* 12, 2984. doi:10.1038/s41467-021-23230-9

Hao, J., Song, X., Song, B., Liu, Y., Wei, L., Wang, X., et al. (2008). Effects of Lentivirus-Mediated HIF-1α Knockdown on Hypoxia-Related Cisplatin Resistance and Their Dependence on P53 Status in Fibrosarcoma Cells. *Cancer Gene Ther.* 15, 449–455. doi:10.1038/cgt.2008.4

He, Q., and Shi, J. (2014). MSN Anti-cancer Nanomedicines: Chemotherapy Enhancement, Overcoming of Drug Resistance, and Metastasis Inhibition. *Adv. Mater.* 26, 391–411. doi:10.1002/adma.201303123

He, Y., Lei, L., Cao, J., Yang, X., Cai, S., Tong, F., et al. (2021). A Combinational Chemo-Immune Therapy Using an Enzyme-Sensitive Nanoplatform for Dual-Drug Delivery to Specific Sites by cascade Targeting. *Sci. Adv.* 7, eaba0776. doi:10.1126/sciadv.aba0776

Huo, Q., Zhu, J., Niu, Y., Shi, H., Gong, Y., Li, Y., et al. (2017). pH-triggered Surface Charge-Switchable Polymer Micelles for the Co-delivery of Paclitaxel/disulfiram and Overcoming Multidrug Resistance in Cancer. *Ijn* 12, 8631–8647. doi:10.2147/ijn.s144452

Ishizawa, K., Rasheed, Z. A., Karisch, R., Wang, Q., Kowalski, J., Susky, E., et al. (2010). Tumor-initiating Cells Are Rare in many Human Tumors. *Cell Stem Cell* 7, 279–282. doi:10.1016/j.stem.2010.08.009

Izumi, H., Torigoe, T., Ishiguchi, H., Uramoto, H., Yoshida, Y., Tanabe, M., et al. (2003). Cellular pH Regulators: Potentially Promising Molecular Targets for Cancer Chemotherapy. *Cancer Treat. Rev.* 29, 541–549. doi:10.1016/s0305-7372(03)00106-3

Jeong, H., Lee, S. H., Hwang, Y., Yoo, H., Jung, H., Kim, S. H., et al. (2017). Multivalent Aptamer-RNA Conjugates for Simple and Efficient Delivery of Doxorubicin/siRNA into Multidrug-Resistant Cells. *Macromol Biosci.* 17, 1600343. doi:10.1002/mabi.201600343

Jiang, Z.-S., Sun, Y.-Z., Wang, S.-M., and Ruan, J.-S. (2017). Epithelial-mesenchymal Transition: Potential Regulator of ABC Transporters in Tumor Progression. *J. Cancer* 8, 2319–2327. doi:10.7150/jca.19079

Jing, X., Yang, F., Shao, C., Wei, K., Xie, M., Shen, H., et al. (2019). Role of Hypoxia in Cancer Therapy by Regulating the Tumor Microenvironment. *Mol. Cancer* 18, 157. doi:10.1186/s12943-019-1089-9

Joshi, U., Filipczak, N., Khan, M. M., Attia, S. A., and Torchilin, V. (2020). Hypoxia-sensitive Micellar Nanoparticles for Co-delivery of siRNA and Chemotherapeutics to Overcome Multi-Drug Resistance in Tumor Cells. *Int. J. Pharmaceutics* 590, 119915. doi:10.1016/j.ijpharm.2020.119915

Kc, R. B., Thapa, B., and Xu, P. (2012). pH and Redox Dual Responsive Nanoparticle for Nuclear Targeted Drug Delivery. *Mol. Pharm.* 9, 2719–2729. doi:10.1021/mp300274g

Ke, L., Li, Z., Fan, X., Loh, X. J., Cheng, H., Wu, Y.-L., et al. (2021). Cyclodextrin-Based Hybrid Polymeric Complex to Overcome Dual Drug Resistance Mechanisms for Cancer Therapy. *Polymers* 13, 1254. doi:10.3390/polym13081254

Kim, D., Xue, J. Y., and Lito, P. (2020). Targeting KRAS(G12C): From Inhibitory Mechanism to Modulation of Antitumor Effects in Patients. *Cell* 183, 850–859. doi:10.1016/j.cell.2020.09.044

Kobayashi, H., Watanabe, R., and Choyke, P. L. (2013). Improving Conventional Enhanced Permeability and Retention (EPR) Effects; what Is the Appropriate Target? *Theranostics* 4, 81–89. doi:10.7150/thno.7193

Lackner, M. R., Wilson, T. R., and Settleman, J. (2012). Mechanisms of Acquired Resistance to Targeted Cancer Therapies. *Future Oncol.* 8, 999–1014. doi:10.2217/fon.12.86

Lamouille, S., Xu, J., and Derynck, R. (2014). Molecular Mechanisms of Epithelial-Mesenchymal Transition. *Nat. Rev. Mol. Cel Biol.* 15, 178–196. doi:10.1038/nrm3758

Lang, T., Liu, Y., Zheng, Z., Ran, W., Zhai, Y., Yin, Q., et al. (2019). Cocktail Strategy Based on Spatio-Temporally Controlled Nano Device Improves Therapy of Breast Cancer. *Adv. Mater.* 31, e1903844. doi:10.1002/adma.201903844

Lee, J. E., Park, H. S., Lee, D., Yoo, G., Kim, T., Jeon, H., et al. (2016). Hippo Pathway Effector YAP Inhibition Restores the Sensitivity of EGFR-TKI in Lung Adenocarcinoma Having Primary or Acquired EGFR-TKI Resistance. *Biochem. Biophysical Res. Commun.* 474, 154–160. doi:10.1016/j.bbrc.2016.04.089

Li, J., Dirisala, A., Ge, Z., Wang, Y., Yin, W., Ke, W., et al. (2017). Therapeutic Vesicular Nanoreactors with Tumor-Specific Activation and Self-Destruction for Synergistic Tumor Ablation. *Angew. Chem.* 129, 14213–14218. doi:10.1002/ange.201706964

Li, J., Ge, Z., Toh, K., Liu, X., Dirisala, A., Ke, W., et al. (2021). Enzymatically Transformable Polymersome-Based Nanotherapeutics to Eliminate Minimal Relapsable Cancer. *Adv. Mater.* Online ahead of print, e2105254. doi:10.1002/adma.202105254

Li, J., Han, Y., Chen, Q., Shi, H., Ur Rehman, S., Siddiq, M., et al. (2014). Dual Endogenous Stimuli-Responsive Polyplex Micelles as Smart Two-step Delivery Nanocarriers for Deep Tumor Tissue Penetration and Combating Drug Resistance of Cisplatin. *J. Mater. Chem. B.* 2, 1813–1824. doi:10.1039/c3tb21383h

Li, J., and Kataoka, K. (2021). Chemo-physical Strategies to Advance the *In Vivo* Functionality of Targeted Nanomedicine: The Next Generation. *J. Am. Chem. Soc.* 143, 538–559. doi:10.1021/jacs.0c09029

Li, J., Ke, W., Li, H., Zha, Z., Han, Y., and Ge, Z. (2015). Endogenous Stimuli-Sensitive Multistage Polymeric Micelleplex Anticancer Drug Delivery System for Efficient Tumor Penetration and Cellular Internalization. *Adv. Healthc. Mater.* 4, 2206–2219. doi:10.1002/adhm.201500379

Li, J., Shu, Y., Hao, T., Wang, Y., Qian, Y., Duan, C., et al. (2013). A Chitosan-Glutathione Based Injectable Hydrogel for Suppression of Oxidative Stress Damage in Cardiomyocytes. *Biomaterials* 34, 9071–9081. doi:10.1016/j.biomaterials.2013.08.031

Li, L., He, S., Yu, L., Elshazly, E. H., Wang, H., Chen, K., et al. (2019). Codelivery of DOX and siRNA by Folate-Biotin-Quaternized Starch Nanoparticles for Promoting Synergistic Suppression of Human Lung Cancer Cells. *Drug Deliv.* 26, 499–508. doi:10.1080/10717544.2019.1606363

Liu, L., Ning, X., Sun, L., Zhang, H., Shi, Y., Guo, C., et al. (2008). Hypoxia-inducible Factor-1 Alpha Contributes to Hypoxia-Induced Chemoresistance in Gastric Cancer. *Cancer Sci.* 99, 121–128. doi:10.1111/j.1349-7006.2007.00643.x

Liu, Q., Cai, J., Zheng, Y., Tan, Y., Wang, Y., Zhang, Z., et al. (2019). NanoRNP Overcomes Tumor Heterogeneity in Cancer Treatment. *Nano Lett.* 19, 7662–7672. doi:10.1021/acs.nanolett.9b02501

Longley, D., and Johnston, P. (2005). Molecular Mechanisms of Drug Resistance. *J. Pathol.* 205, 275–292. doi:10.1002/path.1706

Lord, A. C., D'souza, N., Shaw, A., Rokan, Z., Moran, B., Abulafi, M., et al. (2021). MRI-diagnosed Tumour Deposits and EMVI Status Have superior Prognostic Accuracy to Current Clinical TNM Staging in Rectal Cancer. *Ann. Surg.* Online ahead of print. doi:10.1097/SLA.0000000000004499

Lu, J., Tan, M., and Cai, Q. (2015). The Warburg Effect in Tumor Progression: Mitochondrial Oxidative Metabolism as an Anti-metastasis Mechanism. *Cancer Lett.* 356, 156–164. doi:10.1016/j.canlet.2014.04.001

Mani, S. A., Guo, W., Liao, M.-J., Eaton, E. N., Ayyanan, A., Zhou, A. Y., et al. (2008). The Epithelial-Mesenchymal Transition Generates Cells with Properties of Stem Cells. *Cell* 133, 704–715. doi:10.1016/j.cell.2008.03.027

Mao, J., Li, Y., Wu, T., Yuan, C., Zeng, B., Xu, Y., et al. (2016). A Simple Dual-pH Responsive Prodrug-Based Polymeric Micelles for Drug Delivery. *ACS Appl. Mater. Inter.* 8, 17109–17117. doi:10.1021/acsami.6b04247

Markman, J. L., Rekechenetskiy, A., Holler, E., and Ljubimova, J. Y. (2013). Nanomedicine Therapeutic Approaches to Overcome Cancer Drug Resistance. *Adv. Drug Deliv. Rev.* 65, 1866–1879. doi:10.1016/j.addr.2013.09.019

Marson, D., Laurini, E., Aulic, S., Fermeglia, M., and Pricl, S. (2019). Evolution from Covalent to Self-Assembled PAMAM-Based Dendrimers as Nanovectors for siRNA Delivery in Cancer by Coupled In Silico-Experimental Studies. Part I: Covalent siRNA Nanocarriers. *Pharmaceutics* 11, 351. doi:10.3390/pharmaceutics11070351

Marusyk, A., and Polyak, K. (2010). Tumor Heterogeneity: Causes and Consequences. *Biochim. Biophys. Acta (Bba) - Rev. Cancer* 1805, 105–117. doi:10.1016/j.bbcan.2009.11.002

Mckeown, S. R. (2014). Defining Normoxia, Physoxia and Hypoxia in Tumours-Implications for Treatment Response. *Bjr* 87, 20130676. doi:10.1259/bjr.20130676

Milla, P., Dosio, F., and Cattel, L. (2012). PEGylation of Proteins and Liposomes: a Powerful and Flexible Strategy to Improve the Drug Delivery. *Cdm* 13, 105–119. doi:10.2174/138920012798356934

Min, H.-Y., Lee, S.-C., Woo, J. K., Jung, H. J., Park, K. H., Jeong, H. M., et al. (2017). Essential Role of DNA Methyltransferase 1-mediated Transcription of Insulin-like Growth Factor 2 in Resistance to Histone Deacetylase Inhibitors. *Clin. Cancer Res.* 23, 1299–1311. doi:10.1158/1078-0432.ccr-16-0534

Miraglia, E., Viarisio, D., Riganti, C., Costamagna, C., Ghigo, D., and Bosia, A. (2005). Na+/H+ Exchanger Activity Is Increased in Doxorubicin-Resistant Human colon Cancer Cells and its Modulation Modifies the Sensitivity of the Cells to Doxorubicin. *Int. J. Cancer* 115, 924–929. doi:10.1002/ijc.20959

Mitchell, M. J., Billingsley, M. M., Haley, R. M., Wechsler, M. E., Peppas, N. A., and Langer, R. (2021). Engineering Precision Nanoparticles for Drug Delivery. *Nat. Rev. Drug Discov.* 20, 101–124. doi:10.1038/s41573-020-0090-8

Moitra, K. (2015). Overcoming Multidrug Resistance in Cancer Stem Cells. *Biomed. Res. Int.* 2015, 635745. doi:10.1155/2015/635745

Nagrath, S., Sequist, L. V., Maheswaran, S., Bell, D. W., Irimia, D., Ulkus, L., et al. (2007). Isolation of Rare Circulating Tumour Cells in Cancer Patients by Microchip Technology. *Nature* 450, 1235–1239. doi:10.1038/nature06385

Nigam, S. K. (2015). What Do Drug Transporters Really Do? *Nat. Rev. Drug Discov.* 14, 29–44. doi:10.1038/nrd4461

Olson, E. S., Jiang, T., Aguilera, T. A., Nguyen, Q. T., Ellies, L. G., Scadeng, M., et al. (2010). Activatable Cell Penetrating Peptides Linked to Nanoparticles as Dual Probes for *In Vivo* Fluorescence and MR Imaging of Proteases. *Proc. Natl. Acad. Sci.* 107, 4311–4316. doi:10.1073/pnas.0910283107

Pallis, M., Turzanski, J., Higashi, Y., and Russell, N. (2002). P-glycoprotein in Acute Myeloid Leukaemia: Therapeutic Implications of its Association with Both a Multidrug-Resistant and an Apoptosis-Resistant Phenotype. *Leuk. Lymphoma* 43, 1221–1228. doi:10.1080/10428190290026277

Pastorek, J., and Pastorekova, S. (2015). Hypoxia-induced Carbonic Anhydrase IX as a Target for Cancer Therapy: from Biology to Clinical Use. *Semin. Cancer Biol.* 31, 52–64. doi:10.1016/j.semcancer.2014.08.002

Pérez-Tomás, R. (2006). Multidrug Resistance: Retrospect and Prospects in Anti-cancer Drug Treatment. *Cmc* 13, 1859–1876. doi:10.2174/092986706777585077

Pieretti, J. C., Pelegrino, M. T., Nascimento, M. H. M., Tortella, G. R., Rubilar, O., and Seabra, A. B. (2020). Small Molecules for Great Solutions: Can Nitric Oxide-Releasing Nanomaterials Overcome Drug Resistance in Chemotherapy? *Biochem. Pharmacol.* 176, 113740. doi:10.1016/j.bcp.2019.113740

Polyak, K. (2014). Tumor Heterogeneity Confounds and Illuminates: a Case for Darwinian Tumor Evolution. *Nat. Med.* 20, 344–346. doi:10.1038/nm.3518

Robey, R. W., Pluchino, K. M., Hall, M. D., Fojo, A. T., Bates, S. E., and Gottesman, M. M. (2018). Revisiting the Role of ABC Transporters in Multidrug-Resistant Cancer. *Nat. Rev. Cancer* 18, 452–464. doi:10.1038/s41568-018-0005-8

Rohwer, N., and Cramer, T. (2011). Hypoxia-mediated Drug Resistance: Novel Insights on the Functional Interaction of HIFs and Cell Death Pathways. *Drug Resist. Updates* 14, 191–201. doi:10.1016/j.drup.2011.03.001

Rohwer, N., Dame, C., Haugstetter, A., Wiedenmann, B., Detjen, K., Schmitt, C. A., et al. (2010). Hypoxia-Inducible Factor 1α Determines Gastric Cancer Chemosensitivity via Modulation of P53 and NF-Kb. *PLoS One* 5, e12038. doi:10.1371/journal.pone.0012038

Saxena, M., Stephens, M. A., Pathak, H., and Rangarajan, A. (2011). Transcription Factors that Mediate Epithelial-Mesenchymal Transition lead to Multidrug Resistance by Upregulating ABC Transporters. *Cell Death Dis.* 2, e179. doi:10.1038/cddis.2011.61

Scarberry, K. E., Dickerson, E. B., Mcdonald, J. F., and Zhang, Z. J. (2008). Magnetic Nanoparticle–Peptide Conjugates for *In Vitro* and *In Vivo* Targeting and Extraction of Cancer Cells. *J. Am. Chem. Soc.* 130, 10258–10262. doi:10.1021/ja801969b

Schütz, C. A., Juillerat-Jeanneret, L., Mueller, H., Lynch, I., and Riediker, M. (2013). Therapeutic Nanoparticles in Clinics and under Clinical Evaluation. *Nanomedicine* 8, 449–467. doi:10.2217/nnm.13.8

Semenza, G. L. (2010). HIF-1: Upstream and Downstream of Cancer Metabolism. *Curr. Opin. Genet. Dev.* 20, 51–56. doi:10.1016/j.gde.2009.10.009

Son, S., Shin, S., Rao, N. V., Um, W., Jeon, J., Ko, H., et al. (2018). Anti-Trop2 Antibody-Conjugated Bioreducible Nanoparticles for Targeted Triple Negative Breast Cancer Therapy. *Int. J. Biol. Macromolecules* 110, 406–415. doi:10.1016/j.ijbiomac.2017.10.113

Song, L., Jiang, Q., Liu, J., Li, N., Liu, Q., Dai, L., et al. (2017). DNA Origami/gold Nanorod Hybrid Nanostructures for the Circumvention of Drug Resistance. *Nanoscale* 9, 7750–7754. doi:10.1039/c7nr02222k

Song, X., Feng, L., Liang, C., Yang, K., and Liu, Z. (2016). Ultrasound Triggered Tumor Oxygenation with Oxygen-Shuttle Nanoperfluorocarbon to Overcome Hypoxia-Associated Resistance in Cancer Therapies. *Nano Lett.* 16, 6145–6153. doi:10.1021/acs.nanolett.6b02365

Spugnini, E. P., Sonveaux, P., Stock, C., Perez-Sayans, M., De Milito, A., Avnet, S., et al. (2015). Proton Channels and Exchangers in Cancer. *Biochim. Biophys. Acta (Bba) - Biomembranes* 1848, 2715–2726. doi:10.1016/j.bbamem.2014.10.015

Sun, M., Gu, P., Yang, Y., Yu, L., Jiang, Z., Li, J., et al. (2021). Mesoporous Silica Nanoparticles Inflame Tumors to Overcome Anti-PD-1 Resistance through TLR4-Nfkb axis. *J. Immunother. Cancer* 9, e002508. doi:10.1136/jitc-2021-002508

Taylor, S., Spugnini, E. P., Assaraf, Y. G., Azzarito, T., Rauch, C., and Fais, S. (2015). Microenvironment Acidity as a Major Determinant of Tumor Chemoresistance: Proton Pump Inhibitors (PPIs) as a Novel Therapeutic Approach. *Drug Resist. Updates* 23, 69–78. doi:10.1016/j.drup.2015.08.004

Tian, H., Luo, Z., Liu, L., Zheng, M., Chen, Z., Ma, A., et al. (2017). Cancer Cell Membrane-Biomimetic Oxygen Nanocarrier for Breaking Hypoxia-Induced Chemoresistance. *Adv. Funct. Mater.* 27, 1703197. doi:10.1002/adfm.201703197

Vaghasiya, K., Ray, E., Sharma, A., Katare, O. P., and Verma, R. K. (2020). Matrix Metalloproteinase-Responsive Mesoporous Silica Nanoparticles Cloaked with

Cleavable Protein for "Self-Actuating" On-Demand Controlled Drug Delivery for Cancer Therapy. *ACS Appl. Bio Mater.* 3, 4987–4999. doi:10.1021/acsabm.0c00497

Van Der Meel, R., Vehmeijer, L. J. C., Kok, R. J., Storm, G., and Van Gaal, E. V. B. (2013). Ligand-targeted Particulate Nanomedicines Undergoing Clinical Evaluation: Current Status. *Adv. Drug Deliv. Rev.* 65, 1284–1298. doi:10.1016/j.addr.2013.08.012

Vasan, N., Baselga, J., and Hyman, D. M. (2019). A View on Drug Resistance in Cancer. *Nature* 575, 299–309. doi:10.1038/s41586-019-1730-1

Vaupel, P., and Multhoff, G. (2018). Hypoxia-/HIF-1α-Driven Factors of the Tumor Microenvironment Impeding Antitumor Immune Responses and Promoting Malignant Progression. *Adv. Exp. Med. Biol.* 1072, 171–175. doi:10.1007/978-3-319-91287-5_27

Vaupel, P., Schmidberger, H., and Mayer, A. (2019). The Warburg Effect: Essential Part of Metabolic Reprogramming and central Contributor to Cancer Progression. *Int. J. Radiat. Biol.* 95, 912–919. doi:10.1080/09553002.2019.1589653

Villani, A. C., Satija, R., Reynolds, G., Sarkizova, S., Shekhar, K., Fletcher, J., et al. (2017). Single-cell RNA-Seq Reveals New Types of Human Blood Dendritic Cells, Monocytes, and Progenitors. *Science* 356, eaah4573. doi:10.1126/science.aah4573

Vishwakarma, S. K., Sharmila, P., Bardia, A., Chandrakala, L., Raju, N., Sravani, G., et al. (2017). Use of Biocompatible Sorafenib-Gold Nanoconjugates for Reversal of Drug Resistance in Human Hepatoblatoma Cells. *Sci. Rep.* 7, 8539. doi:10.1038/s41598-017-08878-y

Vitale, I., Manic, G., De Maria, R., Kroemer, G., and Galluzzi, L. (2017). DNA Damage in Stem Cells. *Mol. Cel* 66, 306–319. doi:10.1016/j.molcel.2017.04.006

Vivek, R., Thangam, R., Nipunbabu, V., Rejeeth, C., Sivasubramanian, S., Gunasekaran, P., et al. (2014). Multifunctional HER2-Antibody Conjugated Polymeric Nanocarrier-Based Drug Delivery System for Multi-Drug-Resistant Breast Cancer Therapy. *ACS Appl. Mater. Inter.* 6, 6469–6480. doi:10.1021/am406012g

Wang, D., Zhao, C., Xu, F., Zhang, A., Jin, M., Zhang, K., et al. (2021a). Cisplatin-resistant NSCLC Cells Induced by Hypoxia Transmit Resistance to Sensitive Cells through Exosomal PKM2. *Theranostics* 11, 2860–2875. doi:10.7150/thno.51797

Wang, J., Wu, C., Qin, X., Huang, Y., Zhang, J., Chen, T., et al. (2021b). NIR-II Light Triggered Nitric Oxide Release Nanoplatform Combined Chemo-Photothermal Therapy for Overcoming Multidrug Resistant Cancer. *J. Mater. Chem. B* 9, 1698–1706. doi:10.1039/d0tb02626c

Wang, L., Chang, Y., Feng, Y., Li, X., Cheng, Y., Jian, H., et al. (2019a). Nitric Oxide Stimulated Programmable Drug Release of Nanosystem for Multidrug Resistance Cancer Therapy. *Nano Lett.* 19, 6800–6811. doi:10.1021/acs.nanolett.9b01869

Wang, L., Lin, X., Wang, J., Hu, Z., Ji, Y., Hou, S., et al. (2014). Novel Insights into Combating Cancer Chemotherapy Resistance Using a Plasmonic Nanocarrier: Enhancing Drug Sensitiveness and Accumulation Simultaneously with Localized Mild Photothermal Stimulus of Femtosecond Pulsed Laser. *Adv. Funct. Mater.* 24, 4229–4239. doi:10.1002/adfm.201400015

Wang, M., Liu, W., Zhang, Y., Dang, M., Zhang, Y., Tao, J., et al. (2019b). Intercellular Adhesion Molecule 1 Antibody-Mediated Mesoporous Drug Delivery System for Targeted Treatment of Triple-Negative Breast Cancer. *J. Colloid Interf. Sci.* 538, 630–637. doi:10.1016/j.jcis.2018.12.032

Wang, Y., Sun, S., Zhang, Z., and Shi, D. (2018a). Nanomaterials for Cancer Precision Medicine. *Adv. Mater.* 30, 1705660. doi:10.1002/adma.201705660

Wang, Y., Wang, F., Liu, Y., Xu, S., Shen, Y., Feng, N., et al. (2018b). Glutathione Detonated and pH Responsive Nano-Clusters of Au Nanorods with a High Dose of DOX for Treatment of Multidrug Resistant Cancer. *Acta Biomater.* 75, 334–345. doi:10.1016/j.actbio.2018.06.012

Wang, Z., Li, X., Wang, D., Zou, Y., Qu, X., He, C., et al. (2017). Concurrently Suppressing Multidrug Resistance and Metastasis of Breast Cancer by Co-delivery of Paclitaxel and Honokiol with pH-Sensitive Polymeric Micelles. *Acta Biomater.* 62, 144–156. doi:10.1016/j.actbio.2017.08.027

Wang, Z., Xu, Z., and Zhu, G. (2016). A Platinum(IV) Anticancer Prodrug Targeting Nucleotide Excision Repair to Overcome Cisplatin Resistance. *Angew. Chem. Int. Ed.* 55, 15564–15568. doi:10.1002/anie.201608936

Wei, G., Yang, G., Wei, B., Wang, Y., and Zhou, S. (2019a). Near-infrared Light Switching Nitric Oxide Nanoemitter for Triple-Combination Therapy of Multidrug Resistant Cancer. *Acta Biomater.* 100, 365–377. doi:10.1016/j.actbio.2019.10.002

Wei, X., Liu, L., Li, X., Wang, Y., Guo, X., Zhao, J., et al. (2019b). Selectively Targeting Tumor-Associated Macrophages and Tumor Cells with Polymeric Micelles for Enhanced Cancer Chemo-Immunotherapy. *J. Controlled Release* 313, 42–53. doi:10.1016/j.jconrel.2019.09.021

Wen, Z.-M., Jie, J., Zhang, Y., Liu, H., and Peng, L.-P. (2017). A Self-Assembled Polyjuglanin Nanoparticle Loaded with Doxorubicin and Anti-kras siRNA for Attenuating Multidrug Resistance in Human Lung Cancer. *Biochem. Biophysical Res. Commun.* 493, 1430–1437. doi:10.1016/j.bbrc.2017.09.132

Wirthner, R., Wrann, S., Balamurugan, K., Wenger, R. H., and Stiehl, D. P. (2008). Impaired DNA Double-Strand Break Repair Contributes to Chemoresistance in HIF-1 -deficient Mouse Embryonic Fibroblasts. *Carcinogenesis* 29, 2306–2316. doi:10.1093/carcin/bgn231

Wu, H., Wang, C., Sun, J., Sun, L., Wan, J., Wang, S., et al. (2019). Self-Assembled and Self-Monitored Sorafenib/Indocyanine Green Nanodrug with Synergistic Antitumor Activity Mediated by Hyperthermia and Reactive Oxygen Species-Induced Apoptosis. *ACS Appl. Mater. Inter.* 11, 43996–44006. doi:10.1021/acsami.9b18086

Xiao, B., Ma, L., and Merlin, D. (2017). Nanoparticle-mediated Co-delivery of Chemotherapeutic Agent and siRNA for Combination Cancer Therapy. *Expert Opin. Drug Deliv.* 14, 65–73. doi:10.1080/17425247.2016.1205583

Xu, M., Zhang, C. Y., Wu, J., Zhou, H., Bai, R., Shen, Z., et al. (2019). PEG-detachable Polymeric Micelles Self-Assembled from Amphiphilic Copolymers for Tumor-Acidity-Triggered Drug Delivery and Controlled Release. *ACS Appl. Mater. Inter.* 11, 5701–5713. doi:10.1021/acsami.8b13059

Xu, R., Luo, X., Ye, X., Li, H., Liu, H., Du, Q., et al. (2021). SIRT1/PGC-1α/PPAR-γ Correlate with Hypoxia-Induced Chemoresistance in Non-small Cell Lung Cancer. *Front. Oncol.* 11, 682762. doi:10.3389/fonc.2021.682762

Yan, J., Zhang, Z., Zhan, X., Chen, K., Pu, Y., Liang, Y., et al. (2021). *In Situ* injection of Dual-Delivery PEG Based MMP-2 Sensitive Hydrogels for Enhanced Tumor Penetration and Chemo-Immune Combination Therapy. *Nanoscale* 13, 9577–9589. doi:10.1039/d1nr01155c

Yan, Y., Zuo, X., and Wei, D. (2015). Concise Review: Emerging Role of CD44 in Cancer Stem Cells: A Promising Biomarker and Therapeutic Target. *Stem Cell Transl Med* 4, 1033–1043. doi:10.5966/sctm.2015-0048

Yang, Y. (2015). Cancer Immunotherapy: Harnessing the Immune System to Battle Cancer. *J. Clin. Invest.* 125, 3335–3337. doi:10.1172/jci83871

Yao, Q., Kou, L., Tu, Y., and Zhu, L. (2018). MMP-responsive 'Smart' Drug Delivery and Tumor Targeting. *Trends Pharmacol. Sci.* 39, 766–781. doi:10.1016/j.tips.2018.06.003

Yu, P., Yu, H., Guo, C., Cui, Z., Chen, X., Yin, Q., et al. (2015). Reversal of Doxorubicin Resistance in Breast Cancer by Mitochondria-Targeted pH-Responsive Micelles. *Acta Biomater.* 14, 115–124. doi:10.1016/j.actbio.2014.12.001

Yuan, Y.-Y., Mao, C.-Q., Du, X.-J., Du, J.-Z., Wang, F., and Wang, J. (2012). Surface Charge Switchable Nanoparticles Based on Zwitterionic Polymer for Enhanced Drug Delivery to Tumor. *Adv. Mater.* 24, 5476–5480. doi:10.1002/adma.201202296

Zellmer, V. R., and Zhang, S. (2014). Evolving Concepts of Tumor Heterogeneity. *Cell Biosci* 4, 69. doi:10.1186/2045-3701-4-69

Zeng, Y., Yang, Z., Li, H., Hao, Y., Liu, C., Zhu, L., et al. (2017). Multifunctional Nanographene Oxide for Targeted Gene-Mediated Thermochemotherapy of Drug-Resistant Tumour. *Sci. Rep.* 7, 43506. doi:10.1038/srep43506

Zhang, J., Du, Z., Pan, S., Shi, M., Li, J., Yang, C., et al. (2018). Overcoming Multidrug Resistance by Codelivery of MDR1-Targeting siRNA and Doxorubicin Using EphA10-Mediated pH-Sensitive Lipoplexes: *In Vitro* and *In Vivo* Evaluation. *ACS Appl. Mater. Inter.* 10, 21590–21600. doi:10.1021/acsami.8b01806

Zhang, J., Wang, L., Fai Chan, H., Xie, W., Chen, S., He, C., et al. (2017). Co-delivery of Paclitaxel and Tetrandrine via iRGD Peptide Conjugated Lipid-Polymer Hybrid Nanoparticles Overcome Multidrug Resistance in Cancer Cells. *Sci. Rep.* 7, 46057. doi:10.1038/srep46057

Zhang, L., Zhang, Y., Strong, J. M., Reynolds, K. S., and Huang, S.-M. (2008). A Regulatory Viewpoint on Transporter-Based Drug Interactions. *Xenobiotica* 38, 709–724. doi:10.1080/00498250802017715

Zhang, P.-Y., and Yu, Y. (2020). Precise Personalized Medicine in Gynecology Cancer and Infertility. *Front. Cel Dev. Biol.* 7, 382. doi:10.3389/fcell.2019.00382

Zhang, W., Wang, F., Wang, Y., Wang, J., Yu, Y., Guo, S., et al. (2016). pH and Near-Infrared Light Dual-Stimuli Responsive Drug Delivery Using DNA-Conjugated Gold Nanorods for Effective Treatment of Multidrug Resistant Cancer Cells. *J. Controlled Release* 232, 9–19. doi:10.1016/j.jconrel.2016.04.001

Zhu, M., Nie, G., Meng, H., Xia, T., Nel, A., and Zhao, Y. (2013). Physicochemical Properties Determine Nanomaterial Cellular Uptake, Transport, and Fate. *Acc. Chem. Res.* 46, 622–631. doi:10.1021/ar300031y

Conflict of Interest: The authors declare that the research was conducted in the absence of any commercial or financial relationships that could be construed as a potential conflict of interest.

Publisher's Note: All claims expressed in this article are solely those of the authors and do not necessarily represent those of their affiliated organizations, or those of the publisher, the editors, and the reviewers. Any product that may be evaluated in this article, or claim that may be made by its manufacturer, is not guaranteed or endorsed by the publisher.

frontiers in Bioengineering and Biotechnology

ORIGINAL RESEARCH
published: 07 December 2021
doi: 10.3389/fbioe.2021.762489

Resveratrol-Loaded TPGS-Resveratrol-Solid Lipid Nanoparticles for Multidrug-Resistant Therapy of Breast Cancer: *In Vivo* and *In Vitro* Study

Wenrui Wang[1], Mengyang Zhou[1,2], Yang Xu[1], Wei Peng[1], Shiwen Zhang[1], Rongjie Li[1], Han Zhang[1], Hui Zhang[1], Shumin Cheng[1], Youjing Wang[1], Xinyu Wei[3], Chengxu Yue[1], Qingling Yang[3]* and Changjie Chen[3]**

[1]Anhui Province Key Laboratory of Translational Cancer Research, Department of Biotechnology, Bengbu Medical College, Anhui, China, [2]Department of Life Sciences, Anhui Medical University, Anhui, China, [3]Department of Biochemistry, School of Laboratory Medicine Bengbu Medical College, Anhui, China

OPEN ACCESS

Edited by:
Jinbing Xie,
Southeast University, China

Reviewed by:
Jiao Wang,
Purdue University, United States
Ling Zhi Wu,
Nanjing University of Posts and Telecommunications, China

***Correspondence:**
Wenrui Wang
wenrui-wang1983@163.com
Changjie Chen
tochenchangjie@163.com
Qingling Yang
yqlmimi@163.com

Specialty section:
This article was submitted to Biomaterials, a section of the journal Frontiers in Bioengineering and Biotechnology

Received: 22 August 2021
Accepted: 04 November 2021
Published: 07 December 2021

Citation:
Wang W, Zhou M, Xu Y, Peng W, Zhang S, Li R, Zhang H, Zhang H, Cheng S, Wang Y, Wei X, Yue C, Yang Q and Chen C (2021) Resveratrol-Loaded TPGS-Resveratrol-Solid Lipid Nanoparticles for Multidrug-Resistant Therapy of Breast Cancer: In Vivo and In Vitro Study. Front. Bioeng. Biotechnol. 9:762489. doi: 10.3389/fbioe.2021.762489

Multidrug resistance (MDR) is a serious problem during cancer therapy. The purpose of the present study was to formulate D-α-Tocopheryl polyethylene glycol 1000 succinate-resveratrol-solid lipid nanoparticles (TPGS-Res-SLNs) to improve its therapeutic efficacy against breast cancer. In this study, the solvent injection method was used to prepare the TPGS-Res-SLNs. It was found that the TPGS-Res-SLNs exhibited zeta potential and drug-loading of −25.6 ± 1.3 mV and 32.4 ± 2.6%, respectively. Therefore, it was evident that the TPGS-Res-SLNs can increase cellular uptake of chemotherapeutic drugs, induce mitochondrial dysfunction, and augment tumor treatment efficiency by inducing apoptosis. Moreover, it was found that SKBR3/PR cells treated with TPGS-Res-SLNs exhibited significant inhibition of cell migration and invasion, as compared with free resveratrol. In addition, results from *in vivo* SKBR3/PR xenograft tumor models revealed that TPGS-Res-SLNs has better efficacy in promoting apoptosis of tumor cells owing to high therapeutic outcomes on tumors when compared with the efficacy of free resveratrol. In conclusion, the findings of the present study indicate significant potential for use of TPGS-Res-SLNs as an efficient drug delivery vehicle to overcome drug resistance in breast cancer therapy.

Keywords: multidrug resistance, drug delivery, resveratrol, solid lipid nanoparticle, breast cancer

INTRODUCTION

Globally, breast cancer (BC) is the second leading cause of cancer-related deaths in women (Malvezzi et al., 2019). The American Cancer Society predicts that, an estimated 281,550 new cases of invasive breast cancer will be diagnosed, resulting in 43,600 deaths in 2021 (Siegel et al., 2021). Reports indicate that genetic mutations, endocrine disorders, and a decline in immune function increases the risk of developing breast cancer (Sun et al., 2017; Sui et al., 2015; Rojas and Stuckey, 2016).

Current methods of treatment for this condition include surgery, chemotherapy, radiotherapy, or combined strategy (Untch et al., 2014; Willers et al., 1997). For instance, use of paclitaxel (PTX) has been recognized as the first-line chemotherapy in treatment of breast cancer. However, the efficacy of

PTX is often limited by multidrug resistance (MDR) (Xu et al., 2016). Therefore, there is need to develop a novel strategy for overcoming this limitation and provide a safe, economically-friendly, and effective therapeutic agent against BC.

The development of MDR poses a major challenge to the existing conventional chemotherapies against BC. Functionally, an ATP-binding cassette (ABC) transporter family, comprising P-glycoprotein (P-gp), multidrug resistance-associated protein (MRP) and BC resistance protein (BCRP), utilizes ATP-derived energy to pump chemotherapy drugs out of tumor cells and protect tumor tissues from chemical toxicity (Yuan et al., 2016; Tang et al., 2016). This leads to insufficient intracellular levels of chemotherapeutic drugs and hence a poor therapeutic efficiency of the drugs. Effective reversal of P-gp-mediated MDR and maintaining accumulation of chemotherapeutic drugs in tumor tissues is imperative to management of MDR and for successful treatment of BC.

Over the past decades, considerable attempts have been made to develop P-gp inhibitors to overcome MDR. Consequently, several inhibitors, such as verapamil and disulfiram, have been identified with their co-encapsulation into nanocarriers found to reduce MDR of cancer cells *in vitro*. However, results from *in vivo* studies have been unsatisfactory, mainly because of poor aqueous solubility and low intracellular concentration (Chen et al., 2015; Alamolhodaei et al., 2017; Zhang et al., 2018). Furthermore, MDR inhibitors may have inherent toxicity on the normal cells.

D-α-Tocopheryl polyethylene glycol 1000 succinate (TPGS), as a derivative of natural vitamin E (α-tocopherol). It has been widely applied in the food and drug industry as a solubilizer, absorption enhancer, and a vehicle for nanodrug delivery system. The biological and physicochemical properties of the compound provide multiple advantages for its applications in drug delivery, including enhancement of drug solubility, improvement of drug permeation, and selective antitumor activity (Yang et al., 2018; Zhang et al., 2017; Gorain et al., 2018). Notably, TPGS can inhibit activity of ATP-dependent P-gp and act as a potent excipient for overcoming MDR in tumor tissues.

Nanotechnology has rapidly developed and plays an important role in anti-tumor, immunology as well as inflammation research (Cho, et al., 2008; Zhu et al., 2018; Zheng et al., 2019). Recently, solid lipid nanoparticles (SLNs) have attracted the most attention among all known nanocarriers in the field of drug delivery. This, owing to several unique material properties of SLNs such as small particle size, biocompatibility, chemical, and mechanical stability as well as easy functionalization potential (Banerjee et al., 2019; Shen et al., 2019; Wang et al., 2015). In addition, SLNs can modulate release of kinetics, improve blood circulation time, and increase overall therapeutic efficacy of anticancer drugs (Jiang et al., 2016). In the present study, resveratrol was successfully loaded into SLNs for treatment of breast cancer (Wang et al., 2017a). Moreover, some research studies have shown that SLNs is a promising platform for the delivery of therapeutic agents for MDR cancer chemotherapy (Majidinia et al., 2020). Based on these considerations, the current study designed TPGS-functionalized SLNs for loading drugs to overcome MDR in breast cancer.

In this study, a novel drug delivery system was developed to overcome MDR in BC, based on the findings of our previous research. First, TPGS-Res-SLNs was successfully synthesized using emulsification and low-temperature solidification methods and then characterized them using transmission electron microscopy (TEM) and zeta potential detection. The release behaviors of TPGS-Res-SLNs *in vitro* in PBS at different pH values was then measured. Second, anti-tumor efficacy of the synthesized compounds in the SKBR3/paclitaxel resistant (SKBR3/PR) cells was explored *in vitro*. The effect of these compounds on cell uptake and cytotoxicity against SKBR3/PR cells as well as anti-tumor efficacy in mice bearing an SKBR3/PR tumor were then evaluated. Further, animal studies were used to validate the treatment with TPGS-Res-SLNs, and compare the resulting effects to those of free drug. Finally, the present study examined the probable underlying mechanism of MDR inhibition in breast cancer.

MATERIALS AND METHODS

Materials

Resveratrol, D-α-Tocopheryl polyethylene glycol 1000 succinate (TPGS) was obtained from Aladdin Chemicals (Shanghai, China). Stearic acid, lecithin chloroform, and Tween80 were acquired from Sinopharm Chemical Reagent Co, Ltd. (Shanghai, China). Dulbecco's Modified Eagle Medium (DMEM), fetal bovine serum (FBS), penicillin G, and trypsin-EDTA were purchased from Thermo Fisher Scientific (MA, United States). Other chemicals used in this study were of analytical grade. The primary antibodies used in the experiment including P-gp, BCRP, N-cadherin, Vimentin, MMP-2, and MMP-9 were purchased from Proteintech (Beverly, MA, United States). Horseradish peroxidase (HRP) which are conjugated secondary antibodies used against rabbit or mouse immunoglobulin were purchased from Santa Cruz Biotechnology (Santa Cruz).

Preparation of Res-SLNs and TPGS-Res-SLNs

D-α-Tocopheryl polyethylene glycol 1000 succinate-resveratrol-solid lipid nanoparticles (TPGS-Res-SLNs) were prepared using the emulsification and low-temperature solidification method. A total of 10 ml solution containing resveratrol (0.15 g), stearic acid (0.2 g), lecithin (0.1 g), and TPGS (0.1 g) were prepared in chloroform and then added into 30 ml of H_2O containing Myrj52 (0.25 g) under fast stirring. The mixture was stirred at 1,000 rpm at 75°C for about 1 h till the total volume reduced to 5 ml, 10 ml of cold water was then added and the solution was stirred at 1,000 rpm for another 2 h at ice bath. To remove both impurities and large particles, the formulated TPGS-Res-SLNs were centrifuged at 20,000 rpm (Avanti J25 centrifuge, JA25.50 rotor, Beckman) for 1 h to collect the synthesized materials. The productive TPGS-Res-SLNs was dried for 24 h at −56°C in vacuum. Blank SLNs were developed following the same procedure without the addition of resveratrol whereas the

preparation of Res-SLNs was done using the same protocol without the use of TPGS.

Morphological, ζ-potential Characterization of Res-SLNs and TPGS-Res-SLNs

The Res-SLNs and TPGS-Res-SLNs formulation was initially imaged under TEM to investigate its morphology. A drop of a diluted suspension of Res-SLNs and TPGS-Res-SLNs formulation was placed on the carbon-coated copper grid of TEM to form a thin liquid film. This was followed by staining them with phosphotungstic acid solution (2%, w/v) for 5 min. The prepared samples were examined under a transmission electron microscope (JEOL, Tokyo, Japan). Theζ-potential of Res-SLNs and TPGS-Res-SLNs were determined using a Malvern Zeta-size Nano ZS (Malvern Instruments, Malvern, United Kingdom).

Quantifying the Loading Efficiency of Resveratrol by UV-Vis Spectroscopy

The current study also determined the drug loading of Res-SLNs and TPGS-Res-SLNs. Briefly, 500 µl diluted Res-SLNs and TPGS-Res-SLNs formulation was placed into a 0.5 ml centrifugal Amicon® filter tube (Millipore, Carrigtwohill, Ireland) and centrifuged at 14,000 rpm for 30 min at 4°C using an eppendorf centrifuge (Eppendorf AG, Germany). The loaded SLNs remained in the filter tube and the free resveratrol passed through the filter. The amount of free resveratrol in the supernatant was then quantified by UV-vis at 304 nm. The drug loading of SLNs were determined using the following equations:

$$DL\% = \frac{W_{total} - W_{free}}{W_{lipids}} \times 100\%$$

Where: W_{free} is the amount of resveratrol measured in the supernatant; W_{total} is the theoretical amount of resveratrol that was added; W_{lipids} is the total mass of lipids in the SLNs or in the TPGS-SLNs.

In Vitro Drug Release Kinetics

To increase the solubility of resveratrol, the *in vitro* release of resveratrol from TPGS-Res-SLNs was tested using pH 7.4 and pH 5.5 buffer solutions [1:1 mixture of water and ethanol (v/v)]. Briefly, 5 ml freshly prepared TPGS-Res-SLNs solution (equivalent resveratrol dose of 30 µM) was put into dialysis tube and dialyzed against 50 ml of the medium with constant shaking at 37°C. At predetermined time points, 1 ml of the dialysis solution was removed and an equal volume of fresh medium was added. Resveratrol release was determined by measuring the absorption intensity at 304 nm using UV-visible spectrometer.

In Vitro Cytotoxicity

The relative cytotoxicity of free resveratrol, Res-SLNs, and TPGS-Res-SLNs were separately evaluated *in vitro* through CCK-8 assay. The SKBR3/PR cells were seeded in 96-well plates at a density of 5×10^3 cells per well in 100 µl DMEM and grew for 24 h. Subsequently, cells were incubated with free Resveratrol, Res-SLNs, and TPGS-Res-SLNs at different concentrations (0, 20, 30, and 40 µM) for 24 or 48 h. Cell viability was measured using a CCK-8 kit (Dojindo Laboratories, Japan) according to the manufacturer's instructions and absorbance was measured at 450 nm wavelength using a spectrophotometer.

Cell Uptake

Considering the no fluorescent property of Resveratrol, C6 was chosen as the probe for investigating the cellular uptake behavior of SKBR3/PR cells (Al-Kassas et al., 2017). The cells were seeded overnight in a 24-well plate and incubated with free C6 or C6-loaded-TPGS-SLNs at an equivalent concentration of C6 (100 ng/ml) in a medium supplement with 10% FBS. After 0.5- and 4-h incubation, the cells were washed twice with precooled PBS, fixed using 4% paraformaldehyde, and stained with DAPI dye solution for 5 min. Fluorescent images of the cells were analyzed under a TCS SP2 confocal microscope (Leica, Germany) to investigate the cellular uptake of free C6 and C6-TPGS-SLNs.

P-gp Activity Assay

To investigate the transport activity of P-gp, Rho-123 comprising fluorescent substrates of P-gp were used (Kumar et al., 2020). Briefly, SKBR3/PR cells were pretreated with Resveratrol, Res-SLNs, and TPGS-Res-SLNs in culture medium in the dark and then co-treated with Rho-123 (0.5 µg/ml) for 1 h at 37°C. After accumulation of Rho-123, the cells were washed with ice-cold PBS and collected using trypsinization. Intracellular fluorescence of Rho-123 was measured using a FACS can flow cytometer (BD Biosciences).

Scratch Wound Healing Assay

The wound healing assay was carried out to confirm the migration ability. The SKBR3/PR cells were first seeded in six-well plates and cultured to confluency. A single wound was created by scratching the confluent monolayer of the cell using a 10-µl sterile pipette tip. The cells were then washed two times with phosphate buffered saline (PBS) and incubated with DMEM supplemented with 1% FBS. Images were then taken using an inverted microscope at 0 and 24 h.

Transwell Invasion Assay

The invasion assays of transfected SKBR3/PR cells were performed using Transwell cell-culture chambers (Corning, United States). The chamber was coated with the admixture of Matrigel (BD, United States). A total of 3,000 cells were the seeded into upper chamber with 100 µl serum-free medium. On the other hand, the lower chamber was supplemented with 750 µl medium containing 10% FBS. A total of 3,000 treated cells were seeded into the upper chamber with 100 µl serum-free medium and the bottom chamber was supplemented with 750 µl medium containing 10% FBS. After 24 h of incubation, these cells were washed, fixed with 4% polyoxymethylene and then stained with 0.1% crystal violet. The invaded cells were

then counted and photographed under a microscope (Hanrong Company, Shanghai). Five visual fields were selected and the average number was taken.

Cell Apoptosis

To quantitatively analyze apoptosis in SKBR3/PR cells, Annexin V-FITC/PI double staining was performed in the current study. The SKBR3/PR cells were seeded into a six-wells plate at the density of 2×10^5 per well and cultured for 24 h. The SKBR3/PR cells were later washed with PBS (the culture medium) and was then replaced with TPGS-Res-SLNs, Res-SLNs or free resveratrol at a concentration equivalent to 30 μM Res for 24 h at 37°C and 5% CO_2. The cells with no treatment were used as the control. Thereafter, the cells were washed with cold PBS and harvested using 0.25% trypsin (no EDTA). The collected cells were washed twice with cold PBS and resuspended in 500 μl 1×binding buffer. Five of Annexin V-Fluorescein isothiocyanate (FITC) and 5 μl Propidium Iodide (PI) were then into the resuspended cells according to the manufacture's protocol. The plate was incubated in the dark for 30 min at 37°C before it was placed in an ice bath in preparation for flow cytometry analysis (BD Biosciences). Results were analyzed using Flowjo7.6 software.

Cell Cycle

The SKBR3/paclitaxel resistant cells were seeded in six-wells plates at the destiny of 2×10^5 per well for 24 h and then treated with TPGS-Res-SLNs, Res-SLNs or free Res for 24 h (equivalent dose of resveratrol 30 μM). The cells were then washed with cold PBS and harvested after trypsinization with 0.25% trypsin (no EDTA). Then, the cells were washed with PBS and fixed in cold 70% ethanol for 24 h. After fixation, the cells were spun again and washed with cold PBS and sequentially treated with RNase (100 μg/ml) and propidium iodide (50 μg/ml) for 20 min at 37°C in the dark. Cell cycle stages were determined and analyzed using flow cytometry.

Immunofluorescent Staining

The SKBR3/PR cells were grown on surface-treated coverslips in 24 well plates (approximately 50,000 cells per well) for 24 h until between 50 and 60% confluence. The cells were later exposed to different formulations of Resveratrol, Res-SLNs, and TPGS-Res-SLNs (equivalent dose of free resveratrol 30 μM). After a 12-h period of drug treatment, the cells were fixed with 4% paraformaldehyde (Solarbio, Beijing, China) for 18 min, permeabilized for 8 min with 0.2% Triton X-100, and blocked for 55 min with 1% bull serum albumin (Amresco) at room temperature. The cells were probed overnight with a primary antibody against E-Cadherin (Sigma; 1:100 dilution) at 4°C and Alexa Fluor 488-conjugated goat anti rabbit IgG (Molecular Probes, Eugene, OR, 1:100) in the dark for 1 h at room temperature. After three further washes, the cells were counterstained using 4, 6-diamidine-2-phenylindole (Beyotime, 1:1000) in the dark for 5 min at room temperature. All reagents were diluted in phosphate buffered saline (PBS) with all the steps followed by three-times-5 min PBS washing. Images were captured using ZEN version 2012 software (Zeiss, Gottingen, Germany) under a laser scanning confocal microscope LSM 780 (Zeiss).

Western Blot Analysis

The SKBR3/PR cells (approximately 5×10^5) were seeded in six-well plates (cells per well) and exposed to resveratrol, Res-SLNs, or TPGS-Res-SLNs (equivalent dose of free resveratrol 30 μM) for 24 h. The medium was removed and the cells washed several times using PBS (pH 7.4) in a lysis buffer for 15 min. After centrifugation at 12,000 rpm, a BCA protein assay kit (KeyGen Biotech, Nanjing, China) was used to measure the total protein concentration of the supernatant with cell lysates. Then, equal amounts of total protein (30 μg) were analyzed on 10% SDS-polyacrylamide gel electrophoresis and transferred onto a polyvinylidene fluoride (PVDF) membranes. The samples were blocked with 5% BSA and incubated overnight with primary antibodies at 4°C. The blots were incubated with horseradish peroxidase (HRP)-coupled secondary antibody, and the bands were visualized using ImageQuant LAS4000 mini (GE Healthcare Life Science, United States). The primary antibodies used in the experiment included P-gp, BCRP, N-cadherin, Vimentin, MMP-2, MMP-9, and β-actin (included as a control). HRP-conjugated secondary antibodies were purchased from KeyGEN (Nanjing, China).

Xenograft Models in Nude Mice

All animal assay were performed in accordance with the Guidelines for Care and Use of Laboratory Animals of Bengbu medical University and approved by the Animal Ethics Committee of Animal Experiments at Bengbu medical University (Permit No. SYXK Wan 2019081). Female BALB/c nude mice, aged between 5 and 6 weeks were use in this study. They were obtained by the Experimental Animal Center of the Bengbu medical college. The SKBR3/PR cells we suspended in PBS, at a concentration of 2×10^7/ml. A 10 μl of the cell suspension was subcutaneously injected into the dorsal right flank of each mouse. When tumor volume reached ~100 mm^3, the mice were randomized into four groups as follows (n = 4 per group): 1) the control group: where mice were administered with a daily dose of 100 μl PBS; 2) Resveratrol group: in which mice were treated with 20 mg/kg resveratrol; 3) Resveratrol-SLNs group: where mice were treated with Resveratrol-SLNs at doses equivalent to 20 mg/kg resveratrol; 4) TPGS-Res-SLNs group: in which mice were treated with TPGS-Res-SLNs at doses equivalent to 20 mg/kg resveratrol. The tail intravenous injection is a difficult technique and it is hard to ensure the accuracy of the dose given to mice every time. Therefore, all treatments were given intraperitoneally (IP) daily for five times, to guarantee the equivalent concentration of resveratrol and improve the accuracy of this study. The shortest (S) and longest (L) diameters of the mouse tumors were measured and recorded every after 2 days using a Vernier caliper and the tumor volume (V) was calculated using the following formula:

$$\text{Tumor volume}\,(V) = L \times S^2/2$$

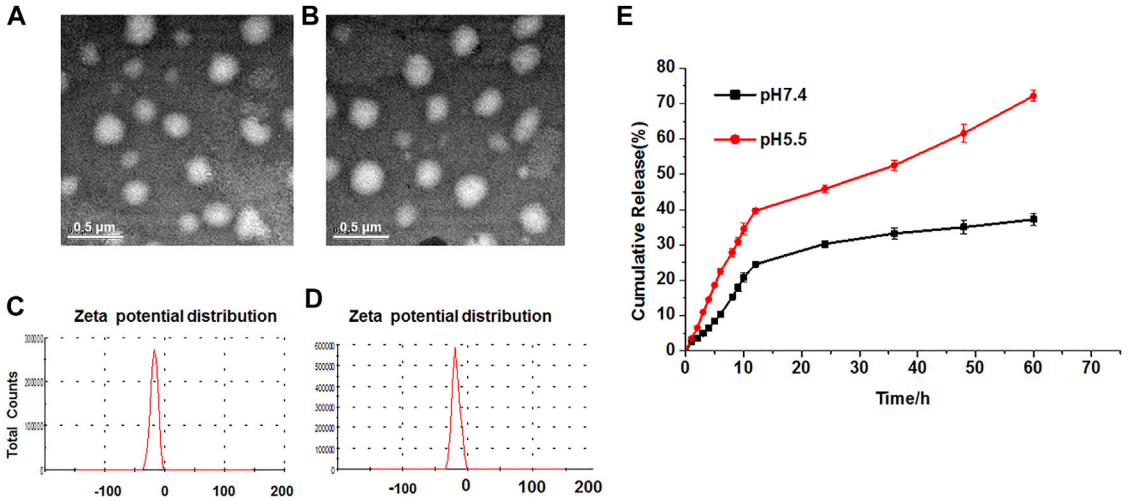

FIGURE 1 | Characterization and in vitro drug release of TPGS-Res-SLNs. TEM image (scale bar: 500 nm) of **(A)** Res-SLNs and **(B)** TPGS-Res-SLNs in the suspension. The Zeta potentials of **(C)** Res-SLNs and **(D)** TPGS-Res-SLNs. **(E)** *In vitro* release profiles of Resveratrol from TPGS-Res-SLNs at different pH (pH 7.4 and pH 5.5). Data are expressed as the mean ± S.D. (n = 3).

After 21 days, the mice were anesthetized, the tissues were excised, and the major organs (heart, liver, spleen, lung, and kidney) were collected for subsequent analyses.

Immunohistochemical Staining

Expression of E-cadherin and N-cadherin was examined by immunohistochemical (IHC) staining. Briefly, paraffin-embedded tumor tissues were sliced into 3 μm sections, deparaffinized with xylene, rehydrated with alcohol gradient and then rinsed using deionized water. The tissue antigen was the retrieved by heating it for about 10 min in Tris-EDTA solution (pH 8.0), and the sections were blocked in 3% H_2O_2 solution. The blocked sections were incubated overnight with antibodies against E-cadherin (diluted 1:200) or Vimentin (diluted 1:100) at 4°C, washed three times with PBS, and then incubated with goat anti-rabbit IgG for 30 min. The sections were stained with freshly-prepared 3, 3′-diaminobenzidine (DAB), observed under the microscope, and pictures taken for analysis using the image processing software.

In Vivo TUNEL Assay

In the current study, TUNEL assays were performed to detect DNA fragmentation, which is characteristic of apoptotic cells (Tang, et al., 2010). Tumor sections (4 μm) were deparaffinized in xylene and rehydrated in a series of graded ethanol to water. Thereafter, 50 ml of proteinase K (50 mg/ml) in TBS (pH 8.0) was added onto the slides and incubated for 30 min at room temperature. The slides were rinsed three times with PBS and then incubated for 1 h with 50 ml tunel cocktail (a mixture of 2 ml enzyme solution and 48 ml label solution) at 37°C in a humidified atmosphere in the dark. Finally, 1 μl of 1,000× DAPI stock (0.2 mg/ml) was allowed to stand in the dark for a few minutes, covered using slips and the slides analyzed under CLSM using 488 nm excitation and 530 nm emission. The cells showing green fluorescence were categorized as apoptotic. Cell nuclei staining using DAPI was also performed and the mean fluorescence intensity was measured using ImageJ software.

Histological Examination

In the current study histopathological analysis was performed on organs and tumor tissues, using hematoxylin and eosin (H&E) staining. The main organs (heart, lung, liver, spleen, and kidney) were harvested and fixed overnight in 4% paraformaldehyde and then embedded in paraffin. The tissues were cut into 5 μm sections for H&E staining according to the standard procedures. This was followed by examination of the tissues under a light microscope (Olympus Corporation, Tokyo, Japan).

Statistical Analysis

All results of the present study were presented as means ± standard deviation (SD). The statistical difference between two groups was tested using one-way analysis of variance (ANOVA) followed by t-test. The data were considered as statistically significant at $p < 0.05$ or 0.01.

RESULTS

Characterization of Res-SLNs and TPGS-Res-SLNs

Generally, the Res-SLNs and TPGS-Res-SLNs were successfully prepared in the present study. The morphology and size of these compounds were first characterized through transmission electron microscopy (TEM). Both Res- and TPGS-Res-SLNs were spherical in shape with mean diameters of 169 and 203 nm, respectively (**Figures 1A,B**). The zeta potential of Res-SLNs and TPGS-Res-SLNs was −27.8 ± 1.6 and −25.6 ± 1.3 mV, respectively (**Figures 1C,D**).

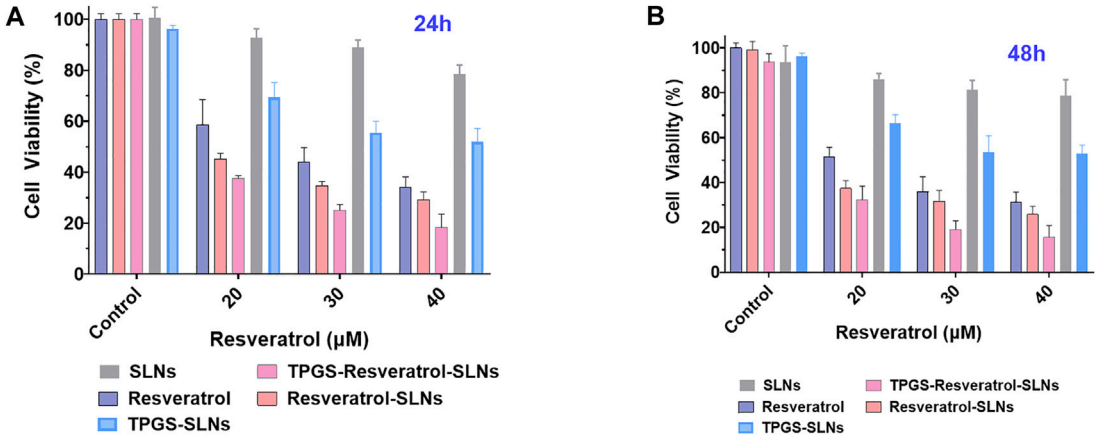

FIGURE 2 | *In vitro* cell viability assay using CCK8 reagents. The cell viability of SKBR3/PR cell treated with SLNs, free resveratrol, Res-SLNs and TPGS-Res-SLNs after 24 h **(A)** and 48 h **(B)**. Data are presented as the mean ± S.D. (n = 3 wells). The significant difference of the results was analyzed. $^{**}P < 0.01$, $^{*}P < 0.05$.

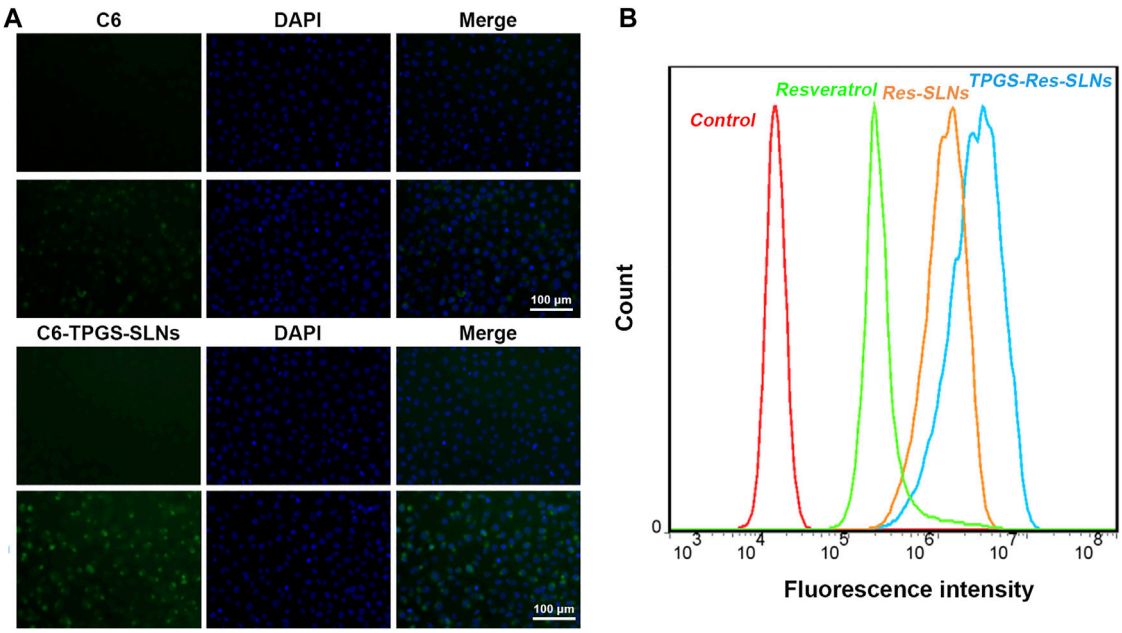

FIGURE 3 | Cellular uptake and P-gp inhibition ability. **(A)** Confocal laser scanning microscopy (CLSM) images of SKBR3/PR cells after 0.5 and 4 h incubation with the coumarin-6-loaded-TPGS-SLNs (C6-TPGS-SLNs), respectively. The image was obtained from FITC channel (green), DAPI channel (blue) and the overlay of the two channels. The C6-TPGS-SLNs were green and the nucleus was stained by DAPI (blue). **(B)** P-gp inhibition ability of Resveratrol, Res-SLNs and TPGS-Res-SLNs increased uptake of Rho-123 in SKBR3/PR cells.

The surface charge and size of nanoparticles are important parameters that affect cellular damage of cancer cells. The resultant uniform sizes of the Res-SLNs and TPGS-Res-SLNs enables better solubility and bioavailability (Bai et al., 2013).

Zeta potential is a significant factor in maintaining stability of nanoparticles in suspension through electrostatic repulsion between particles (Gao et al., 2011). In this study, zeta potential of the studied particles was negative enough to sustain the stability of TPGS-Res-SLNs dispersed system. The drug-loading of Res by TPGS-SLNs was 32.4 ± 2.6%. In addition, the release curves of resveratrol from TPGS-Res-SLNs were investigated under different pH conditions ranging from 5.5 to 7.4. Results of the current study showed that 30.27% of resveratrol was released from the TPGS-Res-SLNs at 48 h in PBS buffers (pH 7.4), whereas 45.8% of resveratrol in the PBS with pH 5.5 (**Figure 1E**). These results suggested that the TPGS-SLNs could be utilized for controlling the release of resveratrol in a pH-sensitive manner.

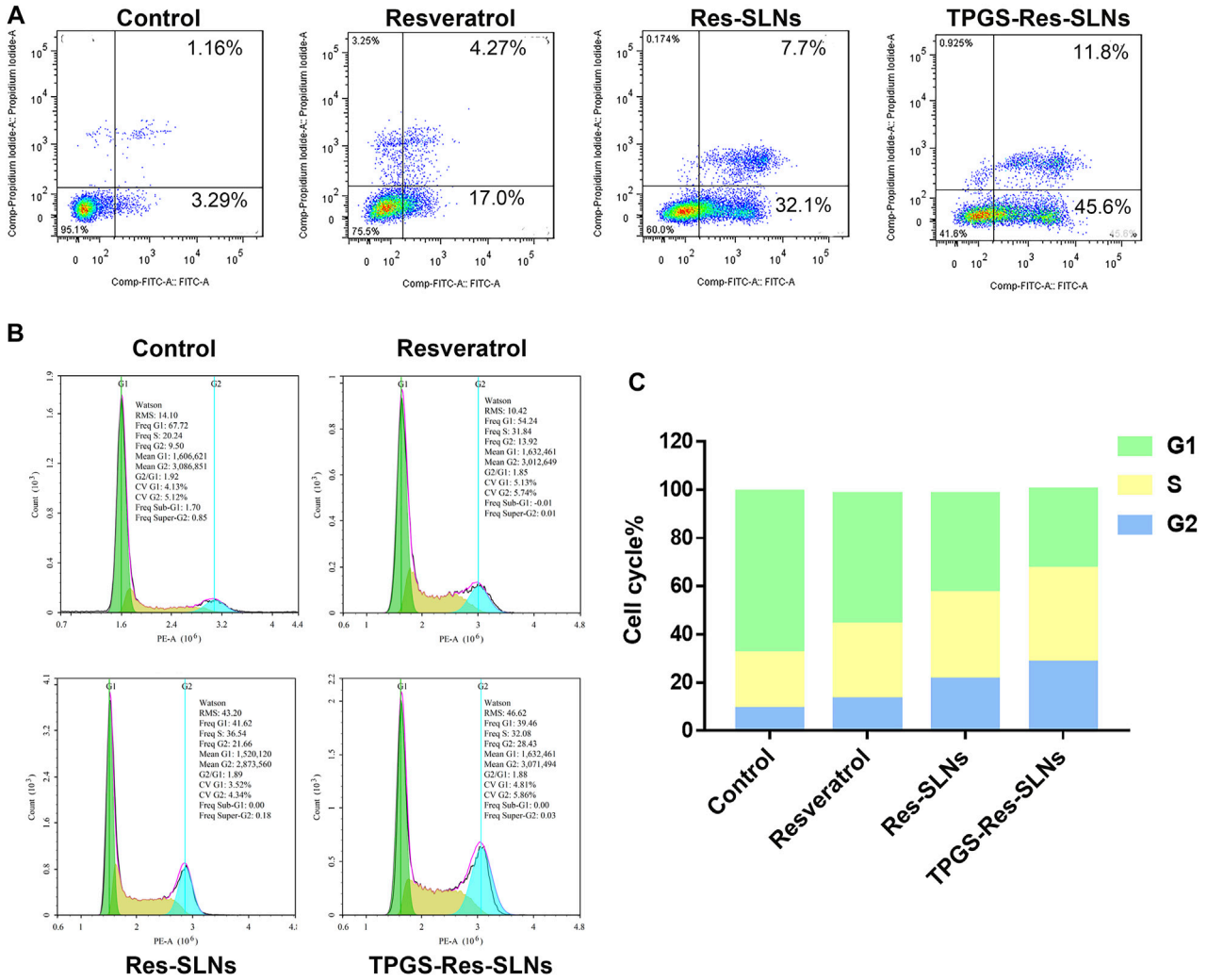

FIGURE 4 | TPGS-Res-SLNs induced apoptosis of SKBR3/PR cells. **(A)** Assessment of cellular death (apoptosis and necrosis) using Annexin V-FITC/PI staining after incubation for 24 h. SKBR3/PR cells were incubated with Resveratrol, Res-SLNs and TPGS-Res-SLNs for 24 hours. **(B)** Flow cytometry analysis of cell cycle phase distribution in SKBR3/PR cells. **(C)** Histogram showing the cell cycle distribution after treatment with Resveratrol, Res-SLNs and TPGS-Res-SLNs.

Cytotoxicity of Res-SLNs and TPGS-Res-SLNs on SKBR3/PR

To assess the potential of different drug formulations to inhibit growth of SKBR3/PR cells, a CCK8 assay was performed at 24 and 48 h. It was found that there was no toxicity caused by the nanocarrier against the SKBR3/PR cells (**Figures 2A,B**). After 24 h of incubation, the TPGS-Res-SLNs showed a slightly higher toxicity than free resveratrol and Res-SLNs to SKBR3/PR cells. After the incubation period, a higher cytotoxicity was recorded in TPGS-Res-SLNs relative to Res-SLNs and free Res. These results can be attributed to the fact that free resveratrol have low solubility and instability in aqueous solution. The solubility and stability of resveratrol were enhanced by loading it in SLNs or in TPGS-SLNs and this resulted in prolonged inhibition of proliferation to drug resistant cancer cells. Additionally, the rate of cell survival for TPGS-Res-SLNs was always lower than that of Res-SLNs and free resveratrol at each dose level (**Figure 2**).

Efficient Cellular Uptake of TPGS-Res-SLNs

The uptake of different drug formulations in drug-resistant cell-line SKBR3/PR was also studied under a fluorescence microscope using the fluorescence dye, coumarin-6 (C6), and the cellular uptake was compared between C6 loaded TPGS-SLNs and coumarin-6 solution. The C6@TPGS-SLNs exhibited stronger fluorescence intensities compared to C6 after 0.5 h of incubation (**Figure 3A**). Thia suggested that there was a rapid internalization of C6@TPGS-SLNs into the cells within the period. Prolonging incubation time to 4 h, resulted into the entry of C6 into the SKBR/PR and into a marked increase intensity of fluorescence. When compared with C6, C6@ TPGS-SLNs showed significantly stronger green

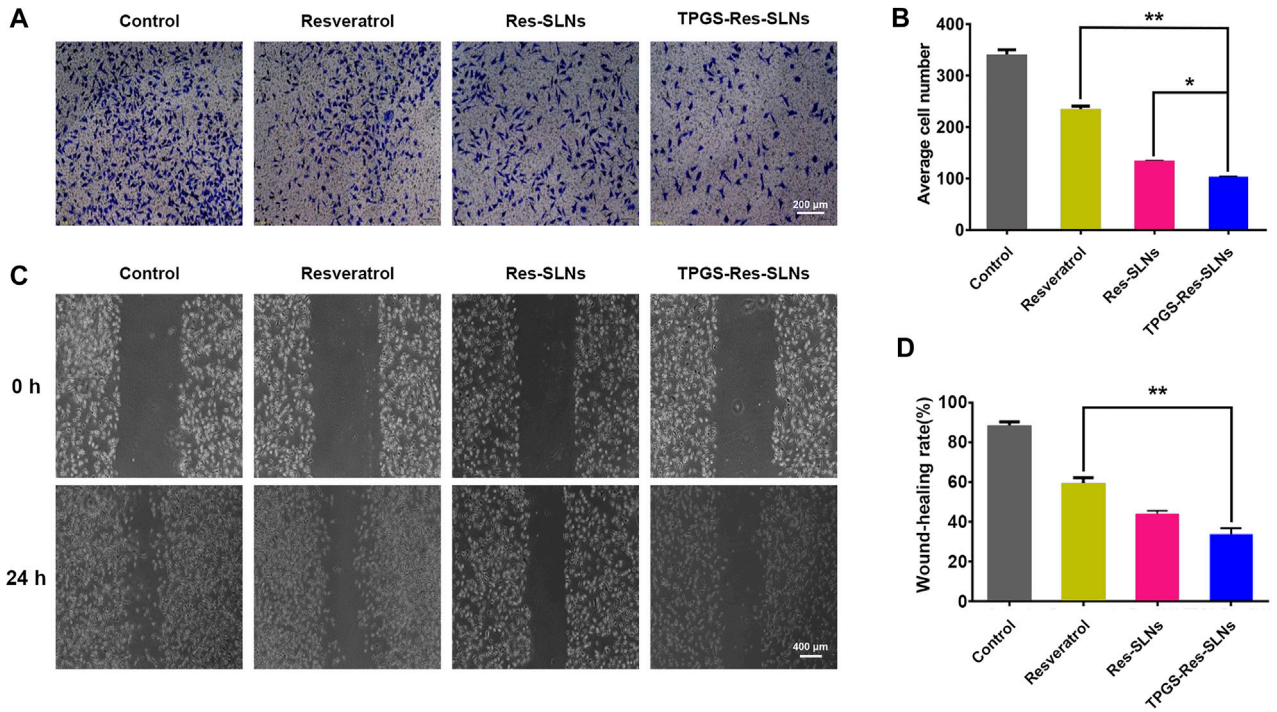

FIGURE 5 | TPGS-Res-SLNs inhibited invasion and migration ability of SKBR3/PR cells *in vitro* **(A)** Transwell migration assay was used to detect the number of trans-membrane cells. Representative microphotographs of the Boyden chamber assay of SKBR3/PR cells. **(B)** The quantitative data for the Boyden chamber assay. The bar graph represents the number of invasive cells present per unit area in different treated groups. **(C)** Wound-healing assays were performed to assess cell migration. Cells were treated with Resveratrol, Res-SLNs and TPGS-Res-SLNs for 0 and 24 h or untreated. Representative images of treated and untreated cells are shown. **(D)** Distance migrated by cells at the 24 h are shown. The values represent the mean ± SD of three independent experiments. (**$p < 0.01$, *$p < 0.05$).

fluorescence after 4 h of incubation. The results of this study indicated that uptake of C6 loaded TPGS-SLNs and C6 solution was time dependent.

P-gp Inhibition Improves Intracellular Accumulation

The P-gp has been recognized as an active efflux transporter and plays an important role in paclitaxel resistance in various cancers including breast cancer (Che et al., 2019). To investigate the functions of free resveratrol, Res-SLNs, and TPGS-Res-SLNs on P-gp mediated drug efflux, their influence on intracellular cell uptake of Rhodamine-123 (Rho123) in SKBR3/PR cells was also assessed in the present study.

It was evident that the cells treated with free resveratrol showed significantly enhanced fluorescence relative to the control group (**Figure 3B**). On the other hand, the cells treated with TPGS-Res-SLNs exhibited stronger fluorescence as compared with those treated with Res-SLNs and Resveratrol. These results showed that TPGS significantly enhanced Rho123 accumulation in SKRR3/PR cells and this indicates that the inhibition of p-gp by TPGS-Res-SLNs can prevent drug efflux and increase chemosensitivity of SKBR3/PR cells.

Effect of TPGS-Res-SLNs on Cell Cycle and Apoptosis

To determine the anticancer effect of free resveratrol, Res-SLNs, and TPGS-Res-SLNs, the method of Annexin V-FITC & PI Double Staining was used in the present study. A 21.27% of apoptotic cells (early apoptosis 4.27% plus late apoptosis17%) was recorded in the sample incubated with free Resveratrol as compared with the untreated control group (**Figure 4A**). It was found that when the cells were treated with Res-SLNs, the total apoptotic SKBR3/PR cells increased to 39.80% (7.70 and 32.10% for early and late apoptosis, respectively). In addition, the percentage of total apoptotic cells treated with TPGS-Res-SLNs was 57.40%, which represented 45.60 and 11.80% for early and late apoptosis, respectively. These findings suggest that TPGS-Res-SLNs display the strongest anti-apoptotic effect in SKBR3/PR cells.

To determine the mechanism of cytotoxicity, the present study analyzed progression of the cell cycle and DNA content in SKBR3/PR cells after treatment with free resveratrol, Res-SLNs, and TPGS-Res-SLNs through flow cytometry. Incubating the cells with the three compounds revealed an increase at the G2/M phase from 9.5 to 13.92, 21.66, and 28.43%, respectively (**Figures 4B,C**). This indicated that all the three formulations could induce different levels of cell cycle arrest at the G2/M phase. In particular, TPGS-Res-SLNs resulted in the most significant cell cycle arrest in SKBR3/PR cells. Furthermore, these findings were consistent with the results of *in vitro* cytotoxicity.

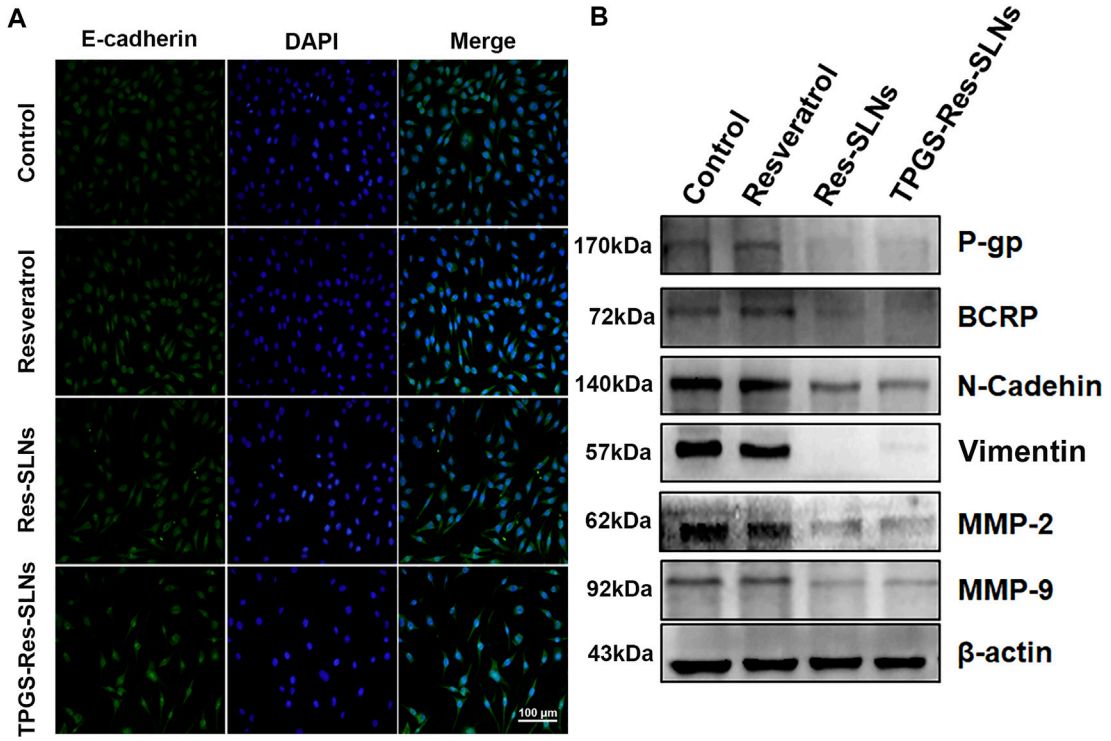

FIGURE 6 | The effect of TPGS-res-SLNs on the EMT-related protein level of SKBR3/PR cells by Immunofluorescence assay and Western blot. **(A)** Immunofluorescence assay was used to detect EMT re lated proteins. SKBR3/PR cell treated with Resveratrol, Res-SLNs and TPGS-Res-SLNs for 48 h. Untreated cells served as the control. E-cadherin was stained in green, and nuclei stained with DAPI were in blue. **(B)** Expression level of P-gp, BCRP, E-cadherin, N-cadherin, Vimentin, MMP-2, and MMP-9 in protein extracted from SKBR3/PR cells analyzed by Western blot.

Effect of TPGS-Res-SLNs on Cell Migration and Invasion

To further investigate whether the TPGS-Res-SLNs treatment had a negative effect on cell invasion, a transwell invasion assay was conducted using matrigel. It was found that there was a significant reduction in the number of invasive cells when treated with TPGS-Res-SLNs for 24 h as compared with when treated with Res-SLNs and the free resveratrol (**Figures 5A**,**B**).

The effect of TPGS-Res-SLNs on SKBR3/PR migration was also investigated in the current study using a wound-healing assay (**Figures 5C,D**). After TPGS-Res-SLNs treatment, the cell migration distance was notably shorter. This indicate that resveratrol has a negative effect on cell migration when carried by the nanoparticles. In addition, it was noted that cellular motility was also inhibited after different treatment times (0 and 24 h). The cell images and quantitative analyses revealed that there were three times fewer migratory cells in the TPGS-Res-SLNs-treated group as compared with those treated with resveratrol group.

Mechanism by TPGS-Res-SLNs Prevents MDR

Previous studies have reported that SKBR3/PR cells shows enhanced migratory ability, which is associated with EMT phenotype (Smith and Bhowmick, 2016; Wang et al., 2017b; Laiolo et al., 2018). Therefore, the present study explored the effect of nano formulations on SKBR3/PR cells by transforming the EMT phenotype. Considering that EMT is characterized by a loss of epithelial markers including E-cadherin and upregulation of mesenchymal markers including N-cadherin and vimentin, the present study investigated the expressions of EMT-related proteins using western blot analysis and immunofluorescent (IF) assay. Immunofluorescence analysis revealed elevated E-cadherin protein levels were in SKBR3/PR cells (**Figure 6A**). Conversely, results of the western blot analysis showed that treatment with Resveratrol, Res-SLNs, and TPGS-Res-SLNs resulted in decreased levels of vimentin and N-cadherin (**Figure 6B**).

Multi-drug resistance (MDR) is common in patients and has been linked to overexpression of drug efflux transporters P-gp and BCRP (Chiu et al., 2016). Overexpression of P-gp is associated with resistance to a wide range of anticancer drugs, including several natural product substances such as paclitaxel (Wang et al., 2017c). Previous studies eports have implicated some nanodrugs in inhibition of MDR in tumor cells and down-regulation of P-gp expression, thus reducing drug efflux (Wang et al., 2019). Based on this, the present study used western blot analysis to investigate the effects of different nano-formulations on P-gp and BCRP expression in SKBR3/PR cells. It was evident that treatment with free resveratrol did not result in a significant decrease in P-gp and BCRP protein levels, but a significant reduction in expression of P-gp and BCRP in the two (Res-

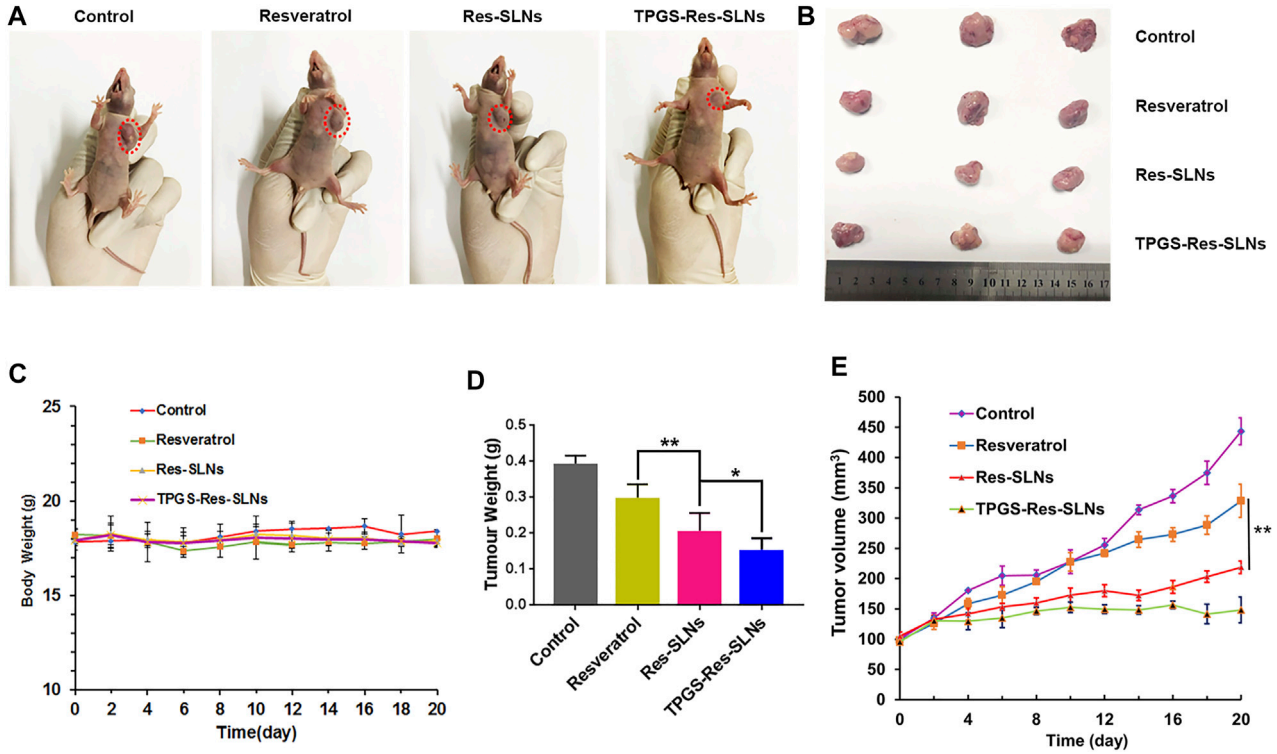

FIGURE 7 | The *in vivo* efficacies of Resveratrol, Res-SLNs and TPGS-Res-SLNs on mice bearing SKBR3/PR xenografts. **(A)** Representative images of mice at the 16th day in the different treatment groups. **(B)** Digital images of tumors excised from representative mice after the indicated treatments. **(C)** Body weight vs. time curves for mice treated with the indicated formulations. **(D)** Tumor weight of mice in the different treatment groups. **(E)** Tumor volume vs. time curves for mice treated with the indicated formulations. he data represented mean ± SD (n = 4). *p < 0.05, **p < 0.01.

SLNs, and TPGS-Res-SLNs) drug formulations was observed (**Figure 6B**).

Many herbal medicines against drug resistance have been reported in multiple cancer types. Resveratrol was assessed on various types of cancers as a chemotherapy sensitizer including pancreatic cancer, breast cancer, and colon cancer. The mechanisms by which resveratrol chemosensitizes cancer cells include by inhibition of tumor cell proliferation, metastasis, and angiogenesis. Resveratrol was assessed as a chemotherapy sensitizer on various types of cancers, including pancreatic cancer, breast cancer, and colon cancer. The mechanisms by which resveratrol chemosensitizes cancer cells include by inhibition of tumor cell proliferation, metastasis, and angiogenesis.

Docetaxel–resveratrol combined treatment provides a promising future for gastric cancer patients to postpone drug resistance and prolong survival. D-α-Tocopheryl polyethylene glycol 1000 succinate can inhibit P-gp, thus sensitizing MDR cells. In the present study, the effect of SLNs with TPGS on sensitizing MDR cells was investigated in SKBR3/PR cells. Solid lipid nanoparticles serve as potential anticancer drug delivery nanocarriers, because they exhibit great superiority to modulate drug release, improve anticancer activity, and overcome MDR. Res-SLNs exhibited high cytotoxicity and allowed efficient intracellular drug delivery. This dual inhibitory strategy can have a significant potential in the clinical management of MDR in cancer.

Matrix metalloproteinases, especially MMP-2/-9, play important roles in breaking down the extracellular matrix (ECM) (Dia and Pangloli, 2017). Loss of the ECM of blood or lymph vessels allows cancer cells to invade into the blood or lymphatic system and spread to other tissues and organs. The present study evaluated whether different nano-formulations suppresses cancer cell invasion and motility by affecting the expression of matrix metalloproteinases. This was performed through a western blot analysis assay to examine the expression of MMP-2 and MMP-9 in cancer cells after treatment with different nano-formulations. Particularly, it was found that there was a significant decrease in MMP-2/MMP-9 expression in SKBR3/PR cells following treatment with resveratrol, Res-SLNs, TPGS-Res-SLNs as compared with the controls (**Figure 6B**). These results corroborated with the findings obtained from the transwell-based migration assay.

In Vivo Anti-Tumor Efficacy in SKBR3/PR Subcutaneous Bearing Nude Mice

Having confirmed the good performance of TPGS-Res-SLNs through *in vitro* experiments, we further investigated the antitumor effect of the nanoparticles *in vivo* in SKBR3/PR

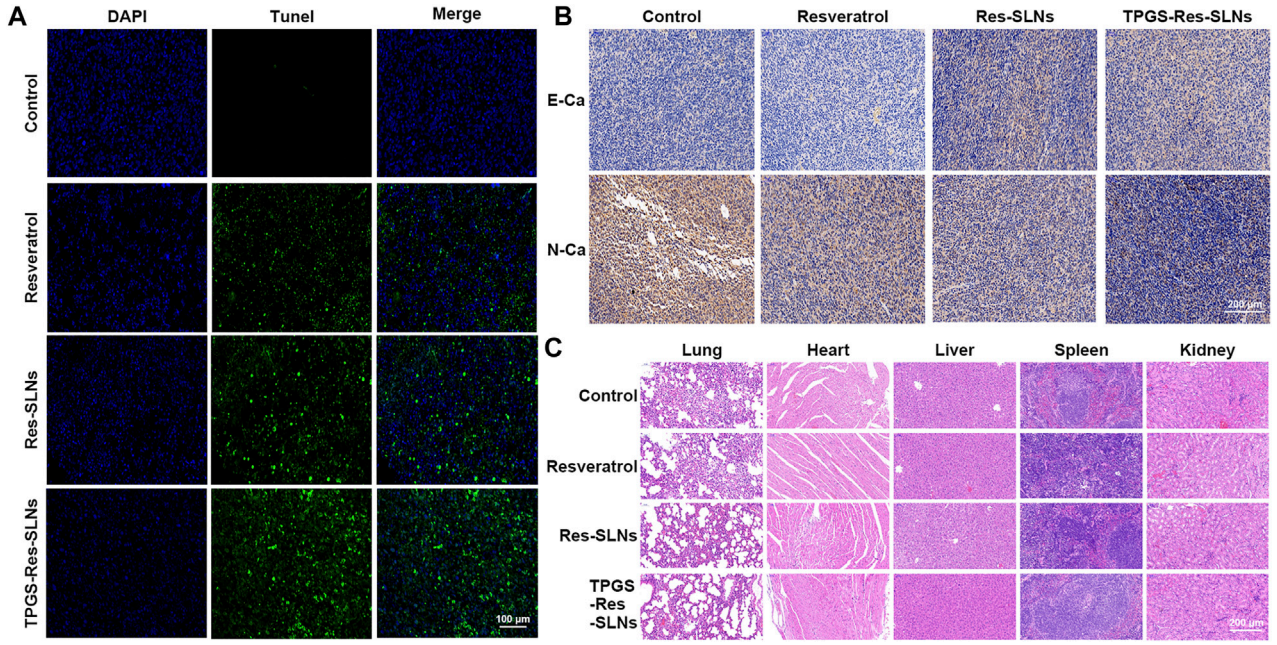

FIGURE 8 | The antitumor effect of TPGS-Res-SLNs on SKBR3/PR tumor bearing BALB/c nude mice. **(A)** Apoptosis detection by TUNEL assay in slices of tumors collected from different groups of mice two days after the end of the indicated treatments. Original magnification ×400. **(B)** IHC staining of E-cadherin (E-Ca), N-cadherin (N-Ca), and positive cells of differently treated subcutaneous tumor. **(C)** H8E staining of vital organs of SKBR3-bearing nude mice after intravenous injection of PBS, Resveratrol, Res-SLNs and TPGS-Res-SLNs.

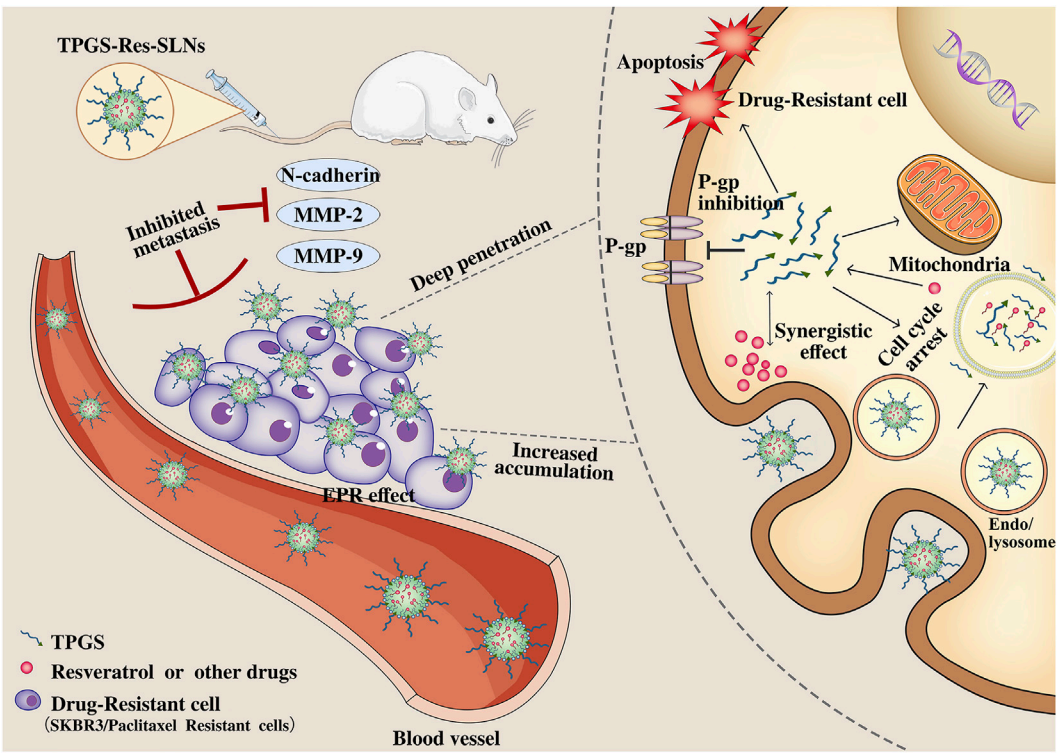

FIGURE 9 | Schematic illustration of the mechanism of TPGS-Res-SLNs regulates paclitaxel resistance in breast cancer.

tumor-bearing mice. Different formulations of drugs were intraperitoneally injected into the mice. Of note, the body weights of mice were not significantly altered in all treatment groups during the entire experimental period (**Figure 7C**). Mice treated with PBS showed faster tumor growth, whereas those treated with free resveratrol only showed slightly slower tumor growth. Comparatively, Res-SLNs and TPGS-Res-SLNs groups showed higher anti-tumor effects than groups treated with PBS and free resveratrol (**Figure 7A**). Images of excised tumors revealed that TPGS-Res-SLNs had a remarkably higher inhibition effect compared to other treatments (**Figure 7B**). In addition, mice treated with Res-SLNs and TPGS-Res-SLNs had lower tumor weight compared to control groups (**Figure 7D**). Analysis of tumor growth curves showed that TPGS-Res-SLNs had significantly ($p < 0.05$) higher antitumor activity than free Resveratrol and Res-SLNs (**Figure 7E**). These results suggested that TPGS-Res-SLNs had stronger tumor growth suppression effect due to two reasons; it had a higher cellular uptake, and prevented the inhibitory effect of TPGS on paclitaxel efflux in a P-gp-dependent manner.

To investigate anti-tumor effects at the cellular level, the TUNEL assay was performed to analyze cell apoptosis. Similar to the tumor growth inhibition assay, we found that PBS-treated groups had no tumor cell apoptosis (**Figure 8A**). Groups treated with TPGS-Res-SLNs had significantly higher apoptosis compared to other groups. These findings reinforced the conclusion that TPGS-Res-SLNs had the highest therapeutic efficacy of all treatments. Taken together, these results demonstrate that TPGS-Res-SLNs can effectively load resveratrol and enhance its efficacy against breast cancer *in vivo*.

Previous studies have shown that EMT is associated with paclitaxel resistance in breast cancer cells (Tian et al., 2017). During EMT, several epithelial surface markers, primarily E-cadherin, are downregulated, whereas mesenchymal markers such as N-cadherin are upregulated. This phenomenon predominantly occurs at the invasive front (IF) of the tumor. We, therefore, examined expression of E-cadherin and N-cadherin in the tumor through immunohistochemistry. Results showed that E-cadherin expression was higher in TPGS-Res-SLNs than in free resveratrol and Res-SLNs-treated groups (**Figure 8B**). By contrast, N-cadherin expression was significantly lower in TPGS-Res-SLNs compared to free resveratrol and Res-SLNs treated groups.

Generally, cancer chemotherapeutics have been shown to cause severe toxicity to normal tissues. Therefore, we further explored the effect of each treatment on histopathology of major organs, heart, liver, spleen, lung, and kidney through H&E staining. It was evident that free Resveratrol, Res-SLNs, and TPGS-Res-SLNs treatments induced no obvious histological changes (**Figure 8C**). These results demonstrated that TPGS-Res-SLNs treatment did not induce organ damage, and can therefore be considered as a safe and effective therapeutic agent for breast cancer treatment.

CONCLUSION

Although several strategies have been developed to combat multi-drug resistance in cancer cells, it remains an obstacle that limit efficacy of chemotherapy. In this study, we developed a TPGS-SLNs-based delivery strategy as illustrated in **Figure 9**. The TPGS-Res-SLNs and TPGS-SLNs were successfully fabricated, then loaded with Resveratrol. The morphology and size distribution of these nanoparticles were examined and their inhibitory effects on growth, apoptosis, and invasion of SKBR3/PR cells were investigated. The therapeutic effects of different formulations of these compounds were explored *in vivo* using nude mice models of SKBR3/PR, and expression of P-gp, BCRP, E-cadherin, N-cadherin, MMP-2 and MMP-9 was quantified using western blots to reveal the mechanism by which the TPGS-Res-SLNs exert their therapeutic effects. Collectively, the results demonstrated that TPGS-Res-SLNs showed great potential to treat breast cancer.

DATA AVAILABILITY STATEMENT

The raw data supporting the conclusions of this article will be made available by the authors, without undue reservation.

ETHICS STATEMENT

The animal study was reviewed and approved by the Animal Ethics Committee of Bengbu Medical University (Permit No. SYXK Wan 2019081).

AUTHOR CONTRIBUTIONS

WW, CC, and QY conceived the idea of study. WW wrote the manuscript. MZ, YX, WP, SZ, RL, HaZ, and HuZ conducted the experiments and analyzed the data. YW, SC, YW, and CY performed the data analyses. All authors contributed to the article and approved the submitted version.

FUNDING

This work was supported by the 512 Talent Cultivation Program of Bengbu Medical College (by51201206), the Key Projects of Anhui Province University Outstanding Youth Talent Support Program (gxyqZD2019037), the Nature Science Research Project of Anhui province (2108085MH294), the Science and Technology Program of Bengbu City (BYLK201811), the Major Program of Anhui Educational Committee (KJ2019ZD28), and the program for graduates research of Bengbu Medical College (China) (Byycxz20013).

REFERENCES

Al-Kassas, R., Bansal, M., and Shaw, J. (2017). Nanosizing Techniques for Improving Bioavailability of Drugs. *J. Controlled Release* 260, 202–212. doi:10.1016/j.jconrel.2017.06.003

Alamolhodaei, N. S., Tsatsakis, A. M., Ramezani, M., Hayes, A. W., and Karimi, G. (2017). Resveratrol as MDR Reversion Molecule in Breast Cancer: An Overview. *Food Chem. Toxicol.* 103, 223–232. doi:10.1016/j.fct.2017.03.024

Bai, F., Wang, C., Lu, Q., Zhao, M., Ban, F.-Q., Yu, D.-H., et al. (2013). Nanoparticle-mediated Drug Delivery to Tumor Neovasculature to Combat P-Gp Expressing Multidrug Resistant Cancer. *Biomaterials* 34, 6163–6174. doi:10.1016/j.biomaterials.2013.04.062

Banerjee, I., De, M., Dey, G., Bharti, R., Chattopadhyay, S., Ali, N., et al. (2019). A Peptide-Modified Solid Lipid Nanoparticle Formulation of Paclitaxel Modulates Immunity and Outperforms Dacarbazine in a Murine Melanoma Model. *Biomater. Sci.* 7, 1161–1178. doi:10.1039/c8bm01403e

Che, L., Liu, Z., Wang, D., Xu, C., Zhang, C., Meng, J., et al. (2019). Computer-assisted Engineering of Programmed Drug Releasing Multilayer Nanomedicine via Indomethacin-Mediated Ternary Complex for Therapy against a Multidrug Resistant Tumor. *Acta Biomater.* 97, 461–473. doi:10.1016/j.actbio.2019.07.033

Chen, H. H., Huang, W. C., Chiang, W. H., Liu, T. I., Shen, M. Y., Hsu, Y. H., et al. (2015). pH-Responsive Therapeutic Solid Lipid Nanoparticles for Reducing P-Glycoprotein-Mediated Drug Efflux of Multidrug Resistant Cancer Cells. *Int. J. Nanomedicine* 10, 5035–5048. doi:10.2147/IJN.S86053

Chiu, K.-Y., Wu, C.-C., Chia, C.-H., Hsu, S.-L., and Tzeng, Y.-M. (2016). Inhibition of Growth, Migration and Invasion of Human Bladder Cancer Cells by Antrocin, a Sesquiterpene Lactone Isolated from Antrodia Cinnamomea, and its Molecular Mechanisms. *Cancer Lett.* 373, 174–184. doi:10.1016/j.canlet.2015.11.046

Cho, K., Wang, X., Nie, S., Chen, Z., and Shin, D. M. (2008). Therapeutic Nanoparticles for Drug Delivery in Cancer. *Clin. Cancer Res.* 14, 1310–1316. doi:10.1158/1078-0432.ccr-07-1441

Dia, V. P., and Pangloli, P. (2017). Epithelial-to-mesenchymal Transition in Paclitaxel-Resistant Ovarian Cancer Cells Is Downregulated by Luteolin. *J. Cel. Physiol.* 232, 391–401. doi:10.1002/jcp.25436

Gao, Y., Chen, Y., Ji, X., He, X., Yin, Q., Zhang, Z., et al. (2011). Controlled Intracellular Release of Doxorubicin in Multidrug-Resistant Cancer Cells by Tuning the Shell-Pore Sizes of Mesoporous Silica Nanoparticles. *ACS Nano* 5, 9788–9798. doi:10.1021/nn2033105

Gorain, B., Choudhury, H., Pandey, M., and Kesharwani, P. (2018). Paclitaxel Loaded Vitamin E-TPGS Nanoparticles for Cancer Therapy. *Mater. Sci. Eng. C* 91, 868–880. doi:10.1016/j.msec.2018.05.054

Jiang, S., Zhu, R., He, X., Wang, J., Wang, M., Qian, Y., et al. (2016). Enhanced Photocytotoxicity of Curcumin Delivered by Solid Lipid Nanoparticles. *Ijn* 12, 167–178. doi:10.2147/ijn.s123107

Laiolo, J., Tomašič, T., Vera, D. M. A., González, M. L., Lanza, P. A., Gancedo, S. N., et al. (2018). Analogues of the Lignan Pinoresinol as Novel lead Compounds for P-Glycoprotein (P-gp) Inhibitors. *ACS Med. Chem. Lett.* 9 (12), 1186–1192. doi:10.1021/acsmedchemlett.8b00324

Majidinia, M., Mirza-Aghazadeh-Attari, M., Rahimi, M., Mihanfar, A., Karimian, A., Safa, A., et al. (2020). Overcoming Multidrug Resistance in Cancer: Recent Progress in Nanotechnology and New Horizons. *IUBMB Life* 72, 855–871. doi:10.1002/iub.2215

Malvezzi, M., Carioli, G., Bertuccio, P., Boffetta, P., Levi, F., La Vecchia, C., et al. (2019). European Cancer Mortality Predictions for the Year 2019 with Focus on Breast Cancer. *Ann. Oncol.* 30, 781–787. doi:10.1093/annonc/mdz051

Rojas, K., and Stuckey, A. (2016). Breast Cancer Epidemiology and Risk Factors. *Clin. Obstet. Gynecol.* 59, 651–672. doi:10.1097/grf.0000000000000239

Senthil Kumar, C., Thangam, R., Mary, S. A., Kannan, P. R., Arun, G., and Madhan, B. (2020). Targeted Delivery and Apoptosis Induction of Trans-resveratrol-ferulic Acid Loaded Chitosan Coated Folic Acid Conjugate Solid Lipid Nanoparticles in colon Cancer Cells. *Carbohydr. PolymersPolym* 231, 115682. doi:10.1016/j.carbpol.2019.115682

Shen, M.-Y., Liu, T.-I., Yu, T.-W., Kv, R., Chiang, W.-H., Tsai, Y.-C., et al. (2019). Hierarchically Targetable Polysaccharide-Coated Solid Lipid Nanoparticles as an Oral Chemo/thermotherapy Delivery System for Local Treatment of colon Cancer. *Biomaterials* 197, 86–100. doi:10.1016/j.biomaterials.2019.01.019

Siegel, R. L., Miller, K. D., and Dvm, A. J. (2021). Cancer Statistics. *2021ca-cancer J. Clin.* 71, 33. doi:10.3322/caac.21654

Smith, B., and Bhowmick, N. (2016). Role of EMT in Metastasis and Therapy Resistance. *Jcm* 5, 17. doi:10.3390/jcm5020017

Sui, X., Wang, X., Han, W., Li, D., Xu, Y., Lou, F., et al. (2015). MicroRNAs-mediated Cell Fate in Triple Negative Breast Cancers. *Cancer Lett.* 361, 8–12. doi:10.1016/j.canlet.2015.02.048

Sun, Y.-S., Zhao, Z., Yang, Z.-N., Xu, F., Lu, H.-J., Zhu, Z.-Y., et al. (2017). Risk Factors and Preventions of Breast Cancer. *Int. J. Biol. Sci.* 13, 1387–1397. doi:10.7150/ijbs.21635

Tang, D.-W., Yu, S.-H., Ho, Y.-C., Mi, F.-L., Kuo, P.-L., and Sung, H.-W. (2010). Heparinized Chitosan/poly(γ-Glutamic Acid) Nanoparticles for Multi-Functional Delivery of Fibroblast Growth Factor and Heparin. *Biomaterials* 31, 9320–9332. doi:10.1016/j.biomaterials.2010.08.058

Tang, Y., Wang, Y., Kiani, M. F., and Wang, B. (2016). Classification, Treatment Strategy, and Associated Drug Resistance in Breast Cancer. *Clin. Breast Cancer* 16, 335–343. doi:10.1016/j.clbc.2016.05.012

Tian, J., Xu, S., Deng, H., Song, X., Li, X., Chen, J., et al. (2017). Fabrication of Self-Assembled Chitosan-Dispersed LDL Nanoparticles for Drug Delivery with a One-step green Method. *Int. J. Pharmaceutics* 517, 25–34. doi:10.1016/j.ijpharm.2016.11.030

Untch, M., Konecny, G. E., Paepke, S., and von Minckwitz, G. (2014). Current and Future Role of Neoadjuvant Therapy for Breast Cancer. *The Breast* 23, 526–537. doi:10.1016/j.breast.2014.06.004

Wang, J., Wang, H., Zhu, R., Liu, Q., Fei, J., and Wang, S. (2015). Anti-inflammatory Activity of Curcumin-Loaded Solid Lipid Nanoparticles in IL-1β Transgenic Mice Subjected to the Lipopolysaccharide-Induced Sepsis. *Biomaterials* 53, 475–483. doi:10.1016/j.biomaterials.2015.02.116

Wang, W., Zhang, L., Chen, T., Guo, W., Bao, X., Wang, D., et al. (2017a). Anticancer Effects of Resveratrol-Loaded Solid Lipid Nanoparticles on Human Breast Cancer Cells. *Molecules* 22, 1814. doi:10.3390/molecules22111814

Wang, W., Zhang, L., Wang, Y., Ding, Y., Chen, T., Wang, Y., et al. (2017b). Involvement of miR-451 in Resistance to Paclitaxel by Regulating YWHAZ in Breast Cancer. *Cell. Death Dis* 8, e3071. doi:10.1038/cddis.2017.460

Wang, Y., Gong, T., Zhang, Z., and Fu, Y. (2017c). Matrix Stiffness Differentially Regulates Cellular Uptake Behavior of Nanoparticles in Two Breast Cancer Cell Lines. *ACS. Appl. Mater. Inter.* 9, 31. doi:10.1021/acsami.7b08751

Wang, Y. Y., Yan, L., Yang, S., Xu, H. N., Chen, T. T., Dong, Z. L., et al. (2019). Long Noncoding RNA AC073284.4 Suppresses Epithelial-Mesenchymal Transition by Sponging miR-18b-5p in Paclitaxel-Resistant Breast Cancer Cells. *J. Cel. Physiol* 234, 23202–23215. doi:10.1002/jcp.28887

Willers, H., Würschmidt, F., Janik, I., Bünemann, H., and Heilmann, H. P. (1997). Combined Breast-Preserving Surgery, Chemotherapy and Radiotherapy in the Treatment of Breast Carcinoma. *Strahlenther. Onkol* 173, 148–154. doi:10.1007/BF03039273

Xu, J. H., Hu, S. L., Shen, G. D., and Shen, G. (2016). Tumor Suppressor Genes and Their Underlying Interactions in Paclitaxel Resistance in Cancer Therapy. *Cancer Cel. Int* 16, 13. doi:10.1186/s12935-016-0290-9

Yang, C., Wu, T., Qi, Y., and Zhang, Z. (2018). Recent Advances in the Application of Vitamin E TPGS for Drug Delivery. *Theranostics* 8, 464–485. doi:10.7150/thno.22711

Yuan, Y., Cai, T., Xia, X., Zhang, R., Chiba, P., and Cai, Y. (2016). Nanoparticle Delivery of Anticancer Drugs Overcomes Multidrug Resistance in Breast Cancer. *Drug Deliv.* 23, 3350–3357. doi:10.1080/10717544.2016.1178825

Zhang, D., Kong, Y., Sun, J., Huo, S., Zhou, M., Gui, Y., et al. (2017). Co-delivery Nanoparticles with Characteristics of Intracellular Precision Release Drugs for Overcoming Multidrug Resistance. *Int. J. Nanomed* 12, 2081–2108. doi:10.2147/ijn.s128790

Zhang, Y., Wu, J., Ye, M., Wang, B., Sheng, J., Shi, B., et al. (2018). ETS1 Is Associated with Cisplatin Resistance through IKKα/NF-Kb Pathway in Cell Line MDA-MB-231. *Cancer.Cell. Int.* 18, 86. doi:10.1186/s12935-018-0581-4

Zheng, N., Liu, W., Li, B., Nie, H., Liu, J., Cheng, Y., et al. (2019). Co-delivery of Sorafenib and Metapristone Encapsulated by CXCR4-Targeted PLGA-PEG Nanoparticles Overcomes Hepatocellular Carcinoma Resistance to Sorafenib. *J. Exp. Clin. Cancer Res.* 38, 232. doi:10.1186/s13046-019-1216-x

Zhu, J., Huo, Q., Xu, M., Yang, F., Li, Y., Shi, H., et al. (2018). Bortezomib-catechol Conjugated Prodrug Micelles: Combining Bone Targeting and Aryl Boronate-Based pH-Responsive Drug Release for Cancer Bone-Metastasis Therapy. *Nanoscale* 10, 1039. doi:10.1039/c8nr03899f

Conflict of Interest: The authors declare that the research was conducted in the absence of any commercial or financial relationships that could be construed as a potential conflict of interest.

Publisher's Note: All claims expressed in this article are solely those of the authors and do not necessarily represent those of their affiliated organizations, or those of the publisher, the editors and the reviewers. Any product that may be evaluated in this article, or claim that may be made by its manufacturer, is not guaranteed or endorsed by the publisher.

frontiers in Bioengineering and Biotechnology

METHODS
published: 07 February 2022
doi: 10.3389/fbioe.2022.806238

Development of Metal-Organic Framework-Based Dual Antibody Nanoparticles for the Highly Specific Capture and Gradual Release of Circulating Tumor Cells

Mingchao Hu[1†], Cheng Li[2], Zhili Wang[2], Pi Ding[2], Renjun Pei[2], Qiang Wang, Hua Xu[3]* and Chungen Xing[1]**

[1]Department of Gastrointestinal Surgery, The Second Affiliated Hospital of Soochow University, Suzhou, China, [2]School of Nano-Tech and Nano-Bionics, University of Science and Technology of China, Hefei, China, [3]Department of General Surgery, The Affiliated Jiangsu Shengze Hospital of Nanjing Medical University, Suzhou, China

OPEN ACCESS

Edited by:
Jinbing Xie,
Southeast University, China

Reviewed by:
Min Liu,
Jianghan University, China
Ting-Yuan Tu,
National Cheng Kung University, Taiwan

***Correspondence:**
Renjun Pei
rjpei2011@sinano.ac.cn
Hua Xu
szyyxh2000@163.com
Chungen Xing
xingcg@suda.edu.cn

†ORCID:
Mingchao Hu
0000-0002-5567-338X

Specialty section:
This article was submitted to Nanobiotechnology, a section of the journal Frontiers in Bioengineering and Biotechnology

Received: 31 October 2021
Accepted: 17 January 2022
Published: 07 February 2022

Citation:
Hu M, Li C, Wang Z, Ding P, Pei R, Wang Q, Xu H and Xing C (2022) Development of Metal-Organic Framework-Based Dual Antibody Nanoparticles for the Highly Specific Capture and Gradual Release of Circulating Tumor Cells. Front. Bioeng. Biotechnol. 10:806238. doi: 10.3389/fbioe.2022.806238

Circulating tumor cells (CTCs) have been well-established as promising biomarkers that can be leveraged to gauge the prognosis of patients with cancers and to guide patient treatment efforts. Although the scarcity of CTCs within peripheral circulation and the associated phenotypic changes that they exhibit owing to the epithelial-mesenchymal transition (EMT) process make the reliable isolation of these cells very challenging. Recently, several studies have discussed platforms capable of mediating the efficient and sensitive isolation of CTCs, but these approaches are nonetheless subject to certain limitations that preclude their clinical application. For example, these platforms are poorly-suited to minimizing damage in the context of cellular capture and release or the *in vitro* culture of captured cells for subsequent molecular analyses, which would better enable clinicians to select appropriate precision treatments on an individualized basis. In this study, we report the layer-by-layer assembly approach to synthesize a novel composite nanomaterial consisting of modified zirconium-based metal-organic-frameworks (MOFs) on the surface of magnetic beads with dual antibody surface modifications capable of capturing CTCs without being hampered by the state of cellular EMT process. Our analyses indicated that these dual antibody-modified nanomaterials exhibited greater capture efficiency than that observed for single antibody. Importantly, captured cells can be gradually released following capture and undergo subsequent *in vitro* proliferation following water molecule-induced MOF structural collapse. This release mechanism, which does not require operator intervention, may be effective as a means of minimizing damage and preserving cellular viability such that cells can be more reliably utilized for downstream molecular analyses and associated treatment planning. To further confirm the potential clinical applicability of the developed nanomaterial, it was successfully utilized for capturing CTCs from peripheral blood samples collected from cases diagnosed with gastrointestinal tumors.

Keywords: circulating tumor cells, metal organic frameworks, isolation, cell release, layer-by-layer assembly method

INTRODUCTION

Cancer is one of the principal reasons for human morbidity and mortality globally. Despite notable advancements in the treatment and diagnosis of various cancers, metastatic disease progression remains a leading driver of patient death (Jolly et al., 2019). As tumors grow, malignant cells may travel through the leaky local vasculature and ultimately enter into systemic circulation, at which time they are referred to as circulating tumor cells (CTCs) (Joosse et al., 2015). Previous research indicates that the spreading and migration of these CTCs is an important contributor to metastatic tumor progression (Yap et al., 2014). These CTCs also offer value as biomarkers amenable to use in the early diagnosis of specific cancers (Baek et al., 2019; Tsai et al., 2019), the monitoring of patient treatment responses (Turano et al., 2019; Khattak et al., 2020; Rau et al., 2020; Reduzzi et al., 2020), and the gauging of patient prognosis (Yang et al., 2018; Trapp et al., 2019; Wang et al., 2019; Wang et al., 2020). These CTCs consist of cells taken from primary tumors or/and metastatic tissue sites that can be evaluated to gain comprehensive insights regarding the molecular status of the underlying disease, providing valuable feedback to inform clinical decision-making. However, these CTCs are scarce and heterogeneous regarding their molecular phenotypes, making their reliable isolation and identification challenging.

Several platforms have been advanced in recent decades that facilitate the isolation of CTCs based upon either the cellular physical characteristics or on specific cell surface antigens present on these CTCs (Nagrath et al., 2016). Physical characteristic-based cell capture methods include those based on cell size- (Vona et al., 2000; Oh et al., 2017), density- (Weitz et al., 1998; Rosenberg et al., 2002), inertia- (Warkiani et al., 2015), electrophoretic- (Gascoyne et al., 2009; Moon et al., 2011), and photoacoustic-based approaches (Galanzha and Zharov, 2013; Nedosekin et al., 2013). Immunoaffinity-based capture methods generally facilitate the isolation of CTCs through the binding of EpCAM, which is expressed at high levels on the surface of many such tumor cells. However, EpCAM is downregulated on CTCs undergoing the EMT process wherein epithelial cells acquire mesenchymal-like characteristics conducive to invasive, aggressive growth (Satelli et al., 2015; Wu et al., 2017; Liu et al., 2019b). Various recent investigations have shown that the EMT phenotype is closely tied to prognostic outcomes for a range of cancers (Satelli et al., 2015; Wu et al., 2017; Liu et al., 2019b; De et al., 2019; Nicolazzo et al., 2019; Yousefi et al., 2020). Developing a platform capable of simultaneously capturing CTCs exhibiting both mesenchymal and epithelial cell surface characteristics would offer an opportunity to better understand the mechanistic basis for tumor metastasis while offering new therapeutic targets and therapeutic options aimed at the effective treatment of cancers.

MOFs are crystalline porous hybrid nanomaterials consisted of metal clusters or ions joined by organic connectors (Ou et al., 2019). MOFs are widely employed for the catalytic purification of wastewater, gas adsorption, and separation applications (Furukawa et al., 2013; Zhang et al., 2018). As they are highly flexible and exhibit a very large surface area with extensive internal porosity, MOFs have also drawn the interest of researchers in the fields of biosensing (He et al., 2014a; Dong et al., 2018; Wang et al., 2018; Afreen et al., 2020), cancer treatment (He et al., 2014b; Chen et al., 2017), and drug delivery (Horcajada et al., 2010; Della Rocca et al., 2011). Several recent studies have sought to employ MOFs as tools to enhance the efficiency and purity of CTC capture. For example, in one recent report, researchers detected MCF-7 tumor cells using a MOFTA sensor constructed from PCN-224 and DNA tetrahedron coupled to dual aptamers (AS1411 & MUC1) (Ou et al., 2019). In a separate study, researchers proposed to design of a core-shell-based MOF nanoparticle that had been modified with an EpCAM-specific antibody to facilitate the capture and release of CTCs (Xie et al., 2019). However, most MOFs are limited by their poor stability in water, with their structures being susceptible to collapse as a consequence of the slow substitution of metal-ligand linkers by water molecules (Burtch et al., 2014; Yuan et al., 2018; Ding et al., 2019). Zr-based MOFs represent the most thermally and chemically stable MOFs produced to date (Cavka et al., 2008), and the Zr-based MOF UIO-67 has been repeatedly shown to exhibit good stability in aqueous solutions (Zhu et al., 2015; Øien-Ødegaard et al., 2016; Pankajakshan et al., 2018). In a previous report, we developed a dual antibody-based CTC capture platform with specificity for both N-cadherin and EpCAM, thereby facilitating the highly efficient isolation of CTCs with both epithelial and mesenchymal characteristics (Liu et al., 2019a). Here, we employed a layer-by-layer approach to generate UIO-67-modified Fe_3O_4 nanoparticles that underwent further dual antibody modification to facilitate the recognition of CTCs irrespective of EMT state. The generated composite nanomaterial was able to capture cells and then gradually release them for subsequent *in vitro* culture following the collapse of this structure upon water exposure.

EXPERIMENTAL SECTION

Materials and Reagents

Ferric chloride hexahydrate ($FeCl_3.6H_2O$), trisodium citrate (TSC), bovine serum albumin (BSA), polyvinyl pyrrolidone (PVP, Mw: 10,000), Zirconium(IV) chloride ($ZrCl_4$), 1,1′-biphenyl-4,4′-dicarboxylic acid (BPDC), Streptavidin (SA), carbodiimide (EDC), N-hydroxysuccinimide (NHS) were provided from Sigma Aldrich (MO, United States). Polyethylene glycol (PEG, MW: 4000) was acquired from Aladdin Co., Ltd. (Shanghai, China), sodium acetate trihydrate ($NaAc{\cdot}3H_2O$), ethylene glycol (EG), N,N-Dimethylformamide (DMF) were provided from Sinopharm Chemical Reagent Co., Ltd. (Shanghai, China), Hoechst 33342, AF488-conjugated CD45 mouse mAb, AF555-conjugated Pan-Keratin mouse mAb, 1,1′-dioctadecyl-3,3,3′,3′-tetramethylindo-carbocyanine perchlorate (DiI), 3-3′-dioctadecyloxa-carbocyanine perchlorate (DiO) were procured from Cell Signaling Technology, Inc. (Danvers, MA). Biotinylated antibodies specific for human EpCAM and N-cadherin were obtained from Univ-bio Co. Ltd. (Shanghai, China).

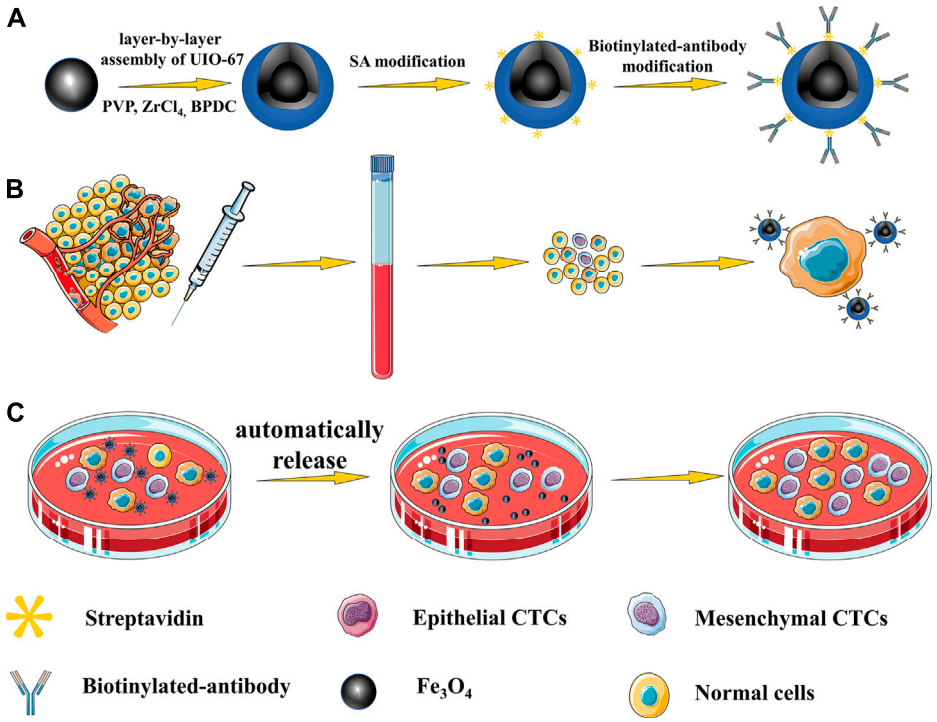

FIGURE 1 | (A) Nanoparticles with a core-shell structure were prepared via a layer-by-layer method. **(B)** Highly specific CTC capture approach using dual antibody-modified nanoparticles. **(C)** UIO-67 gradually collapses in aqueous solutions, thereby facilitating the gradual automated release of captured cells.

Fe_3O_4 Nanoparticle Synthesis

A solvothermal method was used to synthesize Fe_3O_4 nanoparticles as reported previously (Guo et al., 2016). Briefly, $FeCl_3.6H_2O$ (0.945 g, 3.50mmool), PEG (0.50 g, 0.125 mmol), and TSC (0.70 g, 2.38 mmol) were combined with gentle mixing in 70 ml of EG solution until the solvent was fully dissolved to yield a transparent solution, after which $NaAc{\cdot}3H_2O$ (6.96 g, 51.15 mmol) was added and the mixture was stirred vigorously at ambient temperature for 1 h. The mixture was then poured into a reactor and heated to 200°C for 10 h, following which the obtained product was washed thrice in anhydrous ethanol, dissolved in anhydrous ethanol, and stored at 4°C.

Dual-Antibody-Fe_3O_4@UIO-67 Synthesis

A layer-by-layer method was used to synthesize core-shell structure nanoparticles. Briefly, nanoparticles were prepared by dispersing 50 mg of Fe_3O_4 in 50 ml of 10 mg/ml PVP aqueous solution and stirring the resultant mixture for 24 h at ambient temperature. The resultant product was collected, rinsed thrice with anhydrous ethanol, added to 20 ml of DMF along with 0.2 mmol of $ZrCl_4$, and stirred at ambient temperature for 30 min. The product was then collected *via* magnetic separation, rinsed using DMF, and nanoparticles were then dispersant in 20 ml of 10 mmol/L BPDC DMF solution and heated for 40 min at 70°C followed by an additional wash with DMF. This procedure was repeated five times to achieve layer-by-layer assembly, yielding UIO67-coated Fe_3O_4 particles hereafter referred to as Fe_3O_4@UIO-67. Reaction product concentrations were measured, dissolved with anhydrous ethanol, and stored at 4 °C for subsequent utilization.

Next, antibody surface modification was achieved by washing 200 μg of Fe_3O_4@UIO-67 with PBS three times and transferring them into 0.1 M MES buffer containing 0.025 M NHS and 0.1 M EDC with shaking at 37°C for 30 min. The resultant products were then magnetically separated, rinsed thrice with PBS, and then suspended in 900 uL of PBS and 100 ul of SA solution (20 μg/ml in PBS) with gentle shaking at ambient temperature for 10 h. Samples were again rinsed thrice with PBS, yielding SA-modified particles that were subsequently incubated at room temperature with appropriate biotinylated antibodies (2 μg/ml anti-EpCAM or anti-N-cadherin in PBS) for 2 h with constant shaking. The resultant particles were again washed and then suspended in 2% (w/v) BSA for 2 h with constant shaking to prevent non-specific binding to the prepared composite nanomaterial.

Dual Antibody-Modified Fe3O4@UIO-67 Characterization

Fe_3O_4@UIO-67 morphological characteristics were identified *via* transmission electron microscopy (TEM) employing a Hitachi-HT7700 instrument (accelerating voltage: 120 kV). Fe_3O_4@UIO-67 particle size was assessed by implementing a Dynamic Light Scattering (DLS) instrument (Zetasizer Nano ZS ZEN3600, Malvern Instruments Ltd. United Kingdom). Following layer-by-layer assembly, composite nanomaterial surface morphology

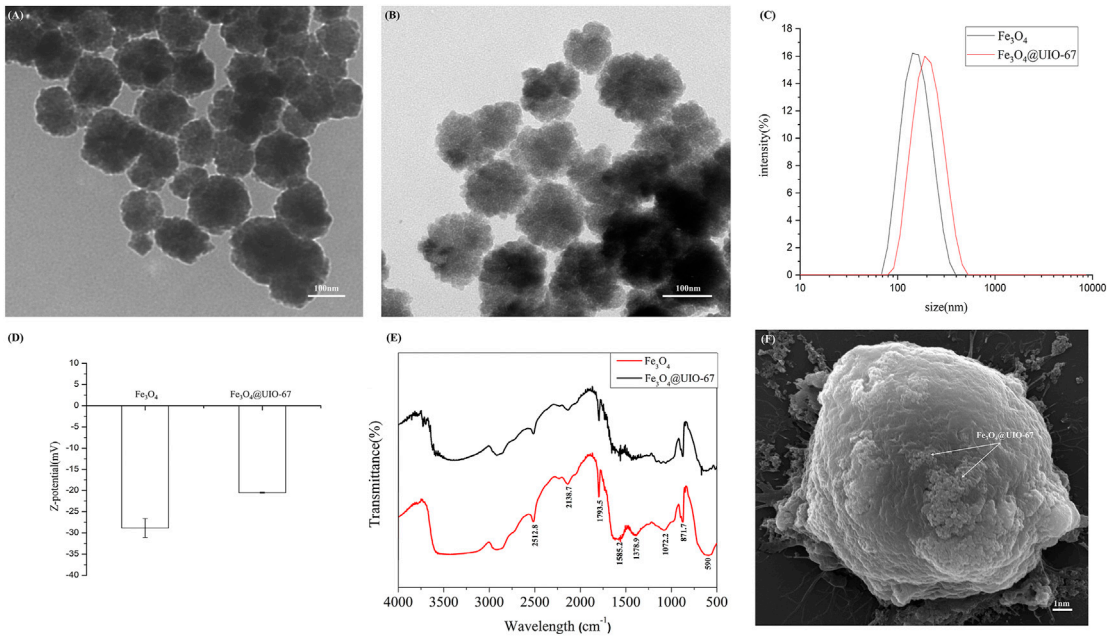

FIGURE 2 | (A) Images of TEM for pure Fe_3O_4. **(B)** Images of TEM for Fe_3O_4@UIO-67. **(C)** Hydrodynamic diameter values for Fe_3O_4 and Fe_3O_4@UIO-67 preparations measured *via* DLS. **(D)** Zeta potential values for Fe_3O_4 and Fe_3O_4@UIO-67 preparations. **(E)** Fe_3O_4 and Fe_3O_4@UIO-67 FTIR spectra. **(F)** Representative MCF-7 cell images following capture using dual antibody-modified Fe_3O_4@UIO-67.

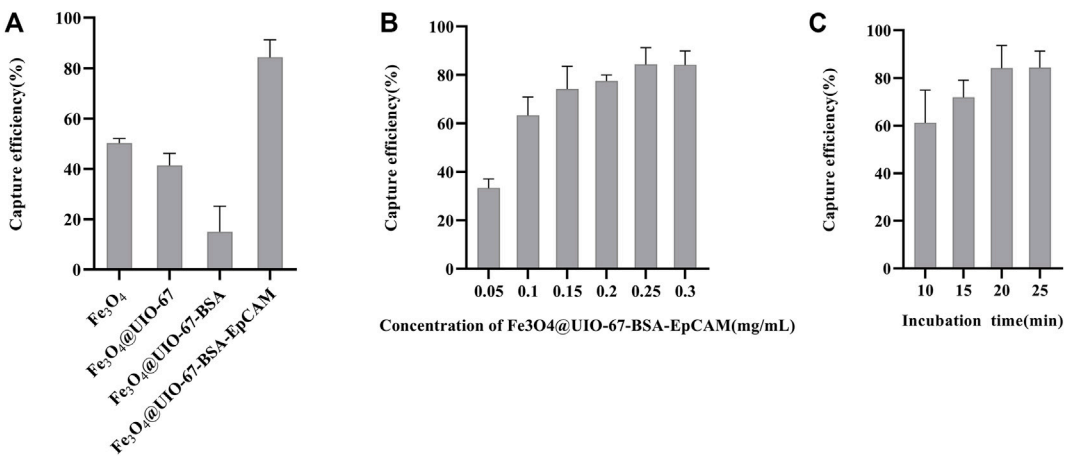

FIGURE 3 | (A) Analysis of the nanoparticle modification status on MCF-7 cell capture efficiency. **(B)** Analysis of the effects of nanoparticle concentration on MCF-7 cell capture efficiency. **(C)** Analysis of the effects of time on MCF-7 cell capture efficiency.

was additionally assessed *via* scanning electron microscopy (SEM, 20.0 kV, FEI Quanta 400F).

Cell Culture

The human MCF-7 breast cancer (EpCAM+, N-cadherin-), HeLa cervical cancer (EpCAM-, N-cadherin+), and CCRF-CEM acute lymphoblastic leukemia T lymphocyte (EpCAM-, N-cadherin-) cell lines were used as models in the present study. HeLa and MCF-7 cells were cultivated in DMEM comprising 1% penicillin/streptomycin and 10% fetal bovine serum (FBS), while CCRF-CEM cells were cultured in RPMI-1640 containing 1% penicillin/streptomycin and 10% FBS. All cells were cultivated in a 5% CO_2 37°C incubator, with media being replaced every other day. Prior to cell capture assays, cells were harvested employing 0.05% trypsin.

Antibody-Functionalized Fe_3O_4@ UIO-67-Mediated Cell Capture Studies

A hemocytometer was used to count model cells, which were then combined with antibody-modified composite nanomaterials at

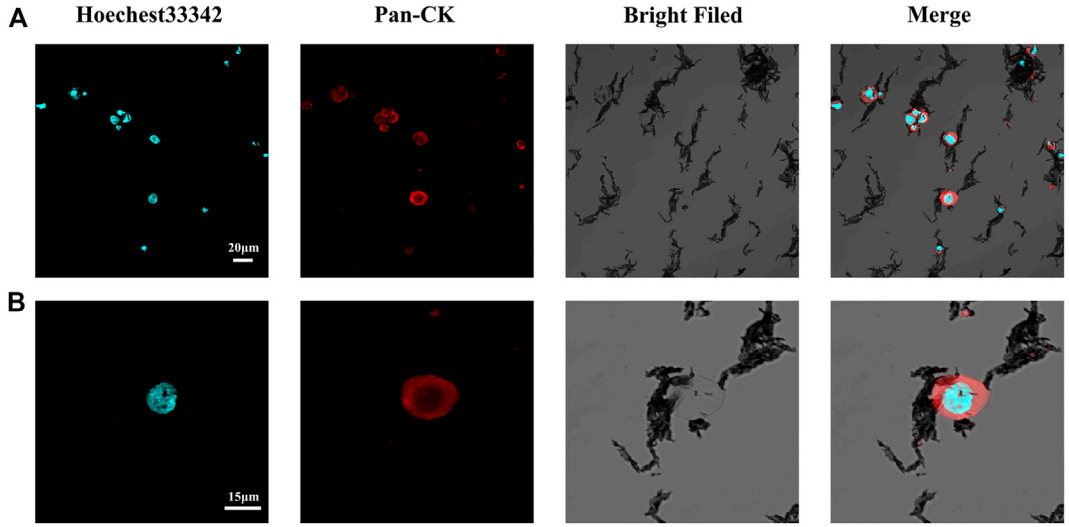

FIGURE 4 | (A) Representative confocal microscopy images of captured MCF-7 cells. **(B)** Representative confocal microscopy images of single captured MCF-7 cells.

experimentally appropriate concentrations for 30 min at ambient temperature to assess cell capture dynamics. Capture efficiency was determined as the ratio of the total number of cells captured by the prepared nanomaterial to the starting cell number. Analyses were repeated in triplicate, with results being reported as the mean ± standard deviation. Associations between co-incubation time and cell capture efficiency for prepared composite nanomaterials, 100,000 MCF-7 cells were incubated with anti-EpCAM-modified magnetic beads for 10, 15, 20, or 25 min, after which samples were magnetically separated, washed thrice with PBS, and cell capture efficiency was calculated. The sensitivity of dual antibody-modified Fe_3O_4@UIO-67 particles as a tool for capturing low numbers of CTCs, 20, 50, 100, or 200 HeLa or MCF-7 cells that had been pre-stained by utilizing Dio dye were suspended in 1 ml of PBS or healthy human donor blood to simulate peripheral blood samples from cancer patients. Following a 30 min co-incubation at 37°C, samples were magnetically separated, rinsed with PBS, and capture efficiency was computed.

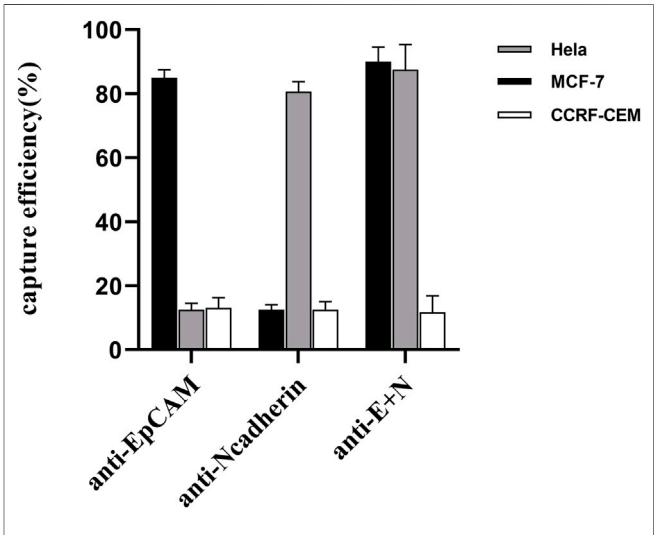

FIGURE 5 | Comparing the rates of capture efficiency when using anti-EpCAM-modified, anti-N-cadherin-modified, and dual antibody-modified nanoparticles to capture model target cell lines.

Culture and Proliferation Analyses of Captured CTCs

After cells had been captured using modified nanoparticle preparations, they were rinsed thrice with PBS and added to DMEM for subsequent culture under standard conditions as described above. Cellular fluorescence was assessed by staining cells with the Dio dye after 24, 48, 72, or 96 h. In addition, a CCK-8 assay was used based on provided protocols to assess cellular proliferation, while cellular viability was quantified with a Calcein-AM/PI Double Stain Kit. Briefly, 50,000 HeLa cells were incubated for 30 min with dual antibody-modified Fe_3O_4@UIO-67 at 37 °C, after which samples were rinsed with PBS and captured cells were stained with 2 μM calcein-AM (green) and 4.5 μM PI (red) for 20 min at 37°C. After a subsequent rinse with PBS, cells were imaged *via* fluorescence microscopy, and the ImageJ application was employed for counting dead (red) and live (green) cells. All analyses were repeated in triplicate.

CTC Capture From Cancer Patient Peripheral Blood Samples

Samples of whole peripheral blood of cancer patients were accumulated from the Second Affiliated Hospital of Soochow University and The Affiliated Jiangsu Shengze Hospital of

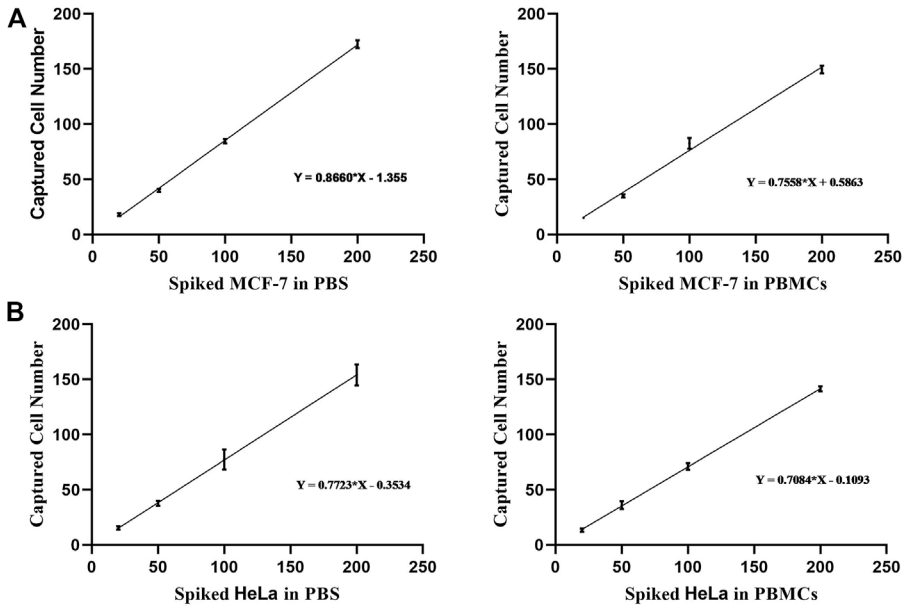

FIGURE 6 | (A) Analysis of the capture efficiency for low numbers of MCF-7 cells in PBS or PBMC-containing solutions. **(B)** Analysis of the capture efficiency for low numbers of HeLa cells in PBS or PBMC-containing solutions.

Nanjing Medical University in tubes comprising Ethylene Diamine Tetraacetic Acid (EDTA) as an anticoagulant. The ethics committees of the participating hospitals approved all aspects of the present study. All samples were processed within 48 h following collection. In total, 5 ml of peripheral blood was collected from each of 10 cancer patients. Each sample was then diluted to a 10 ml total volume using HBSS (Hank's balanced salt solution) and layered atoll 5 ml of Ficoll-Paque (Sigma-Aldrich), after which peripheral blood mononuclear cells (PBMCs) were isolated through centrifuging samples at ambient temperature for 30 min at 2,000 rpm, rinsing the interface later with HBSS three times, and then incubating samples for 30 min with dual antibody-functionalized magnetic beads at 37°C. Captured cells were then washed with PBS, fixed with 4% paraformaldehyde for 20 min, and suspended for 1 h in blocking buffer (1× PBS with 5% FBS and 0.3% Triton X-100). CTCs were identified with Alexa Fluor 555-conjugated anti-PanCK, while leukocytes were identified using Alexa Fluor 488-conjugated anti-CD45, with Hoechst 33342 being used for nuclear counterstaining. Cells were then imaged *via* confocal microscopy, enabling the differentiation between CTCs (CK+/CD45-/Hoechest+) and leukocytes (CK-/CD45+/Hoechest+).

RESULTS

Fe_3O_4@UIO-67 Preparation and Characterization

We began by synthesizing Fe_3O_4 *via* a hydrothermal method, after which UIO-67 was used to modify the surface of these particles *via* a layer-by-layer assembly approach to yield a composite nanomaterial with a stable core-shell structure as shown in **Figure 1**. The surface morphology of these prepared Fe_3O_4 and Fe_3O_4@UIO-67 particles was assessed *via* TEM (**Figure 2A,B**), while DLS was employed for confirming the size and Zeta potential of these particles following UIO-67 modification. The diameters of unmodified Fe_3O_4 and UIO-67-modified Fe_3O_4 in this analysis were 169.90 ± 9.37 nm and 231.91 ± 16.22 nm, respectively, which indicated that UIO-67 was successfully modified on the surface of the Fe_3O_4 using the layer-by-layer assembly method (**Figure 2C**). Zeta potential values indicated that while Fe_3O_4@UIO-67 is relatively stable in water, it is more labile than Fe_3O_4 (**Figure 2D**). The gradual collapse of the prepared MOF structure in aqueous solutions would thus have the capability to facilitate the release of captured CTCs for subsequent culture and analysis. In Fourier-transform infrared (FTIR) spectra analyses of Fe_3O_4, the absorption peak at 590 cm^{-1} was attributed to the stretching vibration of the Fe-O functional group, while the peak at 1,585.2 cm^{-1} corresponded to carboxyl group vibrations as a consequence of the red-shift of the carboxyl peak when the carboxylic acid ligand interacts with the metal ion in the context of coordination, thus reducing its energy and increasing associated stability (**Figure 2E**). The peak at 871.7 cm^{-1} was further assigned to the flexural vibration of C-H within the benzene ring. Comparisons of the FTIR spectra for pure Fe_3O_4 and the prepared composite nanoparticles confirmed that UIO-67 had successfully been used to modify the surfaces of these Fe_3O_4 nanoparticles. Representative images of SEM for MCF-7 cells captured using dual antibody-modified versions of these composite nanoparticles are shown in **Figure 2F**, demonstrating that many nanoparticles were visible on captured cell surfaces.

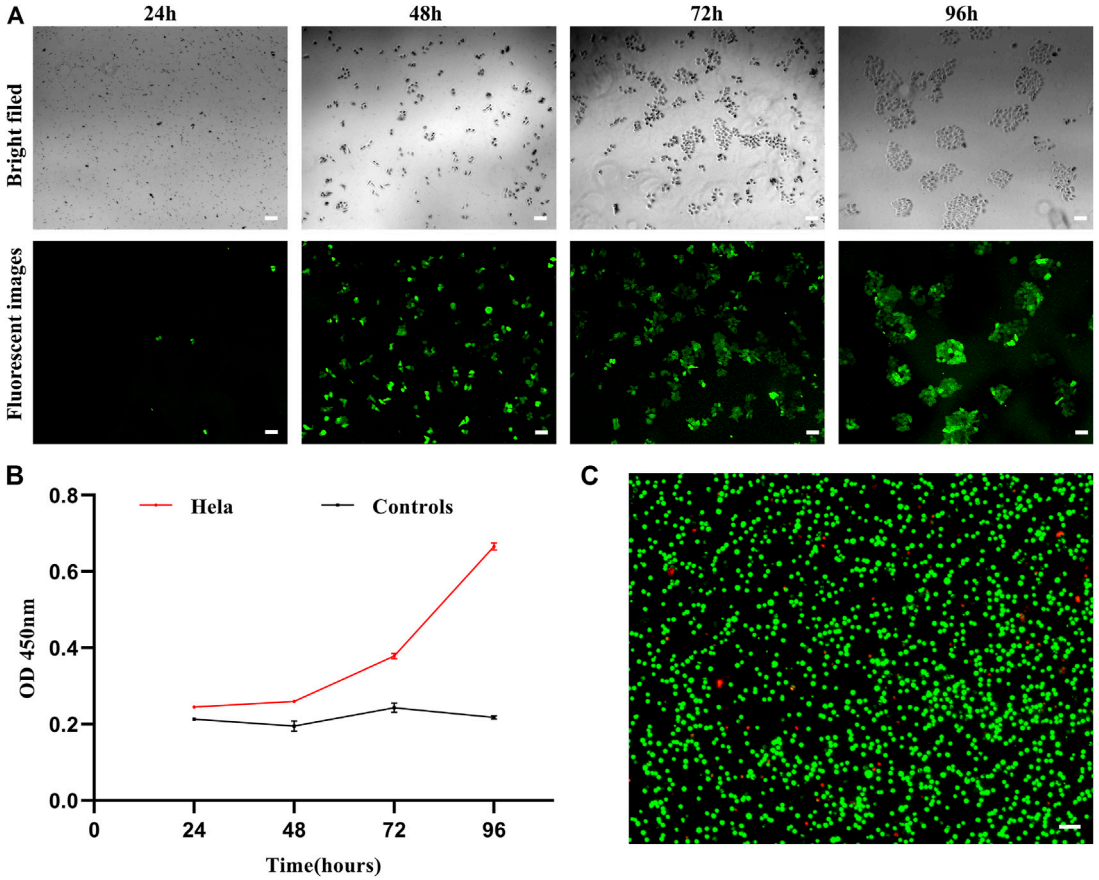

FIGURE 7 | (A) Brightfield and fluorescent images of HeLa cells following dual antibody-modified nanoparticle-mediated capture and subsequent culture for 24, 48, 72, or 96 h. **(B)** Absorbance (OD) at 450 nm for HeLa cell cultures following dual antibody-modified nanoparticle-mediated capture. **(C)** Fluorescent imaging of HeLa cell viability following nanoparticle-mediated capture. Scale bar: 100 μm.

Cell Capture Condition Optimization

To verify the effective capture of target tumor cells employing our dual antibody-modified Fe_3O_4@UIO-67 platform, we next sought to optimize cell capture conditions. To that end, we utilized MCF-7 tumor cells expressing high levels of EpCAM to mimic tumor cells with an epithelial-like phenotype, incubating 10^5 MCF-7 cells with different nanoparticle preparations for 40 min. Samples were then magnetically separated and washed three times, after which capture efficiency was calculated. Modification of UIO-67 using layer-by-layer assembly on these particles did not effectively eliminate non-specific binding in this assay context (**Figure 3A**), leading us to next block the surface of the prepared nanoparticles with 2% (w/v) BSA for 2 h following dual antibody modification, thereby significantly reducing nonspecific cellular adhesion. We next explored the impact of nanoparticle concentrations and incubation duration on the efficiency of MCF-7 capture using our anti-EpCAM-modified nanoparticles, revealing that capture efficiency rose with nanoparticle concentration to a maximum of 84.375 ± 6.884% at a nanoparticle concentration of 0.25 mg/ml (**Figure 3B**). Capture efficiency was also influenced by incubation time, with maximal efficiency being achieved following a 20 min incubation (**Figure 3C**). Representative fluorescent images of MCF-7 cells following dual antibody-modified nanoparticle-mediated capture are shown in **Figure 4A,B**, with isolated MCF-7 cells exhibiting red fluorescence attributable to anti-Pan-CK staining.

Evaluation of the Impact of Modification Status on the UIO-67-Coated Magnetic Nanoparticle Cell Capture Efficiency

We additionally explored the ability of nanoparticles modified with different antibodies to capture simulated CTCs exhibiting different surface phenotypes, with MCF-7 (EpCAM+, N-cadherin-) and HeLa (EpCAM-, N-cadherin+) cells being used to simulate CTCs with epithelial and mesenchymal characteristics, respectively. In addition, CCRF-CEM cells were used to evaluate non-specific nanoparticle cell binding as these cells do not express EpCAM or N-cadherin. Prepared anti-EpCAM-modified nanoparticles exhibited high capture efficiency values for MCF-7 cells (83.75 ± 1.25%) but not for HeLa (12.75 ± 1.79%) or CCRF-CEM (13.125 ± 2.724%) cells, consistent with the feasibility of this specific CTC capture approach (**Figure 5**). Similarly, anti-N-cadherin-modified nanoparticles exhibited high capture efficiency for HeLa cells (80.625 ± 2.724%) but not for MCF-7

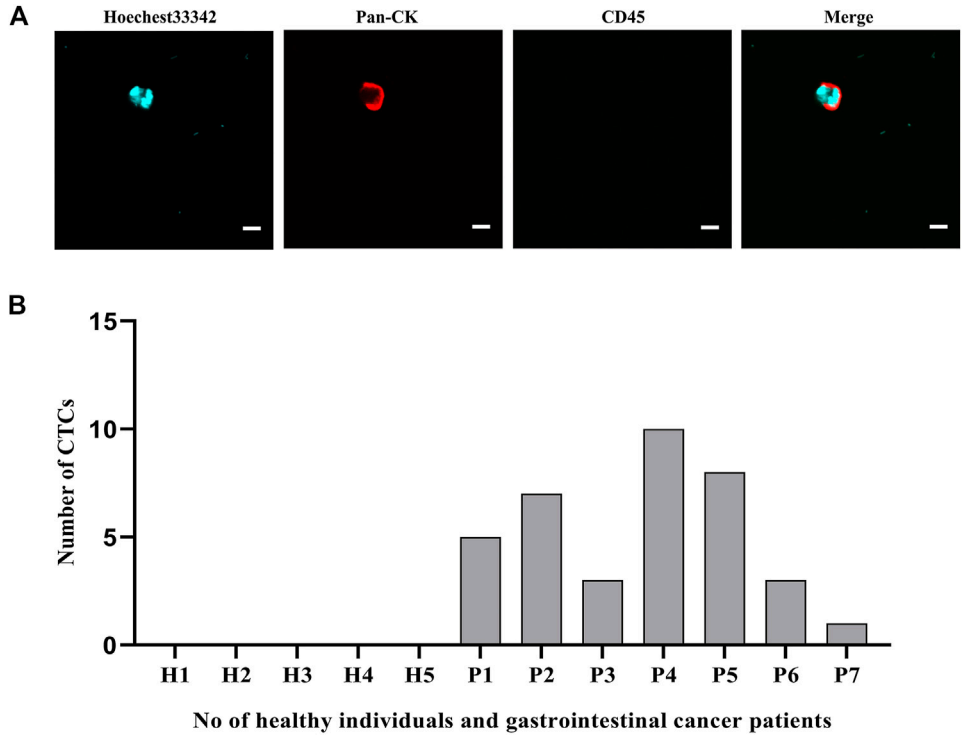

FIGURE 8 | (A) Representative fluorescent images of captured CTCs. **(B)** Quantification of the CTCs captured from the peripheral blood (5 ml) of patients with gastrointestinal tumors. Scale bar: 20 μm.

or CCRF-CEM cells (2.5 ± 1.44% and 12.5 ± 2.04%, respectively). Dual antibody-modified nanoparticles were also able to more efficiently capture both MCF-7 (90 ± 3.95%) and HeLa (87.5 ± 6.85%) cells as compared to single antibody-modified nanoparticles, consistent with the ability of these nanoparticles to capture CTCs irrespective of EMT progression status.

Analysis of Rare Cell Capture Efficiency

Prior experimental studies suggest that dual antibody-modified nanoparticles that had been blocked with BSA (2%, w/v) were well-suited to the efficient capture of target cells of interest with minimal non-specific adsorption. To further confirm the specificity of the developed call capture platform, we sought to assess the ability of our modified composite nanomaterial to detect rare simulated CTCs by adding low numbers of Dio-labeled MCF-7 or HeLa cells (20, 50, 100, or 200 cells) in 1 ml of PBS. Subsequent analyses indicated that over 86% of MCF-7 cells and 77% of HeLa cells were captured through prepared dual antibody-modified nanoparticles under these conditions (**Figure 6A**). We then repeated these experiments following the addition of Dio-stained tumor cells to healthy donor PBMCs to better mimic the complex milieu present within peripheral blood-derived samples gathered from cancer patients. Under these conditions, the capture efficiency rates for MCF-7 and HeLa cells declined slightly to 75 and 70%, respectively, likely owing to the interference stemming from the large numbers of background cells present within these whole blood-derived PBMC samples.

Analysis of Captured Cell Release and Viability

Given their rarity, the ability to transiently capture CTCs *in vitro* and to subsequently culture them for use in subsequent mutational or gene expression analyses would be invaluable as a means of better guiding patient care and more fully understanding the mechanisms shaping tumor pathogenesis. As such, we next co-cultured captured cells and nanoparticles *in vitro* and then evaluated the viability and proliferation of cells over time. This analysis revealed that after an initial quiescent period, these captured cells were able to proliferate in culture (**Figure 7A,B**), consistent with their gradual release from the MOF structure as it collapses in water. This progressive dissolution of the MOF structure following interaction with water can thus facilitate the automated release of captured cells in a non-damaging manner, thus enabling their subsequent proliferation and *in vitro* culture for downstream molecular analyses while maintaining high levels of viability (**Figure 7C**).

Dual Antibody-Modified Fe_3O_4@UIO-67-Mediated Capture of Peripheral Blood CTCs From Gastrointestinal Cancer Patients

To confirm the potential clinical viability of these dual antibody-modified nanoparticles, we next utilized them in an effort for

capturing CTCs from the peripheral blood of gastrointestinal cancer cases (n = 7) and healthy controls (n = 5) using blood samples collected from the Second Affiliated Hospital of Soochow University and The Affiliated Jiangsu Shengze Hospital of Nanjing Medical University. Following nanoparticle-mediated CTC capture, immunofluorescent staining was conducted to differentiate between leukocytes (CK-/CD45+/Hoechest+) and CTCs (CK+/CD45-/Hoechest33342+). Representative images of captured CRCs are shown in **Figure 8A**, with the quantification of the numbers of peripheral blood CTCs captured from each gastrointestinal cancer patient being shown in **Figure 8B**. On average, 1-10 CTCs were collected in the peripheral blood samples from these cancer cases, whereas 0 CTCs were evident in any of the healthy control blood samples. Together, these data thus demonstrate that these dual antibody-modified nanoparticles can reliably capture CTCs within the peripheral blood of cases harboring gastrointestinal tumors.

CONCLUSION

In conclusion, we herein employed a layer-by-layer assembly approach to develop a novel composite nanomaterial *via* the modification of MOF structures on the surfaces of magnetic beads with dual-antibodies targeting epithelial and mesenchymal antigens expressed on the surfaces of CTCs. The constructed MOF structure underwent gradual collapse in water, thereby facilitating the gradual release of captured cells which can then undergo subsequent proliferation in culture. This composite nanomaterial offers many advantages include ease-of-synthesis, a low cost, and excellent biocompatibility, and its ability to capture viable CTCs for subsequent culture makes it amenable to use in the context of a variety of downstream molecular analyses.

DATA AVAILABILITY STATEMENT

The raw data supporting the conclusions of this article will be made available by the authors, without undue reservation.

ETHICS STATEMENT

Written informed consent was obtained from the individual(s) for the publication of any potentially identifiable images or data included in this article.

AUTHOR CONTRIBUTIONS

MH and CL contributed to the idea for the article, ZW, PD and HX contributed to the capture experiments, RP and CX contributed to the manuscript review.

FUNDING

This study was funded by the Chinese Natural Science Foundation (Grant number: 81672970), Project from Jiangsu Provincial Health and Family Planning Commission (Grant number: CXTDA2017016 and BE2020766) Suzhou Introduce Team Program (Grant number: SS202088).

ACKNOWLEDGMENTS

The authors would like to thank all the reviewers who participated in the review, as well as MJEditor (www.mjeditor.com) for providing English editing services during the preparation of this manuscript.

REFERENCES

Afreen, S., He, Z., Xiao, Y., and Zhu, J.-J. (2020). Nanoscale Metal-Organic Frameworks in Detecting Cancer Biomarkers. *J. Mater. Chem. B* 8 (7), 1338–1349. doi:10.1039/c9tb02579k

Baek, D. H., Kim, G. H., Song, G. A., Han, I. S., Park, E. Y., Kim, H. S., et al. (2019). Clinical Potential of Circulating Tumor Cells in Colorectal Cancer: A Prospective Study. *Clin. Translational Gastroenterol.* 10 (7), e00055. doi:10.14309/ctg.0000000000000055

Burtch, N. C., Jasuja, H., and Walton, K. S. (2014). Water Stability and Adsorption in Metal-Organic Frameworks. *Chem. Rev.* 114 (20), 10575–10612. doi:10.1021/cr5002589

Cavka, J. H., Jakobsen, S., Olsbye, U., Guillou, N., Lamberti, C., Bordiga, S., et al. (2008). A New Zirconium Inorganic Building brick Forming Metal Organic Frameworks with Exceptional Stability. *J. Am. Chem. Soc.* 130 (42), 13850–13851. doi:10.1021/ja8057953

Chen, R., Zhang, J., Chelora, J., Xiong, Y., Kershaw, S. V., Li, K. F., et al. (2017). Ruthenium(II) Complex Incorporated UiO-67 Metal-Organic Framework Nanoparticles for Enhanced Two-Photon Fluorescence Imaging and Photodynamic Cancer Therapy. *ACS Appl. Mater. Inter.* 9 (7), 5699–5708. doi:10.1021/acsami.6b12469

De, T., Goyal, S., Balachander, G., Chatterjee, K., Kumar, P., Babu K., G., et al. (2019). A Novel *Ex Vivo* System Using 3D Polymer Scaffold to Culture Circulating Tumor Cells from Breast Cancer Patients Exhibits Dynamic E-M Phenotypes. *J. Clin. Med.* 8 (9), 1473. doi:10.3390/jcm8091473

Della Rocca, J., Liu, D., and Lin, W. (2011). Nanoscale Metal-Organic Frameworks for Biomedical Imaging and Drug Delivery. *Acc. Chem. Res.* 44 (10), 957–968. doi:10.1021/ar200028a

Ding, M., Cai, X., and Jiang, H.-L. (2019). Improving MOF Stability: Approaches and Applications. *Chem. Sci.* 10 (44), 10209–10230. doi:10.1039/c9sc03916c

Dong, S., Peng, L., Wei, W., and Huang, T. (2018). Three MOF-Templated Carbon Nanocomposites for Potential Platforms of Enzyme Immobilization with Improved Electrochemical Performance. *ACS Appl. Mater. Inter.* 10 (17), 14665–14672. doi:10.1021/acsami.8b00702

Furukawa, H., Cordova, K. E., O'Keeffe, M., and Yaghi, O. M. (2013). The Chemistry and Applications of Metal-Organic Frameworks. *Science* 341 (6149), 1230444. doi:10.1126/science.1230444

Galanzha, E., and Zharov, V. (2013). Circulating Tumor Cell Detection and Capture by Photoacoustic Flow Cytometry *In Vivo* and *Ex Vivo*. *Cancers* 5 (4), 1691–1738. doi:10.3390/cancers5041691

Gascoyne, P. R. C., Noshari, J., Anderson, T. J., and Becker, F. F. (2009). Isolation of Rare Cells from Cell Mixtures by Dielectrophoresis. *Electrophoresis* 30 (8), 1388–1398. doi:10.1002/elps.200800373

Guo, X., Wu, Z., Li, W., Wang, Z., Li, Q., Kong, F., et al. (2016). Appropriate Size of Magnetic Nanoparticles for Various Bioapplications in Cancer Diagnostics and

Therapy. *ACS Appl. Mater. Inter.* 8 (5), 3092–3106. doi:10.1021/acsami.5b10352

He, C., Lu, K., and Lin, W. (2014a). Nanoscale Metal-Organic Frameworks for Real-Time Intracellular pH Sensing in Live Cells. *J. Am. Chem. Soc.* 136 (35), 12253–12256. doi:10.1021/ja507333c

He, C., Lu, K., Liu, D., and Lin, W. (2014b). Nanoscale Metal-Organic Frameworks for the Co-delivery of Cisplatin and Pooled siRNAs to Enhance Therapeutic Efficacy in Drug-Resistant Ovarian Cancer Cells. *J. Am. Chem. Soc.* 136 (14), 5181–5184. doi:10.1021/ja4098862

Horcajada, P., Chalati, T., Serre, C., Gillet, B., Sebrie, C., Baati, T., et al. (2010). Porous Metal-Organic-Framework Nanoscale Carriers as a Potential Platform for Drug Delivery and Imaging. *Nat. Mater* 9 (2), 172–178. doi:10.1038/Nmat2608

Jolly, M. K., Somarelli, J. A., Sheth, M., Biddle, A., Tripathi, S. C., Armstrong, A. J., et al. (2019). Hybrid Epithelial/mesenchymal Phenotypes Promote Metastasis and Therapy Resistance across Carcinomas. *Pharmacol. Ther.* 194, 161–184. doi:10.1016/j.pharmthera.2018.09.007

Joosse, S. A., Gorges, T. M., and Pantel, K. (2015). Biology, Detection, and Clinical Implications of Circulating Tumor Cells. *EMBO Mol. Med.* 7 (1), 1–11. doi:10.15252/emmm.201303698

Khattak, M. A., Reid, A., Freeman, J., Pereira, M., McEvoy, A., Lo, J., et al. (2020). PD-L1 Expression on Circulating Tumor Cells May Be Predictive of Response to Pembrolizumab in Advanced Melanoma: Results from a Pilot Study. *Oncologist* 25 (3), e520–e527. doi:10.1634/theoncologist.2019-0557

Liu, H., Wang, Z., Chen, C., Ding, P., Sun, N., and Pei, R. (2019a). Dual-antibody Modified PLGA Nanofibers for Specific Capture of Epithelial and Mesenchymal CTCsfic Capture of Epithelial and Mesenchymal CTCs. *Colloids Surf. B: Biointerfaces* 181, 143–148. doi:10.1016/j.colsurfb.2019.05.031

Liu, X., Li, J., Cadilha, B. L., Markota, A., Voigt, C., Huang, Z., et al. (2019b). Epithelial-type Systemic Breast Carcinoma Cells with a Restricted Mesenchymal Transition Are a Major Source of Metastasis. *Sci. Adv.* 5 (6), eaav4275. doi:10.1126/sciadv.aav4275

Moon, H.-S., Kwon, K., Kim, S.-I., Han, H., Sohn, J., Lee, S., et al. (2011). Continuous Separation of Breast Cancer Cells from Blood Samples Using Multi-Orifice Flow Fractionation (MOFF) and Dielectrophoresis (DEP). *Lab. Chip* 11 (6), 1118–1125. doi:10.1039/c0lc00345j

Nagrath, S., Jack, R. M., Sahai, V., and Simeone, D. M. (2016). Opportunities and Challenges for Pancreatic Circulating Tumor Cells. *Gastroenterology* 151 (3), 412–426. doi:10.1053/j.gastro.2016.05.052

Nedosekin, D. A., Sarimollaoglu, M., Galanzha, E. I., Sawant, R., Torchilin, V. P., Verkhusha, V. V., et al. (2013). Synergy of Photoacoustic and Fluorescence Flow Cytometry of Circulating Cells with Negative and Positive Contrasts. *J. Biophoton.* 6 (5), 425–434. doi:10.1002/jbio.201200047

Nicolazzo, C., Raimondi, C., Gradilone, A., Emiliani, A., Zeuner, A., Francescangeli, F., et al. (2019). Circulating Tumor Cells in Right- and Left-Sided Colorectal Cancer. *Cancers* 11 (8), 1042. doi:10.3390/cancers11081042

Oh, B. Y., Kim, J., Lee, W. Y., and Kim, H. C. (2017). A New Size-Based Platform for Circulating Tumor Cell Detection in Colorectal Cancer Patients. *Clin. Colorectal Cancer* 16 (3), 214–219. doi:10.1016/j.clcc.2017.01.007

Øien-Ødegaard, S., Bouchevreau, B., Hylland, K., Wu, L., Blom, R., Grande, C., et al. (2016). UiO-67-type Metal-Organic Frameworks with Enhanced Water Stability and Methane Adsorption Capacity. *Inorg. Chem.* 55 (5), 1986–1991. doi:10.1021/acs.inorgchem.5b02257

Ou, D., Sun, D., Liang, Z., Chen, B., Lin, X., and Chen, Z. (2019). A Novel Cytosensor for Capture, Detection and Release of Breast Cancer Cells Based on Metal Organic Framework PCN-224 and DNA Tetrahedron Linked Dual-Aptamer. *Sensors Actuators B: Chem.* 285 (APR), 398–404. doi:10.1016/j.snb.2019.01.079

Pankajakshan, A., Sinha, M., Ojha, A. A., and Mandal, S. (2018). Water-Stable Nanoscale Zirconium-Based Metal-Organic Frameworks for the Effective Removal of Glyphosate from Aqueous Media. *ACS Omega* 3 (7), 7832–7839. doi:10.1021/acsomega.8b00921

Rau, K.-M., Liu, C.-T., Hsiao, Y.-C., Hsiao, K.-Y., Wang, T.-M., Hung, W.-S., et al. (2020). Sequential Circulating Tumor Cell Counts in Patients with Locally Advanced or Metastatic Hepatocellular Carcinoma: Monitoring the Treatment Response. *J. Clin. Med.* 9 (1), 188. doi:10.3390/jcm9010188

Reduzzi, C., Vismara, M., Silvestri, M., Celio, L., Niger, M., Peverelli, G., et al. (2020). A Novel Circulating Tumor Cell Subpopulation for Treatment Monitoring and Molecular Characterization in Biliary Tract Cancer. *Int. J. Cancer* 146 (12), 3495–3503. doi:10.1002/ijc.32822

Rosenberg, R., Gertler, R., Friederichs, J., Fuehrer, K., Dahm, M., Phelps, R., et al. (2002). Comparison of Two Density Gradient Centrifugation Systems for the Enrichment of Disseminated Tumor Cells in Blood. *Cytometry* 49 (4), 150–158. doi:10.1002/cyto.10161

Satelli, A., Mitra, A., Brownlee, Z., Xia, X., Bellister, S., Overman, M. J., et al. (2015). Epithelial-mesenchymal Transitioned Circulating Tumor Cells Capture for Detecting Tumor Progression. *Clin. Cancer Res.* 21 (4), 899–906. doi:10.1158/1078-0432.CCR-14-0894

Trapp, E., Janni, W., Schindlbeck, C., Jückstock, J., Andergassen, U., de Gregorio, A., et al. (2019). Presence of Circulating Tumor Cells in High-Risk Early Breast Cancer during Follow-Up and Prognosis. *J. Natl. Cancer Inst.* 111 (4), 380–387. doi:10.1093/jnci/djy152

Tsai, W.-S., You, J.-F., Hung, H.-Y., Hsieh, P.-S., Hsieh, B., Lenz, H.-J., et al. (2019). Novel Circulating Tumor Cell Assay for Detection of Colorectal Adenomas and Cancer. *Clin. Translational Gastroenterol.* 10 (10), e00088. doi:10.14309/ctg.0000000000000088

Turano, M., Delrio, P., Rega, D., Cammarota, F., Polverino, A., Duraturo, F., et al. (2019). Promising Colorectal Cancer Biomarkers for Precision Prevention and Therapy. *Cancers* 11 (12), 1932. doi:10.3390/cancers11121932

Vona, G., Sabile, A., Louha, M., Sitruk, V., Romana, S., Schütze, K., et al. (2000). Isolation by Size of Epithelial Tumor Cells. *Am. J. Pathol.* 156 (1), 57–63. doi:10.1016/s0002-9440(10)64706-2

Wang, H., Jian, Y., Kong, Q., Liu, H., Lan, F., Liang, L., et al. (2018). Ultrasensitive Electrochemical Paper-Based Biosensor for microRNA via Strand Displacement Reaction and Metal-Organic Frameworks. *Sensors Actuators B: Chem.* 257, 561–569. doi:10.1016/j.snb.2017.10.188

Wang, L., Zhou, S., Zhang, W., Wang, J., Wang, M., Hu, X., et al. (2019). Circulating Tumor Cells as an Independent Prognostic Factor in Advanced Colorectal Cancer: a Retrospective Study in 121 Patients. *Int. J. Colorectal Dis.* 34 (4), 589–597. doi:10.1007/s00384-018-03223-9

Wang, P.-P., Liu, S.-H., Chen, C.-T., Lv, L., Li, D., Liu, Q.-Y., et al. (2020). Circulating Tumor Cells as a New Predictive and Prognostic Factor in Patients with Small Cell Lung Cancer. *J. Cancer* 11 (8), 2113–2122. doi:10.7150/jca.35308

Warkiani, M. E., Khoo, B. L., Wu, L., Tay, A. K. P., Bhagat, A. A. S., Han, J., et al. (2015). Ultra-fast, Label-free Isolation of Circulating Tumor Cells from Blood Using Spiral Microfluidics. *Nat. Protoc.* 11 (1), 134–148. doi:10.1038/nprot.2016.003

Weitz, J., Kienle, P., Lacroix, J., Willeke, F., Benner, A., Lehnert, T., et al. (1998). Dissemination of Tumor Cells in Patients Undergoing Surgery for Colorectal Cancer. *Clin. Cancer Res.* 4 (2), 343–348.

Wu, F., Zhu, J., Mao, Y., Li, X., Hu, B., and Zhang, D. (2017). Associations between the Epithelial-Mesenchymal Transition Phenotypes of Circulating Tumor Cells and the Clinicopathological Features of Patients with Colorectal Cancer. *Dis. Markers* 2017, 1–6. doi:10.1155/2017/9474532

Xie, W., Yin, T., Chen, Y.-L., Zhu, D.-M., Zan, M.-H., Chen, B., et al. (2019). Capture and "Self-Release" of Circulating Tumor Cells Using Metal-Organic Framework Materials. *Nanoscale* 11 (17), 8293–8303. doi:10.1039/c8nr09071h

Yang, C., Zou, K., Yuan, Z., Guo, T., and Xiong, B. (2018). Prognostic Value of Circulating Tumor Cells Detected with the CellSearch System in Patients with Gastric Cancer: Evidence from a Meta-Analysis. *OncoTargets Ther.* 11, 1013–1023. doi:10.2147/OTT.S154114

Yap, T. A., Lorente, D., Omlin, A., Olmos, D., and de Bono, J. S. (2014). Circulating Tumor Cells: a Multifunctional Biomarker. *Clin. Cancer Res.* 20 (10), 2553–2568. doi:10.1158/1078-0432.CCR-13-2664

Yousefi, M., Ghaffari, P., Nosrati, R., Dehghani, S., Salmaninejad, A., Abarghan, Y. J., et al. (2020). Prognostic and Therapeutic Significance of Circulating Tumor Cells in Patients with Lung Cancer. *Cell Oncol.* 43 (1), 31–49. doi:10.1007/s13402-019-00470-y

Yuan, S., Feng, L., Wang, K., Pang, J., Bosch, M., Lollar, C., et al. (2018). Stable Metal-Organic Frameworks: Design, Synthesis, and Applications. *Adv. Mater.* 30 (37), 1704303. doi:10.1002/adma.201704303

Zhang, L., Wang, J., Ren, X., Zhang, W., Zhang, T., Liu, X., et al. (2018). Internally Extended Growth of Core-Shell NH2-MIL-101(Al)@ZIF-8 Nanoflowers for the Simultaneous Detection and Removal of Cu(II). *J. Mater. Chem. A.* 6 (42), 21029–21038. doi:10.1039/c8ta07349j

Zhu, X., Li, B., Yang, J., Li, Y., Zhao, W., Shi, J., et al. (2015). Effective Adsorption and Enhanced Removal of Organophosphorus Pesticides from Aqueous Solution by Zr-Based MOFs of UiO-67. *ACS Appl. Mater. Inter.* 7 (1), 223–231. doi:10.1021/am5059074

Conflict of Interest: The authors declare that the research was conducted in the absence of any commercial or financial relationships that could be construed as a potential conflict of interest.

Publisher's Note: All claims expressed in this article are solely those of the authors and do not necessarily represent those of their affiliated organizations, or those of the publisher, the editors and the reviewers. Any product that may be evaluated in this article, or claim that may be made by its manufacturer, is not guaranteed or endorsed by the publisher.

frontiers in Bioengineering and Biotechnology

ORIGINAL RESEARCH
published: 08 March 2022
doi: 10.3389/fbioe.2021.763486

Janus Magnetic Nanoplatform for Magnetically Targeted and Protein/Hyperthermia Combination Therapies of Breast Cancer

Shuting Zuo[1], *Jing Wang*[1], *Xianquan An*[2] *and Yan Zhang*[1]*

[1]Department of Breast Surgery, The Second Hospital of Jilin University, Changchun, China, [2]Department of Anesthesiology, The Second Hospital of Jilin University, Changchun, China

Protein therapeutics have been considered a promising strategy for cancer treatment due to their highly specific bioactivity and few side effects. Unfortunately, the low physiological stability and poor membrane permeability of most protein drugs greatly limit their clinical application. Furthermore, single-modality protein therapeutics show insufficient efficacy. To address these issues, Janus magnetic mesoporous silica nanoparticles (Janus MSNNPs) were developed to preload ribonuclease A (RNaseA) to simultaneously realize the magnetically enhanced delivery of protein drugs and magnetic hyperthermia-enhanced protein therapy. Janus MSNNPs showed a high RNaseA loading ability and pH-responsive drug release behavior. Furthermore, an external magnetic field could remarkably enhance the therapeutic effect of RNaseA-loaded Janus MSNNPs due to the improved intracellular internalization of RNaseA. Importantly, Janus MSNNPs possessed an outstanding magnetic hyperthermia conversion efficiency, which could generate hyperthermia under an alternating magnetic field, effectively supplementing protein therapy by a combined effect. *In vitro* and *in vivo* experiments confirmed the high anticancer outcome and low side effects of this intriguing strategy for breast cancer based on Janus MSNNPs. Hence, Janus MSNNPs might be an effective and safe nanoplatform for magnetically combined protein therapy.

Keywords: combination therapies, Janus, breast cancer, magnetic targeting, nanocarriers

OPEN ACCESS

Edited by:
Wang Zheng,
Suzhou Institute of Nano-tech and Nano-bionics (CAS), China

Reviewed by:
Hang Zhou,
Harbin Medical University, China
Wen-Fei Dong,
Suzhou Institute of Biomedical Engineering and Technology (CAS), China

***Correspondence:**
Yan Zhang
zhangy01@jlu.edu.cn

Specialty section:
This article was submitted to Nanobiotechnology, a section of the journal Frontiers in Bioengineering and Biotechnology

Received: *24 August 2021*
Accepted: *16 September 2021*
Published: *08 March 2022*

Citation:
Zuo S, Wang J, An X and Zhang Y (2022) Janus Magnetic Nanoplatform for Magnetically Targeted and Protein/Hyperthermia Combination Therapies of Breast Cancer. Front. Bioeng. Biotechnol. 9:763486. doi: 10.3389/fbioe.2021.763486

INTRODUCTION

Breast cancer is the most frequently diagnosed life-threatening cancer in females and the second leading cause of cancer deaths among women. An estimated million cases of breast cancer are diagnosed worldwide every year (Waks and Winer, 2019; Mckinney et al., 2020). Of all breast cancers, ~10–20% are described as triple-negative. Triple-negative breast cancer (TNBC), which is negative for estrogen receptors, progesterone receptors and human epidermal growth factor receptor 2, is a highly malignant cancer that does not respond to hormonal therapy or specific therapy targeting HER2 receptors (Garrido-Castro et al., 2019; Yin et al., 2020). Surgery and chemotherapy are considered the standard therapies for breast cancer. Unfortunately, surgical resection only works for noninvasive TNBC, while most TNBC patients do not meet the criteria for surgery (Chang-Qing et al., 2020). Moreover, chemotherapy is restricted by severe side effects and multidrug resistance in a

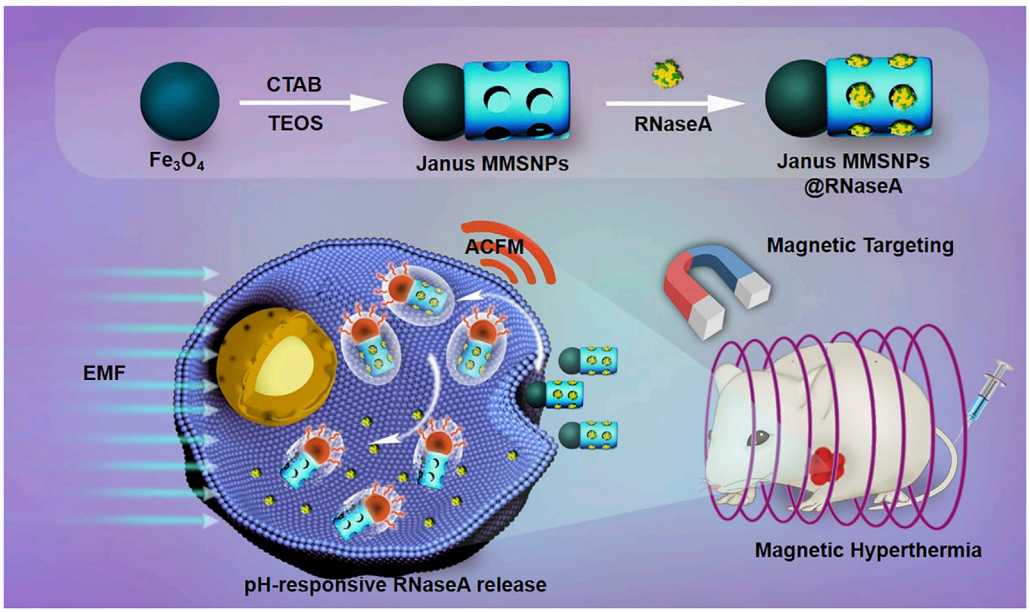

SCHEME 1 | Schematic illustration of the preparation of RNaseA-loaded Janus MMSNPs and their application for magnetically targeted and protein/hyperthermia combination therapies of breast cancer.

considerable number of TNBC patients (Pearce et al., 2017; Nedeljković and Damjanović, 2019). Thus, there is a pressing need to seek novel strategies for the efficient and safe treatment of TNBC.

Protein therapeutics, as a new mechanism for cancer therapy, have attracted great attention due to their highly specific bioactivity and few side effects (Kordalivand et al., 2018; Si et al., 2020). Unlike gene therapy, protein drugs can generate therapeutic efficacy by cell apoptosis activation, blockage of proliferation and antiangiogenesis without inducing permanent genetic alterations or adverse effects, thus holding great promise in the clinic, especially to treat chemotherapy-resistant cancers (Shao et al., 2018). Ribonuclease A (RNaseA), a relatively small protein with a size of 2.2 × 2.8 × 3.8 nm, has been applied as an alternative drug by virtue of its ability to catalyze the degradation of cellular RNA and subsequently inhibit protein production in the cytosol (Yu et al., 2017; Zhu et al., 2020). Compared with traditional chemotherapeutic drugs, RNaseA shows considerable advantages of highly specific bioactivity and avoids multidrug resistance. Although promising, the therapeutic efficacy of RNaseA is highly compromised by its low physiological stability, short half-life, and poor membrane permeability. Moreover, RNaseA alone is insufficient to control the progression of TNBC (Yu et al., 2017; Jia et al., 2019; Zhao et al., 2019). Consequently, developing a high-performance strategy for the protein therapy of TNBC is an urgent task facing the scientific community.

The combination of nanotechnology and biomedicine has allowed new approaches for cancer theranostics with high efficiency, specificity and personalization (Bjornmalm et al., 2017; Yue et al., 2018). The immobilization of proteins into nanoparticles has been shown to enhance the stability, activity and cellular internalization efficiency, leading to the development of multifunctional structures with synergistic effects as hybrid nanoplatforms (Iype et al., 2017; Xu et al., 2019). Among them, magnetic mesoporous silica nanoparticles (MMSNPs) provide good biocompatibility, high surface area and unique magnetic target properties, and thus they are considered ideal nanocarriers to achieve magnetically guided protein delivery since the cellular uptake and tumor accumulation of MMSNPs can be improved by using an external magnetic field (Chang et al., 2018). More importantly, M-MSNs can produce hyperthermia under an alternating current magnetic field (ACMF), termed magnetic hyperthermia therapy, a noninvasive treatment, which can effectively supplement the antitumor efficacy of RNaseA (Xing et al., 2018). Therefore, MMSNPs might be an excellent candidate for the protein therapy of TNBC. Nevertheless, the potential of magnetically enhanced RNaseA therapy by MMSNPs has not yet been explored.

Janus nanomaterials, named after the double-faced Roman mythology god, are compartmentalized particles with two sides of different chemical compositions, and they have gained considerable interest due to their noninterfering properties on anisotropic surfaces (Zhang et al., 2020; Shao et al., 2021). Janus metallic mesoporous silica nanocarriers have been demonstrated to have unique optical, magnetic, thermal, and electric properties in comparison to the conventional core-shell structures, thus showing a potentially synergistic and stimuli-responsive manner in combined diagnosis and therapy of cancer (Hernández-Montoto et al., 2019; Zhang et al., 2019; Xing et al., 2020). In this work, Janus MMSNPs were developed using a sol-gel method and functionalized with carboxyl groups for RNaseA loading and

pH-responsive release. Janus MMSNPs showed a high RNaseA loading efficiency, magnetic response performance and magnetic hyperthermia conversion efficiency. Then, we investigated their performance in magnetically targeted and hyperthermia-enhanced suicide protein therapy *in vitro* and *in vivo*. In light of the good therapeutic outcome and biosafety, Janus MMSNPs might be a promising platform for efficient protein therapy of TNBC (**Scheme 1**).

METHODS

Preparation of Janus MMSNPs

Polyacrylic acid (PAA)-stabilized Fe_3O_4 NPs were fabricated using a high-temperature hydrolysis reaction. Polyacrylic acid (PAA)-stabilized Fe_3O_4 NPs were fabricated using a high-temperature hydrolysis reaction. Briefly, 0.13 mg $FeCl_3$ was dissolved into the 34 ml of diethylene glycol under the stirring at 30°C. At the same time, 2.0 g NaOH was dissolved into the 20 ml of diethylene glycol with stirring at 120°C. After 1 h, the diethylene glycol solution of $FeCl_3$ was heated to 265°C for 30 min under the protection of nitrogen gas. Then, 3.4 ml diethylene glycol solution of NaOH was added into the diethylene glycol solution of $FeCl_3$ and reacted at 265°C for 1 h. Then, the polyacrylic acid (PAA)-stabilized Fe_3O_4 NPs were obtained after washed with ethyl alcohol and water and centrifugation. Then, Janus MMSNPs were fabricated by a modified sol-gel method. Briefly, 1 ml of Fe_3O_4 NP solution (8.4 mg/ml) was mixed with 10 ml of CTAB solution (5 mg/ml) under ultrasonication for 30 min. Then, 40 μL of tetraethyl orthosilicate (TEOS) was added dropwise into the mixture, followed by 0.5 ml of ammonium hydroxide (14.8 M). After 20 min of stirring at 40°C, the products were collected by magnetic separation using a magnet and washed with deionized water and ethyl alcohol three times. To form a mesoporous structure, the prepared products were dispersed in a NH_4NO_3 solution and refluxed for 12 h to extract CTAB. For RNaseA loading and PEG conjugation, carboxylate groups were introduced on the surface of Janus MMSNPs. First, Janus MMSNPs were modified with -NH_2 groups using ammonium persulfate (APS) through postgrafting according to a previous report. Then, 20 mg of Janus MMSNPs was dispersed in a DMF solution of succinic anhydride (100 ml, 2 wt%) and stirred overnight at the room temperature. The obtained Janus MMSNPs with -COOH functionalization were collected and washed. Finally, PEG was conjugated onto the Janus MMSNPs through an EDC/NHS reaction. Briefly, the Janus MMSNP suspension was mixed with an EDC/NHS aqueous solution and sonicated for 30 min. Then, PEG was added into the mixture with stirring for 24 h. Finally, PEG-grafted Janus MMSNPs were collected and stored at 4°C for further use.

RNaseA Loading and Release

20 mg of RNaseA was added into 10 ml of deionized water to prepare a protein stock solution. Then, 20 ml of Janus MMSNPs (2 mg/ml) was mixed with 10 ml of the prepared protein stock solution, and the mixture was stirred at 4°C for 24 h. After centrifugation, the loading amount of RNaseA was determined by detecting the absorbance of the supernatant at 280 nm and calculated using the following equation: Loading content (%) = Mass of drug in NPs/Mass of drug-loaded NPs. For the RNaseA release test, 5 mg of RNaseA-loaded Janus MMSNPs was encapsulated into a dialysis bag and placed in 10 ml of PBS solutions with different pH values (pH = 5.5 and 7.4). Then, the amount of RNaseA released was detected at predetermined time points by the UV-vis spectrometry.

Intracellular Internalization and Drug Release

MCF-7 cells were obtained from ATCC and cultured at 37°C in RPMI 1640 medium with 10% fetal bovine serum penicillin and streptomycin. MCF-7 cells were seeded in a 6-well plate and maintained overnight. To detect the cellular uptake of Janus MMSNPs, FITC-labeled Janus MMSNPs were incubated with MCF-7 cells at a concentration of 12.5 μg/ml for 6 h. For the EMF-treated groups, small NdFeB permanent magnets (surface magnetic field of 0.2 T) were placed on the bottom of the 6-well plate for 30 min. Then, the cells were stained with Hoechst 33258 and LysoTracker Red DND-99 (Invitrogen) for observation by CLSM. To quantify the intracellular internalization of Janus MMSNPs, the cells were washed, trypsinized and resuspended after the same treatment with Janus MMSNPs and measured by FACS. To investigate the intracellular release of RNaseA, RNaseA was labeled with Cy5.5 and preloaded into Janus MMSNPs. Then, RNaseA-loaded Janus MMSNPs were incubated with MCF-7 cells for 6 h and detected by CLSM and FACS using the same protocol.

In vitro Therapeutic Effect of Janus MMSNPs@RNaseA

MCF-7 cells were seeded in a 96-well plate and cultured overnight. Then, these cells were treated with various concentrations of Janus MMSNPs, RNaseA and Janus MMSNPs@RNaseA for 24 h with or without 30 min of external magnetic field (EMF) exposure. For the EMF treatment groups, a small NdFeB permanent magnets (0.2T) were placed under the 96-well plates during the incubation of 0.5 h. Notably, the amount of RNaseA in Janus MMSNPs@RNaseA was equal to that of free RNaseA in the same parallel groups. Then, cell viability was assessed using WST assays, and untreated cells were used as the control group.

To investigate the magnetic hyperthermia conversion efficacy of Janus MMSNPs, cell culture medium containing various concentrations of Janus MMSNPs@RNaseA was placed and exposed to an alternating magnetic field (ACFM, 325 Oe, 262 kHz), and the temperature change was monitored at predetermined time points. To investigate the magnetic hyperthermia therapy of Janus MMSNPs, MCF-7 cells were treated with various concentrations of Janus MMSNPs with or without an ACFM (325 Oe, 262 kHz) in the absence or presence of an EMF. For the ACFM treatment groups, the cells were exposed in

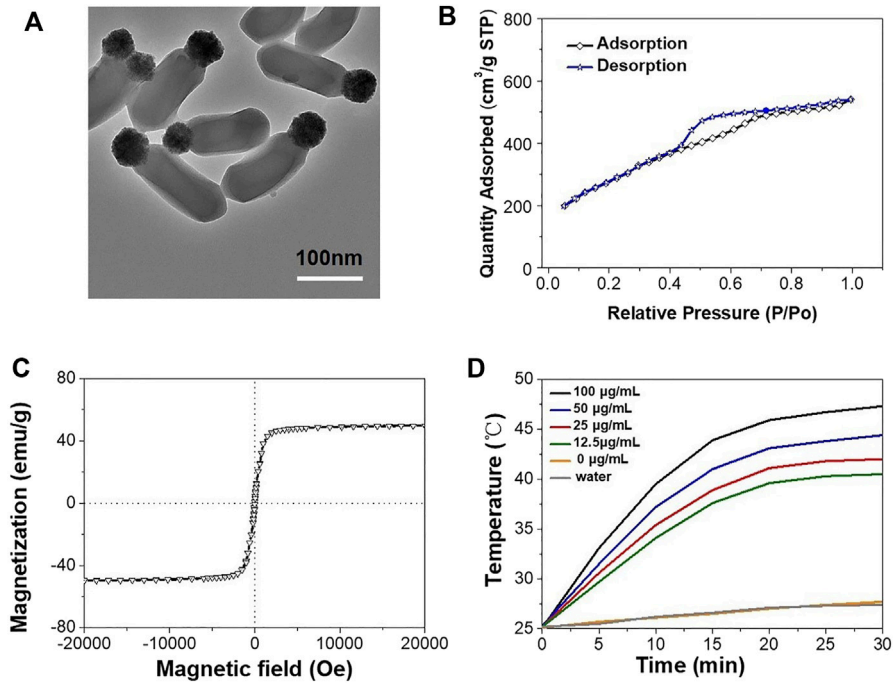

FIGURE 1 | Characterization of Janus MMSNPs. **(A)** TEM images of Janus MMSNPs, scale bar = 100 nm. **(B)** N_2 adsorption-desorption isotherms of Janus MMSNPs. **(C)** Magnetization curve of Janus MMSNPs. **(D)** Temperature-time curves of various concentration of Janus MMSNPs solutions.

an ACFM for 30 min during the incubation of 6 h. After 24 h of incubation, the cell viability was measured using the same method.

In vivo Combined Therapies and Biosafety

All animal experiments were approved by the Ethics Committee for the Use of Experimental Animals of Jilin University. To establish MCF-7 tumor-bearing nude mice, 5×10^6 MCF-7 cells were orthotopically injected into the mammary fat pads of female nude mice weighing approximately 20 g. When the volume of these tumors grew to approximately 80 mm^3, all of the mice were separated into six groups and intravenously administered PBS, free RNaseA (5 mg/kg), Janus MMSNPs (20 mg/kg) and Janus MMSNPs@RNaseA (25 mg/kg) every 3 days. For the EMF-treated groups, a NdFeB permanent magnet (surface magnetic field of 0.5 T) was placed on the skin over the tumor site for 1 h at 1 h after administration. For the ACMF-treated groups, the mice were placed under an alternating magnetic field (325 Oe, 262 kHz) for 1 h at 24 h after administration. The tumors and body weight in each group were recorded every 3 days. Tumor volumes were caculated using the equation: tumor volume = the length of tumor × the width of tumor × the width of tumor $^2 \times 0.52$. All the mice were sacrificed at the 23rd days. The tumors were harvested and weighed. The liver, spleen, kidneys, lungs and heart were harvested, sliced and stained with hematoxylin-eosin. The serum was separated from the collected blood, and the serum biochemical indices, including aminotransferase (AST), phosphocreatine kinase (CK), alanine aminotransferase (ALT), total bilirubin (TBIL), alkaline phosphatase (ALP), blood urea nitrogen (BUN), creatinine (CR), cholesterol (TC) and triglyceride (TG) were assessed using the manufacturer's protocol.

RESULTS AND DISCUSSION

Janus MMSNPs were constructed using a sol-gel method, in which Fe_3O_4 nanoparticles were used as a substrate, TEOS was used as a silica source, and CTAB was used as a template. Transmission electron microscopy (TEM) in **Figure 1A** clearly revealed that Janus MMSNPs showed a uniform morphology and good monodispersity, which consisted of a Fe_3O_4 head with a size of approximately 50 nm and a silica body with dimensions of approximately 150 nm. Subsequently, Janus MMSNPs were modified with carboxyl groups and conjugated with polyethylene glycol (PEG) amine. After PEG decoration, Janus MMSNPs showed long-term stability in cell medium for 5 days of storage (Supplementary Figure S1). Then, we investigated the magnetic properties of these Janus MMSNPs. As shown in the **Figure 1C**, Janus MMSNPs possess good magnetic properties with a saturation magnetization value of 49 $emu \cdot g^{-1}$. We next investigated the mesoporous properties of Janus MMSNs. The N_2 adsorption-desorption isotherm curve in **Figure 1B** indicated that Janus MMSNPs have a large pore volume (0.57 cm^3/g), a high BET surface area (578.2 m^2/g) and a uniform pore diameter (4.2 nm). The excellent mesoporous properties of Janus MMSNs suggested a high drug loading efficiency. To investigate the magnetic hyperthermia conversion ability of Janus MMSNPs,

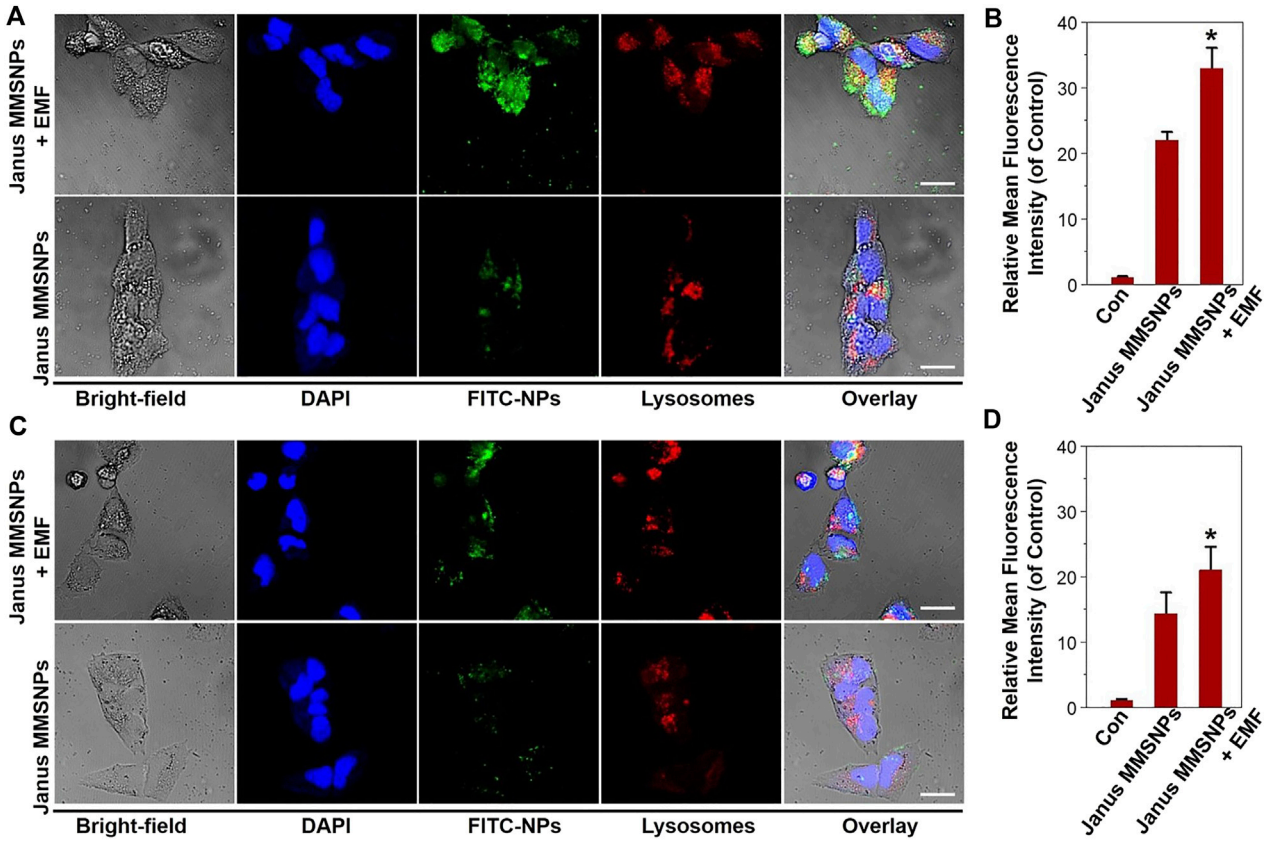

FIGURE 2 | Cellular uptake of Janus MMSNPs. CLSM images of MCF-7 cells **(A)** and MCF 10A cells **(C)** incubated with Janus MMSNPs for 6 h with or without an EMF, scale bars = 10 μm. Quantitative FACS analysis of the endocytosis of Janus MMSNPs in MCF-7 cells **(B)** and MCF 10A cells **(D)** after 6 h of incubation with or without an EMF. Mean values ± SD. *$p < 0.05$ vs. the Janus MMSNPs group, $n = 3$.

we measured the temperature change of cell culture media containing various concentrations of Janus MMSNPs under an alternating current magnetic field (ACMF). As shown in **Figure 1D**, the temperature of pure water and cell culture medium without Janus MMSNPs only increased by 6°C under an ACMF, whereas the temperature increase in Janus MMSNP solutions was in a time- and concentration-dependent manner with the exposure to ACMF. At a Janus MMSNP concentration of 50 μg/ml after less than 20 min of exposure to ACMF, the temperature of the cell medium rose to 43°C, a crucial temperature to induce cancer cell death.

Numerous studies have demonstrated that an external magnetic field (EMF) could improve the cellular uptake of magnetic nanocarriers and direct their transportation to tumor sites, which was also named as "magnetic targeting". Thus, we investigated the cellular internalization of Janus MMSNPs under a magnetic field stimulus. As shown in **Figures 2A, C**, the colocalization of FITC-labeled Janus MMSNPs with endolysosomes was observed after 6 h of incubation with MCF-7 cells and MCF 10A cells with or without an EMF by CLSM, indicating that the Janus MMSNPs could enter into the cells and internalize in the endolysosomes. As expected, higher fluorescence signals were found in the magnetic field treated groups than that those of EMF-untreated groups, which was in line with the FACS results (**Figures 2B, D**), confirming the utility of the EMF to promote the cellular internalization of Janus MMSNPs. Notably, more Janus MMSNPs distributed in MCF-7 cells compared with MCF 10A cells at the same EMF-treated condition, indicated that Janus MMSNP could induce a higher cellular uptake in cancer cells than normal cells.

To explore the potential for protein delivery, the carboxyl-functionalized Janus MMSNPs were loaded with Ribonuclease A (RNaseA), a cytotoxic protein drug commonly used in the breast cancer therapy. The zeta potential change indicated that RNaseA was successfully loaded into the Janus MMSNPs (Supplementary Figure S3). As determined by UV-visible spectrophotometry, the drug loading content of RNaseA was as high as 250.6 μg mg^{-1}. To investigate the drug release behavior, the cumulative release of RNaseA from RNaseA-loaded Janus MMSNs (Janus MMSNs@RNaseA) was measured in PBS solution at different pH values (5.5 and 7.4). As shown in **Figure 3A**, less than 20% of RNaseA was released from Janus MMSNs@RNaseA after 96 h of dialysis at a pH of 7.4, whereas a rapid release of RNaseA occurred at a pH of 5.5, and the cumulative release reached 66.1% at 96 h. The pH-

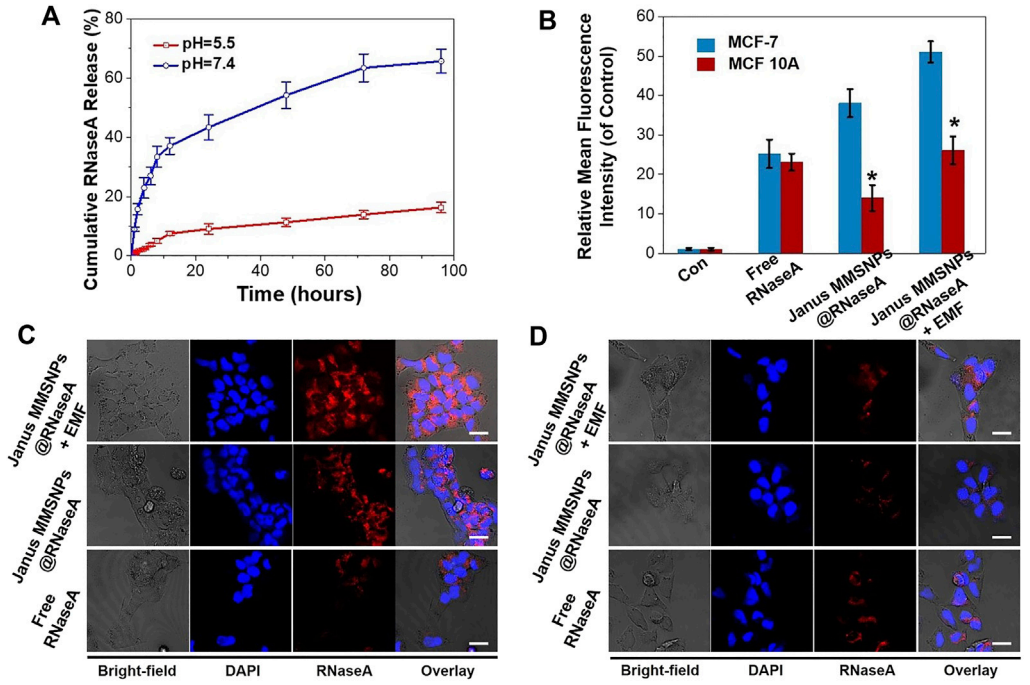

FIGURE 3 | Drug release behavior of Janus MMSNPs@RNaseA. **(A)** Drug-release behavior of Janus MMSNPs@RNaseA at different pH value. **(B)** Quantitative FACS analysis of the intracellular distribution of RNaseA in free RNaseA-, Janus MMSNPs@RNaseA -, or Janus MMSNPs@RNaseA plus an EMF-treated MCF-7 or MCF 10A cells for 6 h. Mean values ± SD. *$p < 0.05$ vs. the MCF-7 cell group, $n = 3$. **(C)** CLSM images of MCF-7 cells after treated with free RNaseA or Janus MMSNPs@RNaseA with or without an EMF for 6 h **(D)** CLSM images of MCF cells after treated with free RNaseA or Janus MMSNPs@RNaseA with or without an EMF for 6 h. Scale bar = 10 μm.

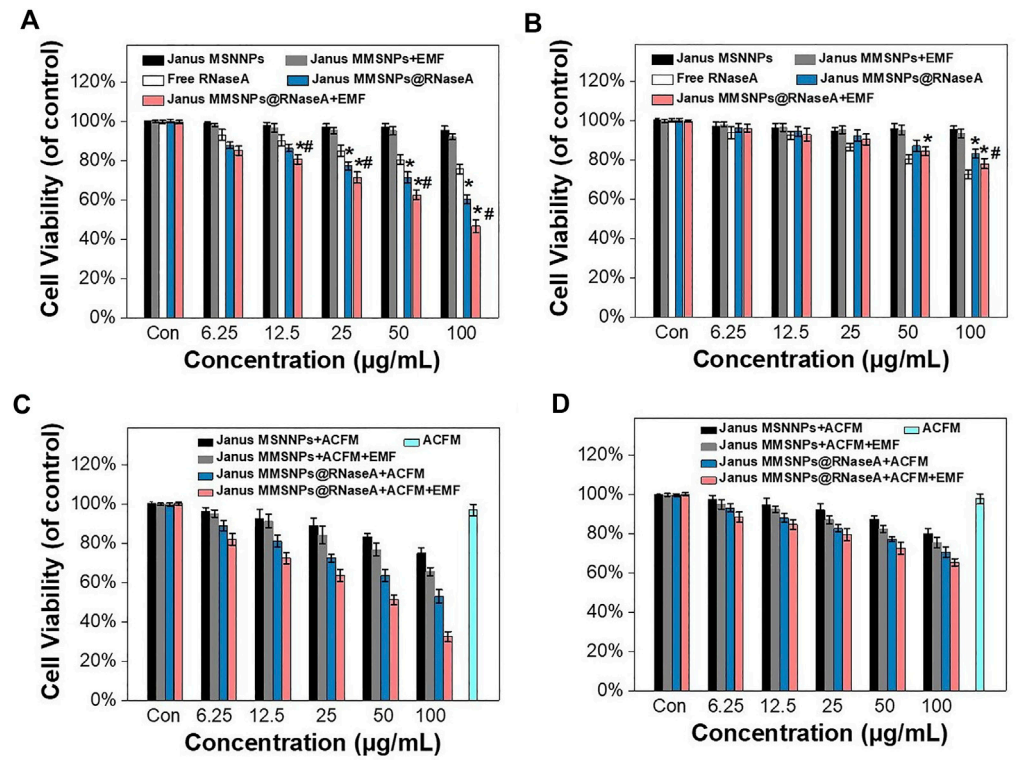

FIGURE 4 | Combination therapies of Janus MMSNPs@RNaseA *in vitro*. Cell viability of **(A)** MCF-7 and **(B)** MCF 10A after incubation with free RNaseA, Janus M-MSNs or Janus MMSNPs@RNaseA with or without an EMF for 24 h *$p < 0.05$ vs. free RNaseA group; #$p < 0.05$ vs. Janus MMSNPs@RNaseA group. The cytotoxicity of Janus MMSNPs@RNaseA in the absence or presence of an ACMF with or without EMF towards **(C)** MCF-7 cells and **(D)** MCF 10A for 24 h. Mean values ± SD, $n = 4$.

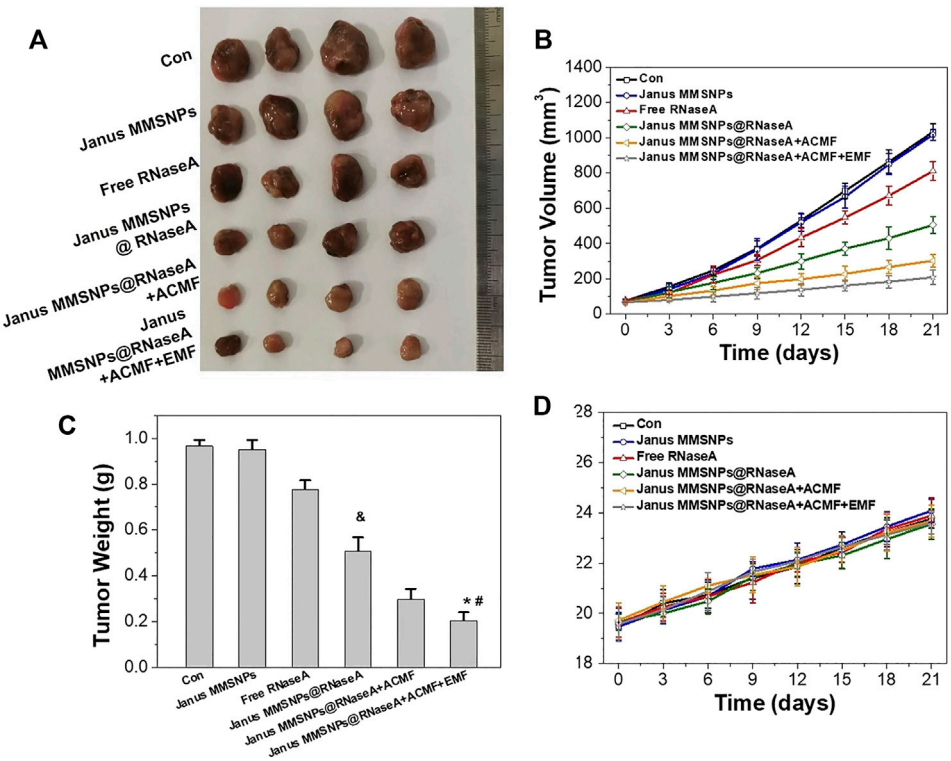

FIGURE 5 | *In vivo* combined protein/magnetic hyperthermia therapes of Janus MMSNPs@RNaseA. **(A)** Tumor photographs. **(B)** Tumor growth curves. **(C)** Tumor weights Mean values ± SD, $n = 4$. $^{*}p < 0.05$ vs. the Janus MMSNPs@RNaseA, $^{\#}p < 0.05$ vs. Janus MMSNPs@RNaseA plus ACFM, and $^{\&}p < 0.05$ vs. the free RNaseA groups. **(D)** Body weight change.

responsive drug release phenomenon could be explained by RNaseA becoming more water soluble at low pH because of the protonation of amine groups. Since endolysosomes and the local environment of tumor tissues are acidic, pH-responsive drug release behavior can improve the anticancer effect and reduce the side effects in normal tissues. To investigate the intracellular drug release, RNaseA was labeled with Cy 5.5, and the red fluorescence signals of RNaseA were detected in MCF-7 cells and MCF-10A cells after 6 h of incubation using CLSM and FACS. As shown in **Figures 3B–D**, more green fluorescent signals were detected in MCF-7 cells after treated with Janus MMSNPs@RNaseA than those treated with free RNaseA, indicating Janus MMSNPs are effective carriers to improve the cellular internalization of RNaseA in cancer cells. On the contrary, Janus MMSNPs@RNaseA groups showed a lower intracellular RNaseA distribution than free RNaseA, which could be attributed to the weak cellular internalization of Janus MMSNPs and the low RNaseA release in normal cells. Additionally, an external magnetic field obviously improved the RNaseA accumulation in both MCF-7 cells and MCF 10A cells after treated with Janus MMSNPs@RNaseA. Other studies have demonstrated that in comparison to the core-shell nanoparticles, Janus magnetic nanoparticles have a higher cellular uptake efficiency due to the rod-like morphology and stronger magnetic responsive property because of the non-interfering feature (Shao et al., 2016). The magnetically-enhanced performance indicated that Janus MMSNPs might be a superior nanoplatform for protein therapies of cancer.

Endocytosis and drug distribution play important roles in the therapeutic effect. The WST assay was subsequently performed to evaluate the cytotoxicity of Janus MMSNPs@RNaseA with the aim of an EMF. As shown in **Figures 4A,B**, Janus MMSNPs showed a negligible cytotoxicity towards MCF-7 cells or MCF 10A cells even at a concentration of 100 μg/ml with or without an EMF, indicating that Janus MMSNPs have a good biocompatibility. The anticancer effect of Janus MMSNPs@RNaseA and free RNaseA was concentration-dependent in MCF-7 cells. Janus MMSNPs@RNaseA showed a higher killing effect towards MCF-7 cells than free RNaseA when the amount of RNaseA was equal, whereas Janus MMSNPs@RNaseA induced lower death of MCF 10A cells than free RNaseA, which was in line with the results of intracellular RNaseA accumulation. These results indicated the anticancer efficacy of Janus MMSNPs@RNaseA originated from the selective endocytosis and pH-responsive drug release in cancer cells rather than in normal cells. Notably, the applied EMF remarkably improve the therapeutic efficiency of Janus MMSNPs@RNaseA, which was due to the magnetically enhanced endocytosis. Given the ability of Janus MMSNPs to generate magnetic hyperthermia, we investigated the therapeutic effect of magnetic hyperthermia on

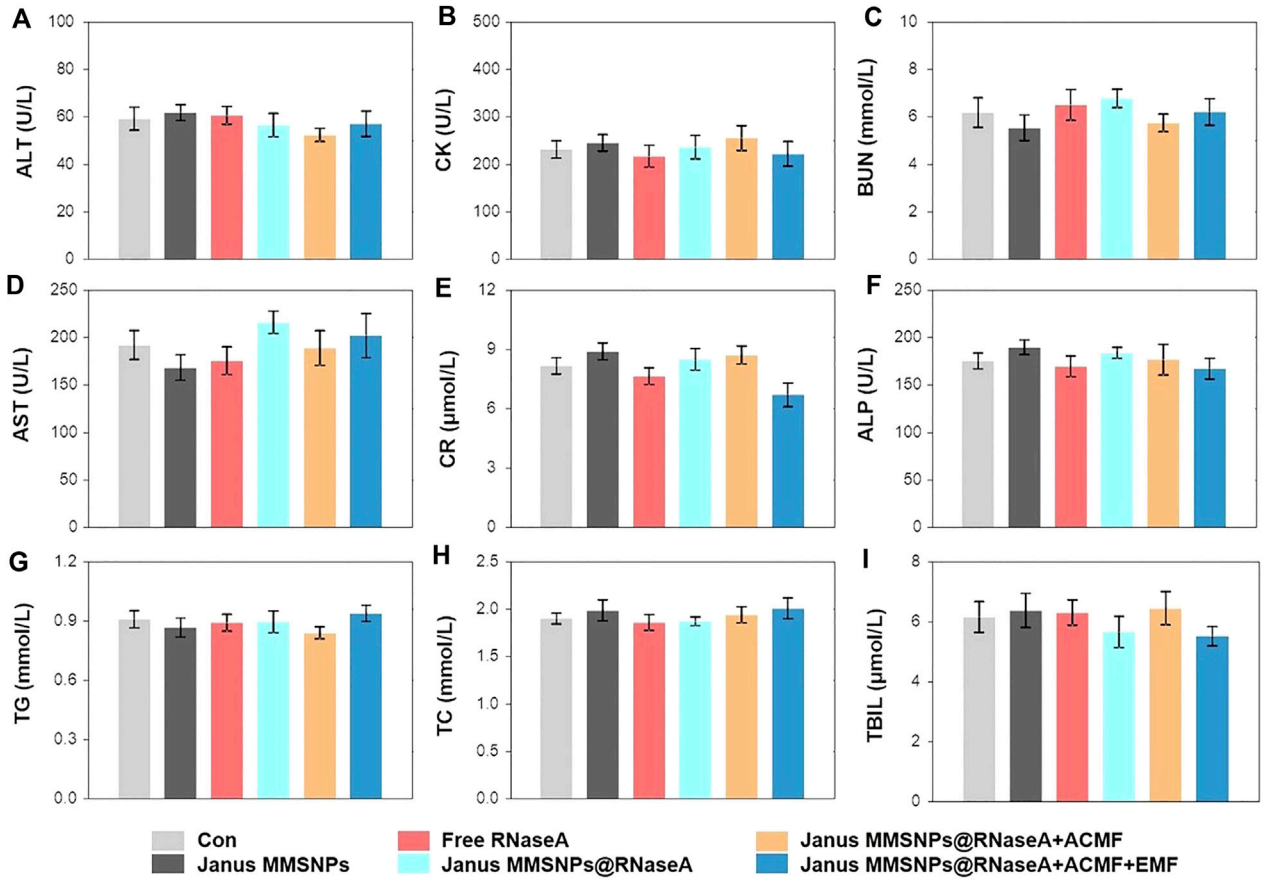

FIGURE 6 | Serum biochemistry indicators assessment. **(A)** Alanine aminotransferase (ALT). **(B)** Phosphocreatine kinase (CK). **(C)** Blood urea nitrogen (BUN). **(D)** Aspartate aminotransferase (AST). **(E)** Creatinine (CR). **(F)** Alkaline phosphatase (ALP). **(G)** Triglyceride (TG). **(H)** Cholesterol (TC). **(I)** Total bilirubin (TBIL) of MCF-7 tumor-bearing nude mice. Mean values ± SD, n = 4.

Janus MMSNP-treated MCF-7 cells. As shown in **Figures 4C,D**, the cell viability of MCF-7 cells and MCF 10 A cells was not decreased only after exposure to ACMF in the absence of Janus MMSNPs, indicating the biosafety of the applied ACMF. As expected, Janus MMSNPs plus ACMF showed a concentration-dependent anticancer effect, and the therapeutic effect of magnetic hyperthermia could be improved by an EMF due to magnetically enhanced endocytosis. We subsequently explored the combined effect of magnetic hyperthermia therapy with protein therapy. The **Figures 4C,D** revealed that Janus MMSNPs@RNaseA plus ACMF could induce more deaths of MCF-7 cells than single Janus MMSNPs@RNaseA or Janus MMSNPs plus ACMF. Additionally, Janus MMSNPs@RNaseA plus ACMF with EMF showed the best anticancer effect among all the treatment groups. These results indicated that both ACMF and EMF could improve the outcome of protein therapy and that the combination of these two stimuli could result in the best therapeutic efficacy.

After confirming the Janus MMSNPs@RNaseA-based combination therapies *in vitro*, we further investigated magnetically enhanced protein therapy *in vivo*. MCF-7 tumor-bearing nude mice were established and randomly divided into six groups. As shown in **Figures 5A–C**, tumors in the Janus MMSNP-treated groups grew similarly to those in the control groups, indicating that Janus MMSNPs have no inhibitory effect on tumor growth. Janus MMSNPs@RNaseA showed delayed growth in the relative tumor volumes and tumor weights compared with the control groups or the free RNaseA groups. Additionally, the inhibitory rate of tumor growth was remarkably higher in the Janus MMSNPs@RNaseA plus ACMF groups than in the Janus MMSNPs@RNaseA groups, and Janus MMSNPs@RNaseA plus ACMF with EMF showed the highest therapeutic efficacy among all of the treatment groups, indicating the magnetically enhanced combination therapy based on our Janus MMSNPs@RNaseA.

Encouraged by the outstanding therapeutic efficacy, we evaluated the systemic toxicity of the combination therapies. As shown in **Figure 5D** and **Figure 6**, none of the mice experienced weight loss, and no observable changes occurred in serum biochemical indices, including aspartate aminotransferase (AST), phosphocreatine kinase (CK), alkaline phosphatase (ALP), alanine aminotransferase (ALT), blood urea nitrogen (BUN), creatinine (CR), total bilirubin (TBIL), cholesterol (TC) and triglyceride (TG), after being subjected to a full course of any treatments. Furthermore,

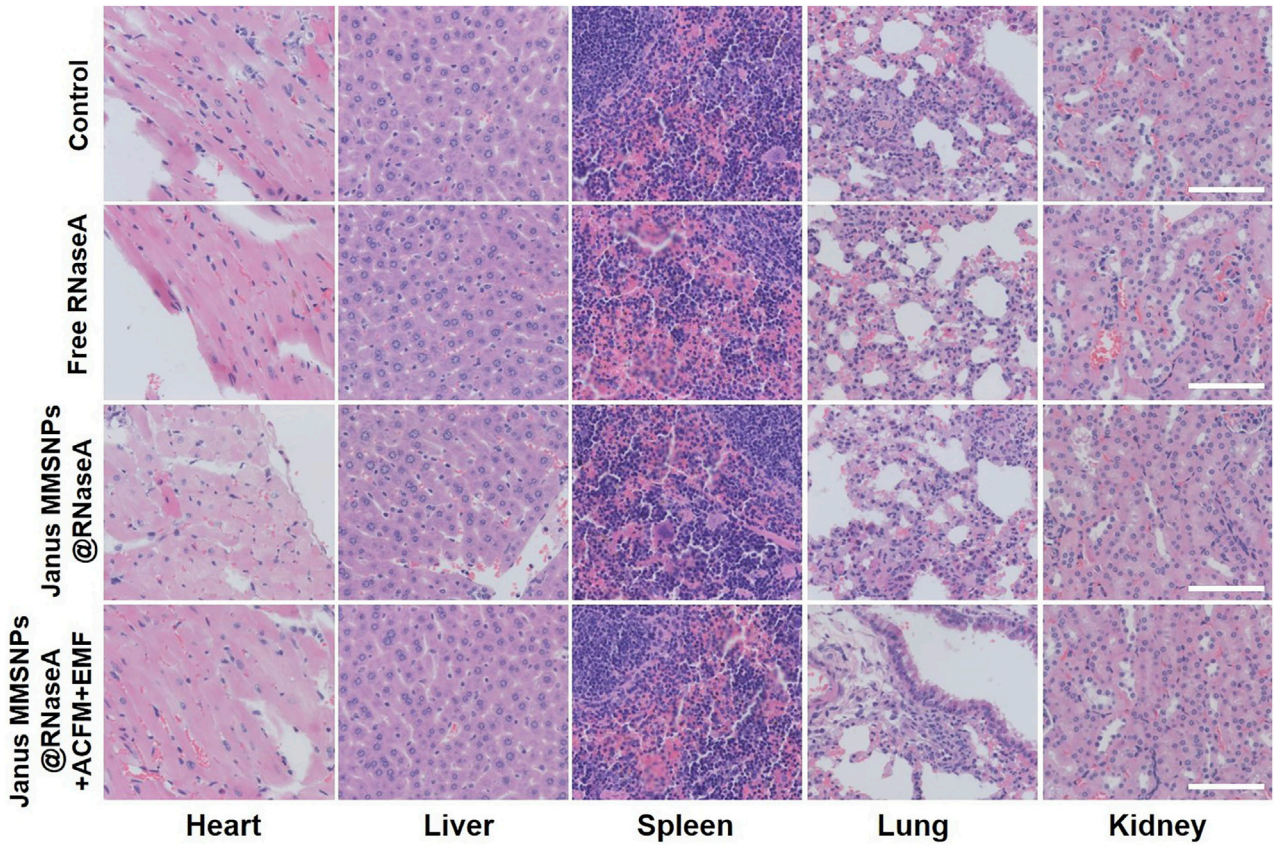

FIGURE 7 | Effect of protein/hyperthermia combination therapies on the histopathology of heart, liver, spleen, lung and liver from MCF-7 tumor bearing nude mice. Scale bar = 100 μm.

hematoxylin-eosin staining images of the heart, liver, spleen, lungs and kidneys in **Figure 7** indicated a normal physiology of all of the mouse organs after receiving any treatment. Collectively, consistent with our *in vitro* results, Janus MMSNPs@RNaseA exposed to an EMF displayed a magnetically enhanced protein therapeutic outcome *in vivo* with negligible side effects.

CONCLUSION

In summary, Janus MMSNPs were fabricated to preload RNaseA for realizing magnetically enhanced protein therapy of breast cancer. The prepared Janus MMSNPs showed a high RNaseA loading efficiency, pH-responsive protein release property and improved protein delivery with the help of an external magnetic field. Importantly, the therapeutic effect of Janus MMSNPs could be promoted by magnetically enhanced tumor accumulation and their combination with magnetic hyperthermia therapy. Given their good magnetic targeting abilities and the remarkable combined effect of magnetic hyperthermia therapy with protein therapy, Janus MMSNPs might be a potentially superior candidate for the protein therapy of breast cancer.

DATA AVAILABILITY STATEMENT

The original contributions presented in the study are included in the article/Supplementary Material, further inquiries can be directed to the corresponding author.

ETHICS STATEMENT

The animal study was reviewed and approved by the Ethics Committee for the Use of Experimental Animals of Jilin University.

AUTHOR CONTRIBUTIONS

SZ made substantial contributions to conception and design as well as the experimental section. JW provide purely technical help. XA contributes acquisition of data and generous contribution on the culture cells. YZ did great help in revising this manuscript critically for important intellectual content and final approval of the version to be published.

FUNDING

This study was supported by Scientific Development Program of Jilin Province (20180201054YY), Finance Department Program of Jilin Province (2020SCZT028).

SUPPLEMENTARY MATERIAL

The Supplementary Material for this article can be found online at: https://www.frontiersin.org/articles/10.3389/fbioe.2021.763486/full#supplementary-material

REFERENCES

Björnmalm, M., Thurecht, K. J., Michael, M., Scott, A. M., and Caruso, F. (2017). Bridging Bio-Nano Science and Cancer Nanomedicine. *ACS nano* 11, 9594–9613. doi:10.1021/acsnano.7b04855

Chang, Z.-M., Wang, Z., Shao, D., Yue, J., Lu, M.-M., Li, L., et al. (2018). Fluorescent-magnetic Janus Nanorods for Selective Capture and Rapid Identification of Foodborne Bacteria. *Sensors Actuators B: Chem.* 260, 1004–1011. doi:10.1016/j.snb.2018.01.123

Chang-Qing, Y., Jie, L., Shi-Qi, Z., Kun, Z., Zi-Qian, G., Ran, X., et al. (2020). Recent Treatment Progress of Triple Negative Breast Cancer. *Prog. Biophys. Mol. Biol.* 151, 40–53. doi:10.1016/j.pbiomolbio.2019.11.007

Garrido-Castro, A. C., Lin, N. U., and Polyak, K. (2019). Insights into Molecular Classifications of Triple-Negative Breast Cancer: Improving Patient Selection for Treatment. *Cancer Discov.* 9, 176–198. doi:10.1158/2159-8290.cd-18-1177

Hernández-Montoto, A., Llopis-Lorente, A., Gorbe, M., Terrés-Haro, J. M., Cao Milán, R., Díaz De Greñu-Puertas, B., et al. (2019). Janus Gold Nanostars-Mesoporous Silica Nanoparticles for NIR-Light-Triggered Drug Delivery. *Chemistry-A Eur. J.* 25, 8471–8478. doi:10.1002/chem.201900750

Iype, T., Thomas, J., Mohan, S., Johnson, K. K., George, L. E., Ambattu, L. A., et al. (2017). A Novel Method for Immobilization of Proteins via Entrapment of Magnetic Nanoparticles through Epoxy Cross-Linking. *Anal. Biochem.* 519, 42–50. doi:10.1016/j.ab.2016.12.007

Jia, J., Zhang, S., Wen, K., and Li, Q. (2019). Nano-scaled Zeolitic Imidazole Framework-8 as an Efficient Carrier for the Intracellular Delivery of RNase A in Cancer Treatment. *Int. J. Nanomedicine* 14, 9971–9981. doi:10.2147/ijn.s210107

Kordalivand, N., Li, D., Beztsinna, N., Sastre Torano, J., Mastrobattista, E., Van Nostrum, C. F., et al. (2018). Polyethyleneimine Coated Nanogels for the Intracellular Delivery of RNase A for Cancer Therapy. *Chem. Eng. J.* 340, 32–41. doi:10.1016/j.cej.2017.12.071

Mckinney, S. M., Sieniek, M., Godbole, V., Godwin, J., Antropova, N., Ashrafian, H., et al. (2020). International Evaluation of an AI System for Breast Cancer Screening. *Nature* 577, 89–94. doi:10.1038/s41586-019-1799-6

Nedeljković, M., and Damjanović, A. (2019). Mechanisms of Chemotherapy Resistance in Triple-Negative Breast Cancer—How We Can Rise to the challenge. *Cells* 8, 957. doi:10.3390/cells8090957

Pearce, A., Haas, M., Viney, R., Pearson, S.-A., Haywood, P., Brown, C., et al. (2017). Incidence and Severity of Self-Reported Chemotherapy Side Effects in Routine Care: A Prospective Cohort Study. *PloS one* 12, e0184360. doi:10.1371/journal.pone.0184360

Shao, D., Li, J., Zheng, X., Pan, Y., Wang, Z., Zhang, M., et al. (2016). Janus "Nano-Bullets" for Magnetic Targeting Liver Cancer Chemotherapy. *Biomaterials* 100, 118–133. doi:10.1016/j.biomaterials.2016.05.030

Shao, D., Li, M., Wang, Z., Zheng, X., Lao, Y.-H., Chang, Z., et al. (2018). Bioinspired Diselenide-Bridged Mesoporous Silica Nanoparticles for Dual-Responsive Protein Delivery. *Adv. Mater.* 30, 1801198. doi:10.1002/adma.201801198

Shao, D., Wang, Z., Chang, Z., Chen, L., Dong, W.-F., and Leong, K. W. (2021). Janus Metallic Mesoporous Silica Nanoparticles: Unique Structures for Cancer Theranostics. *Curr. Opin. Biomed. Eng.* 19, 100294. doi:10.1016/j.cobme.2021.100294

Si, X., Ma, S., Xu, Y., Zhang, D., Shen, N., Yu, H., et al. (2020). Hypoxia-sensitive Supramolecular Nanogels for the Cytosolic Delivery of Ribonuclease A as a Breast Cancer Therapeutic. *J. Controlled Release* 320, 83–95. doi:10.1016/j.jconrel.2020.01.021

Waks, A. G., and Winer, E. P. (2019). Breast Cancer Treatment. *Jama* 321, 288–300. doi:10.1001/jama.2018.19323

Xing, H., Wang, Z., Shao, D., Chang, Z., Ge, M., Li, L., et al. (2018). Janus Nanocarriers for Magnetically Targeted and Hyperthermia-Enhanced Curcumin Therapy of Liver Cancer. *RSC Adv.* 8, 30448–30454. doi:10.1039/c8ra05694c

Xing, Y., Zhou, Y., Zhang, Y., Zhang, C., Deng, X., Dong, C., et al. (2020). Facile Fabrication Route of Janus Gold-Mesoporous Silica Nanocarriers with Dual-Drug Delivery for Tumor Therapy. *ACS Biomater. Sci. Eng.* 6, 1573–1581. doi:10.1021/acsbiomaterials.0c00042

Xu, C., Lei, C., and Yu, C. (2019). Mesoporous Silica Nanoparticles for Protein protection and Delivery. *Front. Chem.* 7, 290. doi:10.3389/fchem.2019.00290

Yin, L., Duan, J. J., Bian, X. W., and Yu, S. C. (2020). Triple-negative Breast Cancer Molecular Subtyping and Treatment Progress. *Breast Cancer Res.* 22, 61–13. doi:10.1186/s13058-020-01296-5

Yu, M., Gu, Z., Ottewell, T., and Yu, C. (2017). Silica-based Nanoparticles for Therapeutic Protein Delivery. *J. Mater. Chem. B.* 5, 3241–3252. doi:10.1039/c7tb00244k

Yue, J., Wang, Z., Shao, D., Chang, Z., Hu, R., Li, L., et al. (2018). Cancer Cell Membrane-Modified Biodegradable Mesoporous Silica Nanocarriers for Berberine Therapy of Liver Cancer. *RSC Adv.* 8, 40288–40297. doi:10.1039/c8ra07574c

Zhang, F., Jia, Y., Zheng, X., Shao, D., Zhao, Y., Wang, Z., et al. (2019). Janus Nanocarrier-Based Co-delivery of Doxorubicin and Berberine Weakens Chemotherapy-Exacerbated Hepatocellular Carcinoma Recurrence. *Acta Biomater.* 100, 352–364. doi:10.1016/j.actbio.2019.09.034

Zhang, L., Yang, Z., Gong, T., Pan, R., Wang, H., Guo, Z., et al. (2020). Recent Advances in Emerging Janus Two-Dimensional Materials: from Fundamental Physics to Device Applications. *J. Mater. Chem. A.* 8, 8813–8830. doi:10.1039/d0ta01999b

Zhao, S., Duan, F., Liu, S., Wu, T., Shang, Y., Tian, R., et al. (2019). Efficient Intracellular Delivery of RNase A Using DNA Origami Carriers. *ACS Appl. Mater. Inter.* 11, 11112–11118. doi:10.1021/acsami.8b21724

Zhu, X., Tang, R., Wang, S., Chen, X., Hu, J., Lei, C., et al. (2020). Protein@Inorganic Nanodumpling System for High-Loading Protein Delivery with Activatable Fluorescence and Magnetic Resonance Bimodal Imaging Capabilities. *ACS nano* 14, 2172–2182. doi:10.1021/acsnano.9b09024

Conflict of Interest: The authors declare that the research was conducted in the absence of any commercial or financial relationships that could be construed as a potential conflict of interest.

Publisher's Note: All claims expressed in this article are solely those of the authors and do not necessarily represent those of their affiliated organizations, or those of the publisher, the editors and the reviewers. Any product that may be evaluated in this article, or claim that may be made by its manufacturer, is not guaranteed or endorsed by the publisher.

frontiers in Materials

REVIEW
published: 18 March 2022
doi: 10.3389/fmats.2022.857385

Research Advance in Manganese Nanoparticles in Cancer Diagnosis and Therapy

*Dengyun Nie[1], Yinxing Zhu[1], Ting Guo[2], Miao Yue[1] and Mei Lin[2,3]**

[1]Nanjing University of Chinese Medicine, Nanjing, China, [2]Clinical Laboratory of Taizhou People's Hospital Affiliated to Nanjing Medical University, Taizhou, China, [3]Clinical Laboratory, Taizhou People's Hospital Affiliated to Nanjing University of Chinese Medicine, Taizhou, China

As the second reason of causing death after cardiovascular disease for human being, cancer is damaging people all over the world. Fortunately, rapidly developing in the past decade, nanotechnology has become one of the most promising technologies for cancer theranostics. Recent studies have demonstrated that metal nanoparticles, especially manganese nanoparticles (Mn-NPs), exhibit amazing potential for application in multifarious oncology fields according to their characteristic fundamental properties. Although global scientists have developed a variety of new Mn-NPs and have proved their preponderance in cancer diagnosis and treatment, Mn-NPs are still not approved for clinical use. In this paper, the recent research progress of Mn-NPs in the fields of cancer diagnosis and therapy is reviewed. Besides, the future prospect and challenges of Mn-NPs are discussed to explore wider applications of Mn-NPs in clinic. Here, we hope that this review will show a better overall understanding of Mn-NPs and provide guidance for their design in clinical applications for cancer.

Keywords: cancer, diagnosis, therapy, manganese, nanoparticles

OPEN ACCESS

Edited by:
Jinbing Xie,
Southeast University, China

Reviewed by:
Eunsoo Yoo,
North Carolina Agricultural and Technical State University, United States
Xianglong Hu,
South China Normal University, China

****Correspondence:***
Mei Lin
l_mei@163.com

Specialty section:
This article was submitted to Biomaterials, a section of the journal Frontiers in Materials

Received: *18 January 2022*
Accepted: *04 March 2022*
Published: *18 March 2022*

Citation:
Nie D, Zhu Y, Guo T, Yue M and Lin M (2022) Research Advance in Manganese Nanoparticles in Cancer Diagnosis and Therapy. Front. Mater. 9:857385. doi: 10.3389/fmats.2022.857385

1 INTRODUCTION

Cancer, a morbid state caused by aberrant cell proliferation, is the second leading cause of death globally. Cancer caused almost ten million deaths in 2020 on the basis of data released by the World Health Organization (WHO), and unfortunately the incidence of cancer is still rising year by year (Siegel et al., 2021). Cancer is undoubtedly a major risk to the health and lives of people in the world. Molecular imaging technology has high veracity and dependability in elucidating biological processes and monitoring disease status, and particularly has important value in tumor detection and prognosis monitoring. The main types of cancer therapy include surgery, chemotherapy, radiotherapy, immunotherapy and so on. However, current imaging techniques have their own limitations of applications in clinical cases and traditional treatments are accompanied by diverse side effects. Therefore, it is desirable to develop a better medical strategy for diagnosis and treatments of cancer. In recent years, the rapid development of nanomedicine seems to be a promising option to overcome these challenges of cancer.

A series of nanoparticles (NPs) have been developed and increasingly entered the stage of clinical application (Kim et al., 2010; Baetke et al., 2015). Among them, manganese nanoparticles (Mn-NPs) show good biocompatibility and low side effects because manganese (Mn) is a basic building of cells and a cofactor for many metabolic enzymes (Felton et al., 2014). Thus, a considerable number of researches have been conducted, focusing on the development of Mn-NPs and their potential

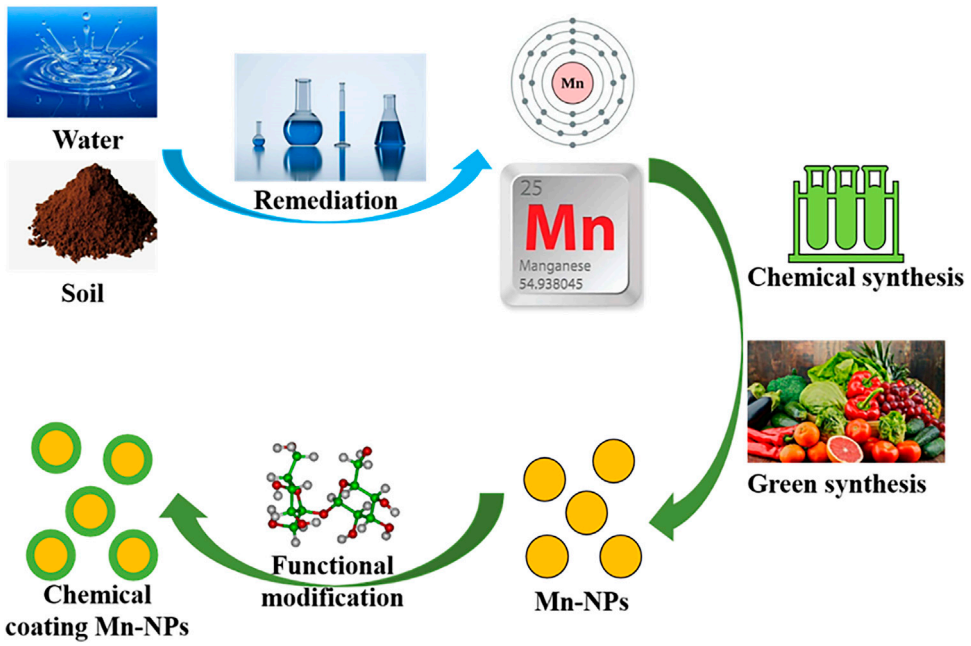

FIGURE 1 | Source and synthesis of Mn-NPs.

applications in multipurpose diagnosis and therapy of cancer. Herein, we provide a review of the studies that have been conducted on Mn-NPs over the past decade, describe the synthesis and surface functionalization of Mn-NPs as well as the use of Mn-NPs in cancer diagnosis and treatments in detail, and briefly discuss the possible molecular mechanisms underlying cancer.

2 CLASSIFICATION AND SYNTHESIS

Mn as the third most abundant transition metal on earth can be prepared into various Mn nanostructures through different nanotechnologies, such as NPs, nanorods, nanobelts, nanosheets, nanowires, nanotubes, nanofibers and other hierarchical structures. Thereinto, Mn-NPs are divided into two main categories: Mn oxide NPs and Mn-doped NPs, and their preparation methods are not universal due to their customization and complexity of configurations. Although a brief overview of the synthesis of MnO_2 NPs, which are the simplest Mn-NPs, will be described here for an instance, readers are encouraged to view other reviews to obtain detailed information about the synthesis of other kinds of Mn-NPs. A representative synthesis procedure of MnO_2 NPs is as follows: 60 ml of saturated argon aqueous solution containing 0.1 mM $KMnO_4$ in a glass container is irradiated in a water bath, and the temperature of the water bath is maintained at 20°C using a cold water circulation system. The container is installed in a constant position and closed from air during the irradiation (Abulizi et al., 2014). Besides, green synthesis of Mn-NPs has received great attention in recent years, which is a new evolved means from the nanobiotechnology and is the latest available method to manufacture Mn-NPs combining materialogy and biotechnology (**Figure 1**) (Hoseinpour and Ghaemi, 2018). Green synthesis of Mn-NPs using raw materials, vegetables and fruits, plant extracts, microorganisms and fungi has advantages of non-toxic, environmentally friendly, clean and low-cost, and it can be completed at room temperature and normal pressure (Singh et al., 2016; Ahmed et al., 2017). Using genetic engineering, molecular cloning, plant extracts and other biotechnologies to green synthesize Mn-NPs with controllable shape and size will be a major advancement in the nanobiotechnology, and how to achieve this achievement is also a huge challenge.

3 CHARACTERISTICS AND MODIFICATION

Mn shows efficient redox performance because it has different oxidation states, ranging from −3 to +7, and has ability to form compounds with a coordination number up to 7.5 (Haque et al., 2021), which led to the use of high oxidation-state Mn species as strong oxidants (Li and Yang, 2018). Mn is effective in improving the catalytic activity in several oxidation reactions. Mn^{2+} can trigger Fenton reaction that converts overexpressed endogenous hydrogen peroxide (H_2O_2) (100 μM~1 mM) (An et al., 2020) into highly toxic reactive oxygen species (ROS) in the acidic tumor microenvironment (TME) at pH 6.5~7.0 (Qian et al., 2019; Anderson and Simon, 2020). Also, Mn in the form of oxides possesses strong redox property and surface nanoarchitectures property. Therefore, Mn-NPs show oxidase-like features for their catalytic properties (Liu et al., 2012), and are widely used in cancer diagnosis and therapy. The activity of Mn-NPs is dependent on their size, morphology, surface area and redox functions (Haque et al.,

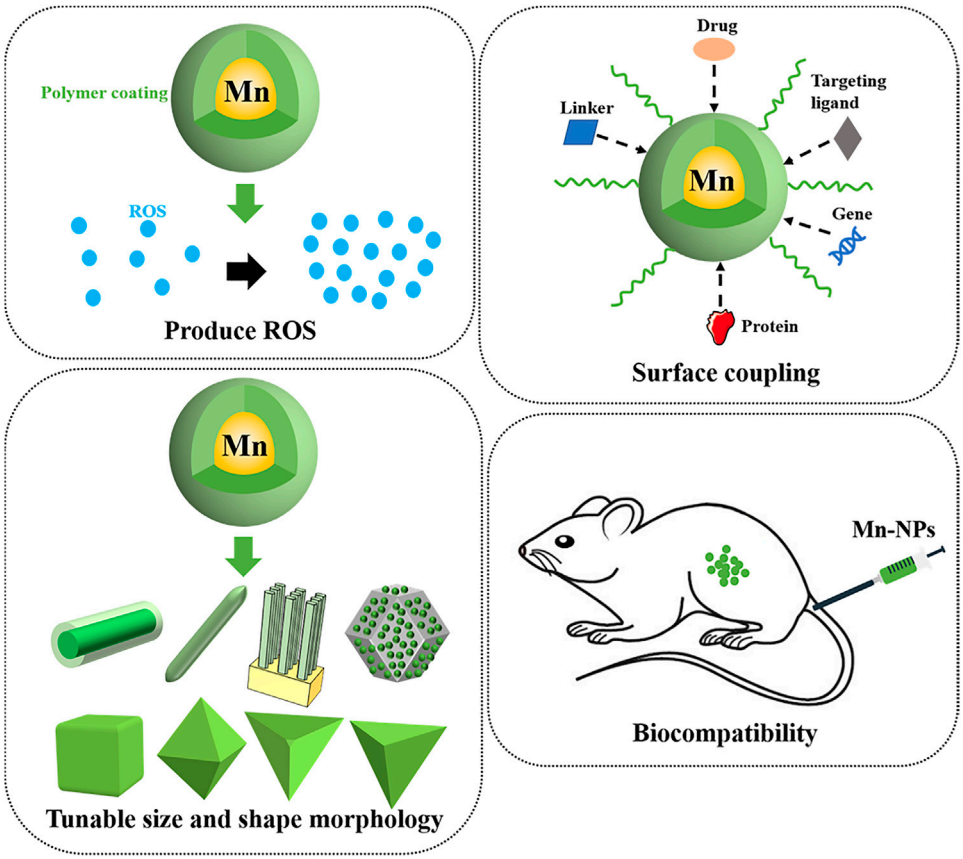

FIGURE 2 | Important properties of Mn-NPs.

2021). Mn-NPs with the diameter ≤100 nm generally exhibit great chemical and physical properties due to fundamental properties of their main part (Mn) and are being used in drug delivery studies owing to their large surface to volume ratio, which can increase the sensitivity to TME. In addition, Mn-NPs have advantages of good biocompatibility and environmental compatibility, high specific capacitance, strong adsorption property and so on.

The negative charge on the surface of Mn-NPs makes them easy to couple, which means that they can be functionalized easily by adding diversified biomolecules such as drugs, targeting ligands, protein, genes and more. Additionally, different kinds of coating provide surface chemistry that facilitates the integration of functional ligands (**Figure 2**). Surface chemical modification contributes to the versatility of Mn-NPs, such as combined treatment of multimodal imaging and chemotherapy-drug delivery (Xi et al., 2017; Yuan et al., 2019).

4 CYTOTOXICITY

Mn is non-toxic metal, so Mn-NPs are also less-toxic materials than other NPs-based compounds, such as various chalcogenides (Hoseinpour and Ghaemi, 2018). Razumov et al. tested toxicity of different kinds of Mn-NPs against glioblastoma U-87MG and U-251 cells and normal human cells and confirmed that Mn oxide NPs exhibited low cytotoxicity (Razumov et al., 2017). Furthermore, Mn-doped NPs also exhibited low cytotoxicity. Islam et al. examined the cytotoxicity of polysaccharide chitosan (CS)-coated Mn ferrite NPs ($MnFe_2O_4$-NPs) in HeLa cells cultured to a confluent state, and found that the cells' survival was 100% and 95% in the absence and presence of these NPs after 24 h incubation, respectively. Thus, no cytotoxic effect was visibly observed for $MnFe_2O_4$ NPs *in vitro* (Islam et al., 2020). However, Mn in the form of complexus still had certain weaknesses *in vivo* such as short blood circulation time and accumulation in the brain (Bellusci et al., 2014), leading to damage to the central nervous system followed by cognitive and movement abnormalities in a few animal models (Sárközi et al., 2009; Oszlánczi et al., 2010; Li et al., 2014; Haque et al., 2021). Bellusci et al. discovered complete clearance of $MnFe_2O_4$ NPs in the kidneys, spleen and brain of mice at day 7. Fortunately, there was no evidence of irreversible histopathological damage to any of the organs examined (Bellusci et al., 2014). Sarkozi et al. reported that rats were injected with a nanosuspension of MnO_2 with approximately 23 nm nominal particle diameter at doses of

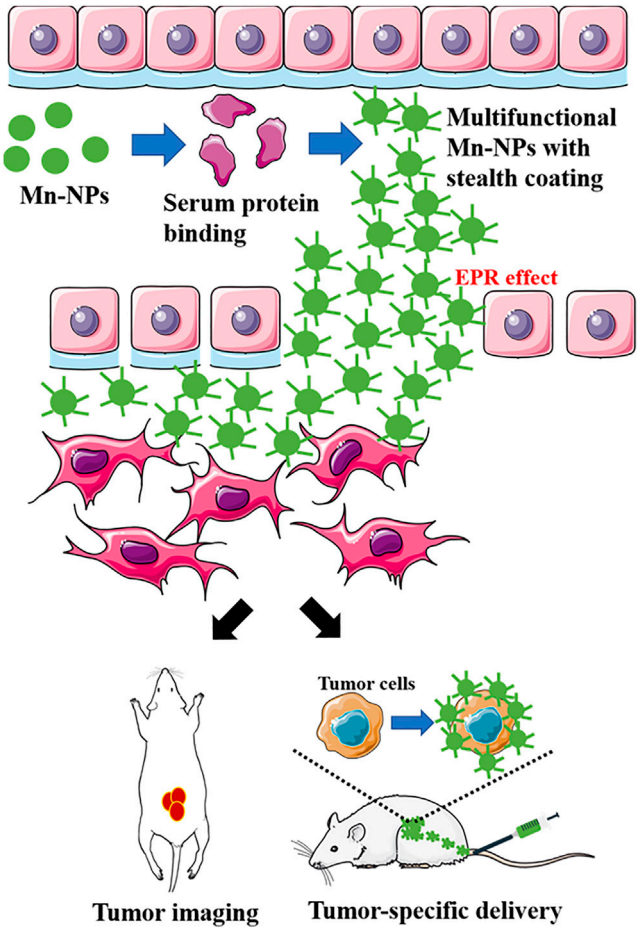

FIGURE 3 | Different approaches of Mn-NPs in cancer diagnosis and treatment.

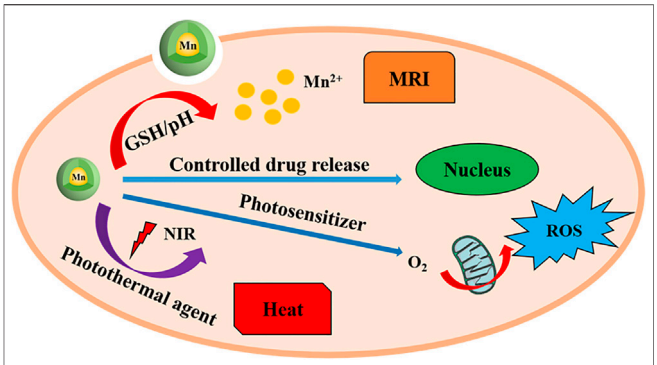

FIGURE 4 | The mechanism of Mn-NPs-based nanotheranostic agents for imaging guided chemotherapy/PDT/PTT and tumor MR imaging.

2.63 and 5.26 mg Mn/kg into the trachea for 3, 6 and 9 weeks. Mn could be examined in their lung and brain samples after treatment. In the open field activity, the proportion of walking and rearing decreased, while the proportion of local activity and inactivity increased. The evoked potential latency was prolonged, and the tail nerve conduction velocity was decreased. These results suggested that the Mn content of perfused NPs could enter the brain through the airway, causing nerve damage and reducing exercise capacity (Sárközi et al., 2009). The biocompatibility and non-toxic properties of Mn-NPs make them an all-right option for biomedical applications. Nevertheless, Mn-NPs have cytotoxicity properties against tumor cells (Al-Fahdawi et al., 2015), which is especially beneficial to their applications for cancer diagnosis and therapy.

5 DIFFERENT APPLICATIONS IN CANCER DIAGNOSIS AND THERAPY

Tumor tissue generally has a leaky vasculature, which allows Mn-NPs to accumulate at tumor site easily. This is referred to as the enhanced permeation and retention (EPR) effect of Mn-NPs. Incubation of polymeric Mn-NPs in plasma or serum could result in surface enrichment with multifunctional proteins. The targeting ligands of tumor specific biomarkers were conjugated on to Mn-NPs with the opsonization of serum protein to interact with receptors on the tumor cells, allowing for endocytosis and subsequent release of the drug (Moghimi and Szebeni, 2003). For instance, folic acid (FA) receptors are highly expressed on the surface of liver cancer cells and breast cancer cells (Law et al., 2020; Tao Gong et al., 2021), so the targeted uptake of tumor cells can be achieved by FA-modified Mn-NPs. Mn-NPs have been studied to be used for a great diversity of biomedical applications in cancer diagnosis and treatment based on their above properties (**Figure 3**), such as magnetic resonance imaging, positron emission tomography, chemotherapy, radiotherapy, all of which are discussed in the following subsections.

5.1 Diagnosis

The cancer has a recognizable latent or early asymptomatic stage. A large number of clinical practices have proved that the key to the prognosis of malignant tumors is whether early detection and diagnosis can be achieved so as to take corresponding treatment measures. A shorter interval between diagnoses may contribute to improve five-year survivals in five common cancers (Tørring et al., 2013). Various medical imaging techniques have played an important role in the early detection and diagnosis of cancer for their convenient and precise diagnostic capabilities at the systemic, molecular, and cellular levels, such as magnetic resonance imaging (MRI), positron emission tomography (PET), photoacoustic imaging (PAI) and fluorescence imaging (FI) (**Figure 4**) (Zanzonico, 2019). In this part, we make a detailed introduction of Mn-NPs as contrast agents (CAs) for above imaging techniques.

5.1.1 Magnetic Resonance Imaging

Magnetic resonance imaging (MRI) is a non-invasive detection technique based on the principle of nuclear spins, which is of great value in the clinical diagnosis of cancer. However, most contrast agents used in MRI are nonspecific and fast-excretory, and only can act extracellularly with localization imaging of

tumor cells (Fan et al., 2020). The logical design of theranostic nanoparticles shows synergistic turn-on of therapeutic potency and enhanced diagnostic imaging in response to TME (Hu et al., 2015). Mn was one of the earliest reported paramagnetic contrast materials for MRI based on its potent positive contrast enhancement. The increased accessibility of Mn centers to adjacent water molecules due to the porous architecture of Mn-NPs greatly enhances the contrast capacity of T1-weighted MRI, thus Mn-NPs appear to be a potential choice for MRI tool exploration. Among them, a variety of Mn oxide NPs, such as MnO, MnO_2, Mn_3O_4, and MnO_x NPs have been extensively researched as T1-weighted MRI CAs owing to the short cycle time of Mn^{2+} chelate and the size-controlled cycle time of colloidal NPs(Cai et al., 2019). The high loading content of Mn^{2+} chelate helps Mn-NPs exert a better effect in MRI (Liu et al., 2015). For instance, Yang et al. reported that Mn dioxide on silk fibroin NPs (SF@MnO_2-NPs) could significantly enhance water proton relaxation and improve MRI contrast (Yang et al., 2019).

In order to further improve imaging contrast sensitivity, various Mn-doped NPs as T1- or T2-MRI CAs have been developed (Zhao et al., 2018). Kuo et al. developed gadolinium-Mn-doped magnetism-engineered iron oxide NPs (Gd-MnMEIO-NPs) as a novel contrast agent with enhancement effects in both T1- and T2-weighted MRI of liver with high relaxivity r1 and r2 values. The average hydrodynamic size of Gd-MnMEIO-NPs was 20 nm, and the zeta potential was close to 0 mV, which could effectively avoid their removal from the reticuloendothelial system and prolong their residence time. Gd-MnMEIO-NPs could not only enhance normal liver and living tumor tissues but also improve the visualization of vascular trees. Haemodynamic information from dynamic contrast-enhanced T1-weighted MRI images using Gd-MnMEIO-NPs was helpful to diagnose liver tumors (Kuo et al., 2016).

Prussian blue (PB) as a clinically applied drug has drawn extensive attention in the theranostics of cancer, such as MRI (Dacarro et al., 2018), so PB NPs doped with Mn seemed to display a great performance in the CAs of MRI (Zhu et al., 2015). Then, diversiform multifunctional Mn-doped PB NPs were developed and researched universally, and they all had peculiar longitudinal nuclear MRI relaxivity values (Ali et al., 2018; Gao et al., 2020). Dumont et al. synthesized Mn-containing PB NPs (MnPB-NPs) as CAs for molecular MRI of pediatric brain tumors. The surfaces of these NPs were modified with biotinylated antibodies targeting neuron-glial antigen 2 or biotinylated transferrin which were protein markers overexpressed in pediatric brain tumors. These NPs showed great capacity in MRI quality of pediatric brain tumors *in vitro* (Dumont et al., 2014). These show that Mn-NPs have been widely applicated in the MRI of cancer.

5.1.2 Positron Emission Tomography Imaging

Positron emission tomography (PET) is a reversely progressive clinical imaging technology based on positrons released after decay of positron radionuclides (Fan et al., 2020), which is especially appropriate for early diagnosis of cancers (Tarkin et al., 2020). Combinations of different imaging modalities may be the great trend of future clinical diagnosis, because each of imaging technique has its own unique advantages and limitations in terms of spatial and temporal resolution, tissue penetration depth, detection sensitivity and veracity, and convenience and cost. In this regard, the integration of PET and MRI is developing rapidly and is currently in clinical trials for cancer detection and diagnosis owing to the extremely high sensitivity of PET and the ultra-high spatial resolution of MRI. Mn oxide NPs as a class of typical Mn-NPs, which seemingly have excellent potency as CAs of PET/MRI, are successfully developed and updated in recent years. Likewise, Zhan et al. reported that Mn_3O_4-NPs with conjugation to the anti-CD105 antibody TRC105 and radionuclide copper-64 (^{64}Cu-NOTA-Mn_3O_4@PEG-TRC105-NPs) had excellent specific targeting the vascular marker CD105, and were successfully used in PET/MRI of breast tumors *in vivo* (Zhan et al., 2017). Zhan et al. also synthesized copper-64 labeling of Mn_3O_4-NPs (^{64}Cu-NOTA-FA-FI-PEG-PEI-Ac-Mn_3O_4-NPs) and resoundingly put them into applications for PET/MRI of human cervical cancer xenografts which overexpress folate receptor in mice (Zhu et al., 2018). Otherwise, Shi et al. developed Mn ferrite NPs conjugated with integrin $\alpha_v\beta_3$ over-expressed targeting cyclic arginine-glycine-aspartic acid-peptide and labeled with positron radionuclide copper-64 (^{64}Cu-$MnFe_2O_4$-NPs-dopa-PEG-DOTA/RGD). *In vivo* PET/MRI of mice showed that these NPs could accurately image the tumor site with over expression of $\alpha_v\beta_3$ locally (Shi and Shen, 2018). All of these indicate Mn-NPs, particularly Mn oxide NPs, play a crucial part in PET/MRI, which is expanded for early detection and diagnosis of cancer.

5.1.3 Photoacoustic Imaging

Photoacoustic imaging (PAI) is a mixed imaging modality that merges optical illumination and ultrasound detection (Attia et al., 2019). The photothermal effect, which kills tumor cells, produces sound waves that can be detected and converted into imaging signals. This technique is capable of detecting changes of several biologically relevant signals in the TME, such as acidic pH, certain enzymes and ROS. Furthermore, PAI is useful to help the surgical removal of tumor because of its instant diagnostic functions. Photothermal transduction agents (PTAs) have a strong photothermal effect, which can harvest energy from light and convert it into heat, thereby increasing the temperature of the surrounding environment to 41~55°C and inducing tumor cells death, so PTAs can be used for PAI to build intrinsic theranostic platforms, in which imaging probes can clearly emerge the presence of tumors (Shah et al., 2008). PTAs are expected to only increase the temperature of TME locally to reduce damage to healthy tissues, where PTAs are absent or outside the range of laser irradiation.

A series of Mn oxide NPs have been widely and successfully used as PTAs due to their high absorption cross-section and strong redox property, such as Hu et al. developed a new smart nanoplatform based on degradable MnO_2-NPs (PBP@MnO_2-NPs) and a near-infrared (NIR) absorptive polymer conjugated with BODIPY molecules for dual-activatable tumor MRI/PAI. The designed smart probe had two PAI channels, in

which H_2O_2-/pH-sensitive MnO_2-NPs provide a clear PAI signal at 680 nm, and H_2O_2-/pH-inert polymer-NPs provide a bright PAI signal at 825 nm. PBP@MnO_2-NPs acted as a proportional agent with slight interference for PAI *in vivo*, and the Mn^{2+} ions released by PBP@MnO_2-NPs under TME could accurately reveal the location and size of the tumor by activated MRI (Hu et al., 2019). Beyond that, Rich et al. designed ultra-small $NaYF_4$:Nd^{3+}/$NaGdF_4$ nanocrystals coated with MnO_2 (MnO_2@ $NaYF_4$:Nd^{3+}/$NaGdF_4$-NPs) to treat head and neck squamous cell carcinomas (HNSCC), and the ability of which to increase the release of oxygen (O_2) in TME both *in vitro* and *in vivo* had been confirmed using MRI/PAI (Rich et al., 2020). Hence, these studies promise the discovery of Mn-NPs as theranostic PTAs for fast and accurate diagnosis of cancer.

5.1.4 Fluorescence Imaging

Fluorescence imaging (FI) is a common testing method in biology and medical experiments, especially broad adhibition of which in cancers. This means has superior value in accurate and early detection of tumor cells in clinical trials. Mn-NPs can selectively accumulate at the tumor site by functionalized modifications. Take advantage of this characteristic of Mn-NPs, some fluorescent dyes modifications of Mn-NPs can improve the molecular imaging of ultra-small tumor cells that cannot be detected by other imaging methods. However, the limited tissue penetration depth and autofluorescence limit its application in deep tissues (Leblond et al., 2010), thus combining MRI and FI can make up for the shortcomings of each individual pattern. MRI can provide a macroscopic boundary of the tumor for preoperative planning, while high-resolution FI can directly display the edge of the tumor during surgery, ensuring that the tumor is completely removed during surgery and normal tissue is preserved. For instance, Abbasi et al. developed polymeric theranostic NPs (PTNPs) containing a fluorescent dye (Myrj 59) and MnO-NPs for dual modal MRI/FI of breast cancer, and these NPs showed effective tumor accumulation and enhancement of MRI/FI signal in a mice xenograft orthotopic human breast tumor model (Abbasi et al., 2015). Banerjee et al. found that pyrrolidin-2-one (Pyrr)-capped Mn oxide NPs (MnO^{pyrr}-NPs) not only were qualified for Cas of MRI, but also had good photoluminescent property due to the modification of Pyrr during the thermal treatment (Banerjee et al., 2019). In the previous content, the application of SF@MnO2-NPs for MRI/FI was also reported (Yang et al., 2019). Beyond that, Mn-doped PB NPs showed excellent performance in MRI/FI of pediatric brain tumors *in vivo* (Dumont et al., 2014). We are convinced that the great potential of Mn-NPs in FI would be devoted to assist clinicians to conduct accurate and early detection of tumor cells.

5.1.5 X-Ray Imaging and X-Ray Computed Tomography Imaging

X-ray imaging is the most widely available, fastest and most cost-effective medical imaging technique today. X-ray computed tomography (CT) imaging, which is an upgraded version of X-ray imaging, has some advantages in cancer diagnosis, such as a high density and space distinguishable abilities (Pfeiffer et al., 2020). Mn-NPs have the relatively high atomic number and X-ray absorption coefficient, which makes for an X-ray contrast agent. For instance, Zhao et al. reported that Bi@mSiO_2@MnO_2/DOX-NPs could be used as excellent contrast agents for CT imaging of tumors with a high CT value (Zhao et al., 2021). Besides, Wang et al. found that multifunctional MnO_2-mSiO_2@Au-HA-NPs could simultaneously perform significant multispectral optoacoustic tomography (MSOT)/CT/MR imaging (Siyu Wang et al., 2019). Wang et al. developed MPDA-WS_2@MnO_2-NPs as trimodality contrast agents for MSOT/CT/MRI that could accomplish real-time guidance and monitoring during cancer treatment (Yidan Wang et al., 2019). It can be seen that the addition of MnO_2 into NPs will help expand their functions and enhance their applications in CT.

5.2 Therapy

The most traditional cancer therapies include chemotherapy, radiotherapy, and surgery, in which the patients may suffer from severe side effects and unsatisfied treatment outcomes. These treatment failures have inspired the development of more safe and effective treatment strategies for cancer. The emerging cancer therapies include but are not limited to photodynamic therapy (PDT), photothermal therapy (PTT), magnetic hyperthermia, immunotherapy, gene therapy (**Figure 5**), which have or may improve treatment outcomes (Liu et al., 2019a). Particularly, the simultaneous therapy of tumors by loading therapeutic drugs in Mn-NPs or combining certain clinical treatments has been widely studied and has been a hot area of current research.

5.2.1 Chemotherapy

Chemotherapy is a common treatment for cancer which makes use of chemical drugs. Traditional delivery of chemotherapeutic drugs involves oral or intravenous administration, which results in a systemic distribution of the drug, with only a small part of it reaching the tumor site. Consequently, these chemotherapeutic drugs are inevitably endocytosed by normal cells, causing serious side effects. Furthermore, chemotherapeutic drug resistance usually occurs owing to over-expression of drug efflux pumps, increased drug metabolism, and alteration of drug targets in tumor cells under constant drug stimulation. These imperfections of cancer chemotherapy are overcome by targeted drug delivery approaches, in which specific drugs or bioactive substances are released at a specific location in a controlled way (Singh et al., 2018). The fast development of nanomedicine offers great possibilities for targeted drug delivery. The ligands of tumor specific biomarkers such as monoclonal antibodies, aptamers, peptides, and vitamins all can be conjugated on to the surface of Mn-NPs containing chemotherapeutic drugs to realize targeted drug delivery. Then, these ligands interact with receptors on tumor cells, allowing endocytosis and subsequent release of the drug. Due to the small size of Mn-NPs, they can efficiently cross the capillaries to approach their target tumor cells. Mn-NPs have great biocompatibility, non-toxic nature and especially high loading capacity (Felton et al., 2014). According to these properties of Mn-NPs, they are considered as a potential drug delivery system which can be used in chemotherapy of cancer.

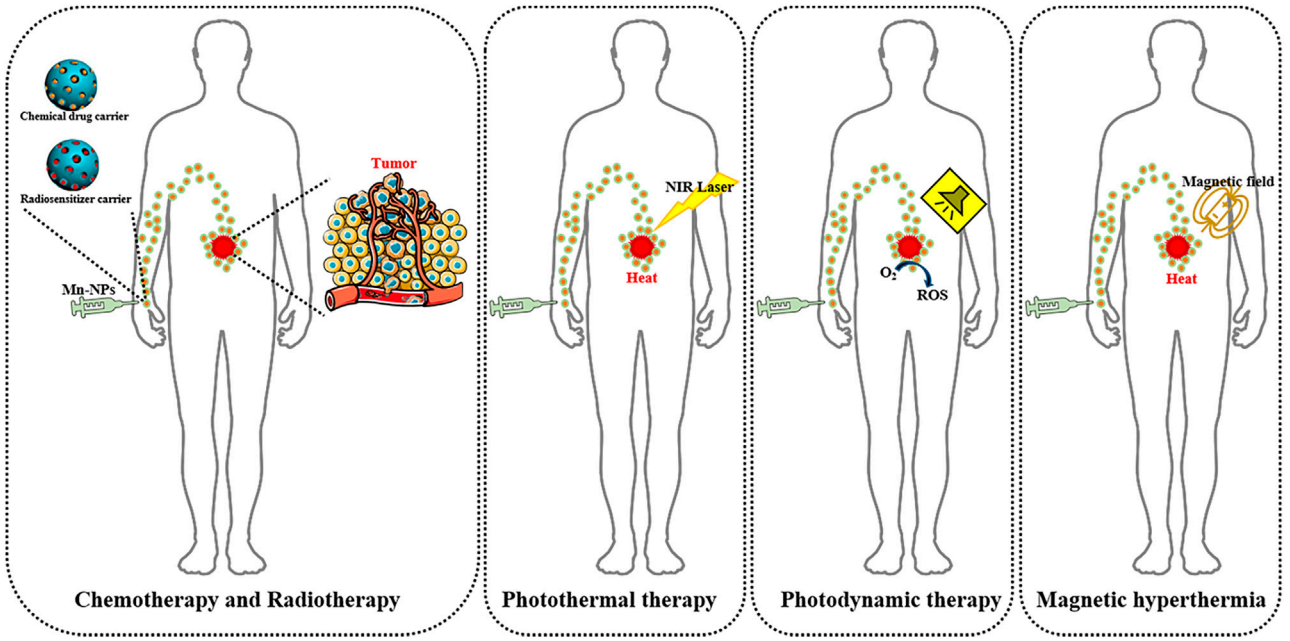

FIGURE 5 | Different approaches of Mn-NPs in cancer treatment.

Song et al. reported that high responsiveness of MnO_2-NPs to H_2O_2, which concurrently generated O_2 and regulated pH, could effectively alleviate tumor hypoxia and contribute to improve chemotherapy response in solid tumors. Additionally, hyaluronic acid (HA) modification was helpful to further enhance this ability of MnO_2-NPs. The HA-coated, mannan-conjugated MnO_2-NPs (Man-HA-MnO_2-NPs) treatment notably increased tumor oxygenation and down-regulated the expression of hypoxia-inducible factor-1α (HIF-1α) and vascular endothelial growth factor (VEGF) in breast tumor. Compared with single classical chemotherapeutic drug doxorubicin (DOX) treatment, Man-HA-MnO_2-NPs combined with DOX treatment of breast tumor observably increased the diffusion coefficient and inhibited tumor growth and tumor cell proliferation (Song et al., 2016). Yang et al. synthesized SF@MnO_2-NPs, which were co-loaded with a photodynamic agent indocyanine green (ICG) and DOX to produce a SF@MnO_2/ICG/DOX nanocomplex (SMID-NC). They demonstrated that SMID-NC could effectively accumulate in tumor-specific site via EPR effect using FI and MRI *in vivo*, and significantly improved tumor suppressive efficacy of chemotherapy with minimal systemic side effects (Yang et al., 2019).

In addition, Hou et al. reported that DOX could be enveloped in amorphous porous Mn phosphate NPs (PL/APMP-DOX). These NPs had remarkable antitumor efficacy in prolonging the lifetime of the tumor-bearing mice (Hou et al., 2020). Ren et al. described that DOX could be also packeted inside the lumen of hollow Mn/cobalt oxide NPs (MCO-DOX-NPs) and be fast released under the condition of increased glutathione (GSH) in acidic TME. MCO-DOX-NPs showed great inhibition effects in brain tumor growth both *in vitro* and *in vivo* (Ren et al., 2019). Another anticancer chemotherapeutic drug docetaxel (DTX) was co-loaded into PTNPs, and PTNPs exhibited high-efficiency drug loading, continuous and steady drug release, and higher cytotoxicity to human breast cancer cells than DTX alone *in vitro* (Abbasi et al., 2015). Moreover, Tang et al. discovered that Mn-doped silica NPs containing a special chemotherapeutic drug for liver cancer sorafenib (FaPEG-MnMSN@SFB-NPs) had efficient antitumor activity (Tang et al., 2020). These Mn-based targeted drug delivery systems provide evidence for the potential applications of Mn-NPs in cancer chemotherapy.

5.2.2 Radiotherapy

Radiotherapy (RT) is another frequently-used treatment for cancer, which depends on employing high-energy radiation to kill tumor cells. Radiosensitizers can efficiently increase the radiation dose at the cellular level, consequently improving the effect of RT. Mainstream radiosensitizers include alkylating agents that cause DNA damage, inhibitors that block DNA repair, and cell cycle synchronization agents that arrest tumor cells at the more radiosensitive G_2/M phase (Liuyun Gong et al., 2021). However, the efficient and specific delivery of these radiosensitizers, same as chemotherapeutic drugs, is also a challenge of RT. In addition, the hypoxic TME induces the radioresistance of tumors, which brings many troubles to clinicians.

Several research groups have demonstrated that inorganic NPs-based radiosensitizers are a promising choice for RT (Calugaru et al., 2015). Thereinto, Mn oxide NPs showed excellent potentials for their unique properties. They could function as not only a good radiosensitizer carrier, but also both a catalase and an oxidant that promoted decomposition of H_2O_2 into O_2 to convert the hypoxic TME, thus enhancing

RT efficacy (Siyu Wang et al., 2019). Let us cite, Meng et al. delivered the HIF-1 inhibitor acriflavine toward the tumor site to surmount hypoxia-induced radioresistance via a ROS responsive nanoplatform based on MnO_2-NPs, thus enhancing tumor oxidative repair of DNA damage and initiating O2-dependent HIF-1α degradation at the same time (Meng et al., 2018). In particular, Cho et al. discovered that MnO_2-NPs treatment had striking cytotoxic effects on non-small-cell lung cancer (NSCLC) cells and could achieve extra dose-dependent therapeutic effects (Cho et al., 2017). Besides, various functional modifications of Mn dioxide NPs contribute to optimize their aforesaid properties. Liu et al. also reported that acridine orange (AO), which can cause DNA damage under X-ray irradiation, was loaded onto MnO_2-NPs, making it a potential approach to enhance the efficacy of RT (Liu et al., 2020). Yao et al. fabricated a new kind of Bi_2Se_3-MnO_2 nanocomposites that were templated by bovine serum albumin (BSA) (Bi_2Se_3-MnO_2@BSA) via biomineralization. In this, MnO_2 as catalase could increase the O_2 concentration in TME via facilitating the decomposition of endogenous H_2O_2 in order to improve the hypoxia-induced radiation resistance of tumors (Yao et al., 2021). Tao et al. designed PEG-modified reduced nano-graphene oxide-Mn dioxide (rGO-MnO_2-PEG) nanocomposites, and used the radioisotope (^{131}I) to label these nanocomposites as radiosensitizers for *in vivo* tumor RT, ultimately obtaining significant tumor killing effects and further raising the therapeutic effects of RT (Tao et al., 2018). Shin et al. suggested that fucoidan-coated MnO_2-NPs (Fuco-MnO_2-NPs) might enhance the therapeutic effects of RT by dual targeting of tumor hypoxia and angiogenesis (Shin et al., 2018).

Meanwhile, numerous Mn-doped NPs also received elaborative studies. Bao et al. showed the whole process of a nanoscale metal-organic framework based on hafnium (Hf) cluster and Mn(III)-porphyrin ligand (fHMNM) development and production in details, and put them into use as a high-powered multifunctional theranostic agent of RT sequentially getting amazing therapeutic effect (Bao et al., 2020). Wang et al. demonstrated a nanoparticle-loaded block copolymer micellar system, based on HA-modified Mn-zinc ferrite magnetic NPs (MZF-HA-NPs), was able to be used for RT of NSCLC and played good performance in RT efficacy (Haimei Wang et al., 2020). Li et al. synthesized Au@MnS@ZnS NPs with PEG functionalization (Au@MnS@ZnS-PEG-NPs) and found that these NPs could enhance RT induced tumor cells killing efficiency (Li et al., 2016). These researches indicate that Mn-NPs have broad application prospect in the field of RT.

5.2.3 Photothermal Therapy

Photothermal therapy (PTT) is a novel cancer treatment technology that utilizes NPs to convert NIR light energy into thermal energy to ablate tumors (Zhi et al., 2020). Additionally, the PA cavitation can excite water to generate abundant ROS such as superoxide radical (O_2^-), which further spontaneously reacts with the *in situ* released NO to burst highly cytotoxic peroxynitrite ($ONOO^-$), resulting in promoting mitochondrial damage and DNA fragmentation to initiate programmed tumor cell death to treat cancer (Wang et al., 2021). This treatment technology has attracted much current attention owe to its remarkable advantages, such as non-traumatic, a short treatment time and high special spacetime control. In most cases, Mn-NPs as PTAs could be used for both PAI and PTT synchronously because of their powerful oxidizing property to establish expedient theranostic platform for monitoring and evaluating therapeutic effects. To illustrate, SMID-NC exerted a mighty and jarless photothermal effect with NIR irradiation for PTT owing to the distinct photothermal response of SF@MnO_2(Yang et al., 2019). Liu et al. prepared PEGylated amorphous MnO_2 coated polydopamine (PDA) core-shell NPs (PDA@MnO_2-PEG-NPs) with regular morphology and uniform dimensions for acid-sensitive MRI-guided tumor PTT (Liu et al., 2019b). Wen et al. showed that MnO_2-ICG@BSA had a strong singlet O_2-generation ability as well as high photothermal conversion efficiency and stability, especially possessed a significant inhibitory effect on the melanoma *in vitro* and *in vivo* (Wen et al., 2021).

PTT with the combination of other treatments is able to acquire great outcomes. Besides above, Wang et al. designed a gold with MnO_2 core-shell nanostructure (Au@MnO_2) as a GSH-triggered intelligent theranostic agent for dual-MRI/PAI-guided chemodynamic therapy (CDT) and PTT, and confirmed their excellent synergistic treatment effects in CDT/PTT (Yijue Wang et al., 2020). Soratijahromi et al. synthesized a gold with MnO_2 nanocomposite (Au/MnO_2-NC) as a new type photo- and sono-responsive nanomedicine that worked upon laser irradiation or ultrasound exposure for applications in PTT and sonodynamic therapy (SDT) of cancer (Soratijahromi et al., 2020). In addition, some Mn-doped NPs also had broad application prospects in PTT, such as Wu et al. discovered that magnetic-luminescent folic acid-conjugated NPs ($MnFe_2O_4$-$NaYF_4$ Janus-NPs) had a high cellular uptake efficiency in human esophageal carcinoma cells (Eca-109 cells) own to their upconversion luminescence properties and folate targeting potential. These NPs could strongly absorb light in the NIR range and fast convert to thermal energy, in order to remarkedly kill Eca-109 cells upon 808 nm laser irradiation. Furthermore, the growth of Eca-109 cells tumors in mice was availably restrained by the photothermal effects of $MnFe_2O_4$-$NaYF_4$ Janus-NPs(Wu et al., 2017). Zhang et al. developed a therapeutic nanoplatform based on Mn-doped iron oxide NPs that were modified denatured BSA (MnIO-dBSA-NPs). *In vitro* experiments showed great photothermal effects of MnIO-dBSA-NPs, and *in vivo* experiments further proved that these NPs could effectively ablate the tumor tissue achieved light irradiation (Zhang et al., 2015). Yang et al. also reported that graphene oxide (GO)/$MnFe_2O_4$-NPs had strong light absorption capacity and good photothermal stability in NIR region, and could give rise to the worthy photothermal ablation of cancer cells (Yang et al., 2016). These studies showed that Mn-NPs possessed enormous potential and application values in PTT of cancer.

5.2.4 Photodynamic Therapy

Photodynamic therapy (PDT) is a clinically approved cancer therapy that uses non-toxic dyes and harmless visible light in combination with O_2 to produce high level of ROS to kill tumor

cells (Castano et al., 2006). As we all known, the hypoxic TME is a challenge for cancer treatments. The obtained product of Mn oxide NPs could reactive with endogenous H_2O_2 in TME strongly, which was decomposed into O_2 to improve PDT of cancer (Yang et al., 2019). Liu et al. prepared the hybridized nanoplatform (R-MnO_2-FBP) by assembly of Rhodamine B (RhB)-encapsulated MnO_2 as O_2 supplier and indicator, and fluorescein isothiocyanate (FITC)-labelled peptide-functionalized black phosphorus as the theranostic agent. After specific delivery towards tumor cells, R-MnO_2-FBP decomposed in the acidic and H_2O_2-rich TME and produced O_2 to confront hypoxia-induced PDT resistance, in which released Mn^{2+} and RhB dye to realize dual-mode MRI/FI monitoring of O_2 self-supply process. Importantly, imaging-guided PDT using R-MnO_2-FBP showed 51.6% of apoptosis in hypoxic cells (Liu et al., 2019c). Yin et al. developed a H_2O_2-responsive nanozyme (AuNCs@mSiO_2@MnO_2) for off/on modulation and enhancement of MRI-guided PDT, in which MnO_2 nanosheets were wrapped as switch shielding shell. In a neutral physiological environment, the stable MnO_2 shell could eliminate the production of singlet O_2, thereby turning off MRI and PDT. Nevertheless, the reaction of MnO_2 shell with H_2O_2 could induce the degradation of MnO_2 to turn on MRI and PDT in the acidic TME, and the generated O_2 further enhanced PDT (Yin et al., 2021). Liang et al. developed the core-shell gold nanocage with MnO_2 NPs (AuNC@MnO_2-NPs) as TME responsive O_2 generators and NIR-triggered ROS producers for O_2-boosted immunogenic PDT against metastatic triple-negative breast cancer (Liang et al., 2018).

Similarly, PDT combined with other treatment methods can achieve better curative effect. The combination of PDT and enzyme therapy is a very suitable treatment for tumors because it exploits the dimensional control of PDT and efficient enzyme-catalyzed biological reactions. However, co-encapsulation of hydrophilic enzymes and hydrophobic photosensitizers is a challenge, because these two agents often interfere with each other. The development of Mn-doped NPs is expected to solve this problem. For example, Zhu et al. developed a protocell-like nanoreactor, in which hydrophilic glucose oxidase (GOx) was loaded in the pores of mesoporous silica NPs, and hydrophobic Mn phthalate (MnPc) was loaded in the membrane layer of liposomes middle, for synergistic starvation therapy and PDT. The spatial separation of these two payloads protected GOx and MnPc from the cellular environment and avoided mutual influence. GOx catalyzed the oxidation of glucose to generate H_2O_2 and gluconic acid, causing cancer cells to undergo starvation therapy by consuming glucose while disrupting cellular redox balance. MnPc could generate cytotoxic singlet O_2 under 730 nm laser irradiation to conduct PDT. A single treatment of GOx-MSN@MnPc-LP could effectively inhibit tumor growth, indicating a strong synergistic effect of starvation therapy and PDT, which was validated *in vitro* and vivo experiments (Zhu et al., 2020). Additionally, Irmania et al. synthesized Mn-doped green tea-derived carbon quantum dots (Mn-CQDs) as a targeted dual imaging and PDT nanoplatform, and *in vitro* cell viability studies verified Mn-CQDs upon 671 nm irradiation were able to kill more than 90% of tumor cells in PDT (Irmania et al., 2020). Atif et al. reported that Mn-doped cerium nanocomposites enhanced the antibacterial activity and effectiveness of PDT, which might be related to the maximal ROS generation from targeted toxicity and maximal antioxidant activity in bacterial growth inhibition (Atif et al., 2019). As can be seen, Mn-NPs might provide additional benefits to enhance PDT.

5.2.5 Magnetic Hyperthermia

Magnetic hyperthermia is a treatment technique that raises the temperature of a specific tissue above 46°C, which is pretty above the normal physiological temperature (36~37°C), to kill tumor cells under the controlled magnetic field (Farzin et al., 2020). Cancerous cells are more sensitized to hyperthermia compared to normal cells, due to the reducation of the pH at TME causing decreased thermotolerance. The implement of magnetic hyperthermia is inseparable from the use of magnetic NPs (MNPs) (Iacovita et al., 2019). Magnetite (Fe_3O_4) and maghemite (γ-F_2O_3) are the only category of MNPs approved for clinical use by the US Food and Drug Administration (Wilczewska et al., 2012). However, iron oxide MNPs have limited value in magnetic moments, causing the restrictive heating capacity. To figure out these difficulties, new kinds of MNPs have been persistently developed, aimed to obtain better magnetic properties.

Mn becomes a good option for this improvement approach of MNPs owing to its outstanding biocompatibility. For instances, Haghniaz et al. firstly reported that the dextran-coated lanthanum strontium MnO_3-NPs (Dex-LSMO-NPs) had strong ferromagnetism and low Curie temperature and were suitable for hyperthermia applications *in vivo* (Haghniaz et al., 2016). Other than that, CS-coated $MnFe_2O_4$ NPs also showed great magnetic properties, especially used in hyperthermia studies for biomedical research (Islam et al., 2020). MZF-HA-NPs were developed for synergistic therapy under alternating magnetic field and radiation field (Haimei Wang et al., 2020). We believe that MNPs will obtain better effectiveness and wider applications in diagnosis and treatment of cancer, with the further research in Mn coating.

5.2.7 Immunotherapy

Cancer immunotherapy has drawn much attention and achieved continued advancements especially for its safety and amazing prognosis (Yang et al., 2021). Yang et al. developed an intelligent biodegradable hollow Mn dioxide (H-MnO_2) nanoplatform that served for on-demand drug release and modulation of hypoxic TME to enhance cancer immunotherapy. H-MnO_2 nanoshells post modification with polyethylene glycol (PEG) were co-loaded with a photodynamic agent chlorine e6 (Ce6) and DOX (H-MnO_2-PEG/C&D-NPs). As a result, an arresting *in vivo* synergistic therapeutic effect was gained via the combined chemo-PDT, which also triggered a series of anti-tumor immune responses at the same time (Yang et al., 2017). Cyclic GMP-AMP synthase (cGAS) and stimulator of interferon genes (STING) are vital components of the innate immune sensors to cytosolic DNA. Mn was reported to comprehensively induce the activation of cGAS and STING from heightening cGAMP

TABLE 1 | Summary of the application of Mn-NPs in cancer diagnosis and therapy.

NPs	Size	Applications	Cell lines	Animal model	Ref
SMID-NC	60 nm	MRI, FI, chemotherapy, PTT, PDT	4T1 cells	Balb/c 4T1 tumor-bearing mice	Yang et al. (2019)
Gd-MnMEIO-NPs	12 nm	MRI	CT26 cells	Balb/c CT26 xenograft liver tumor mice	Kuo et al. (2016)
MnPB-NPs	33 nm	MRI, FI	brainstem glioma (BSG) D10 cells	Balb/c BSG D10 tumor-bearing mice	Dumont et al. (2014)
^{64}Cu-NOTA-Mn_3O_4@PEG-TRC105-NPs	7 nm	MRI, PET	4T1 cells, HEK-293 cells, HUH-7 cells, MCF-7 human breast cancer cells, human umbilical vein endothelial cells	Balb/c 4T1 tumor-bearing mice	Zhan et al. (2017)
^{64}Cu-NOTA-FA-FI-PEG-PEI-Ac-Mn_3O_4-NPs	7.29 nm	MRI, PET	HeLa cells	Nude HeLa tumor-bearing mice	Zhu et al. (2018)
^{64}Cu-$MnFe_2O_4$-NPs-dopa-PEG-DOTA/RGD	5 nm	MRI, PET	U87MG cells	Nude U87MG tumor-bearing mice	Shi and Shen, (2018)
PBP@MnO2-NPs	93 nm	MRI, PAI	4T1 cells	Xenograft 4T1 tumor mice	Hu et al. (2019)
MnO_2@ $NaYF_4$:Nd^{3+}/$NaGdF_4$-NPs	4.13 nm	MRI, PAI	None	SCID mice bearing tumor from a HNSCC patient-derived xenograft	Rich et al. (2020)
PTNPs	13 nm	MRI, FI, chemotherapy	MDAMB-231 cells	SCID breast tumor-bearing mice	Abbasi et al. (2015)
MnO^{pyrr}-NPs	8.1 nm	MRI, FI	HeLa cells, HepG2 cells	None	Banerjee et al. (2019)
Bi@$mSiO_2$@MnO_2/DOX-NPs	30 nm	MRI, CT, chemotherapy, PTT, CDT	human umbilical vein endothelial cells, HeLa cells	Nude HeLa tumor-bearing mice	Zhao et al. (2021)
MnO_2-$mSiO_2$@Au-HA-NPs	196.9 nm	MRI, CT, MSOT, RT, PTT	4T1 cells	Nude 4T1 tumor-bearing mice	Siyu Wang et al. (2019)
MPDA-WS_2@MnO_2-NPs	170 nm	MRI, CT, MSOT, RT	4T1 cells	Nude 4T1 tumor-bearing mice	Yidan Wang et al. (2019)
Man-HA-MnO_2-NPs	203 nm	Chemotherapy	4T1 cells	Balb/c 4T1 tumor-bearing mice	Song et al. (2016)
PL/APMP-DOX	3.88 nm	Chemotherapy	4T1 cells	Balb/c 4T1 tumor-bearing mice	Hou et al. (2020)
MCO-DOX-NPs	70 nm	MRI, chemotherapy	U87MG cells	Nude U87MG tumor-bearing mice	Ren et al. (2019)
FaPEG-MnMSN@SFB-NPs	101 nm	Chemotherapy	HepG2 cells	Nude HepG2 tumor-bearing mice	Tang et al. (2020)
MnO_2-NPs	30 nm	RT	CT26 cells, 4T1 cells	CT26 tumor-bearing mice, 4T1 tumor-bearing mice	Meng et al. (2018)
MnO_2-NPs	49.81 nm	RT	NSCLC cells	None	Cho et al. (2017)
MnO_2-NPs	155.5 nm	RT	H1299 cells	Nude H1299 xenograft tumor mice	Liu et al. (2020)
Bi_2Se_3-MnO_2@BSA	38 nm	RT	4T1 cells	Balb/c 4T1 tumor-bearing mice	Yao et al. (2021)
rGO-MnO_2-PEG	24 nm	RT	4T1 cells	Balb/c 4T1 tumor-bearing mice	Tao et al. (2018)
Fuco-MnO_2-NPs	17 nm	RT	human pancreatic cancer cell lines (AsPC-1 and BxPC-3)	Balb/c nude mice bearing BxPC3 xenograft tumors	Shin et al. (2018)
fHMNM	4 nm	MRI, PAI, CT, RT, PTT	Hela cells, 4T1 cells, MCF10A cells and S180 cells	Balb/c S180 tumor-bearing mice	Bao et al. (2020)
MZF-HA-NPs	150 nm	RT, magnetic hyperthermia	A549 cells, Beas-2B cells	Balb/c nude A549 tumor-bearing mice	Haimei Wang et al. (2020)
Au@MnS@ZnS-PEG-NPs	110 nm	MRI, RT	4T1 cells	Balb/c 4T1 tumor-bearing mice	Li et al. (2016)
PDA@MnO_2-PEG-NPs	120 nm	MRI, PTT	4T1 cells	Balb/c 4T1 tumor-bearing mice	Liu et al. (2019b)
MnO_2-ICG@BSA	44.67 nm	PTT, PDT	B16F10 cells	Nude B16F10 tumor-bearing mice	Wen et al. (2021)
Au@MnO_2	25 nm	MRI, PAI, PTT, CDT	4T1 cells	Balb/c 4T1 tumor-bearing mice	Yijue Wang et al. (2020)
Au/MnO_2-NC	2 μm	PTT, sonodynamic therapy	Mouse threatening melanoma cell line C540 (B16/F10)	Balb/c C540 tumor-bearing mice	Soratijahromi et al. (2020)
$MnFe_2O_4$-$NaYF_4$ Janus-NPs	13.1 nm	PTT	QSG-7701 cells, Eca-109 cells	Balb/c Eca-109 tumor-bearing mice	Wu et al. (2017)
MnIO-dBSA-NPs	5 nm	MRI, PTT	4T1 cells	Balb/c 4T1 tumor-bearing mice	Zhang et al. (2015)
GO/$MnFe_2O_4$-NPs	170 nm	MRI, chemotherapy, PTT	HeLa cells, L929 cells	Nude HeLa tumor-bearing mice	Yang et al. (2016)
R-MnO_2-FBP	120 nm	MRI, FI, PDT	HeLa cells	Nude HeLa tumor-bearing mice	Liu et al. (2019c)
AuNCs@$mSiO_2$@MnO_2	140 nm	MRI, PDT	MDA-MB-435 cells	Nude MDA-MB-435 tumor-bearing mice	Yin et al. (2021)

(Continued on following page)

TABLE 1 | (*Continued*) Summary of the application of Mn-NPs in cancer diagnosis and therapy.

NPs	Size	Applications	Cell lines	Animal model	Ref
AuNC@MnO_2-NPs	91 nm	MRI, PAI, FI, PDT	4T1 cells	Balb/c 4T1 tumor-bearing mice	Liang et al. (2018)
GOx-MSN@MnPc-LP	177 nm	PDT	4T1 cells	Balb/c 4T1 tumor-bearing mice	Zhu et al. (2020)
Mn-CQDs	5 nm	MRI, FI, PDT	HeLa cells	Nude HeLa tumor-bearing mice	Irmania et al. (2020)
Mn-doped ceria nanocomposite	27.2 nm	PDT	MCF-7 cells	None	Atif et al. (2019)
Dex-LSMO-NPs	25–50 nm	magnetic hyperthermia	B16F1 cells	C57BL/6J B16F1 tumor-bearing mice	Haghniaz et al. (2016)
H-MnO_2-PEG/C&D-NPs	3.94 nm	Chemotherapy, PDT, immunotherapy	4T1 cells	Balb/c 4T1 tumor-bearing mice	Yang et al. (2017)
DCMNs	78 nm	Chemotherapy, PDT, immunotherapy	HeLa cells, 4T1 cells	Balb/c 4T1 tumor-bearing mice	Geng et al. (2021)
Mn@CaCO3/ICG-NPs	107.5 nm	PDT, gene therapy	Lewis lung tumor cells	Balb/c Lewis lung tumor-bearing mice	Liu et al. (2019d)
HART nanoassembly	314 nm	MRI, chemotherapy, gene therapy	MCF7/ADR cells	None	Rajendrakumar et al. (2019)
MnO_2 nanosheets	6 nm	Chemotherapy, gene therapy	A549 cells, MDA-MB-231 cells	Nude MDA-MB-231 xenograft tumor mice	Nie et al. (2020)

production to strengthening cGAMP/STING binding affinity (Wang et al., 2018). Thus, DOX was enveloped in APMP-NPs to gain better synergetic antitumor effects through the activation of cGAS/STING pathway (Hou et al., 2020). A battery of antibodies targeting cellular immune checkpoints, such as PD-1/PD-L1 and CTLA-4, have been developed to promote the activation of T cells and succedent tumor treatment (Van Allen et al., 2015; McGranahan et al., 2016; Le et al., 2017). The rapid development of Mn-NPs is helpful for making use of these antibodies. Geng et al. synthesized Ce6 and DOX coating Mn-NPs (DCMNs) to increase antitumor responses of PD-1 via the combination of chemotherapy and PDT (Geng et al., 2021). The properties of Mn-NPs can greatly improve the efficacy of immunotherapy.

5.2.6 Gene Therapy

Gene therapy was first used genetic material to treat inherited diseases, but it was soon used in cancer treatment (Husain et al., 2015). One of the most important advances in gene therapy of cancer is the application of small interfering RNA (siRNA), which is able to regulate the expression of genes by RNA interference (RNAi). However, despite the potential and powerful functions of these molecules, several shortcomings make their clinical application difficult, including delivery problems, off-target effects, interference with physiological functions of cellular mechanisms involved in gene silencing, and induction of innate immune responses. The appearance of NPs systems provides an ideal opportunity to conquer these troubles (Miele et al., 2012; Zaimy et al., 2017).

Mn-NPs are an excellent gene delivery system which is able to efficiently package siRNA, avoiding its degradation along with serious immune response in the organisms (Bae et al., 2011). Liu et al. synthesized Mn@CaCO3/ICG-NPs loaded with PD-L1-targeting siRNA to enhance the effect of PDT while inhibiting tumor cell resistance/escape with the combination of PDT and immunotherapy. *In vivo* experiments showed that Mn@CaCO3/ICG-NPs could effectively deliver drugs to tumor tissues, significantly redress tumor hypoxia, and further enhance the therapeutic effect of PDT. Besides, the synergistic benefit of siRNA silenced PD-L1 gene that mediated immune resistance/evasion, bringing an amazing therapeutic effect by rousing the immune system (Liu et al., 2019d). Rajendrakumar et al. packaged DOX and antiapoptotic protein B-cell lymphma 2 (Bcl-2) shRNA encoded plasmid into Mn_3O_4 and Fe_3O_4 NPs (HART nanoassembly) with a green-synthesized method. The synergistic cytotoxic effect of Bcl-2 silencing and DOX was acquired by successfully transfecting these NPs into MCF7 multidrug-resistant breast cancer cells (Rajendrakumar et al., 2019).

The RNA-cleaving DNA zyme (DZ) has better prospects for RNAi applications than siRNA because of its higher chemical stability, biocompatibility, predictable activity, and substrate versatility. However, its pharmaceutical applications for disease treatment are confined by the need of metal cofactor for activation and the lack of reliable co-delivery systems in combination with other therapeutic manners. Nie et al. developed metal organic framework coated MnO_2 nanosheets to realize the co-delivery of a survivin inhibiting DZ and DOX for combined chemo-gene therapy in cancer (Nie et al., 2020). Thereout, Mn-NPs provide a good model for designing efficient, customizable nanocarriers for gene therapy of cancer.

Table 1 summarized the application of Mn-NPs in cancer diagnosis and therapy in details.

6 FUTURE PERSPECTIVE AND CHALLENGES

As we all known, cancer is a multi-system disease caused by numerous factors. Therefore, the combination of diagnosis and therapy modalities is significantly necessary for anti-cancer work. The use of multifunctional therapeutic agents in multimodal imaging and therapy is a promising strategy to overcome the limitations of single modality diagnosis and therapy, which can

effectively improve the accuracy of diagnosis and prognosis after treatment in affected cancer patients. As mentioned above, many multifunctional Mn-NPs were developed to realize the early imaging and dual even more trimodality therapy of cancer simultaneously (Xi et al., 2017; Siyu Wang et al., 2019; Yang et al., 2019).

The hypoxic TME as a major mechanism of resistance to tumor treatment may be the most severe difficulty in cancer therapy, which results in insignificant therapeutic effects and poor patient survivals (Siemer et al., 2020), and is urgent for researchers and clinicians to overcome it. Interestingly, Mn-NPs can exert anti-tumor effects through not only as a drug delivery system but also as an oxygenation agent according to past researches. When Mn-NPs are specifically distributed in tumor sites, the decomposition reaction of Mn-NPs promotes H_2O_2 into oxygen molecules, which can relieve tumor hypoxia (Meng et al., 2018). Moreover, Mn-NPs induced that disruption of redox balance would lead to apoptosis and ROS-dependent ferroptosis of tumor cells (Tang et al., 2020). Ferroptosis is a newly discovered form of cell death, which is different from apoptosis, autophagy and pyroptosis, and has unique morphological and biological metabolic changes in cells. Its mechanism is mainly characterized by the production of iron-dependent ROS: When too much ROS is produced and its antioxidant capacity is insufficient to fight it, ROS production and clearance are out of balance, leading to ferroptosis. In recent years, ferroptosis has become a research hotspot in the field of oncology (Liang et al., 2019). With the continuous attempts and applications of Mn-NPs in clinical practice, more and more studies believe that inducing the ferroptosis of tumor cells may become an effective tumor treatment.

Although the current researches on Mn-NPs for biomedical applications in cancer diagnosis and therapy have made great progress, there are still some problems that need to be alerted. Firstly, the large size of Mn-NPs has difficulty excreting from the kidney and causes accumulation in the visceral organ. Secondly, the nerve damage caused by Mn-NPs is not properly addressed. These two issues are still the biggest barriers to the inability of Mn-NPs to be used in the clinic. Thirdly, the diversity of cancer types and progression as well as the differences between affected cancer patients are hard for researchers and clinicians to make the right choice for functional modification of Mn-NPs, which require abundant efforts to resolve. Fortunately, numerous advanced computer simulation techniques can now predict the target and affinity of well-designed NPs, which can greatly reduce our workload for modifier selection of NPs including Mn-NPs. Considered the success of Mn-NPs for biological imaging and cancer treatment, we believe that Mn-NPs offer unique opportunities to translate the insights of basic research into clinical applications.

AUTHOR CONTRIBUTIONS

DN and YZ drafted the original manuscript; TG and MY contributed to writing the review; ML conceived and edited the manuscript, and was responsible for the overall direction of the paper.

FUNDING

This work was supported by the National Natural Science Foundation of China (81571797), the Social Development Plan of Taizhou, China (TS202004), the Natural Science Foundation of Nanjing University of Chinese Medicine China (XZR2020093), and Taizhou People's Hospital Medical Innovation Team Foundation, China (CXTDA201901).

ACKNOWLEDGMENTS

Special thanks to my fiancee Han Zhang, you gave me the enthusiasm for life and study. I sincerely hope to marry you soon and spend the rest of my life with you happily.

REFERENCES

Abbasi, A. Z., Prasad, P., Cai, P., He, C., Foltz, W. D., Amini, M. A., et al. (2015). Manganese Oxide and Docetaxel Co-loaded Fluorescent Polymer Nanoparticles for Dual Modal Imaging and Chemotherapy of Breast Cancer. *J. Controlled Release* 209, 186–196. doi:10.1016/j.jconrel.2015.04.020

Abulizi, A., Yang, G. H., Okitsu, K., and Zhu, J.-J. (2014). Synthesis of MnO2 Nanoparticles from Sonochemical Reduction of MnO4– in Water under Different pH Conditions. *Ultrason. Sonochem.* 21 (5), 1629–1634. doi:10.1016/j.ultsonch.2014.03.030

Ahmed, S., Annu, fnm., Chaudhry, S. A., and Ikram, S. (2017). A Review on Biogenic Synthesis of ZnO Nanoparticles Using Plant Extracts and Microbes: A prospect towards green Chemistry. *J. Photochem. Photobiol. B: Biol.* 166, 272–284. doi:10.1016/j.jphotobiol.2016.12.011

Al-Fahdawi, M. Q., Rasedee, A., Al-Qubaisi, M. S., Alhassan, F. H., Rosli, R., El Zowalaty, M. E., et al. (2015). Cytotoxicity and Physicochemical Characterization of Iron-Manganese-Doped Sulfated Zirconia Nanoparticles. *Int. J. Nanomedicine* 10, 5739–5750. doi:10.2147/IJN.S82586

Ali, L. M. A., Mathlouthi, E., Kajdan, M., Daurat, M., Long, J., Sidi-Boulenouar, R., et al. (2018). Multifunctional Manganese-Doped Prussian Blue Nanoparticles for Two-Photon Photothermal Therapy and Magnetic Resonance Imaging. *Photodiagnosis Photodynamic Ther.* 22, 65–69. doi:10.1016/j.pdpdt.2018.02.015

An, J., Hu, Y.-G., Cheng, K., Li, C., Hou, X.-L., Wang, G.-L., et al. (2020). ROS-augmented and Tumor-Microenvironment Responsive Biodegradable Nanoplatform for Enhancing Chemo-Sonodynamic Therapy. *Biomaterials* 234, 119761. doi:10.1016/j.biomaterials.2020.119761

Anderson, N. M., and Simon, M. C. (2020). The Tumor Microenvironment. *Curr. Biol.* 30 (16), R921–r925. doi:10.1016/j.cub.2020.06.081

Atif, M., Iqbal, S., Fakhar-E-Alam, M., Ismail, M., Mansoor, Q., Mughal, L., et al. (2019). Manganese-Doped Cerium Oxide Nanocomposite Induced Photodynamic Therapy in MCF-7 Cancer Cells and Antibacterial Activity. *Biomed. Res. Int.* 2019, 7156828. doi:10.1155/2019/7156828

Attia, A. B. E., Balasundaram, G., Moothanchery, M., Dinish, U. S., Bi, R., Ntziachristos, V., et al. (2019). A Review of Clinical Photoacoustic Imaging: Current and Future Trends. *Photoacoustics* 16, 100144. doi:10.1016/j.pacs.2019.100144

Bae, K. H., Lee, K., Kim, C., and Park, T. G. (2011). Surface Functionalized Hollow Manganese Oxide Nanoparticles for Cancer Targeted siRNA Delivery and

Magnetic Resonance Imaging. *Biomaterials* 32 (1), 176–184. doi:10.1016/j.biomaterials.2010.09.039

Baetke, S. C., Lammers, T., and Kiessling, F. (2015). Applications of Nanoparticles for Diagnosis and Therapy of Cancer. *Br. J. Radiol.* 88 (1054), 20150207. doi:10.1259/bjr.20150207

Banerjee, A., Bertolesi, G. E., Ling, C.-C., Blasiak, B., Purchase, A., Calderon, O., et al. (2019). Bifunctional Pyrrolidin-2-One Terminated Manganese Oxide Nanoparticles for Combined Magnetic Resonance and Fluorescence Imaging. *ACS Appl. Mater. Inter.* 11 (14), 13069–13078. doi:10.1021/acsami.8b21762

Bao, J., Zu, X., Wang, X., Li, J., Fan, D., Shi, Y., et al. (2020). Multifunctional Hf/Mn-TCPP Metal-Organic Framework Nanoparticles for Triple-Modality Imaging-Guided PTT/RT Synergistic Cancer Therapy. *Int. J. Nanomedicine* 15, 7687–7702. doi:10.2147/ijn.s267321

Bellusci, M., La Barbera, A., Padella, F., Mancuso, M., Pasquo, A., Grollino, M. G., et al. (2014). Biodistribution and Acute Toxicity of a Nanofluid Containing Manganese Iron Oxide Nanoparticles Produced by a Mechanochemical Process. *Int. J. Nanomedicine* 9, 1919–1929. doi:10.2147/IJN.S56394

Cai, X., Zhu, Q., Zeng, Y., Zeng, Q., Chen, X., and Zhan, Y. (2019). Manganese Oxide Nanoparticles as MRI Contrast Agents in Tumor Multimodal Imaging and Therapy. *Int. J. Nanomedicine* 14, 8321–8344. doi:10.2147/ijn.s218085

Calugaru, V., Magné, N., Hérault, J., Bonvalot, S., Le Tourneau, C., and Thariat, J. (2015). Nanoparticules et radiothérapie. *Bull. du Cancer* 102 (1), 83–91. doi:10.1016/j.bulcan.2014.10.002

Castano, A. P., Mroz, P., and Hamblin, M. R. (2006). Photodynamic Therapy and Anti-tumour Immunity. *Nat. Rev. Cancer* 6 (7), 535–545. doi:10.1038/nrc1894

Cho, M. H., Choi, E.-S., Kim, S., Goh, S.-H., and Choi, Y. (2017). Redox-Responsive Manganese Dioxide Nanoparticles for Enhanced MR Imaging and Radiotherapy of Lung Cancer. *Front. Chem.* 5, 109. doi:10.3389/fchem.2017.00109

Dacarro, G., Taglietti, A., and Pallavicini, P. (2018). Prussian Blue Nanoparticles as a Versatile Photothermal Tool. *Molecules* 23 (6), 1414. doi:10.3390/molecules23061414

Dumont, M. F., Yadavilli, S., Sze, R. W., Nazarian, J., and Fernandes, R. (2014). Manganese-containing Prussian Blue Nanoparticles for Imaging of Pediatric Brain Tumors. *Int. J. Nanomedicine* 9, 2581–2595. doi:10.2147/IJN.S63472

Fan, M., Han, Y., Gao, S., Yan, H., Cao, L., Li, Z., et al. (2020). Ultrasmall Gold Nanoparticles in Cancer Diagnosis and Therapy. *Theranostics* 10 (11), 4944–4957. doi:10.7150/thno.42471

Farzin, A., Etesami, S. A., Quint, J., Memic, A., and Tamayol, A. (2020). Magnetic Nanoparticles in Cancer Therapy and Diagnosis. *Adv. Healthc. Mater.* 9 (9), e1901058. doi:10.1002/adhm.201901058

Felton, C., Karmakar, A., Gartia, Y., Ramidi, P., Biris, A. S., and Ghosh, A. (2014). Magnetic Nanoparticles as Contrast Agents in Biomedical Imaging: Recent Advances in Iron- and Manganese-Based Magnetic Nanoparticles. *Drug Metab. Rev.* 46 (2), 142–154. doi:10.3109/03602532.2013.876429

Gao, X., Wang, Q., Cheng, C., Lin, S., Lin, T., Liu, C., et al. (2020). The Application of Prussian Blue Nanoparticles in Tumor Diagnosis and Treatment. *Sensors (Basel)* 20 (23), 6905. doi:10.3390/s20236905

Geng, Z., Chen, F., Wang, X., Wang, L., Pang, Y., and Liu, J. (2021). Combining Anti-PD-1 Antibodies with Mn2+-Drug Coordinated Multifunctional Nanoparticles for Enhanced Cancer Therapy. *Biomaterials* 275, 120897. doi:10.1016/j.biomaterials.2021.120897

Haghniaz, R., Umrani, R. D., and Paknikar, K. M. (2016). Hyperthermia Mediated by Dextran-Coated La0.7Sr0.3MnO3 Nanoparticles: *In Vivo* Studies. *Int. J. Nanomedicine* 11, 1779–1791. doi:10.2147/IJN.S104617

Haque, S., Tripathy, S., and Patra, C. R. (2021). Manganese-based Advanced Nanoparticles for Biomedical Applications: Future Opportunity and Challenges. *Nanoscale* 13 (39), 16405–16426. doi:10.1039/d1nr04964j

Haimei Wang, H., An, L., Tao, C., Ling, Z., Lin, J., Tian, Q., et al. (2020). A Smart Theranostic Platform for Photoacoustic and Magnetic Resonance Dual-Imaging-Guided Photothermal-Enhanced Chemodynamic Therapy. *Nanoscale* 12 (8), 5139–5150. doi:10.1039/c9nr10039c

Hoseinpour, V., and Ghaemi, N. (2018). Green Synthesis of Manganese Nanoparticles: Applications and Future Perspective-A Review. *J. Photochem. Photobiol. B: Biol.* 189, 234–243. doi:10.1016/j.jphotobiol.2018.10.022

Hou, L., Tian, C., Yan, Y., Zhang, L., Zhang, H., and Zhang, Z. (2020). Manganese-Based Nanoactivator Optimizes Cancer Immunotherapy via Enhancing Innate Immunity. *ACS Nano* 14 (4), 3927–3940. doi:10.1021/acsnano.9b06111

Hu, X., Liu, G., Li, Y., Wang, X., and Liu, S. (2015). Cell-penetrating Hyperbranched Polyprodrug Amphiphiles for Synergistic Reductive Milieu-Triggered Drug Release and Enhanced Magnetic Resonance Signals. *J. Am. Chem. Soc.* 137 (1), 362–368. doi:10.1021/ja5105848

Hu, X., Zhan, C., Tang, Y., Lu, F., Li, Y., Pei, F., et al. (2019). Intelligent Polymer-MnO2 Nanoparticles for Dual-Activatable Photoacoustic and Magnetic Resonance Bimodal Imaging in Living Mice. *Chem. Commun.* 55 (43), 6006–6009. doi:10.1039/c9cc02148e

Husain, S. R., Han, J., Au, P., Shannon, K., and Puri, R. K. (2015). Gene Therapy for Cancer: Regulatory Considerations for Approval. *Cancer Gene Ther.* 22 (12), 554–563. doi:10.1038/cgt.2015.58

Iacovita, C., Florea, A., Scorus, L., Pall, E., Dudric, R., Moldovan, A. I., et al. (2019). Hyperthermia, Cytotoxicity, and Cellular Uptake Properties of Manganese and Zinc Ferrite Magnetic Nanoparticles Synthesized by a Polyol-Mediated Process. *Nanomaterials (Basel)* 9 (10), 1489. doi:10.3390/nano9101489

Irmania, N., Dehvari, K., Gedda, G., Tseng, P. J., and Chang, J. Y. (2020). Manganese-doped green tea-derived Carbon Quantum Dots as a Targeted Dual Imaging and Photodynamic Therapy Platform. *J. Biomed. Mater. Res.* 108 (4), 1616–1625. doi:10.1002/jbm.b.34508

Islam, K., Haque, M., Kumar, A., Hoq, A., Hyder, F., and Hoque, S. M. (2020). Manganese Ferrite Nanoparticles (MnFe2O4): Size Dependence for Hyperthermia and Negative/Positive Contrast Enhancement in MRI. *Nanomaterials* 10 (11), 2297. doi:10.3390/nano10112297

Kim, B. Y. S., Rutka, J. T., and Chan, W. C. W. (2010). Nanomedicine. *N. Engl. J. Med.* 363 (25), 2434–2443. doi:10.1056/nejmra0912273

Kuo, Y.-T., Chen, C.-Y., Liu, G.-C., and Wang, Y.-M. (2016). Development of Bifunctional Gadolinium-Labeled Superparamagnetic Nanoparticles (Gd-MnMEIO) for *In Vivo* MR Imaging of the Liver in an Animal Model. *PloS one* 11 (2), e0148695. doi:10.1371/journal.pone.0148695

Law, S., Leung, A. W., and Xu, C. (2020). Folic Acid-Modified Celastrol Nanoparticles: Synthesis, Characterization, Anticancer Activity in 2D and 3D Breast Cancer Models. *Artif. Cell Nanomedicine, Biotechnol.* 48 (1), 542–559. doi:10.1080/21691401.2020.1725025

Le, D. T., Durham, J. N., Smith, K. N., Wang, H., Bartlett, B. R., Aulakh, L. K., et al. (2017). Mismatch Repair Deficiency Predicts Response of Solid Tumors to PD-1 Blockade. *Science* 357 (6349), 409–413. doi:10.1126/science.aan6733

Leblond, F., Davis, S. C., Valdés, P. A., and Pogue, B. W. (2010). Pre-clinical Whole-Body Fluorescence Imaging: Review of Instruments, Methods and Applications. *J. Photochem. Photobiol. B: Biol.* 98 (1), 77–94. doi:10.1016/j.jphotobiol.2009.11.007

Li, L., and Yang, X. (2018). The Essential Element Manganese, Oxidative Stress, and Metabolic Diseases: Links and Interactions. *Oxid Med. Cel Longev* 2018, 7580707. doi:10.1155/2018/7580707

Li, T., Shi, T., Li, X., Zeng, S., Yin, L., and Pu, Y. (2014). Effects of Nano-MnO2 on Dopaminergic Neurons and the Spatial Learning Capability of Rats. *Int. J. Environ. Res. Public Health.* 11 (8), 7918–7930. doi:10.3390/ijerph110807918

Li, M., Zhao, Q., Yi, X., Zhong, X., Song, G., Chai, Z., et al. (2016). Au@MnS@ZnS Core/Shell/Shell Nanoparticles for Magnetic Resonance Imaging and Enhanced Cancer Radiation Therapy. *ACS Appl. Mater. Inter.* 8 (15), 9557–9564. doi:10.1021/acsami.5b11588

Liang, R., Liu, L., He, H., Chen, Z., Han, Z., Luo, Z., et al. (2018). Oxygen-boosted Immunogenic Photodynamic Therapy with Gold Nanocages@manganese Dioxide to Inhibit Tumor Growth and Metastases. *Biomaterials* 177, 149–160. doi:10.1016/j.biomaterials.2018.05.051

Liang, C., Zhang, X., Yang, M., and Dong, X. (2019). Recent Progress in Ferroptosis Inducers for Cancer Therapy. *Adv. Mater.* 31 (51), e1904197. doi:10.1002/adma.201904197

Liu, X., Wang, Q., Zhao, H., Zhang, L., Su, Y., and Lv, Y. (2012). BSA-templated MnO2 Nanoparticles as Both Peroxidase and Oxidase Mimics. *Analyst* 137 (19), 4552–4558. doi:10.1039/c2an35700c

Liu, R., Jing, L., Peng, D., Li, Y., Tian, J., and Dai, Z. (2015). Manganese (II) Chelate Functionalized Copper Sulfide Nanoparticles for Efficient Magnetic Resonance/Photoacoustic Dual-Modal Imaging Guided Photothermal Therapy. *Theranostics* 5 (10), 1144–1153. doi:10.7150/thno.11754

Liu, Y., Bhattarai, P., Dai, Z., and Chen, X. (2019). Photothermal Therapy and Photoacoustic Imaging via Nanotheranostics in Fighting Cancer. *Chem. Soc. Rev.* 48 (7), 2053–2108. doi:10.1039/c8cs00618k

Liu, Y., Xu, J., Liu, L., Tan, J., Gao, L., Wang, J., et al. (2019). Amorphous Manganese Dioxide Coated Polydopamine Nanoparticles for Acid-Sensitive Magnetic Resonance Imaging-Guided Tumor Photothermal Therapy. *J. Biomed. Nanotechnol* 15 (8), 1771–1780. doi:10.1166/jbn.2019.2806

Liu, J., Du, P., Liu, T., Córdova Wong, B. J., Wang, W., Ju, H., et al. (2019). A Black Phosphorus/manganese Dioxide Nanoplatform: Oxygen Self-Supply Monitoring, Photodynamic Therapy Enhancement and Feedback. *Biomaterials* 192, 179–188. doi:10.1016/j.biomaterials.2018.10.018

Liu, Y., Pan, Y., Cao, W., Xia, F., Liu, B., Niu, J., et al. (2019). A Tumor Microenvironment Responsive Biodegradable CaCO3/MnO2- Based Nanoplatform for the Enhanced Photodynamic Therapy and Improved PD-L1 Immunotherapy. *Theranostics* 9 (23), 6867–6884. doi:10.7150/thno.37586

Liu, J., Zhang, W., Kumar, A., Rong, X., Yang, W., Chen, H., et al. (2020). Acridine Orange Encapsulated Mesoporous Manganese Dioxide Nanoparticles to Enhance Radiotherapy. *Bioconjug. Chem.* 31 (1), 82–92. doi:10.1021/acs.bioconjchem.9b00751

Liuyun Gong, L., Zhang, Y., Liu, C., Zhang, M., and Han, S. (2021). Application of Radiosensitizers in Cancer Radiotherapy. *Int. J. Nanomedicine* 16, 1083–1102. doi:10.2147/ijn.s290438

McGranahan, N., Furness, A. J. S., Rosenthal, R., Ramskov, S., Lyngaa, R., Saini, S. K., et al. (2016). Clonal Neoantigens Elicit T Cell Immunoreactivity and Sensitivity to Immune Checkpoint Blockade. *Science* 351 (6280), 1463–1469. doi:10.1126/science.aaf1490

Meng, L., Cheng, Y., Tong, X., Gan, S., Ding, Y., Zhang, Y., et al. (2018). Tumor Oxygenation and Hypoxia Inducible Factor-1 Functional Inhibition via a Reactive Oxygen Species Responsive Nanoplatform for Enhancing Radiation Therapy and Abscopal Effects. *ACS Nano* 12 (8), 8308–8322. doi:10.1021/acsnano.8b03590

Miele, E., Spinelli, G. P., Miele, E., Di Fabrizio, E., Ferretti, E., Tomao, S., et al. (2012). Nanoparticle-based Delivery of Small Interfering RNA: Challenges for Cancer Therapy. *Int. J. Nanomedicine* 7, 3637–3657. doi:10.2147/IJN.S23696

Moghimi, S. M., and Szebeni, J. (2003). Stealth Liposomes and Long Circulating Nanoparticles: Critical Issues in Pharmacokinetics, Opsonization and Protein-Binding Properties. *Prog. Lipid Res.* 42 (6), 463–478. doi:10.1016/s0163-7827(03)00033-x

Nie, Y., Li, D., Peng, Y., Wang, S., Hu, S., Liu, M., et al. (2020). Metal Organic Framework Coated MnO2 Nanosheets Delivering Doxorubicin and Self-Activated DNAzyme for Chemo-Gene Combinatorial Treatment of Cancer. *Int. J. Pharmaceutics* 585, 119513. doi:10.1016/j.ijpharm.2020.119513

Oszlánczi, G., Vezér, T., Sárközi, L., Horváth, E., Kónya, Z., and Papp, A. (2010). Functional Neurotoxicity of Mn-Containing Nanoparticles in Rats. *Ecotoxicol Environ. Saf.* 73 (8), 2004–2009. doi:10.1016/j.ecoenv.2010.09.002

Pfeiffer, D., Pfeiffer, F., and Rummeny, E. (2020). Advanced X-ray Imaging Technology. *Recent Results Cancer Res.* 216, 3–30. doi:10.1007/978-3-030-42618-7_1

Qian, X., Zhang, J., Gu, Z., and Chen, Y. (2019). Nanocatalysts-augmented Fenton Chemical Reaction for Nanocatalytic Tumor Therapy. *Biomaterials* 211, 1–13. doi:10.1016/j.biomaterials.2019.04.023

Rajendrakumar, S. K., Venu, A., Revuri, V., George Thomas, R., Thirunavukkarasu, G. K., Zhang, J., et al. (2019). Hyaluronan-Stabilized Redox-Sensitive Nanoassembly for Chemo-Gene Therapy and Dual T1/T2 MR Imaging in Drug-Resistant Breast Cancer Cells. *Mol. Pharmaceutics* 16 (5), 2226–2234. doi:10.1021/acs.molpharmaceut.9b00189

Razumov, I. A., Zav'yalov, E. L., Troitskii, S. Y., Romashchenko, A. V., Petrovskii, D. V., Kuper, K. E., et al. (2017). Selective Cytotoxicity of Manganese Nanoparticles against Human Glioblastoma Cells. *Bull. Exp. Biol. Med.* 163 (4), 561–565. doi:10.1007/s10517-017-3849-0

Ren, Q., Yang, K., Zou, R., Wan, Z., Shen, Z., Wu, G., et al. (2019). Biodegradable Hollow Manganese/cobalt Oxide Nanoparticles for Tumor Theranostics. *Nanoscale* 11 (47), 23021–23026. doi:10.1039/c9nr07725a

Rich, L. J., Damasco, J. A., Bulmahn, J. C., Kutscher, H. L., Prasad, P. N., and Seshadri, M. (2020). Photoacoustic and Magnetic Resonance Imaging of Hybrid Manganese Dioxide-Coated Ultra-small NaGdF4 Nanoparticles for Spatiotemporal Modulation of Hypoxia in Head and Neck Cancer. *Cancers* 12 (11), 3294. doi:10.3390/cancers12113294

Sárközi, L., Horváth, E., Kónya, Z., Kiricsi, I., Szalay, B., Vezér, T., et al. (2009). Subacute Intratracheal Exposure of Rats to Manganese Nanoparticles: Behavioral, Electrophysiological, and General Toxicological Effects. *Inhal Toxicol.* 21 (Suppl. 1), 83–91. doi:10.1080/08958370902939406

Shah, J., Park, S., Aglyamov, S., Larson, T., Ma, L., Sokolov, K., et al. (2008). Photoacoustic Imaging and Temperature Measurement for Photothermal Cancer Therapy. *J. Biomed. Opt.* 13 (3), 034024. doi:10.1117/1.2940362

Shi, X., and Shen, L. (2018). Integrin α V β 3 Receptor Targeting PET/MRI Dual-Modal Imaging Probe Based on the 64 Cu Labeled Manganese Ferrite Nanoparticles. *J. Inorg. Biochem.* 186, 257–263. doi:10.1016/j.jinorgbio.2018.06.004

Shin, S. W., Jung, W., Choi, C., Kim, S. Y., Son, A., Kim, H., et al. (2018). Fucoidan-Manganese Dioxide Nanoparticles Potentiate Radiation Therapy by Co-targeting Tumor Hypoxia and Angiogenesis. *Mar. Drugs* 16 (12). doi:10.3390/md16120510

Siegel, R. L., Miller, K. D., Fuchs, H. E., and Jemal, A. (2021). Cancer Statistics, 2021. *CA A. Cancer J. Clin.* 71 (1), 7–33. doi:10.3322/caac.21654

Siemer, S., Westmeier, D., Vallet, C., Becker, S., Voskuhl, J., Ding, G.-B., et al. (2020). Retraction of "Resistance to Nano-Based Antifungals Is Mediated by Biomolecule Coronas". *ACS Appl. Mater. Inter.* 12 (13), 15953. doi:10.1021/acsami.9b23592

Singh, P., Kim, Y.-J., Zhang, D., and Yang, D.-C. (2016). Biological Synthesis of Nanoparticles from Plants and Microorganisms. *Trends Biotechnol.* 34 (7), 588–599. doi:10.1016/j.tibtech.2016.02.006

Singh, P., Pandit, S., Mokkapati, V. R. S. S., Garg, A., Ravikumar, V., and Mijakovic, I. (2018). Gold Nanoparticles in Diagnostics and Therapeutics for Human Cancer. *Int. J. Mol. Sci.* 19 (7), 1979. doi:10.3390/ijms19071979

Song, M., Liu, T., Shi, C., Zhang, X., and Chen, X. (2016). Bioconjugated Manganese Dioxide Nanoparticles Enhance Chemotherapy Response by Priming Tumor-Associated Macrophages toward M1-like Phenotype and Attenuating Tumor Hypoxia. *ACS Nano* 10 (1), 633–647. doi:10.1021/acsnano.5b06779

Soratijahromi, E., Mohammadi, S., Dehdari Vais, R., Azarpira, N., and Sattarahmady, N. (2020). Photothermal/sonodynamic Therapy of Melanoma Tumor by a Gold/manganese Dioxide Nanocomposite: *In Vitro* and *In Vivo* Studies. *Photodiagnosis Photodynamic Ther.* 31, 101846. doi:10.1016/j.pdpdt.2020.101846

Siyu Wang, S., You, Q., Wang, J., Song, Y., Cheng, Y., Wang, Y., et al. (2019). MSOT/CT/MR Imaging-Guided and Hypoxia-Maneuvered Oxygen Self-Supply Radiotherapy Based on One-Pot MnO2-mSiO2@Au Nanoparticles. *Nanoscale* 11 (13), 6270–6284. doi:10.1039/c9nr00918c

Tang, H., Li, C., Zhang, Y., Zheng, H., Cheng, Y., Zhu, J., et al. (2020). Targeted Manganese Doped Silica Nano GSH-Cleaner for Treatment of Liver Cancer by Destroying the Intracellular Redox Homeostasis. *Theranostics* 10 (21), 9865–9887. doi:10.7150/thno.46771

Tao, Y., Zhu, L., Zhao, Y., Yi, X., Zhu, L., Ge, F., et al. (2018). Nano-graphene Oxide-Manganese Dioxide Nanocomposites for Overcoming Tumor Hypoxia and Enhancing Cancer Radioisotope Therapy. *Nanoscale* 10 (11), 5114–5123. doi:10.1039/c7nr08747k

Tao Gong, T., Wang, X., Ma, Q., Li, J., Li, M., Huang, Y., et al. (2021). Triformyl Cholic Acid and Folic Acid Functionalized Magnetic Graphene Oxide Nanocomposites: Multiple-Targeted Dual-Modal Synergistic Chemotherapy/photothermal Therapy for Liver Cancer. *J. Inorg. Biochem.* 223, 111558. doi:10.1016/j.jinorgbio.2021.111558

Tarkin, J. M., Ćorović, A., Wall, C., Gopalan, D., and Rudd, J. H. (2020). Positron Emission Tomography Imaging in Cardiovascular Disease. *Heart* 106 (22), 1712–1718. doi:10.1136/heartjnl-2019-315183

Tørring, M. L., Frydenberg, M., Hansen, R. P., Olesen, F., and Vedsted, P. (2013). Evidence of Increasing Mortality with Longer Diagnostic Intervals for Five Common Cancers: a Cohort Study in Primary Care. *Eur. J. Cancer* 49 (9), 2187–2198. doi:10.1016/j.ejca.2013.01.025

Van Allen, E. M., Miao, D., Schilling, B., Shukla, S. A., Blank, C., Zimmer, L., et al. (2015). Genomic Correlates of Response to CTLA-4 Blockade in Metastatic Melanoma. *Science* 350 (6257), 207–211. doi:10.1126/science.aad0095

Wang, C., Guan, Y., Lv, M., Zhang, R., Guo, Z., Wei, X., et al. (2018). Manganese Increases the Sensitivity of the cGAS-STING Pathway for Double-Stranded DNA and Is Required for the Host Defense against DNA Viruses. *Immunity* 48 (4), 675–687. e7. doi:10.1016/j.immuni.2018.03.017

Wang, Z., Zhan, M., Li, W., Chu, C., Xing, D., Lu, S., et al. (2021). Photoacoustic Cavitation-Ignited Reactive Oxygen Species to Amplify Peroxynitrite Burst by

Photosensitization-free Polymeric Nanocapsules. *Angew. Chem. Int. Ed.* 60 (9), 4720–4731. doi:10.1002/anie.202013301

Wen, L., Hyoju, R., Wang, P., Shi, L., Li, C., Li, M., et al. (2021). Hydrogen-Peroxide-Responsive Protein Biomimetic Nanoparticles for Photothermal-Photodynamic Combination Therapy of Melanoma. *Lasers Surg. Med.* 53 (3), 390–399. doi:10.1002/lsm.23292

Wilczewska, A. Z., Niemirowicz, K., Markiewicz, K. H., and Car, H. (2012). Nanoparticles as Drug Delivery Systems. *Pharmacol. Rep.* 64 (5), 1020–1037. doi:10.1016/s1734-1140(12)70901-5

Wu, Q., Lin, Y., Wo, F., Yuan, Y., Ouyang, Q., Song, J., et al. (2017). Novel Magnetic-Luminescent Janus Nanoparticles for Cell Labeling and Tumor Photothermal Therapy. *Small* 13 (39). doi:10.1002/smll.201701129

Xi, J., Da, L., Yang, C., Chen, R., Gao, l., Fan, L., et al. (2017). Mn2+-coordinated PDA@DOX/PLGA Nanoparticles as a Smart Theranostic Agent for Synergistic Chemo-Photothermal Tumor Therapy. *Int. J. Nanomedicine* 12, 3331–3345. doi:10.2147/ijn.s132270

Yang, Y., Shi, H., Wang, Y., Shi, B., Guo, L., Wu, D., et al. (2016). Graphene Oxide/manganese Ferrite Nanohybrids for Magnetic Resonance Imaging, Photothermal Therapy and Drug Delivery. *J. Biomater. Appl.* 30 (6), 810–822. doi:10.1177/0885328215601926

Yang, G., Xu, L., Chao, Y., Xu, J., Sun, X., Wu, Y., et al. (2017). Hollow MnO2 as a Tumor-Microenvironment-Responsive Biodegradable Nano-Platform for Combination Therapy Favoring Antitumor Immune Responses. *Nat. Commun.* 8 (1), 902. doi:10.1038/s41467-017-01050-0

Yang, R., Hou, M., Gao, Y., Lu, S., Zhang, L., Xu, Z., et al. (2019). Biomineralization-inspired Crystallization of Manganese Oxide on Silk Fibroin Nanoparticles for *In Vivo* MR/fluorescence Imaging-Assisted Tri-modal Therapy of Cancer. *Theranostics* 9 (21), 6314–6333. doi:10.7150/thno.36252

Yang, M., Li, J., Gu, P., and Fan, X. (2021). The Application of Nanoparticles in Cancer Immunotherapy: Targeting Tumor Microenvironment. *Bioactive Mater.* 6 (7), 1973–1987. doi:10.1016/j.bioactmat.2020.12.010

Yao, Y., Li, P., He, J., Wang, D., Hu, J., and Yang, X. (2021). Albumin-Templated Bi2Se3-MnO2 Nanocomposites with Promoted Catalase-like Activity for Enhanced Radiotherapy of Cancer. *ACS Appl. Mater. Inter.* 13 (24), 28650–28661. doi:10.1021/acsami.1c05669

Yin, Z., Ji, Q., Wu, D., Li, Z., Fan, M., Zhang, H., et al. (2021). H2O2-Responsive Gold Nanoclusters @ Mesoporous Silica @ Manganese Dioxide Nanozyme for "Off/On" Modulation and Enhancement of Magnetic Resonance Imaging and Photodynamic Therapy. *ACS Appl. Mater. Inter.* 13 (13), 14928–14937. doi:10.1021/acsami.1c00430

Yidan Wang, Y., Song, S., Lu, T., Cheng, Y., Song, Y., Wang, S., et al. (2019). Oxygen-supplementing Mesoporous Polydopamine Nanosponges with WS2 QDs-Embedded for CT/MSOT/MR Imaging and Thermoradiotherapy of Hypoxic Cancer. *Biomaterials* 220, 119405. doi:10.1016/j.biomaterials.2019.119405

Yijue Wang, Y., Zou, L., Qiang, Z., Jiang, J., Zhu, Z., and Ren, J. (2020). Enhancing Targeted Cancer Treatment by Combining Hyperthermia and Radiotherapy Using Mn-Zn Ferrite Magnetic Nanoparticles. *ACS Biomater. Sci. Eng.* 6 (6), 3550–3562. doi:10.1021/acsbiomaterials.0c00287

Yuan, X., Yin, Y., Zan, W., Sun, X., and Yang, Q. (2019). Hybrid Manganese Dioxide-Bovine Serum Albumin Nanostructure Incorporated with Doxorubicin and IR780 for Enhanced Breast Cancer Chemo-Photothermal Therapy. *Drug Deliv.* 26 (1), 1254–1264. doi:10.1080/10717544.2019.1693706

Zaimy, M. A., Saffarzadeh, N., Mohammadi, A., Pourghadamyari, H., Izadi, P., Sarli, A., et al. (2017). New Methods in the Diagnosis of Cancer and Gene Therapy of Cancer Based on Nanoparticles. *Cancer Gene Ther.* 24 (6), 233–243. doi:10.1038/cgt.2017.16

Zanzonico, P. B. (2019). Benefits and Risks in Medical Imaging. *Health Phys.* 116 (2), 135–137. doi:10.1097/hp.0000000000001038

Zhan, Y., Shi, S., Ehlerding, E. B., Graves, S. A., Goel, S., Engle, J. W., et al. (2017). Radiolabeled, Antibody-Conjugated Manganese Oxide Nanoparticles for Tumor Vasculature Targeted Positron Emission Tomography and Magnetic Resonance Imaging. *ACS Appl. Mater. Inter.* 9 (44), 38304–38312. doi:10.1021/acsami.7b12216

Zhang, M., Cao, Y., Wang, L., Ma, Y., Tu, X., and Zhang, Z. (2015). Manganese Doped Iron Oxide Theranostic Nanoparticles for Combined T1 Magnetic Resonance Imaging and Photothermal Therapy. *ACS Appl. Mater. Inter.* 7 (8), 4650–4658. doi:10.1021/am5080453

Zhao, Z., Zhou, Z., Bao, J., Wang, Z., Hu, J., Chi, X., et al. (2018). Octapod Iron Oxide Nanoparticles as High-Performance T_2 Contrast Agents for Magnetic Resonance Imaging. *Nat. Commun.* 4 (3), 2266. doi:10.1038/ncomms3266

Zhao, H., Wang, J., Li, X., Li, Y., Li, C., Wang, X., et al. (2021). A Biocompatible Theranostic Agent Based on Stable Bismuth Nanoparticles for X-ray Computed Tomography/magnetic Resonance Imaging-Guided Enhanced Chemo/photothermal/chemodynamic Therapy for Tumours. *J. Colloid Interf. Sci.* 604, 80–90. doi:10.1016/j.jcis.2021.06.174

Zhi, D., Yang, T., O'Hagan, J., Zhang, S., and Donnelly, R. F. (2020). Photothermal Therapy. *J. Controlled Release* 325, 52–71. doi:10.1016/j.jconrel.2020.06.032

Zhu, W., Liu, K., Sun, X., Wang, X., Li, Y., Cheng, L., et al. (2015). Mn2+-doped Prussian Blue Nanocubes for Bimodal Imaging and Photothermal Therapy with Enhanced Performance. *ACS Appl. Mater. Inter.* 7 (21), 11575–11582. doi:10.1021/acsami.5b02510

Zhu, J., Li, H., Xiong, Z., Shen, M., Conti, P. S., Shi, X., et al. (2018). Polyethyleneimine-Coated Manganese Oxide Nanoparticles for Targeted Tumor PET/MR Imaging. *ACS Appl. Mater. Inter.* 10 (41), 34954–34964. doi:10.1021/acsami.8b12355

Zhu, Y., Shi, H., Li, T., Yu, J., Guo, Z., Cheng, J., et al. (2020). A Dual Functional Nanoreactor for Synergistic Starvation and Photodynamic Therapy. *ACS Appl. Mater. Inter.* 12 (16), 18309–18318. doi:10.1021/acsami.0c01039

Conflict of Interest: The authors declare that the research was conducted in the absence of any commercial or financial relationships that could be construed as a potential conflict of interest.

Publisher's Note: All claims expressed in this article are solely those of the authors and do not necessarily represent those of their affiliated organizations, or those of the publisher, the editors and the reviewers. Any product that may be evaluated in this article, or claim that may be made by its manufacturer, is not guaranteed or endorsed by the publisher.

Advantages of publishing in Frontiers

OPEN ACCESS
Articles are free to read for greatest visibility and readership

FAST PUBLICATION
Around 90 days from submission to decision

HIGH QUALITY PEER-REVIEW
Rigorous, collaborative, and constructive peer-review

TRANSPARENT PEER-REVIEW
Editors and reviewers acknowledged by name on published articles

Frontiers
Avenue du Tribunal-Fédéral 34
1005 Lausanne | Switzerland

Visit us: www.frontiersin.org
Contact us: frontiersin.org/about/contact

REPRODUCIBILITY OF RESEARCH
Support open data and methods to enhance research reproducibility

DIGITAL PUBLISHING
Articles designed for optimal readership across devices

FOLLOW US
@frontiersin

IMPACT METRICS
Advanced article metrics track visibility across digital media

EXTENSIVE PROMOTION
Marketing and promotion of impactful research

LOOP RESEARCH NETWORK
Our network increases your article's readership